

Lecture Notes in Electrical Engineering

Volume 197

For further volumes:
<http://www.springer.com/series/7818>

Society of Automotive Engineers of China
(SAE-China) · International Federation of
Automotive Engineering Societies (FISITA)
Editors

Proceedings of the FISITA 2012 World Automotive Congress

Volume 9: Automotive Safety Technology



Editors

SAE-China
Beijing
People's Republic of China

FISITA
London
UK

ISSN 1876-1100

ISSN 1876-1119 (electronic)

ISBN 978-3-642-33804-5

ISBN 978-3-642-33805-2 (eBook)

DOI 10.1007/978-3-642-33805-2

Springer Heidelberg New York Dordrecht London

Library of Congress Control Number: 2012948289

© Springer-Verlag Berlin Heidelberg 2013

This work is subject to copyright. All rights are reserved by the Publisher, whether the whole or part of the material is concerned, specifically the rights of translation, reprinting, reuse of illustrations, recitation, broadcasting, reproduction on microfilms or in any other physical way, and transmission or information storage and retrieval, electronic adaptation, computer software, or by similar or dissimilar methodology now known or hereafter developed. Exempted from this legal reservation are brief excerpts in connection with reviews or scholarly analysis or material supplied specifically for the purpose of being entered and executed on a computer system, for exclusive use by the purchaser of the work. Duplication of this publication or parts thereof is permitted only under the provisions of the Copyright Law of the Publisher's location, in its current version, and permission for use must always be obtained from Springer. Permissions for use may be obtained through RightsLink at the Copyright Clearance Center. Violations are liable to prosecution under the respective Copyright Law.

The use of general descriptive names, registered names, trademarks, service marks, etc. in this publication does not imply, even in the absence of a specific statement, that such names are exempt from the relevant protective laws and regulations and therefore free for general use.

While the advice and information in this book are believed to be true and accurate at the date of publication, neither the authors nor the editors nor the publisher can accept any legal responsibility for any errors or omissions that may be made. The publisher makes no warranty, express or implied, with respect to the material contained herein.

Printed on acid-free paper

Springer is part of Springer Science+Business Media (www.springer.com)

Contents

Part I Automotive Structure Crashworthiness

The New ECE Regulation Brings Challenge on Commercial Vehicle	3
F2012-F01-001	
Lilin Zhou, Yanhui Wang, Shifei Wang, Wei Li and Shuli Zhao	
BIW Safety Performance Research Based on Vehicle Frontal Crash	13
F2012-F01-003	
Zhida Shen, Xin Qiao and Haishu Chen	
Development of an Impact Absorbing Component by Gimlet Form for any Crushes	27
F2012-F01-004	
Tauchi Hideki	
Study on the Spot-Weld Failure Prediction Model in Auto Crash Simulation	39
F2012-F01-005	
Xiao Feng	
Ultra High Strength Steel B Pillar Reinforcement Structure to Enhance Side Impact and Roof Crash as Reducing Weight.	53
F2012-F01-006	
Do Hoi Kim, Chan Young Kang, Jong Weon Seo, Jung Han Kim and Yong Bai Joo	
The Design of Car's Crash Box Based on the Section Force	73
F2012-F01-007	
Man Yang	

Vehicle Front Crash Design Accounting for Uncertainties	83
F2012-F01-009	
Markus Zimmermann	
The Initial Velocity Value of Coach in Frontal Impact Research	91
F2012-F01-010	
Zhaokai Li, Qiang Yu, Junjie Chen, Qiang Li, Guosheng Zhang and Xiao Yuan	
Study on Correlation Method of C-NCAP Full Frontal Impact	105
F2012-F01-026	
Feng Huang, Yongxing Chao and Weigang Chen	
Study on Vehicle Body Structure Deformation Modes in Frontal Crash	117
F2012-F01-028	
Huihong Liao, Weiguo Liu, Dayong Zhou, Chun Wang and Fuquan Zhao	
Part II Occupant and Child Safety Protection	
An Analysis on Optimization of Side Impact Performance for X Project Using Madymo	133
F2012-F02-003	
Lijuan Hu, Minhui Liu and Houjun Zhang	
Optimization Analysis of Chest Injury of a Dummy in a Vehicle Subjected to Side Collision	147
F2012-F02-004	
Yan Liu and Haishu Chen	
Ejection of Passengers in Bus Rollover Accidents	161
F2012-F02-005	
Matolcsy Mátyás	
Enhancement Vehicle's Occupant Safety by Using Vehicle Dynamics Control Systems in Vehicle-to-Barrier Offset Frontal Collision	179
F2012-F02-006	
Mustafa Elkady and Ahmed Elmarakbi	
Research on a New Airbag in the Seat Back of Vehicle	193
F2012-F02-013	
Zhi Wang, Huili Yu, Taisong Cui and Hui Zhao	

Study of the Sled Test Simulation for 40 % Offset Deformable Barrier Crash Test	201
F2012-F02-014	
Zhi Wang, Bi-na Dai and Hui Zhao	
Development of a Six-Year Old Digital Human Body Model for Vehicle Safety Analysis	207
F2012-F02-015	
Jesse Ruan, Stephen Rouhana and Saeed Barbat	
New Concept for Neck Injury Lessening System Development	223
F2012-F02-019	
SangDo Park, DongWoo Jeong, Hak Gyun Kim and Jin Young Nam	
Evaluation of the Testing Capabilities of the Q10 Prototype Dummy	237
F2012-F02-022	
Alejandro Longton, Marianne Hynd, Kees Waagmeester, Erik Salters and Serge Cirovic	
Improvement of the Child Injury Risk Curves for Road Accidents	247
F2012-F02-023	
Alejandro Longton, Philippe Lesire, Heiko Johannsen, Philippe Beillas, Anita Fiorentino and Alan Kirk	
Optimization of Passive Head Restraint for IIHS Low Speed Rear Impact	257
F2012-F02-026	
Dong Ming	
Optimization Study on Whiplash Injury Reduction in Rear Impact	269
F2012-F02-027	
Yuanbo Wang	
The Safety of Body Structure and Occupant Protection Research of Medium Bus Under Three Kinds of Frontal Impact Forms.	279
F2012-F02-038	
Zhaokai Li, Yuan Xiao, Wenyan Zhu and Hanxue Zhao	

Part III Pedestrian Protection

Development of a Parametric Vehicle Front Structure Model for Pedestrian Impact Simulations	295
F2012-F03-004	
Bingbing Nie, Jun Huang, Yong Xia, Qing Zhou, Bing Deng and Mark Neal	
Front Stop Lamps for a Safer Traffic	311
F2012-F03-006	
Ovidiu Antonescu	
Study on Headlamp with Spot Light	315
F2012-F03-007	
Byoungsuk Ahn, Youngsub Oh, Hootaeck Cho, Myunggug Bang and Sunkyoung Park	
Analysis of Pedestrian Kinematics and Injury Mechanism in Real World Accidents	325
F2012-F03-010	
Daisuke Murakami, Chinmoy Pal, Yoshiko Kawabe and Tomosaburo Okabe	
Development of an On-Board Pedestrian Detection System Using Monocular Camera for Driver Assistance Applications	341
F2012-F03-013	
Pongsathorn Raksincharoensak, Yuichi Sakai, Ikuko Shimizu, Masao Nagai, Dirk Ulbricht and Rolf Adomat	
Pedestrian Detection by Neuromorphic Visual Information Processing	351
F2012-F03-017	
Han Woo Joon, Kim Chulsoo and Han Il Song	
Development of an On-Board Crosswalk Detection for Pedestrian Protection Using a Monocular Camera	363
F2012-F03-019	
Yuichi Sakai, Pongsathorn Raksincharoensak, Ikuko Shimizu, Masao Nagai, Dirk Ulbricht and Rolf Adomat	

Part IV Crash Biomechanics

Development and Validation of a Finite Element Model of the Human Thoracic for Rib Fractures Prediction in Automobile Collisions	375
F2012-F04-001	
Zhihua Cai, Fengchong Lan, Jiqing Chen and Fuquan Zhao	

**Part V Crash Pre-judge Technology/Traffic Accident
Analysis and Reconstruction**

A Study on Injury Prediction Method and Influential Factors in Side Impact Crashes Using Accident Data	391
F2012-F05-003	
Hiroshi Kuniyuki	
Research on Vehicle Transportation Safety Risk Assessment and Control	407
F2012-F05-004	
Jie Yang and Xinpeng Tang	

Development of an Integrated Test Bed and Virtual Laboratory for Safety Performance Prediction in Active Safety Systems	417
F2012-F05-005	
Thomas Helmer, Thomas Kühbeck, Christian Gruber and Ronald Kates	

Finite Element Analysis of Cervical Spinal Nerve Tissue Tolerance to Whiplash Injury: A Preliminary Study	433
F2012-F05-006	
Chaoyang Chen, Bo Cheng, Chuanhua Huang, Binhu Jiang, Dawei Chen and Xin Tao	

A Rear View Camera Based Tailgate Warning System	449
F2012-F05-007	
Chong Sun, Guanglinx Ma, Manoj Dwivedi, Yi Zeng and Xubo Song	

Part VI Driving Action Perception and Safety Assistance System

On Electric Vehicle Alert for Detection and Emergency Response	463
F2012-F07-002	
Juan J. Garcia, Yannick Blecon and M. J. Dalmau	

On-Demand Driver Vigilance Enhancement Without Drowsiness Detection	477
F2012-F07-003	
Shane Chang	
Pre-Crash Performance of Collision Mitigation and Avoidance Systems: Results from the Assess Project	489
F2012-F07-006	
Andrés Aparicio, Sébastien Baurès, Jordi Bargalló, Carmen Rodarius, John Vissers, Oliver Bartels, Patrick Seiniger, Paul Lemmen, Thomas Unsel, Maminirina Ranovona, Tatsuhiro Okawa and Swen Schaub	
Optical Self Diagnostics for Camera Based Driver Assistance	507
F2012-F07-008	
HadjHamma Tadjine, Dehgani Anoushirvan, Dick Eugen and Karsten Schulze	
Object Detection and Classification Using a Rear In-Vehicle Fisheye Camera	519
F2012-F07-009	
HadjHamma Tadjine, Markus Hess and Schulze Karsten	
Abnormal Driving Behavior Detection Using a Linear Non-Gaussian Acyclic Model for Causal Discovery	529
F2012-F07-010	
Zujie Zhang, Yuta Inoue, Kazushi Ikeda, Tomohiro Shibata, Takashi Bandou and Takayuki Miyahara	
euroFOT: Field Operational Test and Impact Assessment of Advanced Driver Assistance Systems: Final Results	537
F2012-F07-012	
Mohamed Benmimoun, Andreas Pütz, Adrian Zlocki and Lutz Eckstein	
A New Risk Evaluation Index for Rear-End Collisions Considering Drivers' Risk Perception	549
F2012-F07-023	
Hui Zhang, ShaoBo Qiu, Hongjian Li and Bin Liu	
Study on the Highway Vehicle Collision Avoidance and Warning System	557
F2012-F07-025	
Yuncheng Wang, Xie Fei, Jianhua Wang and Xu Hao	

Effectiveness Assessment of Human–Machine Interface in Driver Assistance System	567
F2012-F07-027	
Bo Li, Weiguo Liu, Xiaolin Zhang, Zhijie Pan and Fuquan Zhao	
 Part VII Vehicle Controls on Handing and Stability	
Sliding Mode Control for All-Wheel Steering of Four-Axle Vehicle	577
F2012-F08-001	
Kaifeng Zheng and Sizhong Chen	
Vehicle Control via Real-Time Flow Modeling and Flow Manipulation	589
F2012-F08-003	
Hiroshi Tokutake, Taro Tsukada and Eiji Itakura	
Road Test for Interaction Between Differential Lock and Driving Control System	599
F2012-F08-005	
Jian Zhao, Bing Zhu, Jing Li, Jian Wu and Hui Lu	
Evaluation of the Effectiveness of Active Safety Systems in Vans with Respect to Real World Accident Analysis	609
F2012-F08-006	
Francisco Javier Páez Ayuso, Arturo Furones Crespo, Francisco Aparicio Izquierdo and Blanca Arenas Ramírez	
High Accuracy Yaw Rate Sensor for Preventive Safety System	619
F2012-F08-008	
Masamoto Kawaguchi, Naoki Fujimoto, Takashi Katsumata and Masaaki Tanaka	
The Exploration and Improvement of Steering Heavy for Heavy Dumper	631
F2012-F08-009	
Jian Chen	
Sidewise Adaptive Single-Track Vehicle Model for ESC	645
F2012-F08-012	
Zhenfu Chen, Georg Roll, Alfred Eckert and Peter Rieth	

Dynamic Stability Control Strategy Development for an In-Wheel Motorized Electric Vehicle	657
F2012-F08-013	
Jianwu Zhang, Yan-e Zhao, Xiqiang Guan and Tongli Lu	
A Study of Cornering Braking Control Strategy Based on Road Identification	669
F2012-F08-014	
Xiqiang Guan, Yao Li, Tengyue Ba and Jianwu Zhang	
Van Traffic Accident Analysis. A Holistic Approach	681
F2012-F08-015	
Blanca Arenas Ramírez, Javier Páez Ayuso, José M. Mira McWilliams, Felipe Jiménez Alonso, Arturo Furones Crespo and Francisco Aparicio Izquierdo	
Study on Rollover Prevention of Heavy-Duty Vehicles by Using Flywheel Energy Storage Systems	693
F2012-F08-016	
Suda Yoshihiro, Huh Junhoi, Aki Masahiko, Shihpin Lin, Ryoichi Takahata and Naomasa Mukaiide	
Part VIII Safety Standards and International Regulations	
Iso 26262 Impact on Development of Powertrain Control System	705
F2012-F09-003	
Hui Guo, Jiaxi Liu, Shitao Yu and Jun Li	
Analysis and Improvement for the Failure of Seat Belt Anchor of a Car Based on Simulation and Experiment	717
F2012-F09-004	
Yongsheng Li, Hong Peng, Bing Rong, Yongxin Men and Fuquan Zhao	
Passengers' Safety Evaluation Research Based on Vehicle with Freeway Guardrail Impact.	733
F2012-F09-005	
Hui Tang, Yongxin Men, Qingxiang Guo, Jianxun Liu and Fuquan Zhao	
Protection of Occupants for Survival Space as per ECE R29: A Study of Regulatory Requirements, New Proposals and Challenges of Implementation in Global Context	747
F2012-F09-008	
Mukesh Sharma	

Contents	xiii
Automotive Functional Safety Compliance Requirements with ISO 26262: HW Architectural Metrics with an Example	769
F2012-F09-009	
T. Chitra	
Part IX Other	
Research on Vehicle Transportation Safety Risk Assessment and Control	783
F2012-F10-002	
Jie Yang and Xinpeng Tang	
Reliability in Automotive Engineering by Fuzzy Rule-Based FMEA	793
F2012-F10-003	
László Pokorádi and Tímea Fülep	
Back Muscle Activity While Operating a Vehicle	801
F2012-F10-010	
Chaoyang Chen, Bo Cheng, Zhengguang Wang, Dawei Chen, Xin Tao and John M. Cavanaugh	
Development of Lightweight Front Side Member Through Hydroforming Technology	813
F2012-F10-017	
K. J. Sung, D. H. Kim, K. S. Kim and Y. K. Kim	

Part I

Automotive Structure Crashworthiness

The New ECE Regulation Brings Challenge on Commercial Vehicle

Lilin Zhou, Yanhui Wang, Shifei Wang, Wei Li and Shuli Zhao

Abstract *Research and/or Engineering Questions/Objective* 03 series of regulation No 29 of the Economic Commission for Europe of the United Nations (UN/ECE) entry into force on January, 2011. In this new regulation, most important is that it adds a new A-Pillars impact test and a modified roof strength test to evaluate the resistance of cab in rollover accident. *Methodology* Firstly, mechanism of commercial vehicle rollover accidents are analyzed in this paper and results show that A-Pillars, side sill, side and front door provide significant enhancements on impact. Then, working procedure verifies the contribution of structure modifications based on relative comparisons. Moreover, AHSS (Advanced High Strength Steel) is also discussed to increase the strength of the great weakness on current cab. *Results* All of the proposed methods are examined in FEM models and simulation results are confirmed to be satisfactory for giving enough survival space for occupant in frontal and roof impact tests. *Limitations of this study* Experimental validations will be included in scope of the next work. *What does the paper offer that is new in the field in comparison to other works of the author* This study has almost carried simultaneously with the discussion of new version R29 from 2010 to now. The achievement involves relevant approaches acting at crumple zones and the determination of transfer paths between point of concern for deformation and place of impacting. *Conclusion* The aim is to develop a new or refined quantification methodology for improving commercial vehicle safety, based on computational, experimental and hybrid analyses.

Keywords ECE R29 · Commercial vehicle cab · Rollover · Structure crashworthiness · CAE

F2012-F01-001

L. Zhou (✉) · Y. Wang · S. Wang · W. Li · S. Zhao
IAT Automobile Technology CO., LTD, Ningbo, China

1 Introduction

Reports from the OICA (The International Organization of Motor Vehicle Manufacturers) shows that, during the past 30 years, the count of traffic accidents in Europe increasing nearly for three times and an average of almost 40,000 persons lost their life in traffic accident per year, which means more than 100 deaths occur in one day. These are shocking, but the good news is that, the number of terrible traffic accidents seems to be tailing off: it falls by nearly one half of 30 years ago.

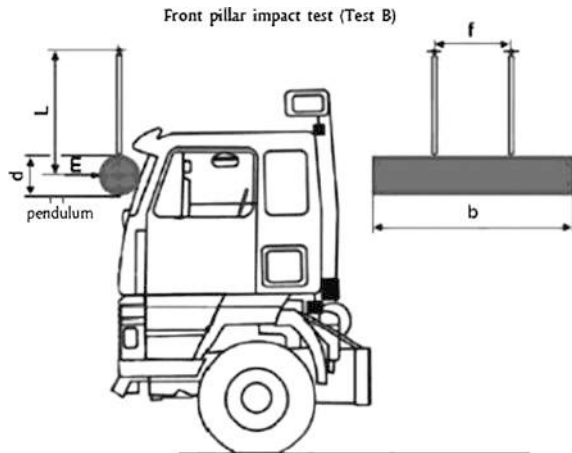
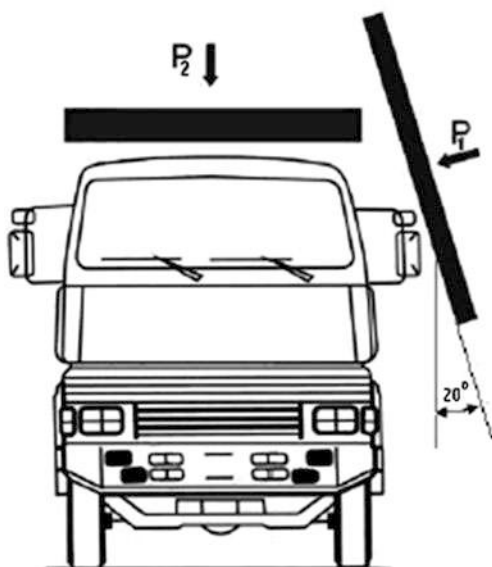
In U.S., the average percent of persons involved in accidents that matched the rollover query was 18 %. In China, approximately 15,000 people are killed each year in heavy trucks crashes, rollover or accidents(around 20 % of the overall fatalities) and three or four times as many are injured—directly costing around hundreds million RMB annually.

Rollovers are probably the most common truck accidents. In order to understand further in vehicle crashworthiness and occupant safety for rollovers, the body structure should be designed to absorb part of the crash energy by controlled plastic deformations, so that the driver and passenger compartment can give adequate space to the truck occupants.

2 New Policy Description

03 series of amendments, regulation No 29(UN/ECE) concerning the approval of vehicles with regard to the protection of the occupants of the cab of a commercial vehicle, which enter into force by the date of January 2011 [1]. In new regulation, most important is that it adds new Test B (90°rollover test) and optimizes the requirement of roof strength test C (180°rollover test).

- Test A is almost still the same to 02 series, the only difference is that the impact energy for N2 series ($GVW > 7.5\text{ T}$) and N3 series increase from 44 to 55 kJ (+25 %).
- The new Test B is an impact test to the A-Pillars of the cab intended to evaluate the resistance of a cab in a 90° rollover accident with subsequent impact. The total impact energy is 29.4 kJ, and the direction of impact shall be horizontal and shall be parallel to the median longitudinal plane of the vehicle.
- The improved Test C means a cab roof strength test intended to evaluate the resistance of a cab in a 180° rollover accident. It concludes two cases: on step P1, the striking face of the impactor is at an angle of 20° to the median longitudinal plane of the cab, impact energy should be no less than 17.6 kJ; the step P2 is equal to the old ECE R29 02 series, a normal roof strength test (Figs. 1 and 2).

Fig. 1 Test B**Fig. 2** Test C**Roof strength test (Test C)****Compelling**

Old UN/ECE R29 (R29.02)

- Applies to all N vehicles (N1 + N2 + N3)
- Two mandatory tests: frontal impact test, roof strength test
- One optional test: rear wall test

Current UN/ECE R29 (R29.03)

Fig. 3 90° rollover accident



Fig. 4 180° rollover accident



- All N vehicles (N1 + N2 + N3): Test-A (frontal impact), Test-C:only P2 (roof strength test)
- For N2(GVW > 7.5T) + N3 add new: Test-B (90°rollover), Test-C:P1 + P2(180° rollover)
- Delete: rear wall test

3 Research

Rollover crashes involve vehicles that leave the travel lane and encroach onto the shoulder and hit one or more of any number of natural or artificial objects. Unfortunately, roadside crashes account for far too great a portion of the total fatal highway crashes. So, presents 90 and 180°rollover test, with truck subsequently impacting an obstacle (trees, pillars, poles, safety barriers ...) [2]. See in Figs. 3 and 4.

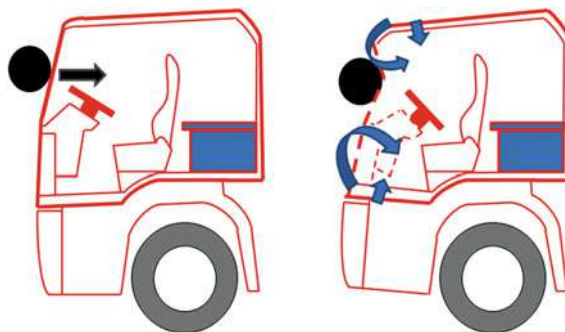


Fig. 5 Cab's deformation in 90° rollover accident

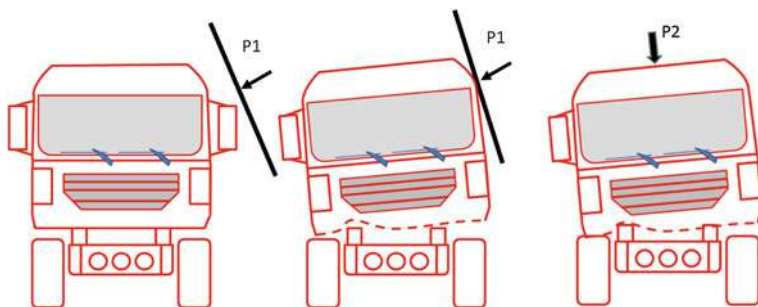


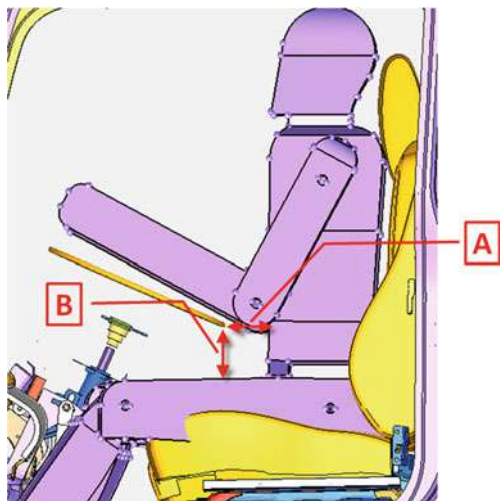
Fig. 6 Cab deformation in 180° rollover accident

In Test B, pendulum hit the cab in horizontal direction on the middle line of windscreens, A-Pillars are general not strong enough to hold the crash energy, soon rush into the passenger compartment. Then roof and floor will follow the front, part of the crash kinetic energy is absorbed by the plastic deformations, in mixed axial and several place's bending mode. The lower structure of front cab is tilting around the y-axis, intrusion of dash panel cause IP and steering wheel going down towards driver's seat, which resulted in smaller survival space for driver's upper leg and lower leg (Fig. 5).

In test C, the pendulum firstly strikes at the side of cab, then P2 load (which corresponds to the maximum mass authorized for the front axle or axles of the vehicle, subject to a maximum of 98 kN) is added on the roof, after two load-steps apply on the cab, over which the energy of the impactor is applied into the roof, side, and especially in floor. Total structure of cab is almost rotating around the x-axis, the main deformation of passenger side floor panel, which produces upward movement on passenger's ankle and leg (Fig. 6).

The outcome for the occupant's survival space is always dependant on the actual energy absorbed by the cabin structure. Even if the total energy of rollover generally is high, but designing for a suitable structure which can manage the crash

Fig. 7 Distance between chest/leg and STG



energy absorption well, like a design process with the capability of dealing the various transfer functions of dash panel, side, roof, and floor energy-absorbing systems deform upon direct impact [3, 4].

4 Principle

In addition, the cab should catch a suitable deformation that satisfies the following requirements for occupant:

1. Front structure with crumple zones absorbs the crash energy, different with passenger vehicle. In the most common commercial vehicle considerations of styling and layout, there gives no much more deformation space causing by frontal collisions, it present the first challenging task to the engineer [5]. In layout works of vehicle, take account of the distance between front zones to occupant compartment, especially the STG (A, B, C and D) system [6]. See in Figs. 7 and 8.
2. Bending deformation mode is an energy absorption process, deformed sharp of a 90° rollover model as shows on Fig. 5, the joints of A-pillar-to-Roof, Hinge-Pillar-to-Rocker, B-Pillar-to-Rocker provided plastic deformation on frontal collisions. Much of the crash energy is absorbed by these parts; the structure should be sufficiently stiff. AHSS (Advanced High Strength Steel) applied in vehicle structure would be an approach to meet all previously requirements. But lower cost cab is appreciated in designs, so it presents the second challenging task to engineer.
3. Properly designed upper side and roof structure (E, F and G) to minimize frontal intrusion. Roof deformation is excessive in rollover, but in Test B, if we

Fig. 8 Distance between leg and steering column

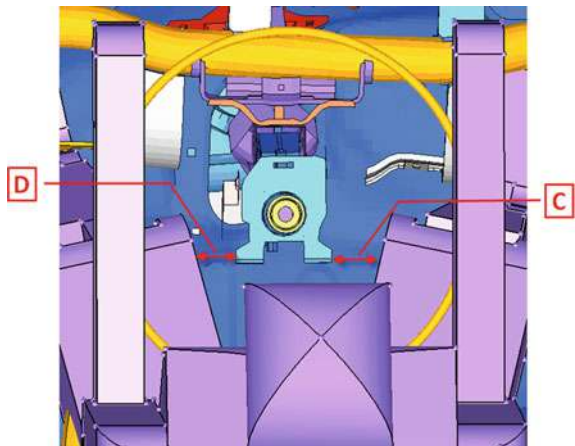
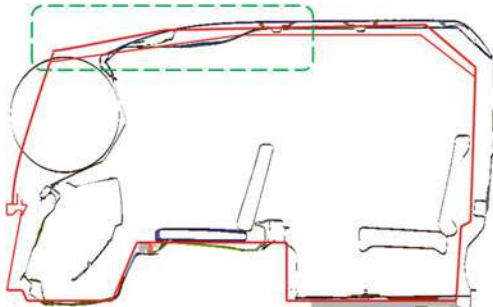


Fig. 9 Roof deformation



could increase the upper corner deformation properly, it can save more space for the occupant in cab. See in Figs. 9 and 10. Comparison on roof deformation in Test B impact, some specific holes or crumple zones could be added on A pillar, B pillar and upper side, and all of these modifications should be validated by other structural performance calculation and test. This is the third challenging task to design.

4. Strong door structure for rollover protection. It can supply additional support from A-Pillar to B-Pillar, lower part of the door must be rigid enough to decrease bending deformation and lower part of the B-Pillar also should be rigid to support the door and then the A-Pillar. So, possible solutions of the reinforced plate are to be applied to optimize the load transmission and to avoid the bending deformation. Light weight is the forth question engineer will face (Figs. 11 and 12).

Fig. 10 Crumple zones add on the cab

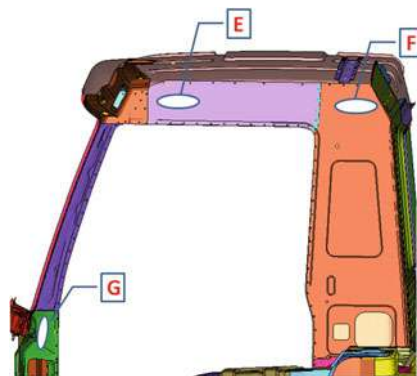


Fig. 11 Strong door structure



Fig. 12 Increase section dimension

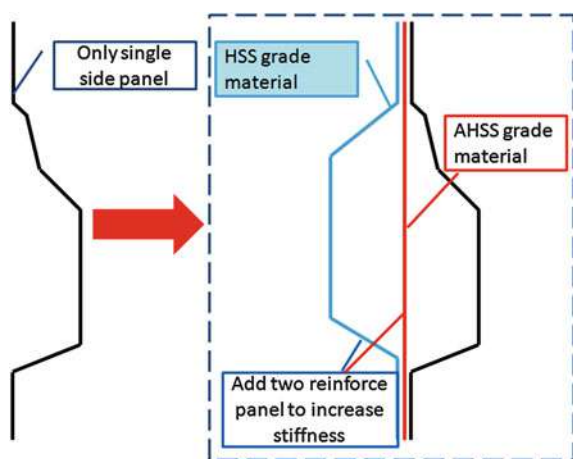
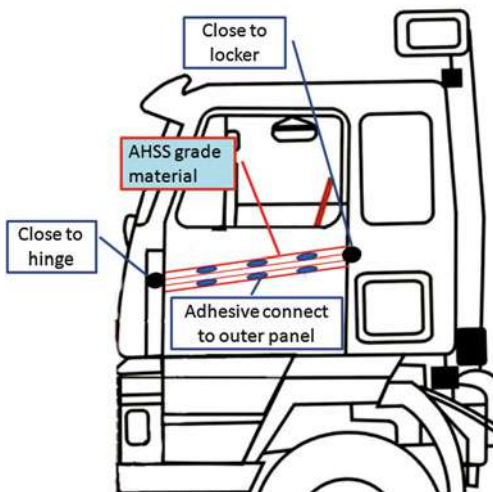


Fig. 13 Strong door structure



5 Calculation and Result

Validation is taken on an 8.5T GVW commercial vehicle cab, which has been marketed for several years. We can fulfil the requirement of new policies by doing some design iteration on this cab, work based on:

Firstly, increase section dimension of lower part of A-Pillar and sill. The original sill part has only single side panel, adding two reinforce panels to strengthen the lower part's bending stiffness, see in Fig. 12. By a meanwhile layout work should be taken simultaneously.

Secondly, apply AHSS (with yield strength of 800–1,000 MPa) grade material and HSS (with yield strength of 600 MPa) to the joint between A-Pillar and sill, which should be handled to ensure an efficiently connection then an efficiently support to the A-Pillar, see in Fig. 12.

Thirdly, new inner panels are designed to optimize the load transmission and to avoid bending of the frontal door. Both ends of this part should be applied as close as to the position of hinge and locker, application of AHSS (with yield strength of 1,000 MPa) grade material suggested for these inner parts, see in Fig. 13.

Output of the simulation show good result on these improvements, after crash, cab can supply enough space for the occupant, which caused by the fact that, pendulum hits the stiffness and strength optimized front structure briefly and load transmission do a good work on the impact.

6 Future and Scope

After 6 years of the date entry into force, Commercial Vehicle manufacturer shall satisfy new approvals under this regulation to the new types of cabs. Existing cabs cannot meet (re-design could result in new approvals!) Safety features such as load absorbing front and roof structures are the safety features designed as new procedures on commercial vehicles.

To meet this safety requirement involves a multidisciplinary procedure that working from concept definition to the end of production. The future's vehicle structure will be smart, light weight, crashworthy in rollover, and front or roof crashes. Achieving vehicle safety also need to integrate with other aspect: cost objective, engineering technology, fuel economy constraints, recyclables requirements, and market performance, some of them will be undoubtedly in conflict with each other. Cab structure will continue to optimize during decades in response to consumer's high demands, increasing government regulation and globalization of the industry.

References

1. Official Journal of the European Union, L304/21 (2010) Regulation No 29 of the Economic Commission for Europe of the United Nations (UN/ECE)—Uniform provisions concerning the approval of vehicles with regard to the protection of the occupants of the cab of a commercial vehicle
2. Montella A, Pernetti M (2010) In-depth investigation of run-off-the-road crashes on the motorway naples-candela. Proceedings of the 4th international symposium on highway geometric design, 2–5 June 2010
3. Ligovic M (2005) Volvo trucks view on truck rollover accidents
4. American Iron and Steel Institute (2004) Vehicle crashworthiness and occupant protection methods
5. de Castro I, Jokuszies M, Altamore P, Lee W (2001) Simulation of occupant response in the ECE R29 safety test. SAE 2001-01-3845
6. Raich H (2003) Safety analysis of the new actros megospace cabin according to ECE-R29/02. Proceedings of the 4th European LS-DYNA users conference, 22–23 May 2003

BIW Safety Performance Research Based on Vehicle Frontal Crash

Zhida Shen, Xin Qiao and Haishu Chen

Abstract This paper introduces the research course of vehicle crash safety performance. A vehicle frontal crash FEA model is established according to CMVDR294. Vehicle frontal crash simulation calculation is conducted by LS-DYNA. Energy absorption area and transmission route of impact force in frontal crash are introduced in details. Affects of longitudinal beams deformation on vehicle crashworthiness are discussed deeply through simulation of the longitudinal beams design plan. Finally, tests are made to verify feasibility of the longitudinal beams design plan and reliability of the vehicle frontal crash model. As result, references are provided for vehicle longitudinal beams design and improvement for the future.

Keywords FEA · Frontal crash · Longitudinal beam · Vehicle crashworthiness

1 Preface

With the development of the society and the progress of human culture, automobile has become necessary means of transport in people's life. Along with increased automobile ownership and rapid development of high grade

F2012-F01-003

Z. Shen (✉) · X. Qiao

CAE Department, Brilliance Automotive Engineering Research Institute, Shenyang, China

H. Chen

Safety Department, Brilliance Automotive Engineering Research Institute, Shenyang, China

expressways, road traffic accidents have increased year by year. In all types of crash accidents, frontal crashes cover about 30 % of the total number of accidents. The injury rate and lethality rate are also very high [1]. Therefore, how to improve vehicle passive safety performance in crash and how to avoid or alleviate injury and death of passengers in crash to the maximum have become an important subject of vehicle passive safety performance research in our country.

Even though vehicle crash tests are indispensable for final authentication and evaluation of vehicle type and passive protective device, yet the preparatory expenses and test costs are extremely expensive. Furthermore, the test results are not stable enough and the repeatability is poor due to some random factors. As shown by related studies home and abroad, computer simulation of vehicle crash course with a dummy can not only predict the crashworthiness of the vehicle structure itself, but also the response and injury degrees of the passenger during the crash more accurately. So it may give better prediction of passive safety performance of the vehicle being developed and accelerate the development pace of new vehicle types.

FEA theory and its application were born in early 1960s. At that time computer simulation research on vehicle crash had been carried out in foreign countries. However, the research was restricted by the development of computer hardware technology and algorithm theory, actual breakthrough started in 1986 when LS-DYNA succeeded in simulating vehicle large deformation for the first time [2]. Ever since then, computer simulation technique based on dynamic explicit nonlinear finite element technology has seen its widespread applications abroad. Their researches are mainly concentrated on the following aspects:

- (1) Computer simulation of 100 % frontal crashes. Frontal crash of vehicle is the most common traffic accidents, in which casualties and property damages are more serious, therefore, the contents of this aspect were the first focus when crash simulation analyses were made and passive safety statutes were drafted in America and some European countries. In 1993, British Transport Research Laboratory conducted simulation calculation of the frontal crash of a car by using a giant computer and dynamic nonlinear FEA software. The vehicle model was composed of 25,000 deformed elements and 100 ms response course of vehicle crash was calculated, in which acceleration curve and vehicle deformation, etc. during the crash were acquired [2]. It showed that the passenger had serious injuries mainly in the head, chest and legs in the frontal crash. In view of the seriousness of passenger's injury in vehicle frontal crash, corresponding statutes related to vehicle frontal crash have been formulated in America and Europe. Therefore, simulation analysis of vehicle frontal crash is very significant to improve vehicle crashworthiness in frontal crash (Fig. 1).
- (2) In 40 % ODB crashes, the obstacles may be rigid walls or deformable objects. This is because when compared with frontal crash, the front end structure of the vehicle body intrudes into the passenger's space more seriously in side crashes, which may easily injure the passenger on the intruded side of the structure. The method for the research is basically similar to the method used

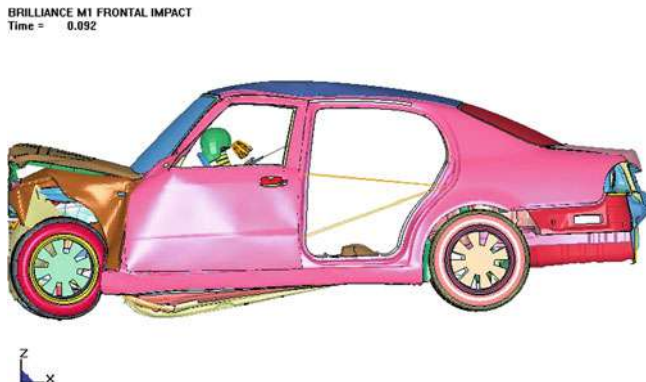


Fig. 1 The 100 % frontal crash simulation

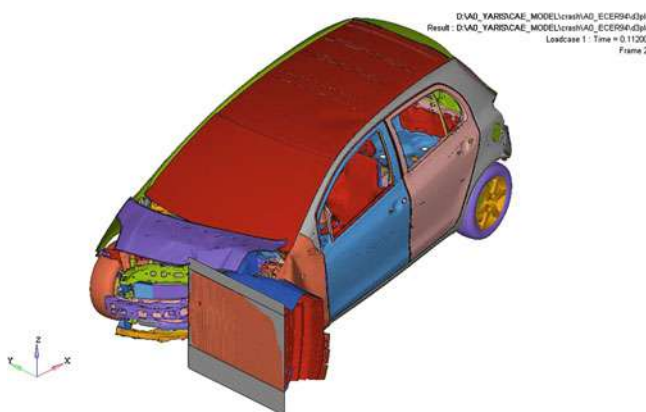


Fig. 2 The 40 % ODB crash simulation

for computer simulation research of vehicle frontal crash, except that the key objects to be considered in the vehicle simulation are not totally the same as those in front crash. Besides front longitudinal beams and dash panel, the front tyre, the front door frame, the steering wheel and the pillar on the side crash side are also the key objects for consideration and research (Fig. 2).

- (3) The side impact simulation. The key point to be considered in side crash simulation is the peripheral structure, including side door, door frame, pillar, roof and floor on the crashed side, passenger seat and so on. The expected objective is that the deformations of the pillar and the door are small. Therefore, The side impact simulation is equally important for the research of vehicle crashworthiness (Fig. 3).

Since crash accidents endanger human safety, definite and stringent requirements for vehicle crashworthiness are specified in automobile codes or standards

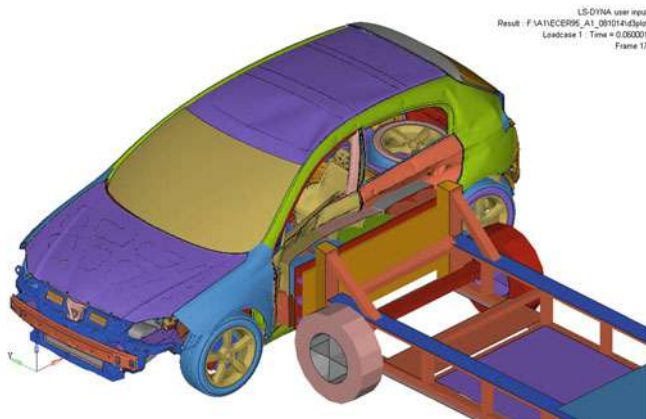


Fig. 3 The side impact simulation

both home and abroad. In foreign countries, safety performance must be evaluated before a vehicle is finalized for production and sales of vehicles that fail to meet the crashworthiness specified by the statute shall not be permitted. On Jan. 1, 2000, the Chinese Government also implemented Regulations for Protective Design of Passengers in Frontal Crash (CMVDR294), which specifies that vehicles to be newly listed in China later than October, 1999 must meet the above Regulations, that the import licensing of imported vehicles that had been sold in China before implementation of the above Regulations must be cancelled if they had not meet the Regulations. As for the vehicles that had been produced and listed but failed to meet the Regulations, they must satisfy the Regulations through structural modification before July 1, 2002, otherwise the production must be stopped.

2 Establishment of Finite Element Model

In modeling thought, the finite element model of vehicle frontal crash is generally the same as those similar crash models. What is different lies only in different concerns for vehicle body components due to differences in the purpose of analysis. The grid of energy absorption components in the front end of vehicle body: front bumper beam, crash box, upper longitudinal beams and lower longitudinal beams must be detailed appropriately, and the connecting relations between components must be simulated as much as possible. The components and structures inside the engine compartment must be detailed as much as possible; the engine and the gearbox may be simplified properly, but accuracy of the overall dimensions must be ensured. Generally speaking, the quality of the simulation model analyzed may affect the precision of the calculation results directly, so it is critically important for the analysis [3]. Therefore, for any complicated crash

simulation model, a set of standardized modeling flow is necessary for accuracy of the simulation model.

A finished automobile has many complicated components, so the establishment of vehicle simulation model is a gigantic work that requires large quantities of manpower and vigor. In establishing the vehicle finite element model, the first thing is to check the 3D dig fax and 3D welding points of the real vehicle structure provided by design section, and show critical concerns about all the structural components affecting the crash analysis. After that, CATIA 3D models of all the vehicle parts and components shall be saved in MODEL format files, geometric contours of parts shall be input via the formatted data conversion interface in Hypermesh software so as to make the grid by using the lines and planes, in which the main characteristic lines must be reserved and the grid must be fitted properly with the geometry.

The modeling method for each subsystem and its parts and components depends upon the structural characteristics and the response features during the crash. Generally, in modeling of frontal crash, the model is established in three categories of components. The first category is body sheet metal parts such as front bumper beam, crash box, upper longitudinal beams and lower longitudinal beams, which are the main components for deformation energy absorption and force transmission, because they are the main objects to express the deformation of the crashed body. The second category is the chassis and power assembly system, whose mass and rigidity are great relative to the vehicle body structure, so the inertia should not be neglected. The third category is body accessories, whose deformation energy absorption ability is very low, but the mass occupies a larger proportion, so they have greater impact on vehicle body response. The elasticity and damping characteristics of front and rear suspensions are particularly important in frontal crash modeling, because rigidity characteristics of rubber suspension and other factors shall affect the response to movement such as body pitching and side deflection in the course of crash, which is just one of the features in modeling of frontal crash [4].

Vehicle model shall be assembled according to automobile manufacturing process (Fig. 4). First thing is the relations between all the small assemblies, then all the subassemblies shall be assembled, and finally the vehicle model shall be assembled [5]. Assembling of vehicle model shall be realized through addition of connecting units (welding points hinged to short beams) or restrictions (e.g. rigid restriction) on the connecting positions. Finally boundary conditions shall be defined and all the contact problems between components during the crash shall be resolved.

Vehicle frontal crash model has large quantities of nodes and units, so it has certain high requirements for software and hardware. This modeling is completed on DELL/T3500 work station by using Hypermesh, which is a common pre-processing software in automobile industry. For more accurate and more effective modeling, a LS-DYNA file [6] may be set up for each crash respectively according to the subsystems of the vehicle, the suffix of the file is key. Subsystems of the model include: BIW system, four doors and two hoods system, chassis system,

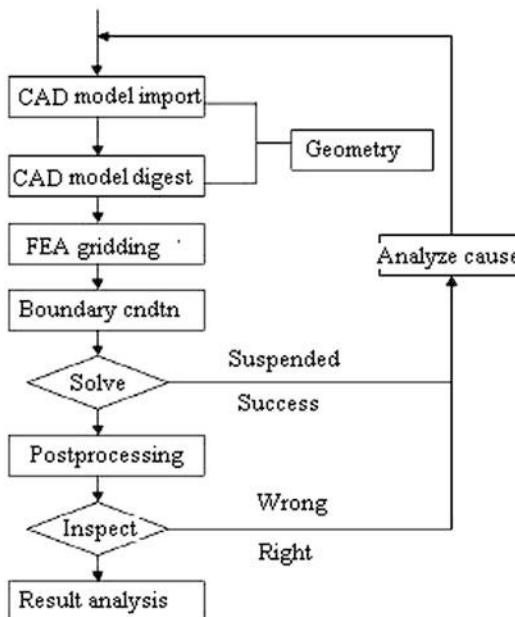


Fig. 4 The FEA modeling process configuration



Fig. 5 The total vehicle frontal crash FEA model configuration

steering system, power transmission system, interior and exterior decoration system and safety system. Finally, all the subsystems are assembled together by means of an associated file. Through statistics, the model is composed of 1,183,754 nodes, 1,291,149 units, 3,698 body welding points, and the mass of the finished vehicle is 1,145 kg. Penetration and interference of parts and components must be avoided in the model so as to ensure that the calculation results of the crash model are accurate.

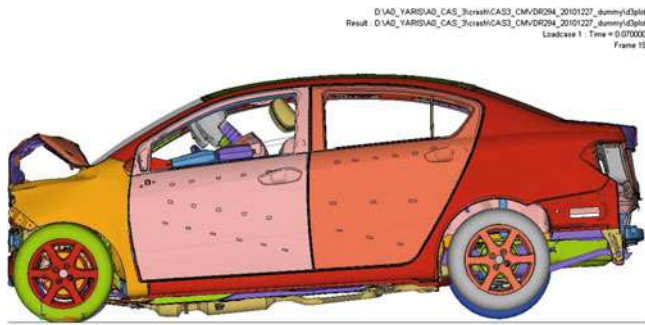


Fig. 6 The vehicle frontal crash simulation result

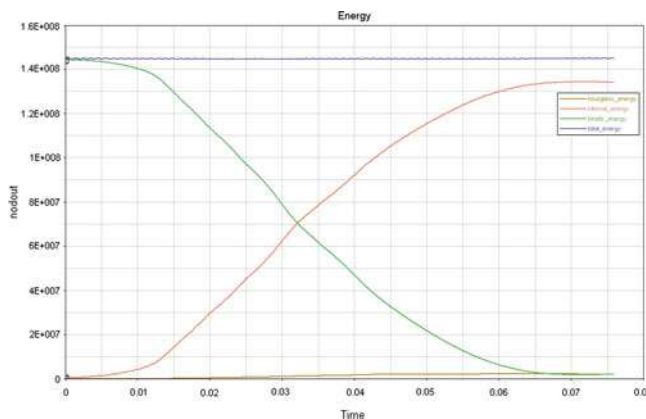
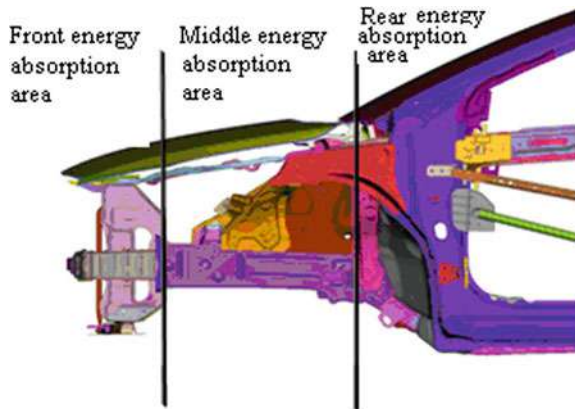


Fig. 7 The system energy curves

Crash simulation was carried out for this type of vehicle according to Regulations for Protective Design of Passengers in Frontal Crash (CMVDR294), which is officially promulgated for execution in our country. The model was stricken against a rigid barrier (as shown in Fig. 5) at a speed of 50 km/h. The body deformation after the crash is as shown in Fig. 6.

Through simulation calculation, the total energy variation tendency of frontal crash model is shown in Fig. 7. After the crash is performed, the general system deformation energy (internal energy) and dynamic energy are about 47 % respectively, the remaining 6 % of energy are crash interfacial energy and hour-glass energy in value calculation, of which the hourglass energy only covers 2.5 % of the total energy. Therefore, it can be seen from the figure and the data that this simulation is believable. The response characteristics of the total energy may be used to evaluate the general crashworthiness of the body structure.

Fig. 8 Division of crash energy absorption areas



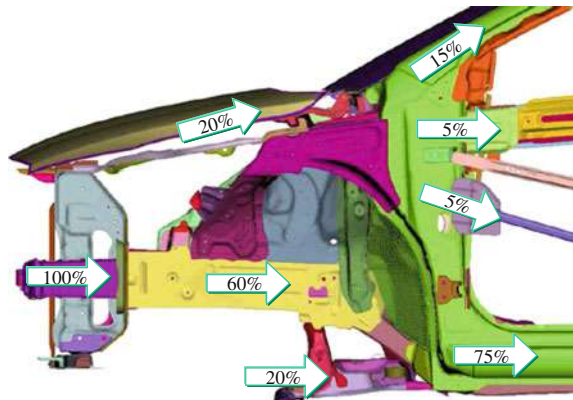
3 Energy Absorption Area of Vehicle Body and Force Transmission Route in Frontal Crash

At present, the method popularly adopted for vehicle body design is to divide the body into three areas: front, middle and rear energy absorption areas [7], as shown in Fig. 8. in which, the front energy absorption area is mainly made up of front bumper beam, bumper beam buffer block, engine hood front end and crash box. Such components are made of high performance plates, which can absorb the energy produced in the impact as much as possible through their deformation, and also continue to split the energy to the left and the right by using the force borne by the structure and transfer the energy rearward. The middle energy absorption area is mainly composed of upper and lower longitudinal beams of the body, fender, engine hood rear part and auxiliary frame. Such structures absorb most energy produced in the crash through reasonable bending deformation. The rear energy absorption area is composed mainly of the driver's cab that is both strong and rigid. In design of rear energy absorption area, deformation that may cause injury to the passengers must be avoided as much as possible so as to guarantee the passengers' safety by reducing the intrusion into the front floor and the crash speed as well as the acceleration of frontal crash.

Crash force transmission routes: The front, middle and rear energy absorption areas are the basis of multiply force transmission routes in frontal crash. Setting of multiply force transmission routes in frontal crash for frontal crash may effectively absorb energy and transmit crash force. Multiply force transmission routes in frontal crash are generally divided into three layers as shown in Fig. 9, which are typical force transmission routes in the course of frontal crash.

It can be seen from the above figure that the upper layer of frontal crash force transmission routes is composed of such components as engine compartment, upper longitudinal beams and front damper mounting hood, which absorb some of the crash energy from the front area, and disperse the rest of energy to Pillar A, front wall and reinforcing beam.

Fig. 9 Division of crash force transmission



The middle layer mainly consists of bumper beam, crash box and lower longitudinal beams, which is the major force transmission route in the course of crash. The bumper beam and the crash box split the energy produced in the crash leftward and rightward and absorb the energy initially, and then through the above components, transmit the energy to such areas as lower longitudinal beams, front floor, middle channel and threshold. The lower layer is mainly made up of the auxiliary frame, which absorbs part of the crash energy from the engine and the gearbox, and transmit the rest of energy to the front floor longitudinal beams, the threshold and other areas.

4 Influence of Longitudinal Beams on the Crash

It is known from the above discussion that the longitudinal beams of the body plays a vital role in frontal crash. Since one of the engines mounted in this type of vehicle has a large volume, the shape of the right longitudinal beams has to be amended according to the proposal of the general arrangement. The most direct scheme is to reduce Y section in the middle of the right longitudinal beams. Design plan (1) is as shown in Fig. 10.

Through simulation calculation, it is discovered that the middle part of the right longitudinal beams has seriously bent before the energy absorption box is entirely squashed. As shown in Fig. 11, this type of state is not favorable to energy absorption in the early stage, which may cause more serious injury to the passenger.

On the basis of Plan 1, Plan 2 is a transition design by using a smooth curve in the variable cross section, which is bound to affect the rigidity of the middle part of the right longitudinal beams.

Therefore, a semi-enclosed reinforcing part is added in the middle part to reinforce the rigidity at this place, as shown in Fig. 12. Through simulation calculation, the right crash box is squashed completely, but the middle part of the

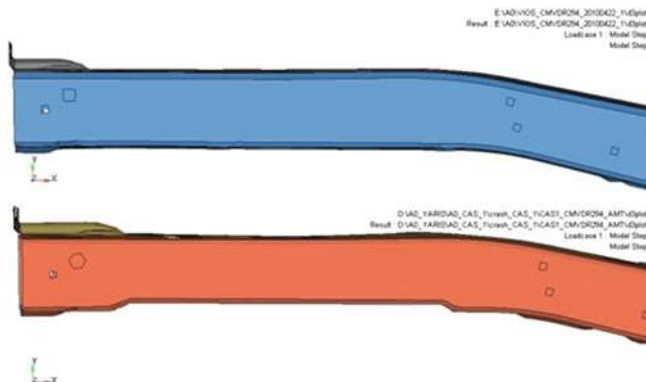
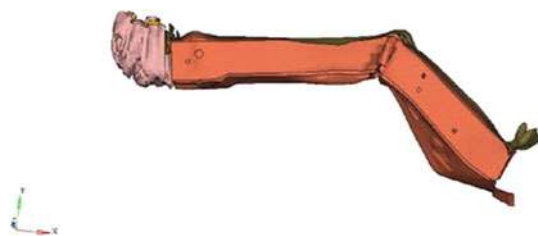


Fig. 10 The right longitudinal beams design plan 1 (The above is the original plan of the longitudinal beams)

Fig. 11 Plan 1 the right longitudinal beams deformation



longitudinal beams is not bent. This state will make the energy transmit directly to the root of the right longitudinal beams and the front floor, and the intrusion of the right fire bulkhead is increased obviously, as shown in Fig. 13.

Plan 3 is made on the basis of Plan 2, in which the semi-enclosed reinforcing part in the middle of the right longitudinal beams is cancelled. In order to reinforce the bending rigidity at this position, two 20 mm stiffeners are added in the weak position in the middle of the right longitudinal beams, as shown in Fig. 14.

Through simulation calculation, the middle of the right longitudinal beams is bent seriously after the crash box at the front end of the right longitudinal beams is completely squashed. This type of design can ensure the bending rigidity of the right longitudinal beams and also most energy produced in the crash is consumed in the area in front of the cab. So this type of deformation is relatively idealistic in frontal crash, as shown in Fig. 15.

5 Design Verification

In order to verify the design feasibility, the design of Plan 3 is used in a real vehicle crash test. Seen from the crash result as shown in Fig. 16, the front energy absorption area and the middle energy absorption area of the vehicle have suffered

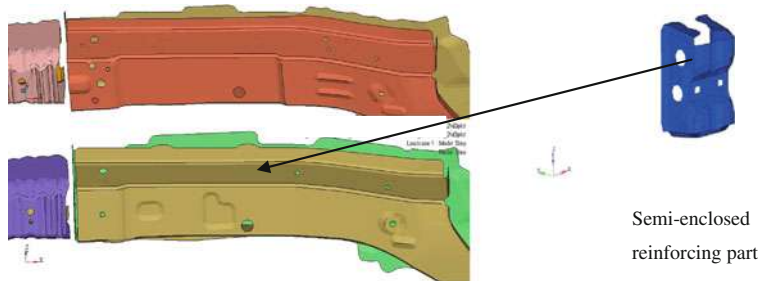


Fig. 12 The right longitudinal beams design plan 2 (the above is plan 1)

Fig. 13 The right longitudinal beams deformation of plan 2



Fig. 14 The right longitudinal beams design plan.3 (the above is plan 2)

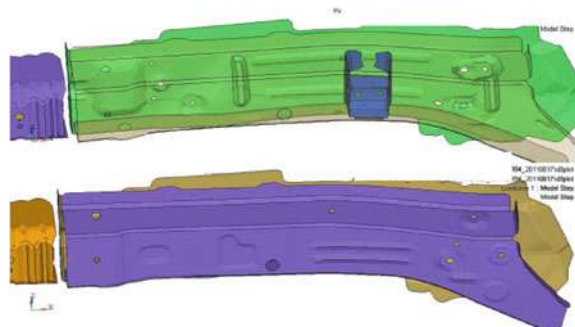
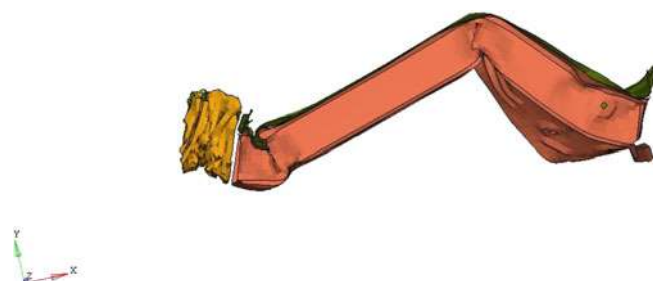


Fig. 15 The right longitudinal beams deformation of plan 3



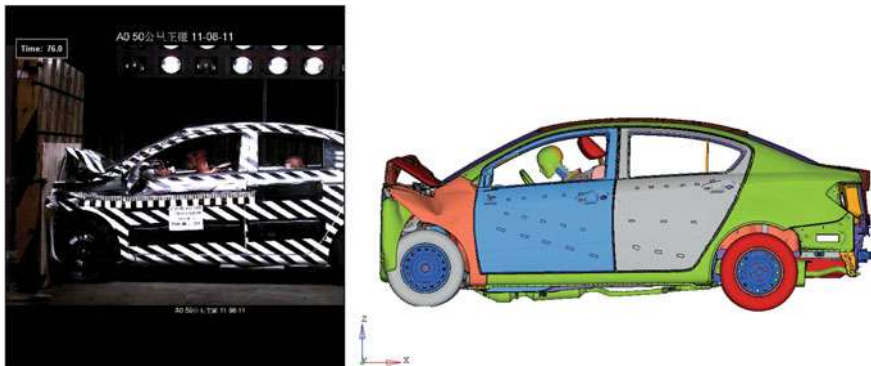


Fig. 16 Comparison between test result and simulation result



Fig. 17 The failure parts after testing

from more serious deformation, which absorbs most of the energy. Behind Pillar A, the area deformation is smaller, the intrusion of the fire bulkhead is smaller, the front floor does not have essential deformation, the door can be opened normally, the fuel tank does not have any leakage. In this test, only the crashworthiness of the vehicle body is verified, so no safety airbag is installed in the test vehicle.

After the real vehicle crash, two places are found to have obvious fractures, one is the connecting position of the engine suspension to the engine body, the other is the lower housing of the gearbox, where serious cracks occur as shown in Fig. 17.

However, the higher simulation result may be because of the different contact mode algorithm, the higher contact rigidity used as well as one-directional mass point instead of the mass of vehicle body accessories and interior decorations. As a whole, the fitness of the wave forms and peak values of the simulation curve and the test curve is higher.

After the failure mode of the corresponding fracture position is adjusted in the crash model, the simulation calculation is carried out for the second time. An acceleration curve corresponding to the time course is output and compared with the acceleration signal collected in the test, as shown in Fig. 18. It can be seen that

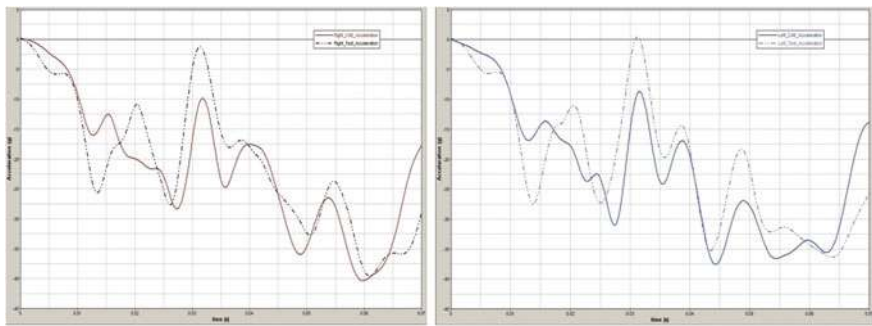


Fig. 18 Comparison between acceleration curves of left and right B pillars (solid line is simulation value, dotted line is test value)

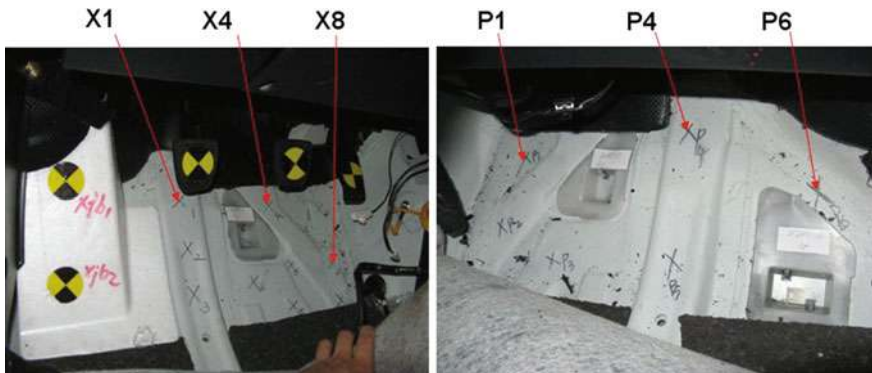


Fig. 19 The measuring points of floor intrusion

the left side acceleration peak appears near 45 ms while the right side acceleration peak appears near 60 ms. It is measured that the variations of the two acceleration curves are basically the same, but there are certain differences between the peak value and the corresponding time when it appears, the simulation value is a bit higher than the test result. According to the modeling experience, the difference between the test and the simulation time is caused by the instable factors existing in the model, e.g. negative value of contact energy and contact failure.

Similarly, when floor deformation value is acquired from the front floor of the cab, the size of the deformation may directly affect the leg injury value of the passenger, so to control the intrusion of this area is utterly important, as shown in Fig. 19.

The accelerations of simulation value and test value are controlled within 2 g. The intrusion difference at corresponding positions is controlled within 4 mm, which are used to verify the reliability of this simulation and the feasibility of body design. See Table 1 for specific values.

Table 1 Summary of acceleration and intrusion

	B Pillar lower acceleration		Left side front floor intrusion(mm)			Right side front floor intrusion(mm)		
	Left	Right	Point × 1	Point × 4	Point × 8	Point P1	Point P4	Point P6
CAE value	37.29	40.31	10.11	13.1	13.56	15.16	13.54	12.15
Test value	36.41	39.56	8.69	9.02	9.63	13.31	11.33	10.01

6 Conclusion and Prospect

In this paper, with a Class A vehicle of a certain type as the research object, the situation of vehicle crash safety research and development both home and abroad has been introduced, the frontal crash FEA model of this type of vehicle has been established, simulation calculation of the model has been made, frontal crash energy absorption areas have been divided, transmission routes of frontal crash force have been analyzed. Through simulation calculation of vehicle body right longitudinal beams design plan, the longitudinal beams deformation influence on the whole vehicle in the course of crash has been deeply discussed. The optimum design plan of the right longitudinal beams has been used for real vehicle frontal crash test to verify the feasibility of this longitudinal beams design and the reliability of the frontal crash model.

The research method and the simulation results in this paper have provided certain examples for body longitudinal beams design in future and certain references for optimization of related frontal crash structures.

References

1. (2005) Automobile crash and safety. Qinghua University Press
2. Weigang Z, Zhihua Z et al (2007) Research on application of computer simulation technology on improvement of automobile frontal crash safety performance. Mech Eng J
3. Zhihua Z (2008) FEA method for automobile crashworthiness analysis. Autom Eng
4. Watanabe K, Tachibana M, Wiemann M, Frankenberg D (2008) Vehicle side structure. Strength steel and roll forming technology. SAE paper No.01-1403
5. Xichan Z (2007) Research on automobile crash safety performance by application of computer simulation technology. People's Transportation Press, Beijng, pp 16–21
6. Is-dyna_970_manual (user's manual). 165–203
7. Chunyu W, Bing W (2007) Research on car frame structure crashworthiness by application of FEA method. Autom Eng 04:41–46

Development of an Impact Absorbing Component By Gimlet Form for Any Crushes

Tauchi Hideki

Abstract Making vehicles lighter leads to improved fuel efficiency and fuel savings. Impact absorbers play an important role in improving car safety, and improving their performance while reducing their weight will help lower the risk of accidents and support the environmental goal of reduced fuel usage. Polypropylene is used to make impact absorbers, since it is a lightweight and recyclable material. By processing polypropylene into an optimal form, it can be designed to undergo compression buckling when an impact is applied. The impact energy that a material can absorb corresponds to the integral value of the buckling load and displacement when plastic compression buckling arises in the absorber. Consequently, causing more compression buckling can increase the amount of impact absorption. This study considers the optimal form of an absorber to maximize the amount of impact absorption. A crash analysis was performed via computer simulation that compared the amount of impact absorption of a cylindrical shell and polygonal tube. A comparison between the polygonal tube and a pyramid-shaped absorber was also performed. The analysis found that polygonal tubes are superior to cylindrical shells in impact absorption performance. This is because decreasing the width of the planar sections and increasing the number of ridgelines will improve the compression buckling of the impact absorber. It was also found that pyramid-shaped designs are superior to polygonal tubes as impact absorbers. This is because the cross-sectional areas become smaller near the apex, and the pyramid shape gives rise to regular compression buckling from near the apex. Based on these results a new form of impact absorber is proposed that attaches

F2012-F01-004

T. Hideki (✉)

Automotive Group Next Generation Lighter Technology Group, WHITE IMPACT Co., Ltd., Zhenjiang, Japan
e-mail: info@whiteimpact.co.jp

concavo-convex projections on the side of a pyramid shape. These results suggest that by processing into an optimal form to absorb the shock, lightweight polypropylene can provide sufficient amounts of impact absorption.

Keywords Shock absorber · Computer aided engineering · Passive safety · Buckling · Weight saving

1 Introduction

In recent years the demand for fossil fuel has increased around the world, and the acquisition of energy resources has become a major problem for the country. There is a limit to fossil fuel reserves, and many studies have suggested that these reserves will be exhausted within the next 100 years, if present rates of consumption continue.

These trends are especially vital to the automotive industry. One countermeasure for Japan, which has limited domestic energy reserves, is to develop technologies for fuel efficiency. Automobiles consume large amounts of fossil fuel, both during manufacture and through operation. Two ways to reduce automotive fossil fuel consumption are (1) reduce vehicle weight to improve fuel economy, and (2) more fully recycle car components to reduce the usage of raw materials. According to reports from the Ministry of Land, Infrastructure, and Transport in Japan, for every 100 kg reduction in car weight, the average fuel efficiency increases by 1 km/l [1]. Also, increasing the recycling rates for used automotive materials will both lower the amount of waste and reduce the amount of new materials required for vehicle manufacture.

The death toll due to traffic accidents has been decreasing in recent years according to the National Police Agency statistics and Ministry of Internal Affairs and Communications statistics in Japan [2], but continued efforts are needed to lower this number and eventually make it zero. In particular, to reduce injury risk during an accident, technologies are needed to better protect people inside automobiles through impact absorption, and these technologies must be included in the design and manufacture of new automobiles. To achieve the goals of weight saving and easier recycling, we have employed polypropylene as a structural material for automotive impact absorbers, and have characterized the impact absorption performance of polypropylene in order to maximize risk reduction during an accident.

2 The Need for Buckling

The amount of impact energy that can be absorbed by a material is equal to the integrated value of the force-stroke curve (F–S curve) of the buckling load and the displacement when plastic buckling deformation occurs. This value is defined by the fluctuation process of the load accompanied by the deformation. The load, accompanied by the generation of buckling, increases until material buckling occurs, and reaches a maximum just before the onset of buckling. After the initiation of buckling, the value decreases sharply which shows that there is a large fluctuation before and after the buckling. Therefore to increase the impact absorption efficiency of the material, it is necessary to reduce the load fluctuation, and to increase the frequency of buckling under fixed levels of compression [3]. An effective way to accomplish this is to shorten the buckling wavelength and increase the overall buckling load.

3 Manipulation of Buckling Wavelength

3.1 Influence of the Plane Width

We first consider buckling on thin flat plates. As Fig. 1 shows, when dynamic compression is applied in the x-direction on a thin flat plate oriented normal to the z-direction, buckling occurs when the compression limit is reached and will result in deflection on the plate [4].

In the xy plane, when the plate is extended in the x-direction, the deflection w is represented as

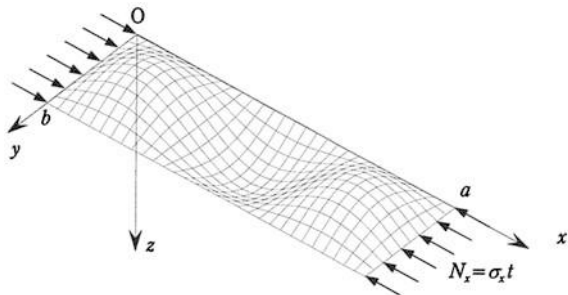
$$w = A_{mn} \sin \frac{m\pi x}{a} \sin \frac{n\pi y}{b}$$

where a is the long side width, b is the short side width, and m and n are integer values

A plate with flexural rigidity D , receiving a uniform in-plane compression stress σ_x in the x-direction, may be described by the following fundamental equation obtained from equilibrium of forces [5].

$$D \left(\frac{\partial^4 w}{\partial x^4} + 2 \frac{\partial^4 w}{\partial x^2 \partial y^2} + \frac{\partial^4 w}{\partial y^4} \right) + \sigma_x t \frac{\partial^2 w}{\partial x^2} = 0$$

$$D = \frac{Et^3}{12(1 - \nu^2)}$$

Fig. 1 Buckling model

In the equation, E is the elastic modulus, ν is the Poisson ratio, and t is the plate thickness. By substituting deflection w from Eq. (1), the relationship between the half wave number of the buckle wave and compressive stress can be determined.

$$\sigma_x \frac{\pi^2 D}{t} \left(\frac{a}{m} \right)^2 \left\{ \left(\frac{m}{a} \right)^2 + \left(\frac{n}{b} \right)^2 \right\}^2$$

No force is applied to the plate's compressive force in an orthogonal direction (i.e., the y-direction). Considering that buckling occurs when only one half-wave exists, the buckling stress σ_{cr} is represented as

$$\sigma_{cr} = \frac{\pi^2 E}{12(1 - \nu^2)} \frac{t^2}{b^2} \left(\frac{m^2 b^2}{a^2} + \frac{a^2}{m^2 b^2} + 2 \right)$$

The half-wave number in the compressive force is m and the buckle length is v when σ_{cr} is added, and $\lambda = \frac{a}{m}$ has the relation

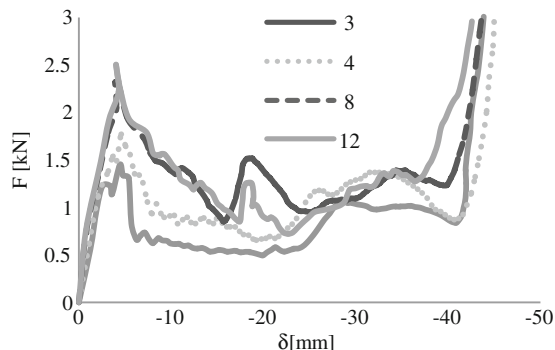
$$\sigma_{cr} = \frac{\pi^2 E}{12(1 - \nu^2)} \frac{t^2}{b^2} \left(\frac{b^2}{\lambda^2} + \frac{\lambda^2}{b^2} + 2 \right)$$

When the same force is applied to two similar plates with constant values of a , but different widths b , the above formula suggests that the plate with the smaller b leads to a lower value of λ . That is, the plate with the smaller width buckles with a shorter buckling length when compressed with the same stress.

3.2 Effect of the Number of Ridgelines

We next examine a polygonal tube, made from plates as considered in Sect. 3.1. In a polygonal tube it is known that the stress is concentrated at the ridgeline, and a plate under stress will buckle along the ridgeline. When the number of ridgelines is increased, the impact energy is shared among all ridgelines, so the energy which each ridgeline receives becomes smaller. In other words, by increasing the number of ridgelines, the amount of absorbable impact energy is increased.

Fig. 2 Effect of the ridgeline in F-S curve



4 The Ideal Shape

4.1 Effect of the Width of the Planar Section and the Number of Ridgelines

The discussion in Sect. 3 suggests an approach to improve the impact absorption ability of a structural material. When a rectangular polygonal tube made from many plates is compressed, making the tube's face width (i.e., the widths of the planar sections) smaller by adding many ridgelines will reduce the buckling length and increase the buckling frequency.

To examine the effect that the number of ridgelines (i.e., the number of corners) has on the behaviour of plastic buckling, an impact analysis was done for 1) a circular tube with radius R fixed at 25 mm and 2) a square tube with the number of ridgelines n fixed at $n = 3, 4, 6, 8$, and 12. The results are shown in Fig. 2. In this figure, the horizontal axis is the loading point displacement δ [mm] and the vertical axis is the buckling load F [kN].

From Fig. 2, before the first load peak, the F-S curve's shape doesn't depend on the ridgeline number n . In particular, when focusing on the maximum value, as the number of ridgelines increases from 3 to 12, the load at the maximum value increases and the frequency of attaining the maximum value increases as well. From this behaviour, it can be seen that the buckling length gets shorter and that the increase in ridgeline number leads to the buckling wave getting shorter by increasing the buckling frequency. However, increasing n does not lead to an increase in the impact absorption ability.

The relationship between the mean value of the number of ridgelines and the buckling load was examined, and the results are shown in Fig. 3. In the figure the horizontal axis is the number of ridgelines n , and the vertical axis is the mean value F_{ave} [N] of the buckling load F where the loading point displacement range is $\delta = 0$ –42 mm.

From Fig. 3, the mean load F_{ave} increases with the increase of the number of ridgelines, and after reaching a maximum at $n = 8$, the mean load tends to

Fig. 3 Comparison of the impact absorption performance

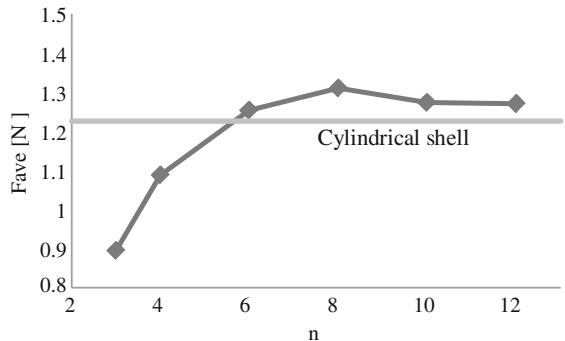


Fig. 4 Comparison with the cylindrical shell in F-S curve

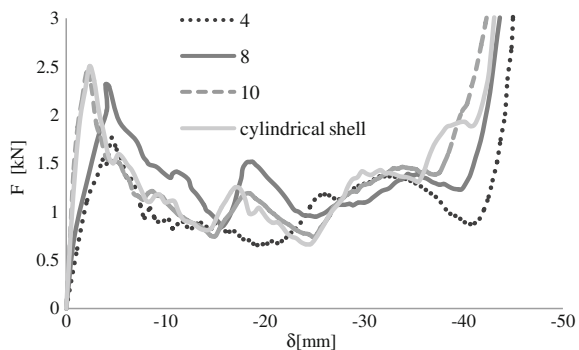
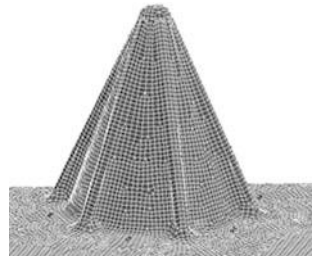


Fig. 5 Development form



decrease. Comparing these data to those of the cylindrical shell, the tubes with hexagonal, octagonal, decagonal, and dodecagonal cross sections have better impact absorbing abilities. From this, it cannot be concluded that the greater number of ridgelines the tube has and the more it buckles, the more it is able to absorb impact.

Figure 4 compares the F-S curves of a cylindrical shell with radius $R = 25$ mm and those of tubes with hexagonal, octagonal, and decagonal cross sections. The relation of the horizontal and vertical axes is the same as in Fig. 2. The

From Fig. 4, it can be seen that the decagon's F-S curve behaviour is very much like that of the cylindrical shell. This is thought to happen because when the number of ridgelines increases while keeping a constant circumference, the

resulting shape approaches that of a cylindrical shell. Even though the planar section width is small, the angles made by two adjacent sides of the polygon are large, and results in a longer buckling length like that of the cylindrical shell. Consequently, to attain high impact absorption ability and to buckle with short buckling length, not only the planar section and the number of ridgelines, but the angle made by the two adjacent sides of the polygon is important.

4.2 The Optimum Form

Based on [Sect. 4.1](#), to make a hollow rectangular polygon-shaped impact attenuator, adding ribs (concavo-convex) to the side will increase the number of ridgelines while avoiding an increase in the size of the angle made by two adjacent sides. In this case, the number of ridgelines and the planar section increases considerably compared to a rectangular polygon, and is considered to make an ideal impact attenuator.

5 Comparing Pyramidal to Cylindrical Absorbers

When comparing a hollow cylindrical and pyramid-shaped material of the same thickness, it is obvious when given a shock from the upper part, the pyramid-shaped material will buckle with a smaller shock than the cylindrical, because of the difference in cross sectional area.

In other words, in a pyramid-shaped material the first buckling will occur at the very top where the cross section is small; this first buckling will become the starting point and the plastic buckling will occur in ascending order of the cross sectional area. This leads to buckling occurring in a bellow-like shape, and it can be predicted that this shape will surely absorb the impact.

6 The Characteristics of the Newly Developed Form

As from [Sect. 4](#), a form with a cross sectional shape which includes ribs and concavo-convex surfaces on the side sections will have high impact absorption abilities. As discussed in [Sect. 5](#), a pyramid-shaped material can absorb impact energy more reliably than one that is cylindrical, from the difference in buckling energy by the difference of the area of cross section. From the two points above, a new shape was developed, as shown in [Fig. 5](#), which includes many concavo-convex surfaces. The reason that the newly developed form is a cone instead of a pyramid is that many concavo-convex surfaces were added to the form, and by the relation of the ridgelines and the planar sections, it is possible to regard this form

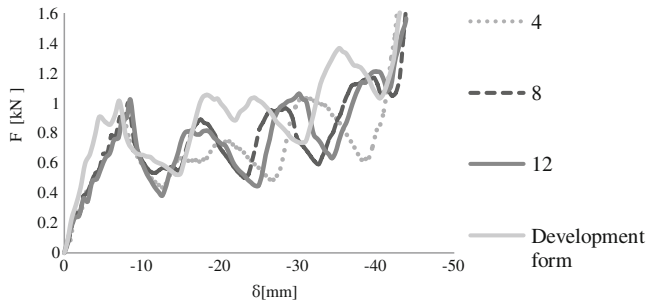
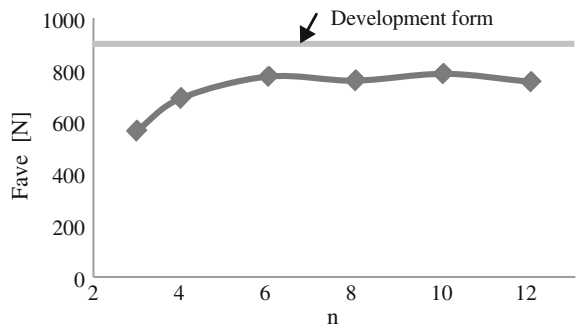


Fig. 6 Comparison with the development form and pyramid forms

Fig. 7 Comparison of the impact absorption performance



as a pyramid. To see if this form is effective in the case of impact absorption, it was compared and verified with other forms such as pyramids.

7 The Analysis Results of the Newly Developed Form

An impact analysis was executed where the circumradius was fixed to $R = 25$ mm, and the number of the pyramid's ridgelines was fixed to $n = 3, 4, 6$, and 8. The result of the analysis compared with the newly developed form is as shown in Fig. 6. In the figure, the horizontal axis is the loading point displacement δ [mm] and the vertical axis is the magnitude of the load F [kN].

As can be seen in Fig. 6, the newly developed form's figures increase before any of the other pyramids, and the number of times it reaches the maximum value is greater than those of the pyramids. Furthermore, the load value is bigger than those exhibited by the pyramids. Comparing Fig. 6 with Fig. 2, it is evident that the pyramid-shaped form surely buckles from the start.

Figure 7 shows the relationship between the number of ridgelines and the mean value F_{ave} [N] of the buckling load, where the loading point displacement range is $\delta = 0\text{--}42$ mm. From the figure, it is evident that the impact absorbing abilities of the developmental form are greater than the pyramid-shaped form by far. When

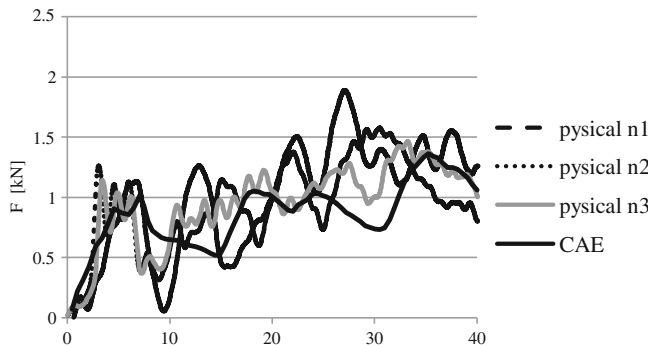


Fig. 8 Force–Stroke curve correlation between pyisical and CAE

buckling under impact, the newly developed form buckles with short buckling wavelength and has large impact absorbing abilities. Therefore, the newly developed form is suitable for an impact attenuator. We have patented this form in and outside the country.

8 Accuracy and Reliability of CAE Analysis

Here, we compare the analysis data to the actual test data. Figure 8 shows the F–S curves and the results from three samples, all of which were of the same form, had the same thickness, and were tested in the same environment. In Fig. 8 the peak positions and the number of times the samples reached these maxima are approximately the same. The integrated values are compared in Fig. 9. Comparing the integrated values of the mean value of the three tests and the CAE analysis, 91.76 % coincide. This observation demonstrates the reliability of the CAE analysis data used in this study.

9 Future Issues

It cannot be said that the position where the buckling occurs is predictable, because during an impact, the exact position where the load is applied at the onset of buckling is uncertain and will vary during multiple repeated experiments. Due to this uncertainty, this material may not be able to show its abilities fully during an accident. To show its abilities fully, it is necessary to design a specific buckling point, without reducing the overall strength of the material. By further experimentation and analysis, and specifying the position of the buckling by making a convexo-concave surface at the buckling point, improvements will be made to maximize the material's ability to absorb impacts and ensure full performance at any time.

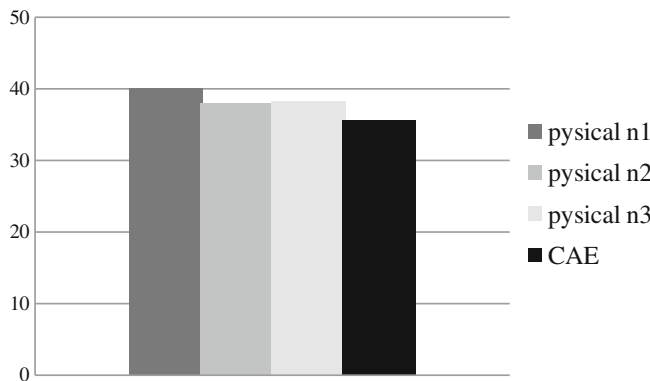


Fig. 9 Numerical integration value (EA amount value) $\delta = 40$ [mm]

10 Summary and Conclusions

In this development, as a result of having analyzed the structure of the impact absorption and carrying out an impact analysis of the impact attenuator, the following conclusions were obtained.

During shock absorption, a polygonal tube with ridgelines was much superior to a cylindrical shell as a shock absorber, and a pyramid shape was superior to a cylindrical shape. The pyramid shape would be made more suitable by increasing the number of ridgelines and decreasing the planar section.

The developmental form presented in this paper was able to absorb larger loads as a result of the increase in ridgelines and decrease in the planar sections by adding ribs. In addition, it is possible to absorb shocks of various load sizes, small to large, as a result of the impact being absorbed progressively, because in the pyramid shape, the plastic deformation occurs from the protruding portion with short circumference.

Further research is needed due to insufficiency in analysis data and experiments. Also, developments to specify the buckling point artificially by processing the form will be the subject of future work.

Acknowledgments We are very thankful to Dr. Kouji Mizuno of Nagoya University, Department of Mechanical Science and Engineering Mechano-Informatics and Systems Biomechanics and Human-Machine Systems Biomechanics Laboratory, and Mr. Yoshiaki Nakazawa of Sumitomo Metal Industries, Ltd, for their cooperation in the experimental analysis. For their instructive advice we also thank Mr. Kenichi Ohmae, CEO of Business-Breakthrough Ltd; Standing Adviser Mr. Yasuo Morimoto of Toshiba Corporation; and Professor Takatoshi Matsumoto of Hosei University, Department of Science and Engineering.

References

1. Ministry of Land, Infrastructure, and Transport in Japan (2008) Published on the performance of automobile fuel efficiency
2. National Police Agency statistics and Ministry of Internal Affairs and Communications statistics in Japan (2010) Changes in traffic fatalities
3. Nakazawa Y (2008) Effects of cross sectional shape on plastic buckling behaviour of thin-Walled polygonal shell members. Kyoto University, Abstract)
4. Timoshenko, Woinowsky Krieger (1973) Setu Hasegawa Burein Publication, Theory of plates and shells
5. Fukumoto Y (1982) Shintaikei Dobokukougaku9 Kouzoubutunozakutu anteikaiseki: Gihoudou Publication

Study on the Spot-Weld Failure Prediction Model in Auto Crash Simulation

Xiao Feng

Abstract The material failure is the essence of the spot-weld failure. TS Model has been constructed by the base material (BM) zone, the heat-affected zone (HAZ) and the nugget, and takes the failure strain as the unique parameter used for judging material failure, so it can be equivalent to the spot-weld failure by simulating the material failure in HAZ. TS Model involves the analysis of five critical problems, which include the spot-weld failure criterion, the reference datum to failure strain, the nugget diameter, the mesh size effect, and the spot-weld material model. TS model takes the material elongation rate as the reference datum of the strain failure. The mesh size in HAZ, which is matched with the material elongation, is determined initially. Meanwhile, the BM consistency assumption is put forward. Finally, the relationship between some factors and the spot-weld failure load has got by TS Model. Because of the simplicity of the failure criterion and the effectiveness of the spot-weld failure prediction, TS Model will have great engineering application value.

Keywords TS Model · Failure strain · Mesh size effect · BM consistency assumption

F2012-F01-005

X. Feng (✉)
Wuhan ShangShan Simulation Technology Co., Ltd, Beijing, China

1 Introduction

The car crashworthiness is one of the most important vehicle performances. In the crash test, body critical areas often appear the structure failure which is caused by the spot-weld failure. It will directly affect the credibility of the calculation that the full-vehicle crash simulation whether or not can predict the spot-weld failure. The “spot-weld failure” is considered as one of the greatest challenges in the crash simulation [1]. Therefore, it is very significant to develop the suitable spot-weld model for the engineering application and to predict the spot-weld failure in the engineering practice. Therefore, it is very significant to develop the spot-weld model that can be suitable for the engineering application and predictable to the spot-weld failure in the engineering practice.

2 Technical Background

All kinds of the spot-weld models have been put forward in a lot of literatures. For example, Omar Faruque et al. [2] use the spring element with two nodes and six degrees to simulate the spot-weld, and the failure criterions are the spot-weld peak force, displacement, and energy and so on. The research of Honda USA [3] shows that using multi solid elements to simulate the spot-weld is more accurate. Toyota makes use of the spot-weld failure model [4] developed by itself to simulate the pull-out failure successfully, and has applied it in the vehicle crash model. The results of numerical simulation agree well with the experimental measurement.

It is found that the spot-weld model can be decomposed into some basic construction elements, which include the research object, the nugget element, the spot-weld mathematical model, the spot-weld failure model, the failure standard and the spot-weld contact model. A kind of the spot-weld model consists of several of those basic construction elements, in other words the combination of basic construction elements can produce different types and levels of the spot-weld models. From the depth of the spot-weld model, it can be divided into three levels. The first is the functional simulation, which only considers the connecting function of the spot-weld, but doesn't consider the spot-weld failure. The second is the failure set, which can simulate the spot-weld failure phenomenon, but cannot predict it. The third is the failure prediction, which is able to predict it.

The choice of basic construction elements decides the hierarchy and complexity of the spot-weld. If the mathematical model and failure model are applied to describe the spot-weld, the spot-weld model has very little correlation problems, and the application is very convenient. But due to the complexity of failure parameters, only failure set can be implemented. If the 3D mesh and the simple failure standard are applied, a lot of correlation problems will appeared in the spot-weld model.

The essence of the spot-weld failure is materials failure, but the spot-weld mechanical function failure is just its failure phenomenon. The traditional

spot-weld models and failure standards adopt the mathematical model to describe the function of spot-weld. It completely avoids the research of the spot-weld correlation problems. Because of the brevity in the form and the convenience in the realization, the traditional spot-weld models are widely used. However the spot-weld failure standard is very complex, it can simulate the spot-weld failure but cannot predict it. The failure simulation needs the support of the database of related spot-weld, for example, the processing requirement to the spot-weld failure in [5] is that just the area of the spot-weld failure through the experience judgment needs to consider the spot-weld failure. How to set the failure parameters will need to refer to the database.

With body-in-white lightweight giving rise to the increase of the high strength materials, the spot-weld appears another kind of universal failure mode—the interface failure, which cannot be reasonably explained by traditional the spot-weld model. Therefore it becomes the trends of research for the spot-weld failure prediction method to the construction of the finer spot-weld model and the adoption of the strain failure model.

3 Research Method

The idea of the spot-weld failure prediction in [6] is of forward-looking in the engineering application. Firstly, according to the microcosmic process of the spot-weld failure, the spot-weld failure is supposed as the localized necking of heat-affected zone (HAZ) material or material failures which is caused by shear along the nugget boundary materials. Secondly, based on the analysis of the spot-weld failure phenomenon, points out the critical strain which according to localized necking or shear failure. Thirdly, based on the judgment of the strain failure, it is predicted that adopting the detailed spot-weld model to predict the spot-weld failure in the vehicle crash model.

3.1 3d Spot-Weld

From the angle of spot-weld correlation, Madasamy et al. [7] put forward the negative view to the detailed FEM or 3D spot-weld model. The spot-weld model were put forward mainly from the 2D angle in its early stage, the view has been widely recognized, so the 2D spot-weld which has less correlation are used widely in actual crash model.

With the development and requirement of the car body lightweight and the view of considering the spot-weld material property, the 3D spot-weld model is adopted and the concept of the “Spot Weld Element” [8] is put forward. Heubrandtner et al. [9] proposed the concept earlier, the essence of which is considering the spot-weld modularization in the engineering practical application. From the researches in recent years, the intensification of the spot-weld model is a major research trend and mean.

3.2 Failure Standard

The spot-weld failure is similar to the material necking failure or shear failure according to the analysis from the micro process [9–11], which supports the point of view of Zuniga [6]. Chao [10] puts forward the material failure standard of “fracturing stress”, and points out that any complex criterion would severely limit its use in engineering applications, and a single material critical stress or strain failure standard complies with the simple principle.

A single strain failure standard [12] is used to the spot-weld model in order to simulate the pullout failure. Wang [13] used a regular mesh to simulate the HAZ and puts forward the determination of failure strain, and points out the correlation between the failure strain and mesh size. Kumagai [14] established a detailed spot weld model using solid elements, and adopts the critical rupture strain to simulate two kinds of failure modes.

3.3 The Research Approach

Sklad et al. [8] give their three-pronged approach for spot-weld model. Firstly, the spot-weld physical model is studied including the spot-weld microstructure, mechanical property testing, welding process and so on. Secondly, the spot-weld mechanical model is summarized based on the spot-weld physical model. Finally, the spot-weld 3D model and failure standard are put forward.

In this paper, the research approach is just opposite. From the need of engineering analysis, the spot-weld model is regarded as pure finite element model and the material elongation rate is treated as the critical value of the material failure. By simulating the spot-weld material failure to predict the spot-weld failure, a spot-weld failure prediction model is constructed directly. In the practical engineering application, it's found that the spot model can be applied in practical engineering problems reasonably. Therefore, the research is the post-mortem study, and the key is the correlation problem for spot-weld failure.

4 TS Spot-Weld Failure Prediction Model

TS spot-weld failure prediction model (for short TS Model) inherits the research ideas in [6]. For example, the finite element meshes have been used to construct the nugget and HAZ and the material elongation rate is referred as the critical value of the spot-weld failure. TS Model is given in [15], as is shown in Fig. 1, the two layers of solid elements are adopted to simulate the nugget, and each layer consists of four solid elements which form an equilateral octagon. The material of the nugget is supposed to be consistent with the base material (BM), then, through

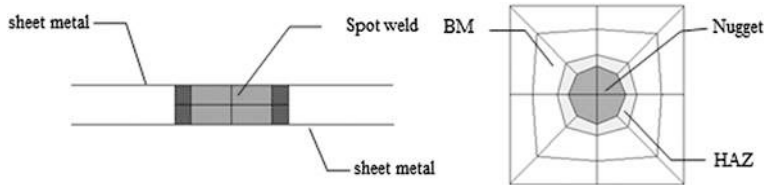


Fig. 1 The side and top viewport of TS Model

Table 1 The results comparison of shear test and TS Model

CASE	Shear failure Load (KN)			
	Thickness	Material	TEST	TS Model
Case1	2.3 mm/1.8 mm	B170P1	15.829	15.712
Case2	1.5 mm/1.5 mm	B340/590DP	18.018	18.141

three circles of shell elements, the meshes are gradually transited to the base mesh size of 10 mm × 10 mm.

TS Model is consistent with the physical structure described in [6]. The HAZ consists of a layer of shell meshes covered at the upper and under the surface of nugget, and the first circle of meshes connected with the upper and under the surface of nugget. The width of the first circle of meshes along the diameter direction of nugget is 1.5 mm. The HAZ and the BM have the same material thickness and type. And the elongation rate of the BM is set as the strain critical value of material failure. The rest of the two circles of meshes are defined as the BM, the most outer boundary of which consists of two elements. Thus, it's corresponded with the requirement that the welding edge must have two rows of meshes. Such meshes complete the transition from the spot-weld mesh size to the basic mesh size. From the angle of the construction of the spot-weld mesh, the VOLVO Spot-weld Model which is applied in the experimental simulation of the 3-point bending beam in [16] is consistent with the meshes of TS Model including the HAZ and nugget, furthermore, considers the change of material property in HAZ.

Two spot-weld shear test results are given in [17, 18], as is shown in Table 1. TS Model, the nugget diameter of which is 8.8 mm, is applied to carry out the simulation analysis of the typical spot-weld shear failure test. The result is consistent with the description of the failure process of spot-weld in [10].

5 Correlation Issues of TS Model

TS Model considers the practical requirement and follows the research trend of the spot-weld simulation. The simplicity of TS Model in essence leads to the complexity of the form, which performs for the five correlation issues: the welding

Table 2 The results comparison of shear test and TS Model in different nugget diameter

	Nugget diameter(mm)	Shear failure load (KN)	Failure mode
Test	6.5	15.829	Pull-out failure
TS model	6.5	13.112	
	8.8	15.712	

edge mesh matching, the node degree of freedom coordination, the size of nugget diameter, the mesh size effect and the spot-weld material model. And the first two problems have been solved in finite element modeling.

5.1 Analysis of the Nugget Size

Traditional spot-weld models take the spot-weld as a mechanical model, avoiding the analysis of the nugget size. In TS Model, the nugget size is an important factor that affects the spot-weld mechanical properties. TS Model is applied to analyze the nugget diameter in ase1. Table 2 is the comparison of the test and simulation of the shear failure load. In Table 2, 6.5 mm refers to the welding technology diameter and 8.8 mm is the nugget diameter which is reversely obtained according to the test results.

Analyzed the result of TS Model, if the nugget size uses the diameter of welding process, it will be smaller than spot-weld physical diameter, as a result, the spot-weld shear failure load is smaller. Therefore, the nugget diameter of finite element model must agree with the nugget physics diameter. The judgment [19] of microscopic section and the size of the spot-weld provide the basis for the determination of spot-weld physical diameter. Heubrandtner et al. [9] directly pointed out that the spot weld radius needed for the analytical expressions for the maximum forces at failure is obtained from micrographs of the spot weld. And the definition of nugget diameter is directly given [20].

Because the welding process performance in low strength materials is better, generally the nugget has a larger diameter. Therefore, the nugget diameter has a major effect to the failure load, but has no influence on the failure mode which mainly is the pullout failure. However, the welding process performance in high strength materials is poor, in the same welding process conditions, the nugget diameter is smaller. Therefore, for high strength materials, the nugget diameter not only has influence on the failure load, but also cause uncertainty of failure mode. When the nugget diameter is too big, the pullout failure happens, and when it is too small, the interface failure happens. The fundamental reason for the interface failure in high strength materials is that the nugget diameter is small. Using finer spot-weld finite element model and the strain failure criteria, Kumagai et al. [14] analyzed the influence of the nugget diameter on the failure mode and gave the satisfactory explanation.

5.2 Mesh Size Effect

For taking the strain failure spot-weld model in the vehicle crash simulation, on the one hand, how to determine the failure strains of different materials and thicknesses are unavoidable; on the other hand, using the finite element method to simulate the large deformation will cause the mesh size effect. Therefore, researching the mesh size effect is very important to the prediction of the material failure.

Bois [21] qualitatively gave the calculation formula of fracture strain and mesh size effect curves. Tyler-Street [22] simulated the materials tensile test in the condition of certain deformation for different mesh size specimens, the curve of the biggest strain and mesh size is consistent with the mesh size effect curve in [21]. Wierzbicki [23] also got similar results, and had a funny description that it is clearly seen that the strain in the finite element simulation is actually an “apparent strain” whereas the actual physical strain may not exist at all.

TS Model adopts the strain as the standard of material failure to simulate spot-weld failure. Researching the mesh size effect aims to solve the problem how to determinate the numerical value of failure strain. Generally, in the finite element analysis, the mesh is finer and the precision is higher.

A finer mesh size is subjectively determined for spot-weld, then the simulation and experimental results are compared, and the failure strain is determined in the simulation model, so the mesh size decides the failure strain. For the same spot-weld test results, because of different mesh size, the numerical value of failure strain is different. Therefore, the subjectivity of the mesh size determination leads to the arbitrary of the failure strain determination. TS Model is just opposite. Because of the existence of the mesh size effect, the numerical value of failure strain is firstly considered, and the unified value standard which is the material elongation rate is determined by different materials. Then, the simulation and experimental results are compared, and the unified spot-weld mesh size is determined by the material elongation rate.

5.2.1 Benchmark of Material Elongation Rate

In order to research the relationship of mesh size and failure strain in TS Model, the shear model is established based on the spot-weld typical mechanical performance tests. The upper and lower welding sheet metal material is B340/590DP, and the material elongation rate is 0.18. The thickness is 1.5 mm respectively, and the HAZ adopts spot-weld mesh transition mode with three kinds of different size including 1.5, 3.25 and 6.5 mm, as are shown in Fig. 2.

The shear models are exerted the same displacement respectively, and the material failure isn't considered. The results of the max plastic strain in HAZ are shown in Table 3. The corresponding relationship between mesh size and max plastic strain is shown in Fig. 3. A (1.5 mm) stands for fine mesh model,

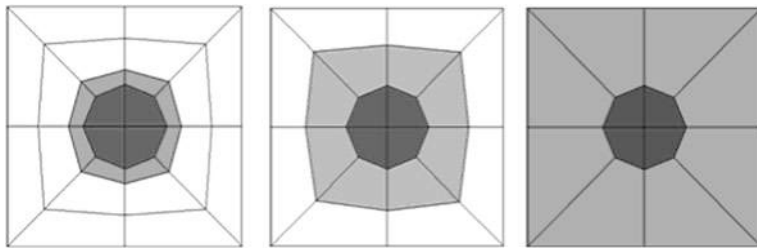


Fig. 2 The different mesh size transition mode for TS Model

Table 3 The max plastic strain in different mesh size

Max plastic strain		
1.5 mm	3.25 mm	6.5 mm
0.285	0.126	0.098

B (3.25 mm) stands for medium mesh model, and C (6.5 mm) stands for coarse mesh model. The physical meaning of the curve is that increasing the mesh size in HAZ, the max plastic strain decreases gradually.

The fine spot-weld model is adopted, and the strain is taken as judgment standard of the material failure. If the spot-weld mesh size is predetermined, the failure of spot-weld must be predicted, so it can only be determined according to the test failure load that how to set the numerical value of failure strain for the sheet metals which are of different material and thickness. In the engineering application, a strain failure database needs to be created. Because of the existence of the mesh size effect, if the mesh size changes, the strain failure database will be invalid.

In order to avoid such defect, TS Model adopts opposite ideas which is predetermining the failure strain, and taking elongation rate as unified reference standards of materials failure. Due to the existence of the mesh size effect, controlling the mesh size can make sure that simulation and test of failure load are consistent. The potential advantage is that spot-weld strain failure database is replaced by material characteristic database.

5.2.2 Mesh Size of the HAZ

Through setting the elongation rate of B340/590DP as the failure strain in HAZ, the shear model can get the shear failure load for different mesh size, as is shown in Table 4. The corresponding relationship between mesh size and shear failure load is shown in Fig. 4. The physical meaning of the curve is that increasing the mesh size in HAZ, the shear failure load increases.

For the shear models represented by A, B and C, if the same load F_A is exerted, according to the Fig. 3, the max plastic strain for A, B and C will decline one by

Fig. 3 The curve of max strain effect

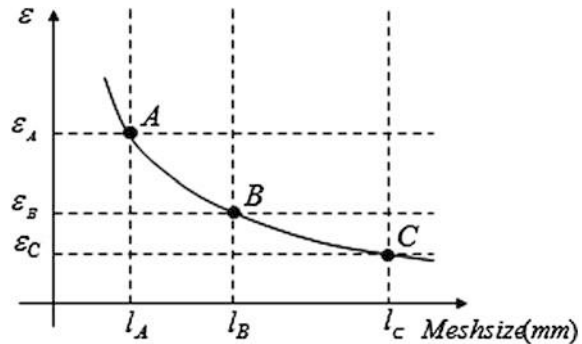
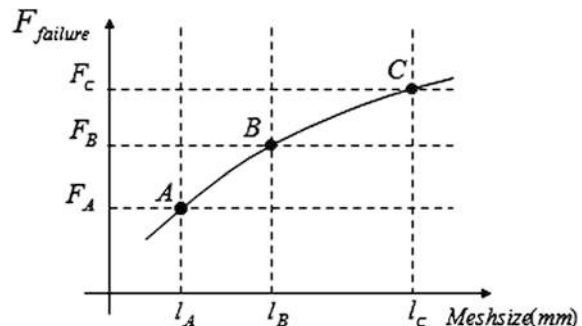


Table 4 The shear failure load in different mesh size

Failure load (K)		
1.5 mm	3.25 mm	6.5 mm
18.10	22.62	25.14

Fig. 4 The curve of shear failure load effect



one. If the load F_A makes ε_A equal to the failure strain in A, it is the shear failure load in the condition of the mesh size. Because the strains in B and C don't reach failure strain value, the load can continue to increase to F_B and F_C , so the shear failure loads in A, B and C increase in turn.

Due to the existence of the mesh size effect, with the increase of the mesh size, shear failure load increases drably. It provides the basis for finding mesh size matching with materials elongation rate, namely there is always a kind of mesh size making simulation failure load equal to test failure load.

The test and simulation analysis [24] are carried out to the bending ability of bumper rail, taking the same failure strain value as material failure standard, the author examines the deformation of the bumper rail and load displacement curve in the condition of three kinds of mesh size of 2, 4 and 8 mm, contrasts with the test results and finds that the data from 4 mm mesh size is more close to the test result.

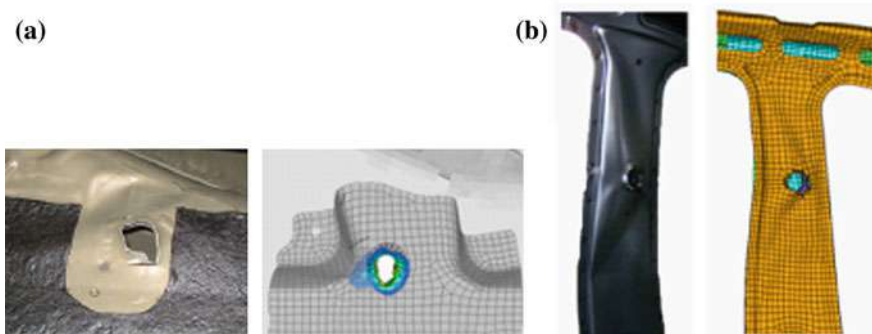


Fig. 5 **a** The correlation of safety belt anchorage failure in rear floor; **b** the correlation of safety belt anchorage failure in B-pillar

5.2.3 Matching of Key Parameters

If the test failure load F_{ture} is equal to the shear failure load F_B , the mesh size in B matches with the material elongation rate. One safety belt anchorage in rear floor was pulled out in the ECE R14 test, as shown in the Fig. 5a. The simulation analysis was carried out according to the test conditions. The metal sheet of bolt holes adopts the 1.5 mm mesh size, and the material elongation rate is referred as the material failure standard. The test failure phenomenon was successfully simulated. In the improvement case, one local reinforcement plate is increased. As a result, the failure does not appear, the result is consistent with the subsequent verification test.

The other safety belt anchorage in B-pillar was pulled out in the test, as shown in the Fig. 5b. The test failure phenomenon was successfully simulated. In the improvement case, the thickness of the local reinforcement plate increases from 1.2 to 1.5 mm, as a result, the result does not appear failure which is consistent with the subsequent verification test.

Based on the above safety belt anchorages strength test and FEA results, the mesh size matching with material elongation rate is preliminary determined as 1.5 mm or so in TS Model, which has nothing to do with material types, in other words, the different material elongation rate can match with the same mesh size.

5.2.4 Quasi-Static and Dynamic

The purpose of researching TS Model is to predict spot-weld failure in the vehicle crash simulation. But TS Model can simulate spot-weld failure effectively in the quasi-static condition. When TS Model is applied to dynamic crushing simulation of top-hat beam, the spot-weld early appears failure phenomenon, namely matching between the mesh size and failure strain in the quasi-static condition is not suitable for dynamic condition. Therefore, the application of TS Model in the



Fig. 6 **a** The deformation of left B-pillar; **b** The deformation of right B-pillar

vehicle crash model needs study mesh size effect fundamentally. The new method of uniaxial tensile test is provided [25], which can obtain the size effect curve between real fracture strain and reference length, and the material true stress–strain curve is redefined. All of these provide the basis of TS Model’s application from quasi-static to dynamic analysis.

5.3 Spot-Weld Material Model

The traditional spot-weld models deals with the spot-weld as a mechanical model, avoiding the material problem. Because of the heat influence in welding process, the material properties in the HAZ and nugget have changed greatly, comparing to the BM.

5.3.1 Spot-Weld Failure Cases

Seeger et al. [26] mentioned a kind of method to deal with the spot-weld material in HAZ. According to the method, the direct inference is that welding will make material performance get better, which is in contradiction to the conclusion that welding will make material performance go bad in the engineering practice.

The right side safety belt anchorage of some vehicle in B-pillar appears serious structural failure phenomenon in the ECE R14 test. In the design, the structure and welding process of left and right B-pillar is consistent. Perhaps because of the negligence, the engineer increases a spot-weld in right B-pillar. It comes out a completely different test result that the right B-pillar takes place serious structural failure, however the left is not. There are four BIWs used to do the test, the deformation results in left and right B-pillar are shown in Fig. 6.

The test results show that increasing the spot-weld does not necessarily lead to B-pillar structure failure, but there is a critical failure strain value, and only when the strain is greater than the critical strain, the B-pillar structure fails. But the instability of welding process leads to that it has different influence to the sheet

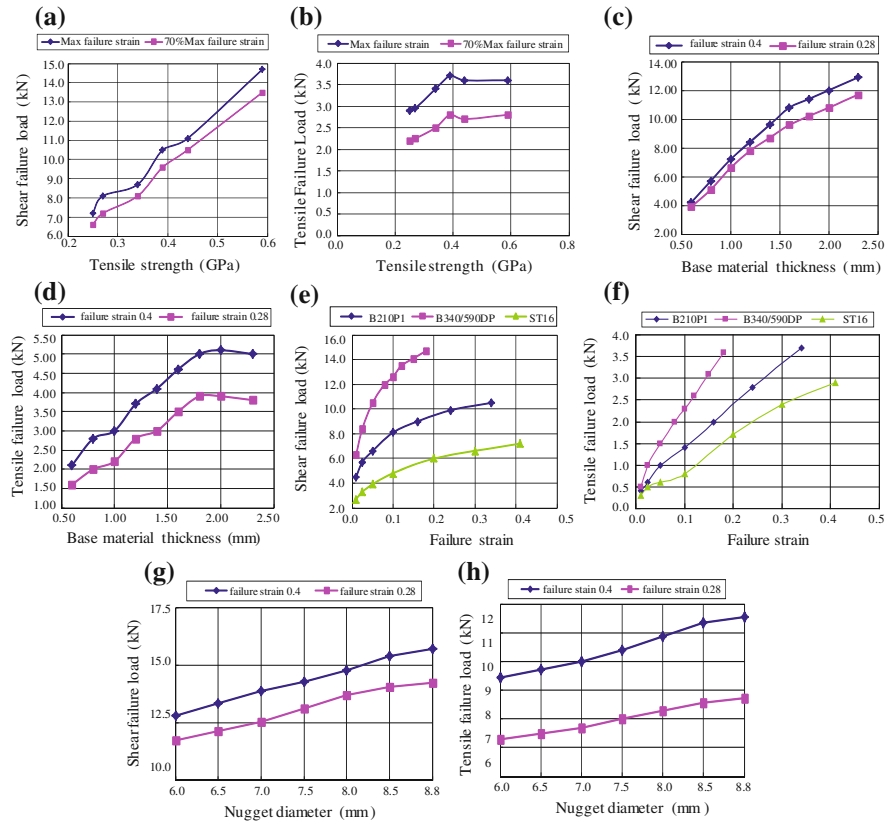


Fig. 7 a The effect of BM strength on shear failure load; b the effect of BM strength on tensile failure load; c the effect of BM thickness on shear failure load; d the effect of BM thickness on tensile failure load; e the effect of failure strain on shear failure load; f the effect of failure strain on tensile failure load; g the effect of nugget diameter on shear failure load; h the effect of nugget diameter on tensile failure load

metal. The strains in right B-pillar numbering for ①, ②, ③ are greater than the critical failure strain value, thus, they fail; the strain in right B-pillar numbering for ④ is less than the critical failure strain value, therefore, it doesn't fail.

5.3.2 Spot-Weld Material Assumption

Based on the judgment that the extent of spot-weld materials getting worse can be ignored to solve engineering problems, the base material consistency assumption is put forward for TS Model, it is mainly based on the following points.

In the first place, the welding process makes the organization structure of BM change and spot-weld material performance becomes poor, but the degree of change is unable to be quantitatively calculated, therefore the change of spot-weld

material properties is ignored in TS Model. On the one hand, it brings great convenience to deal with the engineering problems; on the other hand, the calculation accuracy can meet the engineering requirements.

In the second place, from solving practical engineering problems, the simulation of spot-weld failure is not the purpose of engineering analysis. In the collision analysis, the traditional spot-weld model actually don't simulate spot-weld itself, but simulate the mechanical behavior of spot-weld, and takes the spot-weld evaluation standard as the spot-weld failure standard, thus avoiding the spot-weld material problem. Therefore, the evaluation standard for TS Model is not whether considering the spot-weld material properties, but whether simulating the mechanical behavior of spot-weld.

In the third place, welding process has the same influence to different materials, and the consideration of spot-weld material properties has been embedded in the matching between the elongation rate and the mesh size.

6 Influencing Factor of Spot-Weld Failure

Using TS Model, the influencing factors of the spot-weld failure load, including the material strength, the thickness of sheet metal, the failure strain, the nugget diameter, were studied, as are shown in Fig. 7. The analysis results show that the same welding material, the thin BM firstly tears, while the same welding thickness, the low strength BM firstly tears, and the ability of spot weld to resist shear force much larger than the tensile force.

7 Summary

TS Model is the unity of complexity and simplicity, its complexity lies in the study and verification of the mesh size effect and the spot-weld materials assumption, its simplicity is the modular and the single failure standard. It is in line with the actual requirements of engineering applications that using the simple method to solve the complex problems.

References

1. Kohler J, Frank T (2009) Today's challenges in crash simulation. 7th European LS-DYNA
2. Faruque O, Saha N, Mallela K et al (2006) Modelling of spot weld under impact loading and its effect on crash simulation. SAE Paper 2006-01- 0959
3. Malcolm S, Nutwell E (2007) Spotweld failure prediction using solid element assemblies. 6th European LS-DYNA users conference
4. Kumagai K, Hayashi S, Ohno T (2007) Rupture modeling of spotwelds under dynamic loading for car crash FE analysis. LS-DYNA Anwenderfoyum, Frankenthal

5. Analytical Simulation Procedure for IIHS Side Impact (2005) GM global crash safety
6. Zuniga S, Sheppard SD (1997) Resistance spot weld failure loads and modes in overload conditions. Fatigue and fracture mechanics: 27th volume. In: Piascik RS, Newman JC, Dowling NE (eds) ASTM STP 1296. American Society for Testing and Materials, pp 469–489
7. Madasamy C, Tyan T (2004) Finite element modelling of spot weld connections in crash applications. SAE2004-01-0691
8. Sklad P, Feng Z, Simunovic S (2008) Dynamic characterization of spot welds. Oak ridge national laboratory. Feb 25–28
9. Heubrandtner T, Rangger G, Scherjau D (2005) Advanced spot weld failure modeling based on trefftz formulation LS-DYNA
10. Chao YJ (2003) Ultimate strength and failure mechanism of resistance spot weld subjected to tensile, shear, or combined loads
11. Lin S-H, Pan J, Tyan T, Wu S, Prasad P (2002) Modeling and testing of spot welds under dynamic impact loading conditions. SAE2002-01-0149
12. Cheng C-S (2004) The assessment of a combined methodology for spot weld failure modeling. SAE2004-01-0690
13. Wang J, Xia Y, Zhou Q (2006) Simulation of spot weld pullout by modeling failure around nugget. SAE paper 2006-01-0532
14. Kumagai K, Shirooka M, Ohachi J (2007) Rupture modeling of spot welds suitable for crash FE analysis in vehicle development process. 6th European LS-DYNA users' conference
15. Feng X (2009) The numerical simulation method for spot-weld failure prediction. China Patent Application No.200910302830.9
16. Bergwall M, Dahlström S (2010) The new volvo S60 car body. Euro-car-body
17. Xiaowei Z (2007) The performance and application analysis of automotive hot rolled dual phase steel. Chery J 1
18. Yunquan J (2007) Research about the effect of append the pastern in the resistance welding. Chery J 1
19. Sun X, Stephens EV et al (2007) Effects of fusion zone size and failure mode on peak load and energy absorption of advanced high strength steel spot welds under lap shear loading conditions
20. Fan X, Masters I, Roy R (2007) Simulation of distortion induced in assemblies by spot welding. Proceedings of the IMechE, vol. 221 Part B: journal of engineering manufacture
21. Du Bois PA (2006) Crashworthiness and impact engineering with LS-DYNA
22. Tyler-Street M (2009) Developing failure criteria for application to ship structures subjected to explosive blast loadings. 7th European LS-DYNA conference
23. Wierzbicki T (2006) Fracture of advanced high strength steels
24. Wang H, Slvasamy S et al (2006) Material failure approaches for ultra high strength steel. LS-DYNA Anwenderforum, Bamberg
25. Feng X (2010) The data measuring and calculation method for new uniaxial tensile test. China Patent Application No.201010501697.2
26. Seeger F, Michel G et al (2008) Investigation of spot weld behavior using detailed modeling technique. LS-DYNA Anwenderforum, Bamberg

Ultra High Strength Steel B Pillar Reinforcement Structure to Enhance Side Impact and Roof Crash as Reducing Weight

**Do Hoi Kim, Chan Young Kang, Jong Weon Seo,
Jung Han Kim and Yong Bai Joo**

Abstract At present, the issues of most importance are the environment and fuel efficiency. Thus, automobile companies have endeavored to reduce the weight of cars and develop eco-friendly fuel. The other issue is for the safety of passengers. Especially the new NCAP and IIHS's regulations involving roof crash test have strengthened for a few years. The automobile industry should increase the weight of cars for the improved regulation for the safety of passengers. OEMs have to satisfy the two confrontational requirements as developing the new vehicle. Therefore this paper will present the way to fulfill the confrontational goal by making a new B pillar structure through TRIZ and adjusting 980 Mpa high strengthened steel into the Center Pillar Outer.

Keywords Reinforcement • B Pillar • Side impact • Roof crash • Weight • Cost

1 Introduction

In recent years, the development of fuel-efficient vehicles is becoming an issue. Along with environmental-friendly cars that make up the topic of the global automotive industry of the development of environmentally friendly fuels. The recent Motor Show, the fuel efficiency and the development of new alternative energy is to

F2012-F01-006

D. H. Kim (✉) · C. Y. Kang · J. W. Seo · J. H. Kim · Y. B. Joo
Senior Research Engineer, Hyundai/Structure Engineering Design Team1,
Gyeonggi-do, Korea

Fig. 1 Side Impact Test



be mainstreamed with a focus on small cars than large cars. Saving vehicle's weight has emerged as an important challenge with the development of new fuel [1–4].

In addition, while the passenger's safety is emphasized, the B-pillar's deflections (passenger survival space) are often measured at the time of the passenger side collision in IIHS. Even when the vehicle overturned, increasing the stiffness is required of the body through the ROOF CRASH TEST in order to protect passengers. In order to protect passengers and vehicles, the thickness of BIW should be increased to improve the performance of the collision and the strength of vehicle. However, in order to improve fuel economy, weight should be reduced at the same time; the OEM must satisfy the two contrary conditions.

As improving both fuel economy and safety of passengers, weight should be reduced compared to the existing vehicle.

In this paper, we focus on the HMC to develop new vehicles that meet the two opposing goals. The grade of the vehicle was preceded as B-SEGMENT. Considering worldwide products and side-impact crash, US side impact is set as the standard in this paper. The contents of this paper can be fully deployed horizontally in spite of a little difference.

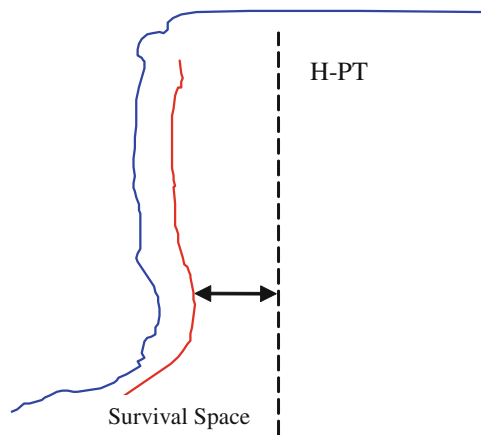
First, US collision performance related to B Pillar can be divided into three major. (Figs. 1 and 2 references)

1. US IIHS Side impact Performance
2. US IIHS Roof Crash Performance
3. US SINCAP Crash Performance

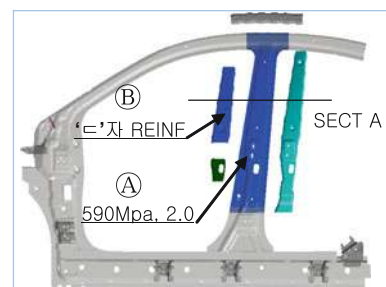
The ratings in the case of North American IIHS are divided into GOOD/ACCEPTABLE/MARGINAL/POOR. SINCAP is classified into 5★/4★/3★/2★/1★.

R vehicle of the HMC set up the highest goal to attain IIHS—Good, SINCAP—5★.

IIHS competitive survival space of the B-pillar is shown as Fig. 3. In the case of previous vehicle's space of R (HMC) was 97 mm; thus the goal of the new vehicle—R is selected by 125 mm (GOOD)

Fig. 2 Roof Crash Test**Fig. 3** Survival space comparison

차종	생존공간(mm)	차체 RATING
T company Y	101mm	Acceptable
H company F	103mm	Acceptable

Fig. 4 Previous REINF-SIDE OTR COMPLE

Finally, in the case of Roof Crash Test Fig. 2 Good level of Roof Crash Test is SWR 4.0. Therefore the goal of R vehicle is aimed at SWR 4.2 by considering margin.

In this paper, while the goal of R vehicle collision was satisfied, the enhanced B pillar compared to conventional B-pillar is to shown as reducing the cost/weight using TRIZ techniques.

Moreover This paper will present how the B pillar of R vehicle was made by protecting patents and how it was optimized through DFSS.

2 Concept Development

2.1 Concept of New B Pillar

2.1.1 The Problem of Previous B Pillar

REINF-SIDE OTR COMPLE at BIW is a direct effect on the side impact and roof crash performance (Fig. 4).

The previous REINF-SIDE OTR COMPLE has been used in HMC, Japan and European companies (Fig. 4).

R T-car added the previous vehicle into reinforcement and brackets after crash analysis.

And the final T-CAR crash test results that the B-pillar's deformation was sustained up to 111 m. IIHS vehicle passenger survival space transformation 125 mm (GOOD) was not achieved.

In the case of roof crash test, SWR 3.97 was not satisfied with the goal 4.0 (GOOD). In addition, the fuel efficiency was worsen because of adding the weight of 5 kg/per car (Fig. 5).

2.1.2 Competitive Cars' Analysis

As in Sect. 2.1.1 in order to reinforce low performance, the other's vehicle's analysis was carried out. First, through QFD-1 (Fig. 6), roof crash and side impact was chosen as the selection criteria. The following six kinds of additional selection criteria were taken into as the standard of concept evaluation.

The selected evaluation's criteria

1. Roof crash
2. Side Impact
3. B-pillar's design freedom
4. Formability
5. Weight
6. Cost

The primary evaluation matrix is shown as Fig. 7 as comparing R vehicle to competitive cars with six kinds of evaluation's criteria.

구분	P/NAME	RB 종곡	구TD	RB 2차해석 (TD 비교)	RB복미 T-CAR안	YARIS (코롤라참조)
RH	① PLR-CTR OTR UPR/LWR	440E, 2.0/1.2	440E, 1.4/0.8	440E, 2.0/1.2	590 1.8/ 440E 1.2	590, 1.8/ 440E 1.2
	② REINF-CTR PLR OTR	590, 1.6	440 1.4	590, 1.8	590, 2.0 (307H ~1538H)	590, 2.9
	③ REINF-CTR PLR OTR UPR	-	-		590, 2.0	
	④ REINF-CTR PLR OTR MID	-	-		440E, 1.2	-
	⑤ RAIL-ROOF SIDE OTR	590, 1.4	590, 1.4	590, 1.4	590, 1.4	440E, 1.6
	⑥ REINF-S/SILL OTR	1180Y, 1.2	1180Y, 1.2	1180Y, 1.2	1180Y, 1.2	590, 1.6
	⑦ SUPT-S/SILL OTR CTR	440 0.8	590 1.0	440 1.4	440, 1.4	440, 1.4
	⑧ REINF-S/SILL OTR RR	-	590 1.4	590 1.0	590 1.0	-
	⑨ SUPT-ROOF SIDE OTR FR	-	-	590 1.6	-	-
	⑩ SUPT-ROOF SIDE OTR CTR	-	-		590 1.8	590 1.8
ROOF	⑪ GUSSET-SIDE SILL OTR	-	-	440 0.7	440 0.7	-
	⑫ PNL-CTR PLR INR	440E,1.0	590 0.8	590,1.0	590,1.0	440, 1.2
	⑬ RAIL-ROOF CTR NO.1	440, 1.2	440 1.4	590 1.4	780 1.2	340, 2.3
	⑭ REINF-ROOF CTR NO.1,L/R	-	-		440,2.0	440, 1.0
IIHS 변형량			73mm	89mm	111mm	103mm

Fig. 5 R T-CAR material and thickness

When the B pillars of the competitive cars are comparing. The Y vehicle and M vehicle are good at side impact, roof crash performance. In the other hand, Y has a disadvantage of weight and M vehicle has a disadvantage of cost because of HOTSTAMPING.

In addition, through the analysis, W section type was developed. It's strength to weigh ratio (SWR) was improved by 0.4 from SWR 3.8 to SWR 4.2 than U section type (Fig. 8). Therefore, after adding W cross-section into B pillar in order to improve roof crash, ULTRA HIGH STRENGHTH STEEL was to be considered.

2.1.3 980 Mpa B PILLAR

First in the case of HOTSTAMPING, the elevation of cost is 13,000 won/per vehicle. Therefore it is impossible to apply B-SEGMENT.

Thus 980 Mpa Ultra cold high strengthen steel was pushed.

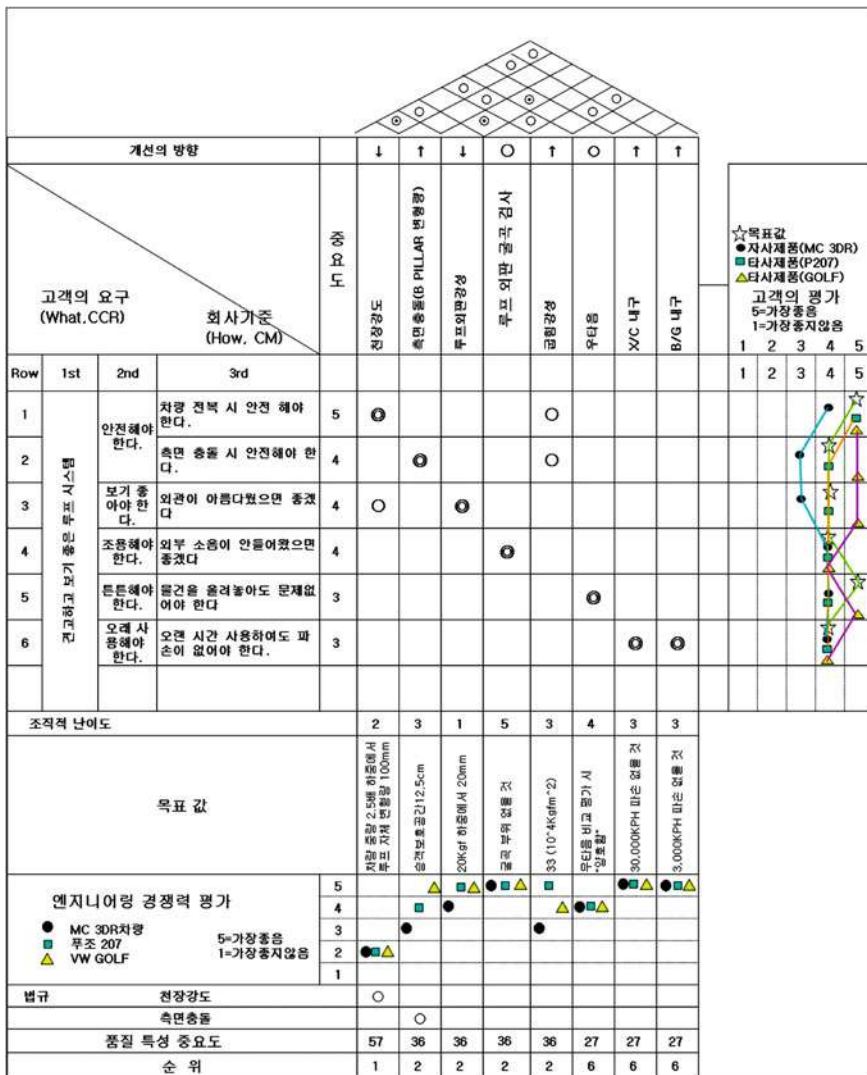
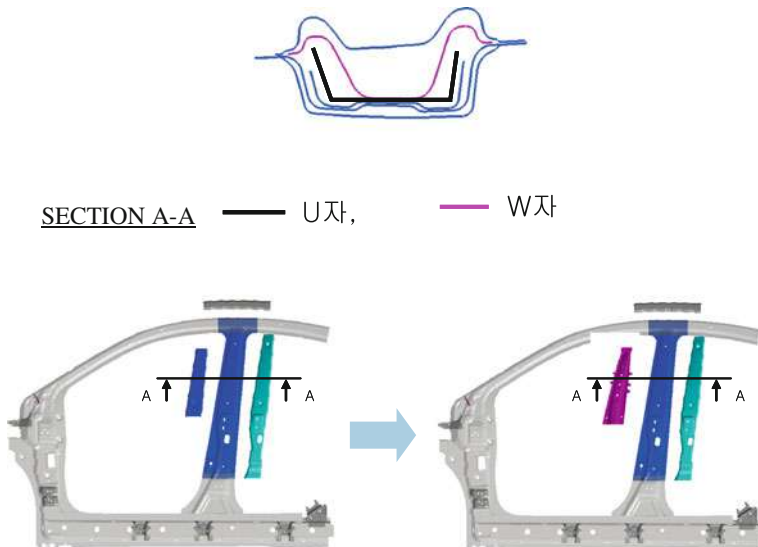


Fig. 6 QFD-1

It is possible that 980 Mpa B pillar's cost is equivalent to the existing REINF-S/OTR COMPLE. It is because the other part's thickness can be thinner after applying 980 Mpa CTR PLR OTR. The material's cost of 980 Mpa is a little expensive owing to same cold stamping method. However the analysis of formability is resulted that the tearing of panel occurred (Fig. 9).

The change of this area is very difficult because it is related to the vehicle's design and the gap between CTR-PLR OTR and PNL-SIDE OTR should be held constant. If 980 Mpa, CTR-PLR UPR is used, the performance is not only

	개념1(아리스-코볼라장조)	개념 2 신 TD구조]	개념3(부조 307-MD)	개념 4(메르소-구 TD구조)
	1.80L SPH1600 + 1.4L SPHC440 SPH1600: 2.00x	SGARIC440 1.60x SGARIC440 2.00x SPHC440 1.60x + SPHC440 1.25	SGCEN 0.80x SPFC140 1.50	SGARIC440 1.60x SGARIC440 1.20x SGARIC440 2.00x
한정강도 [SWR]	3.78	+ [4.0]	+ [4.0]	- [3.2]
측면총높 (mm)	103mm	- [90mm]	+ [128mm]	- [100mm]
디자인 자유도	D A T U M	S	-	S
성형성	S	-	-	S
원가	S	-	-	+
증명	-	-	+	-
+	1	3	3	+1
-	-2	3	3	-3
결과		-1	0	-2

Fig. 7 The primary matrix**Fig. 8** REINF-CTR PLR UPR COMPARISON

improved, but the weight and cost is also reduced. However the formability should be solved.

2.1.4 “W + t B PILLAR” DEVELOPMENT

To solve the above technical contradiction, TRIZ's Altshuller contradiction Table was used.

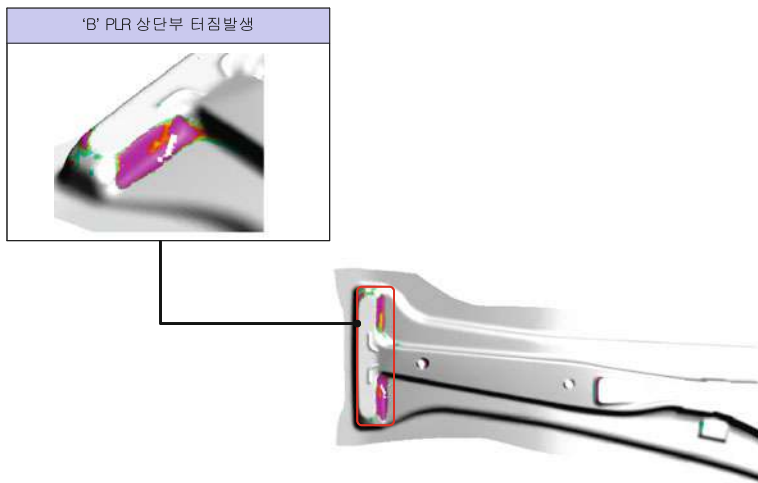


Fig. 9 The analysis of 980 Mpa formability

IF: To improve the strength of CTR PLR UPR

Then: Apply to 980 Mpa into B pillar

But: The formability fall

It resulted in “Local Quality”.

- (Local Quality) -

- Change the target and environments of the same structure to be heterogeneous.
- Let the target of each part perform different functions.
- Let each part of the target be operated in the optimal condition.

Through the combination of the above three, the following result can be derived.

Separating CTR PLR UPR’s function and combining with the surrounding environment, Changed the existing shape into heterogeneous structure.

The existing REINF-SIDE OTR was changed with the above result (Fig. 10).

First, the upper area of CTR-PLR UPR(A) was separated from the existing shape as the principle of TRIZ because of the problem of the formability.

Second, the cross-section of the ‘B’ part was changed from ‘U’ to ‘W’.

Third, Combine T shape’s upper panel with ‘W’ cross-section.

Finally the “W + T B Pillar” was developed as the heterogeneous structure (Fig. 11).

In addition, while developing “W + T B PILLAR (WTBP)”, the totals of 15 patents involved in NEW BRKT-SEAT BELT fitted in “W + T B PILLAR were registered. When the new REINF-SIDE OTR was compared with the good structures in the primary matrix (Fig. 7), it is proved that the new REINF-SIDE OTR (WTBP) is the most excellent structure than the existing structures (Fig. 12).

Fig. 10 The existing REINF-SIDE OTR

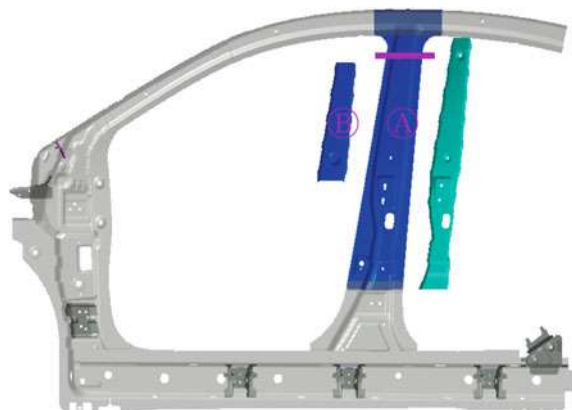
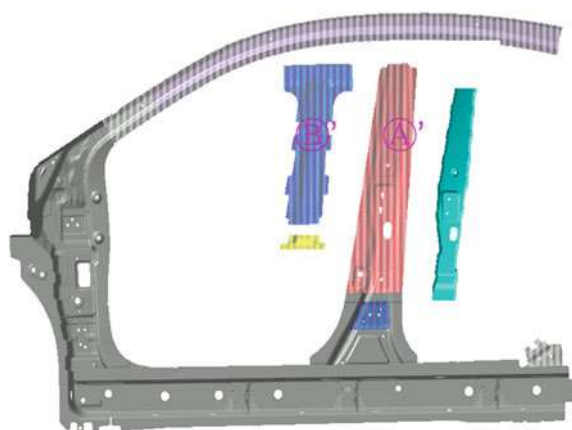


Fig. 11 The new REIF-SIDE OTR



2.2 Failure Mode and Effect Analysis (FMEA)

2.2.1 FMEA Function Hierarchy

“W + T B PILLAR” is the first structure in the world; it is not verified in a new vehicle. The quality problems may be happened in the field. Therefore FMEA was conducted. After analysis of the function of each part of WTBP.

The road pass of each part was made to know the connections with all parts of WTBP.

The function of B pillar has a central role to connect roof and floor while keeping body stiffness and supporting Doors. The main function parts of B pillar are as follows that applied WTBP in R vehicle in HMC.

- (1) REINF-CTR PLR OTR UPR
- (2) REINF-CTR PLR OTR
- (3) BRKT-CTR PLR OTR CTR
- (4) REINF-CTR PLR OTR UPR

	개념1(야리스-코롤라)	개념2(신 TD구조)	개념5(W+T자구조)
천정강도		+	+
측면충돌	D	-	S
디자인 자유도	A	S	S
성형성	T	S	-
원가	U	S	+
중량	M	-	+
+		1	+3
-		-2	-1
합계		-1	+2

Fig. 12 The second matrix (Fig. 7)

Fig. 13 FMEA function hierarchy

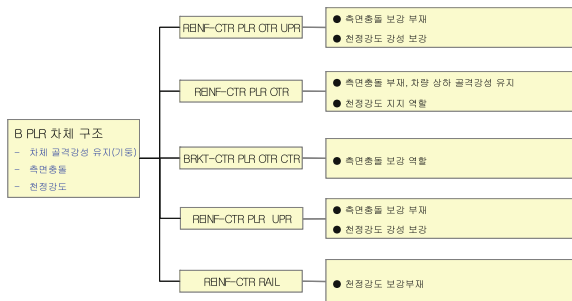


Figure 13 is the function hierarchy which shows the body structure of B pillar and role.

2.2.2 FMEA Application

Based on the analysis of R vehicle's function (Fig. 13), potential failure modes of the FMEA and recommendations are as follows: (Fig. 14)

- (1) Lack of side-impact crash performance
→ Material/thickness/length optimization
- (2) Lack of roof crash performance
→ Material/thickness/length optimization

System : 차체 v Subsystem : REINF-SIDE OTR COMPLETE Component : REINF-CTR PLR OTR, REINF-ROOF RAIL				설계 FMEA										FMEA No.: Page 1 of 1 작성자 / 소속 : 김도희/차체설계팀 승인자 / 소속 : 김도희/차체설계팀 작성일 : 09.10.15 개정일 : 10.02.01			
부품/기능	장재적 고장 모드	장재적 고장 양형	장재적 고장 예상 원인/ 메커니즘	현재				권고조치 사항	조치 침입 및 목표일	조치 결과				조치 결과			
				제작	설계	제작	설계			장재적 고장 예상 원인/ 메커니즘	장재적 고장 예방	장재적 고장 검증	장재적 고장 예상 원인/ 메커니즘	장재적 고장 예방	장재적 고장 검증	장재적 고장 예상 원인/ 메커니즘	장재적 고장 예방
B PLR : 차체 강성 : 차체 강성 부족 : 충돌 충수 : 충돌 충수 : 차체 강성 부족 : 차체 강성 부족 : 전착성능 부족	충연충돌 충격흡수미흡	충연충돌 시 습격 의 심각한 상해	9 부적절한 재질, 두께 길이선정	6 충연충돌 해석	충연충돌 평가	3 162	재질, 두께, 길이 최적화 (DFSS)	재질, 두께, 길이 최적화 (DFSS)	DFSS를 통한 재질, 두께 최적화	9 2 3 54							
	현경강도 충격흡수미흡	차량현봉시 습격 의 심각한 상해	9 부적절한 재질, 두께 길이선정	6 충돌 충수 증가 확보	현경강도 평가	4 216	재질, 두께, 길이 최적화 (DFSS)	재질, 두께, 길이 최적화 (DFSS)	DFSS를 통한 재질, 두께 최적화	9 2 4 72							
	차체 강성 부족 (장치)	NVH성능저하	5 부적절한 재질 두께선정	5 차체 경감성 해석	실차 TEST	2 50											
	차체 강성 부족 (주행)	NVH성능저하	5 부적절한 재질, 두께선정	5 차체 경감성 해석	실차 TEST	2 50											
	S/BELT 강성부족	S/BELT ANCHOR 벽구 불안족	9 S/BELT 전단력에 경강이 부족한 구조	5 S/BELT 해석	실차 TEST	2 90	구조 변경	차체설계1팀 (08.11/15)	CO2 구조 -> SPOT 구조 W+T 자형에 맞는 구조 개발	9 2 2 36							
	전착성능 부족	내구부식발생	6 전착액이 유동될 수 있는 HOLE 부족	6 전착 TEST	5 180	HOLE 추가	차체설계1팀 (08.11/20)	전착 HOLE 추가	6 3 5 135								

Fig. 14 FMEA of WTBP

(3) Lack of body stiffness

→ Conduct the R vehicle's stiffness analysis

(4) Lack of the mounting stiffness of SEAT BELT

→ Make the new structure fitted in WTBP

(Patent)

(5) Lack of electrodepositing performance

→ The holes of Side sill are added for improving electro-deposition

In particular, The WTBP's SEAT BELT MOUNTING can be assembled through CO₂ welding owing to W-shaped cross-section, because SEAT BELT MOUNTING which applied in WTBP is the first applied structure. However the excessive CO₂ welding can make quality problems. So thus as improving W-shaped cross-section's angle in order to apply spot welding, the dispersion quality of SPOT welding was enhanced (Fig. 15b).

3 Optimization of the New Structure

3.1 WTBP Optimization

3.1.1 QFD-2

The WTBP was optimized through the method of DFSS. The result which was conducted by QFD-2 is that the following factors are selected (Fig. 16).

(1) REINF-CTR ROOF RAIL thickness, length

(2) REINF-CTR PLR OTR UPR thickness, length

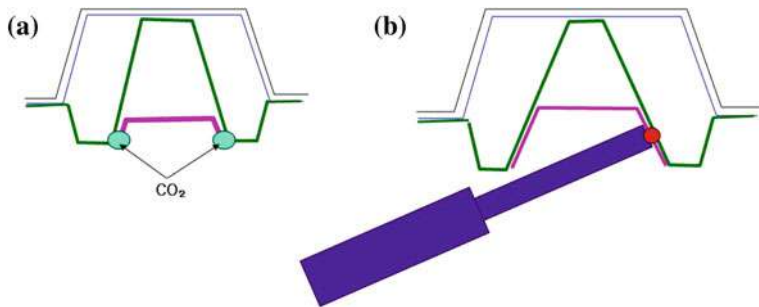


Fig. 15 SEAT BELT MTG DEVELOPMENT. **a, b** SEC A-A

설계파라미터	중요도	SIDE COMP'L 시스템												목표값	달성값			
		REINF-CTR ROOF RAIL		REINF-CTR PLR OTR UPR		REINF-CTR PLR OTR UWR		SIDE SILL OTR		BRKT-CTR PLR OTR UPR		REINF-CTR PUR UPR		REINF-CTR PUR OTR UPR				
CCM	두께 (mm)	길이 (mm)	두께 (mm)	길이 (mm)	두께 (mm)	길이 (mm)	두께 (mm)	길이 (mm)	두께 (mm)	길이 (mm)	두께 (mm)	길이 (mm)	두께 (mm)	길이 (mm)	두께 (mm)	길이 (mm)		
성능	현행값도	5	◎	◎	◎	◎	○	○	○	○	△	○	◎	◎	△	◎	SWR 4.2이상	4.0
	측면충돌	4	◎	◎	◎	◎	△	△	△	△	○	◎	◎	◎	◎	◎	B PLR면 현방 (105mm)이상	114mm
	차체감성	3	△	△	○	△	○	○	△	△	△	○	○	○	△	△	NVH 7-	NVH 7-
구조	초기값	1.8t	243mm	1.8t	SPPC598	1.2t	SPPC440	1.2t	SPPC1180Y	1.8t	SPPC598	1.8t	410mm	2.0t	710			
	최적값	1.4t	243mm	1.6t	SPPC598					1.8t		1.4t	410mm		710			
절대적 중요도		54	54	48	54	20	20	26	26	44	28	48	48	44	54			

Fig. 16 QFD-2

- (3) BRKT-CTR PLR OTR CTR UPR thickness
- (4) REINF-CTR PLR UPR thickness, length
- (5) REINF-CTR PLR OTR UPR length

3.1.2 Definition of Ideal Function

The input factors of the ideal function were selected by the velocity of side impact and roof crash test. The output resulted in the safety space of passengers in BIW and roof crash strength (Fig. 17).

Roof strength and side impact crash TEST have a dynamic characteristic behavior. However all of the impact speed limits were in progress at fixed speed. So the static characteristic behavior was applied (Fig. 18).



Fig. 17 Definition of ideal function

3.1.3 P-DIAGRAM

(Static: Larger the Better Characteristics)

The control factors were 5 parts' s material

And thickness which were selected by QFD-2

Noise factor are as follows (Fig. 17):

1. The effect of reducing the thickness according to the panel formation ($\pm 3\%$)
2. The differences of the tensile strength of the material

The output signal is set up as Side impact (B Pillar passenger survival space) and Roof Crash (SWR) in the condition of Larger the Better Characteristics. The weight and cost Were considered as the optimized was selected (Fig. 19).

3.1.4 Control Parameters

The control parameters' material, thickness and length through QFD-2 were selected by comparing HMC's vehicles with the competitive cars as follows:

- REINF-CTR PLR OTR UPR's material:
440E/590DP,
Thickness: 1.6/1.8/2.0t
- REINF-CTR ROOF RAIL's length:
220/243/260 mm,
Thickness:1.4/1.6/1.8t
- REINF-CTR PLR UPR's length:
210/410/610 mm,
Thickness:1.4/1.6/1.8t
- REINF-CTR PLR OTR CTR's thickness:
1.6/1.8/2.0 t
- REINF-CTR PLR OTR's length:
620/710/800 mm

Fig. 18 The static characteristic behavior

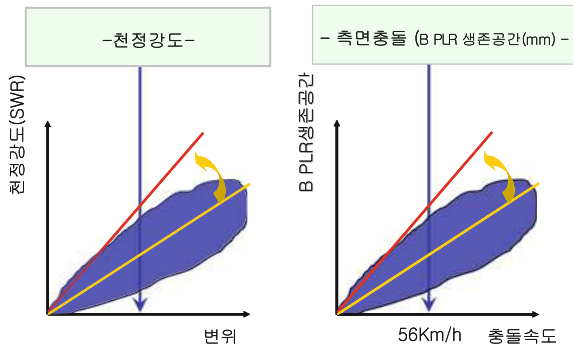


Fig. 19 P-DIAGRAM



3.1.5 The Experiment Results Obtained by the Orthogonal Table L18 and the Contents of Analysis

The orthogonal Table analysis were performed and the result of roof crash test is as follows:

The result (Figs. 20 and 21) of the orthogonal experiment is S/B ratio and MEAM as Fig. 22.

The result of S/N ratio and Mean of B pillar's survival space is Fig. 23.

WTBP's role is very important at ROOF CRASH. While WTBP support the upper area of B pillar which the bending happened and make a moment at ROOF-RAIL SIDE OTR, the bending of the upper area of CTR-PLR UPR and the connection area with ROOF did not happen. Rather the lower area of CTR-PLR OTR which has a large cross-section was deformed instead of the upper area as absorbing Impact Energy. So thus, the ROOF CRASH PERFORMANCE is enhanced (Figs. 24, 25 and 26).

The result of ROOF CRASH came out far above the goal (SWR 4.2). Therefore while keeping the performance of SIDE IMPACT, the weight and cost saving took a consideration for optimization. As a result, the optimized factors are shown as follows (Fig. 27);

	A	B	C	D	E	F	G	F	최적화도		S/N	MEAN
	1	2	3	4	5	6	7	8	N1	N2		
BASE	2	2	2	2	2	2	2	2	4.58	4.52	13.16	4.55
1	1	1	1	1	1	1	1	1	4.31	4.31	12.69	4.31
2	1	1	2	2	2	2	2	2	4.31	4.37	12.75	4.34
3	1	1	3	3	3	3	3	3	4.32	4.28	12.67	4.3
4	1	2	1	1	2	2	3	3	4.46	4.38	12.91	4.42
5	1	2	2	2	3	3	1	1	4.35	4.35	12.77	4.35
6	1	2	3	3	1	1	2	2	4.38	4.42	12.87	4.4
7	1	3	1	2	1	3	2	3	4.42	4.38	12.87	4.4
8	1	3	2	3	2	1	3	1	4.39	4.37	12.83	4.38
9	1	3	3	1	3	2	1	2	4.39	4.40	12.86	4.395
10	2	1	1	3	3	2	2	1	4.35	4.31	12.73	4.33
11	2	1	2	1	1	3	3	2	4.45	4.44	12.96	4.445
12	2	1	3	2	2	1	1	3	4.34	4.29	12.7	4.315
13	2	2	1	2	3	1	3	2	4.38	4.52	12.96	4.45
14	2	2	2	3	1	2	1	3	4.39	4.45	12.91	4.42
15	2	2	3	1	2	3	2	1	4.47	4.40	12.94	4.435
16	2	3	1	3	2	3	1	2	4.64	4.47	13.17	4.555
17	2	3	2	1	3	1	2	3	4.41	4.32	12.8	4.365
18	2	3	3	2	1	2	3	1	4.56	4.41	13.03	4.485
최적안	2	1	2	1	2	1	2	1	4.51	4.44	13.02	4.475

Fig. 20 ROOF CRASH—SWR

	A	B	C	D	E	F	G	F	측면충돌		S/N	MEAN
	1	2	3	4	5	6	7	8	N1	N2		
BASE	2	2	2	2	2	2	2	2	115.65	113.21	41.14	114.05
1	1	1	1	1	1	1	1	1	114.77	109.10	40.97	111.9
2	1	1	2	2	2	2	2	2	114.21	112.40	41.08	113.3
3	1	1	3	3	3	3	3	3	117.19	112.64	41.2	114.9
4	1	2	1	1	2	2	3	3	115.47	112.49	41.13	114
5	1	2	2	2	3	3	1	1	114.90	110.89	41.05	112.9
6	1	2	3	3	1	1	2	2	115.90	110.12	41.05	113
7	1	3	1	2	1	3	2	3	114.09	111.24	41.03	112.7
8	1	3	2	3	2	1	3	1	113.26	112.42	41.05	112.8
9	1	3	3	1	3	2	1	2	115.51	110.65	41.06	113.1
10	2	1	1	3	3	2	2	1	116.29	112.01	41.14	114.2
11	2	1	2	1	1	3	3	2	114.30	112.40	41.09	113.4
12	2	1	3	2	2	1	1	3	115.78	111.37	41.1	113.8
13	2	2	1	2	3	1	3	2	116.80	112.74	41.19	114.8
14	2	2	2	3	1	2	1	3	116.59	108.17	41	112.4
15	2	2	3	1	2	3	2	1	114.76	113.71	41.16	114.2
16	2	3	1	3	2	3	1	2	116.26	111.42	41.12	113.8
17	2	3	2	1	3	1	2	3	116	112.79	41.17	114.4
18	2	3	3	2	1	2	3	1	113.55	112.62	41.07	113.1
최적안	2	1	2	1	2	1	2	1	114.24	113.86	41.17	114.43

Fig. 21 SIDE IMPACT (B-PLR SURVIVAL SPACE)

- weight and cost reducing factor while keeping SIDE IMPACT → B,D,F
- Performance → A,H, C
- Cost → E,G

3.1.6 The Optimal Results by DFSS

The result that estimates ROOF CRASH by DFSS is that S/N: -2.1 %, MEAN: -0.5 %. In the case of SIDE IMPACT, S/N: +0.1 %, MEAN: +0.17 % (Fig. 28).

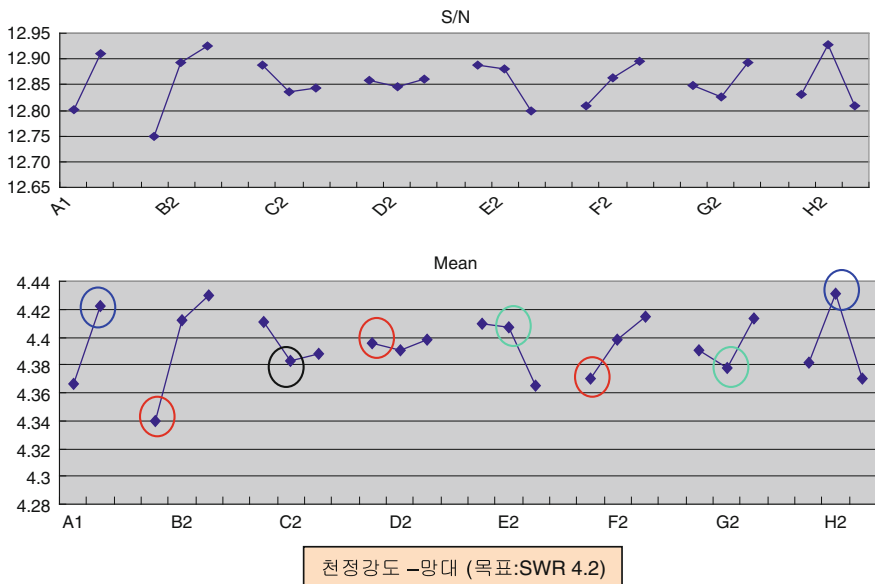


Fig. 22 ROOF CRASH S/N and MEAN

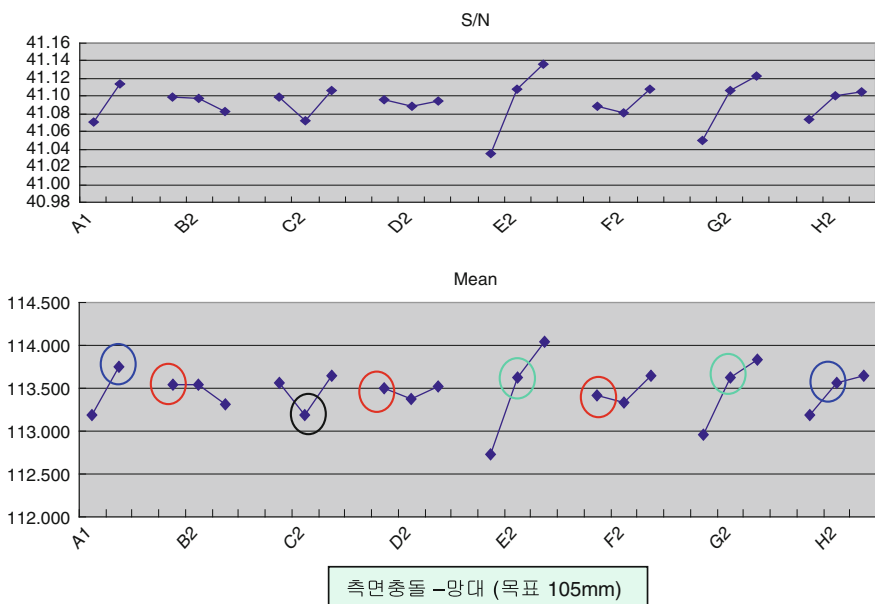


Fig. 23 Side Impact S/N and MEAN

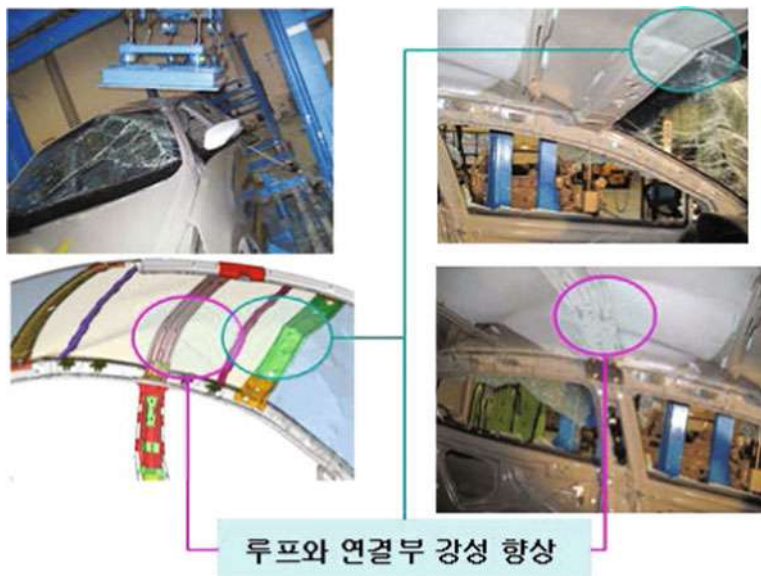
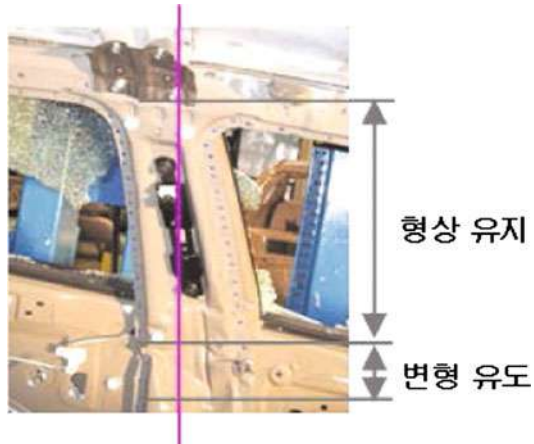


Fig. 24 WTBP ROOF CRASH TEST1

Fig. 25 WTBP ROOF
CRASH TEST 2



The result comes out as predicted initially. Thus the additional reduction of the weight and cost is possible. Although the result of the confirmation analysis in the performance of ROOF CRASH and SIDE IMPACT is different as expected, the volume of difference is small and is able to be considered as same level.

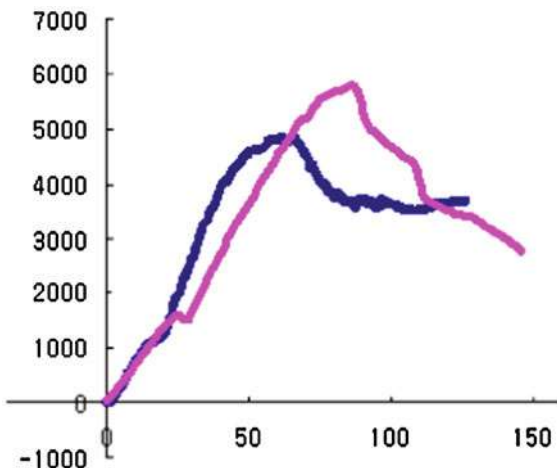


Fig. 26 THE RESULT OF ROOF CRASH

	A	B	C	D	E	F	G	H
초기안	레벨 2							
최적안	레벨 2	레벨 1	레벨 2	레벨 1	레벨 2	레벨 1	레벨 2	레벨 2

	제어인자	1수준	현수준	
			2수준	3수준
A	① REINF-CTR PLR OTR UPR 재질	SPRC440E	SPRC590	
B	② REINF-CTR PLR OTR UPR 두께	1.6	1.6	2.0
C	③ REINF-CTR ROOF RAIL 길이	220	243	260
D	④ REINF-CTR ROOF RAIL 두께	1.4	1.6	1.8
E	⑤ REINF-CTR PLR UPR 길이	210	410	610
F	⑥ REINF-CTR PLR UPR 두께	1.4	1.6	1.8
G	⑦ REINF-CTR PLR OTR CTR 두께	1.6	1.6	2.0
H	⑧ REINF-CTR PLR OTR 길이	620	710	800

Fig. 27 THE RESULT OF OPTIMIZATION

3.1.7 The Effects of WTBP

The WTBP makes SIDE IMPACT be improved from 97 to 125 mm (IIHS passenger survival space) and ROOF CRASH be enhanced from 3.7 to 5.2 innovatively. In the other hand, the new structure is able to reduce 5.5 kg/per vehicle by applying 980 Mpa and change the material and thickness of the other parts. The cost saving is approximately 5,500 won/per vehicle.

구분	천정강도		측면충돌	
	S/N	MEAN	S/N	MEAN
BASE 사양	12.99	4.484	41.12	113.751
최적사항	12.81	4.44	41.13	113.949
이득	-0.18 (-2.1%)	-0.024 (-0.5%)	0.1%	0.17%

구분	천정강도		측면충돌	
	S/N	MEAN	S/N	MEAN
BASE 사양	13.16	4.55	41.14	114.05
최적사항	13.02	4.475	41.17	114.43
이득	-1.6%	-1.6%	0.3%	0.3%

Fig. 28 Optimal specifications of analysis

4 Conclusion

- (1) The WTBP which had not seen in the existing vehicle was developed that improved the ROOF CRASH and SIDE IMPACT performance. And through TRIZ, WTBP is able to confirm 15 patents.
- (2) The CTR PLR OTR was developed by applying 980 Mpa ultra high tensile strength improving performance and reducing the weight and cost.
- (3) As applying cold ultra high strength steel into the B-pillar by patent, the freedom of the design was increased.
- (4) The WTBP development with SEAT BELT MT'G gave a help to improve the body structure of the HMC.

References

1. Rollover crash Study—Vehicle design and occupant injuries, George Rechnitzer, SAE 05-13-1996
2. Roof Strength Requirement for Vehicles Involved in Rollover Crash, Sreekantha Das, SAE, 04-14-2008
3. Crashworthiness Assessment of Side Impact of an Autobody with 60TRIP Steel for Side Members
4. A study of various side-impact configurations, P. Cooley, SAE, 01-01-1979

The Design of Car's Crash Box Based on the Section Force

Man Yang

Abstract The crash box plays a key role in the car's low speed crash performance, and also important for high speed crash. Currently, the styling design goes ahead of structure design in a car's development, leading to the poor performance of the crash box which is designed under the constraint of styling. In this paper, a new method is put forward for coupling the design of styling and crash box's crash performance in the styling design phase of an B-class car. In this method, basing on the crash load case, the crash box's section force target is deduced by its energy absorption ratio. Then the design parameter is deduced. With this method, the compatibility between the styling and crash performance is evaluated during the early phase of the car's development. A compatible design of styling and crash performance can be acquired by the optimization of styling and under this method. Finally, the B-class car's crash result is shown in this paper for the verification of the effectiveness and engineering-feasibility of this method.

Keywords Finite element analysis · Structural optimization · Section force · Crash box · Crash and safety

F2012-F01-007

M. Yang (✉)

Guangzhou Automobile Group Co., LTD., GAC Automotive Engineering Institute,
Guangzhou, Guangdong 510640, China

1 Backgound

The vehicle's maintenance due to low speed crash is an important part of the auto claims. Rearch council for automobile repairs (RCAR) recommends a regulation of 15 km/h offset rigid barrier crash, which is call RCAR15 for short in this paper, to evaluate the low speed crash performance of the vehicle. In this regulation, the vehicle's low speed crash performance is acceptable if the structure (the frontal rail always), behind the crash box remains intact [1, 2]. Due to the influence of this regulation, the low speed crash performance discussed in this paper is based on this RCAR15 regulation (Figs. 1 and 2).

Currently, CAE optimization base on the FEA method is quite effective for the design of crash box [3–5]. However, this traditional method is CAD data dependent. In fact, the CAD data cannot be available until the vehicle's frontal styling is finished, when the package of the engine bay is finished. Under this method, if the performance of the crash box is poor, the compensation is replacement of a higher strength material which leads to a higher crush force. As a result, a poor deformation mode of “severe buckle/crush of the rail, together with intact crash box” is quite probable during high speed crash .

The problem above shows that, the balance between high speed crash performance and low speed crash performance is difficult with the traditional, CAD data dependant CAE optimization.

2 A Method Based on Section Force for Crash Box Design

The author puts forward a new method for crash box design, basing on section force. With this method, the detailed design of the crash box is simultaneous and coupled with the design of the styling as well as engine bay package. With this method, a detailed crash box CAD data with good low speed crash performance becomes an input condition of the BIW's CAD model building, and therefore, a good balance between high and low speed crash performance is imaginable.

Briefly, in this method, the initial crash energy is calculated based on the vehicle's kerb mass first. The crush force is then deduced based on its length and the energy it absorbs. Third, the candidate gauges for the crash box is determined with the crush force formula. Finally, the design is accomplished under the requirement of the optimization method.

In case the final gauge is engineering unacceptable, the crash box's length is reset with balance with the engine bay package and styling, and the 4 steps above go through again until the suitable gauge is engineering unacceptable.

The precondition of this method is that, the crash box, with good low speed crash performance, crush axially with the deformation as Fig. 3 and crush force like Fig. 4.

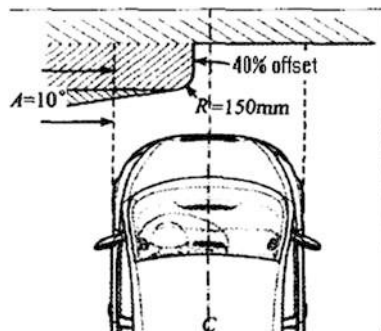


Fig. 1 The RCAR15 loadcase

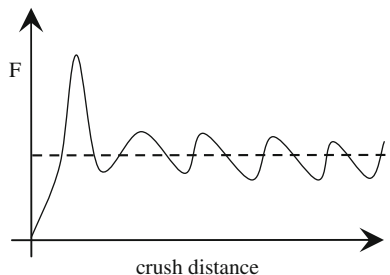


Fig. 2 A typical lowspeed crash accident



Fig. 3 An axial crush

Fig. 4 Section force of axial crush



The crash box design of a B-class car is shown below as a detailed example of this method.

2.1 Calculate the Initial Crash Energy

In the preliminary of this car's concept design, the kerb mass, which is 1500 kg, is available. Therefore, the initial crash energy of RCAR15 can be calculated by the formula below.

$$E = 1/2mV^2 \quad (1)$$

In this case, the energy is 13,021 J.

2.2 Deduce the Crash Box's Crush Force

Based on the CAE experience of the benchmark cars, the crash box absorbs about 45–50 % of the initial crash energy during RCAR15 crash. As a conservative estimate, 50 % is adopted in this paper. The length of the crash box is set to 120 mm temporally under the compromise of styling and engine bay package. Therefore, the crush force can be deduced,

$$F = E * \eta/d = 13021 * 0.5/0.12 = 54.2 \text{ KN} \quad (2)$$

In other words, the crush force must be greater than 54.1 KN to meet a reasonable low speed crash performance.

2.3 Determine the Candidate Gauges of the Crash Box

Because of the rectangular transection of the crash box discussed in the paper, the formula below is recommended for the determination of the crash box's material and the size.

Table 1 The crush force of the gauges with 1.5 mm thickness

No.	Thickness (t/mm)	Width (a/mm)	Length (d/mm)	Material	Area/mm ²	Crush force (F/KN)
1	1.5	50	100	H220BD	441	27.79
2	1.5	55	105	H220BD	471	28.24
3	1.5	60	110	H220BD	501	28.67
4	1.5	65	115	H220BD	531	29.09
5	1.5	50	100	SPHD	441	28.70
6	1.5	55	105	SPHD	471	29.17
7	1.5	60	110	SPHD	501	29.61
8	1.5	65	115	SPHD	531	30.04
9	1.5	50	100	H340LAD	441	39.24
10	1.5	55	105	H340LAD	471	39.88
11	1.5	60	110	H340LAD	501	40.49
12	1.5	65	115	H340LAD	531	41.07
13	1.5	50	100	HC420LA	441	48.08
14	1.5	55	105	HC420LA	471	48.86
15	1.5	60	110	HC420LA	501	49.60
16	1.5	65	115	HC420LA	531	50.32

$$F = 6.69(a + b)^{\frac{1}{4}} t^{\frac{7}{4}} \left(\int_0^{\varepsilon_f} \sigma(\varepsilon) d\varepsilon / \varepsilon_f + \sigma_y \right) \quad (3)$$

In the formula, F is the crush force. a is the length of the rectangular transition, with the width b. T is the thickness. σ_y is the yield stress of the material. $\sigma(\varepsilon)$ is the plastic stress-strain function. ε is the plastic strain, with the failed plastic strain ε_f .

The wildly used thickness for crash box panel including, 1.5, 1.8, 2.0 and 2.2 mm; the common transection sizes is, 50 mm × 100 mm, 55 mm × 105 mm, 60 mm × 110 mm and 65 mm × 115 mm; the typical material is steel, including the steel type of, DC54, H220BD H340LAD, HC420LA.

Based on the formula 3, an orthogonal experimental calculation, throughout the parameter of thickness, transection size, steel type is required, to get the crush force. The results is listed out from Tables 1, 2, 3 and 4.

Based on this method, the gauges with crush force greater than 54.2 KN, can be list into the candidates for the crash box of this car.

2.4 Determine the Best Gauge for the Crash Box

Currently, the economy optimization, with the consideration of performance, is the principle for a car's development. As for the crash box's economy, mass optimization of the structure is the most important, followed by the steel type (the high

Table 2 The crush force of the gauges with 1.8 mm thickness

No.	Thickness (t/mm)	Width (a/mm)	Length (d/mm)	Material	Area/mm ²	Crush force (F/KN)
1	1.8	50	100	H220BD	527.04	38.24
2	1.8	55	105	H220BD	563.04	38.86
3	1.8	60	110	H220BD	599.04	39.45
4	1.8	65	115	H220BD	635.04	40.02
5	1.8	50	100	SPHD	527.04	39.49
6	1.8	55	105	SPHD	563.04	40.13
7	1.8	60	110	SPHD	599.04	40.74
8	1.8	65	115	SPHD	635.04	41.33
9	1.8	50	100	H340LAD	527.04	53.99
10	1.8	55	105	H340LAD	563.04	54.87
11	1.8	60	110	H340LAD	599.04	55.71
12	1.8	65	115	H340LAD	635.04	56.51
13	1.8	50	100	HC420LA	527.04	66.15
14	1.8	55	105	HC420LA	563.04	67.22
15	1.8	60	110	HC420LA	599.04	68.25
16	1.8	65	115	HC420LA	635.04	69.23

Table 3 The crush force of the gauges with 2 mm thickness

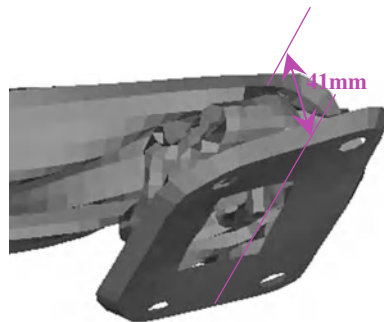
No.	Thickness (t/mm)	Width (a/mm)	Length (d/mm)	Material	Area/mm ²	Crush force (F/KN)
1	2.0	50	100	H220BD	584	45.98
2	2.0	55	105	H220BD	624	46.73
3	2.0	60	110	H220BD	664	47.44
4	2.0	65	115	H220BD	704	48.12
5	2.0	50	100	SPHD	584	47.48
6	2.0	55	105	SPHD	624	48.25
7	2.0	60	110	SPHD	664	48.99
8	2.0	65	115	SPHD	704	49.70
9	2.0	50	100	H340LAD	584	64.93
10	2.0	55	105	H340LAD	624	65.98
11	2.0	60	110	H340LAD	664	66.99
12	2.0	65	115	H340LAD	704	67.95
13	2.0	50	100	HC420LA	584	79.54
14	2.0	55	105	HC420LA	624	80.83
15	2.0	60	110	HC420LA	664	82.07
16	2.0	65	115	HC420LA	704	83.25

strength steels is always more expensive than the mild steels). Because of the same density of the candidate steel types, the mass optimization is identical to the transition's area optimization.

Based on the requirements above, the candidate gauge of line 10 in Table 2 is the target. Finally, the superb parameters of the crash box are, 1.8 mm in

Table 4 The crush force of the gauges with 2.2 mm thickness

No.	Thickness (<i>t/mm</i>)	Width (<i>a/mm</i>)	Length (<i>d/mm</i>)	Material	Area/mm ²	Crush force (<i>F/kN</i>)
1	2.2	50	100	H220BD	640.64	54.32
2	2.2	55	105	H220BD	684.64	55.21
3	2.2	60	110	H220BD	728.64	56.05
4	2.2	65	115	H220BD	772.64	56.86
5	2.2	50	100	SPHD	640.64	56.10
6	2.2	55	105	SPHD	684.64	57.01
7	2.2	60	110	SPHD	728.64	57.88
8	2.2	65	115	SPHD	772.64	58.72
9	2.2	50	100	H340LAD	640.64	76.71
10	2.2	55	105	H340LAD	684.64	77.96
11	2.2	60	110	H340LAD	728.64	79.15
12	2.2	65	115	H340LAD	772.64	80.29
13	2.2	50	100	HC420LA	640.64	93.98
14	2.2	55	105	HC420LA	684.64	95.50
15	2.2	60	110	HC420LA	728.64	96.96
16	2.2	65	115	HC420LA	772.64	98.36

Fig. 5 Crash box deformation of CAE result

thickness, 55 mm × 105 mm in transection, with the steel type of HC340LAD. Due to the engineering acceptance(neither expensive nor difficult in process) for these parameters, the design of the crash box is finished at one time.

2.5 Test Verification

With the 4 steps above, the crash box detailed CAD data and material is available during the concept design phrase of the car. The design is adopt into the physical test car. The figures below show the crash box's CAE deformation based on the CAD data, and test (Figs. 5, 6, 7 and 8).

Fig. 6 Crash box deformation of test result



Fig. 7 Rail deformation of CAE result

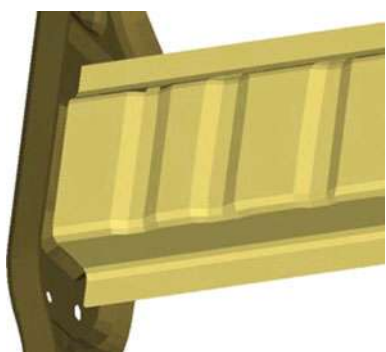


Fig. 8 Rail deformation of test result



The figures above show that, the deformation mode of the CAE result is similar to that of the test. The remained length of the crash box after crash is 38 mm in CAE result, with 41 mm in test result. Meanwhile, the frontal rail behind the crash box remains intact both in the CAE and test result. Obviously, this method is quite effective in the design of crash box.

3 Conclusion

The low speed crash performance is important to the vehicle. The author puts forward a new method based on the section force. With this method, the detailed design of the crash box is simultaneous and coupled with the design of the styling and engine bay package. The crash box economy is good, with the consideration of balance between high and low speed crash performance. Finally, an example of a B-class car's crash box design, is shown in this paper. The comparison between the CAE and test result, proves that this method is quite effective.

References

1. Mahmood HF, Paluszny A (1986) Analytical technique for simulating crash response of vehicle structures composed of beam elements. SAE 860820
2. Mahmood HF, Paluszny A (1988) Crash analysis of thin-walled beam type structure. SAE 880894
3. Castejon L, Cuartero J, Clemente R et al (1998) Energy absorption capability of composite materials applied to automotive crash absorbers design. SAE 980964
4. Tarigopula V, Langseth M, Hopperstad OS et al (2006) Axial crushing of thin-walled high-strength steel sections. Int J Impact Eng 32(2):847–882
5. Han DC, Park SH (1999) Collapse behavior of square thin-walled columns subjected to oblique loads. Thin Walled Struct 35:167–184

Vehicle Front Crash Design Accounting for Uncertainties

Markus Zimmermann

Abstract Uncertainty is naturally present in the early development phase of vehicle design: some parameters cannot yet be specified exactly, others may have to be changed over the course of development. When this results in the loss of required performance, expensive counter measures have to be taken. In vehicle architectures, this problem is even more severe, because several vehicles may be affected. A new approach for the design of robust vehicle structures is presented here and applied to the USNCAP frontal crash. It relies on a systems engineering technique, the V-model, where design goals for the vehicle are systematically broken down into subsystem and component design goals. Design goals for components are admissible ranges, i.e. *solution spaces*, for their functional properties within which the final design can be realized. They are uncoupled in the sense that the admissible range for the properties of one component does not depend on the choice of other components' properties. Every design within the solution space delivers the required performance. Susceptibility to uncertainty is reduced by seeking large solution spaces. Solution spaces are computed using a particular algorithm that was developed at BMW. As an example, the design of a front rail for its respective solution space is shown.

Keywords Crash design · Uncertainty · Robust design · Early design phase · Systems engineering

F2012-F01-009

M. Zimmermann (✉)
Department of Vehicle Safety, BMW, Munich, Germany

1 Introduction

Vehicle development for crash is subject to various uncertainties. In the early design phase, little is known about the final state of the vehicle, and only a coarse layout is specified. Crash analysis or design for crash has to rely on assumptions that are likely to change. During the design process, information becomes available progressively as the design is developed in detail. At the same time, however, it is subject to change due to functional requirements on the vehicle from other disciplines such as acoustics, driving dynamics, etc. Yet another source of uncertainty is the manufacturing process due to limited capabilities to realize an intended design exactly as specified.

Uncertainty may lead to the loss of functional performance. This becomes even more critical, if several vehicles are developed on the same platform with communal body parts. Sensitivities are more difficult to assess, and the loss of robustness may lead to multiple failure. Design corrections in a late design phase are extremely complicated, as they have to be made in accordance with all vehicles involved. Consequently, there is a need to develop vehicles such that they meet design goals *and* are as robust as possible with respect to unintended variations.

Classical optimization techniques are inappropriate development tools in this context, as they maximize functional performance only, which often leads to highly sensitive and less robust designs. More advanced methods like Robust Design Optimization seek for optima that are robust with respect to a specified variability of uncertain parameters. Unfortunately however, this information, i.e. the degree to which uncertain parameters may vary, is not known in an early design phase and should be optimized to increase robustness. Therefore, Robust Design Optimization is not applicable.

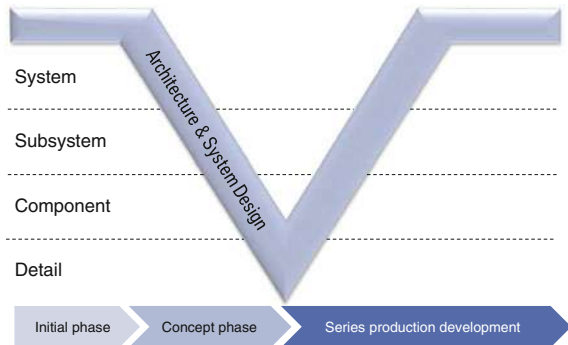
The approach presented here adopts a systems engineering technique so as to separate the vehicle system from its subsystems and components. On each level, performance and robustness can be optimized. On the subsystem level, solution spaces for component design are computed and optimized with respect to size using a special algorithm that was developed at BMW.

2 A Systems Engineering Approach for the USNCAP Front Crash

2.1 The V-Model

In a development process according to the V-Model, see [1], design goals for the vehicle (system level) are broken down into design goals for underlying subsystems, e.g., the vehicle structure. Similarly, component design goals are derived from the subsystem design goals. This process is called *architecture & system design* and is applied top-down to all design disciplines such as crash, driving

Fig. 1 The V-model of systems engineering



dynamics, etc. It is visualized in Fig. 1 as the left leg of the V. Components such as structural members of the vehicle body are then designed to reach their respective design goal. In the *integration & verification* process (bottom-up), components, subsystems and the vehicle are tested so as to ensure that all design goals are reached, shown as the right leg of the V in Fig. 1.

2.2 The USNCAP Frontal Crash

In a frontal crash according to the USNCAP test program, a vehicle hits a rigid barrier at the speed of 56 km/h with 100 % overlap, see Fig. 2a. The crash performance of the vehicle is assessed by injury measures, such as the head injury criterion value or the chest deflection, which are simulated by a crash test dummy.

2.3 System to Subsystems

For the USNCAP frontal crash, the vehicle can be seen as a system of two subsystems: the vehicle structure and the restraint system. The structure decelerates the passenger cell, thus providing the boundary conditions for the restraint system which slows down the passenger. If the maximum value of the acceleration signal a_{\max} (sliding mean filter applied, see Fig. 2b) does not exceed the limit value a_{limit} , the restraint system can avoid critical injury by slowing down the passenger smoothly, as shown in [2]. The subsystems can be separated and designed independently by adopting the design goals that (1) $a_{\max} < a_{\text{limit}}$ for the vehicle structure and (2) the restraint system is to keep the injury levels subcritical for $a_{\max} = a_{\text{limit}}$.

2.4 Subsystem to Components

In a frontal crash, the vehicle acceleration depends on the mechanical behaviour of its structural members. *Structural components* are parts of these members the

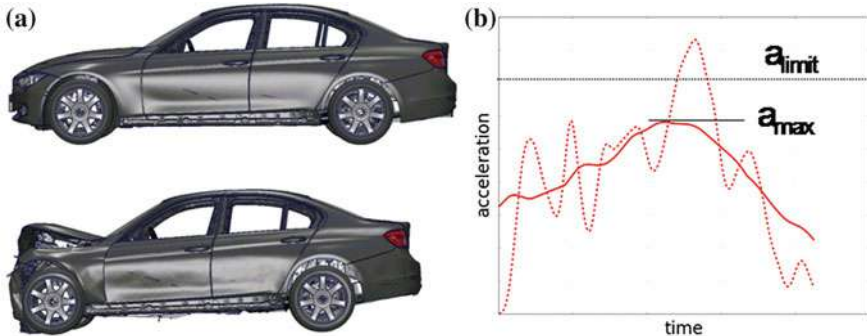


Fig. 2 **a** A vehicle in the USNCAP frontal crash. **b** Acceleration signal measured at the b-pillar (*dotted line* with cfc60 filter, *solid line* with sliding mean filter)

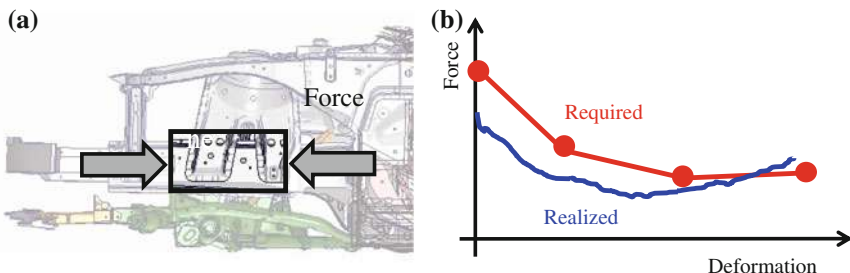


Fig. 3 **a** Vehicle front structure and the component *front rail 02*. **b** Force-deformation characteristics of the component

behaviour of which can be described by a relation between their longitudinal deformation and the associated resisting force, see Fig. 3. It is shown in [2, 3] that these force–deformation characteristics entirely determine the overall vehicle deformation and the vehicle acceleration. Therefore, they have to be specified as component design goals.

In a full vehicle Finite Element simulation, force–deformation characteristics can be measured. One could design a vehicle structure that satisfies the subsystem design goal $a_{\text{max}} < a_{\text{limit}}$ or even try to minimize a_{max} using numerical optimization techniques. The result would be one force–deformation characteristic for each component, serving as a component design goal. Realizing it in the final vehicle design would be practically impossible however, due to the uncertainties previously mentioned. The inevitable deviation from the required state would be difficult to assess, as the crash system is highly sensitive. Therefore, the approach adopted here identifies a *solution space*, i.e. range of permissible force–deformation characteristics. In this range, all elements deliver the required subsystem performance $a_{\text{max}} < a_{\text{limit}}$ in arbitrary combination of their properties.

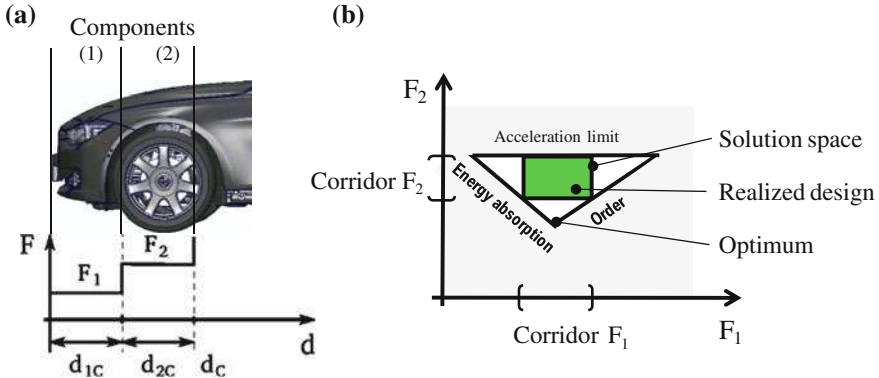


Fig. 4 a Simplified vehicle front structure with two components characterized by the deformation loads F_1 and F_2 . b The solution space in the F_1 - F_2 design space

3 Solution Spaces for Robust Design

3.1 Simplified Crash Structure

In order to explain the concept of solution spaces, a simplified crash structure is considered. The front section consists only of two components as shown in Fig. 4a. The components deform at the forces F_1 and F_2 , respectively. Figure 4b shows the design space for F_1 and F_2 . All feasible designs lie in the triangular region. Outside the triangular region, designs either (1) violate the required order of deformation, (2) do not absorb the kinetic energy entirely causing an abrupt stop of the passenger cell, or (3) deform at a force level at which the acceleration exceeds the limit value.

Within the triangular region lies a solution space. Due to its rectangular shape, it can be expressed as a set of permissible intervals or *corridors* for F_1 and F_2 . Within the corridors, the choice of F_1 is independent of F_2 and vice versa, i.e. they are *decoupled*. Therefore, the corridors may serve as design goals for the components 1 and 2.

Some good designs in the triangular region that are not included in the rectangular solution space are ignored. This loss of solution space is associated with decoupling the parameters in order to obtain independent design goals for each component.

3.2 General Crash Structure

For general crash structures, a solution space may be computed using, first, a substitute crash model as shown in Fig. 5a and, second, a particular algorithm to

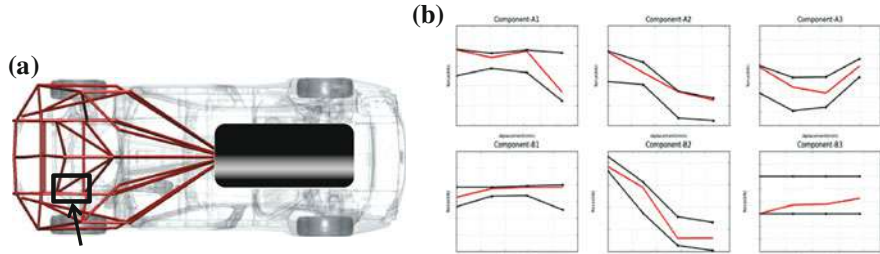


Fig. 5 **a** Substitute crash model. The component *front rail section 2* is highlighted. **b** Example corridors for structural components (black lines) and one random test configuration of force–deformation characteristics (red lines)

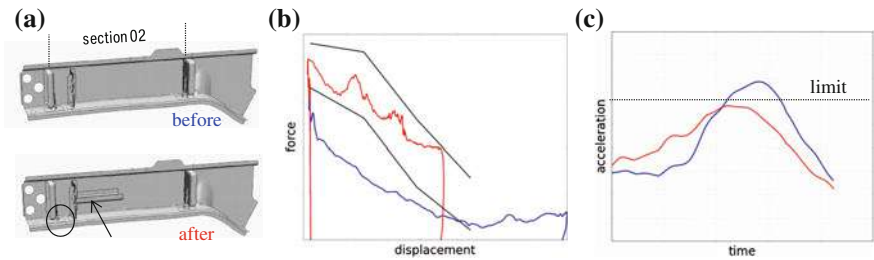


Fig. 6 **a** Front rail section 2, *before* and *after* the modification. Associated **b** corridor and force–deformation characteristics and **c** accelerations

compute solution spaces. The substitute crash model simulates the vehicle acceleration for prescribed force–deformation characteristics of all relevant structural components. Each component is parameterized by four discrete force values, shown as dots in Fig. 3b. One vehicle model includes typically nine structural components to be designed. Associated with this are 36 force values as degrees of freedom. If several vehicle models are considered on one platform, the number of force values may exceed 100.

The solution space algorithm seeks large corridors for all force–deformation characteristics, as described in [4]. Some examples are shown in Fig. 4b. Designs lying within the corridors satisfy $a_{\max} < a_{\text{limit}}$.

4 Example

When all component design goals are known, structural components can be designed. An example for designing the front rail section 2 is shown in Fig. 6. In the initial design, the force–deformation characteristic of the component lies outside the associated corridor and the acceleration of the vehicle structure exceeds the limit value. The front rail section 2 can be immediately identified as

relevant parameter. The modification shown in Fig. 6a shifts the force-deformation characteristic into the corridor, thus decreasing the acceleration maximum below the limit value. Once within the corridor, the distance between the realized force-deformation characteristic and the corridor boundaries quantifies the tolerance to the variation of uncertain parameters.

5 Conclusions

The V-model of systems engineering distinguishes between design work on the system, subsystem and component level. Design goals for one level are successively broken down into design goals of the underlying level. Following this procedure, complex systems such as vehicles sharing communal body parts can be developed systematically such that they reach performance goals and are robust at the same time.

Deriving design goals for structural components in crash development is difficult due to sensitive and non-linear crash mechanics. Vehicle structures may be developed for the USNCAP front crash by computing a solution space and component design goals. In the early design phase, the vehicle layout may be changed to provide larger solution spaces for higher robustness and less susceptibility to uncertainty. In the late design phase, structural members are designed in detail to lie within the solution space, thereby ensuring a robust crash performance.

References

1. Haberfellner R, de Weck O, Fricke E, Vössner S (2012) Systems engineering, Grundlagen und Anwendung. Orell Füssli Verlag, Zürich
2. Kerstan H, Bartelheimer W (2009) Innovative Prozesse und Methoden in der Funktionsauslegung—Auslegung für den Frontcrash. Fahrzeugsicherheit, VDI-Berichte, vol 2078. Düsseldorf, VDI Verlag
3. Fender J, Duddeck F, Zimmermann M (2012) Hybrid Regression and physics based vehicle crash modelling. In preparation for submission to structural and multidisciplinary optimization
4. Zimmermann M, Edler von Hoessle J (2012) Computing solution spaces for robust design. Submitted for publication to the international journal for numerical methods in engineering in 03/2012

The Initial Velocity Value of Coach in Frontal Impact Research

Zhaokai Li, Qiang Yu, Junjie Chen, Qiang Li, Guosheng Zhang and Xiao Yuan

Abstract This paper belongs to the technical field of coach passive safety. The frequent occurrence of frontal collision causes the serious destroyed coaches and heavy casualties for this vehicle have great load and various occupants. So far, not any laws or regulations about coach frontal collision have been formulated yet. Therefore, it is difficult to complete anything whether the theory and test research in frontal collision of coach or safety evaluation of coach structure. The initial impact velocity value will be put forward based on a lot of research. Taking a large-sized coach as the object of study, we built the finite element model accurately and used large deformation finite element analysis method and explicit dynamic analysis software LS-DYNA to simulate impact between the coach and a rigid barrier in a series speeds as 10, 20, 30, 40 and 50 km/h so as to analyse the influences of different speed on coach collision and discuss the initial velocity value in frontal impact of coach. In contrast to deformation of vehicle which at different impact speed, we get the deformation mechanism of the front bus and then further analyse the curve of changed driver space and the energy absorption characteristics of the main assembly in different impact velocities. The results consistently show, 30 km/h could be considered as the of initial impact velocity

F2012-F01-010

L. Zhaokai (✉) · Y. Qiang
School of Automobile, Chang'an University, Xian, China

C. Junjie
Proving Ground for Construction Machinery & Refit Military Vehicles of CAM,
Beijing, China

L. Qiang · Z. Guosheng
Research Institute of Highway Ministry of Transport, Beijing, China

X. Yuan
Xi'an Public Transport Corporation, Xian, China

value in frontal impact. There are few studies in this field domestically and abroad so that some experimental data are needed. This paper preliminarily put forward the initial velocity value that apply to frontal impact test and structural safety evaluation of large bus in the point of the vehicle deformation, driving space change and energy absorption difference of coach assembly and parts. The result can provide reference for simulation analysis, real vehicle test and standard setting in frontal impact of coach speed selection.

keywords Coach · Frontal impact · Initial velocity · Energy absorption · Driving area

1 Introduction

The character of coach which is much larger than the passenger car in gross weight and passenger capacity determine the collision moment is even more serious [1]. However, the coach is far behind of passenger car in the crash safety regulations or standards. Passenger car collision standard (such as FMVSS208,ECE R94 and GB11551-2003, etc.) details the initial impact velocity(IIV) as a basic problem [2, 3].

In coach frontal crash test, inappropriate IIV is not conducive to evaluate the security of coach structure. Coach enterprises are difficult to achieve goals of design and improvement due to lack of a unified IIV standard. The establishment and improvement of coach frontal crash test standard system are also urgently need a reasonable IIV.

2 Creating of Coach Model

2.1 Characteristic of Coach

The 6127-type coach have integral type body, rear engine and independent air suspension. The frame of grille of chassis, side wall and front wall used Q345 or 16Mn steel, and skin used Q235A steel (see Fig. 1). Table 1 shows the part of the information for the coach.

2.2 Finite Element Model

The three-dimensional model was established strictly according to the body frame drawings, (see Fig. 2). The grid density turn sparse from front to back of the coach in order to reduce the non-key areas of the grid scale (see Fig. 3).



Fig. 1 The 6127-type coach

Table 1 Part information for the coach

Length/mm	11,980	Fork overhang/mm	2,400
Width/mm	2,485	Rear overhang/mm	3,380
Height/mm	3,720	Rated passenger capacity	51
Front track/mm	2,020	Complete vehicle shipping mass/t	13.0
Rear track/mm	1,860	Gross vehicle weight/t	17.2

Fig. 2 Body frame model

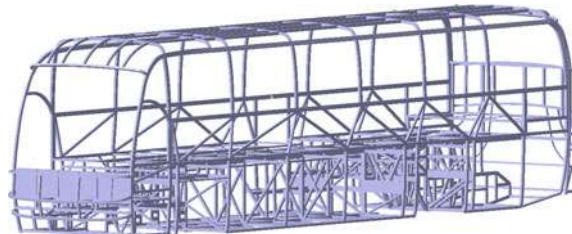


Fig. 3 Finite element model of the coach



Table 2 Coach finite element model information

Part of model	Average grid size(mm)	Material type	Element type
Front frame and skin	10	Piecewise liner plasticity	Shell
Central frame and skin	15		
Rear frame and skin	25		
Transmission shaft	100	Plastic kinematic	Solid
Passenger/Luggage	/	/	Mass

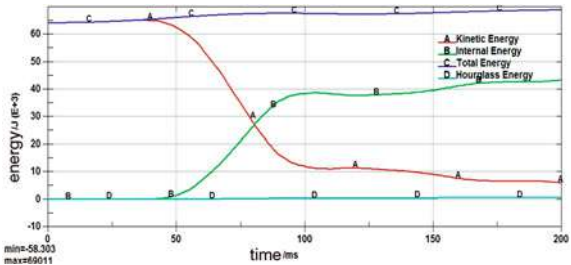
Fig. 4 The energy balance curve

Table 2 show average grid size, material type and element type information of the coach model in different parts.

3 Research Path

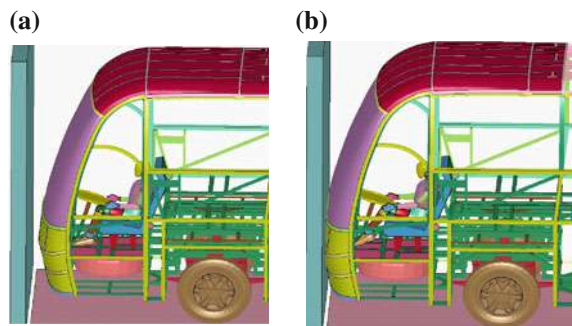
The IIV is selected at the five kinds of levels of 10, 20, 30, 40 and 50 km/h, and the collisions between the coach and rigid barrier are hold under these conditions. The IIV of passenger car is 48.3 km/h which is near 50 km/h. The collision energy under this velocity is several times more than passenger cars. Therefore, 50 km/h can be take as the upper speed limit. But the lower limit of 10 km/h still need some proof.

3.1 The Influence Verification of 10 km/h Collision

3.1.1 Impact Energy

The energy balance curve satisfied the regulation that “the internal energy increases while kinetic energy decreases, the hourglass is less than five percent and the total energy conservation”, which proved the simulation results are correct. The total impact energy is 69 kJ in Fig. 4, which is quite low.

Fig. 5 Body comparison. **a** Before collision, **b** after collision



3.1.2 Body Deformation

Figure 5 shows the body comparison between collision before and after in IIV of 10 km/h. From that, we can see the steering wheel and other parts move small distance backward after collision, and the driving area maintain well and the driver residual space is not be squeezed. The dummy head move forward slightly and have little posture change.

3.1.3 The Conclusion of 10 km/h Collision

The results show that the impact energy of 10 km/h collision is extremely limited. The coach structure have sufficient stiffness to resist the large deformation. The driver would not suffer any harm for the driving space is intact. But it is difficult to form the different evaluation conclusions for the coach that participate in the collision test. Therefore, this velocity does not apply to frontal impact simulation analysis, the real vehicle testing and standards development of coach.

3.2 Research Path for Another Four Kinds of Velocities

20 and 30 km/h make up the lower speed group while 40 and 50 km/h higher, all of which are studied in a comparative way. The research path is shown by Fig. 6.

4 Result Discussion

4.1 Coach Deformation Analysis

The characteristics of coach deformation at different IIV (see Fig. 7) go as following:

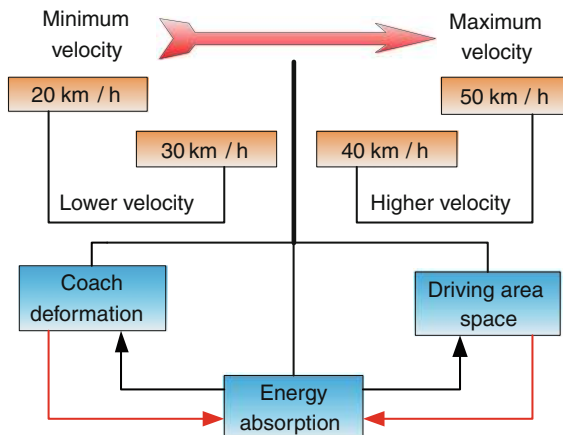


Fig. 6 Research path for four kinds of velocities

IIV	The coach's stress status and deformation	The deformation of the coach	
		In the collision	After the collision
20km/h			
30km/h			
40km/h			
50km/h			

Fig. 7 The body structure deformation at different IIV

20 km/h

- a. Although the front wall's arc beam is crushing as straight beam and the front wall is crumpled to the first pillar, the deformation of coach door is not large.
- b. The frame of the floor in the drive area does not appear the phenomenon of bend and collapse and the seat does not capsize. The steering wheel also does not move backward obviously. The residual space of drive area is intact and not be invaded.

30 km/h

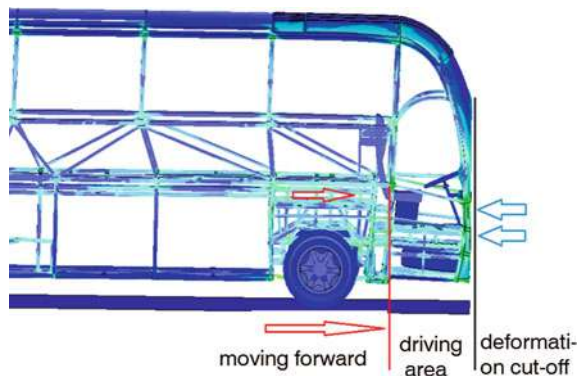
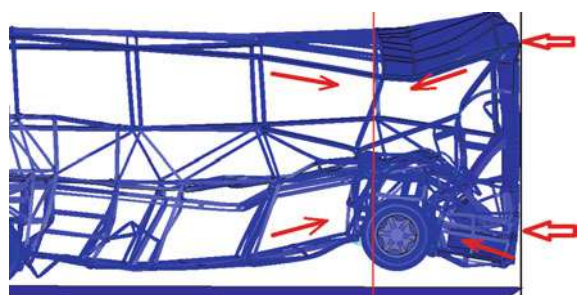
- a. Maximum stress and stress concentration occur in many areas of longitudinal dowel bar's junction.
- b. At last, the front wall's arc beam is crushing into straight beam and the front wall' structure is crushing into the plane. The first pillar on both left and right side wall are close to rigid wall. So the coach door's deformation is more larger and the driver may be hurt as a result of the moving backward of steering wheel.

40 km/h

- a. The front wall is pressed into plane. The frame of the coach body's top cover begin to collapse owing to being squeezed. Because of the squeezing between the central and rear part of coach body and rigid wall, the front of passenger area begin to be heaved and the drive area begin to collapse.
- b. After the collision, it is obviously different for the front space of the vehicle compared with the moment before collision. The distance between the pillar of the coach door became more larger, the front of drive area began to sink, the seat began to turn, the vehicle door's deformation is serious. The driver residual space has been compressed seriously, the top cover's deformation is small. Although the frame of the coach body in the passenger area has deformed to a certain extent, the space kept a good status.

50 km/h

- a. The front wall began to appear a severe plastic deformation and the driver seat continued to turn. The deformation of second pillar, window pillar and coach door is larger than before. The deformation of luggage compartment is quite obvious. The second pillar of the coach door on the right side wall began to collapse down. The drive area's deformation had spread to passenger area.
- b. The top frame began to collapse inward, the holder of the floor in the passenger area sunk. The space structure of passenger area deteriorated severely. At the end of collision, there are no space between the seat and steering wheel. When the seat capsized, it must push the driver out of the window.

Fig. 8 Deformation cut-off**Fig. 9** The force's inclined transfer

4.2 Deformation Mechanism

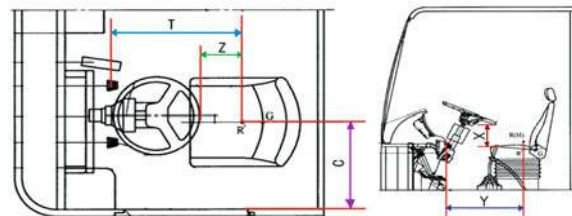
4.2.1 Deformation Cut-Off

At the speed of 30 km/h, the phenomenon of “Deformation cut-off” will occur owing to the “collision” between the front of the bus’s chassis and wall space. But the bus with a huge kinetic energy still moved ahead and extruded the cab continually shown in Fig. 8

4.2.2 The Force’s Inclined Transfer

At the speed of 50 km/h, the collided bus’s front wheel had been lifted greatly and had been off the ground. This is because the back continuous extrusion made the front overhang sink after “deformation cut-off” occur in the drive area. Meanwhile, it made the dowel bar inclined. The inclined dowel bar changed the force transfer direction because the force transfer along them. So, the front axle is lifted under the component force in the front and back inclined bar (Fig. 9).

Fig. 10 Driving area space index



4.3 Spatial Analysis of the Driving Area

4.3.1 Spatial Description of the Driving Area

The spatial of the driving area is the three-dimensional spatial the driver possesses. It will threaten the driver's residual space when the deformation of spatial of the driving area is more larger than a certain value. In this paper, five indexes from three directions can be used to describe the spatial of the driving area (see Fig. 10).

Longitudinal space index: The distance T between the centre of pedal and R point. The distance Z between the steering wheel rim and R point. The distance Y between the dashboard and R point.

Horizontal space index: The distance C between the centre plane of seat and side wall inner shield.

Vertical space index: The distance X between the below rim of the steering wheel and the above surface of the cushion.

4.3.2 The Spatial Curve Analysis of The Driving Area

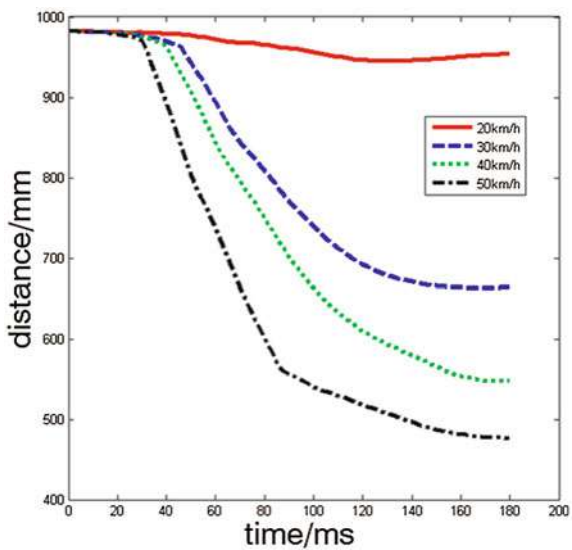
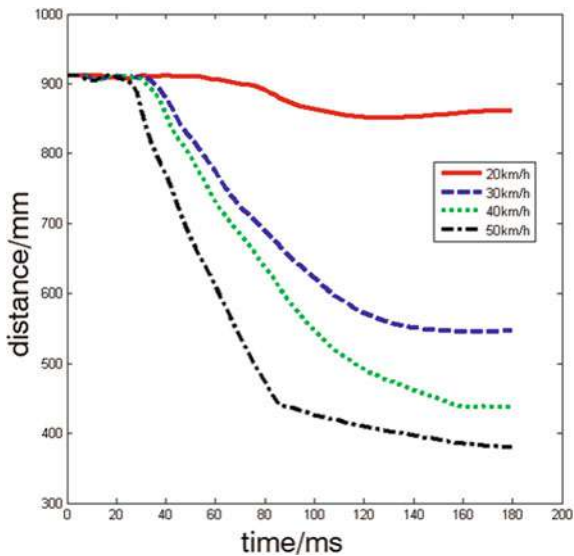
a. The distance of T , Y and Z .

The Figs. 11, 12 and 13 are respectively the curves of T , Y and Z . As are shown in these figures, the terminational value at the speed of 20 km/h is the highest. This illustrates the distance backward change slightly. Z is not the same as T and Y for taking the minimum on the distance curve collided at the speed of 50 km/h, the minimum of Z appear in the collision (80 ms).

b. T , Y and Z curve are in the 30, 40 and 50 showing a faster rate of decline, which are obviously different from 20 km/h curve.

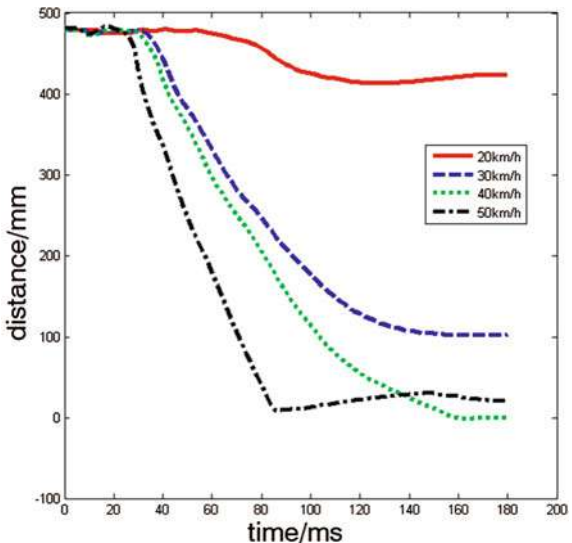
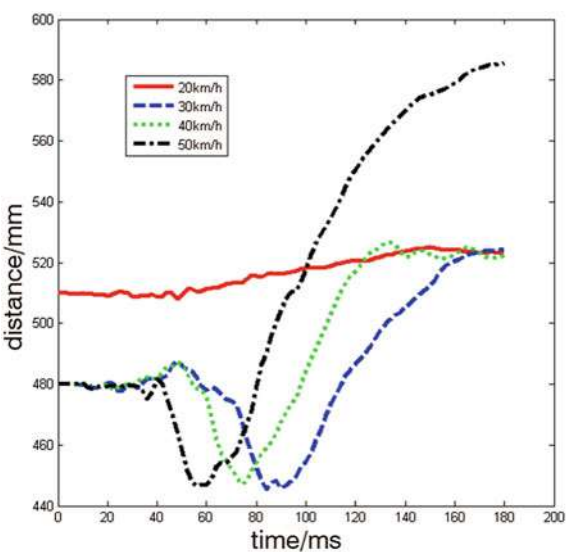
c. The distance of C .

It is C shown in Fig. 14, the curve corresponding to the speed of 20 km/h of collision rise slowly. This illustrates the side wall move slightly outwards at the speed of 20 km/h. But the curves corresponding to the speed of 30, 40 and 50 km/h are different from it. They firstly decrease to the position from the central plane of seat 445 mm and then increase. The final deformation of the speed of 20, 30 and 40 km/h are the same. The final deformation of the speed of 50 km/h increasing sharply.

Fig. 11 Curve of T**Fig. 12** Curve of Y

d. The distance of X

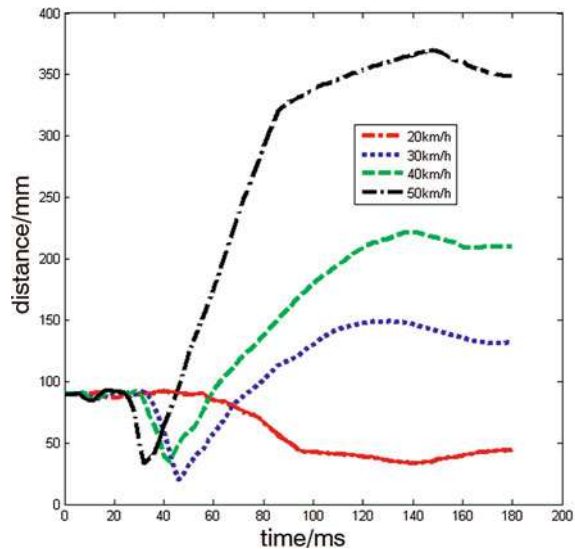
It is X shown in Fig. 15. This illustrates the relative motion of steering wheel and seat along vertical direction. As is shown, the values of distance firstly decrease slightly and increase sharply. Their trends are the same. The curve at the speed of 50 km/h change fastly. The curve at the speed of 20 km/h has been slow decrease to minimum and does not increase obviously.

Fig. 13 Curve of Z**Fig. 14** Curve of C

The above analysis shows, all the corresponding curve can be divided into two categories according to the characteristics of the changes:

The curve corresponds to 30, 40 and 50 km/h have the same trend, and just differ from the rate of change and the magnitude of change.

The curve corresponds to 20 km/h is quite different from the other three curves. The reason is the slow rate of change and small magnitude of change separated it from the others.

Fig. 15 Curve of X

Therefore, we can draw the 30 km/h is “watershed” of the structural deformation of the coach driving area, that means a variety of phenomena of damage on the driver began to appear after the 30 km/h and the extent changed regularly with increasing velocity, which the corresponding value to 30 km/h is lower, 40 km/h is slightly higher, 50 km/h is maximum.

4.4 Analysis of Energy Absorption

4.4.1 Contrast Between the Assemblies

The substance of the different speed collision is different impact energy, which led to the coach results of differentiation in frontal collision. Table 3 listed the energy absorption and adsorption rate of coach assembly in the four kinds IIV.

From the Table 3, we can found four characteristics:

Chassis energy absorption is lower than the front wall frame only in 20 km/h, the rest of the speed, the former are much larger than the latter.

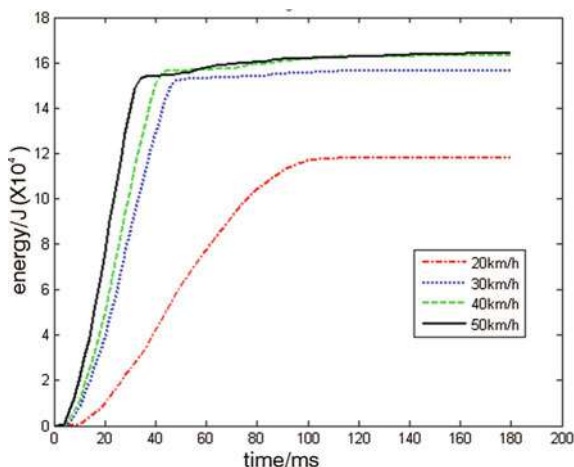
Three types of speed such as 30, 40 and 50 km/h appear that the energy absorption and conversion rate of right side wall frame are higher than left. The reason is the two large open structure (the passenger door and the central door) to reduce the stiffness of the right ride wall make it easier for energy absorption.

Energy absorption of rear wall frame is greater than the top cover in 20 km/h, while the opposite result appeared under the other three kinds of velocities.

Energy absorption of chassis frame become dominant position in speed of 30, 40 and 50 km/h. Energy absorption of other assembly tends to similar values with the increasing velocity.

Table 3 Energy absorption and adsorption rate of coach assembly

Assembly	20 km/ h	Rate/ %	30 km/ h	Rate/ %	40 km/ h	Rate/ %	50 km/ h	Rate/ %
Initial kinetic/kJ	266	/	598.5	/	1061.3	/	1664.5	/
Total energy/kJ	241.22	90.68	571.7	95.52	984.51	92.76	1539.6	92.5
Front wall/kJ	117.8	44.29	152.9	26.74	170.33	17.3	164.06	10.66
Chassis/kJ	57.51	21.62	382.1	63.84	496.11	50.39	849.11	55.15
Right side/kJ	8.92	3.35	75.9	13.28	107.31	10.9	166.3	10.8
Light side/kJ	11.44	4.3	62.8	10.98	95.74	9.72	147.9	9.61
Skin/kJ	16.72	6.29	35.12	6.14	49.07	4.98	68.16	4.43
Top cover/kJ	0.546	0.21 %	8.51	1.49 %	9.62	0.98 %	40.81	2.65 %
Rear wall/kJ	1.29	0.48 %	2.99	0.52 %	3.06	0.03 %	4.30	0.28 %

Fig. 16 The energy absorption contrastive

4.4.2 Energy Absorption of A Certain Assembly and IIV

Figure 15 shows the energy absorption contrastive curve under four kinds of IIV. The result take the front wall frame assembly for example. Energy absorption of a certain assembly increase continuously with the increase of IIV.

The three gathered curve represent the IIV of 30, 40 and 50 km/h, which means that assembly has reached the maximum level of energy absorption in 30 km/h (Fig. 16).

5 Conclusion

If IIV take a too low value, the poor security coach would be neglected and it is hard to give a right evaluation while coach structure deserve it. If IIV take a too high value, the result will be same for all coach can not under so enormous energy.

Fig. 17 The impact test under IIV of 30 km/h curve under different IIV



The IIV of 30 km/h result turn to be moderate and obvious, and from which appeared regular phenomenon and same trend. The energy absorption, as the essential reason of the change, 30 k/h could be used as initial impact velocity.

The first domestic real coach and rigid barrier impact test held under the initial impact velocity of 30 km/h (see Fig. 17), which is a successful test.

References

1. Kwasniewski L, Bojanowski C, Siervogel J, Wekezer JW, Cichocki K (2009) Crash and safety assessment program for paratransit buses. *Int J Impact Eng* 36(0734–743X):235–242
2. Fu-lin S, Jing-tao D, Xu-liang X, Zhi-hua S (2010) Research on simulation and improvement of coach frontal crash. *Chin J Highw Transp* 23(1001–7372):113–118
3. Zhengbao L , Yuhong X, Haixia L (2005) The crashworthiness of structure with large displacement and large deformation. National University of Defense Technology Press, Changsha

Study on Correlation Method of C-NCAP Full Frontal Impact

Feng Huang, Yongxing Chao and Weigang Chen

Abstract Objectives In recent years, CAE is the necessary means in safety performance development of Vehicle Development Process (VDP). How to establish precise CAE model is the most critical problem. Correlation is the most effective means in getting a accurate model. At present, the domestic technology of correlation is rather limited. The results of the published abroad more focus on badered as senior confidential of car companies, so detailed public material lacks. Research on this field is urgent. **Methodology and Results** This paper summarizes common problems in frontal impact simulation, and puts forward a Progressive Correlation Method (PCM). The method is applied to a C-NCAP 50 kph full front impact model correlation. The result shows that the Progressive Correlation Method is very effective and useful. **Limitations and Potential Researches** Progressive Correlation Method (PCM) is only suitable for full frontal rigid impact correlation. We need to develop such a method which is suitable not only for full frontal rigid impact but also for side impact and frontal offset impact. **Conclusions** Progressive Correlation Method (PCM) is very effective in practice. We can find the differences between physical model and FEM quickly and get accurate base models for safety performance development of VDP by PCM. This method has definite physical meaning. To use PCM can improve the efficiency and accuracy significantly in FEA.

Keywords –C-NCAP · Full frontal impact · Correlation · FEA · Crashworthiness

F2012-F01-026

F. Huang (✉) · Y. Chao · W. Chen

Automotive Engineering Research Institute, Beijing Automotive Group Co., Ltd,
Beijing, China

e-mail: huangfeng@beijing-atc.com.cn

1 Introduction

CAE simulation has been widely used in analysis and optimization in order to improve the vehicle crashworthiness performance during vehicle development process. The quality of the model is the key element for following analysis work. Model quality must be verified by correlating analysis results with lab test data. Full vehicle crash modeling is a complicated process, it is needed a reliable standard modeling process, also a common model is needed that it can be shared for frontal, rear and side impact load cases, also it is needed to check and correlate model for frontal impact load case before it is shared by other load cases. Currently, among domestic OEM, successful vehicle model correlation study cases are very few due to lack of data and experience, It is very hard to obtain practical international papers published abroad mostly concentrates in the expression of the basic concept and local structure analysis and optimization, this paper introduces an universal method of Progressive Correlation Method (PCM), then, take a frontal impact correlation analysis of a actual development models as an example, according to the deformation model, acceleration curve and vehicle dynamic crushing of key index in simulation and the comparison with test data, using the proposed PCM, find out the factors influence accuracy of front impact model, then improve the precision of the model and verify this method.

2 Index and Standard

In order to quantitative description of the correlation between test and simulation, it is necessary to define some key parameters, these parameters can make basic description of the vehicle body crashworthiness performance. In the full frontal rigid barrier impact, the body crashworthiness described by the key parameters such as peak acceleration, peak time, effective acceleration, zero crossing time, dynamic crash distance, dash intrusion, crash mode, etc. These indexes related to a new concept, namely effective acceleration, effective acceleration is a comprehensive index that can evaluate vehicle full frontal impact structure crashworthiness performance roundly. Effective acceleration is defined process as follows, get velocity curve by acceleration integral, find out the maximum rebound velocity value v_r , delete the subsequent part, the curve extend along the horizontal direction, draw a straight line through the curve of the initial point $v_i(0, v_i)$ and median point $M_d(t_c, (v_i + v_r)/2)$, the line cut the curve of the extension at point t_f , through the median point M_d drawing a line MN, and it cut horizontal line that trough the initial points v_i and the end point t_f at M and N respectively, suppose C and D were the areas enclosed with the original line $v_i t_f$ and line MN, A and B were the areas enclosed with the line $v_i t_f$ and the curve, the slope of the straight line MN can be determined by the following relationship: $A + B = C + D$, the slope of line MN

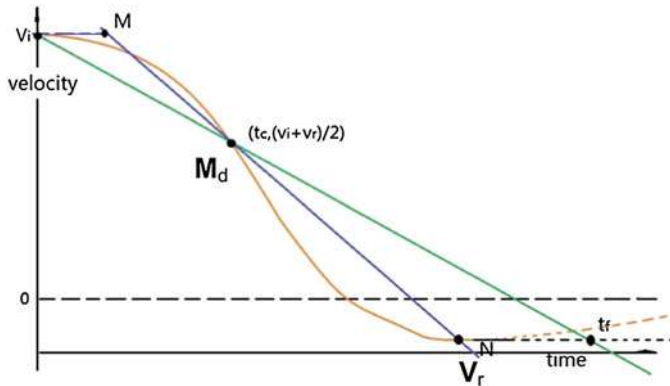


Fig. 1 Definition of effective acceleration

Table 1 Index and standard

Index	Peak G (%)	Peak time (%)	Effective acceleration (%)	Zero crossing time (%)	Dynamic crash distance (%)	Dash intrusion (%)	Deformation mode
Error range	10	10	3	5	5	10	Similar

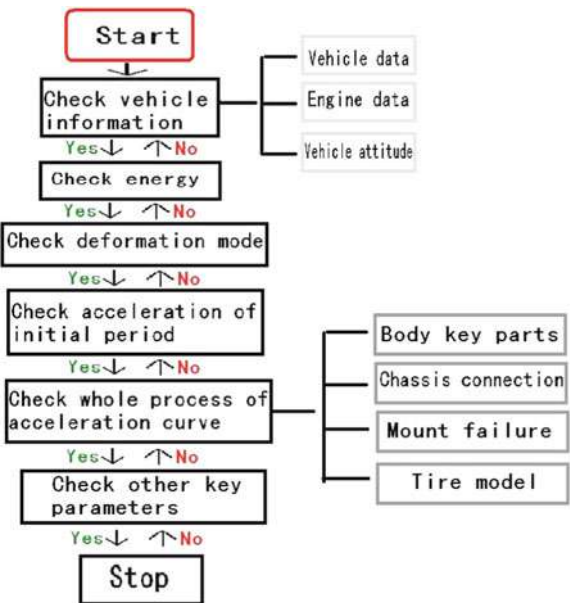
is effective acceleration [1]. Another parameters need to explain, firewall intrusion mainly refers to the intrusion for the foot space (Fig. 1).

In the correlation analysis process, the error of key parameters must meet certain range. When deformation mode of simulation is similar to experiment, all key parameter errors is in the set range, the model correlation can be considered finished, based on past experience of the correlation analysis, the error range of the key parameters is summarized in this paper that is shown in Table 1.

3 Progressive Correlation Method

The vehicle contains many components, and the connection between the parts is very complicated, so simplified method shall be adopted in finite element modeling process, the simplified method should be in line with principle which physical meaning clear and do not produce larger error. Considering the complexity of the model itself, to start correlation task need to construct a basic program, so that the work can be rigorous and orderly, this paper proposed a new method so called Progressive Correlation Method (PCM) that can make the work of correlation analysis standardization, PCM is the method based on the difference between finite element model and physical model, from coarse to fine, from macroscopic to microcosmic, adjust model step by step, it's divided into six main stages. Figure 2 shows a flowchart of the correlation process.

Fig. 2 Correlation flowchart of PCM



3.1 First Stage: Check the Vehicle Information

A newly built finite element model usually cannot fully include the necessary information that engineering analysis needed. The first need to check is some macro information of the vehicle. In general, the first phase of the correlation analysis is mainly to check the following items:

- (a) Check the vehicle data, including the mass and mass center, boundary conditions and initial conditions, check the consistency of the information between FEM and the test vehicle. Vehicle gravity center can be calculated according to the test data of the axis load and wheel load.
- (b) Check the engine data, including model, engine capacity, mass and mass center, the rotation inertia, etc. Check the consistency of the information between FEM and the real engine. Mechanical parameter of the engine is very important to frontal impact simulation and require full attention.
- (c) Check the attitude of the vehicle, the design of the vehicle model is no-load condition in general, the vehicle must be loaded dummy and luggage when in experiment, it makes axis charge redistribution and leads to vehicle attitude change, which cannot be ignored in FEA. The change of the data can be obtained by measuring the distance between fender flares and ground, or according to theoretical calculation, Z displacement of front axle and rear axle can be calculated based on the spiral spring stiffness and Weight difference between test condition and no-load condition, by which the pitch change can be calculate out, so we can get a correct attitude of virtual prototype.

3.2 Second Stage: Check the Energy

Check energy curves of the model such as total energy, kinetic energy, internal energy, sliding energy, hourglass energy, added mass, etc. They are easy to meet requirement in general. If the vehicle information has been checked and the results proved to be correct, energy curves are still abnormal, the reason is generally model quality, at this time, need to examine carefully mesh quality, material parameters and unit, property, interaction, penetration, time step setting, etc. Usually, eliminate the influence of above problems, energy curve can be back to normal.

3.3 The Third Stage: Check the Vehicle and Key Components Deformation Modes

Check the whole vehicle and key components deformation modes respectively, check whether they are similar to those of test data, such as the deformation position, deformation time, deformation mode, etc. This index is easily satisfied, usually no problem. If the deformation mode between simulation and test make great difference, need to check body spot weld, the connections between components, material parameters, etc.

3.4 Stage 4, Check Acceleration of Initial Period

This stage, the main work is to check the first 15 ms acceleration curve, make decision step by step according to C-NCAP full front impact under the speed of 50 km/h, if ignored slight changes in early speed, can calculate vehicle crushing distance that should be less than 208 mm in the top 15 ms time, calculation process seen formula 1.

$$S = V * t < 50 / 3.6 \times 0.015 \times 1000 < 208 \text{ mm} \quad (1)$$

The front of the 208 mm crushing distance mainly involves to the front crash beam, front bumper energy absorbing part and the crash boxes. If gravity center of the model is correct, the acceleration waveform of this stage is mainly related with front bumper energy absorbing part, front crash beam, crash box, including their materials, thickness and connection each other. If the test and simulation appear significant difference in the first 15 ms acceleration curve, need detailed examination from the above three items.

3.5 Stage 5 Check the Whole Process of the Acceleration Curve

If the first 15 ms acceleration curve have good consistency between test and simulation, then we examine the follow-up acceleration curve. The influence factors of acceleration curve after 15 ms is more complicated, which involves material and thickness of body crashworthiness key parts, chassis connection, chassis and body connection, tire model, sub frame model, engine model, engine and sub frame mount failure, stiffness of bushes and spiral springs, damping coefficient of shock absorber and other factors, therefore need to take everything into consideration, and need to examine them from coarse to fine. According to the principle of PCM, if the work of first four stages are completed well, this phase of the body acceleration curve calibration according to the order as follows:

(1) Check the material and thickness of body key parts for Crashworthiness performance, including front rail, kick down, rock, A pillar, firewall beams, etc. check whether the material curve, spot weld position, spot weld number set in these parts and real car are consistent.

(2) Check whether front and rear suspension connection is correct. Usually, McPherson or double wishbone suspension are adopted in front suspension and multi-link or torsion bar suspension in rear suspension. Establish accurate model for frontal impact is based on an adequate understanding of the motion relationship of all chassis components, the stiffness of the spiral spring general is linear, can use spring elements describe it in LS-DYNA. The connection bushes, which between stabilizer bar and sub frame, suspension and sub frame are rather soft, so modelling for these bushes need to input rear stiffness curve. The stiffness of bushes that between the body and the sub frame general is large, it can be simulated by using rigid element.

(3) Check the mount failure, Mount failure of engine and sub frame can be observed from the photos comparison of pre and post collision, the rear mount of engine failure has more possibility, and it is easy to find out from high-speed video, sub frame mount, fix position of rack shell and sub frame, the connection bush of the Lower Sway arms are easy to produce failure too, but it is hard to find them from high-speed video, the failure time is more difficult to determine, it need careful observation, calm analysis to make reasonable judgment.

(4) Check the tire mode, including tire pressure, tire mass, tire size, etc.

3.6 Check Other Security Parameters

When the precision of the acceleration curve and its peak time in simulation meet the requirement well, the next job is checking effective acceleration, speed zero crossing time, dash intrusion etc. These parameters are characterized the macro problems such as whole vehicle stiffness, usually, if the first five stages are in strict accordance with PCM procedure, these parameters can satisfy the requirement of

accuracy too, effective acceleration is a core index, the simulation range of error should be no more than 3 %, if it cannot meet this range, we must return to step 4 to check the model. Dash intrusion is closely related to the dummy tibia scores, especially the intrusion of brake pedal projection points, projection points left 150 mm, projection point right 150 mm and the place such as footrest, need full attention.

4 PCM Application

4.1 Basic Model and Preparation of Test Data

The new protocol method of PCM is used in the actual project development, the model, which has excellent crashworthiness performance, special body structure design, front suspension is McPherson suspension, rear suspension is multi-link suspension. According to the CAD model that design departments provide, by mesh division, the finite element model is built as shown in Fig. 3 below, The model including 1,267,884 elements, 607 components, 5,714 welds. Through preliminary test, the grid quality and penetrate all could meet the basic requirement for crash safety simulation analysis and can be used as the base model for correlation task.

Correlation task in this paper is based on the full frontal impact experimental data of the vehicle according to C-NCAP procedures, the test data including photographs, acceleration curve of a body key position, high speed camera, etc.

4.2 Correlation Process and the Results

Before correlation analysis and calibration, comparison between the simulation results and experimental results, found that the vehicle deformation modes, acceleration curve, sports posture of collision are very different. Figure 4 shows the acceleration curve at B pillar bottom comparison between simulation and experiment.

Check the model according to PCM, found the following problems in base model.

(1) Not input the actual Power Train reference system, the centroid and rotational inertia of the power train that design department provide for is on a reference point for the coordinate system, and the finite element model is not defined local coordinate system, by default, the power train mechanical parameters to the ground for the frame of reference, cause dynamic response of the engine is different from actual impact in serious condition.

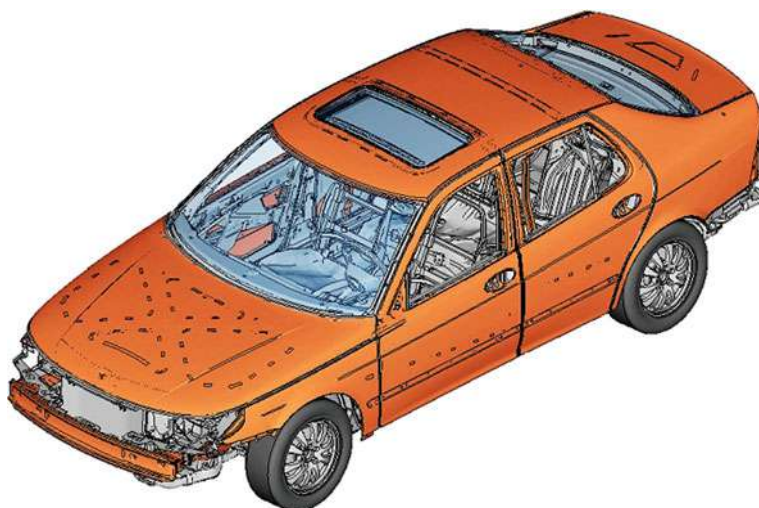


Fig. 3 The base model

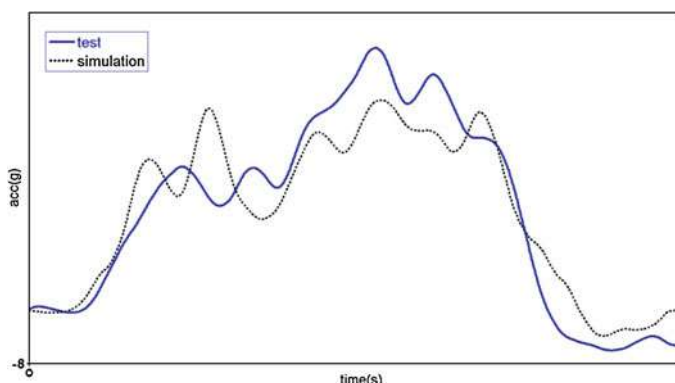


Fig. 4 Comparison of acceleration curve before correlation

- (2) Some body material curves unit is incorrect, cause great influence of simulation results.
- (3) The thickness of upper plate of front rail is incorrect, make the stiffness of front rail itself donot match, therefore, its deformation mode in the simulation is affected.
- (4) Battery bracket and front rail with rigid connection in finite element model, but the actual connection is spot weld, which make front rail local rigidization, and crushing slot can't play a role in simulation.
- (5) Spring element in LS-DYNA is adopted to simulate spiral spring in front and rear suspension, but the stiffness of the set with actual situation are very

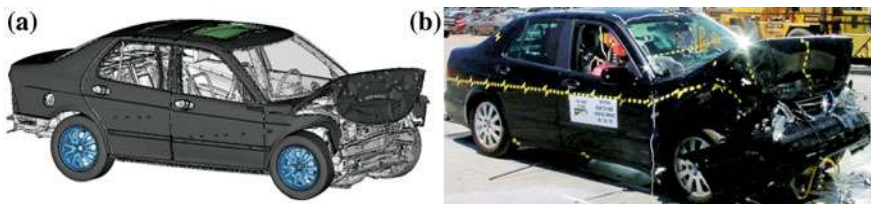


Fig. 5 Comparison of whole vehicle deformation mode. **a** Simulation, **b** Test

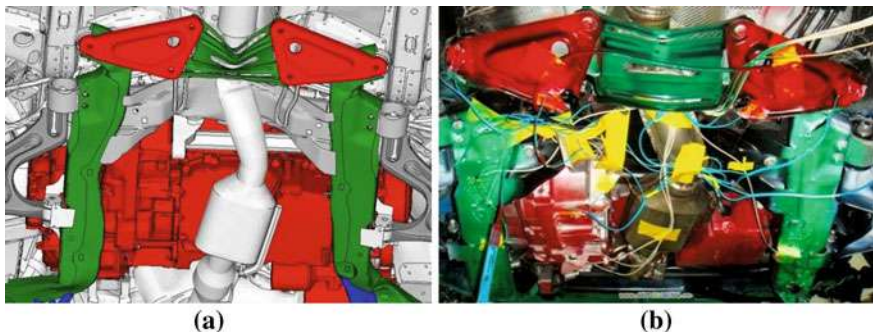


Fig. 6 Comparison of local deformation mode. **a** Simulation, **b** Test

different, make the car movement attitude of the front end sinking, the rear end uplift was not fully reflect in simulation.

(6) The engine rear mount is adopted rigid element in finite element model, but from a test video it can be observed that engine rear mount break in 33 about ms.

(7) The connection bushes between the lower sway arm and sub frame are very soft, which are simulate by rigid element in model, so it can't properly simulate the dynamic chassis.

Compared with conventional method, using the method of PCM can more quickly found that the problems existing in the model, can search out the mistakes in the finite element model by less cases, it only take 12 cases in this paper that finished correlation task well, which need over 50 cases by conventional method in general, the result shows that the precision of the model has improved significantly, as shown in Fig. 5

The bottom of the video in test clearly shows that engine rear mount failure occurred in 33 ms, after the failure being defined in finite element model, the movement of the vehicle bottom in simulation and test meet very well, the comparison of the deformation picture shown as in Figs. 6 and 7.

The acceleration curve of simulation and test after correlation is closer to the before, as shown in Fig. 8, the key parameters error range can meet the design requirements well, such as shown in Table 2.

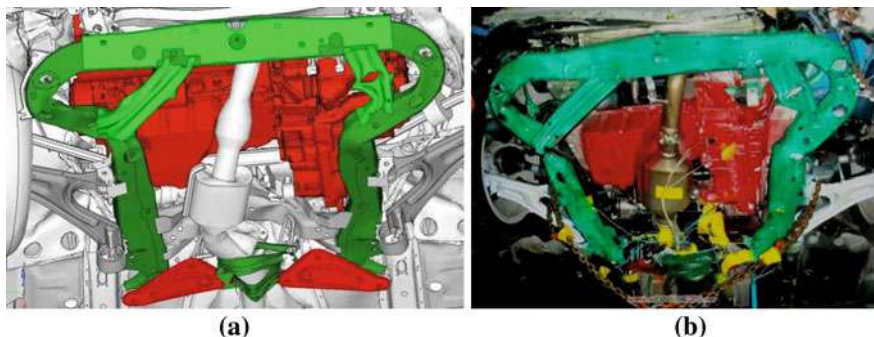


Fig. 7 Comparison of local deformation mode. **a** Simulation, **b** Test

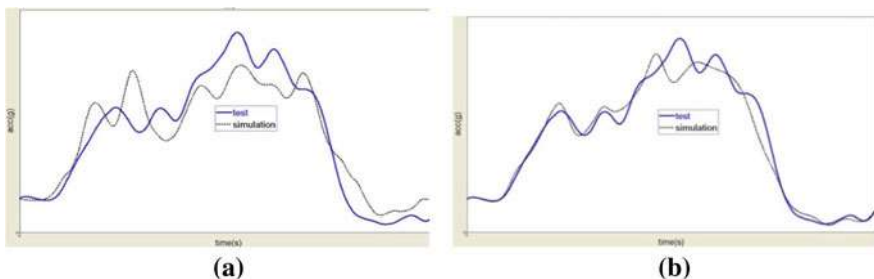


Fig. 8 Comparison of acceleration curve. **a** Before correlation, **b** After correlation

Table 2 Comparison of error range

Index	Peak G (%)	Peak time (%)	Effective acceleration (%)	Zero crossing time (%)	Dynamic crash distance (%)	Dash intrusion (%)	Deformation mode
Error range	10	10	3	5	5	10	Similar
Before correlation	12	2	6	4	8	12	Not similar
After correlation	5	4	2	1	4	7	Similar

5 Conclusion

This paper make full use of CAE analysis experience for many years, construct Progressive Correlation Method, engineer can find the differences between physical model and FEM quickly and get accurate base models for safety performance development of VDP by PCM. Examples of application shows that PCM have definite physical meaning, to use PCM can improve the efficiency and accuracy

significantly in FEA., PCM has certain directive significance for actual project development.

Reference

1. Huang Y-Q (2011) Application of effective acceleration in frontal impact performance evaluation. CSAE auto safety technology international conference proceedings

Study on Vehicle Body Structure Deformation Modes in Frontal Crash

Huihong Liao, Weiguo Liu, Dayong Zhou, Chun Wang
and Fuquan Zhao

Abstract The response of collision velocity waveform to structure deformation in parts dynamic impact simulation was first analyzed in this paper, and a method of deriving structure deformation order by velocity waveform was then determined. By analyzing the relationship between longitudinal rail structure deformation modes and collision velocity waveform in vehicle impact simulation, the reliability of a method of reversely deriving structure deformation modes through speed waveform was verified afterwards. Finally this method was applied in vehicle collision test and the deformation modes of longitudinal rail structure were derived accurately which could provide reference for optimizations of car body structure subsequently.

Keywords Frontal impact · Sensor · Velocity waveform · Deformation behavior

1 Introduction

The main influence factor of passenger response in the vehicle impact is the body acceleration. The faster vehicle acceleration is, the higher acceleration of passenger head becomes, and it is likely to result in higher HIC which reflects the passenger head injury criterion, and vice versa [1]. We can ensure the vehicle structural crashworthiness to a great extent by efficiently control of the engine

F2012-F01-028

H. Liao (✉) · W. Liu (✉) · D. Zhou (✉) · C. Wang (✉) · F. Zhao
Zhejiang Geely Automobile Research Institute CO., LTD, Hangzhou, China

room deformation space [1]. For cars and light buses, the front longitudinal rail is the main energy absorber in the forepart of the body. Its deformation behavior and energy absorbing characteristics have a great influence on the acceleration or the force response during vehicle impact [2]. Therefore, during the performance development of vehicle safety, the injury of passengers is reduced by optimizing the acceleration pulse based on the management of engine compartment deformation.

In the development of structure, conventional methods is optimizing the longitudinal rail according to the finite element simulation result, and then verify the effectiveness of optimization schemes through actual impact test. The crash simulation model after benchmarking can have results similar to the real car test, and it can show the whole process of the structure deformation easily. But in the actual crash test, there is no reliable method to research the deformation of vehicle body structure which is inside the sheet metal and exterior trim. It is hard to verdict if the unsatisfactory impact results are caused by the body structure deformation behavior just by referring to the post-test status. So it's hard to infer the body structure deformation and to judge the consistency of simulation and real test accurately and effectively based on the information we get after the test.

As a consequence, the paper tries to propose one method to restore the body deformation process during the test. The acceleration sensors are allocated on different places of the vehicle body. After the test we can verdict the deformation order through accurate analysis of dynamic change of the velocity curves which are outputted by these sensors. First we can provide reference for body structure optimization. On the other hand, we can verify the consistency of simulation and experiment.

2 Response Research Between Velocity Curves and Structure Deformation

In order to research the response of acceleration sensor to structural deformation in simulation, we first set acceleration sensors in a single spare components simulation model, then contrast the deformation and speed curve of the structure by real-time to find the relationship between them and draw the conclusion that different structural deformation mode embodies in speed curve of fluctuation characteristics. Detailed study of the process and conclusions are shown as follows:

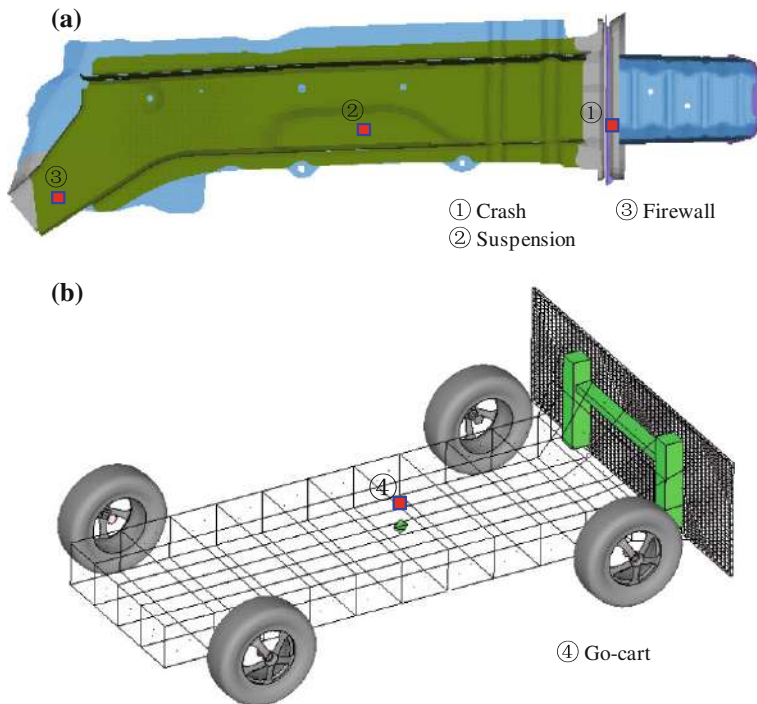


Fig. 1 Sensor placement in parts dynamic impact model **a** sensors on longitudinal rail **b** sensor on go-cart

2.1 Analysis of the Speed Variation Characteristics Based on the Simulation of the Deformation of Component

2.1.1 Layout of Sensors in Components Simulation Model

We set four acceleration sensors in model, including 3 on longitudinal rails and 1 on Go-cart which are shown in Fig. 1:

In the process of impact, crash box and front of longitudinal rail crushed one after another and rear of the longitudinal rail produced only slight deformation. The parts achieve desire behavior by crushing gradually. Related deformation process is listed in Table 1:

2.1.2 Analysis of the Components Deformation Process in Simulation

The essence of the impact is touching of the elasticity and plastic deformation function. The object impact process can be divided into two phases: (1) Compression deformation stage. (2) Restore elasticity stage [3]. Then compression

Table 1 Deformation process of the component crash simulation

Time(s)	Longmember deformation
0	
0.002	
0.004	
0.006	
0.01	
0.02	
0.03	

deformation stage can be divided into elastic deformation stage and plastic deformation stage. After the impact, the plastic deformation can be reused.

In construction engineering, especially cast-in situ concrete template engineering of stents, preloading is demanded before concrete casting in the upper, bracket preloading is to detect stents system of the strength, stiffness and stability, eliminating the elastic deformation and the elastic foundation settlement of bracket, constructs support and templates on one hand. On the other hand, observe the elastic deformation of foundation and the support system under the function of the corresponding load effects, determine the relationship of elastic deformation and load [4].

This paper draws the concept of preloading into the theoretical analysis of vehicle impact. The car itself is a complex composite body. Small gap exists between components. In the early stages when the crash force works, vehicle components make a mutual extruding. Clearance is eliminated and the overall performance produces the non-elastic deformation. With the increasing of crash force, part of the vehicles start to experience material elastic deformation. Crash force continues to increase and part of the vehicles develops into plastic deformation. Some of the material is still in the elastic stage. This paper defines this kind of non-elastic deformation and elastic deformation in the early days of material deformation integrally as preloading deformation. The amount of pre-loading deformation in the vehicle impact curves merged into the plastic deformation displacement, thus the preloading deformation is not obvious acting on the vehicle displacement curve.

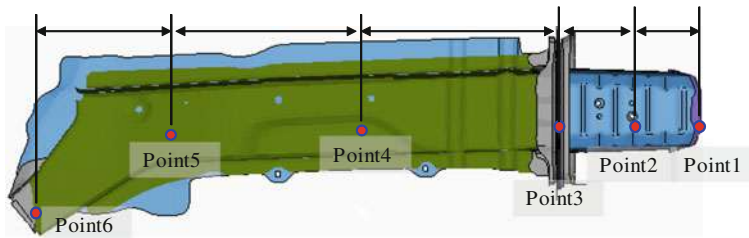


Fig. 2 Point distribution in component models

In order to prove the existence of preloading deformation and determine the rough time in the process of impact, we set up some points (as shown in Fig. 2) in the model and measure the distance between two points and draw curves as shown in Fig. 3.

From the curve in Fig. 3a we can see at 0.004 s in front of the impact process, as a result of the front of the crash box suck the deformation, point 1–2 distance diminishes quickly; In Fig. 4b, from 0.004 to 0.01 s, crash box continue to deformation, point 2–3 distance diminishes quickly. Combined with the deformation process of the model, we conclude that, in Fig. 3c, the displacement of point 3–4 in the period diminished from 0.006 s to the end. While Fig. 4d, point 4–5 happened for tiny deformation, the total length of preloading deformation and plastic deformation is just 4 mm. Figure 4c and d shows both in the 0.002 s positions there is an obvious displacement decline. But the longitudinal rail didn't produce plastic deformation at the final moment, therefore concluded that the impact before 0.002 s is the preloading deformation stage of the longitudinal rail system.

Summarizes the contents of the above, the deformation process of components shows in the list below:

2.1.3 The Analysis of the Speed Response Due to the Parts Deformation Based on the Simulation

Based on the above, the speed curve's responses are studied during the parts deformation process.

In the analysis of the impact waveform, we define the acceleration measured at an undeformed point as the whole acceleration. In the component simulation model, choose the acceleration measured by the accelerometer arranged on Go-cart as a whole acceleration (see Table 2), its speed as other deformation position of speed reference. Each part of the longitudinal rail sensor output speed curve as below after impact:

We can get such conclusions form the curves:

- (1) In the systematic pre-compress deformation stage before 0.002 s, because the component compressed rapidly in the rear-end, the difference between the

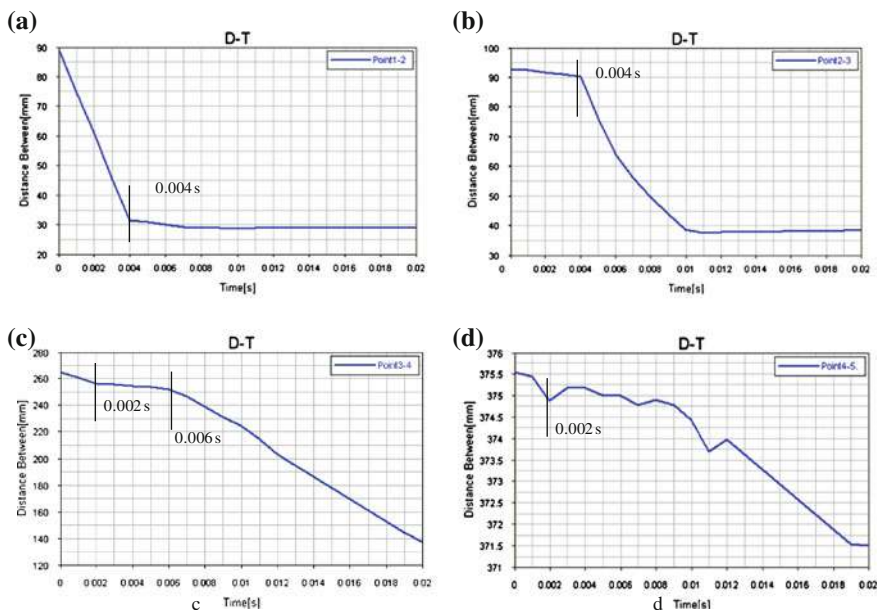
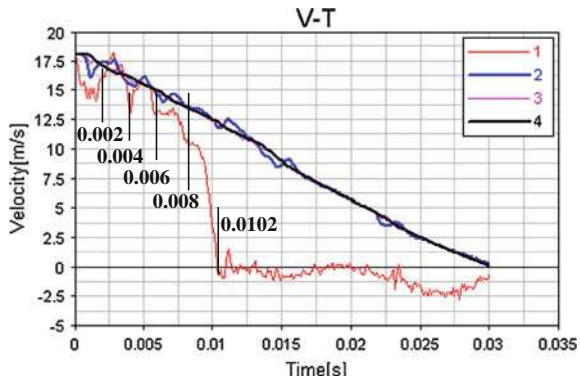


Fig. 3 Partial displacement curve in component models

Fig. 4 Parts impact speed curve



velocity which the front sensors measured and the entirety velocity increased rapidly, and the most forward of the sensors can obviously sense velocity change. The reflection of pre-compress of the rear structure in the velocity curves which put out by the fore-end sensors is the vibration below the whole velocity curve.

- (2) During the phase between 0.002 and 0.08 s, because the crash box in the front-end, middle and later section was collapsed continuously, three times vibration on the velocity curve were generated continuously. At first and second collapses, the velocity curve of NO.1 to NO.3 sensors is higher than the entirety

Table 2 Description of The crash simulation components deformation process

Time(s)	Deformation behavior
0~0.002	System preloading deformation stage, crash box of front-end begin to deformation
0.002~0.004	Front of the crash box continue to deformation and crushing, mid of the crash box begin to deformation
0.004~0.006	Mid of the crash box deformation and crushing, rear-end of the crash box begin deformation
0.006~0.01	Rear-end of the crash box and front of the longitudinal rail deformation
0.01~0.02	Front of the longitudinal rail deformation
0.02~0.03	System thoroughly deformation, speed return to zero

velocity curve. At third collapse, the velocity curve of NO.2 to NO.3 sensors is higher than the entirety velocity curve; whereas NO.1 sensor is lower than before.

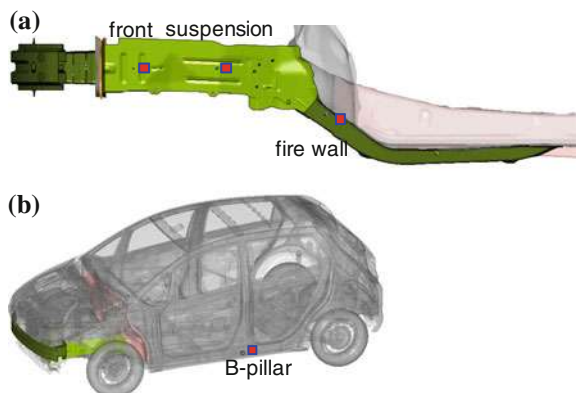
- (3) The crash box completely crushing at 0.0102 s, the speed curve of sensor NO.1 reaches to zero quickly. Then front of the longitudinal rail continues to deformation, causing the speed curve of sensor NO.2, NO.3 fluctuate slightly near the entirety velocity curve;
- (4) After 0.0102 s, the structure near the sensor NO.1 deformation serious, the coordinate of the sensor will change, and the follow-up curve lost its value for reference.

2.1.4 Summary of the Speed Analysis in Components Simulation

According to the analysis above, the process of deduce the trend of velocity curves via the structure deformation character in the Parts dynamic impact are as follows:

- (1) In the process of the system impact, preloading deformation happened at first, preloading deformation including non-elastic deformation and part of the elastic deformation. In preloading deformation stage, the speed curve fluctuates slightly below the vehicle curve. Clearance is eliminated;
- (2) With overall speed curve for reference, when the structure deformation in front of the sensor, the velocity curve vibrates upward higher than the vehicle speed; when the structure deformation at rear of the sensor, the velocity curve vibrates downward below the vehicle speed;
- (3) If there are big deformations near the sensor, the coordinate of the sensor will change, and the follow-up curve lost its value for reference.

Fig. 5 The sensor arrangement in vehicle crash simulation model **a** sensors on longitudinal rail **b** sensor on B-pillar



2.2 Analysis of the Speed Curve Characteristics Based on the Vehicle Crash Simulation

For the further study on the correctness of above conclusions, we arrange acceleration sensor at different position of longitudinal rail in the vehicle impact model, then derivation deformation of the longitudinal rail in vehicle impact though analyze the speed curve vibration characteristics.

In the vehicle impact, we usually take the speed of the sensors arranged under the left B-Pillar as a whole speed, call vehicle impact speed. The location of acceleration sensor arranged in the vehicle impact model as Fig. 5 shows.

As Fig. 6 presents, after frontal impact, crash box and front of the longitudinal rail collapsed completely, rear of the suspension and swan neck area bended. Only by the final state, we cannot know the deformation order of the crash box, the front of the longitudinal rail and the rear of the longitudinal rail (Fig. 7).

After the impact each sensor output speed curve as below:

Introduce the analysis method of Sect. 2.1 into the vehicle crash simulation, according to the vibration feature of the velocity curve which was outputted during the simulation and the final state of the longitudinal rail, the order of the longitudinal rail deformation can be backstopped roughly as follows:

- (1) Before 0.025 s, the longitudinal rail speed curve fluctuate slightly below the vehicle curve, it is the signal of vehicle body preloading deformation;
- (2) For all the 3 speed curves of the longitudinal rail, there are twice upward vibration which higher than the vehicle speed, the curves after 0.025 s are closed to each other, from 0.041 s, the front-end longitudinal rail curve fluctuate violently, it is concluded that there is deformation of the structure nearby this sensor. So the first vibration of the curve emerges at the time when the crash box collapses, the second vibration means crushing of the front-end of the longitudinal rail.
- (3) From 0.033 to 0.041 s, the front-end longitudinal rail velocity curve vibrates downward below the vehicle speed, velocity curves at the suspension and the

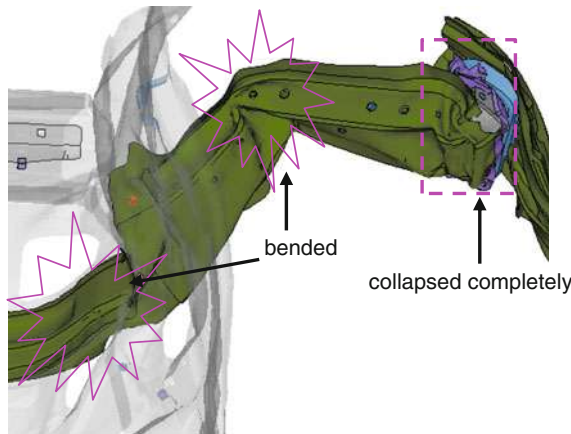


Fig. 6 Front longitudinal rail behavior

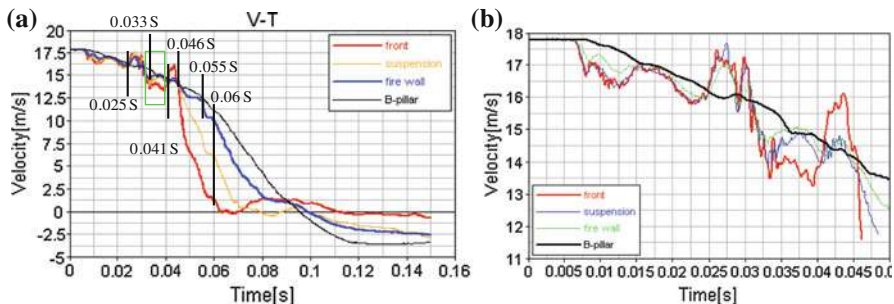


Fig. 7 a The vehicle crash simulation speed pulse b speed pulse former 0.05 s

firewall show vibration upward, the deformation position must be located before the suspension and in the rear of the first sensor. At that moment, velocity curves at the front-end of the longitudinal rail and suspension are both below the vehicle speed curve on the whole, so it is concluded that there is structure deformation behind the suspension.

- (4) 0.055 s, the velocity at the front-end of the longitudinal rail and suspension decline quickly, and the speed curve of the firewall vibrate upward slightly under the vehicle speed, it means the further bending behind the suspension, in the meantime, the swan neck behind the firewall sensor is also in deformation.
- (5) 0.06 s, the three speed curves vibrate upward simultaneously, and there are all lower than the vehicle speed, so it is conclude that the bending of the swan neck is large.

By summing up the above analysis process and contrasting the structure deformation animation and the deform process which is deduced by the velocity

Table 3 Comparison about the structure deformation process during the vehicle impact and the characteristic of speed curve

Time(s)	Status of the longitudinal rail	Description of the deformation	Features of the velocity curve
0		Before the structure deformation	Initial speed
0–0.025		Perloading deformation	Vibration under the vehicle speed curve
0.025–0.033		Collapse of the crash box	Upward vibration higher than the vehicle speed curves
0.033–0.041		Structure deformation between the fore-end sensors of the longitudinal rail and the suspension, the structure behind the suspension is also in deformation	The front-end longitudinal rail velocity curve vibrates and the firewall show vibration upward, velocity curves at the front-end of the longitudinal rail and suspension are both below the vehicle speed curve
0.041–0.046		The front-end of the longitudinal rail crushing	Upward vibration which higher than the vehicle speed, the front-end longitudinal rail curve vibrate violently,
0.046–0.055		Further bending behind the suspension, the swan neck behind the firewall sensor is also in deformation	The velocity at the front-end of the longitudinal rail and suspension decline quickly, and the speed curve of the firewall vibration upward slightly under the vehicle speed
0.055–0.06		Large bending at the swan neck	The three speed curves vibrate upward simultaneously, and three are lower than the vehicle speed
0.096		Maximum deformation moment, vehicle rebound	Speed reach to zero

curves, it is found that there are fitting to each other, see Table 3. So we can draw the conclusion that it is a reliable method for calculating structure deformation behavior on the basis of the collision velocity analysis.

2.3 Summarize of Vehicle Collision Velocity Curve Analysis Methods

According to the analysis results of collision velocity, and combine with the relationship between the fluctuation characteristics of the speed curve and the structure deformation in the component dynamic impact test, the methods of deducing the order of structure deformation in the impact test through vehicle collision speed curve are summarized as follows:

- (1) During the impact, firstly, the preloading deformation which includes the deformation of removing the gap between all parts of the impact system and some elastic deformation emerged. In the stage of preloading deformation, the feature of the velocity curve is the downside and vibration below the overall velocity curve;
- (2) Reference to the vehicle collision velocity curve, the upward vibration of the speed curve is caused by the structure deformation before the sensors, and the downward vibration is caused by the structure deformation which in the back-end of the sensors;
- (3) When the vibration of the speed curve exceed the vehicle velocity, it shows that the rear-end structure is stable, and there is rarely no deformation; on the contrary, if the vibration of the speed curve below the vehicle velocity, it means that there is deformation at the rear-end structure of the sensor;
- (4) If there is big deformation near the sensor, the coordinate of the sensor will change, and the follow-up curve lost its value for reference.

3 Application of the Research Results in the Real Car Test

The results of this paper can be used in the safety development of car body structure. In the real car test, position sensors according to the location of sensors in simulation model and analyze the speed curve getting after crash, so deformation behavior of the longitudinal rail can be detailed understanding during the crash.

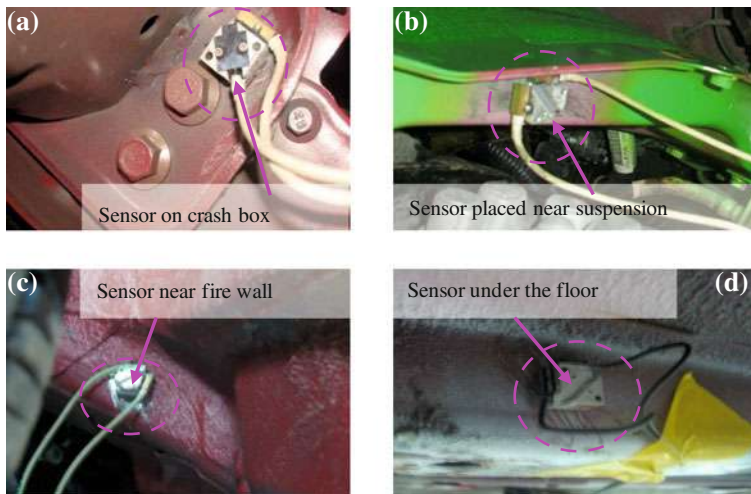


Fig. 8 The impact test longitudinal rail sensor arrangement

3.1 Location of Sensors in Vehicle Crash Test

Position the sensors according to crash simulation results. But there are two requirements for sensors: first sensors have accurate response to noticeable deformation characteristics, second they are not easy to damage. From above, deformation features of longitudinal rail of one model's simulation results are: crush of crash box and front longitudinal rail, Z glyph bending of mount position and longitudinal rail root. At the same time, swan neck will produce vertical bending deformation when Z direction height difference between longitudinal rail weighted height and the center of gravity of whole car is big. So position sensors in fixing board of crash box, mount position, nearby position of fire wall (rear mount bending place), floor bottom position (rear swan neck). In addition, position a sensor under the left side of B pillar. Take the speed getting from this sensor as whole car crash speed. The location of the sensors of longitudinal rail is shown in Fig. 8.

3.2 Analysis of the Vehicle Collision Test Results

Vehicle's deformation after the crash test is shown in Fig. 9. After test crash box completely crushed, front longitudinal rail deformed, mount position and longitudinal rail root Z glyph bended and crushed. The whole deformation accord with the simulation results approximately, as shown in Fig. 10.

Information extracted from sensors on longitudinal rail and under B pillar after test can be drawing a speed curve as shown in Fig. 11. According to the

Fig. 9 Vehicle deformation after the impact



Fig. 10 The impact test longitudinal rail deformation results

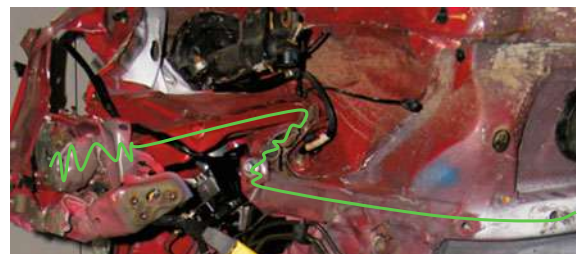
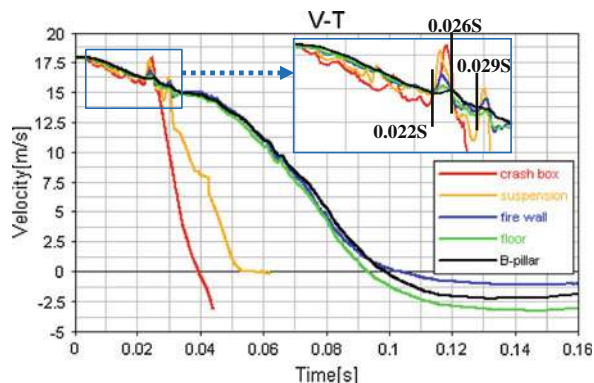


Fig. 11 Vehicle test speed curve



longitudinal rail deformation state and fluctuation characteristics of speed waveform, use method of Sect. 2.3 in this paper, we analyze longitudinal rail deformation modes, determine the deformation period of longitudinal rail's front and rear part as follows:

- (1) Before 0.022 s is the time for system preloading deformation stage;
- (2) 0.022–0.026 s, longitudinal rail speed curve uplink produce higher shock than vehicle speed curve, crash box deformed and crushed;
- (3) 0.026–0.029 s, speed of crash box position quickly reduce, suspension position speed produces the uplink oscillation, fire wall and floor position produces the descending oscillation of the speed, and all speed are lower than vehicle

collision speed. We judge that this period front longitudinal rail and mount rear position deform at the same time;

- (4) After 0.029 s, front longitudinal rail continue to deform, rear longitudinal rail bend and crush severely, suspension position speed reduce quickly, the longitudinal rail mount rear position begin to deform severely, longitudinal rail and mount position speed reduce rapidly.

According to the above analysis, longitudinal rail deformation modes of real car test is deduced : after crash box crushed, longitudinal rail mount position and front longitudinal rail deform at the same time, rear longitudinal rail deform too early to support the front longitudinal rail deformation effectively, the whole longitudinal rail deformation model is not ideal. The longitudinal rail structure can be optimized. The following idea of optimization is to design front longitudinal rail crushing slot reasonable and improve the structure strength of rear mount position.

4 Conclusions

By studying the response of collision velocity waveform to structure deformation from simulation, the fluctuation characteristics of velocity waveform was deduced in the condition of regarding vehicle impact speed as references when longitudinal sensor front-end/back-end structure deformed or when vehicle experienced pre-loading deformation. Thus, a methodology of reversely deriving structure deformation modes according to fluctuation characteristics of collision velocity was concluded. This method of which the reliability was verified by real vehicle test provides reference for optimizations of car body structure subsequently.

Simultaneously, the research results can also be used to verify the consistency of structure deformation sequence between simulation and test.

References

1. Ping Y, Zhigang Y, Xuqiang H, Meilin M, Dazhi W, Xiaodong T, Binyuan P (2008) Front longitudinal rail rail design for vehicle frontal impact. Shanghai: 2008 China international conference of automotive safety technology, pp 245–250
2. Xianfu M, Xianguang G, Zhide F, Youmei Z (2011) Research of thin walled structures crashworthiness. Beijing: 2011 China conference of automotive safety technology, pp 98–101
3. Zhanchun T (2001) Rearch of the impact force response by structure deformation. Beihang University, Beijing
4. Guanlei W, Bin L (2010) Preressing technique for cast-in situ concrete box girder brackets. Word Build Mater 31(2):67–75

Part II

Occupant and Child Safety Protection

An Analysis on Optimization of Side Impact Performance for X Project Using Madymo

Lijuan Hu, Minhui Liu and Houjun Zhang

Abstract Through analyzing the vehicle side impact test data for X project, sub-structure simulation models are built by using PSM of MADYMO to find out optimization directions for current problems, and the optimization results are validated by vehicle test. The optimization plans for this project include decreasing armrest's stiffness; matching SAB to resist direct contact between thorax, abdomen and door trim, increase the points of abdomen and thorax ribs; Adding the pelvis push foam, SAB, CAB can decrease thorax modifier T12 injury significantly and improve thorax protective performance. Vehicle optimization test data indicate that the optimization approaches can increase the total side impact scores effectively and arrive at the target value.

Keywords MADYMO · PSM · T12 · Sled · Stiffness

In our country, road crossings in cities are mainly in the form of level crossing, so the occurrence probability of side impact accidents is extremely high, and the lethality rate is only second to that of frontal impact accidents, but the injury rate ranks the first steadily. Therefore, the research on vehicle side impact safety has become one of the most important contents of automobile passive safety research, and it has received more and more attention from the state, manufacturers and consumers. Since 2006, our country has begun to implement GB 20071-2006, national compulsory standard of side impact and Chine New Car Assessment

F2012-F02-003

L. Hu (✉) · H. Zhang
Brilliance Automobile Engineering Research Institute, Beijing, China

M. Liu
Jinzhou Jinheng Automotive Safety System Co., Ltd, Beijing, China

Program (C-NCAP), in both of which stringent requirements for vehicle side safety performance has been specified. All the OEM and suppliers have made large numbers of simulation designs and vehicle tests so as to improve the side impact safety performance of the vehicle.

Compared with vehicle front structure, the side has fewer energy absorption structures, the space between the passenger and door trim is narrow [1]. In the course of side impact, when the vehicle is intruded by the impacting object, the passenger shall suffer from a strong impact load and have secondary collision with the interior components. When the impact of external force exceeds the bearing limit of human body, impact injury may occur to the passenger inside the vehicle [2, 3]. Factors affecting passenger's safety in side impact include: intruding speed, amount of intrusion, type of intrusion, stiffness of door trim system, the style of door trim and B Pillar trim, seat pattern and performance, side airbag and side air curtain, and so on.

Through analyzing the vehicle side impact test data for X project, sub-structure's simulation models are built by using PSM of MADYMO to find out optimization directions for current problems, and finally validate the result by vehicle test. In this project, the optimization plans that focus on thorax and abdomen which gain little points and modifier T12 problem include decreasing the stiffness of door trim; matching SAB to avoid direct contact between abdomen and door trim and increase the scores of abdomen and thorax ribs; Adding the pelvis foam, SAB, CAB can improve the points of thorax modifier T12 and increase thorax protective performance. Verification test data indicate that the optimization approach can increase the total side impact scores greatly and arrive at the expected goal [4].

1 Dummy's Moving Posture in Impact

Through understanding of positions of the dummy sensors in side impact test, and in combination with the test video and test data, the movement attitude of the dummy in the test may be analyzed to find out the factors that affect the loss of scores in each part of the dummy. Shown in Fig. 1 are the positions of ES|dummy sensors used in the side impact. Before the test, digital signals are acquired from the contact switches mounted on the positions of the impacted dummy such as head, upper arm, upper rib, lower rib, seat cushion wing and seatback wing. The positions and contact times are as shown in Fig. 2.

It is known from the test video that with the movement deformable barrier intruding gradually, B pillar trim contacts the seat back adjuster earliest at 24.5 ms, which rapidly pushes the seat move toward inside the car, and the dummy moves to the opposite direction. At 31.7 ms, the upper arm of the dummy contacts the trim first. At 32.2 ms, the pelvis contacts the door trim, then the abdomen, upper rib and lower rib of the dummy contact the trim successively. At 56.1 ms, the rear part of the head contacts B Pillar trim slightly.

Fig. 1 Map of side dummy sensors

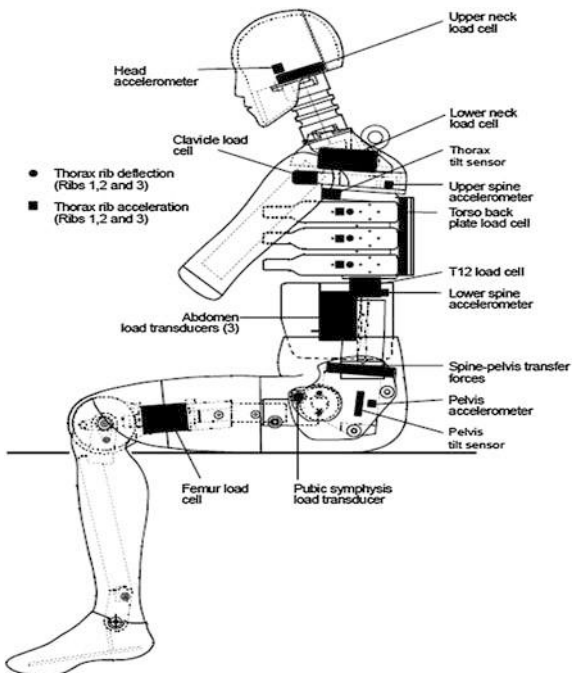


Fig. 2 Contact switch positions and dummy-trim contact time



Dummy head	56.1ms
Upper arm	31.7ms
Upper rib	36.4ms
Lower rib	47.7
Pelvis	32.2ms
Seat regulator	24.5ms

2 Test Data Analysis

In the basic test for X project, the head and the pelvis of the dummy have got full points separately; the thorax and abdomen have lost more points. The deflection of thorax upper rib and viscosity criteria are 33.15 mm and 0.48 m/s respectively, the sum force of abdomen is 1.63 KN, all of which have exceeded the high

Table 1 Scores of basic vehicle side impact test

Injury criteria	Full score	C-NCAP high performance	C-NCAP low performance	Baseline	Score	Total
Head HIC36	4	650	800	75.33	4	12.09
Head 3MS g	4	72	88	28.17		
Thorax upper rib displacement mm	4	22	42	33.15	1.77	
Thorax upper rib VC	4	0.32	1.0	0.48		
Thorax middle rib displacement mm	4	22	42	11		
Thorax middle rib VC	4	0.32	1.0	0.07		
Thorax lower rib displacement mm	4	22	42	4.6		
Thorax lower rib VC	4	0.32	1.0	0.02		
Back plate force FY KN	0	1.0	4.0	0.94		
T12 FY KN	0	1.5	2.0	1.08		
T12 MX N·m	0	150	200	138.7		
Abdominal force KN	4	1.0	2.5	1.63	2.32	
Pubic symphysis force KN	4	3.0	6	1.36	4	

performance threshold. The thorax modifier T12MX is 138.7 N m, which is close to the high performance threshold 150 N.m, requiring serious attention. Specific data of basic vehicle side impact test are listed in Table 1.

Abdomen, thorax and thorax modifier T12 that have lost more points in the test are analyzed for optimization design, and the correctness of simulation results are verified through vehicle test.

2.1 Abdomen Injury Analysis and Protective Performance Improvement

The abdominal force curves in test are as shown in Fig. 3. The abdominal front, middle and rear forces are large. The abdominal middle and rear forces have both exceeded 0.6 KN. However, NCAP requires that sum force of the abdomen is 1.0 KN, which is due to the harder stiffness of the door armrest according to initial analysis.

It is known from the video of the test that, since the door armrest pattern is wide, the armrest intrudes into the passenger's compartment earlier in the course of impact, the dummy abdomen is squeezed seriously, which is the direct cause why the front, middle and rear abdomen forces are big. The armrest end is not smoothened, the middle and rear parts of the dummy abdomen just contact the end of the armrest, where the interaction area is small as shown in Fig. 4, resulting in the middle and rear forces of the abdomen bigger than the front force. Usually, it is recommended that the armrest should be kept flush with the door trim; the

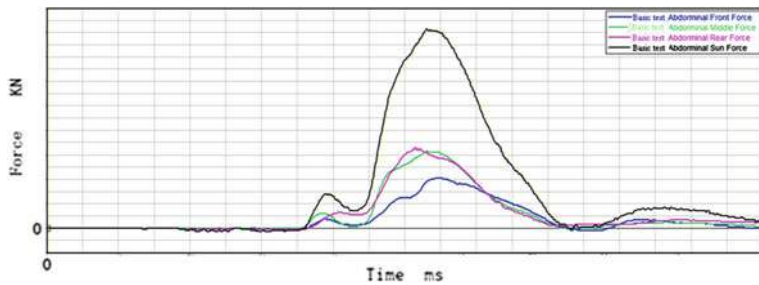


Fig. 3 Abdominal force curves in vehicle test

Fig. 4 Contact between abdomen and armrest after test



Fig. 5 Contact between abdomen and armrest



excessively big armrest would affect rib deformation and movement attitude of the dummy. Shown in Fig. 5 are the screenshots of contacts between dummy abdomen and door trim at 52 ms.

By using Prescribed structure motion (PSM) method of MADYMO software, the intrusion speed, intrusion amount and intrusion pattern of the vehicle side structure that are obtained from structure CAE simulation results are input, as the



Fig. 6 Comparison between dummy movement attitudes

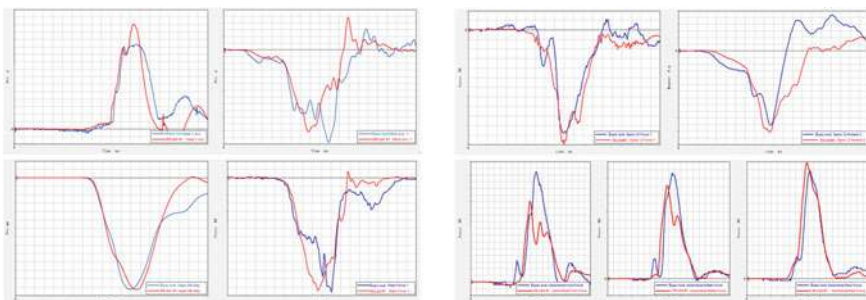


Fig. 7 Comparisons between basic vehicle test data and simulation data

known boundary conditions. The interactions between the restraint systems, dummy, door trim and the inner plate are implemented via defining contacts. This method shall shorten the development cycle and test costs greatly, so it has realistic significance to the development of passenger protection and restraint systems. Based on structure CAE result, the movement of side structure is scaled with PSM-SCALING so that the deformation mode of body structure is similar to the vehicle test process. In order to gain the injury values of all parts of the dummy, the correlation of the model is verified, and a better baseline model is obtained, which is recorded as Model #1 for further optimization analysis. In this project, the comparison between the dummy movement and simulation file at 78 ms in the vehicle test is as shown in Fig. 6.

The comparisons between basic vehicle test data and simulation model #1 are shown in Fig. 7.

It can be seen from the comparisons between basic vehicle test data and simulation data in Fig. 7 that abdominal front, middle and rear forces, T12Fy and T12Mx have better coherence. The armrest stiffness is decreased on the basis of Model #1, and this model is recorded as Model #2. Shown in Fig. 8 are the

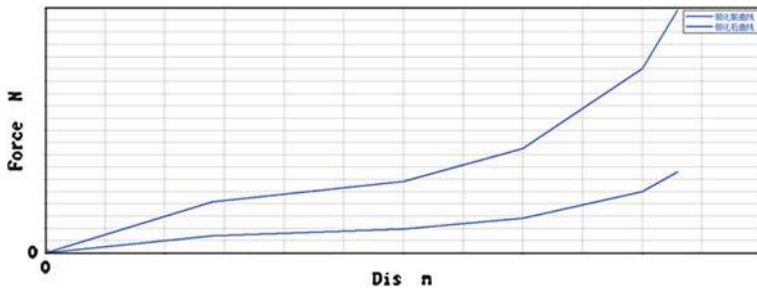


Fig. 8 Compared curves of armrest stiffness

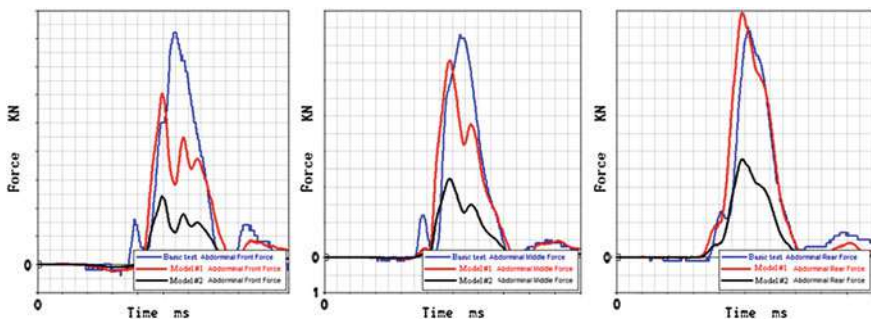


Fig. 9 Abdominal force comparisons between Models #1 and #2

compared curves of the armrest stiffness. Figure 9 shows the comparisons between simulation results of abdominal front, middle and rear forces in simulation models #1 and #2.

It is known from above curves that the abdominal forces may be reduced by soften armrest stiffness. SAB is matched on the basis of Model #2, and this model is recorded as Model 3#. The shape of SAB deployed in the impact is shown in Fig. 16, in which two $\Phi 15$ mm vent holes are used, the fire time is 8 ms, and fold type of airbag is spiral fold. Spiral fold has the advantage over zigzag fold because it may reduce the interference of the airbag with the armrest so that the airbag deploys completely. Adding SAB can avoid direct contact between abdomen and armrest, reduce the middle and rear forces of the abdomen effectively. The simulation results are as shown in Fig. 10.

Based on the simulation results in Model #2, the following measures have been taken in the vehicle optimization test: Added weaken slots in the longitudinal direction inside the armrest and reduced the material thickness from 4 to 2.5 mm, meanwhile, cancelled the button board, softened the integral stiffness of the armrest. According the simulation results of Model #3, installed SAB inside the seat, the gas generator is 135 KPa, the volume of the airbag is 14 L; two $\Phi 15$ mm

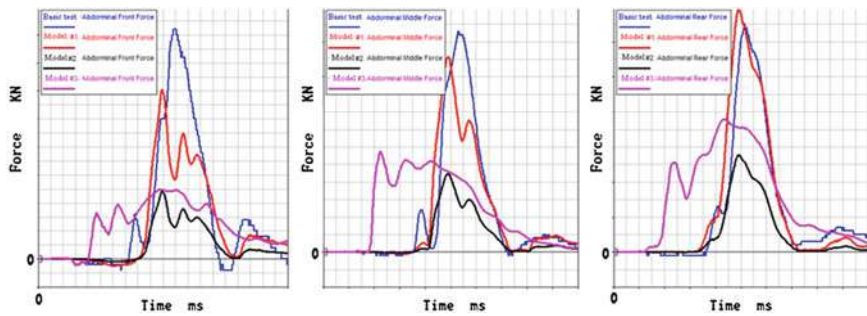


Fig. 10 Comparison between abdominal front, middle and rear forces in Models #1, #2 and #3

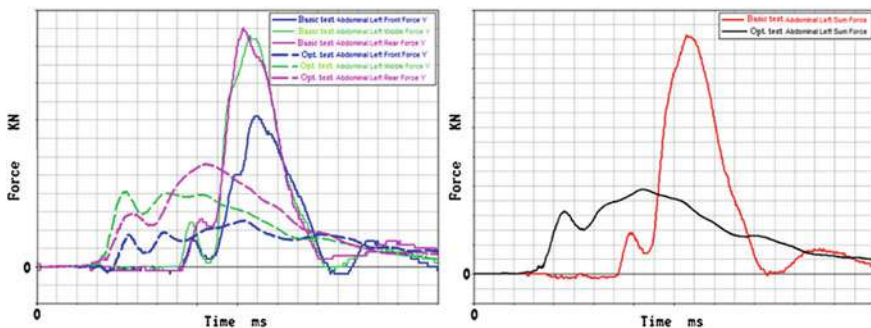


Fig. 11 Comparisons between abdominal forces in basic vehicle test and vehicle optimization test

vent holes are set. The comparison between the vehicle test results is shown in Fig. 11.

It is seen from the curves that after the armrest stiffness is decreased and SAB is fitted, the abdominal front, middle and rear forces have been reduced by 68, 58.7 and 30.7 % respectively, so the dummy abdomen is protected sufficiently.

2.2 Thorax Injury Analysis and Improvement of Protective Performance

In side impact, the ribs of the dummy are the parts with the highest injury rate and the most serious injury due to the deformation caused by door intrusion. The thorax rib deformation reflects the injury degree of thorax ribs. The test results of X project indicate that the deformation of thorax upper rib and the viscosity index of thorax upper rib have both exceeded the lower performance limit specified by C-NCAP. Analysis on the test curves in conjunction with the test video, it

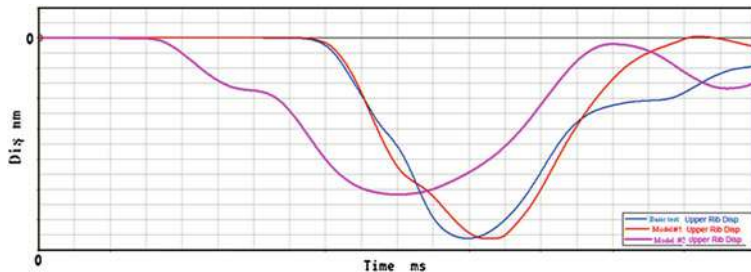


Fig. 12 Comparison between upper rib deformations after SAB is fitted

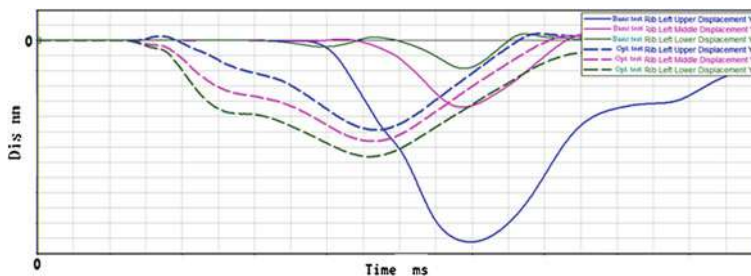


Fig. 13 Comparison between rib deformations in vehicle test

has been discovered that relatively larger displacement occurs when the upper rib gets in contact with the door trim. Therefore, by adding SAB, direct contact of the thorax with the trim is separated. This model is still Model #3, which is not detailed unnecessarily here. See Fig. 12 for the comparison between simulation results before and after SAB is fitted.

After SAB is fitted in the vehicle optimization test, the rib deformation comparison between simulations and vehicle test results is shown in Fig. 13.

The test results show that after the armrest stiffness is decreased and SAB is fitted, the displacement of thorax upper rib is reduced by 55.6 %, SAB has effectively resolved the direct contact between upper rib and door trim, so the upper rib protection is improved. However, the deformations of lower rib and middle rib are increased a bit, because in the basic test, the dummy lower rib and middle rib have not any direct contact with the door trim, so the injury value is very small. After SAB is fitted, the lower rib, middle rib and upper rib of the dummy get in contact with the SAB successively, so the movement attitude of the dummy is changed and the injury value may increase, but not to the extent of injuring the ribs.

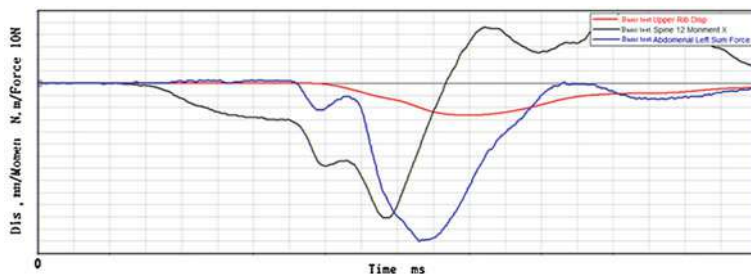


Fig. 14 Comparison between Y-axis accelerations of lower rib, T12 and pelvis in basic test

2.3 Thorax Modifier T12Mx

T12 is the 12th joint and also the last joint of the thoracic vertebra, which is connected to the lumbar vertebra. The spine of the thoracic vertebra is one of the parts that are easily injured, and also one of the critical points in the research of injuries under impact. In C-NCAP, T12 Fy and Mx are used to modify the abdomen score of the dummy. T12 Fy describes the shearing force of the dummy thorax relative to the lateral movement of the loin, while T12 Mx describes the bending moment generated in the thorax rotation around X axis relative to the loin. In the course of the impact test, the impact force on the dummy that the moving barrier intruding the side structure created is a transient force; T12 bears a strong impact force and gets bent at the same time. The whole course takes about 30 sm from the door's intrusion to its contact with the dummy. Therefore, all the anti-collision design of the door plate, the arrangement of the trim structure and the material strength has significant influences on the magnitude of the impact force.

Comprehensive analysis of the three curves of thorax upper rib deformation, T12Mx and abdominal resultant force, as shown in Fig. 14, it is concluded that the armrest corresponding to the abdomen is too wide and the stiffness is too hard, so the intrusion speed into the door is too fast. It gets in contact with the abdomen first, and pushes the abdomen to intrude into the vehicle, so that the lateral movements of the dummy loin and the thorax are relatively violent, thus creates Fy accompanied with axial bending moment in X axis. Therefore adding of pelvis push foam is taken into account to increase the pelvis load-carrying capacity and the lateral displacement of the pelvis, SAB which can cover from thorax to pelvis are fitted so that the thorax, abdomen and pelvis of the dummy move synchronously. Fitting of CAB can prevent the head from contacting with the interior components, and what is more important, it can improve the relative movement of the head and the upper torso of the dummy, which causes harmonious movement of the head, thorax, abdomen and pelvis and reduces T12 injury.

Based on Model #3, pelvis push foam is added, which is recorded as #4. The pelvis push foam is made of polyurethane with a density of 25 kg/m^3 as shown in Fig. 15. The white object is the pelvis push foam, whose area can cover the whole

Fig. 15 Position of pelvis push foam

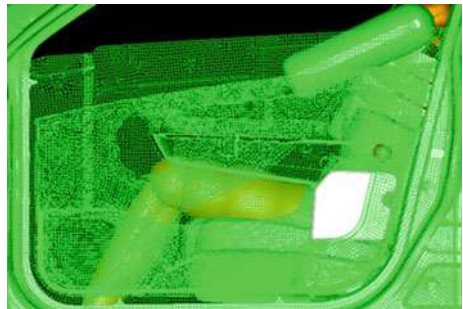
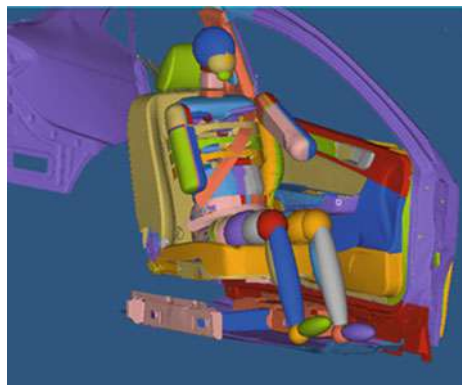


Fig. 16 Deployment diagram of SAB



pelvis. The push foam can push the whole pelvis inward in the course of the movement Fig. 16.

The comparison between the optimized results of MADYMO is shown in Fig. 17. T12 Fy of Model #4 is 0.5 KN less than that of Model #1 and the corresponding T12MX is reduced by 70 N m.

As indicated by the test results in Fig. 18, after the pelvis push foam is added, the armrest stiffness is decreased and SAB & CAB are fitted, the movement attitude of the dummy is changed, and contact time of the dummy with the interior components is changed, finally, T12Mx is 52 N·m, which increases the safety allowance effectively. When compared with the basic test, it is improved by 62.32 %, which meet the target value.

From the above, through optimization of SAB, pelvis push foam and the general stiffness of door armrest, the loss of points are resolved successfully. The optimization test scores are as shown in Table 2. After optimization, C-NCAP has obtained full score-16 point, which is 3.91 point more than the basic test.

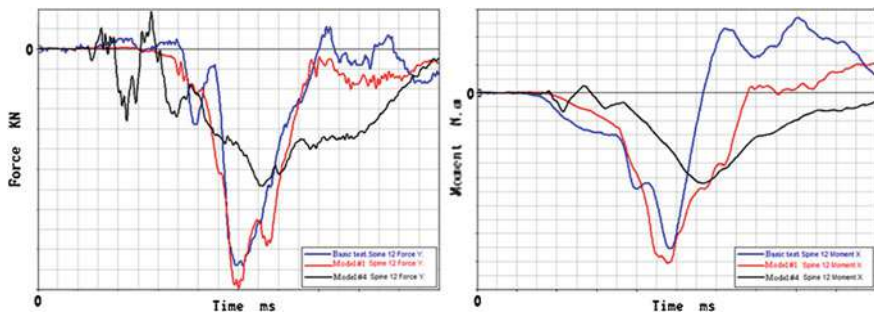


Fig. 17 Comparison between T12Fy and Mx of models #1 and #4

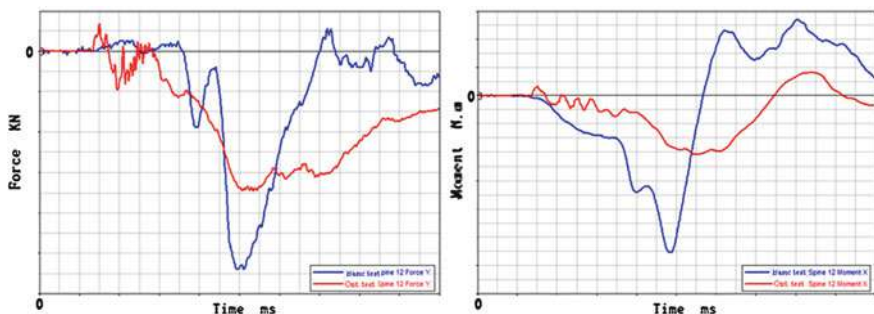


Fig. 18 Comparison between T12Fy and Mx of vehicle test results

Table 2 Scores of vehicle side optimization test

Injury criteria	Full score	C-NCAP high performance	C-NCAP low performance	Optimization Score	Total
Head HIC36	4	650	800	24	4 16
Head 3MS g	4	72	88	23.5	
Thorax upper rib displacement mm	4	22	42	14.71	4
Thorax upper rib VC	4	0.32	1.0	0.07	
Thorax middle rib displacement mm	4	22	42	16.57	
Thorax middle rib VC	4	0.32	1.0	0.077	
Thorax lower rib displacement mm	4	22	42	19.08	
Thorax lower rib VC	4	0.32	1.0	0.086	
Back plate force FY KN	0	1.0	4.0	0.12	
T12 FY KN	0	1.5	2.0	0.68	
T12 MX N·m	0	150	200	52.24	
Abdomen force KN	4	1.0	2.5	0.57	4
Pubic symphysis force KN	4	3.0	6	1.32	4

3 Conclusion

In this paper, aiming at serious loss of score in thorax and abdomen and modifier T12 problems in vehicle side impact test of X Project, sub-structure's simulation models were built using PSM of MADYMO combines with the current problems have been analyzed, the optimization direction has been determined and the correlation has been verified through vehicle test. The protective effects on head, thorax, abdomen and T12 have been improved in the side impact by means of decreasing door armrest stiffness, fitting SAB and CAB as well as adding pelvis push foam, and the expected target has been reached.

References

1. C-NCAP Management Regulations (2009) China Automotive Technology Research Center
2. Yi Z, Gaoji Y, Xuzhou N esc (2010) Dummy T12 injury mechanism in side impact and restraint system analysis optimization [V], 2010 Essay Collection of China Automotive Engineering Society
3. Xuerong Z, Zuqing S (2008) Analysis on influence factors of passengers in side impact. Autom Eng 30(2):146–150
4. Qian Z, Tao X (2009) Research on injury values of dummy positions in side impact [v]. In: The 7th session of international automotive transportation safety academic conference

Optimization Analysis of Chest Injury of a Dummy in a Vehicle Subjected to Side Collision

Yan Liu and Haishu Chen

Abstract A side slide test was carried out in light of score deduction of chest injury of a dummy in a sedan subjected to side impact. A modification in side airbag folding was made thereafter and the dummy chest injury was minimized through the entire vehicle side collision test by resizing the vent hole and adding pelvis foam inside the door trim. Max value of rib compression following the optimization reduced and the dummy chest obtained a perfect score. Meanwhile, the vehicle's side collision C-NCAP scored 16.

Keywords Car collision · Slide test · Side airbag · Vent hole

1 Introduction

Car ownership in China gradually increases along with the continuous improvement of road traffic conditions. Accidents of vehicle collision therefore increase. Among which, side collision occupies 30 %, according to the statistics, ranks next to head-on collision. While in accidents resulted in deaths and serious injuries, side collision occupies 35 % [1]. Side collision protection is therefore very important and China's new vehicle evaluation standard C-NCAP emphasizes more on occupant protection in side collisions. C-NCAP covers not only the dummy injury value of the state mandatory standard, but also three dummy's chest modifiers [2].

F2012-F02-004

Y. Liu (✉) · H. Chen
Brilliance Automobile Engineering Research Institute, Shenyang, China

Increase in the score of side collision dummy requires both the control of side structure of the vehicle body and door trim styling and the adoption of side airbag in dummy protection improvement [3].

This paper describes the minimization of chest injury of a dummy subjected to side impact through side airbag folding and vent hole optimization analysis and deformation of inner paneling of the vehicle door with help of side slide tests and vehicle tests.

2 Injuries Criteria of a Dummy in Side Impact

In C-NCAP side impact test, a EuroSIDE2 dummy was placed in the driver's position for evaluation of occupant injury. Head, chest, abdomen and pelvis were used for scoring. Each of them scored 4 in maximum and 0 in minimum. Scores between limits of injuries shall be calculated by means of linear interpolation, summed up to the score of side collision. Total score was 16 in maximum. Maximum penalty was 4 accumulated from three modifiers of the chest. See Table 1 for detail.

3 Data Analysis of a Sedan in Side Impact

3.1 Test Description

A sedan side impact test was completed with airbag at TIANJIN state test base in Mar. 2011, as shown in Figs. 1 and 2. The airbag was designed for chest and pelvis protection. Two vent holes of $\Phi 25$ mm were made at 2/3 of the airbag and no pelvis foam was provided inside the door trim.

This collision test saw a perfect score in the dummy's head, abdomen and pelvis. Lose points were concentrated in the chest. Maximum compressive deformation of the lower rib was 23.28 mm. V^*C was 0.469 m/s, exceeding the criterion, as shown in Figs. 3 and 4. A score deduction of 0.88 in the dummy's chest was experienced in the sedan subjected to the side impact test.

3.2 Test Analysis

We knew through the test that the dummy's lower rib compressive deformation was of maximum. We paid more attention to the parts in surrounding and found out that the airbag was not fully deployed due to the interference of internal armrest at the door trim (Figs. 5 and 6). As shown by the compressive deformation curve, the airbag outflow too fast, the dummy's lower rib increased obviously in

Table 1 C-NCAP side impact occupant injury criterion and scores

Criterion	Injuries and scores			
	4	3.99 to 2.67	2.66 to 1.33	1.32 to 0.01
Head	HIC(36 ms) 3 ms resultant acceleration (g)	<650 <72 <22	651–766 72.04–77.32 22.05–28.65	767–884 77.36–82.68 28.7–35.35
Thorax	Compressive deformation (mm) $V^*C(m/s)$	<0.32 <1.00	0.322–0.546	0.548–0.774
	Penalty 0–2	Back plate load Fy (kN)		
		<1.50 <150		
		T12 load Fy (kN) T12 Mx (Nm)		
		<1.00 <3.00	1.01–1.50 3.01–4.00	1.51–2.00 4.01–5.00
Abdomen	Resultant force (kN)			
Pelvis	Resultant force (kN)			
				>2.00 >200 >2.5 >6
				2.01–2.50 5.01–5.99

Fig. 1 Before impact**Fig. 2** After impact

the later period, pulse duration was not large enough and the airbag did not function remarkably in the later period of impact. Pelvis foam was not mounted in the test and the dummy's pelvis was pushed hard, while the dummy's chest received a little push from the vehicle's door trim. Therefore, under the situation of insufficient airbag deployment, the dummy's body movement imbalance was increased, resulting in an increase of force by the lower rib and the value of injury.

4 Optimization Analysis of Value of Thorax Injury to a Dummy in Side Impaction

4.1 Slide Test

Slide test is a method of test of low cost and high repeatability used in study of car occupant protection by the side door structure, door trim and side airbag. Cycle of test can be reduced remarkably through simulation of an entire car side impaction.

Airbag used in the slide test was a modification based on the original car side airbag. Due to the limitation of technical level of slide technology, the modification was done only by changing the way of airbag folding, looking at the airbag deploying process, making it deploy fully to provide the best protection effect, as listed in Table 2.

By comparison of color on the airbag taken from the dummy's rib location after the test, we knew where the dummy was in contact with the airbag. As a side protection airbag, the dummy should contact its center as close as possible, as

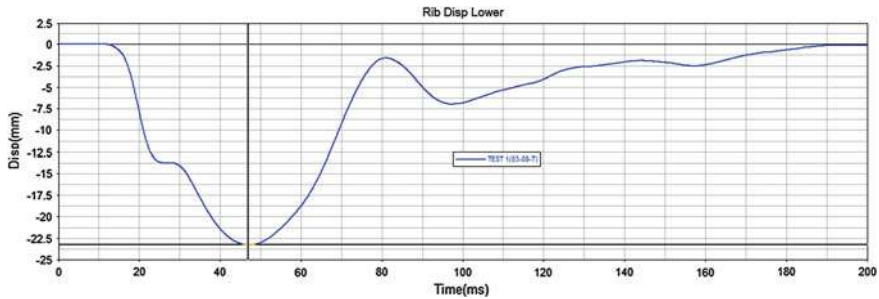


Fig. 3 Dummy's lower rib compressive deformation curve (max 23.28 mm)

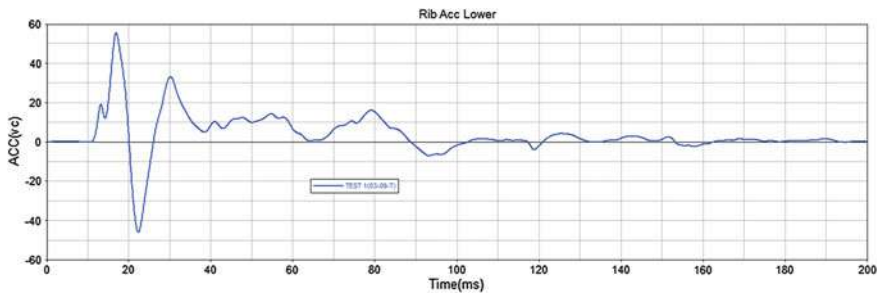


Fig. 4 V^*C is 0.469 m/s

Fig. 5 After Impact



shown in Figs. 7, 8, 9 and 10. The more it contacted close to the center, the better the protective effect. We knew through the test that the existing "Z" folding was not suitable to the car design. Though the "Z" half folding could expand the airbag quickly and correctly, the outstanding of armrest at the door was not in favor of the

Fig. 6 After Impact

airbag's impact deploying. It was found through the test that X direction folding was good to avoid the armrest. The airbag could deploy forward long the surface of the armrest and thus precluded an airbag jamming in deploying. It was decided thereafter that the existing side airbag folding was changed to the method of test 2 to ensure a possibility of a full air bag deploying in car collision.

4.2 Vehicle Side Impact Optimization Test

Side airbag folding was decided through side slide test. Pelvis foam was added at the same time, which was made of polyurethane with a density of 25 kg/m^3 (Fig. 11) and used to ensure a movement coordination of the dummy in collision. Increase contact area between the dummy and the airbag.

Airbag used in the vehicle test was a modification based on side slide test. Due to the limitation of space and structure of parts in surrounding, the modification is only involved in the vent hole size. In 1st test airbag folding style was adopted based on the slide test, with a vent hole size of $\Phi 25 \text{ mm}$, aiming at the impact of the hardness of the airbag on the dummy as a result of increase in contact area between the dummy and airbag. The test saw a full expansion of the airbag, which bypassed the end of armrest at the door and played a role of protection in the chest. As shown by the data, the lower rib compressive deformation decreased in fore phase of the test, but increased again in the later. This meant that the airbag did not function in the late phase of the test. It deployed too fast. Vent hole was

Table 2 Records of airbag modification test

Tests and remarks		1st	2nd	3rd	4th	Remarks
Airbag state	Airbag form	Protection Shape	Chest, pelvis Oval	Chest, pelvis Oval	Chest, pelvis Oval	With side air curtain
		Vent hole size (mm)	Ø25	Ø25	Ø25	Reduced unnecessary air space
		Vent hole location	At 2/3 of airbag	At 2/3 of airbag	At 2/3 of airbag	Basic test data showing that Ø25 mm can satisfy the car's performance requirement
Airbag folding	Number of vent holes	2	2	2	2	Basically between rib and abdomen
Z direction	X direction	“Z” half folded 7 times	Folded in direction of occupant 4 times	Folded in direction of occupant 5 times	“Z” half folded 5 times	In symmetry
Z direction	Long side	Half folded twice	Half folded once	Folded once inward airbag	Half folded once	
	Short side	Half folded once	Half folded once	Folded once inward airbag	Half folded once	

Fig. 7 The first airbag testing laboratories



Fig. 8 Second airbag testing laboratories



completely blocked in 2nd test, based on the 1st, to elongate the airbag pressure maintenance. Location of airbag protection was as required, but the airbag acted negatively against the chest due to the high pressure the moment the door deformed because of the space between the door and dummy. Further modification

Fig. 9 Third airbag testing laboratories



Fig. 10 Fourth airbag testing laboratories



was made in 3rd test, based also on 1st, by reducing the vent hole diameter by 5 mm to strengthen part of the airbag pressure. The test saw a lower rib compressive deformation of 20.03 mm Max while other injury values met the



Fig. 11 Pelvis foam location

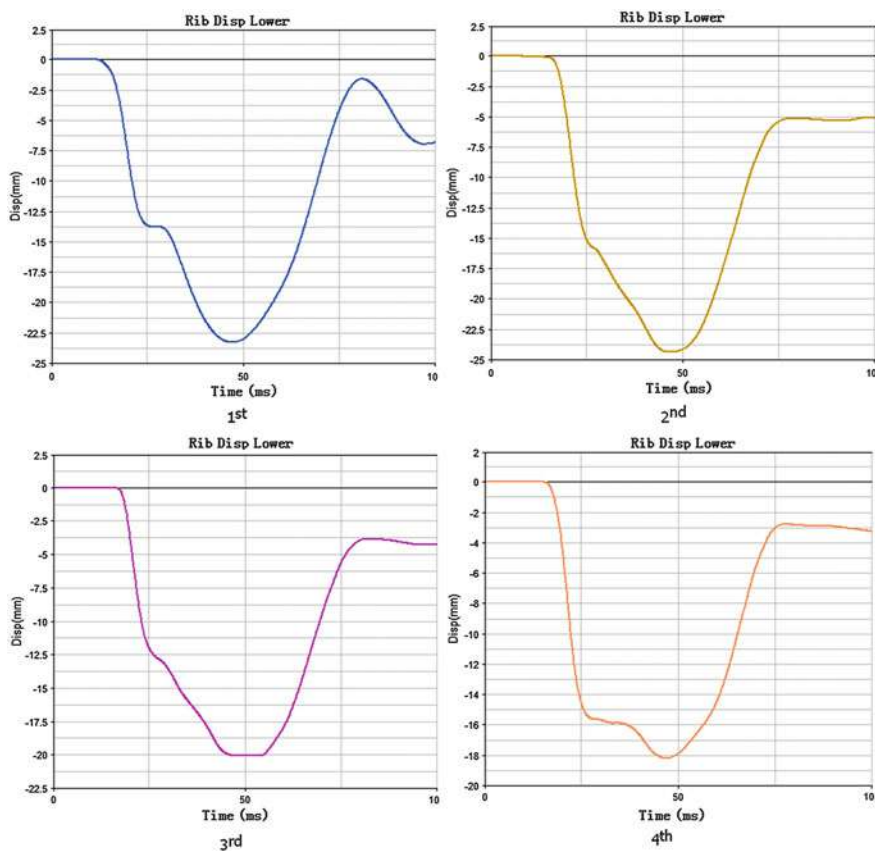


Fig. 12

requirements. V^*C was 0.281 m/s, showing a better effect. However, the compressive deformation of 20.3 mm was 1.7 mm only from the standard 22 mm, very unsafe. Vent hole of the airbag was therefore reduced further, based on 3rd test, to $\Phi 15$ mm. All the rest remained unchanged. The test resulted in a lower rib

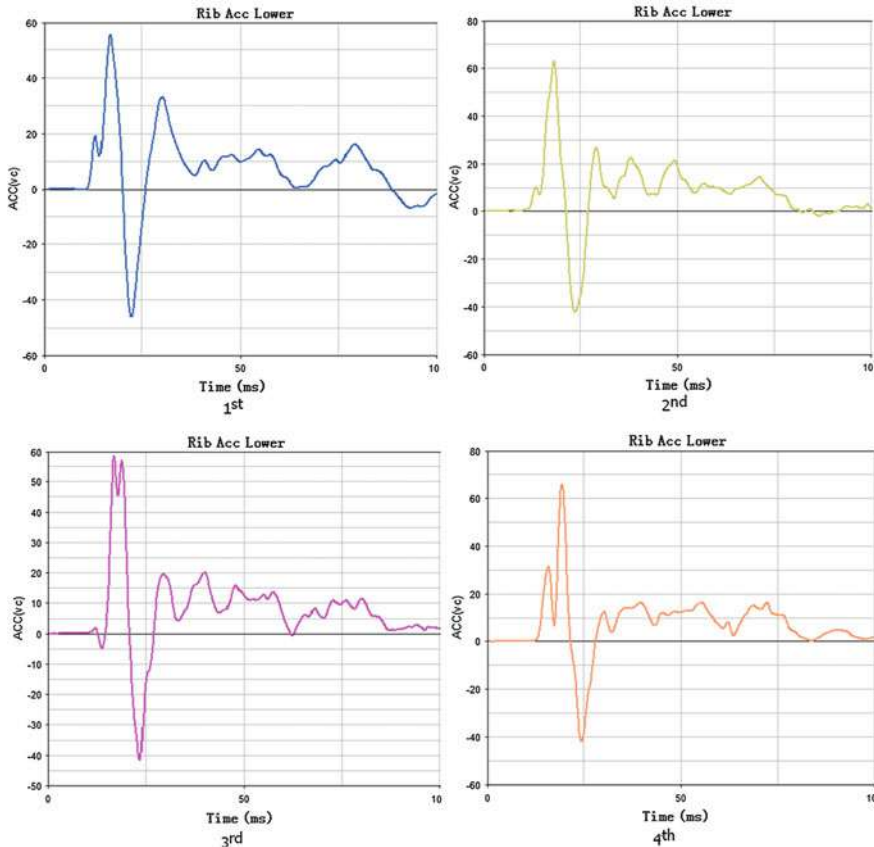


Fig. 13

compressive deformation of 18.21 mm Max and V*C of 0.2247 m/s while making the injury values of other parts of the dummy fall in the range of safety. Based on lower rib compressive deformation and VC in charts 12 and 13 decided in four collision tests, we decided that the state of airbag and parts in surrounding obtained in 4th test was final (Figs. 12, 13).

4.3 Verification Test

Through four impact test optimizations, side airbag of this car employed a turnover folding, with a vent hole of $\Phi 15$ mm and a pelvis foam added inside the door trim. The block was made of polyurethane with a density of 25 kg/m^3 . The final verification test C-NCAP scored 16. Scores of each part are listed in Table 3.

Table 3 C-ncap scores of a sedan in side impact

Vehicle	Evaluation criterion		Driver limit	High performance limit	Low performance limit	Max score	Score of each part	Final score
Impact criterion	Head	Injury values 3 ms resultant acceleration (g)	39.72 20.43	650 72	1000 88	4	4.00	16.00
Chest	Compressive deformation (mm)	18.22	22	42	4	4	4.00	
	Viscous injury response (VC)	0.247	0.3	1	4			
	Back plate Fy (kN)	0.173	1	4	-2	0.00		
	T12 F _y	0.697	1.5	2	-2	0.00		
	T12 M _x	96.86	150	200	-2			
Abdomen	Abdomen force (kN)	0.671	1	2.5	4	4.00		
Pelvis	Pelvis force (kN)	0.904	3	6	4	4.00		

5 Conclusion

Airbag folding style was modified, on the basis of existing side airbag design, from “Z” to turnover. Vent hole diameter was reduced. Pelvis foam was added. Contact area between the dummy and airbag was increased and the side collision C-NACP score was increased by 0.88. It was known through the final verification test that the airbag folding way, vent hole size and the contact area between the dummy and airbag had a great impact on the dummy’s thorax compressive deformation.

References

1. Amcneil L, Holzner DRM, Schoeneburg DRR et al (2005) Current worwide side impact activities-divergence versus harmonization and the possible effect on future car design. In: the 19th ESV conference, paper number 05-0077, Washington DC
2. Wang D, Hu X, Su X (2008) Study of improvement by use of side airbag in protection of occupant subjected to side collision. Shanghai Auto 10:39–42
3. Narayan Y et al (2007) Biomechanics of side impact: injury criteria, aging occupants, and airbag technology. J Biomech 40:227–243

Ejection of Passengers in Bus Rollover Accidents

Matolcsy Mátyás

Abstract The rollover is the most severe, dangerous bus accident. If the weak superstructure collapses in the rollover, the passengers are compressed and killed, or seriously injured. Requiring specified roof strength—UN-ECE, Regulation 66—the severity of bus rollovers were significantly reduced. Later it became clear that another problem—belonging to the rollover accidents, too—the ejection of the passengers from the bus remained unsolved. Some case studies and statistical data are shown in the paper to present the ejection. Two kinds of ejections exist: the total ejection, when the passenger gets out completely from the passenger compartment, and the partial ejection, when only the head, shoulder, chest, arms, and the lower parts of the body remain inside. The injury mechanisms are discussed in the paper. The reason of the ejection is the broken side window. It is not allowed to use laminated safety glass as side window, because the side windows are generally used as emergency exits. The paper proves that the side windows are not needed as emergency exit and the breakable side windows are absolutely unusable as emergency exit. Nowadays it is hoped that the retention of the passengers may be solved by the obligatory use of safety belts. The paper shows that this assumption is faulty; the safety belts have more disadvantages than advantages in rollover. When the bus is lying on its side after a rollover accident, and the passengers are wearing their safety belt, they are hanging in a very unusual position and they cannot release the loaded safety belts. On the other hand, the safety belt can prevent the projection and total ejection, but it is almost ineffective against the partial ejection. In the UN-ECE organization there are different efforts—the author is participating in this work—to solve this problem, but there is no one good solution, because the problem is very complex (obligatory use of safety belts,

F2012-F02-005

M. Mátyás (✉)
GTE, Budapest, Hungary



Fig. 1 Collapsed superstructures in bus rollover

laminated safety glazing, emergency exits, etc.). The paper tries to give a clear picture about the problem—which is an essential, newly recognized issue in the bus safety—and showing the possible ways to the solution.

Keywords Bus · Rollover · Ejection · Safety belt · Emergency window

1 Introduction

In the mid 1970s the bus rollover became known as a very dangerous accident. It may be said that this time it was known as the most severe bus accident. Because of the generally weak superstructures endured large scale plastic deformations or in many cases completely collapsed, so the passengers were compressed, or hard structural elements intruded into their bodies. Typical results of rollover accidents are shown on Fig. 1 proving that the way of large scale deformation is general and similar—when the superstructure is week—in small and large buses, double deckers. The fatality rate was very high in these accidents (30–50 % of the passengers being on the board in the accident). International legislative—and belonging research—work was initiated in UN-ECE (Geneva) which resulted in 1986 the Regulation 66 which required a certain roof strength for Class II and Class III coaches. This regulation was improved and developed in 2004 and now it may be said that the roof strength problem of buses is solved. The coaches, which are approved on the basis of Regulation 66 do not collapse in a wide variety of rollover accidents (excluding of course, when the bus is rolling and falling down into a deep, e.g. 20 m or more precipice).

A brief history of the international activity about rollover protection is given as follows:

- 1974 Hungary raised the problem in Geneva, urged international regulation. The proposal was refused.
- 1976 UK joined to the Hungarian proposal, international work (study, data collection, research, rollover tests) has been started. Germany, Sweden also joined to the action.

- 1986 UN-ECE Regulation 66—about the required strength of the bus superstructure—has been accepted and put into force.
- 2005 The revised, developed version of R.66 has been finished, it became clear—on the basis of accident analysis—that it is a very effective tool to provide „survival space” for the passengers in protectable rollover accidents (PRA) and to reduce drastically the fatality rate.
- 2000 It was recognized that the second most dangerous injury mechanism is the ejection, projection of the passengers.

2 Injury Mechanisms in Rollover

At the beginning—as it was said above—only the intrusion was known and it was thought that all the fatalities and injuries were due to the compression of the passengers. Later more injury mechanism came into the picture. First the differentiation between the causes of the injuries, next the parts of the human body on which the injury happens (e.g. head, neck, thorax, extremities, etc.), and finally the medical form of the injuries (fracture, contusion, distortion, laceration, cut, nerve damage, etc.)

On the basis of the different causes, the following injury mechanisms are considered today:

- Intrusion means that the strongly deformed superstructure—more exactly parts of the superstructure—intrudes into the body of the passenger, compresses, crushes parts of the body (head, chest, pelvis, etc.) This injury mechanism is the most dangerous in rollover, but it can be avoided by a strong superstructure. (see UN-ECE Regulation 66)
- Projection means that—without using restraint system—the passenger leaves the original (seating) position due to an uncontrolled, unwanted motion, “flies” in the passenger compartment or sometimes out of it. During this motion hits rigid, hard parts of the compartment, or bumps against other “flying” passengers, or hits the outside ground when leaving the bus through a broken window. It was thought that the best tool against projection is the compulsory use of safety belt. It is partly true, the problems will be discussed later.
- Ejection means that the passenger—totally or partly—comes out from the passenger compartment, out from the outside contour of the bus through the broken side windows. At the beginning the total and partial ejection were handled together, but later it became clear that they are completely different events, motions, mechanism:
 - Total ejection could be fortunately, if the bus rolls away from the ejected passenger, or tragic, if the bus rolls onto the passenger. The complete ejection could be prevented by the use of safety belt.

- Partial ejection is always dangerous, could cause very severe injury (even fatality) and the safety belt is generally ineffective against it. Only the upper parts of the body (head, shoulder, chest, arms) come outside the bus.

The ejection and projection are—in many cases—overlapping processes, depending on the status of the side windows. If they are not broken, they can keep the passengers inside the bus, if broken, the projection can be ejection.

- Gash, prick (on the passenger body) means a special injury, caused by the broken glass pieces, fragments. The glass fragments can fall onto the passenger, or—if the bus turns on its side only—onto the ground and the passenger (being partially ejected) is injured by the ground and the glass fragments together. This injury is very dangerous, if the bus is sliding further on its side after the turn over. The good solution against this kind of injury would be the use of laminated safety glass in side windows, instead of the toughened glass generally used for the time being.
- Burning means a “fire caused” injury, if the bus gets fire after rollover (as consequence of the rollover). Fire tests of buses proved [1] that—depending on the type, the propagation of the fire and other circumstances—the available evacuation time for the passengers is in the range of 3–5 min.

This brief list shows that there are certain overlaps among the injury mechanisms and there is no one technical solution which could prevent, or at least significantly reduce the injuries in all cases. Or in other words: no one solution having more advantages than disadvantages in all causes.

3 Accident Analysis

At the beginning, when the collection of information about bus rollover accidents was started, first general statistics was collected: bus categories, types of rollover, number of casualties, etc. were only considered. At that time the methods of “case study” and “in-depth accident analysis” were not known and used methods and if some information appeared about the ejection, it did not produce interest. Later on some accident reports called the attention to the problem of passenger ejection. First the total ejection came into the picture, later the partial ejection, too. At the beginning there were no detailed information about other injury mechanisms, only the intrusion into the passengers by the roof. The other injury mechanisms were recognised around the turn of the century and the ejection problem became interesting and discussed. At that time more detailed researches, accident analysis were initiated, e.g. ECBOS project producing working documents, publications [2], and Final Report [3] and a discussion was started in UN-ECE/WP.29/GRSG abut the problem of passenger’s ejection in bus rollover accidents. To prevent the ejection, different solutions were offered and discussed—inside the frame of UN-ECE organisation and outside as well—but for the moment there is no final,



Fig. 2 The bus turned on its side and slid away (Egypt)

accepted, regulated method. Although to solve the roof strength problem was hard task and took a long time (around 10 years), the ejection question is more complex and therefore also time-consumer. The fortune is that the ejection does not cause so high fatality rate, but it is the second most dangerous injury mechanism.

3.1 In-Depth Accident Analysis

Some in-depth accident analyses are listed below, giving examples about the passenger ejection.

Rollover accident in Egypt [4] A HD coach (Class III.)—taking a curve with relative high speed—rolled over with 50 Hungarian tourist on board, turned on its left side, slid 30–50 m away and stopped. The superstructure was strong enough, no significant structural deformation. All the side windows were broken (see Fig. 2.), the casualties were caused by the ejection of passengers, mainly partial ejection. The passengers fell onto the left side of the bus, compressing the people sitting next to the windows, through the broken windows to the concrete road surface and they were rasped by the glass fragments and by the road. The result: 11 fatalities, 29 injured and hospitalized persons, among which 4 were in life danger and 15 seriously injured.

Rollover in Switzerland [5] A tourist coach (Class III)—24 passengers and 2 drivers on board—rolled down from a mountain road. The path of the rolling process is shown on Fig. 2a. The first part was a slight slope, on which the bus had 6–7 rotations, during which the superstructure completely collapsed. Finally the bus fell into the precipice. The result was: 12 fatalities, 15 serious injuries (4 of them in life danger). During the first period of the rollover 21 persons were ejected, 7 of them were dead. (see Fig. 3b and c). The remaining 5 persons were not ejected during the drastic fall, and one of them survived the whole process (in life danger)

Rollover accident in Hungary [6] The driver of an intercity coach (Class II.) on an icy, snowy road lost the control, the coach slipped in a sharp curve and rolled down on a snowy slope with 2½ rotations and stopped on its side. Fifteen passengers

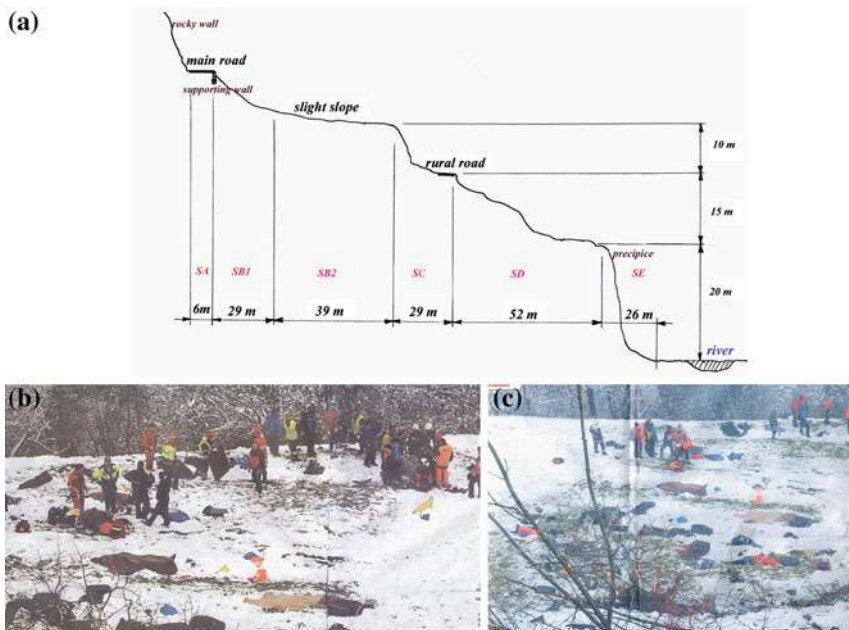


Fig. 3 The path of the rolling process (Switzerland)

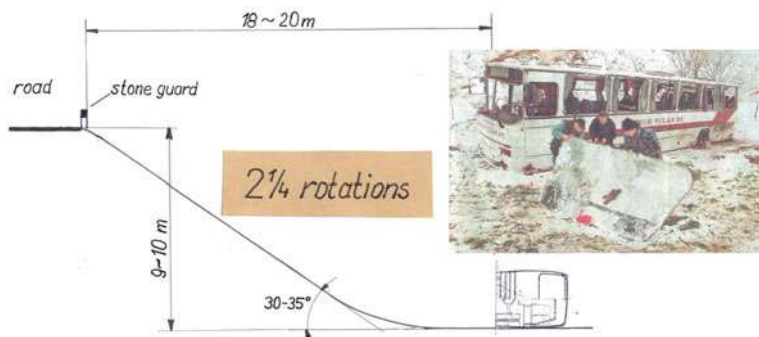


Fig. 4 Rollover on a slope with $2\frac{1}{4}$ rotations

on board, plus driver. The superstructure was strong enough, no significant deformations. The windscreen and the majority of the windows were fallen out without breaking (installation with rubber profiles). The slope and the bus—after the accident—is shown on Fig. 4. The result: 8 serious injuries, 8 light, but 7 of them were hospitalized. Three persons (among them the driver) were totally, three passengers partially ejected. They were partially under the bus, getting very severe injuries. It took more than one hour for the firemen to escape them. They were ejected in the

Table I Casualty rates in different rollover samples

Considered accidents (statistical sample)	Number of events (sample size)	Casualty per accident (CR)				All casualties
		Fatality	Serious injury	Slight injury	Injury without classification	
All rollover accidents	462	11.7	3.1	3.1	7.6	25.5
Protectable rollover accidents (PRA)	278	5.7	2.8	3.6	6.3	18.4
Survival space unharmed	131	1.0	2.1	4.3	5.4	12.8
Survival space damaged	78	13.6	6.8	4.0	10.2	34.6
Bus fire after rollover	15	26.0	3.8	1.6	8.2	39.6

second round. It is interesting to note that the passengers—even the rollover was a relative slow process—could not describe the process, their motion. They estimated 2- 2, 5- 3 and also 4 rotations.

3.2 Statistics

Information were collected about more than 460 bus rollover accidents [7]. It is rather difficult to find out from accident reports whether the bus was approved or not according to Regulation 66. But it is easy to recognize whether the required passenger survival space was harmed or not (partially or completely) by the deformed superstructure. Table 1 compares the casualty rates for different samples of rollover accidents. The casualty rates mean—in this case—the average (fatalities, injuries) value in one accident, belonging to the sample:

$$\text{Casualty Rate } (R_c) = \frac{\text{Number of casualties in the sample}}{\text{Samplesize}} = \frac{N_c}{n}$$

Statistical sample means certain group of (rollover) accidents, in which certain feature, characteristics is common (Protectable Rollovers, or at least one fatality is involved, or all rollovers, etc.) Protectable rollover accident (PRA) is, in which the occupants could be protected [8] (Counterexample: to roll down into a 100 m deep precipice is not a PRA). Among the casualty rates we can specify fatality rate, serious injury, all injury rate, etc. It is interesting to compare the two fatality rates (see Table 1): when the survival space was harmed, or it remained intact. The ratio between them is more than 13:1; more than one order.

It is difficult to get a clear picture about the weight of the ejection in rollover accidents. Earlier the ejection was not important, interesting issue, and later on, when it became interesting, the competent people on the scene of the accident (policemen, ambulance people, firemen) are not expert in this subject and generally they have their own, urgent task after the accident. They do not care too much about ejection. But slowly the interest turns to this problem and more and more reports contain notices about ejections. In the last 2 ears 91 rollover accident information

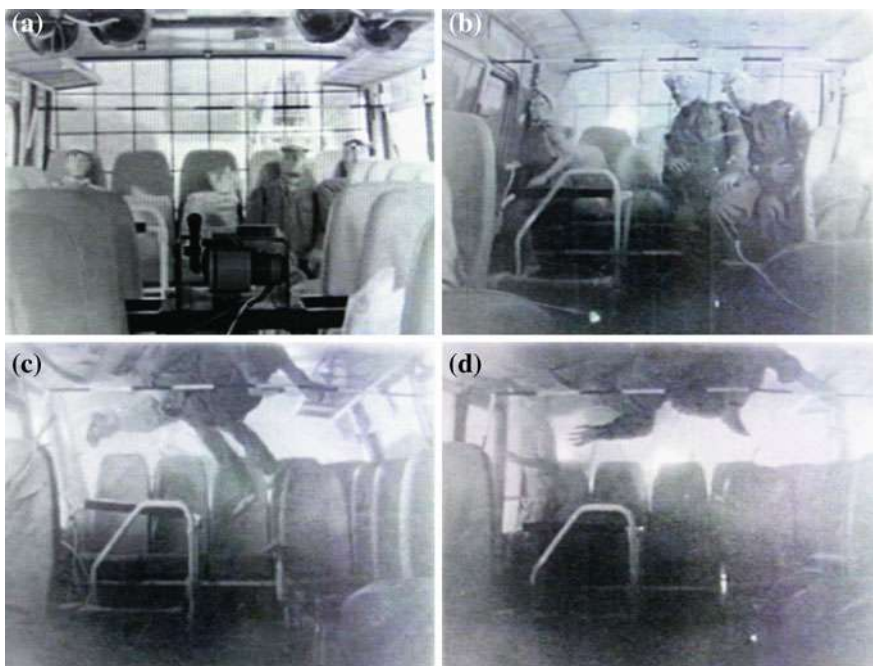


Fig. 5 Motion of unbelted dummies in a rollover test

was collected, among which in nine cases (10 %) the ejection was mentioned. It may be assumed that ejection happens in 15–20 % of the rollover accidents.

3.3 Lessons, Learned From Bus Rollover Tests

In the mid of the 1970s IKARUS made a lot of different rollover and roof strength tests [8]. Rollover tests on a standard 6/4 slope were carried out to study the energy input and energy absorption by the superstructure. In the test with loaded bus all the seats were loaded by a sandbags (68 kg), fixed by ropes to the seats. Many sandbags were “ejected” during 1, 5 rotation, they were scattered on the slope, and the ejection process could be seen on the high-speed film. But our conclusion was—when evaluating the test—that the mass and the inertia of the rolling bus could be changing during the process and we did not recognize it as a dangerous injury mechanism, because the ejection problem was not recognized at that time, as a dangerous injury mechanism. Later on, another similar rollover test was performed with dummies. Three dummies were used—without seatbelt—and filmed. Figure 5a shows their original position sitting on the rearmost seat row, Fig. 5b when two of them are leaving their seats but still in “seating” position, while Fig. 5c and d in “flying” position. During this motion they hit the roof

structure, the windows on both sides and bump each other. The superstructure was strong enough, the side windows did not break, therefore the dummies were not ejected. The evaluation of this process gave good arguments to the international discussion: how to consider the effect of the unbelted, or belted passengers in the rollover, related to the energy input. Matolcsy [9] again, at that time we did not consider the “projection” and “ejection” as injury mechanism just an effect on the energy input, energy balance. Twenty years later an interesting rollover test was produced by VOLVO [10]. Eleven dummies, representing children and adult passengers, using 3 pts safety belt, were used in this test. (Two of them were not belted). This test proved that the 3 pts safety belts are effective against projection, because they kept the dummies on them seats after $3\frac{1}{4}$ rotations. The unbelted dummies were flying around the passengers compartment.

4 How to Prevent Ejection?

Recognizing the serious problem of passenger ejection, generally six feasible possibilities are mentioned [11]:

- (a) To design and use **small side** windows which geometrically prevents the ejection. Small reduction in window’s dimension does not help, large reduction (see airplane windows) is unacceptable for the passengers, bus operators and manufacturers as well.
- (b) To provide **high side wall** under the window rail (900–1,000 mm) in the passenger compartment. This is shoulder height of a sitting passenger related to the floor level under the seat.
- (c) To use **horizontal rails** (hand straps) at the side windows, at shoulder height of the sitting passengers. It was thought that this rail could prevent the partial ejection, but seeing the unbelted dummy’s motion in the rollover (Fig. 5.), it was obviously not true. Later on it was supposed that these rails, together with safety belt could be a good solution. But the question is, whether the safety belt is an effective tool against ejection?
- (d) To use **laminated glazing** in side windows. The laminated glazing is widely used as windscreens and it proved that if there is no large scale structural (plastic) deformation, it could be cracked, but never breaks and falls out from its frame. In the discussions—mainly from the bus manufacturers—a lot of arguments were listed against this solution:
 - it is more expensive than the toughened safety glass. It is true, but it was true when this technology was introduced at windscreens. To increase the safety has a price in any cases.
 - the weight of laminated glass is bigger than the toughened glass. (This is not an a priori truth)
 - using laminated glassing, the side windows can not be used as breakable emergency exit and this significantly decreases the safety.

- (e) Obligatory use of **safety belt** is the most popular idea nowadays. (Safety belt was developed to prevent projection in frontal collision). It was thought that it could prevent the projection and ejection, both the total and partial ejection. Both 2 and 3 pts belts were considered (examples taken from cars and airplanes), but the 3 pts belt does not have reality in buses as general solution. (The driver's seat may be equipped with 3 pts belt). Generally there were two objections against the safety belt:
- It is impossible to force the passengers to use it during the whole journey. In contradiction to the airplane, where the use of the safety belt is obligatory only at take off and landing, so during the flight it can be released. It is not comfortable to be belted during a long trip, for 4–5 h.
 - The standing passengers (see Class II coaches) cannot be belted and their uncontrolled motion strongly influences the position of the sitting passengers as well.
- (f) To use side airbags which could “replace” the broken side windows [11]. The referred example is the side airbag in cars.

Concentrating on prevention of ejection (both total and partial), solution “a” from technical point of view is a good one, but unacceptable for the passengers, operator and manufacturers. Solution “b” and “c” are not sufficient, they cannot prevent the ejection. Solution “f” is more theoretical than practical nowadays. Up to present the safety belt was preferred as reassuming solution. But the laminated glassing should not be neglected, as well.

On the basis of the above said an important conclusion may be drawn: there is no one, only one technical solution against ejection.

5 Supplement to the Safety Belt Issue

The safety belts (both the 2 and 3 pts belts) are very effective tools to keep the passengers in their seats—in their survival space—in frontal collision. To prepare a future test series, preliminary tests were performed in Jáfi-AUTÓKUT Research Institute (Hungary) comparing the effect of 2 and 3 pts belts with Hybrid III 50 % male dummy and also with human body. A coach seat was built into a strong frame which was tilted sideways (both quasi-static and dynamic turn over). Figure 6 shows the arrangement.

The coach seat was fixed to a strong, steel frame, far away from the theoretical bus side wall with ~300 mm, to avoid any kind of damage of the dummy. Quasi static and dynamic tilting tests were performed, having 90° rotation. Figure 7 tries to summarise the main conclusions:



Fig. 6 Tilting tests with seatbelt

- (a) The passenger—using 2 pts belt—can not sit on the seat without massive grasping at tilting of $\alpha = 20^\circ$. At $\alpha = 25^\circ$ it is impossible to remain inside the passenger compartment and at $\alpha = 30^\circ$ the passenger can not control his position, he is partially ejected.
- (b) The dummy with 2 pts belt has certain inclination in the three given tilting position, but much less than the human body. After the dynamic tilting the dummy hit its head to the ground, which was not in the real position, real distance from the seat (see Fig. 9.)
- (c) The dummy with 3 pts belt had smaller inclinations than the dummy with 2 pts belt and after the dynamic tilting its head did not contact the ground. The dummy was completely hanging on the seat belt.

The dummy—hanging on the 3 pts belt—created a very dangerous situation: the belt could not be released—as usual—by finger. Figure 8 shows the hanging position of the dummy, the release of the safety belt by a force transducer (380 N) and the dummy final position, lying on the ground. Figure 9 shows the final dummy positions with 3 pts and 2 pts belt. With 2 pts belt the dummy had larger displacement, its upper part—through its head—was supported somehow by the ground, therefore not the total mass was hanging on the seat belt. The belt release force is smaller in this case (310 N), but also unacceptable high for finger operation. For empty seat, when the belt is not loaded, the releasing force was 29 N , one order less than with loaded by hanging dummies.

Another important result of these tests was, that the Hybrid III dummies are not suitable to study the passenger's (human body) real behaviour in rollover. The dummy is too rigid in crosswise direction, it behaves as a rigid body. The neck, the shoulders, the hip, etc. do not have the necessary flexibility, motion capability. Many studies, computer simulations were published based on these dummies [12, 13]. The results of these studies are questionable in some respect, where the flexibility of the human body was not considered.

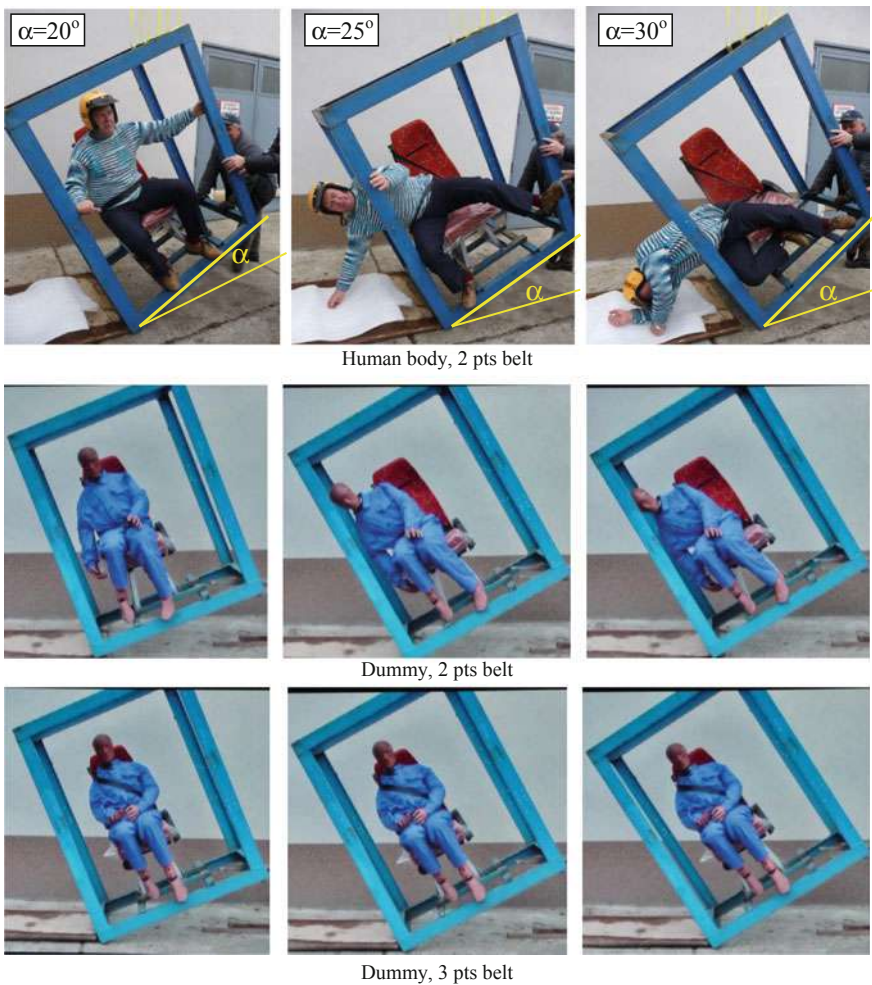


Fig. 7 Different behaviour of the dummy and the human body in the tilting test



Fig. 8 Hanging dummy, 3 pts belt—no way to release the safety belt



Fig. 9 3 pts and 2 pts belted dummies in final position

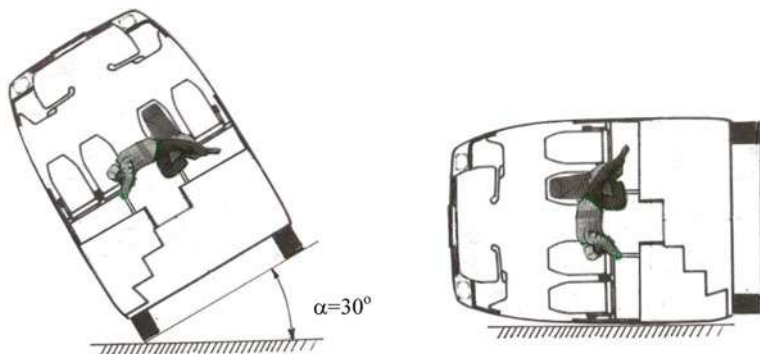


Fig. 10 Hanging passengers in a bus which is lying on its side

This test series highlighted another, new problem to be considered: the passengers hanging on their seat belts cannot release the loaded belt, cannot leave the bus, the bus cannot be evacuated. If they could release the belt—e.g. cutting it—they would fall down onto the passengers having position below them, which also would not make easier the evacuation. Hanging on the safety belt, trying to release it and in the same time to hold their wait by grasping: this is not an easy task. This situation could be fatal if a fire breaks out after the rollover accident. Table 1 shows that it could happen and this is one of the most dangerous accident situations in respect to the fatality and casualty rates. But this hanging position is very disadvantageous if there is no fire. The passengers can not help each other, there is no way to help the injured persons to leave the bus through the rear wall window, roof hatches or windscreens. Figure 10 illustrates the situation at tilting angle $\alpha = 30^\circ$, and we do not have any idea about the passenger's position at $\alpha = 90^\circ$ (when the bus is lying on its side).

Figure 11 shows the driver dummy in original and in final position after $3\frac{1}{4}$ rotations in the VOLVO test, using 3 pts belt [10].



Fig. 11 Original and final position of the “driver” in the VOLVO rollover test

6 Laminated Glazing and Emergency Side Windows

One of the major objection against the use of laminated glazing in side windows is that it would drastically reduce the safety, because this solution prevents the use of the most popular emergency exit, the breakable side windows. To see clearly in this subject: three questions should be study and discussed:

- the emergency exits in general
- the role of the side windows in different emergency situations
- the usability of breakable side windows

6.1 Emergency Exits in General

The following exits may be considered as emergency exit on buses:

service doors side windows
emergency door escape hatches
rear window windscreens

There are four basic post-accident situations, when the bus has to be evacuated as quick as possible:

- the bus is standing on its wheels (after frontal, rear and side collisions, normal fire, rollover after one complete rotation)
- the bus is lying on its side (rollover, turned on its left or right side), this means two positions
- the bus is standing on its roof (rollover, half rotation)

General requirement is to have at least two well usable emergency exits in every basic post accident situation [14], because if one of them is blocked by any reason, the other one could be enough to evacuate the bus in time.



Fig. 12 The bus is standing on its wheels



Fig. 13 The bus lying on its side

6.2 *The Role of Emergency Side Windows*

In the light of the above said, let us examine the role and necessity of side windows in emergency situations.

When the bus is standing on its wheels (Fig. 12): usable emergency exits are two service doors and one emergency door (One door is more than enough to evacuate the bus). There is no need for emergency side windows!

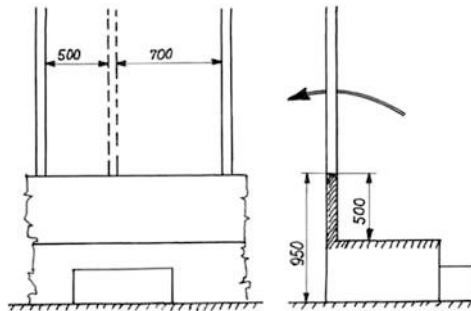
When the bus is lying on its side (Fig. 13): usable emergency exits are the escape hatches and the rear window, or possibly the windscreens. Side windows on one side are blocked by the ground, on the other side it is impossible to break the windows above the head and climb up through the window. There is no need for emergency windows!

The bus is standing on its roof (Fig. 14): The doors (both service and emergency doors) can be used also the rear window and windscreens. There is no need for emergency side windows!



Fig. 14 The bus standing of its roof

Fig. 15 The use of breakable side emergency window



6.3 Usability of Breakable Side Windows

Interesting test was carried out in UK [15], when the UN-ECE Regulation 36. (General safety provisions of large buses) was discussed. 100 voluntary elderly people (average of 73 years) were asked to simulate an emergency evacuation of a bus through side window. The test arrangement is shown on Fig. 15. The participants knew the task, they knew what to do, there was no glass in the window frame (nothing to break) and 44 % refused to pass the test, they were unable to exit through the window simulation. It has to be pointed out that it was a very “lightened” test: in real bus constructions the inside height of the side wall is 700–800 mm (instead of 500 mm), and the outside height is 1,600–1,800 mm (instead of 950 mm)

We also made evacuation test with breakable side window [14]. Thirty years old woman—using protection gloves and face protective mask—was asked to leave the bus through a breakable side window. The measured time was:

- finding and getting the hammer 15 s
- creating a “fire exit” with appropriate size, additional 25 s
- leaving the bus with massive outside help, additional 50 s
- altogether 90 s

The massive outside help meant that two men lifted her out, she could not grasp the window pillar, she could not touch the window rail (waist rail) because of the sharp glass fragments (see Fig. 16).



Fig. 16 Arrangement of evacuation test through side window

The above said proves that there is no essential need for the emergency side windows, and if they are breakable emergency exits, they are unusable for average passengers. This recognition weakens the argument against the laminated safety glazing, because its use do not decrease, but strongly increase the passenger's safety in rollover accident. And one more argument: if—in special cases, like small buses or the lower passenger compartment in a double deck bus—there is a need for side wall emergency window, there are good, approved technical solutions, like hinged type, or “kick out” type window. UN-ECE Regulation 107 (General safety provisions of buses) considers and allows the use of these kind of emergency side windows.

But it has to be underlined that the laminated glazing—even it could be a big step to prevent or significantly reduce the casualties coming from ejection, gash and prick, cannot help against the projections. A general reconsideration is needed, how to increase the passive safety of bus passengers in all kind of accident situations and an optimum protection level should be specified.

7 Summary, Conclusions

- Solving the problem of the strength of bus superstructures, the severity of the injury mechanism **intrusion** (compression) has been drastically reduced, now the second most dangerous injury mechanism is the **ejection**, both total and partial ejection.
- There is no one technical solution which could prevent all the known injury mechanisms in rollover accident.
- It was believed that the safety belt could be a good solution for both the complete and partial ejections. Preliminary tests, shown in this paper prove, that it is not true and the safety belt can introduce a new problem, blocking the evacuation of the bus. The passengers hanging on the belt cannot release it.
- The laminated glazing side windows should not be excluded from the possible solutions preventing the ejection.

- When simulating the passenger's behaviour and motion in rollover (either in test or in computer simulation), the Hybrid III dummies are unusable, they do not represent the human body in this situation, in this process. They are too rigid in cross-wise direction, their flexibility does not represent the human body.
- The passive safety problems of the bus passengers need a new reconsideration involving all kind of bus accident situations.

References

1. Matolcsy M (2009) Analysis of bus fires and belonging safety questions (2009) EAEC Congress. Bratislava, Safety Section, Proceedings on CD, p 12
2. Albertson P et al (2006) Case study: 128 in rollover coach crasher in Sweden. Injury outcome, mechanisms and possible effects of seat belts. *Saf Sci* 44:87–109
3. ECBOS Summary Report (2004) Project of the European Commission, 5th Framework, project number 1999-RD, 11130. Presented also in UN-ECE/WP.29/GRSG, where the reference number is: GRSG-86-4
4. Conclusions of a sever accident. Informal document, No. GRSG-102-03 (2012) Submitted by Hungary. Homepage of UN-ECE: www.unece.org/trans/main/welcwp29.html
5. Matolcsy M (2007) In-depth analysis of a severe bus rollover accident (Was it really a severe one?) EAEC Congress 2007. Budapest. Paper No.CV 01-3, Proceedings on CD, p 11
6. Rollover accident with ejection of occupants. Informal document, No. GRSG-91-07 (2006) Presented by Hungary. Homepage of UN-ECE
7. Matolcsy M (2010) Analysis of bus accident statistics. FISITA Congress, Budapest, Paper No. F2010 F001, p 16
8. Matolcsy M (2001) Standard accident as the basis of vehicle approval test. EAEC Congress. Bratislava, B01, Section Safety, Paper No.SAITS 01122, p 10
9. Matolcsy M (2002) The effect of safety belts in bus rollover process. IMechE publication, Paper No. C601/001/2002, p 10
10. Presson H, Forlund B (2002) Rollover protection of buses and coaches—VOLVO experience. In: 33rd meeting of bus and coach experts. Keszthely, GTE. Session 3; Passive Safety. Paper No. 309a Proceedings on CD
11. Martinez et al (2002) Effectiveness of restrain systems in bus rollover. In: 33rd meeting of bus and coach expert. Keszthely GTE. Session 3; Passive Safety. Paper No. 311a. Proceedings on CD
12. Ruiz S, Millanes M (2002) A contribution to the discussion of the passengers influence in the ECE R.60 rollover test. In: 33rd meeting of bus and coach experts. Keszthely, GTE. Session 3, Passive Safety. Proceeding on CD, p 5
13. Cheng LY et al (1996) Heavy truck crashworthiness—30° rollover accident. 15th ESV conference. Paper No. 96-S11-0-14, p 11
14. Matolcsy M (2011) Evacuation of buses—Emergency exits. Conference on science and vehicle, Belgrade. Reference No. SAFO3, p 13
15. Investigation into the ability of elderly people in climbing out of simulated bus emergency exits (1974) Project report (March, 1974). Industrial ergonomics, Cronfield Institute of Technology, UK, Manuscript

Enhancement Vehicle's Occupant Safety by Using Vehicle Dynamics Control Systems in Vehicle-to-Barrier Offset Frontal Collision

Mustafa Elkady and Ahmed Elmarakbi

Abstract A multi-body occupant mathematical model is developed to capture the occupant kinematics during frontal offset collision. Different cases of vehicle dynamics control systems have been used during the collision to show their effect on the occupant dynamic response. The occupant deceleration and the occupant's chest and head rotational acceleration are used as injury criteria. It is shown from the numerical simulations that the occupant behaviour can be captured and analysed quickly and accurately. Furthermore, it is shown that the VDCS can affect the crash characteristics positively and the occupant safety is improved.

Keywords Collision mitigation · Mathematical modelling · Vehicle dynamics · Vehicle safety · Occupant kinematics

1 Introduction

The development of the vehicle dynamics control systems (VDCS) play an important role in improving vehicle stability, ride characteristics, and passenger safety. The anti-lock braking system (ABS) and the direct yaw control (DYC) system are used to help vehicle stability during emergency manoeuvres, while the

F2012-02-006

M. Elkady · A. Elmarakbi (✉)
University of Sunderland, Sunderland, UK

M. Elkady
Ain Shams University, Cairo, Egypt

active suspension control system (ASC) is used to improve vehicle ride quality and reduce the vehicle vertical acceleration. In addition, the ASC system integrated with the ABS is used to reduce the vehicle stopping distance [1].

With regard to the occupant safety, vehicle body pitch and drop during frontal impact play an important role in driver's neck and head injury [2–4]. Vehicle body pitch and drop have normally been experienced in frontal crash tests. Chang et al. [2] used a finite element (FE) method to investigate frame deformation upon full-frontal impact and discussed the cause and counter-measures design regarding vehicle body pitch and drop. It was found that downward bending generated from the geometric offsets of the frame rails in the vertical direction during a crash is the key feature of the pitching of the vehicle body.

Few researchers have investigated the effect of VDCS on vehicle crashworthiness and collision mitigation. The influence of the braking force on vehicle impact dynamics in low-speed rear-end collisions was studied [5] and this confirmed that the braking force was not negligible in high-quality simulations of vehicle impact dynamics at low speed. The effect of vehicle braking and anti-pitch control systems on the crash routine have been investigated by Hogan [6], who also investigated the possibility of using VDCS to improve vehicle collision performance in full and offset frontal vehicle-to-barrier collision. However, there are no studies have been found that investigate the effect of VDCS on the occupant safety. In this paper, a mathematical multi-body occupant model has been developed and it used to determine the occupant response in offset crash scenario with different cases of VDCSs occupant model.

2 6-DOF Mathematical Vehicle-Barrier Model (Primary Impact)

Using mathematical models in crash simulation is useful for the first design concept to predict the primary impact characteristics because rapid analysis is required at this stage [7, 8]. The primary impact indicates the collision between the front-end structure of the vehicle and an obstacle (a barrier in this paper). This section describes a 6-DOF vehicle dynamics/crash-mathematical model, shown in Fig. 1, which has been former developed by the author [9]. This model has been used to study the effect of vehicle dynamics control systems on vehicle collision mitigation.

Four spring/damper units are used to represent the conventional vehicle suspension system. Each unit has a spring stiffness k_s and damping coefficient c . The subscripts f , r , R and L denote the front wheels, real wheels, right wheels and left wheels, respectively. The ASC system is co-simulated with the conventional suspension system to add or subtract an active force element u , and the ABS is co-simulated with the mathematical model using a simple wheel model to generate the braking force F_b . To represent the front-end structure of the vehicle, four

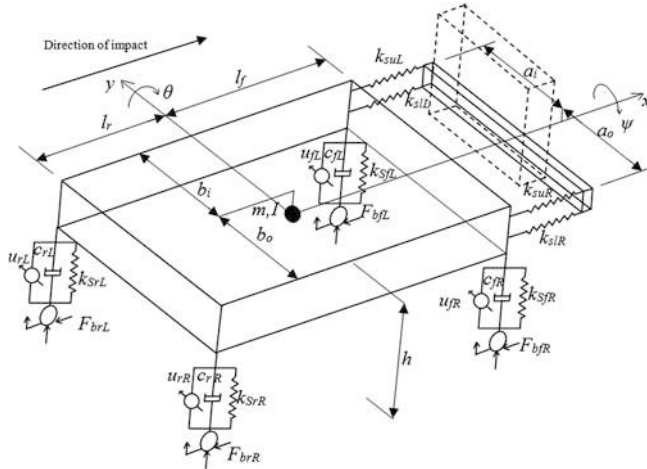


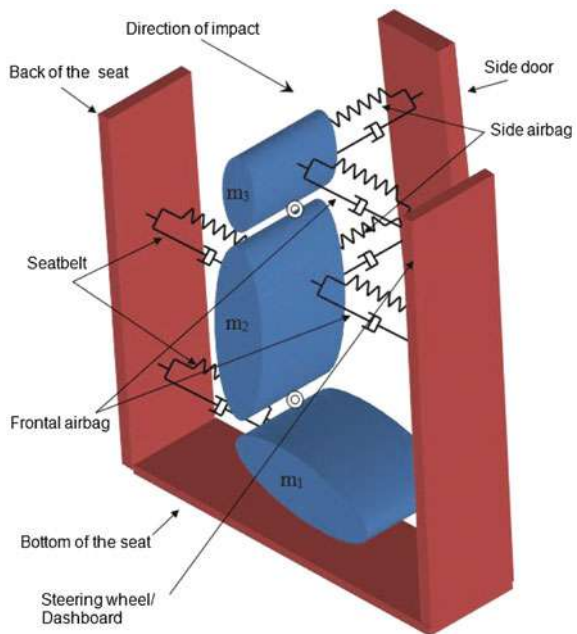
Fig. 1 Vehicle dynamics/crash-mathematical model (primary impact)

nonlinear springs with stiffness k_s are proposed. Two springs represent the upper members (rails) and two springs represent the lower members of the vehicle frontal structure. The subscripts u denotes the upper rails while the subscript l denotes the lower rails. The bumper of the vehicle is represented by a lumped mass m_b and it has only a rotational motion about the point of collision. The equations of motion and control systems have been described in details in a previous study by the author [9] to predict the vehicle deceleration, pitching angle and acceleration, and yawing angle and acceleration. These outputs from the vehicle model are used as input data to the occupant model.

3 Multi-Body Occupant Model (Secondary Impact)

The occupant biodynamic model shown in Fig. 2 is developed to evaluate the occupant kinematic behaviour during the secondary impact. The secondary impact is the interaction between the occupant and the restraint system and/or the vehicle interior due to vehicle collisions. The human body model consists of three bodies, with masses m_1 , m_2 and m_3 . The first body (pelvis), with mass m_1 , represents the legs and the pelvic area of the occupant and it is considered to have a translation motion in the longitudinal direction and rotation motions (pitching, rolling and yawing) with the vehicle body. The second body (chest), with mass m_2 , represents the occupant's abdominal area, the thorax area and the arms and it is considered to have a translation motion in the longitudinal direction and rotation motion around the pivot between the pelvis and the chest bodies (pivot 1). The third body (head), with mass m_3 , represents the head and neck of the occupant and it is considered to have a translation motion in the longitudinal direction and rotation motion around

Fig. 2 Multi-body occupant model (secondary impact)



the pivot between the chest and the head (pivot 2). A rotational coil spring is proposed at each pivot to represent the joint stiffness between the pelvis and the chest areas and between the chest and the head areas, respectively. The seatbelt is represented by two linear spring-damper units between the compartment and the occupant; the frontal and side airbags are represented by tow linear spring-damper units for each one. Figure 3a, b and c shows the side, top and frontal view of the occupant model, respectively. For each figure, the position of the occupant's different bodies is illustrated before and after crash.

3.1 Equation of Motion (EOM) of the Human Body Model

Due to the complexity of obtaining the equation of motions directly from the system, Lagrange's equations have been used to describe the general motions of the multi-body human model as follow:

$$\frac{d}{dt} \left(\frac{\partial E}{\partial \dot{x}_1} \right) - \frac{\partial E}{\partial x_1} + \frac{\partial V}{\partial x_1} + \frac{\partial D}{\partial \dot{x}_1} = 0 \quad (1)$$

$$\frac{d}{dt} \left(\frac{\partial E}{\partial \dot{\theta}_2} \right) - \frac{\partial E}{\partial \theta_2} + \frac{\partial V}{\partial \theta_2} + \frac{\partial D}{\partial \dot{\theta}_2} = 0 \quad (2)$$

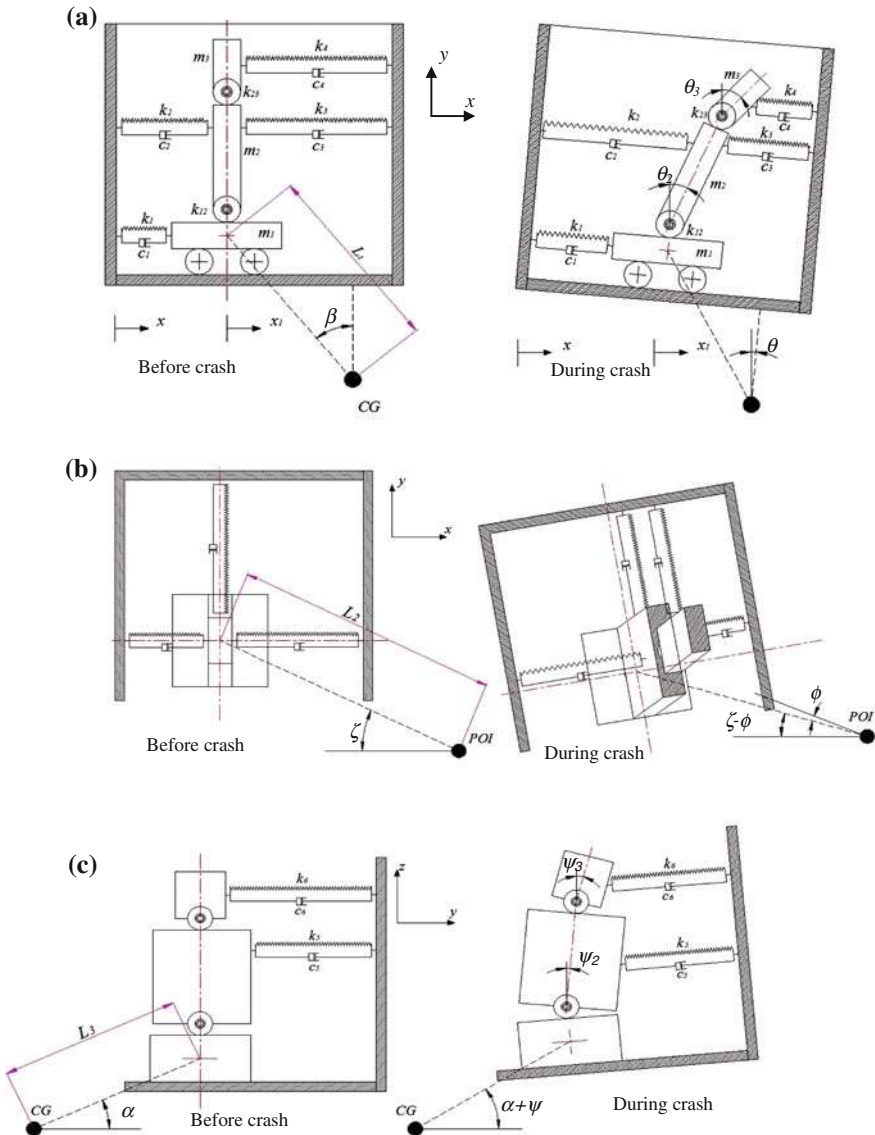


Fig. 3 **a** Side view of the occupant model. **b** Top view of the occupant model (POI point of impact). **c** Frontal view of the occupant model

$$\frac{d}{dt} \left(\frac{\partial E}{\partial \dot{\theta}_3} \right) - \frac{\partial E}{\partial \theta_3} + \frac{\partial V}{\partial \theta_3} + \frac{\partial D}{\partial \dot{\theta}_3} = 0 \quad (3)$$

$$\frac{d}{dt} \left(\frac{\partial E}{\partial \dot{\psi}_2} \right) - \frac{\partial E}{\partial \psi_2} + \frac{\partial V}{\partial \psi_2} + \frac{\partial D}{\partial \dot{\psi}_2} = 0 \quad (4)$$

$$\frac{d}{dt} \left(\frac{\partial E}{\partial \dot{\psi}_3} \right) - \frac{\partial E}{\partial \psi_3} + \frac{\partial V}{\partial \psi_3} + \frac{\partial D}{\partial \dot{\psi}_3} = 0 \quad (5)$$

where E , V and D are the kinetic energy, potential energy and the Rayleigh dissipation function of the system, respectively. x_1 , θ_2 , θ_3 , ψ_2 and ψ_3 are the longitudinal movement of the occupant's pelvis, the rotational angle of the occupant's chest about (y) axis, the rotational angle of the occupant's head about (y) axis, the rotational angle of the occupant's pelvis about (x) axis and the rotational angle of the occupant's head about (x) axis, respectively. \dot{x}_1 , $\dot{\theta}_2$, $\dot{\theta}_3$, $\dot{\psi}_2$ and $\dot{\psi}_3$ are their velocities, respectively. To get the components of the Eqs. 1, 2, 3, 4 and 5, the differentiations of the kinetic energy, potential energy, and Rayleigh dissipation function are determined. To solve these equations, they have been put in an integratable form and then rewritten in a matrix form. After that, different occupant's bodies responses (x_1 , θ_2 , θ_3 , ψ_2 and ψ_3) can be determined based on the input data from the vehicle model by solving the equations using the central difference method.

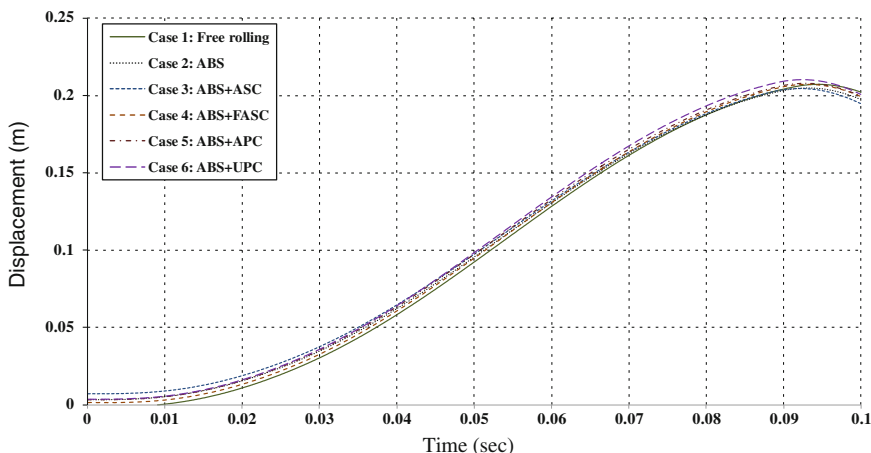
4 Numerical Simulation

The injury criteria in this paper have been taken as occupant's pelvis deceleration, occupant's chest rotational acceleration, and head rotational acceleration. These injury criteria of the occupant have been determined based on the output data obtained from the vehicle model [9]. The vehicle output data (deceleration and pitching and yawing acceleration) due to the collision, are transferred to the occupant as a sudden deceleration to all the body, and rotational movements of the head and chest. Six different cases of VDCS have been applied to the vehicle model 1.5 s prior collision as described in Table 1. The output results of each case have been used as input data to the occupant model to show the influence of these VDCS on the occupant behaviour. The following data is used in the numerical simulation: $m_1 = 26.68$ kg, $m_2 = 46.06$ kg, $m_3 = 5.52$ kg, $k_{R12} = 280$ Nm/rad, $k_{R23} = 200$ Nm/rad, $l_2 = 0.427$ m, $l_3 = 0.24$ m [10]. The total stiffness of the two seatbelt springs is 98.1 kN/m with a damping coefficient of 20 % [11], and then it distributed between the upper and lower seatbelt springs by ratio of 2:3, respectively [12]. Airbag's spring stiffness is 5 kN/m and the damping coefficient is 20 %. The slacks of the seatbelt springs are assumed zero, and the slack of the airbag is 0.05 m.

The longitudinal displacement of the pelvis is depicted for all cases in Fig. 4; it increases forward to reach its maximum position almost at the end of impact,

Table 1 Numerical study matrix

Case number	Description
Free rolling	Vehicle impacted the barrier without any activated control systems
ABS	ABS is applied
ABS + ASC	AS is applied along with ABS
ABS + Frontal ASC	AS is applied for front wheels only along with ABS
Anti pitch control	Anti-pitch control system is applied using the ASC components integrated with ABS
Under pitch condition	ASC is applied to front wheels in upward direction while applied to rear wheels in downward direction to give the vehicle negative pitching angle before crash and ABS is also applied

**Fig. 4** Occupant's pelvis displacement for all cases

and then returns back due to the seatbelt springs effect. It is observed from the figure that there are insignificant differences between the values of the maximum displacement of the occupant's pelvis. Figure 5 shows the pelvis deceleration for all cases; it is shown that it increases during the collision to reach its maximum values at the end of impact and then reduces due to the seat belt effect. The sudden decrease of the deceleration (arrow 1 in the figure) is due to the reverse of the effect of the braking force at the end of impact when the vehicle changes its direction and starts to move backward. It observed that the maximum deceleration for all cases is almost the same.

The relative rotation angle and acceleration around y axis of the occupant's chest for all cases are shown in Figs. 6 and 7, respectively. Because the VDCS is applied to the vehicle 1.5 s before the collision, the rotational angel and acceleration of the chest body at the point of collision is different related to each case. The chest rotational angle is increased to reach its maximum value after about

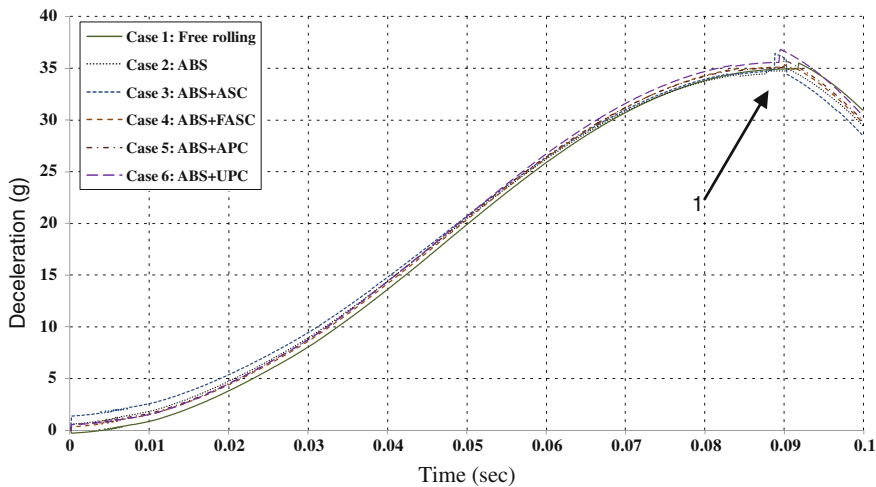


Fig. 5 Occupant's pelvis deceleration for all cases

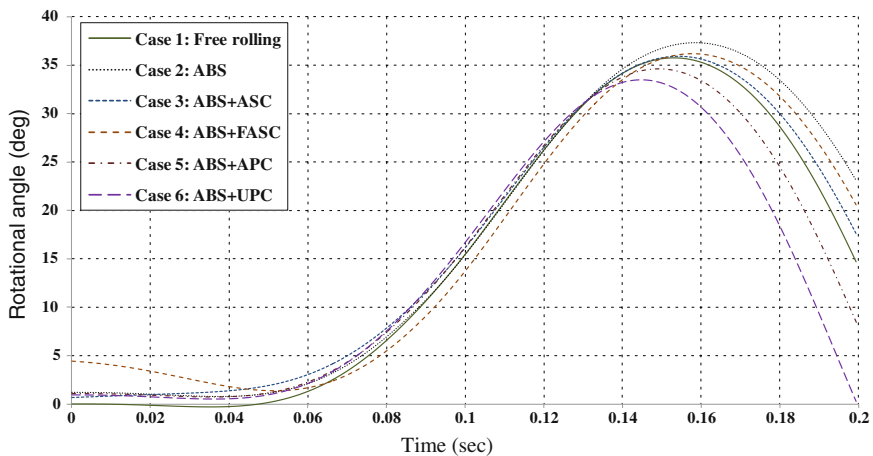


Fig. 6 Rotational angle of the occupant's chest about y axis for all cases

0.06 s from the end of impact. The maximum rotation angle is observed in case 2 (ABS) while the minimum one is observed in case 6 (ABS + UPC). The maximum positive rotational acceleration shown in Fig. 7 is due to the vehicle crash, while the negative maximum acceleration is due to the return of the seatbelt and airbags springs. The same effect of the reversing braking force is shown at the end of collision (arrow 1 in the figure). It is monitored that the minimum positive acceleration is occurred in case 3 while the minimum one in the negative acceleration is happened in case 2.

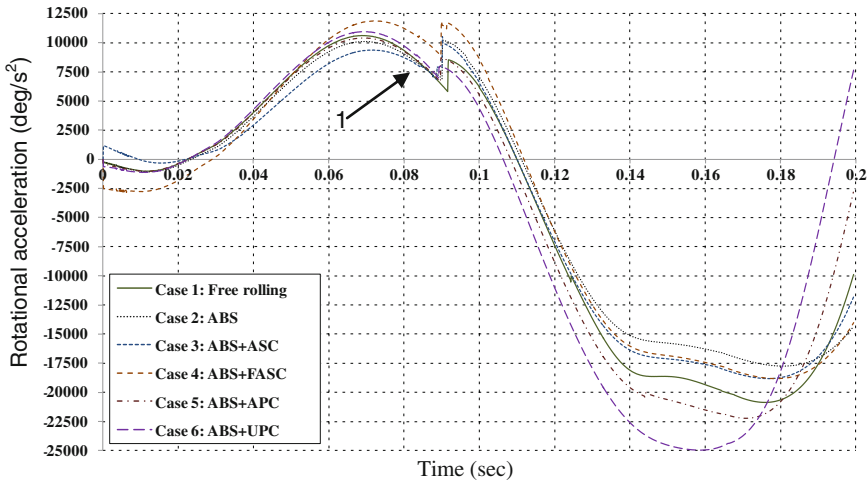


Fig. 7 Rotational acceleration of the occupant's chest about y axis for all cases

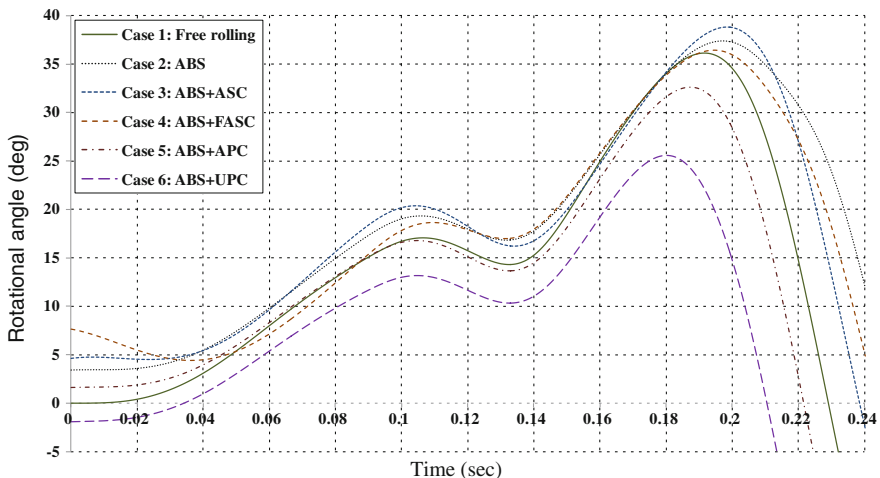


Fig. 8 Rotational angle of the occupant's head about y axis for all cases

The relative rotation angle between the occupant's chest and head about y axis is captured in Fig. 8. The head rotation angle is increased to reach its first peak values, which is occurred during the increase of chest rotating. Then it increased again due to the return of the occupant's chest to reach its second peak values (maximum values). The peak value of the head rotational angle is observed when the ASC is integrated with ABS (case 3) while the minimum one is detected in case 6. Figure 9 shows the relative rotational acceleration of the occupant's head. The maximum negative and positive acceleration are observed in cases 3 and 1

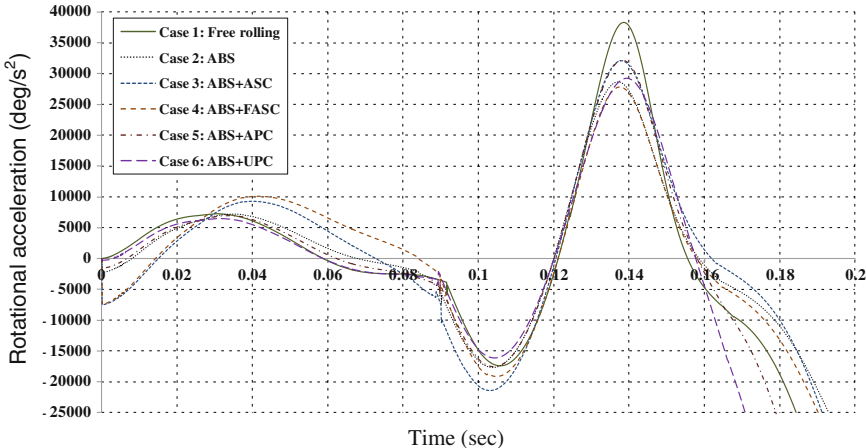


Fig. 9 Rotational acceleration of the occupant's head about y axis for all cases

respectively, while the minimum negative and positive values are seen in cases 6 and (2, 4 and 6), respectively. As observed in the chest results, the head rotational angle and acceleration are started from different points related to the VDCS case.

The relative rotation angle about x axis ($\psi_2 - \psi$) of the occupant's chest for all cases is depicted in Fig. 10. When the occupant chest reaches its maximum rotational angle, it stays for while at this angle while the vehicle is rotated around the point of impact. The maximum rotation angle is observed in case 1 (free rolling) while the minimum one is observed in case 3 (ABS + ASC) and in case 6 with a bit higher value. Figure 11 shows the rotational acceleration of the occupant's chest about x axis for all 6 cases. The first sudden change in this acceleration is due to the activation of the side airbag, while the second one is due to the reversing braking force, arrow 1 and 2 respectively. The third sudden change of the chest acceleration is due to the deactivation of the vehicle's front-end springs, which cause a sudden decrease of the vehicle pitching, yawing and rolling. The maximum positive and negative rotational accelerations are almost the same for all 6 cases. However, case 3 shows the minimum values (by a small difference) among other cases.

The relative rotation angle about x axis between the occupant's chest and head are captured in Fig. 12. During the collision, while the chest takes a positive acceleration and starts rotating toward the vehicle's side door, the head takes a negative small rotation values (about 5 degrees) in the other direction. This maximum negative rotation angle is almost the same for all cases. The positive peak value of the head rotational angle is observed in case 1, while the minimum one is seen in case 2. Figure 13 shows the relative rotational acceleration about x axis of the occupant's head. The effect of the reversing braking force is observed at the end on collision (arrow 1 in the figure). While the maximum positive

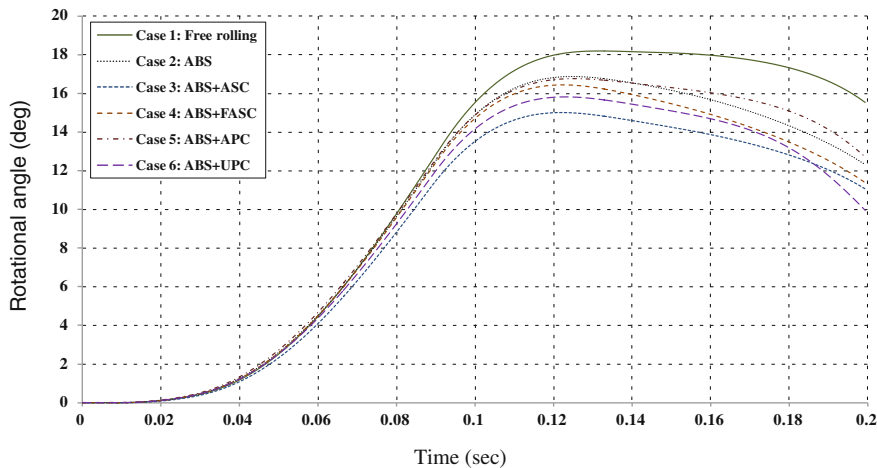


Fig. 10 Rotational angle of the occupant's chest about x axis for all cases

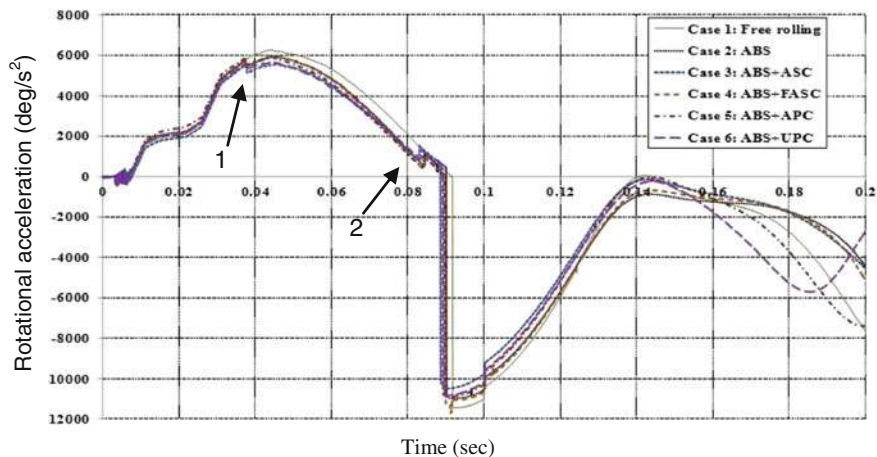


Fig. 11 Rotational acceleration of the occupant's chest about x axis for all cases

acceleration is almost the same for all cases, the maximum negative acceleration caused by the effect of the side airbag is observed in cases 6.

Related to the occupant injury criteria, the occupant's head rotational accelerations appeared to be the major cause of strain-induced brain injury which it contributed to more than 80 % of the brain strain and the peak amplitude of rotational acceleration must not exceed 9.4 krad/s² (538.5 kdeg/s²) [13]. The results show some improvement in the occupant injury criteria, which makes the crash event more survivable. Use of under pitch technique (case 6) can help reduce the chest and head rotation angle, and head rotational acceleration. The VDCS affects the occupant's behaviour with different ways related to the applied case,

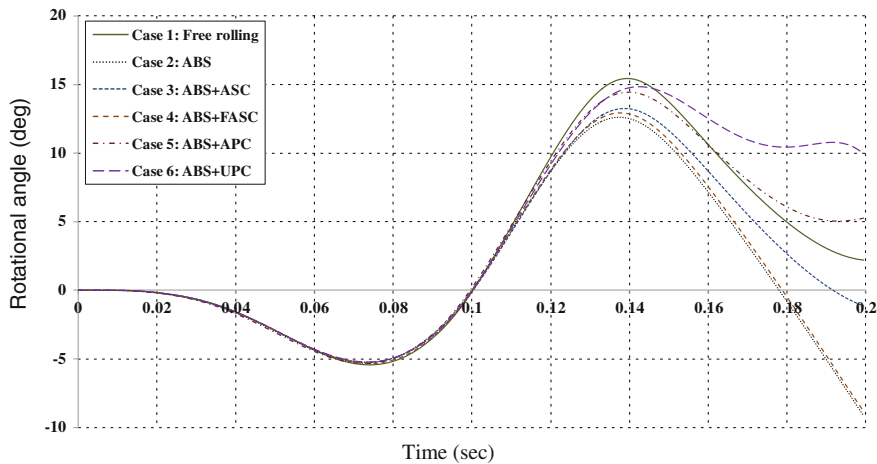


Fig. 12 Rotational angle of the occupant's head about x axis for all cases

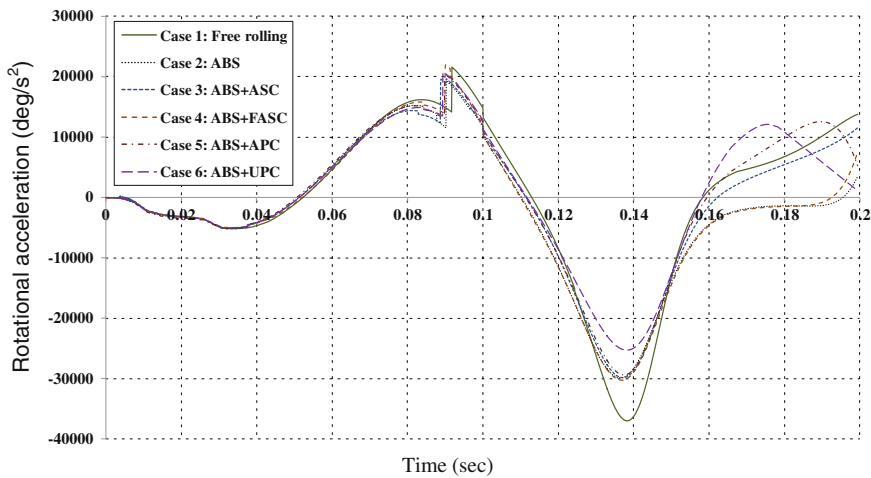


Fig. 13 Rotational acceleration of the occupant's head about x axis for all cases

and it can be seen that the applied of frontal UPC alongside ABS (case 6) can be taken as the best case due to its effect on the occupant's head (the most important part of the occupant's body).

5 Conclusion

A multi-body occupant mathematical model has been developed to study the effect of VDCS on the occupant dynamic response. Different cases of the VDCS have been investigated in case of vehicle-to-barrier frontal offset collision. The results obtained from a previous vehicle model have been used as the input data for the occupant model. The results show that the effect of the VDCS is quite minimal in terms of occupant relative displacement and deceleration. However, there are a significant effect on the rotations angle and acceleration of the occupant chest and head.

Acknowledgments The authors would like to thank the Egyptian Government and the Faculty of Engineering, Ain Shams University for supporting this research.

References

1. Ting W E, Lin JS (2004) Nonlinear control design of anti-lock braking systems combined with active suspensions. In: 5th Asian control conference, 2004, vol 1, pp 611–616
2. Chang JM, Rahman M, Ali M, Tyan T, El-Bkaily M, Cheng J (2005) Modeling and design for vehicle pitch and drop of body-on frame vehicles. In: SAE world congress & exhibition, paper no. 2005-01-0356, Detroit, 2005
3. Chang JM, Ali M, Craig R, Tyan T, El-bkaily M, Cheng J (2006) Important modeling practices in CAE simulation for vehicle pitch and drop. In: SAE world congress & exhibition, paper no. 2006-01-0124, Detroit, 2006
4. Chang JM, Huang M, Tyan T, Li G, Gu L (2006) Structural optimization for vehicle pitch and drop. In: SAE world congress & exhibition, paper no. 2006-01-0316, Detroit, 2006
5. Mastandrea M, Vangi D (2005) Influence of braking force in low-speed vehicle collisions. Proc IMechE 219(2):151–164
6. Hogan I, Manning W (2007) The use of vehicle dynamic control systems for automotive collision mitigation. In: 3rd institution of engineering and technology conference, Warwick, 2007, pp 1–10
7. Emori RI (1968) Analytical approach to automobile collisions. In: SAE world congress & exhibition, paper no. 680016, Warrendale, 1968
8. Kamal MM (1970) Analysis and simulation of vehicle to barrier impact. In: SAE world congress & exhibition, paper no. 700414, Detroit, 1970
9. Elkady M, Elmarakbi A, Crolla D (2011) A numerical study for optimizing vehicle dynamics control systems in offset impacts. In: SAE world congress & exhibition, paper no. 2011-01-0954, Detroit, 2011
10. Ilie S, Tabacu S (2007) Study of the occupant's kinematics during the frontal impact. Ann Oradea Univ Fascicle Manag Technol Eng VI(XVI):542–551
11. Elmarakbi A, Zu J (2004) Dynamic analysis of smart structures for vehicle-to-vehicle frontal collision alleviation. Trans Soc Autom Eng Japan 35:151–156
12. Paultz TJ, Blackketter DM, Rink KK (2006) Constant force restraints for frontal collisions. Proc Inst Mech Eng Part D J Automob Eng 220(9):1177–1189
13. Zhang J, Pintar F (2006) Brain strains in vehicle impact tests. Annu Proc Assoc Adv Autom Med 50:1–12

Research on a New Airbag in the Seat Back of Vehicle

Zhi Wang, Huili Yu, Taisong Cui
and Hui Zhao

Abstract This paper studies a newly patented rear passenger airbag which installed in the seatback to protect the passengers sitting behind it during the frontal crashes. The airbag is packaged in the front row seatback and deployed rearward to cover the head and the chest to reduce the injuries on the passenger at the second row behind the front row of the seat. A CAE model is assembled with front seat, rear passenger airbag, rear dummy, rear seat and the seat belt. A series of the parameters of the rear passenger airbag including the size, shape, installation position, firing time, front seatback angle, belted and unbelted, have been analyzed. It is found that rear passenger airbag can effectively reduce rear dummy injuries especially in the head, neck, and chest areas in the event of frontal crashes with belted or unbelted conditions. Since the rear passenger airbag is installed in the front seatback, the seatback angle will affect rear passenger airbag deployment direction, thus it may not cover the head and the chest when the seatback angles are at the extreme angles (full up or full down). In these positions, the seatback angle sensor is suggested to turn off the rear passenger airbag. When the seatback angle is in between two extreme angles, the rear passenger airbag is designed in the way that the rear passenger airbag surface will mostly match the profile of the rear dummy in order to protect the dummy well.

Keywords Rear passenger airbag · Rear passenger protection · CAE

F2012-F02-013

Z. Wang (✉) · H. Yu · T. Cui · H. Zhao
State Key Laboratory of Vehicle NVH and Safety Technology, Chongqing, China

1 Background

1.1 Technical Requirements

In China, the 2012 version of C-NCAP evaluation procedures implemented in July 2012, compared with the 2009 version of C-NCAP evaluation procedures. The 2012 version have a major changes to the rear passenger of the female dummy injury into a star rating. Three tests of the rear passenger score of 6 points, 9.7 % of the total points. Is the first time in the world to rear adult protection in frontal crash tests.

1.2 Market Demand

Passive safety of adult has been perfect, but rear adult protection is indeed empty, especially the rear frontal protection system. Mainly seat belts provide protection, but only seat belts in the rear passenger of adult head and neck protection ineffective. In this paper, is when frontal crash occurs for the protection of rear passengers airbag design, the rear passengers in a crash can be good protected.

2 Overall Technical Ideas

Mainly divided into three areas:

1. Rear passenger airbag special control strategy: dangerous due to the use of airbags, and rear air bags use of the environment is more complex than the environment of the front airbags. Therefore, to consider a few points: (a) rear passenger airbag in the backrest of the front seats, front seat backrest angle and the front seats have a large range of adjustment, so to determine the protection effect in the rear passenger airbag point of view to allow the airbag fire, beyond the effective scope of protection will not fire airbags. (b) The rear seats need to include monitoring functions to monitor the use of child seats or rear seats not in use (no ride), rear air bags will not fire. Airbag design will be considered low-risk fire, to protect the passenger in the OOP state and the passenger not wearing the seatbelt.
2. Adult protection effect: with other airbags, rear passenger airbag to consider the 5, 50, 95 % protection effect of the dummy.
3. Rear passenger airbag engineered products: contains two things: one, rear air bags installed in the front seat backrest on the way. Rear passenger airbag to be normal used could have a system, which includes the front seat position sensor, front seatback angle sensor, rear seat status sensors, rear seat belt wearing sensor, and integrated so sensor information and analysis to judge whether or not to use the rear passenger airbag ECU controller.



Fig. 1 Analysis model

3 Analysis

3.1 Protection Effect of Rear Passenger Airbag

To the Chang'an develop a high-class cars, for example, the establishment of the vehicle rear passenger restraint system analysis model. Equipped with rear passenger airbag verification rear passenger airbag on the protection effect of 5, 50, 95 % dummy. Note: the front seats in the middle of the travel and the front seat backrest angle is 25° which is the design backrest angle (Fig. 1).

Comparative analysis with or without rear passenger airbag difference on dummy injury:

Contrast no rear passenger airbag and rear passenger airbag in case of dummy injury, can be seen: in the case of a rear passenger airbag, the dummy's head HIC and neck injuries have been improved. The analysis showed that the rear passenger airbag products can increase the protection effect of the rear passenger (Fig. 2, Table 1).

3.2 Rear Passenger Airbag Normal Fire Range: Seats Front and Rear Travel and Seatback Angle Range

The range of the normal fire of the rear air bag identified the need to consider the dummies of different sizes. The basic principle is: the seats around the front position of the position range from 5 % dummy determine, to determine the final

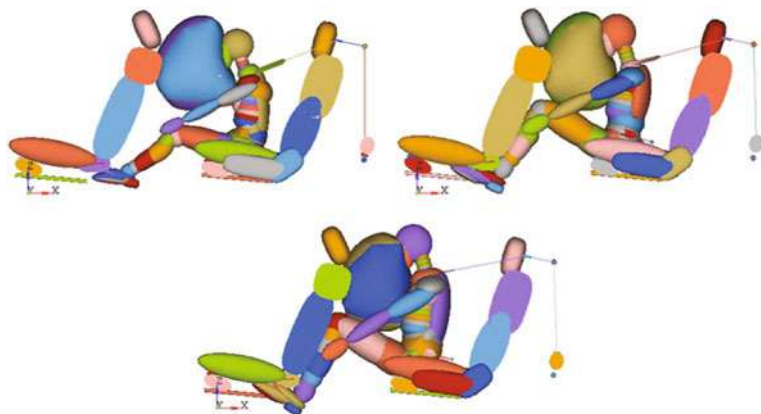


Fig. 2 Rear passenger airbag protection effect

Table 1 Dummy injury contrast

(%)	Head HIC	Neck			Chest
		FX(N)	FZ(N)	My(N*m)	Dis(mm)
5	No RPA	924	1184	29.01	36.7
	RPA	595	316	15.1	35.3
50	No RPA	887	1496	36.67	31.6
	RPA	374	673	8.64	34.6
95	No RPA	756	1254	56.18	40.9
	RPA	293	751	18.73	40.2

position by 95 % dummy; seatback angle maximal from 95 % dummy to determine and the minimum angle from 5 % dummy. Range of travel front and after of the seat position and seat back angle range would be synthesis considered. The range of the rear air bag normal fire for each model will be different, must to analyzed to determine, according to the specific models.

3.2.1 Travel Range Before and After the Seat Analysis

Similarly, the Chang'an develop a high-class cars, for example. The rear seats before and after the travel is not adjustable, the rear seat back angle is not adjustable. Before and after the front seat travel range is 200 mm, the front seat design backrest angle is 25°. Were calculated on the basis of the travel the middle of the 5 % dummy seat forward 50 and 100 mm, and 95 % dummy seat moved back 50 and 100 mm. The results are as follows:

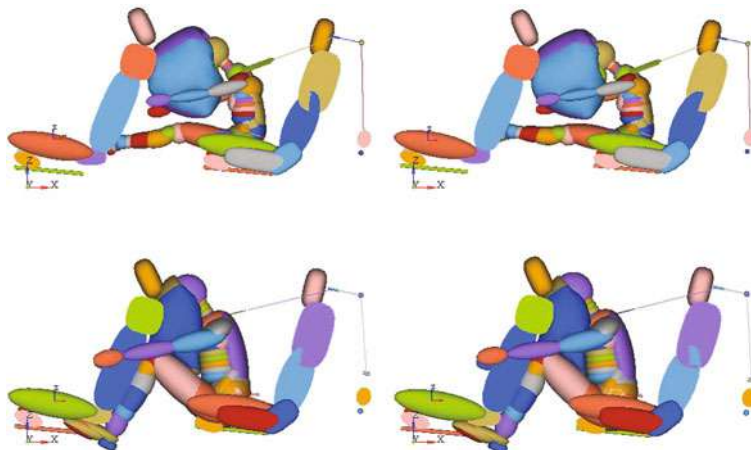


Fig. 3 Travel range before and after the seat analysis

From the results of the analysis, 200 mm within the scope of the front seat of the car before and after the travel can guarantee the protection of air bags on the rear dummy, there was no dummy head off the airbag protected areas (Fig. 3).

3.2.2 Seatback Angle Range Analysis

Similarly, the Chang'an develop a high-class cars, for example. The rear seats before and after the travel is not adjustable, the rear seat back angle is not adjustable. Before and after the travel in the middle position of the front seat. Design backrest angle is 25°. 5 % dummy seatback forward 5° and 10°, and 95 % dummy seatback backward 5° and 10° were calculated on the basis of the design backrest angle. The results are as follows:

From the results of the analysis, 95 % dummy seatback backward 10°, the dummy head beyond the protected area of the rear air bags, head and front seats have contact. Therefore, the rear passenger airbag fire normal range is approached in the design of the backrest angle basis to forward 10°, backward 5° (Fig. 4).

Considering the rear passenger airbag normal fire range of before and after the front seat travel and seatback angle range should be as follows (Fig. 5).

4 Engineering

The rear passenger airbag assembly structure (see Fig. 6) from the rear passenger airbag and cassette bracket connected to the backrest of the seat frame. Cartridge installation bracket have two parts: metal bracket (4 and 5) and a rubber box (2).

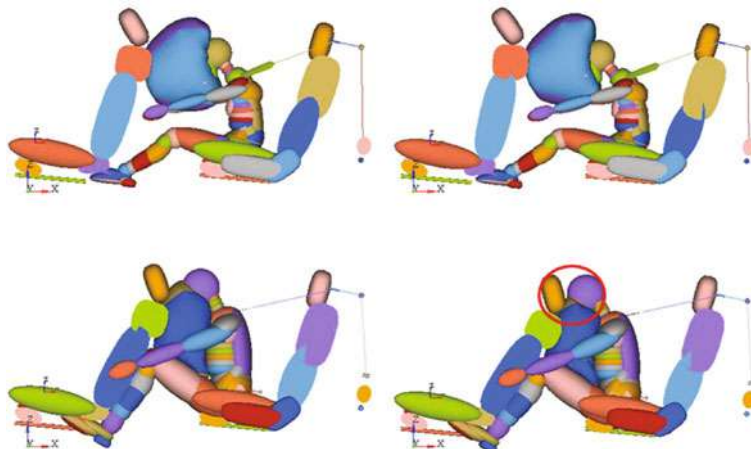
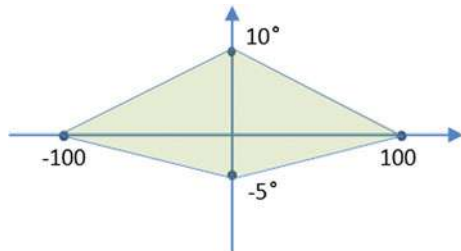


Fig. 4 Seatback angle range analysis

Fig. 5 Rear passenger airbag range



The rubber box (2) located in the seat back bracket and seat fabric, from the bottom to up is the inflater (3), airbags (8) and the air bag guide structure (1). Inflater (3) and airbags structure of (8) is fixed at the bottom of the rubber of the box. Air bag guide structure (1) is located in the top of the rubber box (2), used for airbag deployment direction of the control.

Rubber box (2) front seat backrest side of the plate (6) by the metal bracket welded metal brackets for the two arch-tube (4) and of an L-shaped pallet (5). The rubber box (2) are located within two bow-tube (4), by two bow-tube horizontal welding in the front seat backrest side plate (6). L-type pallet (5) arranged in the bottom of the rubber box (2), longitudinally welded in the front seat backrest bracket.

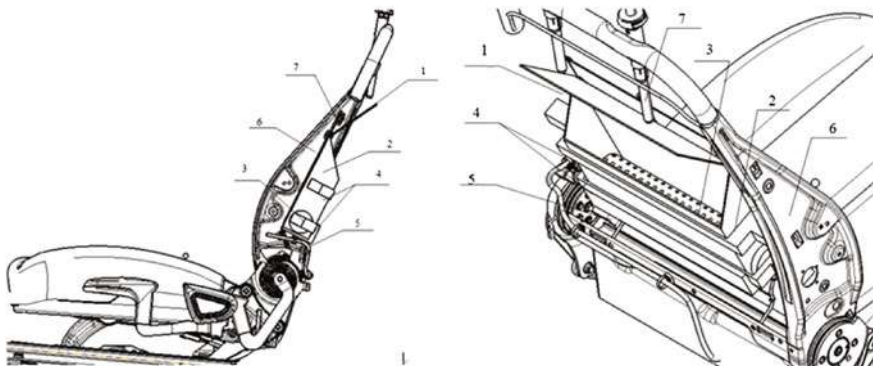


Fig. 6 Rear passenger airbag engineering

5 The Next Test and Development Plan

With the airbag suppliers complete rear passenger airbag sample test protection effect development test.

With ECU suppliers to complete the sensors and logic judgment control development.

With seat suppliers to complete rear passenger airbag installation structure development.

Reference

1. MADYMO theory manual

Study of the Sled Test Simulation for 40 % Offset Deformable Barrier Crash Test

Zhi Wang, Bi-na Dai and Hui Zhao

Abstract Sled test simulation has been one of key tools in developing vehicle restraint systems and been widely used in every OEMs. However, for frontal crashes, traditional sled test facility can only simulate full frontal crash test effectively. It can not simulate frontal 40 % offset crash tests where the vehicle rotates and pinches during the crash. This limitation has become a bottleneck for the restraints developments when the new safety star rating standard—2012 version of the C-NCAP requires both 50 km/h full frontal test and 64 km/h frontal 40 % offset test to be conducted. To develop restraints system by crashing full vehicles clearly is not timely and economically viable. Therefore, it is important to study how to modify the traditional sled test facility to be able to simulate the frontal offset vehicle crashes. This paper uses CAE MADYMO model to successfully find a representative rotation angle in order to guide the sled test set up. The model consists of driver side 50 % male dummy, airbag, seatbelt with pretensioner and load limiter, and a crushable steering column. First, the MADYMO model is constructed and correlated with 64 km/h vehicle test injury numbers. Then, the MADYMO model is rotated along Z axis. A series of angles and the corresponding vehicle pulses are input into the model and the dummy performances including the injury numbers and the movements are analyzed. The author finally finds a representative angle and the vehicle pulse, which can be used for the sled test set up for accurately simulating the 64 km/h 40 % offset frontal vehicle crash test. With the application of this methodology, the traditional sled test facility can be used for both full frontal vehicle crash simulation and offset frontal vehicle crash simulation as well.

F2012-F02-014

Z. Wang (✉) · B. Dai · H. Zhao
State Key Laboratory of Vehicle NVH and Safety Technology, Chongqing, China

Keywords MADYMO · CAE · ODB · Sled test · Vehicle crash safety

1 The Basic Model and the SLED Test Simulation for ODB Crash Test Ideas Introduced

In this paper, the basic model is a model of Chang'an driver side restraint system MADYMO model [1]. The restraint system of the model system is the driver's airbag, the pretensioner and limiter seat belts, crashable steering column. And the model correlation by 64 km/h ODB crash tests, the dummy injury has predictability, simulation and test dummy injury of the standard shown in Fig. 1.

In the sled test to simulate the ODB conditions, the key is how to simulate the vehicle collision conditions when the vehicle hit the barrier occurs vehicle deflection; and vehicle acceleration pulse of the B-pillar on the left and right side was differences, but can only exert an acceleration sled test pulse. The general idea is to solve the initial installation of the fixed body in a sled test on the body and the sled to accelerate the direction to maintain a certain angle, this angle to simulate dummy in the vehicle deflected the course of the relative body deflection of moving gesture; sled acceleration pulse using the lateral acceleration of the vehicle about the B-pillar for a certain percentage of weighted to identify for the acceleration of the sled test pulse. Practical engineering applications, the first analytical model of car to find the goodness of fit of the best CASE, then experimental validation.

1.1 Analytical Methods and Results

Correlation good vehicle bias analysis model, adjusted to the sled test boundary conditions, and the acceleration of the loading direction with the X-axis to a certain angle. Done a large number of simulation analysis on the deflection angle and pulse scale ratio of these two variables in this model before, to find the appropriate range. Therefore, this analysis of variable scope narrow vehicle origin is the center of rotation around the Z-axis rotation angle α ($0^\circ, 6^\circ, 8^\circ, 10^\circ$). The acceleration of the sled to select the two values, namely 30 % synthetic vehicle right side of the B-pillar, left side of the 70 % and the B-pillar acceleration. Analysis matrix, as well as acceleration pulses as follows (Table 1, Fig 2).

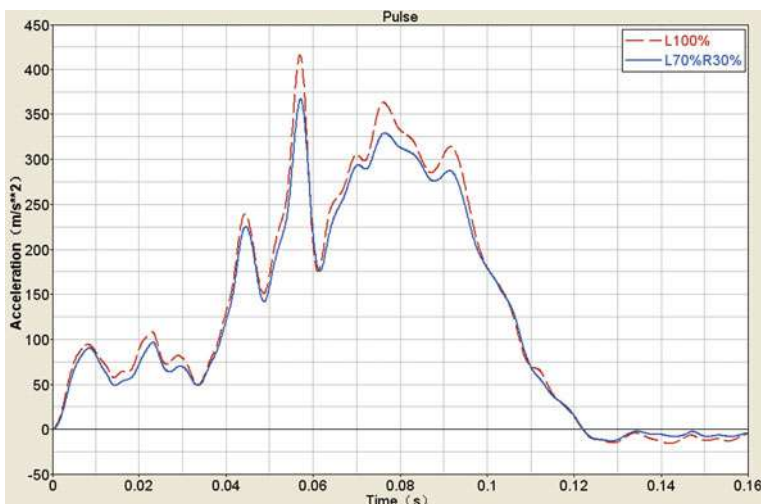
Calculation case1–case7 models, compared to the dummy injury with dummy movement attitude, to find suitable sled of the models to simulate the vehicle 64 km/h ODB angle of rotation of the working conditions mainly on the sled test, dummy injury the response of the head, neck, chest and pelvis fitting. The dummies injury comparison in Table 2.



Dummy	Injury	Test	Simulation
Head	HIC	359/4.0	428/4.0
	3ms G	46.1g/4.0	48.02g/4.0
	Score	4	4
	Fx	4	4
Neck	Mx	16.09Nm/4.0	25Nm/4.0
	Fz	4	4
	Score	4	4
	Dis	36.05mm/1.99	33.4mm/2.37
Chest	3ms G	44.76g/2.77	44.62g/2.8
	Score	1.99	2.37
	Fz	4	4
Femur	Knee Dis	1.03mm/4.0	0.7mm/4.0
	Score	4	4
	Tl	0.72/2.58	0.84/2.04
Tibia	Fz	1.72/4.00	2.37/3.75
	Score	2.58	2.04
	Total Score	12.57	12.41

Fig. 1 The base model**Table 1** Analysis matrix

Case study	0°	6°	8°	10°
L100 %	Case1	Case2	Case4	Case6
L70 %R30 %	–	Case3	Case5	Case7

**Fig. 2** Pulse

From the above case1–case7 models calculated results, a case5 the dummy injury is fitting to the vehicle offset crash test dummy injury. Therefore, the model sled simulation vehicle 64 km/h ODB should be used around the Z axis of rotation 8°

Table 2 The conditions dummy injury comparison table

Results	Base	Case1	Case2	Case3	Case4	Case5	Case6	Case7
Head HIC	428	1765	498	435	567	442	569	469
Head 3 ms	48.02	76.85	51.81	49.74	57.56	48.11	64.1	50.29
Head score	4	0	4	4	4	4	4	4
Neck My	25	44.33	28.79	21.17	21.47	16.92	14.07	17.3
Neck score	4	0	4	4	4	4	4	4
Chest 3ms	44.62	45.91	53.01	48.83	51.74	47.77	50.94	48.73
Chest Dis	33.4	56.9	41.8	38.1	41.6	34.4	38.1	30.6
Chest score	2.37	0	1.17	1.69	1.2	2.22	1.65	2.05

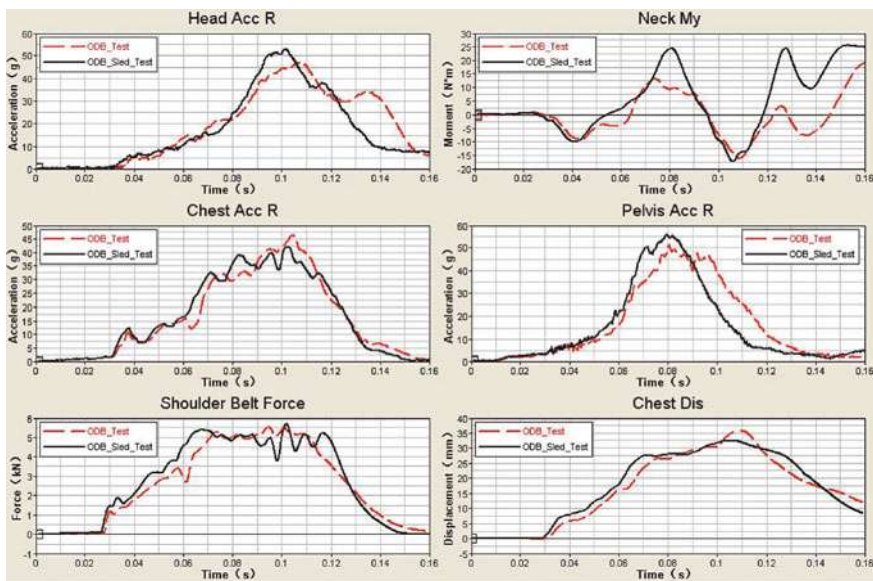
**Fig. 3** Sled test

pulse using the left side of the B-pillar, 70 % and the B-pillar on the right 30 % to simulate.

2 Experimental Validation of the Sled

2.1 Test Methods

ODB sled test method is generally traditional sled test method, the key difference is that is the sled body fixed to keep the sled acceleration loading direction is coincident with the body X direction, but ODB sled body fixed way acceleration direction of the sled body X direction to maintain a certain angle, the angle can be adjusted as needed, and the angle adjustment accuracy to ensure that 1°. In this model, the angle of 8° body mounting sled models using the above-mentioned B-pillar to the 70 % left side of the pulse and the 30 % right side of the pulse (Fig. 3).

**Fig. 4** Curve contrast**Table 3** Dummy injury comparison table

Dummy injury	ODB test	ODB sled test
Head	HIC	359/4.0
	3ms G	46.1 g/4.0
	Score	4
Neck	FX	4
	My	16.09Nm/4.0
	Fz	4
Chest	Score	4
	Dis	36.05 mm/1.99
	3ms G	44.76 g/2.77
	Score	1.99
		33.4 mm/2.51
		40.8 g/3.49
		2.51

Will the ODB sled test dummy injury curve compared with the vehicle ODB crash test results, the curve fit to reach more than 80 %. Key parts of the curve comparison shown in Fig 4.

Dummy injury score also were compared. Comparative results: ODB sled dummy injury and scored to reflect the situation of the vehicle ODB crash test. Table 3 can be drawn from the above results, the ODB sled around the Z-axis rotation of an angle in front sled test to simulate the vehicle ODB crash dummy injury is feasible. The ODB sled can be applied to the integrated development of the restraint system.

3 Conclusion

The overall opinion, this approach is feasible to simulate the ODB conditions in front sled test. 64 km/h ODB conditions in the sled test restraint system to match, reducing the number of vehicle ODB crash test. Saving car resources, testing costs and development time. ODB sled only one deflection and acceleration pulses, so this method can not guarantee the fit of both sides of the front driver and front passenger, it's to fit on one side only.

Reference

1. MADYMO theory manual

Development of a Six-Year Old Digital Human Body Model for Vehicle Safety Analysis

Jesse Ruan, Stephen Rouhana and Saeed Barbat

Abstract Biomechanical differences between children and adults are anatomically obvious and physiologically evident. Nevertheless, scaling laws have been used between child and adult mechanical properties in biomechanical injury studies. These laws may or may not be valid depending on the aging properties of the tissue being studied. Detailed adult human body finite element models have been developed in recent years, but not for children. Therefore, the objective of this study is to develop an industry-first, full-body digital human finite element (FE) model of a six-year old child aimed at helping improve vehicle safety for children and also validating the scaling laws between child and adult mechanical properties. The child digital model was developed based on CT scan images from a living six-year old child⁺⁺. Model geometry was extracted from the CT scans through image analysis. Finite element (FE) mesh for different parts of the body was created from the geometric data obtained in the CT scan image analysis process. While the CT scans were taken with the subject supine, the model in this study is in a standing position, representing a pedestrian posture. Biomechanical properties of each component in the model were obtained from the literature. The model includes a detailed anatomical representation of human organs for a six-year old child, from head to toe. Predicted model responses are compared with test data found in the literature. Forces, displacements for the neck, chest, and abdomen; pressures for the brain are output for injury reference analysis. The analysis of the FE model was performed by using LS-DYNA software. Although the geometric accuracy of the six-year child FE model has been ensured by extracting data from living CT scan images, the mechanical property data used in the model

F2012-F02-015

J. Ruan (✉) · S. Rouhana · S. Barbat
Passive Safety Research and Advanced Engineering, Ford Motor Company, Dearborn, USA

and the impact response used for model comparison can only be considered tentative; since these data are sparse in literature.

Keywords Child safety • FE modeling • Injury biomechanics

1 Introduction

Finite element (FE) models of the human body have been developed for impact biomechanics and injury analysis during vehicle crashes for decades. Most of these models are devoted to body regions such as the head, neck, thorax, abdomen, and upper and lower extremities; a few of them represent a whole human body model. These models are mostly 50th percentile-based because the first crash dummy developed for safety regulations and vehicle safety design was 50th percentile-based. One of the most widely used series of crash dummies is the Hybrid III, which includes a 50th percentile adult male. The injury criteria associated with other crash dummies within the Hybrid III dummy family (95th, 5th, 3, 6, 10 years-old dummies) were scaled from the 50th percentile dummy for the Injury Assessment Reference Values (IARVs) which were derived by the scaling methods (Melvin [1]). Scaling methods have been used to develop human body models that are not 50th percentile-based. For example, Mizuno et al. [2] developed the first 3-year old child human body FE model from a 50th percentile human body model using scaling techniques. While the accuracy and applicability of the scaling techniques need to be further proved, it is justified knowing the lack of tissue property data and dynamic impact responses from human child cadaveric tests in the literature.

There are three major technical hurdles that challenge the modellers to develop a highly biofidelic child human body model: (1) realistic geometric data; (2) realistic material properties of body tissues; (3) impact responses from laboratory-setting child cadaveric tests or real world crashes. In the current study, the emphasis was to tackle the first challenge to develop a six-year old child human body FE model from child geometric data of a living human by means of CT scan images. Material property of body tissues and dynamic impact responses are obtained from the literature, leaving the second and third challenge (both beyond the scope of this research) for further investigation.

2 Methods

2.1 Geometric Data Extraction and 3D Model Generations

The geometric data of the proposed six-year old human child digital model was based on CT scan images of a living six-year old child. The CT scans were taken with the subject supine, with slices space 1 mm from each other. Values of window width and window level used in performing the scans were 300 and 40 Hu, respectively. The CT scan images were deemed necessary for diagnostic purposes and were not taken specifically for the current study. Since these images are in the category of De-identifying materials and not Personal Health Information, they are not subject to the rules of HIPAA (Health Insurance Portability and Accountability Acts).

Figure 1 shows a cross-section of the head, neck, shoulder, thorax, pelvis, and leg/knee from the six-year old CT scans. Figure 2 shows a flow chart describing the process involving geometric data extractions, 3D surface generations, and FE model development. Threshold methods (by adjusting the values of window width and window level) were used to locate areas of interest and to extract three-dimensional data, as shown in Fig. 3. The threshold methods allow users to differentiate the boundary of different tissues and repair unclear masks and fill in holes (if necessary) as seen in Step 2 of Fig. 4. The 3D surfaces were generated by calculating the selected masks to form the NURBS (Non-Uniform Rational B-Spline) surface as visualized in Steps 2 and 3 of Figs. 2 and 4. The generated NURBS surfaces were imported to the FE preprocessor to generate finite element meshes as shown in Step 4 of Figs. 2 and 4.

2.2 Model Descriptions

Figure 5 shows some component bones for the child skull. They include the suture, parietal, frontal, temporal, mandible, Zygomatic, and facial (the occipital, and basal are not shown). All the skull bones were modelled as 8-node hexahedral elements. The overall appearance of the child skull including facial bones is shown in Fig. 6.

Figure 7 shows a more detailed description of the child skull and brain. The skull was modelled as a three-layered structure including the outer table, diploe, and inner table. The brain includes cerebrum, cerebellum, brain stem, corpus callosum, cerebrospinal fluid, ventricles, sinus, falx cerebri, tentorium cerebelli, pia mater, dura mater, grey and white maters (some of these may not show in Fig. 7). Figure 8 shows the neck FE model of the six-year old. It contains all the seven cervical vertebrae, T1 thoracic spine, and major neck muscles.

Figure 9 shows the thoracic model of the six-year old. Its skeleton parts include rib cage, sternum, cartilage, 12 thoracic vertebrae and 5 lumbar vertebrae. Internal

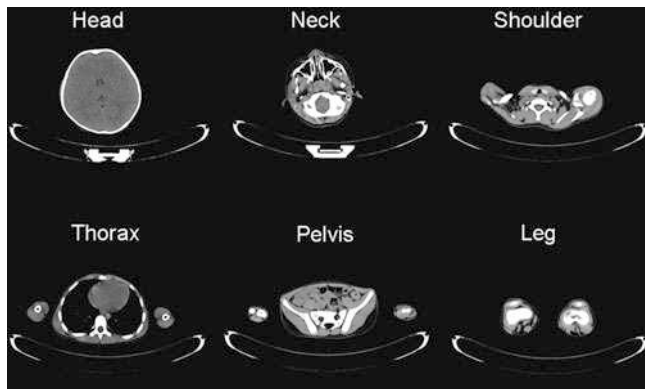
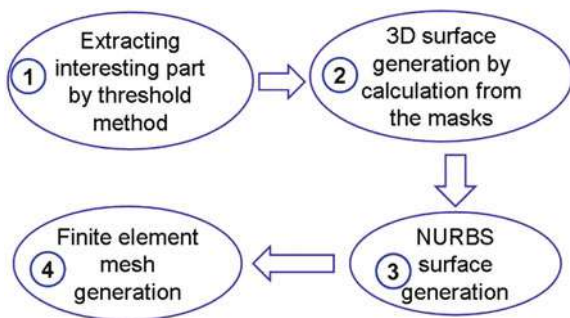


Fig. 1 Cross sections of CT scan images

Fig. 2 Flow chart of model development process



organs include the heart, lungs, aorta, vena cava, bronchus, trachea and esophagus (not shown in Fig. 9). Figure 10 depicts the abdominal model of the six-year old. The internal organs of the abdominal model include the liver, kidneys, spleen, diaphragm, and stomach (not shown in Fig. 10). Also included in the abdominal model were the abdominis which are shown in Fig. 10 as psoas major, quadratus lumborum, and the rectus abdominis not shown. The upper and lower extremities FE models have been developed but details are not shown here for the sake of brevity.

2.3 Material Property Models

Elastic and viscoelastic material constitutive models were used for the six-year old child FE model according to the type of tissues. As aforementioned, tissue material properties of the human child are rare in the literature. Franklyn et al. [3] performed a comprehensive review of material properties of the human child and pointed out that many of the mechanical properties of children were unknown and

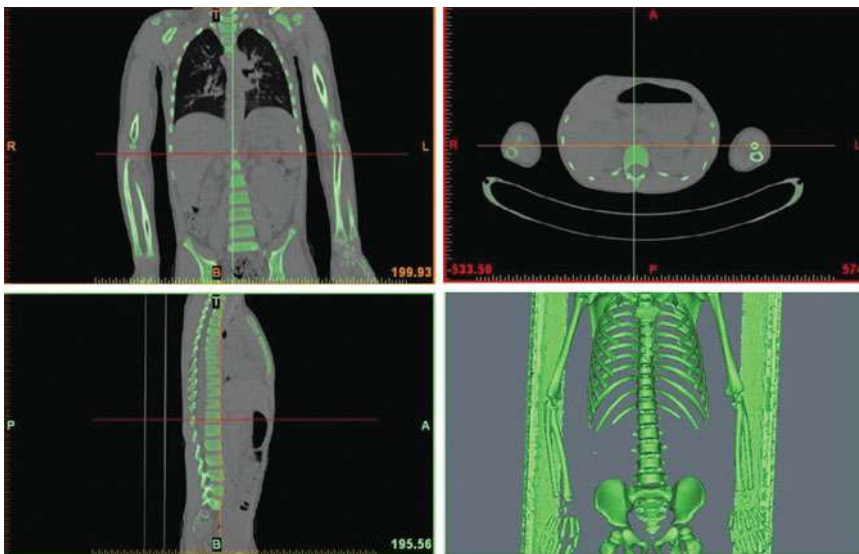


Fig. 3 CT scan image in MIMICS

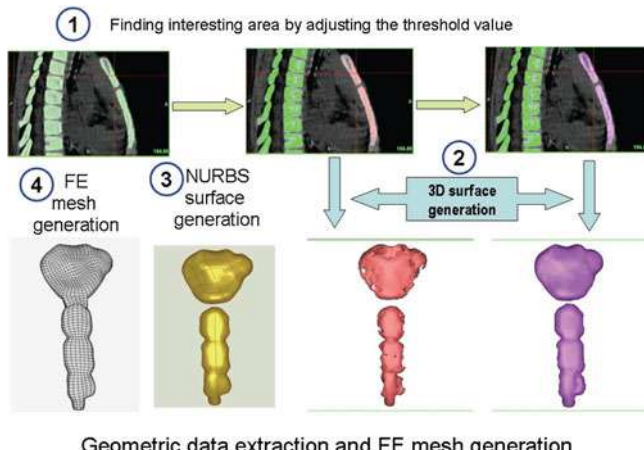


Fig. 4 Illustration of data extraction and FE meshing

further testing was needed. Values defining the constitutive laws of material still need to be determined. In this study, these values were obtained from the available literature (Currey and Butler [4], Lapeer and Prager [5], Mizuno and Namikiri [6], Ouyang et al. [7, 8], Roth et al. [9]); and in some cases values were derived from the adult cadaveric test studies (Cowin [10], Ruan et al. [11, 12], Yamada [13]) (Table 1).

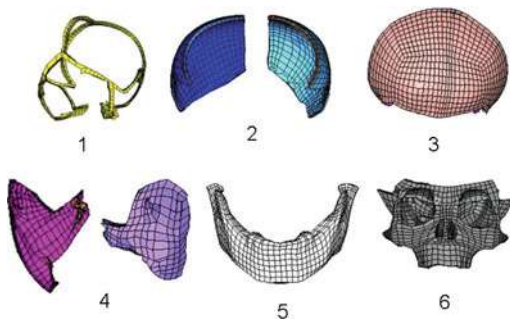


Fig. 5 Six-year old FE components of skull. 1 suture, 2 parietal bone, 3 frontal bone, 4 temporal, 5 mandible, 6 facial bones

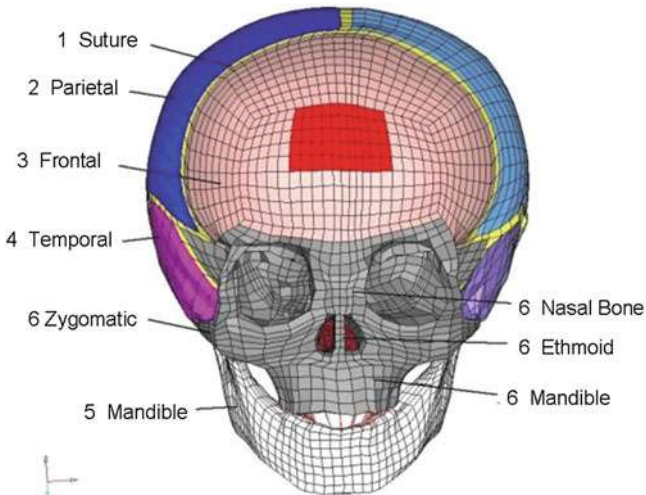


Fig. 6 Six-year old FE skull model

In the current study, the linear viscoelastic model was applied to the brain and other soft tissues such as the ligaments, heart, lungs, liver, kidneys, spleen and muscles. The shear relaxation behaviour was described by:

$$G(t) = G_{\infty} + (G_0 - G_{\infty}) \cdot e^{-\beta t}$$

where, G_{∞} = long-time (infinite) shear modulus, G_0 = short-time shear modulus, β = decay coefficient, t = time. G_0 and G_{∞} varied within a wide range.

The values defined G_0 , G_{∞} , and β are listed in Table 2.

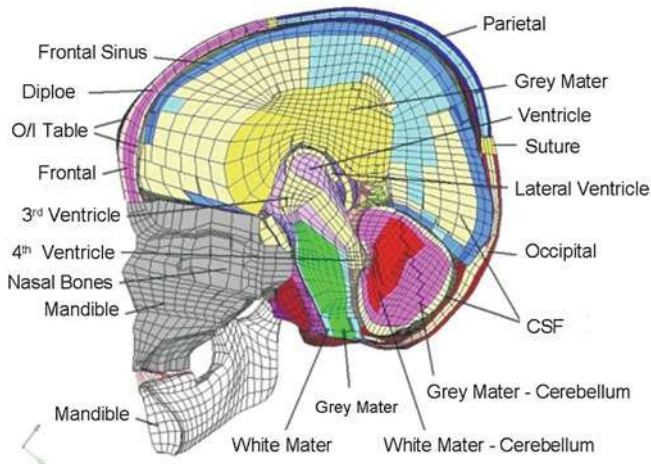


Fig. 7 Six-year old FE skull-brain model

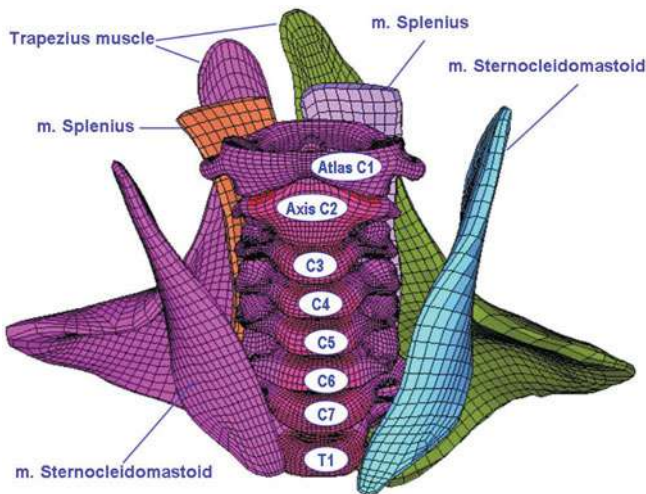


Fig. 8 Six-year old FE neck model

3 Preliminary Results

3.1 Model Characteristics Comparisons

Characteristic dimensions of the six-year old child FE model developed in this study are comparable with those of Hybrid III child dummy, whose dimensions were based on the latest information available on the size and weight of children in

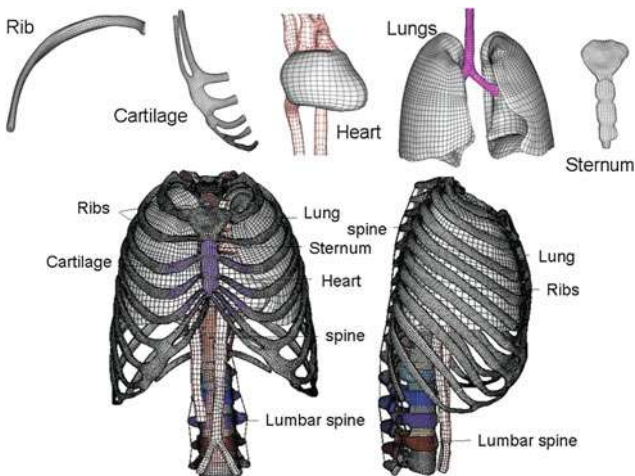


Fig. 9 Six-year old FE thorax model

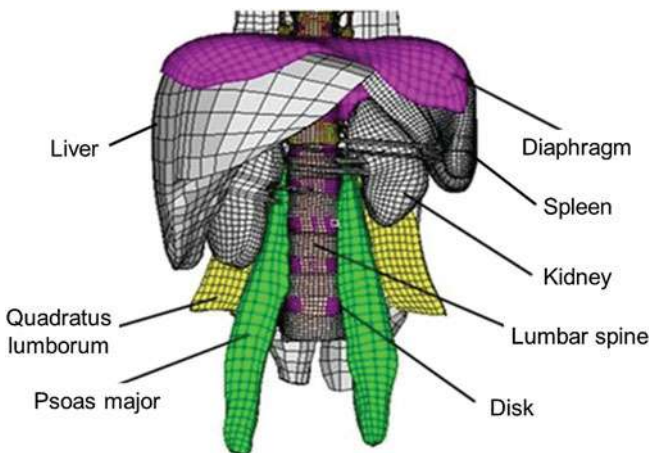


Fig. 10 Six-year old FE abdominal model

the United States (Irwin and Mertz [14]). These comparisons are listed in Tables 3 and 4.

The following sections present the simulation results for the head, neck, thorax, and abdomen. Since there are no appropriate child cadaveric impact tests available, adult cadaveric tests (Nahum et al. [15], Ewing and Thomas [16], Kroell et al. [17], Viano [18]) were chosen for impact response trends comparisons rather than model validation.

Table 1 Elastic material properties of the child model

Tissues	$\rho/(\text{kg/m}^3)$	E/(MPa)	v
Outer/inner table	2120	5733	0.22
Diploe	2150	2662	0.22
Sutures and fontanelles	2150	1500	0.22
Scalp	1200	16.7	0.42
Membranes	1140	31.5	0.45
CSF	1040	0.012	0.49
Compact bone	1830	12000	0.3
Cancellous bone	1000	3450	0.2
End plate	1200	500	0.25
Annulus	1000	4.2	0.45
Trachea	1200	16.7	0.4
Rib	1410	7460	0.30
Sternum	1410	7460	0.30
Blood vessel	1200	4	0.4
Anterior longitudinal ligament	1100	20	0.4
Posterior longitudinal ligament	1100	20	0.4
Supraspinal ligament	1100	15	0.4
Interspinal ligament	1100	11.6	0.4
Intertransverse ligament	1100	58.7	0.4
Capsular ligament	1100	15	0.3
Nuchal ligament	1100	15	0.3
Fiavum ligament	1100	19.5	0.4
Cartilage	1000	20	0.40
Diaphragm	1000	30	0.30

Table 2 Viscoelastic material properties of the child model

Tissues	$\rho/(\text{kg/m}^3)$	K/(MPa)	$G_0/(\text{MPa})$	$G_\infty/(\text{MPa})$	$\beta(\text{s}^{-1})$
Grey Matter	1000	2190	10	5	4.5
White Matter	1000	2110	12.5	6.1	4.5
Brain Stem	1000	2190	23	4.5	4.5
Nucleus	1040	2255	0.2	18	3.5
Heart	1000	2.6	0.44	0.15	3.5
Lung	600	0.22	0.02	0.075	3.5
Rib	2000	9600	1430	1772	1.5
Rib cartilage	1500	53	9	0.096	1.5
Sternum	2000	9592	4423	2.3	1.5
Liver	1100	2.80	0.23	0.044	1.0
Spleen	1100	2.80	0.23	0.044	1.0
Kidney	1100	2.80	0.23	0.044	1.0
Nucleus	1020	2200	90	1.40	1.0
Muscle	1000	0.25	0.115	0.086	1.0
Rectus abdominis	1000	0.25	0.115	0.086	1.0

Table 3 Characteristic dimensions of dummies and FE child model (mm)

Dimension description	3 YO	6 YO	FE 6 YO	50 % Adult
Standing height	953	1168	1136	1751
Head circumference	498	523	511	574
Head breadth	135	141	144	154
Head depth	177	180	175	197
Head height	176	185	189	221
Neck circumference	244	274	282	383
Neck breadth	74	79	76	114
Neck length	90	95	96	142
Shoulder breadth	246	290	274	465
Shoulder to elbow	193	234	221	366
Forearm circumference	158	174	173	275
Chest depth	122	143	131	229
Chest breadth	173	194	189	311
Chest circumference	505	622	574	997
Waist breadth	152	168	174	314
Waist circumference	480	539	508	864
Ankle circumference	148	163	168	261

Table 4 Body segment masses of dummies and FE child model (kg)

Body segment	3 YO	6 YO	FE 6 YO	50 % Adult
Head	3.05	3.48	3.33	4.54
Neck	0.43	0.41	0.56	1.54
Torso	6.61	10.76	9.52	40.23
Upper extremities	1.79	1.98	2.19	8.53
Lower extremities	2.63	4.28	4.31	23.36
Total	14.51	20.91	19.91	78.2

3.2 Head Impact Simulation

Figure 11 shows a head impact condition, which originated from Nahum's et al. [15] cadaver head impact experiments, applied for the head impact simulation. Simulation results are shown in Fig. 12, which is a time-history comparison of intracranial pressures between cadaver test and the six-year child model. Although the logic is vague to compare a child model response to an adult cadaveric testing result, it is justified considering the fact that there is no child cadaveric experimental result available at this time. Nevertheless, the child model simulation shows a correct trend in intracranial pressure change in the adult head and follows a similar kinematic during head impact, only with magnitude differences, as seen in Fig. 12 and Table 5.

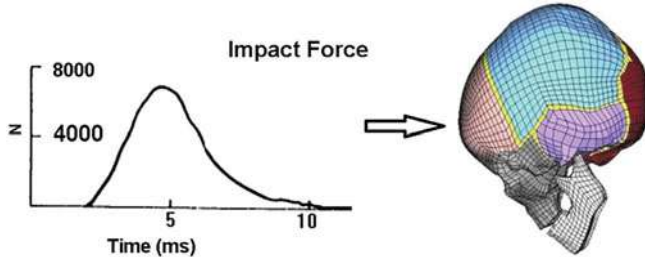


Fig. 11 Impact simulation loading

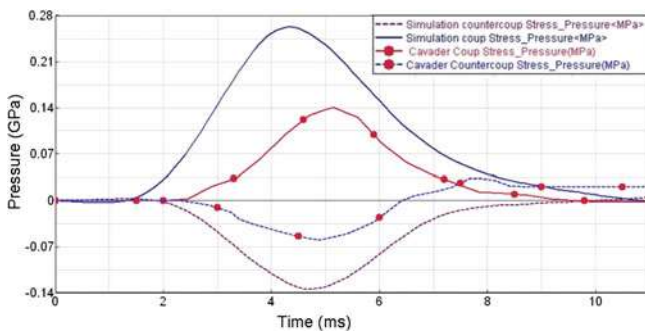


Fig. 12 Pressure responses of head impact

3.3 Neck Impact Simulation

Neck impact simulation was performed using a condition in Ewing's et al. [16] volunteer experiments, where an initial velocity was applied to the T1. Simulation result is shown in Fig. 14, which is displacement-time history. The notion here for the neck impact simulation is the same as in the head impact simulation and further elaboration is no needed Fig. (13).

3.4 Thoracic Impact Simulation

The thoracic impact simulation is shown in Fig. 15, which is an impact condition (impact mass = 23.64 kg, impact speed = 6.7 m/s) from Kroell's et al. [17] frontal cadaveric tests. Force-displacement response from the child model was compared with cadaver corridor, which is shown in Fig. 16. In comparison with model responses from the adult model (Ruan et al. [11]), the child model exhibits a

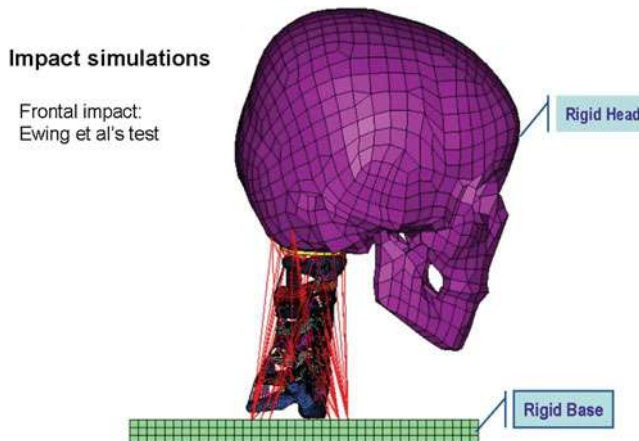


Fig. 13 Neck impact simulation

Table 5 Intracranial pressure comparisons between model and cadaver

Pressure	6 YO FE (kPa)	Cadaver (kPa)
Coup	220.2	140.8
Contrecoup	-135.2	-60.3
Parietal	136.5	73.6
Occipital	-87.1	-45.5

soft thoracic stiffness and respond to impact loading with more compliancy. Here again, the comparisons between child model responses and adult cadaveric testing results may sound naturally exclusive. However, the lack of child cadaveric data, especially thoracic cadaver impact data, makes such comparisons necessary.

3.5 Abdominal Impact Simulation

Abdominal impact simulation conducted in this study mimicked a condition of the cadaveric tests by Viano [18] (shown in Fig. 17) but with reduced impact mass from 23.4 to 8.0 kg. It is shown in Fig. 17. Simulation result is shown in Fig. 18, which presents a force-time history comparison with cadaveric corridor. In comparison with the adult human body model (Ruan et al. [12]), impact force from the child model picks up faster than that of adult model.

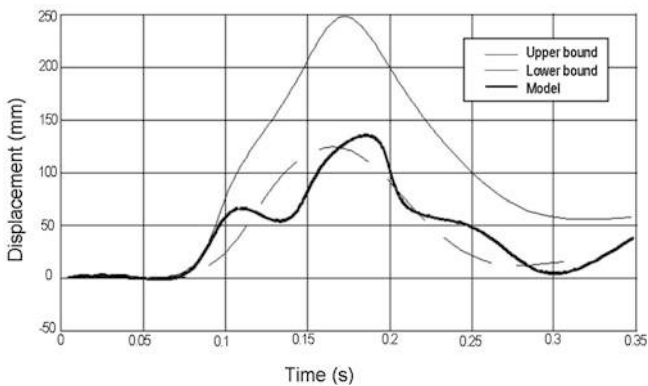


Fig. 14 Displacement–time history comparisons

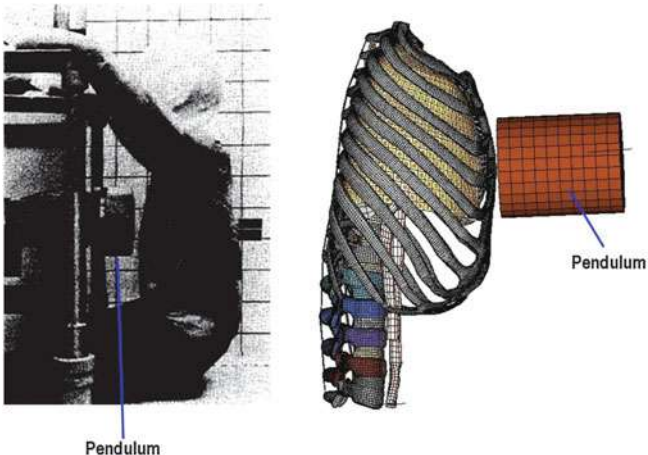


Fig. 15 Frontal thoracic impact simulation

4 Discussion

Due to the lack of cadaveric impact test data, a rigorous model validation process for the proposed six-year old child model is not possible at the present time. However, model validation is required for any digital model validity. To compare the child model responses with the adult cadaveric test results available in the literature is a compromise for model validation and therefore becomes one of the limitations of the current study. Another major limitation of the current study is the lack of experimental study of tissue mechanical properties of human children. Nevertheless, the geometric data on which the proposed six-year child FE model was based are accurate because they were generated from a real living human. This means that one of the three major technical hurdles mentioned earlier for

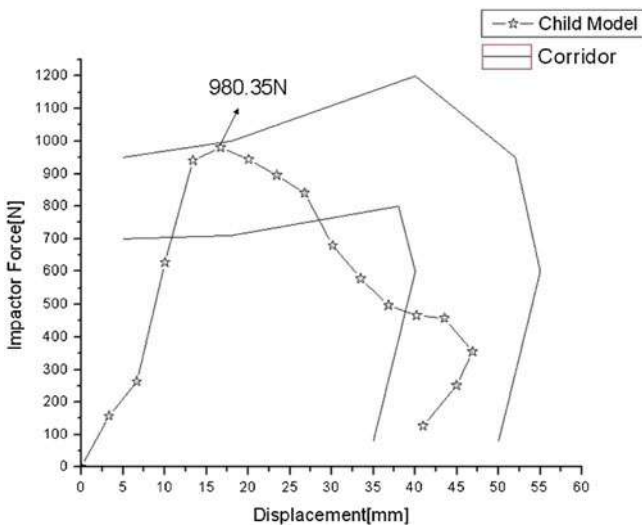


Fig. 16 Force–displacement comparisons

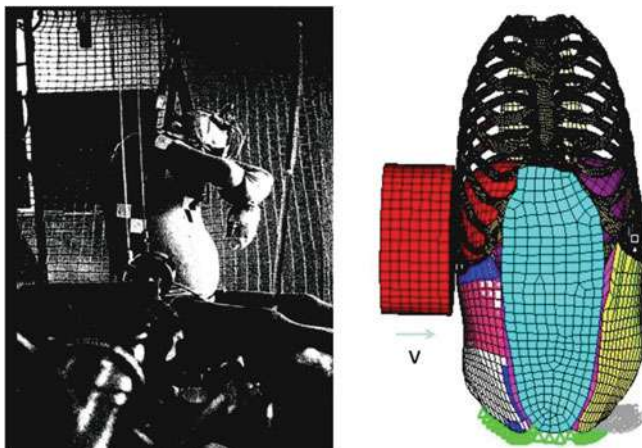


Fig. 17 Lateral abdominal impact simulation

development of a human child model has been addressed. The other two challenges require further investigation, which is beyond the scope of this research. However, this study may help in presenting the first step forward toward future development of more completed and validated child human body digital model.

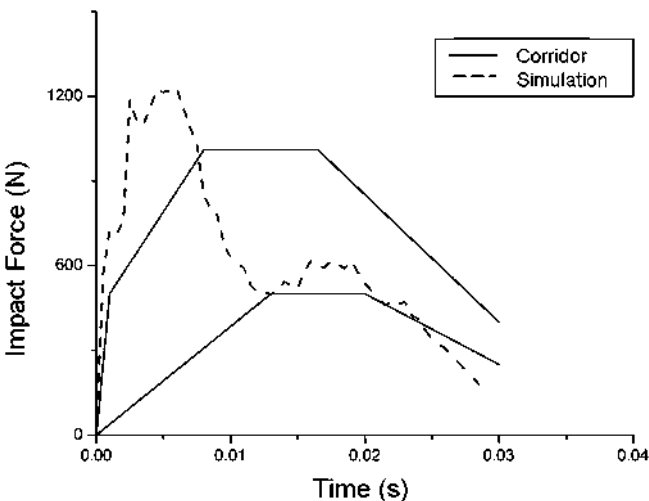


Fig. 18 Force–time history comparisons

5 Conclusions

A geometrically biofidelic six-year old human child finite element model has been developed. Model responses have been tested by comparing them against dynamic trends predicted by the model to adult cadaveric experimental results. More research is needed to obtain tissue mechanical property data to generate more meaningful impact responses for human children to better understand child injury mechanisms in vehicular crashes and help in the further development biomechanically-sound child safety protection systems.

Reference

- Melvin JW (1995) Injury assessment reference values for the CRABI 6-month infant dummy in a rear-facing infant restraint with airbag deployment. SAE paper no. 950872
- Mizuno K, Iwata K, Deguchi T, Ikami T, Kubota M (2005) Development of a three-year-old child FE model. *Traffic Inj Prev* 6:361–371
- Franklyn M, Peiris S, Huber C, Yang KH (2007) Pediatric material properties: A review of human child and animal surrogates. *Crit Rev™ Biomed Eng* 35(3–4):197–342
- Currey JD, Butler G (1975) The mechanical properties of bone tissue in children. *J Bone Joint Surg* 57A(6):810–814
- Lapeer RJ, Prager RW (2001) Fatal head moulding: finite element analysis of a fetal skull subjected to uterine pressure during the first stage of labour. *J Biomech* 34(2001):1125–1133
- Mizuno K, Namikiri T (2007) Analysis of child responses in CRS using child human FE model. In: Proceedings of 20th ESV conference, paper number 07-0145
- Ouyang J, Zhu Q, Zhao W, Xu Y, Chen W, Zhong S (2003) Experimental cadaveric study of lateral impact of the pelvis in children. *Acad J First Med Coll PLA* 23 (5):397–408

8. Ouyang J, Zhu Q, Zhao W, Xu Y, Chen W, Zhong S (2005) Biomechanical assessment of the pediatric cervical spine under bending and tensile loading. *Spine* 30(24):E716–E723
9. Roth S, Raul J, Willinger R (2008) Biofidelic child head FE model to simulate real world trauma. *Comput Methods Programs Biomed* 90(2008):262–274
10. Cowin SC (ed) (2001) Bone mechanics handbook, 2nd edn. CRC Press, Boca Raton
11. Ruan JS, El-Jawahri R, Chai L, Barbat S, Prasad P (2003) Prediction and analysis of human thoracic impact responses and injuries in cadaver impacts using a full human body finite element model. *Stapp Car Crash J* 47:299–321
12. Ruan JS, El-Jawahri R, Barbat S, Prasad P (2005) Biomechanical analysis of human abdominal impact responses and injuries through finite element simulations of a full human body model. *Stapp Car Crash J* 49(2005):299–321
13. Yamada H (1970) Strength of biological materials. In: Evean FG (ed) The Williams & Wilkins Company, Baltimore
14. Irwin A, Mertz HJ (1997) Biomechanical basis for the CRABI and Hybrid III child dummies. In: Child occupant protection 2nd Symposium Proceeding (P-316). SAE paper no. 973317, pp 261–274
15. Nahum AM, Smith RW, Ward CC (1977) Intracranial pressure dynamics during head impact. In: Proceedings of 21st stapp car crash conference, pp 339–366
16. Ewing CL, Thomas DJ (1972) Human head and neck response to impact acceleration. Naval Aerospace Medical Research Laboratory Detachment, New Orleans, Monograph 21, August 1972
17. Kroell CK, Schneider DC, Nahum AM (1971) Impact tolerance and response of the human thorax. In: Proceedings of 15th stapp car crash conference. SAE paper no. 710851
18. Viano DC (1989) Biomechanical responses and injuries in blunt lateral impact. In: Proceedings of 33rd stapp car crash conference. SAE paper no. 892432

New Concept for Neck Injury Lessening System Development

SangDo Park, DongWoo Jeong, Hak Gyun Kim
and Jin Young Nam

Abstract Recently, due to technological evolutions and social demands, motor vehicles are much requested to be enhanced in terms of occupant safety and comfort. As a result, many countries are reinforcing crash regulations and new car assessment programs. Automotive seats as essential parts to the passenger safety and comfort has become most important parts and many automotive companies concentrate on optimization of Neck Injury protection system. The Known factor to reduce neck injury is reducing relative movement between Head and Torso. This study is focused on reducing torso acceleration to minimize neck injuries by controlling seat back frame.

Keywords Frame · Cushion · Back · Whiplash · Neck Injury

1 Introduction

Seat is an engineering design desire's contradictory product where the strength must be reinforced to satisfy ever increasing consumer requirements and various safety regulations while realizing low fuel consumptions and lightweightifications. That is, it is an item where engineering design optimization is a must in the initial stage through optimal concept and systematic CAE. In recent years, the advance automakers are strengthening the seat safety researches in order to reduce the societal cost (Fig. 1) of rear collisions.

F2012-F02-019

S. Park (✉) · D. Jeong · H. G. Kim · J. Y. Nam
HMC, Seoul, Korea

Dymos, Seoul, Korea

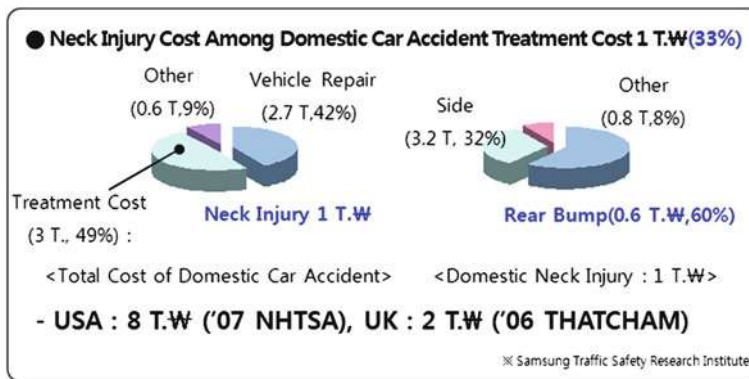


Fig. 1 Domestic/USA/England neck injury societal cost

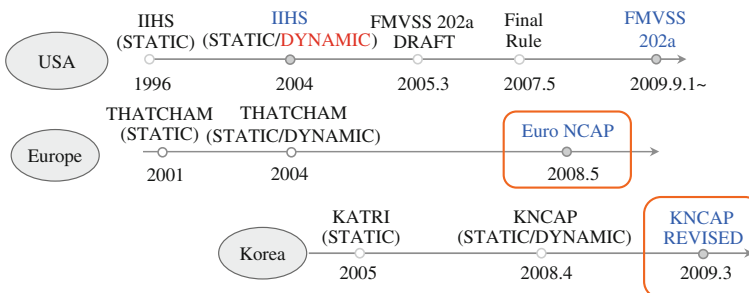


Fig. 2 Regional neck injury evaluation regulations/product value investiture status

Each country steadily enhances the regulations as a method to increase the consumer safety just as shown in Fig. 2, and 2009 collision category combined overall rating is being enforced in domestic, too.

This research, in response to rear collision regulations and product value,

- increases the seat safety by discovering and optimizing neck injury factors,
- presents the engineering design guide/process for the seat safety through validationary CAE/testing,
- establishes criteria for the competitive seat developments [1–5].

2 Main Body

This section presents the seat safety concept & developmental target, explains the supplemental/additional specifications & optimization methodology used to attain the target, observes & analyzes the CAE and test results.

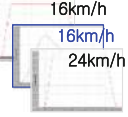
	IIHS (North)	KNCAP	EURO NCAP
Dynamic Injury Criteria	<ul style="list-style-type: none"> • Fx • Fz • T1 • HRCT  16km/h	<ul style="list-style-type: none"> • Fx • Fz • T1 • HRCT • NIC • Nkm • HRV  16km/h	<ul style="list-style-type: none"> • Fx • Fz • T1 • HRCT • NIC • Nkm • HRV  16km/h 16km/h 24km/h
Rating	 GOOD ACCEPTABLE MARGINAL POOR	 5★ 4.9~6 4★ 4.0~4.9 3★ 3.1~4.0 2★ 2.2~3.1 1★ 0~2.2	 GOOD MARGINAL POOR 3.00~4.00 1.50~2.99 0.00~1.49

Fig. 3 Regional regulations/product property summary

2.1 Neck Injury Property and Regulations Status

There are; N. America FMVSS202A for neck injury related regulations; N. America IIHS which measures Fx,Fz,HrCT (T1 Pick) for product properties; EURONCAP/ KNCAP which announces the overall ratings by measuring Fx(Shearing Force), Fz (Tensile Force), T1 (Acceleration), HRCT (Contact Time), NIC (Relative Acceleration), Nkm (Shearing Force + Moment) HRV(head rebound). As for the performance requirements, in the order of KNCAP > EURONCAP > IIHS, KNCAP is the most rigorous of all three; and the assuring the best rating is a must (Fig. 3).

2.2 Neck Injury System and Participant Response Status

The most widely used neck injury lessening system is where the headrest protrudes forward for the head support upon collision and divided into mechanical and electronic according to the operating method. Electronic system offers good performance but expensive; thus, difficult to use in vehicle classes below mid/full sizes. Mechanical system is inexpensive compare to the electronic system, but offers inadequate comfort due to protuberance of operating plate and has operational quality issues.

Accordingly, instead of the headrest protrusion, other OEMs are either implementing the system where the acceleration of head and torso are matched by lowering torso's acceleration through back distortion or researching into eliminating neck injury system to improve neck injury performances.

2.3 HMC Vehicle Status

HMC vehicles with non-standard frame models did not attain the best rating on enhanced KNCAP even active headrest were applied. The standard frame models with the active headrest applications attained the best ratings (Fig. 4).

	MODEL	KNCAP TEST RESULT		EURO NCAP TEST RESULT		IIHS		Note
		ACTIVE	NON ACTIVE	ACTIVE	NON ACTIVE	ACTIVE	NON ACTIVE	
HMC	A	3★	2★	Maginal	Poor	Good	MAGINAL	
	B	4★	3★	Good	-	Good	Good	
	C	3★	-	-	-	Good	-	Electronic Type
	D	5★		-	-	Good	-	
COMPETITOR	A	4★	-	Maginal	-	Good	-	Electronic Type
	B	-	-	Good	-	-	Good	Electronic Type
	C	3★	-	Maginal	-	Good	Maginal	
	D	3★	-	Maginal	-	Good	Maginal	
	E	-	3★		Good	-	Good	

Fig. 4 Seat frame, major rigidity SPEC

2.3.1 Active Headrest Issues

From the perspective neck injury performance enhancement, active headrest that was implemented in all HMC vehicles up until 2010 has made significant contribution in reducing neck injuries; but has reached limits in satisfying enhanced product properties, qualities, and comforts. The comfort deteriorates as upper back is pushed by the plate that is used by the active headrest for its operation, the seat-back pad is damaged by the active operating hinge, has issues with finger jam in pole guide gap. In addition, the profitability has been low as the implementation of active headrest increased the weight and the cost.

2.4 Developmental Target Establishment

The goal of development is to delete the main plate that operates the active headrest and improve below 3 categories.

- (1) Neck Injury Related Regulations and Product Property Enhancements
 - Improve Current System's Margin : All Location 5★ Target
- (2) Develop New Structure to Improve Qualities and Product Properties
 - Upon Sitting, Improve Irritations at Seat-Back Area and Qualities
 - Assure New Technology/New Feature Addition Corresponding Spacing
 - Improve Seat-Back Slimization
- (3) Assure System Competitiveness through Mass/Cost Optimization

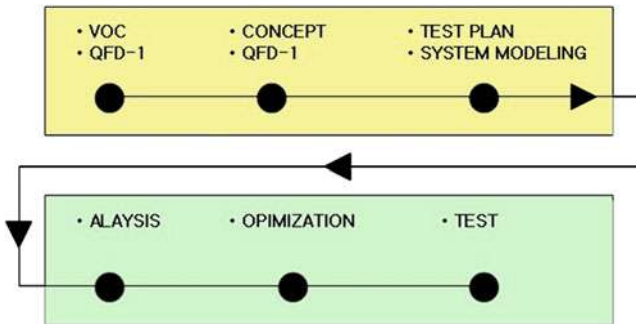


Fig. 5 Research methodology

2.5 Research Methodology

Design For Six Sigma (DFSS) technique was used as a research methodology and research order was as in Fig. 5.

Especially, to assure the strength of new system and to reduce the engineering design variations after the elimination of an active headrest, implemented standard DFSS process composed with the Requirements Definition Stage which analyses the VOC (Voice Of Customer) and company measurement criteria, the Concept Development Stage through its analysis, the engineering design noise considered Optimization Stage in accordance with the defined concepts, etc.

An orthogonal array table was used in formulating experiment plans for the engineering design factors, and the CAE was performed after structural modeling (Solid Modeling) of each concepts. For the collision CAE of KNCAP rear neck injury, PAM CRASHTM was utilized. SLED test was used to validate the optimization effect of factors selected based on the CAE result. The pulse used in SLED test was forward 10G 16 km/h.

2.6 Concept Deduced

Concept deduction was set up as Fig. 6 for the neck injury lessening system's functions and structures. Concept 1: Torso reaction activated headrest protrusion structure currently implemented in HMC where the operating plate is located in Back-Upper. Concept 2, 3: Structure where the operating plate is located in Back-Lower. Concept 5: Electronically operated structure. Concept 6: Structure with operating plate on entire Back. Concept 4: An active system eliminated neck injury lessening structure through frame and Back-Ass'y geometry improvements; most suitable for the developmental target (Fig. 7).

#	Concept #1	Concept #2	Concept #3	Concept #4	Concept #5	Concept #6
Structure	Linkage Activated	Cable Activated, Headrest Protrusion	Cable Activated (Seat-Back Lower)	Shock Reduction Structure	Electrical Active (Sensor Utilized)	Seat-Back Surface Linkage
Operating Principle	① H/REST Ascension ② Torso Recline ③ Rear Bump	Activating Cable Activating Cable	Activation Cable Load	Seat-Back Frame Optimization Structure	Acceleration Sensor Utilized Acceleration Sensor Utilized in the Back Collision Region	Back Frame Upper & H/REST Ascension Torso Recline
Characteristic	• Structure Simple • Back Comfort Inferior	• Mechanism Size Big • Locking Application • H/REST Takeaway Infeasible	• Locking Not Applied	• No Separate Structure • Cost/Mass Advantageous	• Rapid Response • Protuberance Big • Test Deviation Small	• Structure Complicated Back Frame • Back Comfort Inferior
Effective Model	HKMC YF-HM Nissan Altima Ford Mondeo	Kia-Sorento R, Cee'd Toyota-Avensis Opel-Insignia, Saturn	Toyota-RAV4, Corolla	Toyota WH System (Whiplash Injury Lessening) Audi	BMW-X3, 3/5/7 Series	Honda-CIVIC

Fig. 6 Neck injury improvements system concept deduction



Fig. 7 Sports sedan neck injury performance

2.6.1 Concept Supplementation

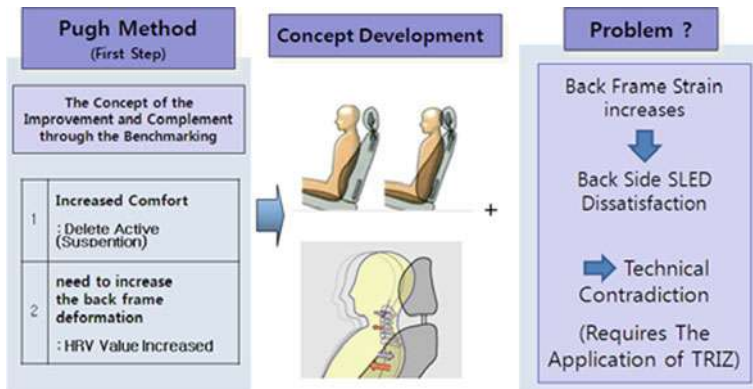
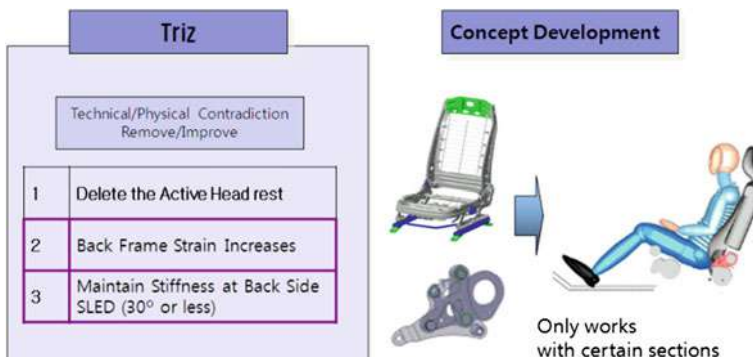
Passenger and RV: Has General Frame and Design Shape

Sports Sedan or Coupe Model: Has Sports Bucket Style. Due to low headrest height, high side support, narrow main width; the attainment of best rating is difficult even an active headrest is implemented and the supplemental system for this is needed.

To supplement this, utilizing Pugh and TRIZ, eliminated the technical/physical contradictions and improved concept is as below (Fig. 8).

While improving the irritations to Back-Upper by removing an active headrest operating plate, it is necessary to have the neck injury lessening feature and must maintain the Seat-Back's strength in rear collision (Fig. 9).

A shock lessening system which operates only in rear collision just as Fig. 10, and in-locking mode in general operating condition which maintains the strength & has no issues with the noise is needed.

**Fig. 8** Pugh method**Fig. 9** TRIZ application

The shock lessening system can improve the continuously indicated comfort issues by removing the existing active, but the cost/weight occurs as the new device is added. Thus, limit the application to the locations with enhanced regulations and special models based on additional margin assurance. For other models, implement neck injury optimization plan without the additional system.

2.6.2 Factor Specific Sensitivity Analysis and Control Factor Selection

Define the engineering design parameters through QFD-2 to optimize the neck injury, and analyze the impacts by identifying sensitivities of each factor. (Fig. 11)

When Backset shrinks; HRCT, F_x , F_z , NIC, N_{km} , HRV performance improves. The 5 mm reduction of Backset improves the overall score by 0.33 points.

Height predominantly impacts the static score and boosts F_z performance. The 6 mm increase in height boosts the overall score by 0.17 points.

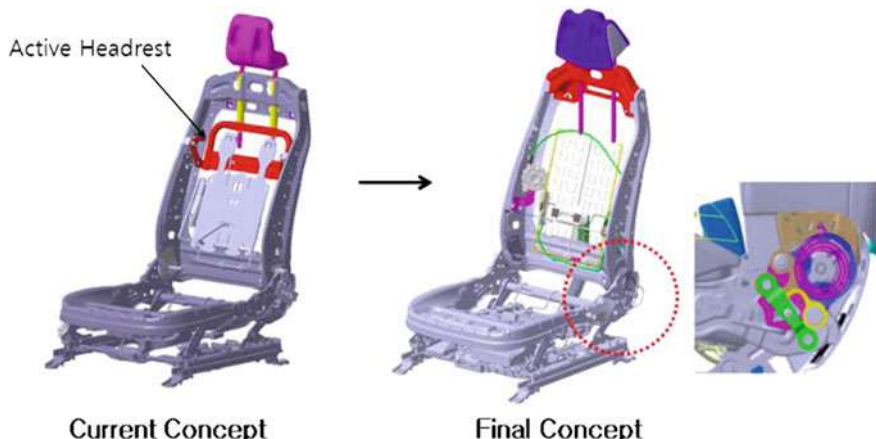


Fig. 10 Impact reduction final concept

- Backset Shrinks HRCT, F_x , F_z , NIC, N_{km} , HRV Performance Improves
 - 5mm Backset Shrinkage Boosts Overall Score by 0.33 Points
- Height Predominantly Impacts Static Score & Boosts F_z Performance
 - 5mm Height Rise Boosts Overall Score by 0.17 Points
- Harder the H/Rest PAD's Physical Property, Thinner the Thickness: Better the Neck Injury Performance
 - 5mm Reduction of PAD Thickness Boosts Overall Score by 0.05 Points

Variables	Deviation	Point
Backset	5mm ↓	0.33 ↑
Height	5mm ↑	0.17 ↑
H/Rest PAD Thickness	5mm ↓	0.05 ↑
Upper Cross Member Thickness	0.2t ↑	0.06 ↑
Cushion Rear Pipe Thickness	0.2t ↑	0.03 ↑
H/Rest Stay Thickness	0.2t ↑	0.05 ↑

Fig. 11 Sensitivity analysis result

Harder the physical property and thinner the H/Rest PAD, better the neck injury performances are. The 5 mm reduction of thickness boosts the overall score by 0.05 points. Greater the structural strength, better the neck injury performance; the 0.2 t increase of Back Frame thickness raises the overall score by 0.10 points; the 0.2 t increase of Upper Cross Member thickness boosts the overall score by 0.06 points; the 0.2 t increase of H/Rest Stay thickness boosts the overall score by 0.05 points; the 0.2 t increase of Cushion Rear Pipe thickness boosts the overall score by 0.03 points.

The final eight control factors were selected using the resulting values of the sensitivity analysis as shown in Figs. 12 and 13.

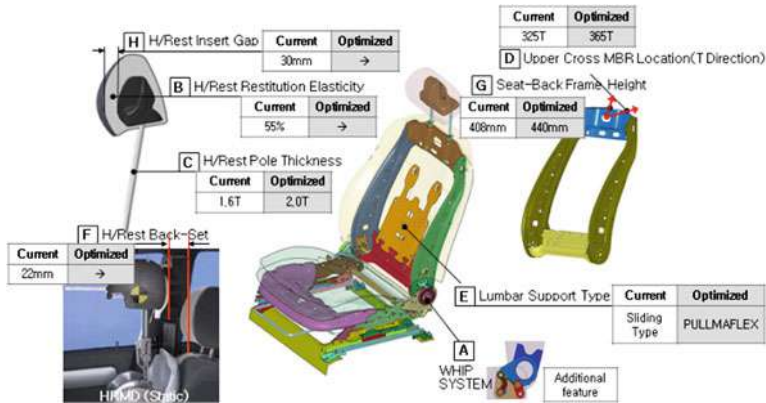


Fig. 12 Neck injury control factor

Fig. 13 Control factor level definition

NO	Level-1	Level-2	Level-3
A	X	O	
B	55%	35%	20%
C	1.6 t	2.0 t	2.3 t
D	YF(T:352mm)	+5mm	+10mm
E	Pullmafex	Horizontal Protrusion	Vertical Protrusion
F	22 mm	40 mm	50 mm
G	YF(H:408mm)	+16mm	+32mm
H	20mm	30mm	40mm

The standards were defined for selected 8 control factors and L18 ($2^1 \times 3^7$) Orthogonal Array Table were generated accordingly (Fig. 14). HRCT, T1, Fx, Fz, Nkm, HRV, NIC were selected (Fig. 15) as test categories; made plan to conduct CAE 72 times using 2 noise factors N1/N2 which could occur during the production or in-use by the consumer at this point, and N1/N2 conditions were set as below.

N1:H-PT Normal Location, Torso Angle (25°)

N2: H-PT 10 mm Upward, Torso Angle (26°)

HRCT/T1	Neck Force (Fx/Fz)	Neck Force (NIC/Nkm/HRV)

Fig. 14 Orthogonal array table generation

		
• HRCT (Head's Rest Contact Time) - Head's Headrest Initial Contact Time	• T1 Acceleration - Thoracic Vertebrae #1(T1) X Directional Acceleration	• NIC (Neck Injury Criterion) - Speed/Acceleration Difference between Cervical Vertebrae & Thoracic Vertebrae
		
• Fx : Upper Neck's Neck Shearing Load • Fz : Upper Neck's Neck Tensile Load	• Nkm - Sum of Neck Moment & Shearing Load	• HRV (Head Rebound Velocity) - Head's Post-Headrest Contact Restitution Rate

Fig. 15 Test category

Based on above proposal, the test plan for new concept of neck injury lessening system was formulated as shown in Fig. 16.

2.7 CAE and Result Analysis

Total 72 CAEs in N1, N2 conditions were conducted and obtained results shown in Fig. 17 [6, 7].

To determine the optimum condition for each HRCT, T1, Fx, Fz, Nkm, HRV, NIC categories; applied the smaller-the-better characteristics to analyze each criteria's impact (Fig. 18).

Large S/N ratio value, small mean value were selected as an optimum condition. And, while WHIPS SYSTEM application has a better performance, factor specific impact reduction structure were applied to non-WHIPS as well to optimize the neck injury reduction (Fig. 19).

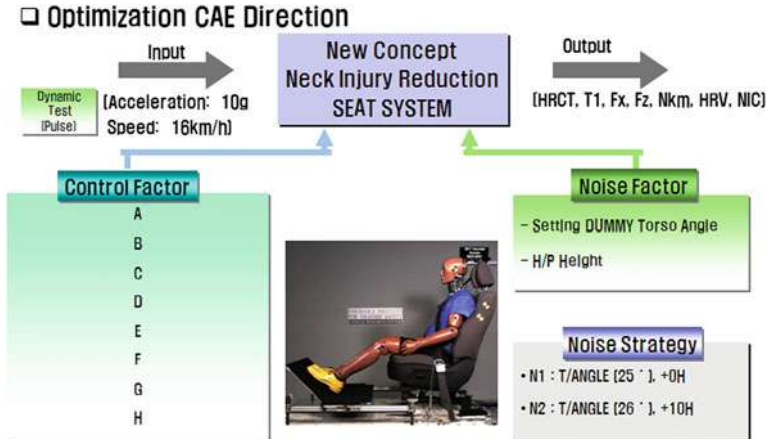


Fig. 16 Test plan formulation

Fig. 17 CAE result

Only the low elasticity headrest and 2 headrest insert gaps were kept in contrasted to the initial condition, and 5 categories including pole thickness were changed (Fig. 20).

2.8 CAE Verification and Result

Upon assuming programs using selected final condition and result verification, the improvements to the neck injury were known compare to the initial specifications (Fig. 21).

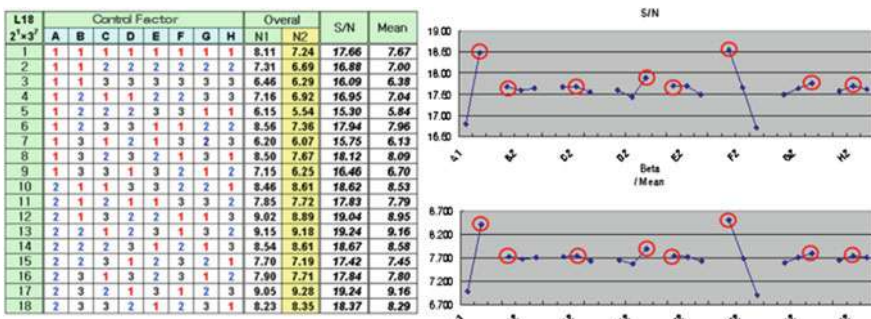


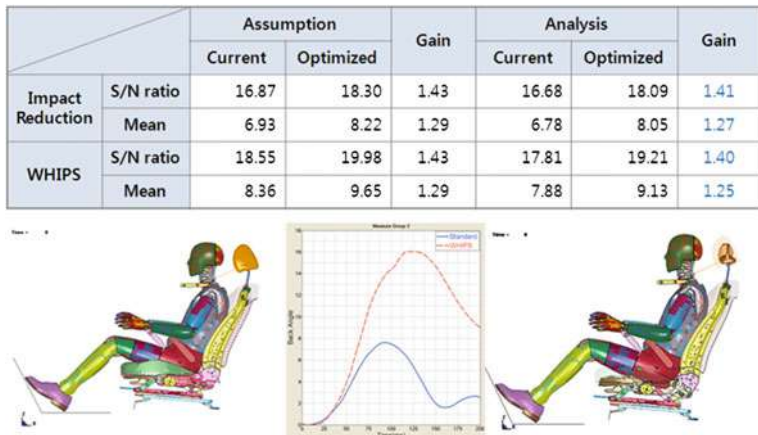
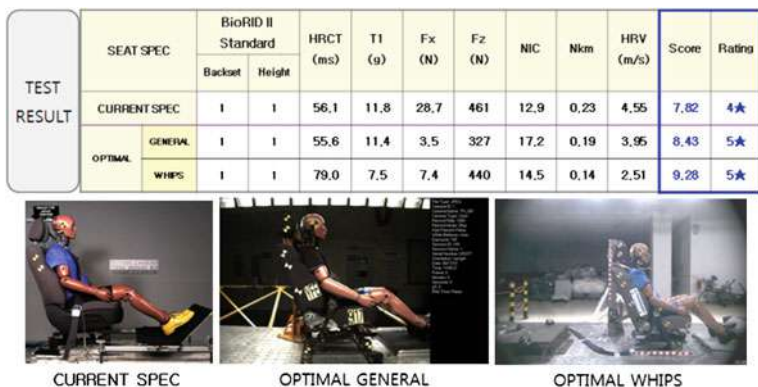
Fig. 18 Category overall analysis result

	A	B	C	D	E	F	G	H
Impact Reduction	1	1	2	3	1	1	3	2
WHIPS	2	1	2	3	1	1	3	2

Fig. 19 Optimal factor

Fig. 20 Optimal factor selection

NO	Level-1	Level-2	Level-3
A	X	O	
B	55%	35%	20%
C	1.6 t	2.0 t	2.3 t
D	YF(T:352mm)	+5mm	+10mm
E	Pullmafex	Horizontal Protrusion	Vertical Protrusion
F	22 mm	40 mm	50 mm
G	YF(H:408mm)	+16mm	+32mm
H	20mm	30mm	40mm

**Fig. 21** CAE verification result**Fig. 22** SLED test result

2.9 Sled Test Result

The rear SLED test were performed in N1/N2 conditions in accordance with each noise conditions with the seat frame, mass production cushion pad, headrest, and belt that were made with the parts material selected as a finalized factor; the same level of results as CAE were obtained and were able to attain 5★ for non-WHIPS structure as well (Fig. 22).

3 Conclusion

In this research, the best rating in neck injury was attained by applying the new impact reduction system concept to meet the enhanced FMVSS202a/European NCAP/KNCAP regulations & product properties (2011 KNCAP HG 5.7★).

- (1) The best rating in neck injury was attained by optimizing the selected 8 control factors through impact analysis, previously relied on the active headrest as a response to existing neck injury.
- (2) The importance of seat frame shape and back pad/headrest's geometry were seen in relation to the HRV value improvements in weak HMC areas.
- (3) Increased the efficiencies through simplization and differentiation of regional specifications, and laid foundation to attain the rating of best in all regions by creating an engineering design guide.
- (4) The Seat-Back irritations and issues with headrest pole guide buoyancy were improved by deleting the active headrest.

After this, plan to supplement and reflect improvements to the standard frame upgrade the result obtained through this research to assure the attainment of the best rating on neck injury in official evaluation safely.

References

1. RCAR (Research Council for Automobile Repairs) (2008) A procedure for evaluating motor vehicle head restraint (Issue3)
2. RCAR-IIWPG (International Insurance Whiplash Prevention Group) (2008) Sear/head restraint evaluation protocol (version 3)
3. EURONCAP (EURO New Car Assessment Program (2008) The dynamic assessment of car seats for neck injury protection test protocol (version 2.8)
4. Ministry of Land, Transport, & Maritime Affairs “Regulations related to the Automobile Safety Evaluation Test”
5. Association of British Insurers (2008) Motor insurance claims data. Association of British Insurers, London
6. Bortenschlager K (2009) Detailed analysis of Biorid-II response variations in hardware and simulation. PDB, Daimler AG, DYNAmore GmbH, ESV 09-0492
7. LS-DYNA Keyword user's Manual—version 971

Evaluation of the Testing Capabilities of the Q10 Prototype Dummy

Alejandro Longton, Marianne Hynd, Kees Waagmeester,
Erik Salters and Serge Cirovic

Abstract *Research objective* The EPOCH project aimed to develop, test and evaluate a Q10 prototype dummy. The tests were split in three main groups. The research aims: (1) for restraint loading were to evaluate the response of the Q10 dummy to different test set-up conditions, (2) for sensitivity to seat design testing were to evaluate the response of the Q10 dummy to different child seat designs, for the durability testing were to evaluate how many tests the Q10 dummy could withstand before damages to occur, to create a maintenance checklist and to identify how frequently it should be checked during a test programme.
Methodology A test matrix was developed to assess the performance of the Q10 prototype dummy. As more than 250 tests were carried out in different crash laboratories and there were only two Q10 prototype dummies available a careful action-plan had to be established. Therefore, a Gantt chart had to be developed. Certification static tests were carried out. Then, tests to compare the P10 dummy with the developed Q10 prototype were carried out. Front impact tests using Reg. 44 were performed to check the dummy behaviour when submitted to an existing

F2012-F02-022

A. Longton (✉)
Applus IDIADA, Tarragona, Spain

M. Hynd
TRL, Berkshire, UK

K. Waagmeester
Humanetics, Delft, The Netherlands

ErikSalters
Dorel, Oldenzaal, Netherlands

S. Cirovic
University of Surrey, Guildford, UK

test procedure. Dynamic tests, following the NPACS side and front impact test procedures, were also conducted. *Results* The certification tests showed that the Q10 prototype dummy correlates well with the biomechanical targets specified in the design brief. From the analysis carried out using the results from the Reg. 44 testing, was concluded that the Q10 dummy is sensitive to changes in the test setup. It was noted that the dummy detected differences in the kinematics and the loading in different setups. From the analysis of the results from the NPACS testing, which were the most severe tests across the testing program, was concluded that the Q10 dummy was capable of detecting differences in the child restraint design and in the test setup in both side and frontal impact tests. The dummy showed good repeatability from the durability front and side impact tests. It was concluded that the dummy is capable of producing repeatable results with up to 30 min recovery time for NPACS side impact tests. A NPACS 5 band scoring system was extended up to the Q10 dummy. *Conclusion* The following conclusions can be made based on results of the front impact testing of the Q10: (1) The Q10 produced the expected loading in the important body regions, (2) the Q10 is capable of producing repeatable results in the important body regions, (3) the Q10 is capable of differentiating between different child restraint designs, (4) the Q10 NPACS scoring system has been expanded, to achieve a rating system, applicable to the Q10.

Keywords Evaluation • Testing • Prototype • Development • Q10

Enabling Protection for Older Children (EPOCh) is a part of the 7th European Community's Seventh Framework Programme (FP7/2007–2013). The consortium, consisting of five partners, set several goals, the achievement of which should improve the child safety in cars.

The implementation of Directive 2003/20/EC from April 8, 2003 means that children of up to 150 cm should use a restraint system when travelling in cars or goods vehicles. As a result, children should be using restraint systems for longer (up to 12 years old, depending on their height). That is why the first objective of the EPOCh project was to produce a 10/12 year old prototype dummy (Fig. 1).

The main goal of the EPOCh project was to develop, test in crash laboratories and evaluate a Q10 prototype dummy. In order to provide better protection the NPACS testing and rating protocols were adjusted and extended for older children, which was the second goal of the project. The last objective of the EPOCh project was to make proposals for dummy's usage in UN-ECE Regulation.

1 Methodology

A test matrix was developed in order to assess the performance of the Q10 prototype dummy. As more than 250 tests were carried out in different crash laboratories and there were only two Q10 prototype dummies available a careful

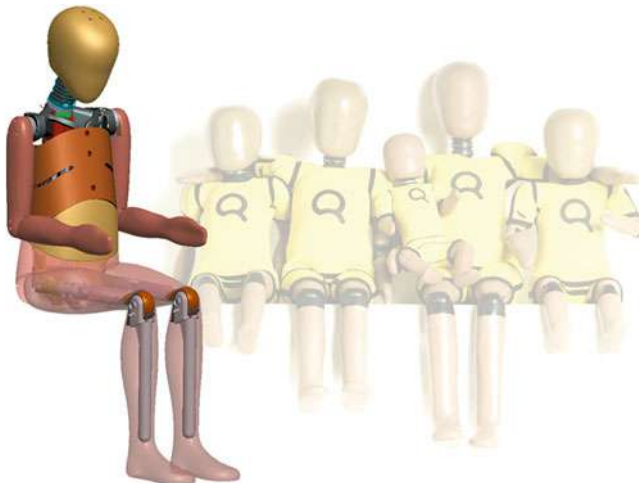


Fig. 1 The Q10 prototype dummy with the other dummies from the Q family

action-plan had to be established. A Gantt chart, showing the starting and finishing dates, the dependency of the work from previous work and allowing some space gaps for unexpected delays, had to be developed.

At the beginning, certification static tests were carried out. Then, tests to compare the P10 dummy with the developed Q10 prototype were carried out. Front impact tests using Reg. 44 were carried out in order to check the dummy behaviour when submitted to an existing test procedure. The dynamic tests, following the NPACS side and front impact test procedures, were conducted in different laboratories and by using both deceleration and acceleration sleds. The tests were split in three main groups in order to check the dummy's sensitivity to restraint loading, sensitivity to child restraint design and durability.

One of the aims of the project was to create a 5 band scoring system for the Q10 prototype dummy. This would then allow it to be used in the NPACS test procedure, which would mean that all child restraint types could be assessed to the NPACS protocols.

2 Test Environment Requirements

The testing of child restraint systems (CRS) is currently done under UNECE Regulation 44 (Reg. 44), using P dummies. The developed Q10 prototype dummy was evaluated according to this regulation. Additionally, a comparison with the P dummy was made. The tests, unless otherwise specified, were set up and executed according to Reg. 44 (Table 1). Prior to each phase a calibration test was conducted as required.

Table 1 Test conditions for dynamic performance testing

Condition	Details
Test bench	Reg. 44 test bench and specified cushions
Anchorages	Belt anchorages A, B ₀ , C Rearmost ISOFIX anchorages
Sled mass	Heavy sled to minimise dummy inertia effects on the pulse TRL—1130 kg, DOREL—752.5 kg
Test pulse	Reg 44 FRONT IMPACT pulse
Impact speed	50 +0/−2 km/h
Test conditions	Pre-impact speed, stopping distance as specified in Reg. 44 (650 = 50 mm)
Setup instrumentation	Sled Uni-axial accelerometers Seat belt force load cells located as prescribed in Reg. 44

The NPACS front impact test was designed to represent a real world frontal impact event at 65 kph (+0/−2). These tests were carried out at IDIADA on an acceleration sled. Also, side impact tests were carried out following the NPACS procedures. Examples of the set-ups are shown on Fig. 2.

3 Results

The Q10 prototype dummy was submitted and evaluated on certification style testing on biomechanical performance, sensitivity, repeatability and durability. These tests were performed at component and full body level, using standard dummy certification test equipment. Certification procedures were developed.

The dummy showed trends in the sensitivity studies that were carried out to validate the Q10 prototype dummy. Additionally, the durability met the requirements specified in Task 1.2 “Biomechanical requirements and design brief” [1]. The results of the testing were repeatable in general and all of the coefficients of variation were within the required 5 %. The certification tests that were carried out showed that the dummy correlates well with the biomechanical targets specified in the design brief for frontal loading conditions. For lateral impact, the response was too stiff initially and too soft at later stages relative to side impact biofidelity corridors.

The Q10 dummy has a total of 71 measuring channels. However, it is expected that for Reg. 44 only a selection of them will be used. In total 114 front impact tests, following the Reg. 44 testing requirements, were conducted in the EPOCh project.

From the analysis carried out using the results from the Reg. 44 testing, can be concluded that the Q10 dummy is sensitive to changes in the test setup. It was noted that the dummy detected differences in the kinematics and the loading in different setups.



Fig. 2 NPACS Front Impact Test bench (*left*) and side impact test bench (*right*) (images distorted to anonymise CRS)

The Q10 prototype dummy's sensitivity to child restraint design was evaluated using the Reg. 44 testing requirements. The dummy distinguished between the different seats in at least one of the tests. In Fig. 3 is shown a comparison of the head acceleration resultants from the tests for sensitivity to child restraint design. This strengthens the conclusion that the Q10 detected the differences between the four different child restraint systems that were tested. The curves of each group of tests are presented in the same colour for easier interpretation of the data dispersion.

It was concluded, after conducting all of the Reg. 44 tests, that the Q10 dummy is durable under this regulation's conditions. A few weaknesses were found and corrected. Additionally, the tests showed that the Q10 is capable of producing repeatable results over extended testing. As a result, it was recommended that the recalibration of the Q10 dummy is conducted after every 20 tests for the Reg. 44 tests, as long as the Q10 does not exceed the 150 % of the loading levels specified.

A comparison between the Q10 and P10 dummies was carried out, comparing the kinematics of each dummy in a number of booster seats and booster cushions Reg. 44 tests. The appropriateness of applying Reg. 44 limits to Q10 was investigated and, where necessary, revised limits were calculated. On Fig. 4 is shown a comparison between Q10 and P10 at the point of maximum head excursion.

In total, 51 frontal and 64 side impact tests were carried out using the NPACS protocol. They evaluated the dummy's sensitivity to restraint loading, sensitivity to child restraint design and durability.

Ten frontal and 12 side impact tests were carried out to determine the dummy's sensitivity to restraint loading. From the results obtained can be concluded that the dummy measured as expected in the major body regions. Additionally, it detected variations in the kinematics response to different loadings. On Fig. 5 is shown that there was a clear difference between the pelvis acceleration loadings measured by

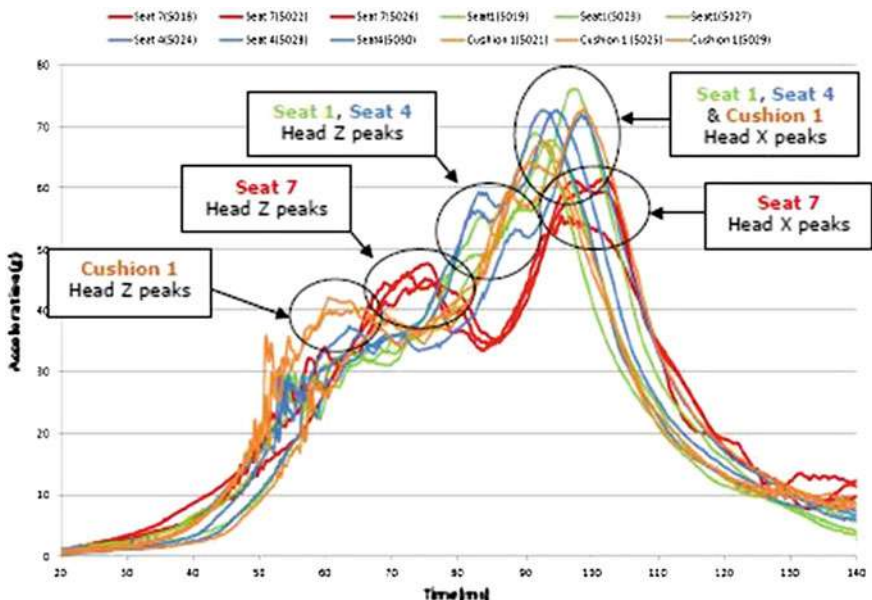


Fig. 3 Sensitivity to child restraint design—head acceleration resultant

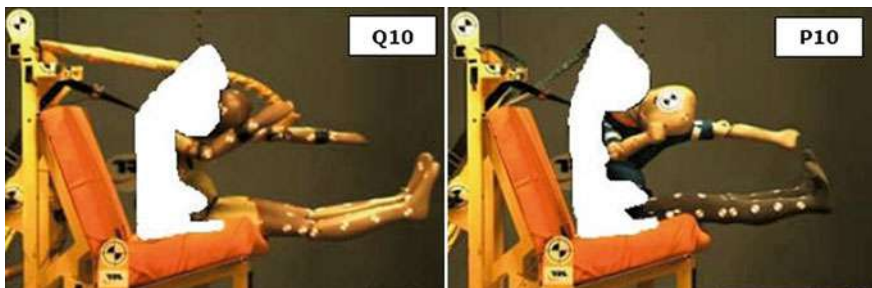


Fig. 4 Comparison between Q10 and P10 at the point of maximum head excursion

the Q10 dummy in the front impact tests with extra belt tension (see red and yellow curves) in comparison to the baseline tests.

From the analysis of the results was concluded that the Q10 dummy was capable of detecting differences in the child restraint design in both side and frontal impact tests. Additionally, differences in the results can be explained by the differences in the child restraint design.

The dummy showed good repeatability from the durability front and side impact tests. A few parts required improvements for their durability, but they were improved and implemented in the final version of the dummy. The investigation into dummy recovery time for side impact NPACS tests found out that the dummy is capable of producing repeatable results with up to 30 min recovery time.

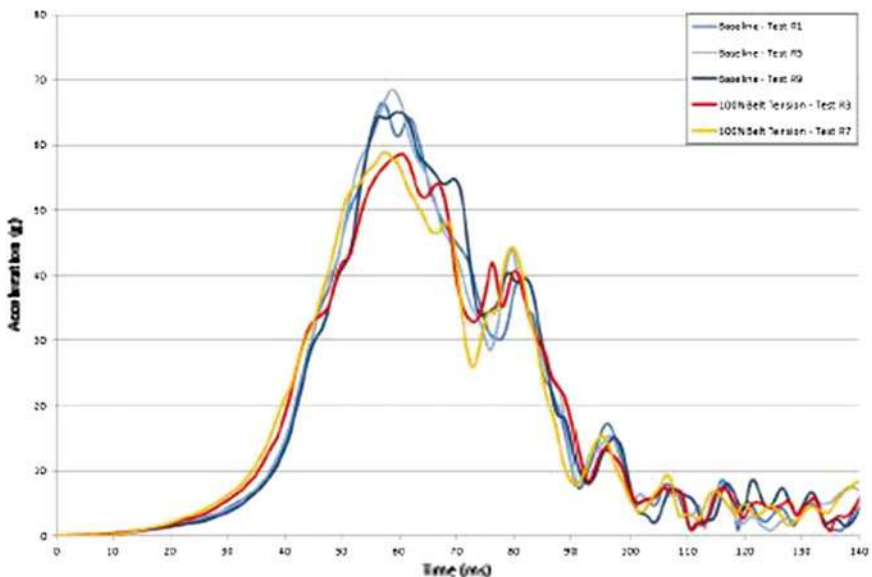


Fig. 5 Front impact: comparing the tests with 100 N seat belt tension to the baseline test for the pelvis resultant acceleration

As already explained, such a large number of tests had to be managed and a Gantt chart was used for this purpose. The following testing results information is available and can be provided if requested:

- Reg. 44
 - Sensitivity to changes in test setup
 - Test matrix
 - Results from the body regions, including: head, upper and lower neck, chest, pelvis
 - Sensitivity to child restraint design
 - Test matrix
 - Results from the body regions, including: head, upper and lower neck, chest, pelvis
 - Durability
 - Test matrix
 - Durability with different seats—results from the body regions, including: head, upper and lower neck, chest, pelvis
 - Durability time dependency testing: tests conducted 15, 30 and 45 min after a previous test. Results from the body regions are available, including: head, upper and lower neck, chest, pelvis

Durability dummy positioning—results from the body regions, including: head, upper and lower neck, chest, pelvis

- Comparison of P10 and Q1

Test matrix

Results from the body regions, including: head, upper and lower neck, chest, pelvis

- NPACS: side and frontal impacts

- Sensitivity to changes in test setup

Test matrix

Results from the body regions, including: head, upper and lower neck, chest, pelvis

- Sensitivity to child restraint design

Test matrix

Results from the body regions, including: head, upper and lower neck, chest, pelvis

- Durability

Test matrix

Durability with different seats—results from the body regions, including: head, upper and lower neck, chest, pelvis

Durability time dependency testing: tests conducted 15, 30 and 45 min after a previous test. Results from the body regions are available, including: head, upper and lower neck, chest, pelvis

Durability dummy positioning—results from the body regions, including: head, upper and lower neck, chest, pelvis.

4 Specification of 5 Band Rating System for Application of NPACS

In the final phase of the EPOCH project a 5 band scoring system for the Q10 dummy was created. This way the NPACS testing procedures were expanded so that all of the child restraint systems can be tested using the NPACS testing protocol.

The first approach for developing this rating system was to apply the already existing scoring tables for both front and side impact results. Ideally, the results of the testing with the Q10 dummy would have evenly spread across the scoring band. However, as this did not happen, a revised scoring table had to be created for both side and frontal tests.

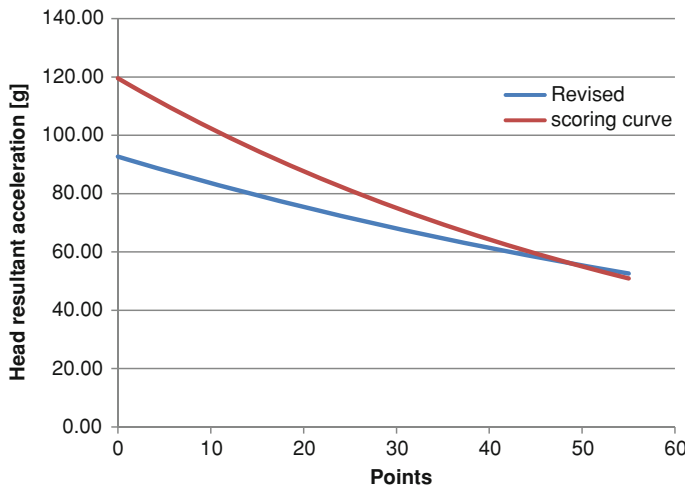


Fig. 6 Front Impact head resultant acceleration revised scoring

The tested samples were chosen in such a way that they can represent the whole range of products available at the market. It was decided that the worst performing child restraint systems should score between 0 and 10 % of the points available per body region. On the other hand, the best performing restraint systems were set to score around 75 %, which will allow some room for possible improvements in child restraint system designs. On Fig. 6 can be seen the revised scoring for front impact head resultant acceleration as an example.

5 Conclusions and Recommendations

The Q10 dummy was developed to the required specifications and was found to be sensitive, durable and repeatable on certification style testing on biomechanical performance. All of the results obtained had a coefficient of variation within the required 5 %. Certification procedures were developed for the Q10 dummy.

Based on the findings from the testing using Reg. 44 testing protocol, the following recommendations and conclusions can be made:

- The Q10 dummy is durable enough to be used in Reg. 44 front impact tests.
- The Q10 is sensitive enough to show differences and specific patterns.
- A recalibration is recommended after every 20 tests.
- The limits have to be revised if Q10 is used, in order to provide an equivalent assessment to the P10. Some of the limits need more investigation.
- Chest vertical should not be assessed for the Q10.
- A minimum of 20 min is the recovery time between tests recommended.

Based on the findings from both the side and frontal testing using NPACS testing protocol, the following recommendations and conclusions can be made:

- The Q10 is sensitive enough to show differences and specific patterns for both side and front impacts.
- The Q10 dummy is durable enough to be used in side impact tests, following the NPACS testing protocol.
- Improved parts would be implemented in the final version of the dummy to prevent the few failures that occurred in the NPACS front impact testing and to reduce the maintenance checks.
- The recommended time between tests is 30 min. This will allow enough time for maintenance checks and dummy recovery.
- The Q10 NPACS scoring system has been expanded, to achieve a rating system, applicable to the Q10.

Reference

1. Waagmeester K, Burleigh M, Lemmen P (2012) D1.2—biomechanical requirements and design brief. EPOCh

Improvement of the Child Injury Risk Curves for Road Accidents

Alejandro Longton, Philippe Lesire, Heiko Johannsen,
Philippe Beillas, Anita Fiorentino and Alan Kirk

Abstract *Research objective* The EC CASPER project aimed at decreasing injuries and fatalities of child travelling in vehicles. One of the ways to achieve this is to obtain knowledge on how injuries occur—identifying the severity and how they can be correlated with the data collected from reconstruction tests. This information leads to improve the injury risk curves by adding new points that were introduced and developed in previous investigation projects. The main idea of these curves is to correlate dummy readings from accident reconstructions with the injury levels recorded in the real cases. These injury risk curves will improve the way children are restraint in cars. *Methodology* The first step to obtain new data for the Injury Risk Curves required collecting information from real accidents. This accident data was collected by road accident investigation teams. Then, some accidents were selected following a certain criteria for reconstructions in crash-test laboratories. The accident reconstructions were carefully prepared, taking into

F2012-F02-023

A. Longton (✉)
Applus IDIADA, Tarragona, Spain

P. Lesire
LAB, Paris, France

H. Johannsen
TUB, Berlin, Germany

P. Beillas
IFSTTAR, Bouguenais, France

A. Fiorentino
Fiat Group Automobiles, Turin, Italy

A. Kirk
Loughborough University, Leicestershire, UK

account the real life travelling situation. Additionally, virtual tests were carried out to ensure the similarity between the EES, kinetics and kinematics of the accident and the proposed test configuration. Once the test results were validated by analysing the deformation of the vehicles and, a correlation is made between the injury/non-injury of the child and the dummy readings, focussed on five body segments. Finally, using the Weibull cumulative distribution of density for the injuries and the confidence interval associated with this, constitute the injury risk curves for each body segment. *Results* The accident database that was developed in previous projects has now information from 806 cases (1300 restrained children) as a result of the efforts of the CASPER accident investigation teams. It is very important to highlight that the database is not representative of the overall European child car passenger population as a selection bias was used to collect the data (a bias for severe injuries and high crash severity was used). CDC descriptions and deformation points of the real accidents and the reconstructions were compared in order to validate the accident reconstructions. The real injuries collected from the accidents were analysed before the reconstructions and compared with the dummies' readings after them. The data collected by performing accident reconstructions was introduced in a reconstruction database. Then, the proposed new points were added to the injury risk curves for their improvement. *Limitations of this study* One of the limitations of this study is the high number of testing variables that can affect the results. For example, unexpected post-crash kinematics of the vehicles and the sensitivity of the impact point. Also, even though the accidents are investigated in-depth, information on the real travelling conditions of the occupants is not always present (e.g. CRS misuse, out of position). These conditions can affect the correlation between real injuries and dummy readings. *What does the paper offer that is new in the field in comparison to other works of the author* Unfortunately, even though the non-orthogonally type of collision carried out in a linear dragging crash ground laboratory was a new experience, this procedure was recently presented in another conference. *Conclusion* The CASPER project took results from previous projects and continued the research to improve the Injury Risk Curves for children in cars. This was done by providing additional points, obtained by accident reconstructions, especially in the ranges that were considered weak in terms of representation. Accidents were collected by investigation teams. Then, some of them were reconstructed in crash test laboratories. Once the reconstruction was validated, the dummies' readings were compared with the injuries from the real accident. These correlations were analysed and new points for the Injury Risk Curves were established. For more information public results have been posted on www.casper-project.eu.

Keywords Reconstruction • Correlation • Accident • Injury risk curves • Validation

Since 1996, several European Union (EU) funded projects have been carried out in order to improve child safety in cars. These projects remarkably enriched the

knowledge of child safety in cars. Even though a significant improvement was achieved, the number of deaths and casualties was still unacceptable. That is why the EC Child Advanced Safety Project for European Roads (CASPER) project aimed at decreasing injuries and fatalities of children travelling in vehicles.

The concept of the accident based injury risk curves was introduced and developed in previous investigation projects. The idea is to correlate dummy readings from accident reconstructions with the AIS levels in the real cases. Data from accidents has been collected, following the protocol defined in the project [1].

1 Casper Accident Database

The first step to obtain new data (points) for the Injury Risk Curves required collecting information from real accidents. The accident data collected in CASPER expanded the existing database with cases from previous European projects. As a result, the available database had information from 806 cases (1300 restrained children). It is also important to highlight that the Database is not representative of the overall European child car passenger population as a selection bias was used to collect the data (a bias for severe injuries and high crash severity was used). However, it contains enough data to allow an indication of the body regions being injured in different CRS types or for different ages of children along with insights into how restraint conditions and the quality of use lead to injury [2]. The cases that best fitted in the project's objectives and that could provide new data for the injury risk curves, as long as they were feasible, were selected for reconstructions. On Fig. 1 is shown the accident scene of an accepted CASPER case from Spain.

2 Accident Reconstruction

Based on some previous studies and database analysis it was agreed to focus on reconstructing frontal and side impact test configurations. Once the accident's data was collected and having the case approved for a full scale reconstruction, a virtual simulation of the accident was carried out. This had to enhance the understanding of the accident conditions and to help for designing the reconstruction. Then, a virtual model of the possible test was carried out. By doing so, the similarity between the accident and the reconstruction test was verified. EES, kinetics and kinematics were compared. Additionally, different impact points were considered and the changes in kinetics and kinematics were examined.

Some cases were considered frontal collision, but a Y-axis component of the velocity was present in the real accident. This component had to be considered as it could affect the kinematics of the occupants. In those cases, the tests were designed with an angle of the convergent vehicles, for a better representation of the real accident. Sometimes different impact velocities were used as well.



Fig. 1 Vehicles on the accident scene of an accepted CASPER case from Spain

Many times these considerations added additional complexity that had to be solved for a successful reconstruction test. Once the configuration was validated, the physical accident reconstruction was prepared and carried out.

2.1 Test Set-Up

A system that uses a trailing cable that can move vehicles simultaneously in two opposite directions was used in most of the accident reconstructions that were performed at IDIADA. This system was used in combination with pulleys to reproduce the collision angles and different impact velocities described previously. For the tests that were considered as complex, some key parameters, such as elasticity of the trailing cable, resonance effects, the trailing motor power peaks and the position at T_0 (The time at which the first impact between the cars occurs) had to be considered.

To carry out reconstructions at an angle different than 180° , pulleys were used. For example, in the accident reconstruction' configuration, shown at Fig. 2, pulleys were used to achieve a crash angle of 240° and to crash the vehicles at different speeds. Using pulleys can also increase or decrease the velocity of one of the vehicles.

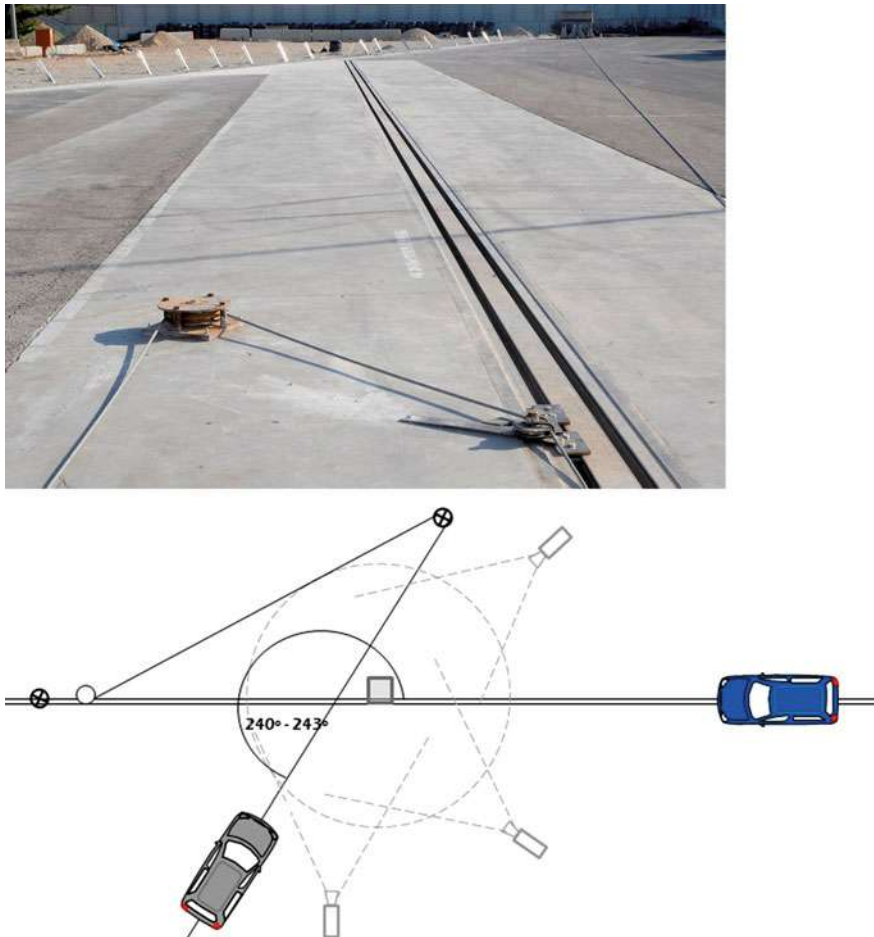


Fig. 2 Accident reconstruction's configuration using pulleys for angled converging vehicles

2.2 Deformation Coding

In order to standardise the descriptions of the deformations of the crashed vehicles and to define the directions of the intruding deformation forces, the Collision Deformation Classification (CDC) was used. This codification system is used by most of the accident investigation teams and it consists of eight fields, explaining clearly the deformation of a car in a collision [3]. CDC coding of the real accidents and the reconstructions could be compared in order to review the accuracy of the test, to help validating the accident reconstruction.

Further detail is recorded of measurements of deformation and intrusion at specific important points on the vehicles (for example, right/left side frontal longitudinal deformation, mid-door lateral intrusion). These are important points as

Table 1 Q-dummies sensors available for reconstructions (P/Q dummies comparison, Longton 2011)

Instrumentation		Dummies					
Sensor	Region	Q0	P0	Q1/Q1½	P1½	Q3/Q6	P3/P6
3-axis accelerometers	Head	✓		✓	✓	✓	✓
	Thorax	✓		✓	✓	✓	✓
	Pelvis	✓		✓	✓	✓	
6-axis load cell	Upper neck	✓		✓	✓	✓	✓
	Lower neck			✓	✓	✓	
	Lumbar spine				✓	✓	
3-axis angular rate sensor	Head			✓		✓	
Displacement sensor	Chest		✓		✓	✓	

they indicate deformation of stiff vehicle structures and intrusion that can influence occupant injuries. Measurements at these points are compared between the accident vehicle and the crash test vehicle.

2.3 Instrumentation

Once the configuration of the crash was finalised and the positions of the occupants and the vehicles were established, the necessary instrumentation for both the dummies and the vehicles was determined, based on the injuries from the real accident. It was required that the vehicles should be equipped with at least one triaxial accelerometer. As for the child restraint system, two accelerometers were typically installed in the reconstructions, a triaxial and a uniaxial, depending on the configuration of the reconstruction.

Medical information indicated what instrumentation was appropriate for the dummies as the main purpose for the in-depth accident investigation and for carrying out accident reconstructions was to correlate the medical injuries with the dummies' readings after validation of the reconstruction accuracy. Therefore, the dummy was instrumented with sensors according to the injuries that the occupants have suffered in the real crash. A special consideration was bore in mind for the neck injuries. For instance, not only loads cells were installed on the dummy's neck, but also gyroscopes on the head were considered. However, uninjured areas were also interesting to measure in order to validate the reconstruction and obtain no injury points that are needed to build injury risk curves.

The Q-dummies family were used in the CASPER project. The dummy that was closest to the age of the child was used as only dummies representing a certain age are available. The sensors available for these dummies are compared with the previously used P-dummies in Table 1.

SEATING POSITION:		Age:
Rear center		approaching 2 years old
Type of restraint:	Use	M.AIS
CRS group 1	Yes	4
Injuries		
Injury	Cause	AIS code
head injury description	Deceleration	XX.06.84.3
GSC=3	Deceleration	XX.08.04.4
lumbar spine injury descr.	Head/chest movement	XX D2.39.2
lumbar spine injury descr.	Head/chest movement	XX D2.02.3
Thorax injury description	Harness	XX 18.02.3
Thorax injury description	Harness	XX 14.10.4
lumbar spine injury descr.		XX 04.01.3
DIED XX DAYS AFTER THE ACCIDENT		

Body region	Max. Values
Head	Acceleration X 29.59g
	Acceleration Y 9.826g
	Acceleration Z 66.39g
	Resultant Acc. 70.17g
	HIC 36 ms 499.98
	Angular speed X 854.9deg/s
Chest	Angular speed Y 2226deg/s
	Angular speed Z 806.7deg/s
	Resultant ang. Sp. 2277deg/s
	Acceleration X 37.35g
	Acceleration Y 17.78g
	Acceleration Z 21.58g
Neck	Resultant Acc. 38.69g
	XMS 3ms Cumul. 34.75
	Fx 440.0N
	Fy 250.0N
	Fz 115.0N
	Resultant F 1181N
Neck	Mx 5.830Nm
	My 13.94Nm
	Mz 3.100Nm
	Resultant M 14.73Nm

Fig. 3 A comparison between real injuries from a CASPER accident (European) and dummy readings

2.4 Injuries

The real injuries collected from the accidents were analysed before the reconstructions and compared with the dummies' readings after them. In Fig. 3 is shown a comparison between the real injuries (child approaching 2 years old) and the dummy's (Q1.5) readings.

3 New Points for the IRC

Once the accident reconstruction was carried out and the data was collected, the test had to be validated. This was done by comparing the car deformation (see Fig. 4) and the CDC of both the real accident and the reconstruction. The dummies' signals, once validated, were correlated with the real accident's injuries. In this way, if the occupant suffered head injuries for example, the peaks and the values that the dummy recorded for the head acceleration curve were examined. Then, the test data was provided for processing in order to create new points for the Injury Risk Curves.

The data collected was introduced in a Reconstruction database (Fig. 5). Once entered, it was available for comprehensive analysis and classification by body region. Then, by biomechanically accepted scaling procedure between the dummies and depending on their biomechanical design parameters, preliminary points were added to the existing curves.



Fig. 4 Visual comparison of the deformation in the real accident (*left*) and the reconstruction (*right*)

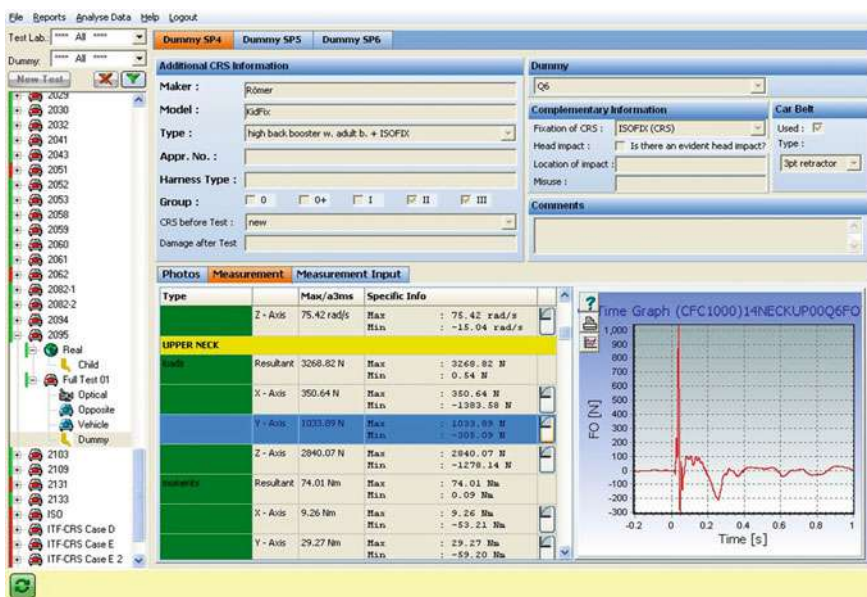


Fig. 5 Reconstruction database

As the normal distribution does not guarantee zero injury risk when no acceleration is applied, a Weibull statistical distribution was applied. Anomalous points were removed and the remaining points were added to the project database of the Injury Risk Curves. Additionally, confidence intervals for the particular distribution were established. Finally, using the Weibull distribution of density the Injury Risk Curves were improved by calculating the cumulative function of the density function [4] (Fig. 6).

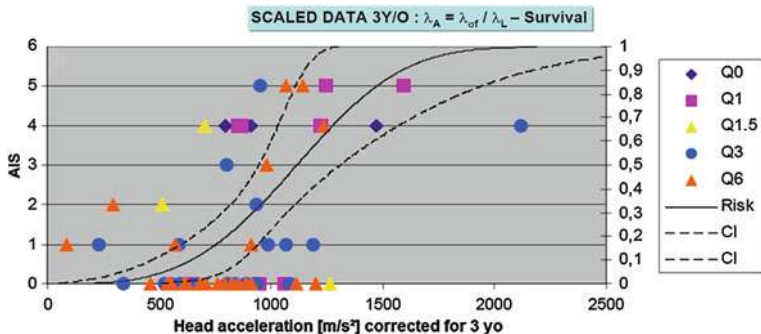


Fig. 6 AIS graph with the established confidence intervals

4 Conclusions

The CASPER project took results from previous projects and continued the research to improve the Injury Risk Curves for children in cars. This was done by providing additional points, obtained by accident reconstructions, especially in the ranges that were considered weak in terms of representation.

Accidents were collected by investigation teams. Then, some of them were reconstructed in crash test laboratories. The CDC and measured deformations of the real accidents and the ones of the reconstructions were compared to validate the test. Additionally, EES, kinetics and kinematics were compared. Once the reconstruction was validated, the dummies' readings were compared with the injuries from the real accident. These correlations were analysed and finally, new points for the Injury Risk Curves were established.

For more information on the other results, public results have been posted on www.casper-project.eu.

Acknowledgments The CASPER project is co-funded by the European Commission under the 7th Framework Programme (Grant Agreement no. 218564).

The members of the CASPER consortium are: GIE RE PR - PSA/RENAULT, Technische Universität Berlin, Université de Strasbourg, APPLUS IDIADA Automotive SA, IFSTTAR, Loughborough University, FIAT Group Automobiles Spa, Medizinische Hochschule Hannover, Chalmers tekniska hoegskola AB, Bundesanstalt für Straßenwesen, TNO, Verein für Fahrzeugsicherheit Berlin e.V., Ludwigs Maximilian Universität, Centre Européen d'Etudes de Sécurité et d'Analyse des Risques, Humanetics Europe GmbH. Further information is available at the CASPER web sites: www.childincarsafety.eu and www.casper-project.eu.

The partners wish to acknowledge all the CREST/CHILD and CASPER data collection teams and their sponsors from all the countries involved in this work.

UK Loughborough cases, collected during the EC CREST/CHILD projects, include accident data from the United Kingdom Co-operative Crash Injury Study, collected up to 2006. CCIS was managed by TRL Ltd on behalf of the Department for Transport (Transport Technology and Standards Division) who funded the project with Autoliv, Ford Motor Company, Nissan Motor Europe and Toyota Motor Europe. The data were collected by teams from the Birmingham Automotive Safety Centre of the University of Birmingham, the Vehicle Safety Research Centre

at Loughborough University, and the Vehicle & Operator Services Agency of the Department for Transport. The views expressed in this work are those of the authors and not necessarily those of the UK CCIS sponsors.

References

1. Kirk A, Lesire P, Schick S (2012) Road reality status (fatality studies), Deliverable 3.2.1 of the EC FP7 Project CASPER
2. Kirk et al (2012) Report on accident analysis, Deliverable 3.2.3 of the EC FP7 Project CASPER
3. Collision Deformation Classification—SAE J224 MAR80
4. Petitjean A, Trosseille X (2011) Statistical simulations to evaluate the methods of the construction of injury risk curves. *Stapp Car Crash J* 55:411–440

Optimization of Passive Head Restraint for IIHS Low Speed Rear Impact

Dong Ming

Abstract *Research and/or Engineering Questions/Objective* Active headrest is usually utilized to mitigate the whiplash injury to the occupant from the rear impact by way of moving forward during the collision to shorten the distance and the contact duration between the occupant head and the headrest thus reduce the neck injury index. But the spread application of the active headrest is limited due to its high cost. This paper explore the approach of applying a passive head restraint to alleviate the whiplash injury during the rear impact. *Methodology* Aimed at earning high rating of GOOD in the rear impact condition in IIHS through minimize the neck injury, this paper presents the method of development and optimization of head restraint insert/surface and seat back suspension and the by way of simulation and vehicle test. *Results* The rigidity distribution of seat back suspension, and quality of the integration design of head restraint foam and insert have great impact to the neck injury resulted from the rear collision. In order to keep the seat comfort, a space between the occupant head and the head restraint surface has to be maintained. In the premise of satisfying the seat comfort to the greatest extend, by way of adjusting seat back suspension and the head restraint insert/surface, the head restraint can rapidly contact the occupant head in the collision, thus reduce the shear load and tension to the neck, and earning highest rating of GOOD in IIHS. *Limitations of this study* This paper study the rear impact load case of IIHS only, does not consider 2012 version NCAP and Euro NCAP. But the approach set forth in this article can be applicable for mitigate the neck injury in the rear impact. *What does the paper offer that is new in the field in comparison to other works of the author* This paper study the development and optimization of passive head restraint to improve the occupant protection

F2012-F02-026

D. Ming (✉)
Pan Asia Technical Automotive Center, Shanghai, China

performance of the head restraint in the rear impact with the minor cost increase. The paper offers the active contribution in lower the cost and the vehicle mass.

Conclusion In the premise of satisfying the seat comfort to the greatest extend, by way of adjusting head restraint insert/surface and seat back suspension, the headrest can rapidly contact the occupant head in the collision, thus reduce the shear load and tension to the neck, and earning highest rating of GOOD in IIHS. This paper study the development and optimization of passive head restraint to improve the occupant protection performance of the headrest in the rear impact without increase the cost. The paper offers the active contribution in lower the cost and the vehicle mass.

Keywords Rear impact • Neck injury • Seat • IIHS • Head restraint

1 The Requirement of IIHS Head Restraint Protocol

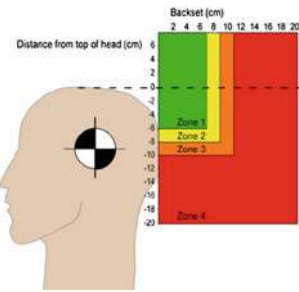
Following a rear impact vehicle crash it is observed that 90 % of all injuries incurred are in fact neck injuries. Around 90 % of these necks injuries occur during a low speed rear impact. The vast majority of these injuries belong to slight injury (AISI) Class [1]. The neck injury will result in a headache, neck pain and neuralgia etc. Symptom for many of the injuries need to be cured over a long period of time and bring very big pain, sufferings and economic loss to the individual. For the purpose of assessing occupant protection ability of seating system, IIHS North America has development test specification of rear impact performance for head restraint. Our researches in this paper are based on target of improve IIHS test rating.

IIHS is the abbreviation of Insurance Institute for Highway Safety. IIHS head restraint rear impact specification is a protocol for evaluating and rating the ability of seats and head restraints to prevent neck injury in moderate and low-speed rear-end crashes. This protocol is developed by Insurance Whiplash Prevention Group (IIWPG). The purpose of the protocol is reduce neck injuries after rear impact and reduce the medical insurance compensation payouts. There are four Classes of performance rating: good, acceptable, marginal and poor assess and provide the car safe information for consumer. IIHS has the following request to the head restraint:

1.1 Measurement and Rating of Static Head Restraint Geometry: The Initial Evaluation

The distance of head, head restraint and headrest height determined static rating of Head Restraint. Such as Fig. 1 shows the use of a head restraint measuring device (HRMD) to carry out static state assessment, and as we can see the higher the

Fig. 1 Diagram of geometric head restraint ratings



headrest is and the closer the headrest is to the head the headrest will have a higher geometric rating. A static evaluation conducted in this way can be used to qualify/disqualify a seat/head restraint design for dynamic testing until the static measurement can be conducted in the vehicle.

1.2 Dynamic Test Requirements

The request that IIHS also stipulated is that the dynamic seat test at the same time, the using a dynamic sled platform to imitate the vehicle while holding the seats still, where the seats will encounter the same weighted rear impact crash condition equivalent to a 10 miles (about 16 km) speed per hour to assess the protection function that seat rear impact to the spine. Pulse of Target Sled Acceleration and Specification Corridors marked by the 'x' as shown as Fig. 2.

These tests should be conducted with a BioRID IIg or later revision dummy. This kind of dummy can simulate the human's spine behaviour and it also has sensors built into detect force and acceleration during a rear impact.

Following are parameter of dynamic test: time to head restraint contact or T1 acceleration (forward acceleration of the seat occupant's torso). Neck Shear (Fx) and Neck Tension (Fz).

The judgment standard that the dynamic state test is as follows:

1. Time to head restraint contact—time to head restraint contact must be less than 70 ms to pass this requirement. OR T1 acceleration (forward acceleration of the seat occupant's torso)—the maximum T1 forward acceleration must be less than 9.5 g to pass this requirement.
2. Neck Shear (Fx) and Tension (Fz)—shown in Fig. 3. Dynamic test rating is determined by matrix shown in Fig. 4.

The static geometry rating and the dynamic rating are combined as shown in Fig. 5 to establish the overall rating for the seat. A seat with a static rating of Poor or Margin will earn a Poor overall rating and need not conduct dynamic test [2].

Fig. 2 Target sled acceleration and specification corridors

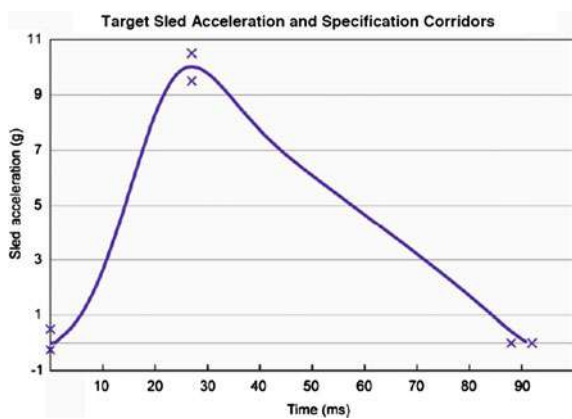
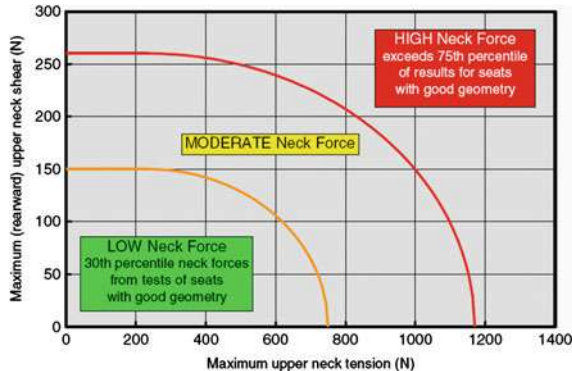


Fig. 3 Rating for the joint distribution



2 Cons of Passive Head Restraint During Lower Speed Rear Impact

During the low speed rear impact, the sooner head restraint contacts to the occupant's head the more protection is generally offered to the head and neck. Make the head restraint as early as possible run into occupant's head is to reduce the distance between head and head restraint and make head restraint higher. But leaves the head restraint too close with occupant's head will produce the problem of occupant comfort. The reason was a backward exercising of the head is restricted by head restraint and makes occupant uncomfortable. Reduce the distance between head restraint and occupant's head can improve head restraint's protection ability for occupant's neck, at the same time, the rigidity distribution of seat back suspension, and the quality of the integration design of head restraint foam and insert have great impact to the neck injury resulted from the rear collision.

Because reducing the distance can improve headrest's protection ability for passenger's neck injury. To reduce the whiplash injury during vehicle rear impact,

Fig. 4 Dynamic rating requirements

Dynamic Rating Requirements		
Seat Design Criteria	Neck Force Classification	Dynamic Rating
T1 X-acceleration ≤ 9.5 g OR Time to head restraint contact ≤ 70 ms	Low	Good
	Moderate	Acceptable
	High	Marginal
T1 X-acceleration > 9.5 g AND Time to head restraint contact > 70 ms	Low	Acceptable
	Moderate	Marginal
	High	Poor

Fig. 5 Formulation of overall rating

Geometric Rating	Dynamic Rating	Overall Rating
Good	Good	Good
	Acceptable	Acceptable
	Marginal	Marginal
	Poor	Poor
Good Height		→ Good
Acceptable	Good	Acceptable
	Acceptable	Acceptable
	Marginal	Marginal
	Poor	Poor
Marginal	No dynamic test	Poor
Poor	No dynamic test	Poor

usually use of active head restraint. Active headrests can deploy forward to eliminate distance between head and head restraint during rear impact, to reduce contact time for lower the whiplash injuries. But the popularize of active head is restricted because its cost is higher. Because passive head restraint has cost benefit, this paper explore the approach of applying a passive head restraint to alleviate the whiplash injury during the rear impact.

3 Occupant's Postures and Injury Principle Analysis During Rear Impact

3.1 The Occupant's Postures Divided into Three Stages During Rear Impact. Shown in Fig. 6

Figure 6 shows three stages of dummy posture during rear impact:

3.1.1 Stage 1 (Shown in Fig. 6. Picture (1) (2)): The Occupant's Head and Torso be Opposite to Move, the Neck Stretches

Torso push by seat back to forward, but because of inertial, the occupant's head still keep in the start position in beginning of crash. Result in spine stretching backward, the neck spine presents a S form. Because the shear force from neck spine to head, the head starts to move rearward, finally whole neck spine will

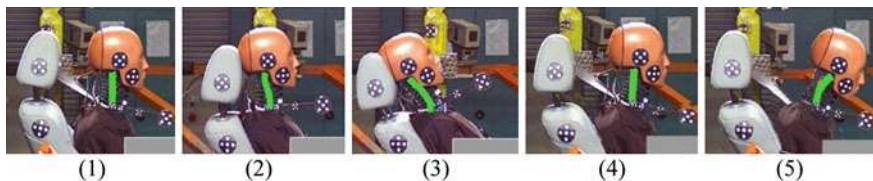


Fig. 6 3 stages of dummy posture during rear impact (1) crash beginning (2) the occupant's head and torso be opposite to exercise, the neck S form transforms (3) head and head restraint full contact, dummy return movement start (4) safety belt beginning function during dummy return (5) The neck is forward bent, crash energy depletion be over

stretch to whiplash to the headrest backward. Upper neck spine change from forward bent to stretch backward. The bent radius of neck is minimum when neck is S form, at this time Neck the Shear (F_x) is the highest. When the head that moves backward to contact with headrest, Neck tension (F_z) will reach highest value. Then head and torso/stretch process be over. Because of the dissimilarity of head restraint position, the head turns angle variety very greatly, but almost wills appear S form under the all condition.

3.1.2 Stage 2 (Shown in Fig. 6. Picture (3) (4)): The Occupant's Head Moves Forward Process

After head gets in touch with headrest, head opposite movement to forward. Because the stored energy of seat release to torso, the occupant will produce to forward return. The head return will not synchronize with torso. If torso return is early than head return, the neck stretches time will become longer, disadvantage is at letting up of Tension (F_z); If torso return is late than head return, will shorten neck stretch time, beneficial to the decrease occupant's neck injury.

3.1.3 Stage 3 (Shown in Fig. 6. Picture (4) (005)): The Neck Stretch/Bent Forward

In this stage, the safety belt starts to function and controls occupant to move forward. The chest is controlled by safety belt to stops move forward, while the head continue to move forward, the neck spine appears ant i- S form. Compare to stage 1 and stage 2. The energy of rear impact is almost exhausted in this stage. So this paper will mainly focus on reduce injure during stage 1 and stage 2.

3.2 Relationship Between IIHS Measurements and Neck Injury Principle

Neck injury principle in the rear impact has various assumptions, up to now have no one can completely explain reason of neck hurt. But all of their theory

foundations is: the movement between head and the torso cause opposite movement of spine. The principle that injury of the neck includes a few kinds assumption as follows [3]:

1. The first assumption thinks that the neck injury caused by neck move to backward and excessively stretching, exceed normal physiology scope of human body. Whether spine excessively stretches, IIHS test to use Tension (Fz) to evaluate.
2. Discover afterwards the neck hurts to also usually appear, even if the neck did not excessively stretch. Reason is before at neck backward flexibility move, S form transform to press a strong moment to change inside the ridge tube, may cause the harm of spine nerve root. The S form transforms mainly caused by shear force. IIHS test to use neck Shear (Fx) to evaluate.
3. During the process of rear impact, occupant's head and head restraint contact time is also important. The contact is more quick, more quick provide protection to the occupant. So IIHS test defined precondition of IIHS good rating is contact time ≤ 70 ms.

4 To Get IIHS Good Rating by Theory

A vehicle now is under production that development for North America market. In order to get competition ability on the cost, installed passive headrest. Although Geometry evaluation of head restraint is in the good zone, seat IIHS overall result is Margin due to dynamic Margin rating in the beginning of development. But the IIHS request of North America for this vehicle is GOOD, therefore, according to occupant's postures and injury principle analysis during rear impact, carried on research to improve the seat dynamic rating.

4.1 Interface Between Occupant and Seat During Rear Impact

Following contact will happen during rear impact: (1) the seat back and torso; (2) head restraint and head;

1. The seat back pushed torso to move forward while rear impact happen. Following parts are included in seat back assembly: foam; wire suspension and seat structure. Seat back isn't a rigid part, while it pushing torso to move forward a certain penetration occurs. As described before: Torso push by seat back in the forward direction, but at this time the occupant's head because of inertial, still keep in the start position. Result in spine stretching backward, that cause neck shear. So reduce rigid of seat back. Increment transformation of back during impact, can lower acceleration for torso that drive by seat back and has advantageous to reduce neck shear force.

For attaining comfort and the request of durable, is needed by the hardness of back foam inside the certain scope, the tension of suspension that behind back foam also will impact comfort of seats. Lower tension of suspension will cause collapse feeling, which leads to customer comfort complaints. How to make transformable seat back but don't influence the basic design parameter is the direction that we study. Is analytical after theory, our detection: while impact occurrence, the back isn't a push torso to parallel forward of, but with depend on rigid distribute of seat back. If upper seat back is more rigid than bottom seat back, while impact occurrence, relative lower rigid bottom of seat back carried smaller movement to the torso, the torso bottom carried under the inertial and stayed around originally position, the torso bottom to sink into a seat back a little bit quickly, upper torso take torso center gravity for the fulcrum, push by relative higher rigid upper seat back, creation of additional of movement forward trend. At this time the head hasn't contact with head restraint, the head still stays originally position because inertial. Additional of forward trend of upper torso increase shear force of neck spine, will bring larger injury to neck spine. Whereas, If bottom seat back is rigid than upper seat back, while impact occurrence, relative lower rigid upper of seat back carried smaller movement to the torso, the torso upper carried under the inertial and stayed around originally position, the torso upper to sink into a seat back a little bit quickly, bottom torso take torso center gravity for the fulcrum, push by relative higher rigid bottom seat back, upper torso creation of additional of movement rearward trend. This will reduce shear force of neck spine. See Fig. 7.

2. Head restraint and head

For comfort reason, head restraint and occupant's head is design to don't get in touch with, need to keep certain distance (Backset). But occupant's torso and seat back is contiguous. As description before: Torso push by seat back to forward during rear impact, because the backset and inertial, head still keep in the start position. Because the shear force from neck spine to head, the head move to rearward, finally whole neck spine will stretch to whiplash to the headrest backward. Neck tension(F_z) reach maximum when the head that move backward to contact with headrest. So, the head restraint more close with occupant's head. The head can be more quicker to get in touch with head restraint and get protection with head restraint. After tear down head restraint, we can found: the head restraint is wrap by soft foam. Parts inside of foam are inserts. Head restraint insert link to seat back frame by rods which attach to insert. Load path of impact force is: from foam to insert, then to rods, finally from rods to seat back frame. Foam not only act as comfort part but also provide safety function. Foam will deformation during crash. The insert of head restraint will provide truly protection after foam deformation. According to theory analysis, we improved head restraint as follows aspects: (a) Reduce back set. After comfort evaluation, back set ≥ 20 mm is acceptable for comfort. Smaller back set let head restraint get in touch with head and provide protection for head quickly, has benefit to reduce neck shear force. At the same time, after head and headrest get in touch, the soft head restraint foam can

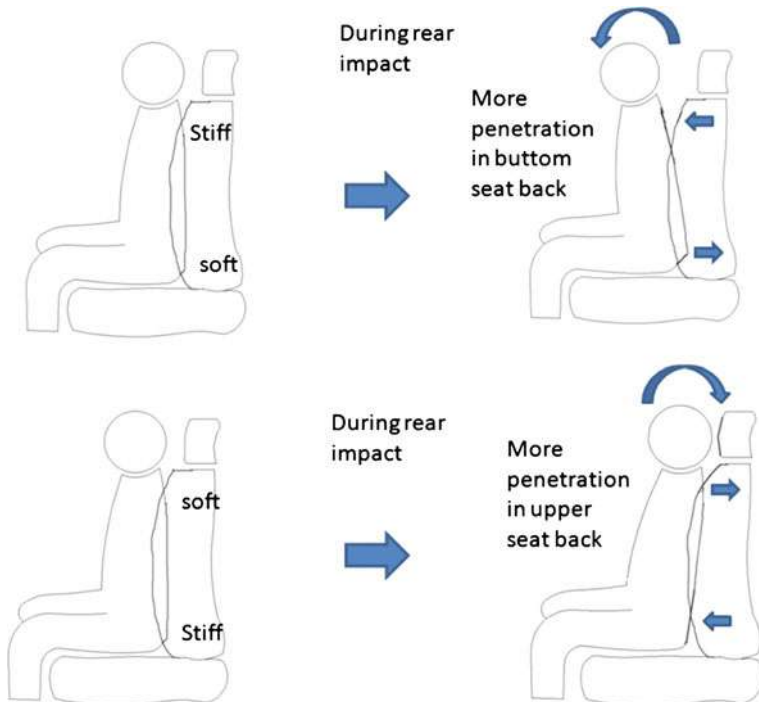


Fig. 7 Occupant posture during rear impact

provide friction resistance to limit extend force of neck spine. (b) Add plastic cover or add EPP to head restraint insert. There parts can improve support ability of head restraint insert. Speed up the load transfer from insert to seat back frame. (c) The height of head restraint. Because seat back is about 25 degrees backward, torso and head have trend to move upward and leave protection area of head restraint during rear impact. So increase the height head restraint properly is help for protection of head restraint.

4.2 Analysis and Study

According to the Interface study between occupant and seat during rear impact, improved seat back and head restraint as following:

1. Carry on improvement to the seat back. The outside layer of seat back is seat foam. Inside of back foam there is back suspension to hold occupant's torso. There will impact styling and comfort if change surface of seat foam. So change foam is not recommended for change rigid distribution of seat back.

Change suspension that inside of seat foam will not influence seats external appearance and less influence comfort, so we change rigid distribution of seat back by change suspension. Is shown as Fig. 8: steel wire suspension attach to back frame by 10 hooks. Cut two hooks in upper of suspension to reduce rigid of back upper area. Temporarily be not carry on strengthening change in back bottom area. Because rigid of back bottom will increase relatively since reduce rigid of back upper area.

2. Carry on improvement to the head restraint.

According to protection theory of head restraint to occupant's head, carried on following improvement to the head restraint: (1) add plastic cover to head restraint insert. That lead to transfer load from head to seat back frame quickly. (2) Bend rods angle forward to reduce backset of seat. (3) Add more foam in front of head restraint to get properly backset. (4) Adjust location of locking pitch in head restraint rod to increase height of headrest.

After apply above change on seat back and head restraint, Test result of IIHS comes to Good.

Test result of step by step improvement show in Fig. 9.

		Improvement				
		Baseline	Improvement 1	Improvement 2	Improvement 3	Improvement 4
Improved items	Seat back suspension	–	No change	No change	Remove up attach hook	Remove up attach hook
	Head rest insert	–	Add plastic cover	Add plastic cover	Add plastic cover	Add plastic cover
	Headrest foam	–	No change	No change	Add foam in front headrest back set 32	Add foam in front headrest back set 22
	Headrest rod	–	No change	Forward 2°, rod height +25 mm	Forward 2°, rod height +25 mm	Forward 2°, rod height +25 mm
Test result (mean value)	Contact time (ms)	73	72	70	68	64
	Neck tension and share	Moderate	Moderate (see picture below)	Moderate (see picture below)	Moderate (see picture below)	Low (see picture below)
	Dynamic rating	Margin	Margin	Acceptable	Acceptable	Good
	Geometric ratings	Good	Good	Good	Good	Good
	IIHS overall rating	Margin	Margin	Acceptable	Acceptable	Good

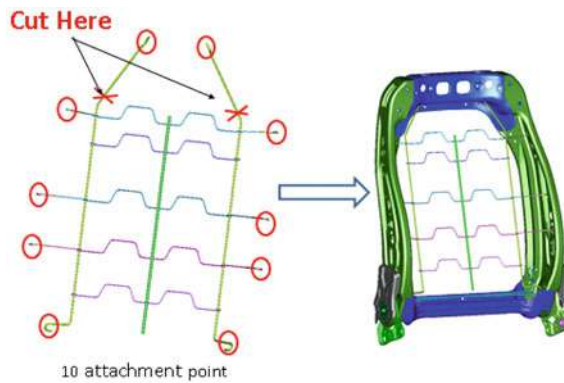


Fig. 8 Proposal of seat back suspension change

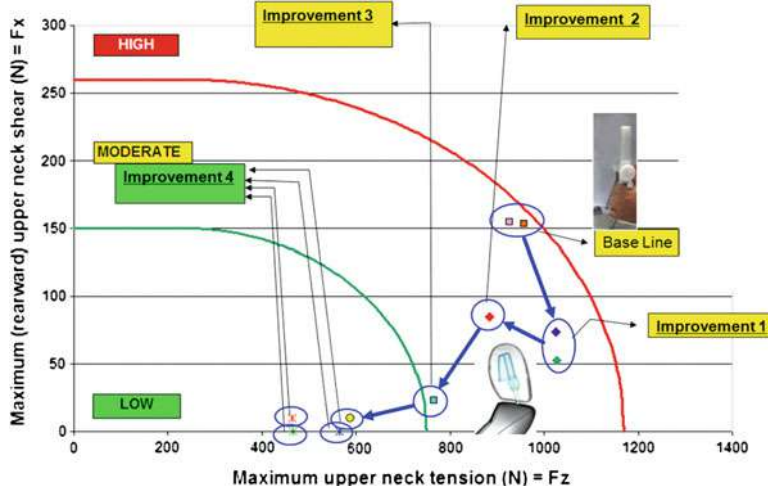


Fig. 9 Test result of step by step improvement

5 Conclusion

By way of adjusting head restraint insert/surface and seat back suspension, the passive headrest can rapidly contact the occupant head in the rear impact, thus reduce the shear load and tension to the neck, and earning highest rating of GOOD in IIHS. An Active headrest isn't an enabler for IIHS good rating. A Passive head restraint can provide enough protection after optimize seat back and head restraint as a matching and complimentary system. That offers the active contribution in lower the cost and the vehicle mass.

References

1. Watanabe Y, Ichikawa H, Kayama O et al (2000) Influence of seat characteristics on occupant motion in low-speed rear impacts. *Accid Anal Prev* 32(3):243–250
2. RCAR-IIWPG Seat/Head Restraint Evaluation Protocol (version 3) (2008) Research Council for Automobile Repairs. Available: <http://www.rcar.org/papers.htm>
3. Xiao Z, Yang J (2007) Simulation on the occupant kinematics response and neck injuries during low speed rear impacts. U461.91 1004-132X(2007)10-1239-05

Optimization Study on Whiplash Injury Reduction in Rear Impact

Yuanbo Wang

Abstract Neck whiplash is a common injury mode in rear impact. Seat design is improved to prevent whiplash injury. DOE study is conducted to determine the sensitivity of geometry and stiffness parameters of seat system based on MADYMO platform. Optimization of design parameters is performed to give the optimized level of seat design parameters to reduce neck whiplash injury.

Keywords Whiplash · DOE · Optimization · Seat · Rear impact

1 Introduction

Rear impact is the most traffic accidental catalog according to accidental statistics in China [1]. Recently, China New Car Assessment Program (CNCAP) has been updated to encourage car makers to provide better protection of occupant neck during rear impact. Neck whiplash is a common injury mode in rear impact. Main counter-measure is taken by most car makers to meet increased safe requirements and reduce the whiplash injury through improved seat design, especially with active headrest. Under these circumstances, study is made on how design parameters of the seat affect whiplash injury and optimize design parameters to minimize neck whiplash.

F2012- F02-027

Y. Wang (✉)
Beijing Automotive Technology Center, Beijing, China

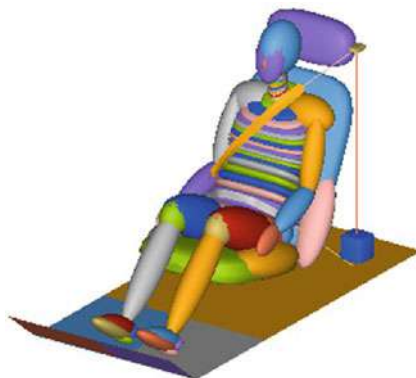


Fig. 1 Sled model

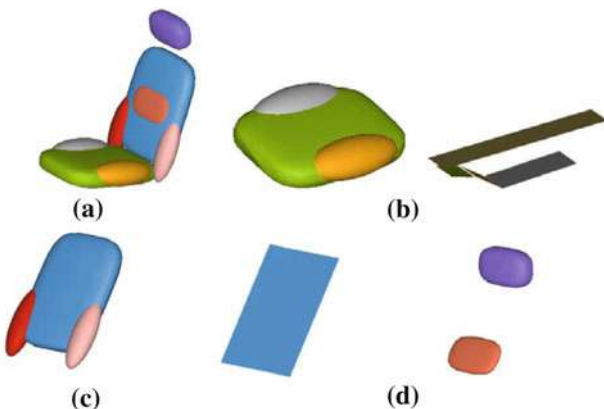


Fig. 2 Details of vehicle seat model (a) Whole seat (b) Seat cushion (c) Seat back (d) Reactive headrest

2 Construction of Madymo Model

It is key factor to have a computationally efficient model in conducting the parametric study. So, this study is done in the multi-body dynamics-based MADYMO platform that simulates dynamic behaviors of physical systems and evaluates injuries sustained by the occupants.

Analysis model is constructed according to sled test for whiplash prevention performance described in NCAP [2], as shown in Fig. 1.

Vehicle seat is main component in the model. For simplified multi-bodies dynamics model, it is important to keep similar the kinematic mechanism and mechanical characteristics between the physical structure and the model. Concept seat in the analysis model uses the combination of multiple ellipsoids, planes, and kinematic joints to describe the physical prototype. Physical seat consists of seat

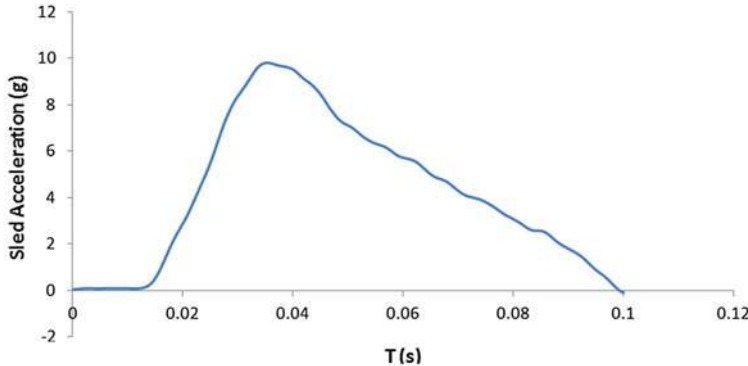


Fig. 3 Sled pulse curve

cushion, seat back and the headrest, which are usually divided to external foam pad and internal metal structure. As shown in Fig. 2, in the model, external foam pads are represented by three connected ellipsoids defining the geometry and their stiffness characteristics derived from the component test of seat foam. Internal metal structures are simplified as connected planes are and their contact characteristics.

Different parts of vehicle seat are joined using kinematics joints according to physical mechanism. The seat back can rotate with respect to the seat cushion through revolute joint. As a main countermeasure to lessen whiplash injury, the reactive headrest is modeled as two ellipsoids rigid connectedly, one representing the headrest and the other the load plate inside the seat back, which move the headrest forward by its rotation relative to the seat back. For each revolute joint, restraint function is defined to give the joint stiffness characteristics.

As described in NCAP whiplash sled test protocol, Biorid II dummy is positioned in the seat and the seat is mounted to the sled with standard pedal referring to vehicle configuration. Crash pulse recorded in sled test given in Fig. 3 is applied to the model. The crash pulse is a triangle shaped pulse with time duration of 100 ms and the resulting change of velocity is 15.65 km/h.

The injury criteria used to assess whiplash injury involves NIC_{max} , Fx_{max} , Fz_{max} and My_{max} of the upper and lower necks. NIC_{max} is the maximum value of $NIC(t)$ during the contact of head with the headrest. It is calculated using the following equations:

$$NIC(t) = 0.2A_x^{rel}(t) + [V_x^{rel}(t)]^2 \quad (1)$$

$$NIC_{max}(t) = Max[NIC(t)] \text{ through } T - HRC_{(end)} \quad (2)$$

where $A_x^{rel}(t)$ is defined as the relative acceleration of the occipital joint to the T1, $A_x^{rel}(t) = A_x^{T1}(t) - A_x^{Head}(t)$, where $A_x^{T1}(t) = \frac{A_x^{T1Left}(t) + A_x^{T1Right}(t)}{2}$ and $A_x^{T1Left}(t)$,



Fig. 4 Animation of whiplash sled test **(a)** $T = 0$ ms **(b)** $T = 60$ ms **(c)** $T = 100$ ms **(d)** $T = 140$ ms **(e)** $T = 160$ ms

$A_x^{T1Right}(t)$ and $A_x^{Head}(t)$ are directly measured by the accelerometers positioned in the occipital joint and the T1. $V_x^{rel}(t)$ is integrated from $A_x^{rel}(t)$, as followed.

$$V_x^{rel}(t) = \int_0^t A_x^{rel}(\tau) d\tau \quad (3)$$

Fx_{max} , Fz_{max} and My_{max} is the maximum value of shear force $Fx(t)$, tension force $Fz(t)$ and the flexion/extension bending moment $My(t)$, respectively. They are obtained from the load cell position at the upper and lower neck.

$$Fx_{max} = \text{Max}|Fx(t)| \text{ through } T - HRC_{(end)} \quad (4)$$

$$Fz_{max} = \text{Max}|Fz(t)| \text{ through } T - HRC_{(end)} \quad (5)$$

$$My_{max} = \text{Max}|My(t)| \text{ through } T - HRC_{(end)} \quad (6)$$

3 Basline Result

Baseline result of whiplash sled test is summarized. Figure 4 is the animation and shows the kinematics of the Biorid II dummy during sled test. The torso firstly contacted and loaded the seat back before the head contacted the headrest. The seat back was rotated rearward by the torso loading with the headrest moving rearward.

Neck Injury Criteria (*NIC*) is the main injury index to assess neck injury and calculated from the accelerometers mounted to the neck, as shown in Fig. 5. Seen from the curve, *NIC* got its maximum value at 109 ms during contact phase. At that time, the head has a large relative motion to the torso. Other injury values including neck forces and moments are listed in Table 1.

4 Doe Analysis and Optimization

Design Of Experiment (DOE) analysis is conducted to determine how seat design parameters affect whiplash injury during rear impact. Design variables are chosen as listed in Table 2, which involves geometry and stiffness variables of the seat

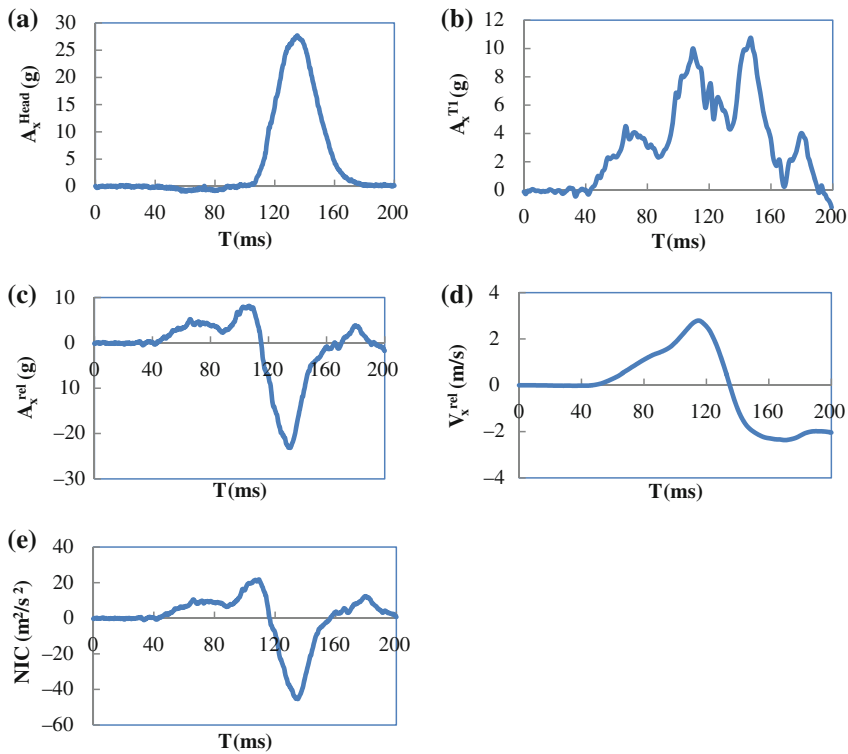


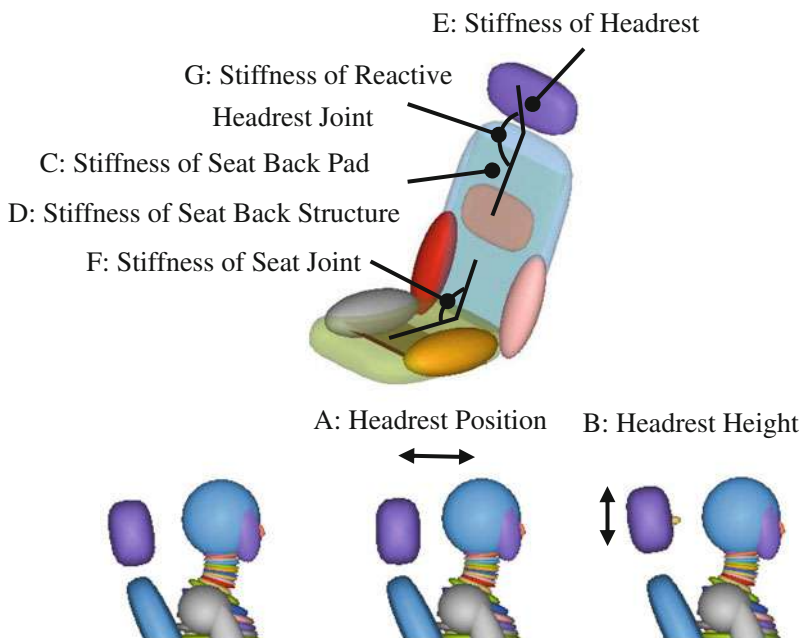
Fig. 5 Baseline result of NIC (a) A_x^{Head} Curve (b) A_x^{TI} Curve (c) A_x^{rel} Curve (d) V_x^{rel} Curve (e) NIC curve

Table 1 Summary of baseline results for whiplash sled test

Injury Index		Baseline
Neck Injury Criteria	$NIC[\text{m}^2/\text{s}^2]$	21.66
Neck Bending Moment	Upper $F_x[\text{N}]$	Shear 147.83
	Upper $F_z[\text{N}]$	Tension 649.57
	Upper $M_y[\text{Nm}]$	Extension 23.37
		Flexion -5.01
	Lower $F_x[\text{N}]$	Shear 469.84
	Lower $F_z[\text{N}]$	Tension 293.11
	Lower $M_y[\text{Nm}]$	Extension 1.44
		Flexion -14.81

Table 2 Summary of design variables for whiplash test

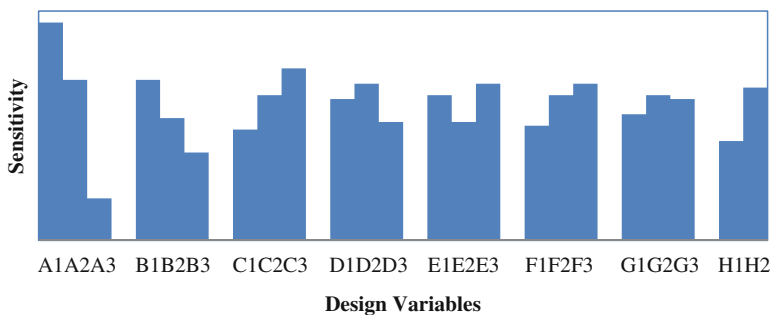
Design variables	Variable levels		
	Low	Middle	High
Geometry variables	A headrest position	A1	A2
	B headrest height	B1	B2
Stiffness variables	C stiffness of seat back pad	C1	C2
	D stiffness of seat back structure	D1	D2
Reactive headrest	E stiffness of headrest	E1	E2
	F stiffness of seat joint	F1	F2
Reactive headrest	G stiffness of headrest joint	G1	G2
	H contact with load plate	H1: No	H2: Yes

**Fig. 6** Seat design variables

and headrest. Since reactive headrest is applied widely to seat system to improve whiplash injury, its influence is also investigated. It is described by design variable H defined as switch time of contact of the torso with load plate of reactive headrest. Switch time means when contact calculation begins to start has two discrete values 0 or 1. Considering end time of simulation is 0.2 s, the value of 0 s means reactive headrest is taken into account for current seat design, while set to 1 s means no reactive headrest. Explanation of design variables are given in Fig. 6.

Table 3 Orthogonal matrix for DOE analysis

Run	A	B	C	D	E	F	G	H
1	1	1	1	1	1	1	1	1
2	1	2	2	2	2	2	2	1
3	1	3	3	3	3	3	3	1
4	2	1	2	2	2	3	3	1
5	2	2	3	3	3	1	1	1
6	2	3	1	1	1	2	2	1
7	3	1	1	1	3	2	3	1
8	3	2	2	2	1	3	1	1
9	3	3	3	3	2	1	2	1
10	1	1	3	3	2	2	1	2
11	1	2	1	1	3	3	2	2
12	1	3	2	2	1	1	3	2
13	2	1	3	3	1	3	2	2
14	2	2	1	1	2	1	3	2
15	2	3	2	2	3	2	1	2
16	3	1	2	2	3	1	2	2
17	3	2	3	3	1	2	3	2
18	3	3	1	1	2	3	1	2

**Fig. 7** Sensitivity of design variables for *NIC*

An L18 Taguchi-style DOE [3] with eight factors is used to analyze the sensitivity of design variables and optimize the seat design to minimize neck injuries. L18 orthogonal matrix is given in Table 3.

As a result, the sensitivity of design variables to *NIC* was obtained in Fig. 7. According to the figure, the geometry of the headrest has the most effective to *NIC* injury index. In fact, seen from formula 2, it is the key to minimize the relative movement of the head to the torso in order to reduce the *NIC* value. So, the head acceleration should be raised faster and the torso be delayed to keep the head and the torso move in harmony. The stiffer and closer headrest can increase the head acceleration faster. And, the softer seat back makes the dummy intrude into the seat back deeper resulting in delayed T1 acceleration. With equipped with reactive load plate, the headrest can be pushed closer to raise the head faster.

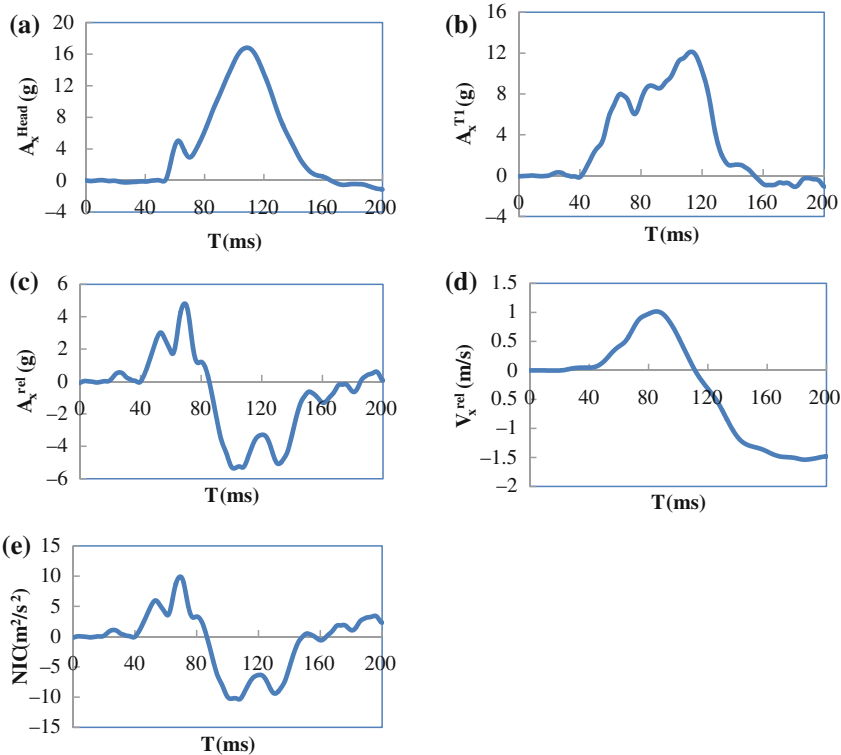


Fig. 8 Optimized result of *NIC* (a) A_x^{Head} Curve (b) A_x^{Tl} Curve (c) A_x^{rel} Curve (d) V_x^{rel} Curve (e) NIC curve

Table 4 Summary of baseline result for whiplash sled test

Injury index		Baseline	Optimization	Change Ratio (%)
Neck injury criteria	$NIC[m^2/s^2]$	21.66	9.84	-54.6
Neck bending moment	Upper $Fx[N]$	Shear	147.83	28.68
	Upper $Fz[N]$	Tension	649.57	118.27
	Upper $My[Nm]$	Extension	23.37	5.46
		Flexion	-5.01	-6.0
	Lower $Fx[N]$	Shear	469.84	97.2
	Lower $Fz[N]$	Tension	293.11	37.67
	Lower $My[Nm]$	Extension	1.44	1.41
		Flexion	-14.81	-4.14

The optimized *NIC* result is shown in Fig. 8 and Table 4. Seen from Table 4, *NIC* is reduced from 21.66 to 9.84, decreased by 54.6 %. Other neck forces and

Table 5 Summary of design variables for whiplash test

Design Variables		Optimized level
Geometry variables	A	A1
	B	B3
Stiffness variables	C	C1
	D	D2
Reactive headrest	E	E3
	F	F1
	G	G1
	H	H2

moments are also summarized in Table 4, which have decreased to some extent. Optimized levels of design variables are given in Table 5.

5 Conclusions

DOE and optimization case study of seat system with reactive headrest is performed to obtain a best protection for whiplash injury during rear impact using design variables chosen. And, the sensitivity of each design variable for the *NIC* injury index is analyzed. It is concluded from the study that

1. NIC is resulted from the relative movement of the head to the torso. The early restraint to the head and the delayed constraint of the torso can reduce the NIC.
2. Judged from DOE result, the headrest geometry and seatback stiffness have the most effect to the NIC.
3. The reactive mechanism helps the headrest move faster and closer to the head which is beneficial to lower NIC.

This study is CAE-based concept analysis and provides optimized seat parameters to reduce the whiplash injury. Further study needs to be carried out considering actual seat structural design and physical prototype validation.

References

1. Traffic Management Bureau. Ministry of Public Security. Road traffic accident statistics compiled of PRC. Beijing: Traffic Management Bureau, Ministry of Public Security, 1996–2009
2. China Automotive Technology and Research Center (2011) C-NCAP Management Regulation. China Automotive Technology and Research Center
3. Chen K (2005) Design and analysis of experiment. Tsinghua University, Beijing

The Safety of Body Structure and Occupant Protection Research of Medium Bus Under Three Kinds of Frontal Impact Forms

Zhaokai Li, Yuan Xiao, Wenyan Zhu and Hanxue Zhao

Abstract This paper belongs to the technical field of bus passive safety. The frequent occurrence of frontal collision causes the serious destroyed buses and heavy casualties for this vehicle have great load and various occupants. So far, there are few research about the collision forms according to the event, and the safety of medium buses are always be neglected. Therefore, it is necessary to discuss these problems. Taking a medium bus as the object of study, we built the finite element model accurately and used large deformation finite element analysis method and explicit dynamic analysis software LS-DYNA to simulate impact under the three conditions of 100 % overlap rate frontal impact, 40 % overlap rate offset impact and the 30° angular impact, and study on the vehicle deformation, energy absorption characteristic of acceleration and their changing regularity. After analysing some indexes as head acceleration, chest compression and pelvic acceleration, conclusion go as following: the second collision is vital to passenger's life safety, the two point seat belt is effective to release the impact from the large acceleration and the space between the seats is also quite important for passenger's protection.

Keywords Medium bus · Frontal impact · Deformation and energy absorption · Dummy injury index · Seat belt

F2012-F02-038

Z. Li (✉) · Y. Xiao · H. Zhao
School of Automobile, Chang'an University, Xian, China

Y. Xiao
Xi'an Public Transport Corporation, Xian, China

W. Zhu
Inner Mongolia Scientific and Technical University, Inner Mongolia, China

1 Introduction

In highway passenger transportation and city communications, medium bus as a major one of the vehicles hold market share far outweigh the large-scale passenger car. According to concerning material introduction, front impact and inclined side collision accounted for 40–60 % of all collision in the passenger car collision accident. Due to the complex operation condition, there are many collision accidents trapped around this type of vehicle. Although its busload is less than large-scale passenger car, the result is also very serious when the accident happened. The front impact forms are varied. But no matter which kind of form happened, there will be a certain extent damage to driver or passengers. This paper use explicit nonlinear finite element software LS-DYNA to simulate the medium bus collide with rigid barrier under three conditions as 100 % overlap rate frontal impact, 40 % overlap offset impact and the 30° angular impact, in order to study body structure safety of this medium bus and driver and passenger's injury.

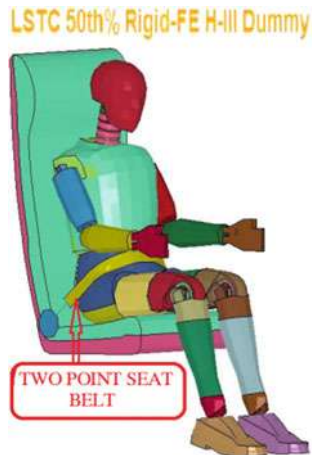
2 Simulation Model Established

2.1 *The Finite Element Model of Vehicle*

According to a CAD drawing of the medium bus, the three-dimensional solid model is established in CATIA [1], and then the model is turned into STP format for importing into HYPERMESH to finish mesh, material defined and other pre-treatment. The body frame use shell element [2, 3]. The frontal structure is the mainly deformation area in frontal impact, so it has a larger mesh density and the average size is 10 mm. The frame and skin select piecewise linear plastic material. The engine choose solid element and bilinear plastic kinematic material. Passenger and luggage use mass element to simulate. The model has 586,782 nodes and 588,297 elements which include 563,083 shell elements, 17,702 solid and 44 lumped mass elements. The first choice of connection is conode way, and the way of spotweld is also used between some nodes which are difficult to use former method.

2.2 *Crash Test Dummies Imported*

Dummy is a type of important tools in vehicle crash test. The regulations such as C-NCAP (China-New Car Assessment Program), CMVDR 294 (design regulation with regard to the protection of the occupants in the event of frontal collision) and GB 11551-2003 (The protection of the occupant in the event of a frontal collision for passenger car) are all use the United States 50 % male adult type Hybrid III

Fig. 1 Hybrid III dummy

dummy as test dummy. And the simulations of this paper take the same kind of dummy as well which is shown in Fig. 1

Most of medium-sized passenger cars are flat head type structure. The driver always encounter strong impact in the event of frontal collision, in addition, the large deformation of floor frame and vehicle acceleration can easily cause passenger's second collision. So adding the driver and passenger dummy to simulate injuries and motion is quite necessary.

The driver seat, both the left and right side of central of bus are location choices for dummy. In the occupant restraint selection, the driver uses the three-point safety belt. The dummy at right side of central bus uses two-point seat belt, while the left dummy with no belt for contradistinction. What should be noted are the front of the left dummy do not lay anything like seat or armrest and the seat space is strictly accordance with the standards. The bus with dummies is shown in Fig. 2.

2.3 Parameter Setting

2.3.1 Initial Conditions Setting

The initial collision velocity is 50 km/h (13.889 mm/ms), adding gravitational acceleration as 0.0098 mm/ms². The contact method of surface-to-surface is used for the vehicle and rigid wall, the vehicle and ground, seat belts and the dummy while the automatic single way is used for the vehicle itself. The six degrees of freedom of rigid wall are restricted.

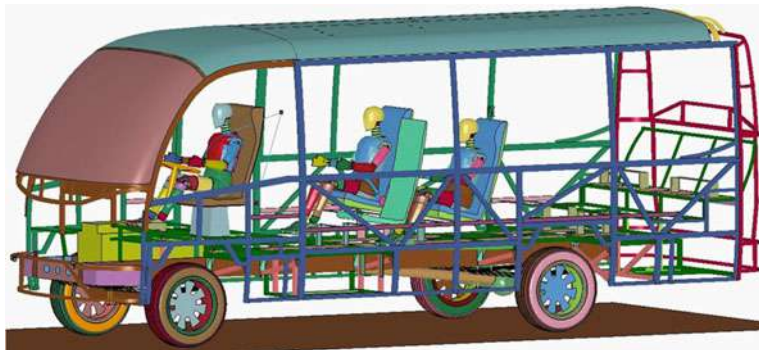


Fig. 2 Relative position of dummy and vehicle

2.3.2 Solving Parameter Setting

The parameters as element algorithm, solving time, time step, the hourglass control, quality zoom and output control are set in LS-PREPOST. Then the K files generated which can be submitted to LS-DYNA for solution.

2.4 Collision Forms Selection

These simulation are about 100 % overlap rate frontal impact, 40 % overlap offset impact and the 30° angular impact, which are shown in Fig. 3. The purpose of these forms selection is to make contrast and complete study the safety of the bus body structure and passenger's injuries.

3 Result Analysis

Due to the large initial kinetic energy, the main injury are driving area's deformation and compression, huge acceleration and the second collision. But the vehicle absorption, the bus acceleration and occupant injury indicator values are varied In different form of collision.

3.1 Analysis of Energy

Energy conservation is an important indicator to certificate the simulation is reasonable. Figure 4 shows that, in the collision process kinetic energy mainly turned into internal energy and the hourglass can maintain in tiny value.

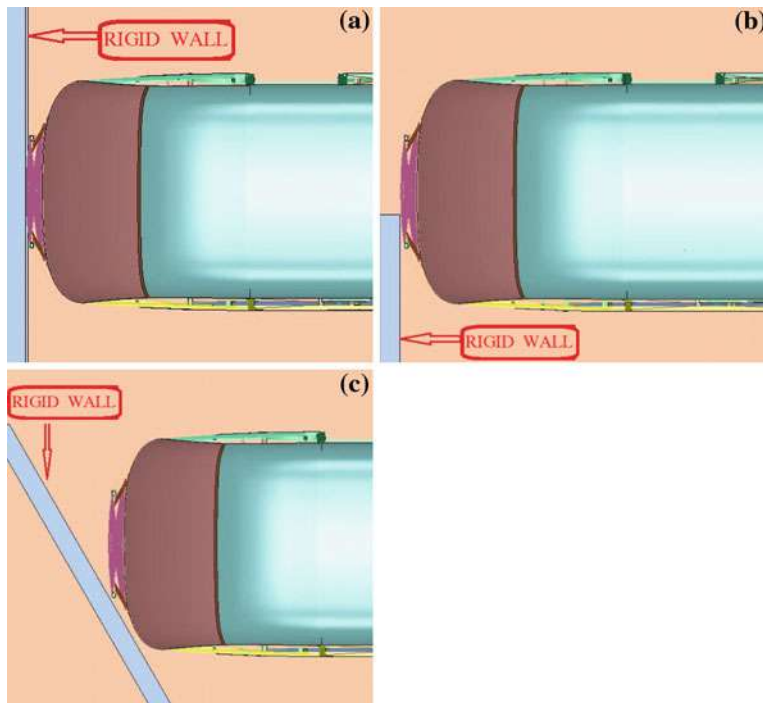


Fig. 3 Three kinds of collision forms **a** 100 % overlap rate frontal impact **b** 40 % overlap rate offset impact **c** 30° angular impact

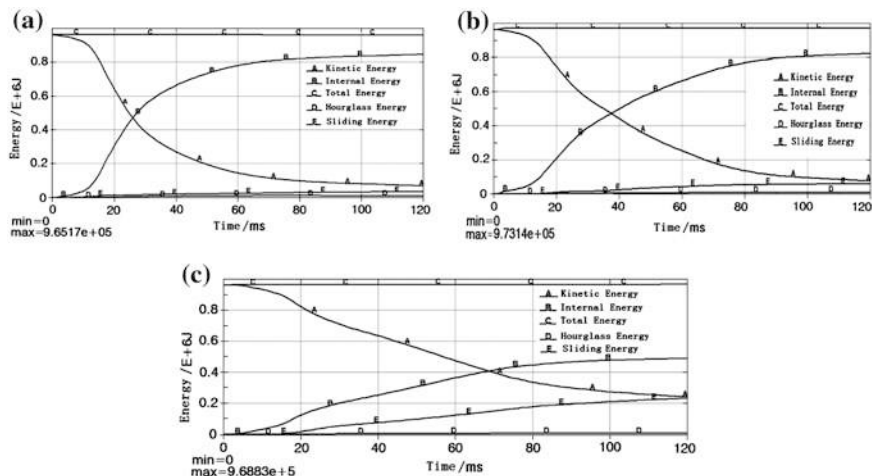


Fig. 4 The energy balance curve **a** 100 % overlap rate frontal impact **b** 40 % overlap rate offset impact **c** 30° angular impact

There was a significant increase of sliding energy between 40 % overlap rate offset crash and 100 % overlap rate frontal Impact, but it has a sharp increase in 30° angular collision. In addition, the body movement (see Fig. 6) shows that, it has a completely deformation fold up in 100 % frontal impact, while it has certain interface slippage in 40 % offset crash, and in 30° angular collision, after bus body contact with rigid wall, it has deformation on the one hand, bus body has a velocity component along the inclined plane, it appears a larger sliding displacement on the other hand for the wall is a cant and part of the kinetic energy turn into sliding energy. In Fig. 4, the point of intersection between kinetic energy curve and internal energy curve retrace in turn in the three forms of the collision, illustrate that the rate of Kinetic energy turned into internal energy was gradually slow, and in 100 % frontal Impact, the kinetic energy decreases soon with the internal energy increases quickly (Fig. 4a). Kinetic energy decreases slowed down with internal energy increases in a lower rate than before (Fig. 4b), Kinetic energy decreases and internal energy increases more gently (Fig. 4c), This situation is connected with that the kinetic energy converted to internal energy and sliding energy at the same time.

3.2 Analysis of Energy Absorption of Vehicle

Under the impact of the huge energy, the vehicle will deform to absorb energy. Because of the difference in contact location, the deformation characteristics is varied, and the absorption degree of frame rail, front wall frame, under frame, left and right side frame, roof frame is different. Figure 5 shows each components absorption curve under these three kinds of collision forms.

In Fig. 5a, frame rail is a main energy absorption component, energy absorption of front wall frame and under frame is approximative equal, and about half of frame rail energy absorption. Energy absorption of left side frame and right side skeleton is nearly equal, both of which have a low value. Figure 5b shows that, front wall frame and frame rail are the main energy absorption, and the front wall frame absorption is slightly smaller than the frame rail, under frame absorption at the center level of absorbing, Left around followed but obviously higher than right side. Figure 5c shows that, front wall frame absorption is the biggest, followed by under frame, energy absorption of frame rail and Left side skeleton is near, all of them less than under frame, the smallest is Right side frame. In these three collision forms, In contrast to other components, roof panel frame absorption is lower.

Table 1 lists the absorption proportions of each components and other energy index, this table shows that, skin has a higher absorption percentage, others such as rear wall frame, seat installation board and dummy all involved in the absorption. In 30° angular collision, the total absorption is 490 kJ which is less than the total absorption in 100 % frontal impact (848 kJ) and 40 % offset crash(825 kJ), at the end of collision, kinetic energy and sliding energy values of 30° angular collision is higher than two kinds of collision form above.

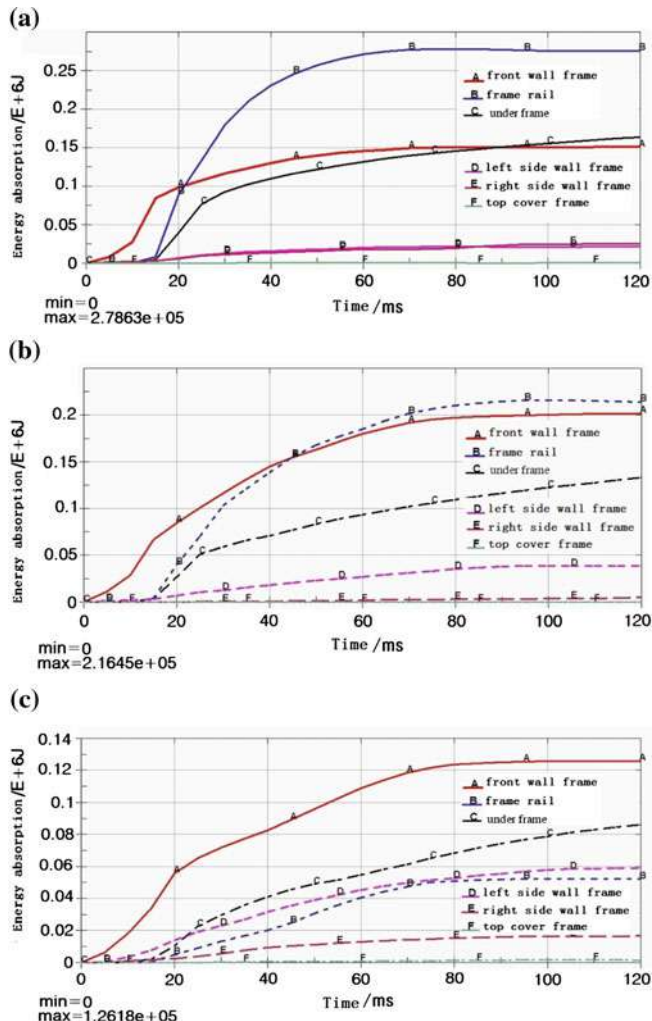


Fig. 5 The energy absorption characteristic curve of the various components **a** 100 % overlap rate frontal impact **b** 40 % overlap rate offset impact **c** 30° angular impact

3.3 The Deformation of Vehicle and the Analysis of Acceleration

With great gross vehicle weight, the bus has very large kinetic energy. When the frontal collision occurs, front wall frame, under frame and frame rail as the main energy-absorbers which absorb a lot of kinetic energy. In Fig. 6a, the deformation in frontal collision mainly focus on front wall frame that deformed seriously made the driver seat flip forward. Although the driver have three-point safety belts,

Table 1 The absorb energy proportions of all the parts and other energy index of three collision forms

Collision form	Front wall frame (%)	Frame rail (%)	Under frame (%)	Left side frame (%)	Right side frame (%)	Skin (%)	Else (%)	Total absorbs energy (kJ)	120 ms kinetic energy (kJ)	120 ms slide energy (kJ)
100 % front impact	17.8	32.9	19.3	2.5	3	1.3	23.5	848	69	35
40 % offset impact	24.5	26.2	16.2	4.7	1.9	4.7	21.8	825	77	61
30° angular impact	25.8	11	17.6	12.1	3.4	3.0	27.1	490	242	231

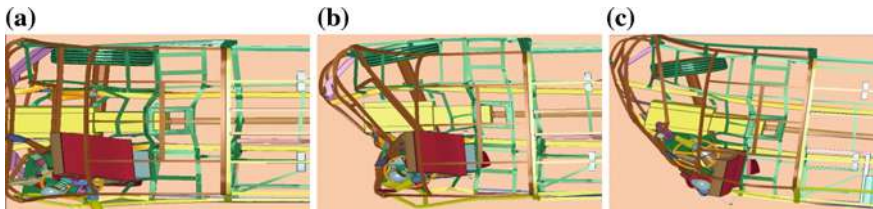
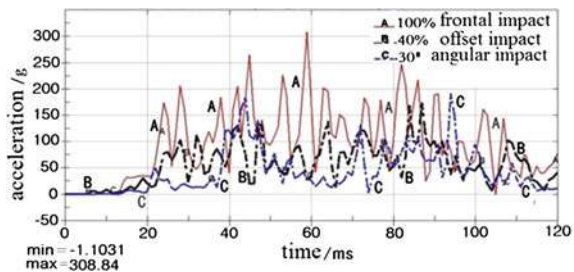


Fig. 6 The deformation of frontal structure under three collision forms **a** 100 % overlap rate frontal impact **b** 40 % overlap rate offset impact **c** 30° angular impact

Fig. 7 The acceleration curve of vehicle under three collision forms



extrusion damage between drivers and steering wheel may happen. In Fig. 6b, collision contact area is less than 100 % frontal collision, but absorption parts is concentrative, the deformation is more obvious; front wall frame is distortion to the left side which bend serious; corresponding to Fig. 5b, the main reduce energy of frame rail absorption translate to the increase of left skeleton energy absorption. As shown in Fig. 6c, the difference of 30° angular collision and two former types, the deforming of front wall frame is similar to slope, The deformation of driver's side is the most serious, and folding up distance is largest; another side space is nearly intact, The body sliding along the wall, which make the driver hurled out of window; combine with absorption curve, the energy of both front wall frame and frame rail is decreasing, but left-right frame energy absorption is increasing, until left side increased amount to under frame, it means left frame is main factor of energy absorption in 30° angular collision.

3.4 The Analysis of Acceleration

From the Fig. 7, the peak acceleration of 100 % frontal impact is occur frequently and the average value is highest in whole process; while 40 % offset collision acceleration is lower than the former, sometimes even about a half; Greater peak difference between the of 30° angular collision and 40 % Offset Crash is more. In the 50–70 ms of interval, 30° angular collision have the lowest value.

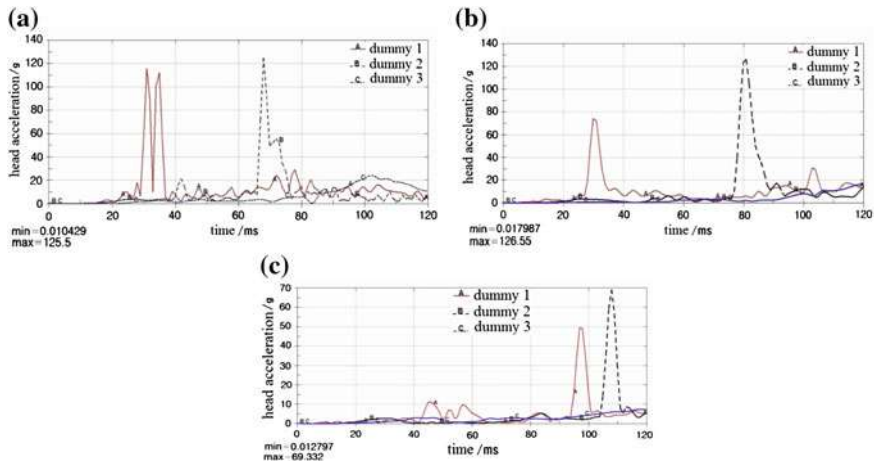


Fig. 8 Head acceleration curve **a** 100 % overlap rate frontal impact **b** 40 % overlap rate offset impact **c** 30°angular impact

In 100 % frontal impact, there have the largest contact area, and the average contact area energy is lowest, vehicle longitudinal stiffness is greater, so deformation is slighter. In 30° angular collision, the slide energy and remaining kinetic energy are larger (see Fig. 4c), which stand impact energy less than 40 % offset collision, but the deformation is still larger than the latter, the reason is that the longitudinal stiffness is even more less. Therefore, stiffness is quite important influence factor to the vehicle acceleration.

3.5 Indexes of Dummy Injury

In order to study the damage to the passenger in frontal collision, three dummies are placed at the bus model. The dummy 1 in the driver's position have three-point seat belt, corresponding to the A curve in Figs. 8, 9, 10; the dummy 2 is located in the left side of the central bus, this dummy is not wearing a seatbelt and there is a seat in the front, which corresponds to the B curve in Figs. 8, 9, 10. With two point seat belt, dummy 3 is on the right side of the Central part and a large space ahead of him, corresponding to C curve in Figs. 8, 9, 10. Table 2 lists head acceleration, chest compression, pelvic acceleration peak values and times of three dummies under the three forms of the collision.

3.5.1 Head Acceleration

For a particular collision form, the dummy 1's head acceleration is higher than dummy 2 and dummy 3, but the peak head acceleration of dummy 2 is higher than

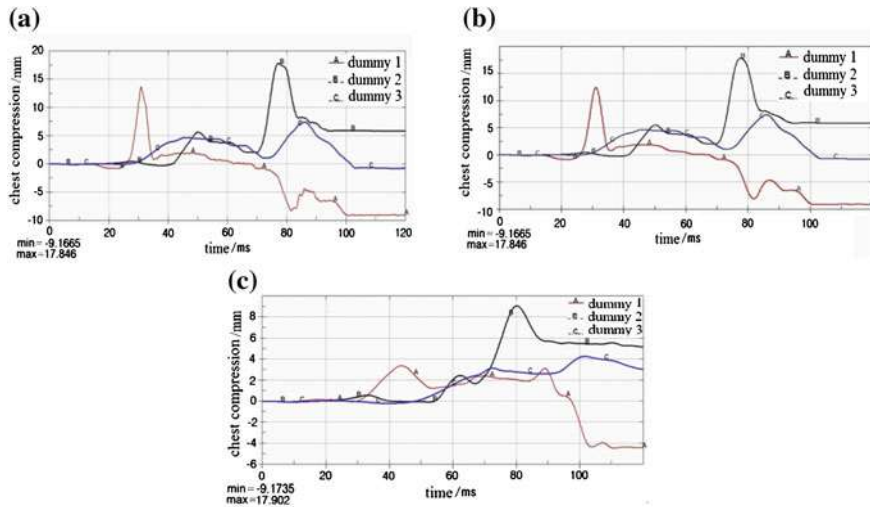


Fig. 9 Chest compression curve **a** 100 % overlap rate frontal impact **b** 40 % overlap rate offset impact **c** 30° angular impact

dummy 1. In the whole process of collision, dummy 1 is in front of the bus and near the front wall, so dummy 1 has a bigger head acceleration; the whole process acceleration of dummy 2 and dummy 3 which are in the central of vehicle, is keep a low level because they are far from the collision area. However, dummy 2 which is not wearing a seatbelt fell from seat for the force of inertia and “second collision” with the front seat, in result of a huge peak acceleration in his head; And dummy 3, which is different from dummy 2, wear a two-point seat belt and no decorate seats and armrest ahead, for the restrictions and free space, he did not happen “second collision”, and the acceleration level is low, also he did not appear particularly large peak acceleration in the whole course time.

3.5.2 Chest Compression

By Fig. 9, the amount of compression on the dummy 1 is largest, dummy 2 is second, dummy 3 is minimum in the form of three kinds of collision. The reason is that dummy 1 wear three-point seat belt and chest is bounded, so he did not crash with other objects; the 2nd dummy is not bounded by the seatbelt and “flying” out by huge inertia, his head first hit the front seat and appeared back, and then his chest hit the front to occur “the secondary impact”. The dummy 3 move forward under the effect of inertia, but he has little effect on the chest due to the constraints of the two-point seat belts and along with the “bend over” action.

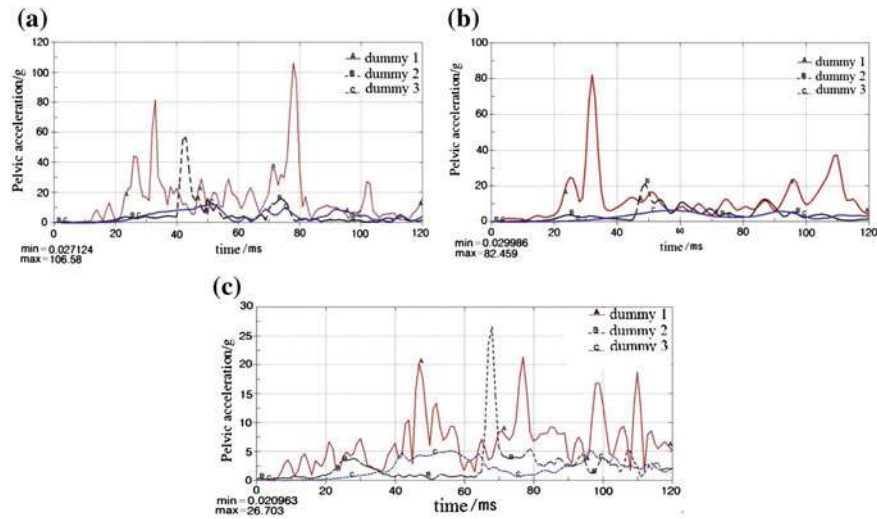


Fig. 10 Pelvic acceleration curve **a** 100 % overlap rate frontal impact **b** 40 % overlap rate offset impact **c** 30° angular impact

3.5.3 Pelvic Acceleration

Figure 10 shows under 100 % frontal impact and 40 % offset collision conditions, the dummy 1 pelvis acceleration mean and peak are greater than dummy 2 and dummy 3; 30° angular collision, dummy 2 once appeared the largest peak pelvis acceleration and dummy 1 had the highest average during the full course. Moreover, all the dummies' value are less than 30 g. In the three kinds of collisions, dummy 2 is higher than dummy 3 which peak value is between 5 and 10 g; In 100 % front collision, peak value of dummy 2 is 60 g. In the 40 % offset collision and 30° angular collisions, peak of dummy 2 is maintained at about 20 g. In addition, the combination of the collision process shows that in 100 % front collision, and 40 % offset collision, dummy 1 has several peaks who suffered steering wheel extrusion; In 30° angular collisions, dummy 1 “thrown” the opposite direction of head of car glide along under the effect of inertia when the front wall slide along the slant rigid wall, (see Fig. 6c), even though it avoided the extrusion of the steering wheel, it will suffer other damages; the pelvis of dummy 2 is under enormous deceleration with moving forward, but because of dummy 3 wear two-point seat belts and pelvis just be bound by the seat belt, tension will be reduced and buffer deceleration.

In Figs. 8, 9, 10, the same location dummy's head acceleration, chest compression and pelvic acceleration showed a significantly decreasing trend under the three forms of collisions (100, 40 % and 30° in turn), that means the passenger most probably suffered the impact damage in 100 % frontal collision, and 40 % offset collision followed it, 30° angular collision is minimum. During occupant injury assessment, the indicators of the former is the most demanding, the latter is loose at most and 40 % offset collision between 100 % frontal and 30° angular collision.

Table 2 The Peak value and time of dummies in different positions under three kinds of collision forms

Collision form	Dummy index	Dummy 1		Dummy 2		Dummy 3	
		Peak value	Time (ms)	Peak value	Time (ms)	Peak value	Time (ms)
100 % frontal impact	Head acceleration	115 g	31	125 g	68	24 g	103
	Chest compression	14 mm	31	18 mm	66	7 mm	85
	Pelvic acceleration	105 g	78	58 g	44	12 g	52
40 % offset impact	Head acceleration	75 g	30	126 g	82	16 g	120
	Chest compression	12 mm	32	18 mm	77	7 mm	87
	Pelvic acceleration	82 g	33	21 g	48	7 g	57
30° angular impact	Head acceleration	49 g	97	69 g	108	7 g	120
	Chest compression	5 mm	45	9 mm	80	4 mm	102
	Pelvic acceleration	21 g	77/47	27 g	69	5 g	76

4 Epilogue

Body structure's stiffness determine deformation and energy absorption, and influence the vehicle and passenger's acceleration. Frame rail in bus has a large stiffness and is the main energy absorption part in 100 % overlap rate frontal impact, while in 40 % offset crash, the main energy absorption assembly are frame rail and front wall. Front wall, under frame and left side skeleton become the main energy absorption assembly together in 30 % angular collision, and frame rail is no longer a main energy absorption part this time. This trend caused collision deformation increase in turn and vehicle acceleration decrease successively in these three collision.

In these three collision forms, all the indexes of the driver are large. Huge collision energy require auxiliary absorbing device or other safety device to reduce the driver injury. Although the passenger area is far away from the collision region and security is much higher than the driver area, the "second collision" between passenger and object inside the bus is the main reason for the injury, and second collision always is vital to passengers. Both the space between the seats and whether the seat belt is effective have an enormous influence on each index. The calculation results also show that the two-point seat belt can effectively avoid the pelvic to stand high acceleration; if the safety belt can restrain dummy movement within the seat space, it can avoid the "second collision".

References

1. Kwasniewski L, Bojanowski C, Siervogel J, Wekezer JW, Cichocki K (2009) Crash and safety assessment program for paratransit buses. *Int J Impact Eng* 36(0734–743X):235–242
2. Fu-lin S, Jing-tao D, Xu-liang X, Zhi-hua S (2010) Research on simulation and improvement of coach frontal crash. *Chin J Highw Transp* 23(1001–7372):113–118
3. Zhengbao L, Yuhong X, Haixia L (2005) The crashworthiness of structure with large displacement and large deformation. National University of Defense Technology Press, Changsha

Part III

Pedestrian Protection

Development of a Parametric Vehicle Front Structure Model for Pedestrian Impact Simulations

Bingbing Nie, Jun Huang, Yong Xia, Qing Zhou, Bing Deng
and Mark Neal

Abstract In this study, a simplified, parametric vehicle front structure was proposed to represent the real vehicle when impacted with full-scale finite element pedestrian human body model (HBM). To capture the real impact responses of human lower limbs, the real vehicle energy-absorbing structures were modeled using distributed beam elements and deformable shell elements to replicate the contact characteristics between vehicle and HBM. An investigation of vehicle front-end profile characteristics in worldwide popular sedan models was conducted to determine the ranges of geometry variables. A local stiffness measurement approach is also proposed. The simplified model is further validated using a detailed sedan model, and the impact responses of HBM in the two simulations correlate quite well with each other. Therefore it can be further used in the DOE study or optimization work in the vehicle front structure design for pedestrian lower limb impact protection.

Keywords Vehicle front structure · Simplified parametric model · Local deformation · Human body model (HBM) · Pedestrian impact

F2012-F03-004

B. Nie (✉) · J. Huang · Y. Xia · Q. Zhou
State Key Laboratory of Automotive Safety and Energy, Department of Automotive
Engineering, Tsinghua University, Beijing, China

B. Deng · M. Neal
General Motors Global Research and Development, Warren, MI, USA

1 Introduction

In car-pedestrian impacts, the lower limbs and head are the most frequently injured body parts [1, 2]. The statistics indicate that 80 % of all pedestrians involved in car-to-pedestrian accidents sustained knee injuries [3]. In regulatory tests, legform impactors such as the TRL and Flex legforms were proposed to evaluate lower limb injuries of pedestrians when laterally impacted with a vehicle [4, 5].

Simplified vehicle front-end models are widely utilized in pedestrian impact analysis, including both FE based models and multi-body models. Due to the high computational efficiency and flexibility of adjusting geometry and stiffness variables, the simplified models could be used in algorithm-based optimization design [6, 7]. Technical flow of parameter analysis for pedestrian lower limb protection has been mentioned in the literature [8–10], including determination of the design variables, Design of Experiments (DOE) study and response surface of the objective function. Therefore a validated parametric vehicle model is an important basis.

Existing simplified models are usually designed for lower legform impactors. These subsystem impactors are usually designed in an over-simplified way to meet the repeatability and reusability requirements. Since the legform impactors do not include the upper body parts, the kinematic responses of the legform impactors are different from those of a full-scale human body [11, 12]. In order to enhance real-life protection of the pedestrian, the finite element (FE) human body model is found to be an effective tool for the study of lower limb injuries. It can provide more realistic kinematic lower limb response and injury characterization. Several studies have documented the development and application of detailed human body models [13–16]. Therefore, a simplified parametric vehicle model for HBM impact is quite important.

The simplified vehicle models in literature usually consist of three parts: bumper, grill and spoiler, which may be too simplified for impact analysis using the HBM. In real-world pedestrian accidents, the vehicle front-end contacts the two lower limbs at different times. Therefore, the deformation near the contact point is much more significant than that at the area far from the contact point. (hereafter named ‘local deformation characteristics’). The grill should also be considered in order to comprehensively reflect the contact characteristics in human body impact with real vehicles.

To capture real impact responses of the human body, it is vital to have accurate local deformation and contact characteristics of the vehicle front structure. With the above considerations, the simplified parametric vehicle model should meet the following requirements:

1. Be flexible to adjust the geometric and stiffness variables to represent different vehicle front end configurations;
2. Be validated against real vehicle front structures to ensure it could accurately predict impact responses of the human body;
3. Have high computational efficiency for DOE and response surface generation.

The goal of this study is to develop a simplified, parametric vehicle front structure, representing the real vehicle when impacted with a full-scale finite element pedestrian human body model (HBM). This parametric vehicle model is validated using a detailed vehicle model, with consideration on the kinematics, injury output, contact forces as well as local deformation of the vehicle. This simplified model can be further used to develop a mathematical tool to optimize the vehicle front structure design for pedestrian lower limb impact protection.

2 Model Setup

2.1 Human Body Model (HBM)

The full-body mid-size pedestrian model (HBM) in this paper was first developed by General Motors (GM) and the University of Virginia (UVA) in 2007 (Fig. 1) [17]. It is a LS-DYNA based finite element model of a 50th percentile pedestrian in a standing position (hereafter referred to as the GM/UVA pedestrian model).

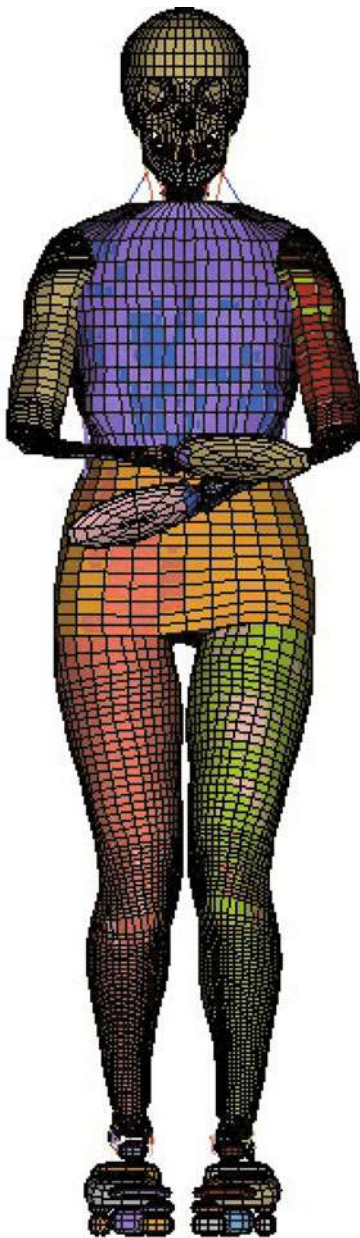
Kinematics of the HBM is validated in the full-scale level using the data from a series of 7 full-scale Post Mortem Human Subjects (PMHS) impact tests conducted in 2004 [18]. The biomechanical fidelity of its lower limbs was validated in component level against component test data from PMHS [19–21]. Therefore it can be used to evaluate the true injuries of human lower limb.

2.2 The Parametric Simplified Vehicle Front-End Model

The parametric vehicle model consists of five parts, representing the front faces of the bonnet leading edge (BLE) (Part 1), upper grill (Part 2), bumper (Part 3), lower grill (Part 4) and spoiler (Part 5), respectively, as shown in Fig. 2. Part 3 and Part 5 are modeled by deformable shell elements to reflect the local deformation of the vehicle in pedestrian-vehicle impact. An array of uniformly distributed beam elements is used to provide the contact stiffness of the bumper and spoiler structures. When impacted with the pedestrian lower limb, such a structure can deform differently at different locations along the length of the structure, and therefore it can accurately predict different contact times of the two lower limbs with the vehicle structure. The stiffness of the beam elements can be adjusted to represent different structural stiffness of the vehicle bumper and spoiler.

The model consists of 5 geometry variables (U_x, U_z, H_3, L_z, L_x) and 7 stiffness variables ($K_1, K_2, K_4, E_3, \sigma_{y3}, E_5, \sigma_{y5}$). For each variable, the number in the subscript indicates the corresponding part number. The five geometry variables define the initial geometry of the model, including the locations and their relative positions, as shown in Fig. 2. Definitions of these 5 geometry variables and 7 stiffness variables are listed in Table 1.

Fig. 1 GM/UVA pedestrian model



Material characteristics of the beam elements behind Part 3 and Part 5 are shown in Fig. 3. The stress-strain curve is divided into 3 phases: the initial slope phase (I), the plateau phase (II) and bottoming out phase (III). A very steep slope, which is artificial, is adopted for the bottoming out phase (III). This definition is also in accordance with the whole crash behaviour of bumper systems, which will

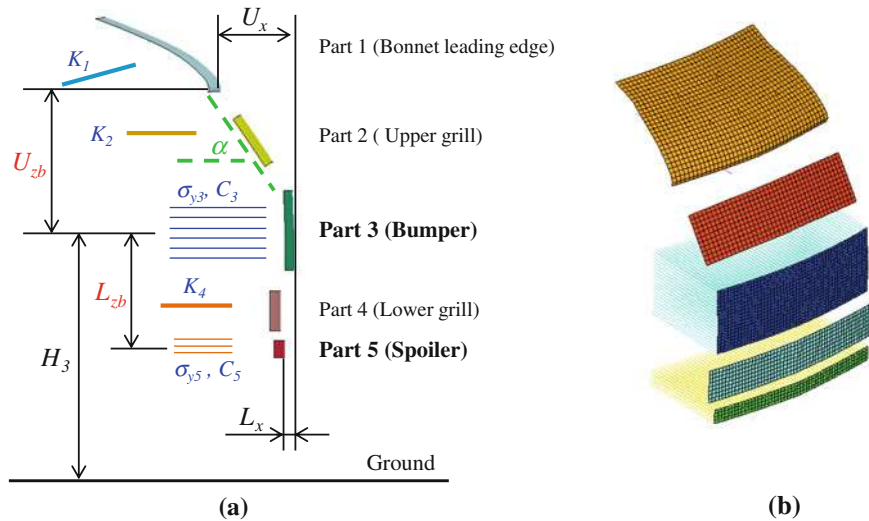


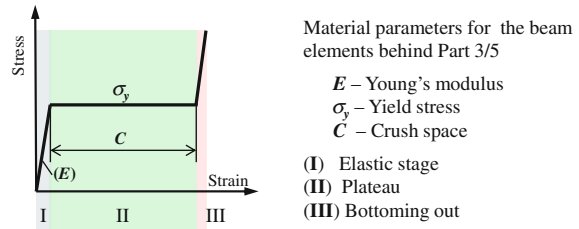
Fig. 2 The simplified parametric vehicle model. **a** Components of the simplified vehicle model. **b** Axonometric drawing

Table 1 Design variables definition of the parametric model

Property	No.	Design variables	Lower bound	Upper bound
Geometry variables	1	U_x X offset of Part 1	60 mm	196 mm
	2	U_z Relative Z offset of Part 1	180 mm	280 mm
	3	H_3 Height of Part 3 center	425 mm	525 mm
	4	L_x X offset of Part 5	0 mm	55 mm
	5	L_z Relative Z offset of Part 5	170 mm	240 mm
Stiffness variables	6	σ_{y3} Yield stress of beam material behind Part 3	0.1 MPa	1.2 MPa
	7	C_3 Crush distance of beam material behind Part 3	20 mm	100 mm
	8	σ_{y5} Yield stress of beam material behind Part 5	0.1 MPa	1.0 MPa
	9	C_5 Crush distance of beam material behind Part 5	10 mm	80 mm
	10	K_1 Scale factor of the beam stiffness behind Part 1	0.5	2
	11	K_2 Scale factor of the beam stiffness behind Part 2	0.5	3
	12	K_4 Scale factor of the beam stiffness behind Part 4	0.5	3

undergo fast and controlled loading [22]. Trial simulations show that the elastic range of the beam material shows almost no influence on the injury parameters, since the structure comes into the plastic stage very soon after impact. Thus for

Fig. 3 Beam material definition for Parts 3 and 5



each of the beams, 2 variables (yield stress σ_y and crush space C) are needed for defining the curve (Fig. 3). 4 variables are needed for the 2 groups of beam elements for the bumper and spoiler respectively.

Part 1, Part 2 and Part 4 do not contribute much to the local deformation during impact. Part 1 only contacts the HBM with the pelvis at later stage; while the stiffness of Part 2/4 is too low to show the local deformation. Therefore their contact surfaces are modeled with rigid shell elements and the stiffness is realized by the deformable beam elements behind the rigid shell elements. Material definition for the beam elements are set to be constant, and the scale factor of the strain–stress curves is taken as independent stiffness design variables, which is shown as K_1 , K_2 , K_4 in Fig. 2a.

For all the 5 geometry variables, bumper height (H_3) is the only one which is measured from the ground level in the Z-direction. It is also one of the most influential variables of the vehicle front-end geometry on knee injury [23]. To provide reasonable vehicle front contours in the DOE sampling process when the geometry variables are changed, two of the geometry variables, U_{zb} and L_{zb} , are set to be the relative dimensions based on bumper height. These two variables also determine the initial position of Part 1 and Part 5.

The initial position of Part 2 is determined by Part 1 and Part 3. Its geometrical center is placed at the midpoint of the connecting line of Part 1 and Part 3. The inclining angle of Part 2 surface (α) is determined by the positions of Part 1 and Part 3, which is shown as α in Fig. 1a. With this dependent variable, the contact surface of the parametric vehicle model is always continuous when the geometric variables are changed. Similarly, the initial position of Part 4 is determined by the relative position of Part 3 and Part 5. All the contact surfaces of the 5 parts deform independently during impact.

2.3 Local Stiffness Measurement

Appropriate ranges and initial values of the stiffness variables need to be determined for the simplified parametric model to better represent the detailed vehicle model. There was a simplified methodology to derive the vehicle bumper stiffness from the acceleration time histories in pedestrian legform impact tests [24]. It is, however, difficult to determine the specific stiffness at the local bumper areas.

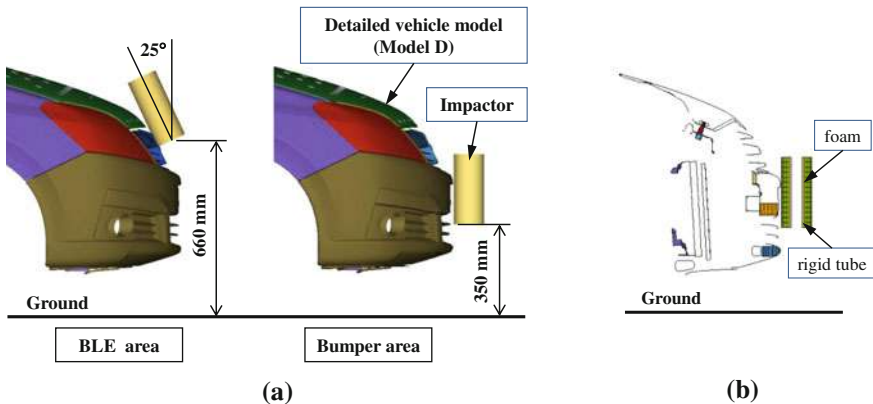


Fig. 4 Measurement of local stiffness on pedestrian lower limb contact areas. **a** Vehicle model I. **b** Vehicle model II

To determine the local stiffness, simulations of impact of certain rigid impactors to the concerned locations on detailed vehicle models were conducted. One detailed real car model is used as an example, as shown in Fig. 4 (hereafter referred to as “Model D”). Model D employed foam structures as energy absorbers in the bumper and spoiler areas. The impactor consists of a rigid tube wrapped by a foam layer, with a height of 280 mm and a mass of 13.4 kg. The initial velocity of the impactor is 11.1 m/s in a direction toward the vehicle, which is the impactor’s only degree of freedom. As an example consider the measurement on the BLE area and the bumper area (in accordance with Part 1 and Part 3 of the simplified model in Fig. 2). For this case the lower edge of the impactor is positioned at 55 and 350 mm from the ground level, respectively (Fig. 4). For the BLE area, the impactor is inclined with an angle of 25 deg to have a more realistic interaction configuration. Node displacements on the vehicle outer surface and contact force were exported to plot the stiffness curve, as shown by the solid lines in Fig. 5.

For the simplified vehicle model, the geometrical variables are set to match the actual dimensions of Model D (hereafter, this specified simplified model is referred to as “Model S”). Correspondingly in Model S, the beam material definition of Part 1 and Part 3 is estimated based on the simplification of the detailed model force-crush behaviors, as shown by the dashed lines in Fig. 5.

For Part 1, the effective plastic strain—stress curve definition for the beam element can be estimated using the following equation:

$$F_1 = \frac{1}{4}\pi D^2 \cdot \sigma_{y1}, C_1 = l \cdot \varepsilon_1 \quad (1)$$

Then K_1 is set as the scaling factor of the effective plastic strain—stress curve

For Part 3, the variable values of yield stress σ_y and crush space C in the beam material definition for Part 3 (Fig. 3) can be estimated similarly.

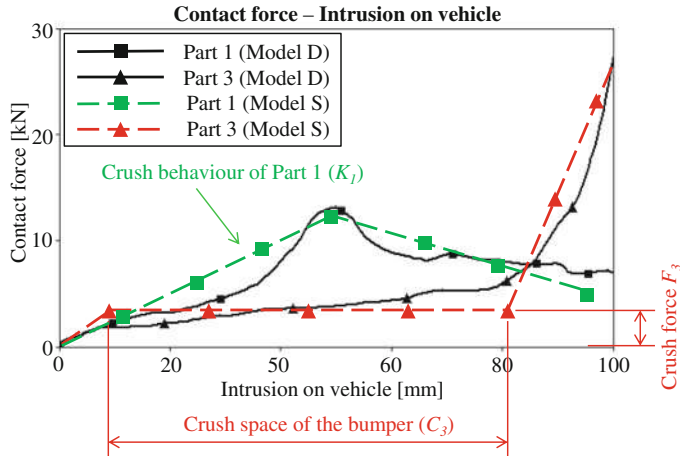


Fig. 5 Force-crush behaviour for Model D and Model S (Part 1/3)

$$F_3 = N \cdot \frac{1}{4} \pi D^2 \cdot \sigma_{y3}, \quad C_3 = l \cdot \varepsilon_3 \quad (2)$$

where N is the number of beam elements that were involved in the impact.

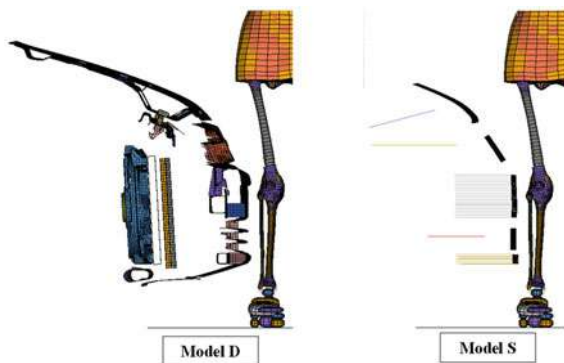
The determination of the initial material definition of Part 2 and Part 4 is similar to that of Part 1 (K_2, K_4); while the determination of beam material of Part 3 is similar to that of Part 5 (σ_{y5}, C_5).

2.4 Determination of the Design Variable Ranges

Using the pre-described 12 variables, the model permits high adjusting flexibility of the structure geometry and stiffness as well as realization of design optimization. The ranges of the geometry variables are determined based on the investigation of vehicle profiles of popular vehicle models produced between 2008 and 2010 (See Appendix). Ranges of the stiffness variables for each part are determined by the previously described approach of measuring the local dynamic stiffness on real vehicle models (See the “Local stiffness measurement” section). The stiffness parameter bounds for simplified vehicle models in previous research [7] were also considered. The upper/lower bounds correspond to the extreme values measured from different vehicle models, and the ranges are slightly widened to cover more vehicle models.

The lower and upper bounds for each of the design variables in the DOE is also shown in Table 1.

Fig. 6 HBM impacts with vehicle models (section view; the muscles on lower limbs are not displayed)



3 Model Validation

To validate the simplified model, impact responses of the HBM impacted with Model D and Model S are compared. In these car-to-pedestrian impact simulations, these vehicle models move into the HBM with an initial velocity of 11.1 m/s, as shown in Fig. 6. The assessed responses in the validation include the human body injury parameters (knee bending angles and ligament elongations of the lower limbs), the contact forces, the lower limb kinematics and local deformations on the vehicle front.

Using the simplified vehicle model, the computation time of HBM-to-vehicle impact simulation is reduced from 5.8 to 1.3 h (6 CPUs on the Massively Parallel Processing server). The reduction in computation time was necessary for response surface generation due to the need for thousands of simulation runs.

Figure 7 shows the comparison of the injury parameters of the lower limbs between the detail and simplified parametric vehicle models. Note that the right leg is the first-struck leg in these simulations. The resultant contact force on HBM (measured on the vehicle side) is compared in Fig. 8a. Figure 8b gives the resultant forces exerted on human body by bonnet leading edge (BLE), bumper and spoiler, which all play significant roles in causing injuries. All the results show good correlations between detailed and simplified parametric vehicle models.

The lower limb kinematics is assessed using five markers on each leg; their locations are shown in Fig. 9a. Comparison of the coordinates for each marker is shown in Fig. 9b. Local deformation on the vehicle parts as well as the strain distribution on the muscles is also validated (Fig. 10). It can be seen that the two models correlate very well with each other.

From the validations results above, it can be seen that the simplified parametric vehicle model can represent a real vehicle model when the design variables are set to match the actual geometry and structural behaviour. With distributed beam elements behind the bumper and spoiler parts, the local deformation and contact characteristics of the vehicle front surface in impact with pedestrians closely

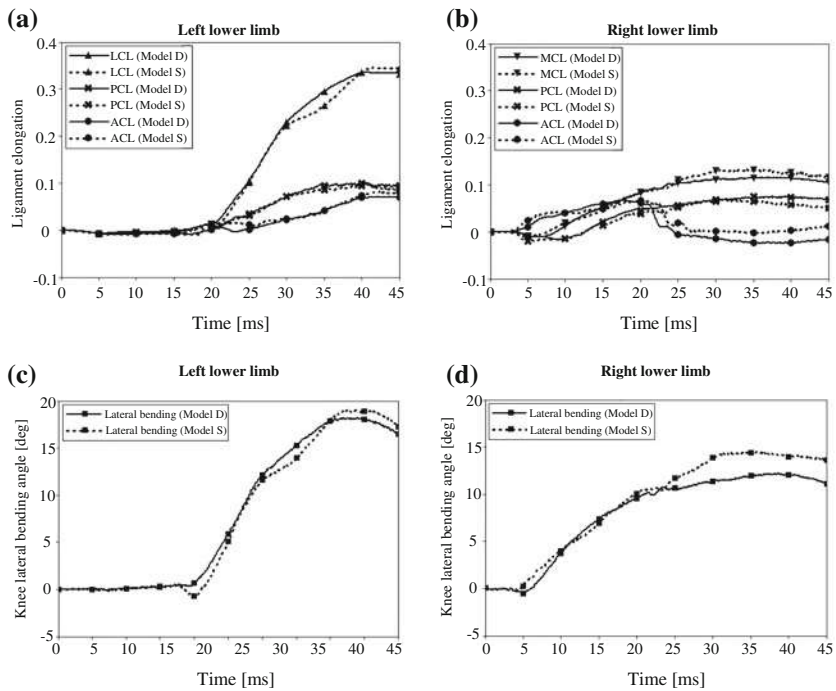


Fig. 7 Validation of HBM injury output. **a** Ligament elongation of left lower limb. **b** Ligament elongation of right lower limb. **c** Knee lateral bending angle of left lower limb. **d** Knee lateral bending angle of right lower limb

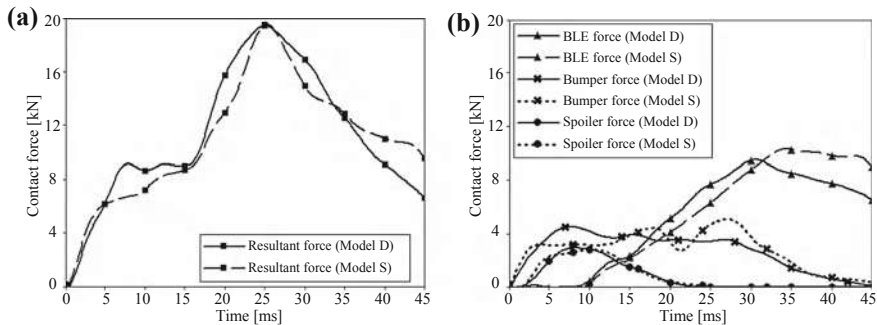


Fig. 8 Validation of contact forces. **a** Resultant force on HBM. **b** Force from BLE/Bumper/Spoiler on right lower limb

match those seen in impact simulations with the detailed model. Injury parameters of the HBM, including the knee bending angle and ligament elongations are similar to those in the detailed vehicle model.

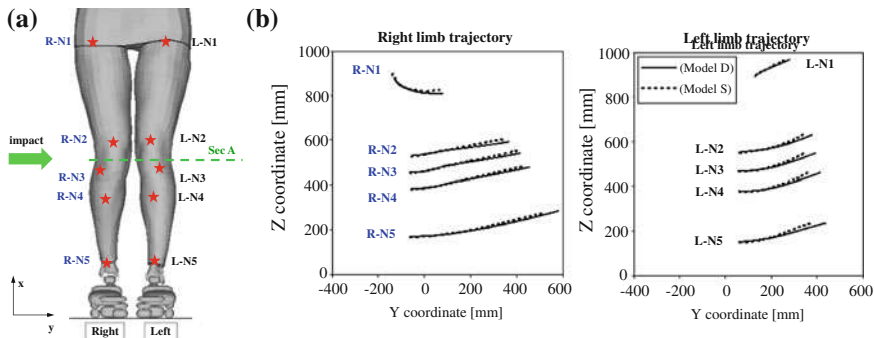


Fig. 9 Kinematics validation. **a** Markers on lower limbs. **b** Comparison of the marker coordinates for Model D and Model S

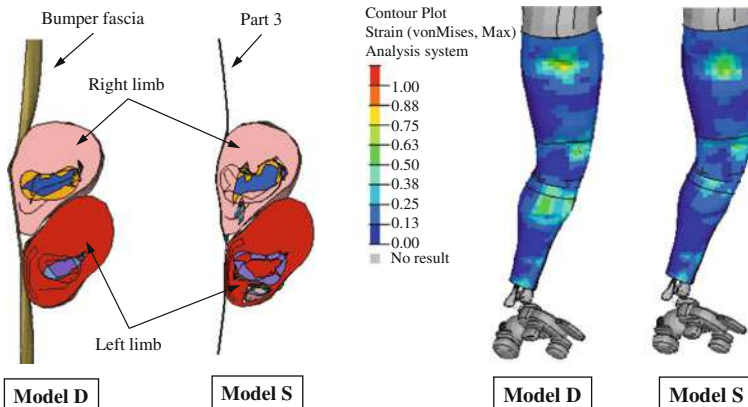


Fig. 10 Validation of local deformation and strain distribution on the lower limb. **a** Local deformation at Section A. **b** Strain distribution on right lower limb

4 Conclusions

A simplified parametric vehicle model has been developed for vehicle-HBM impact simulations. A full-scale, mid-size pedestrian model (GM/UVA model) was used. In real-world pedestrian accidents, the vehicle front-end contacts the two lower limbs at different times. To capture this local deformation of the vehicle front structure, distributed beam elements and deformable shell elements have been used in the simplified model. The grill parts with reasonable geometry are also considered to comprehensively reflect the contact characteristics in human body impact with real vehicles. This simplified model can reduce the calculation time for HBM impact simulation significantly. It also permits high degree of flexibility in adjusting geometry and stiffness variables.

To determine reasonable upper/lower bounds of the design variables, an investigation on vehicle profile characteristics focusing on the worldwide sedan models produced between 2008 and 2010 was conducted. An approach for local stiffness measurement on vehicle front-end was proposed.

This simplified parametric model is further validated by a detailed sedan model. The assessed responses in the validation include the human body injury parameters (knee bending angles and ligament elongations of the two lower limbs), the contact forces, the lower limb kinematics and local deformations on the vehicle front. When the variables on the simplified model are set to match that of the detailed model, it is found that the two models correlate with each other quite well. Therefore this simplified model can represent real vehicle models in impacts with human bodies.

With high calculation efficiency and flexibility of variable adjustment, this simplified parametric model of vehicle front structure can be used in automatic parametric model building for DOE studies and integrated in an optimization loop for improving vehicle design to reduce pedestrian injuries. This is useful in the early phases of vehicle design to give fast predictions on real human injuries of different vehicle design changes.

Appendix: Investigation of Vehicle Profile Characteristics

To determine proper range of the geometry variables, an investigation of vehicle profile characteristics was conducted focusing on the worldwide sedan models produced between 2008 and 2010. The approach is similar to the investigation on vehicle front profile characteristics by International Harmonized Research Activities (IHRA) in 2003 [25]. The profile data were extracted from the Internet, and validated by typical variables published by car manufacturers, such as total length, height, and wheelbase. Then the profile curves of all the sedans were aligned and plotted in one figure, where axis of abscissa is the ground line and axis of ordinates is the vertical longitudinal line of the bumper front edge (Fig. 11). Figure 12 shows the definitions of the measure points for the bumper lead (BL), bumper center-line height (BCH), leading edge height (LEH), bonnet length, bonnet angle, windscreens angle and the bottom depth and height of the front skirt.

The lower and upper bounds and average value of each variable are summarized in Table 2. The results of the vehicle front profile characteristics were used to determine the range of the design variables for further DOE study.

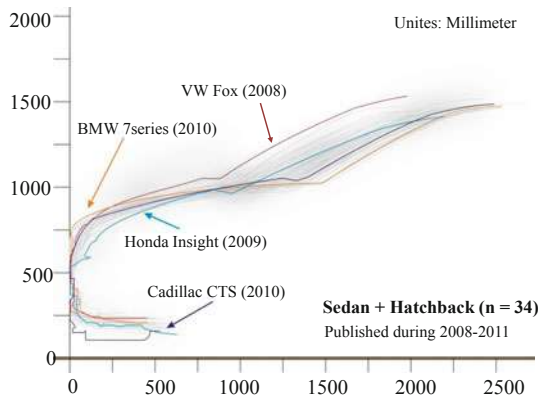


Fig. 11 Sedan front profile corridors

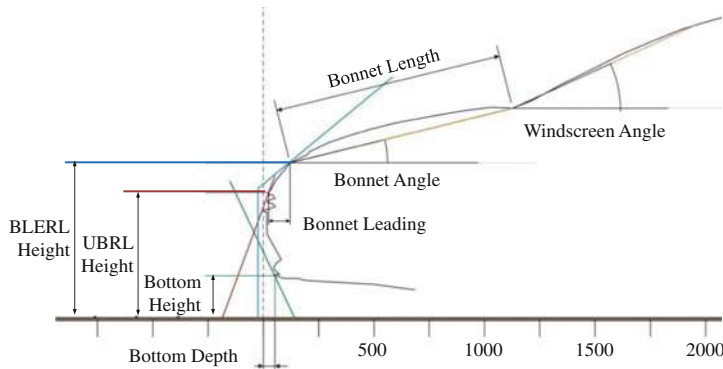


Fig. 12 Definitions of the vehicle front profile parameters

Table 2 Corridors of the vehicle front profile parameters (Sedan + Hatchback, n = 35)

Parameters	Unit	Lower bound	Average	Upper bound
Bottom depth	(mm)	0	10.5	51.9
Bottom height	(mm)	197.6	263	301.4
UBRL height	(mm)	521.2	623.5	667.6
Bonnet leading	(mm)	20.5	111.6	192.7
BLERL height	(mm)	703.9	784.9	847.5
Bonnet length	(mm)	814.6	1170.3	1474.1
Bonnet angle	(°)	9.0	11.0	19.0
Windscreen angle	(°)	21.0	28.0	31.0

Acknowledgments The authors would like to thank Altair for providing us with the educational license for HyperWorks. We also thank LSTC for providing us with the educational license for LS-DYNA.

References

1. IHRA (2001) International harmonized research activities pedestrian safety working group, report. Version 2, December 2001
2. Yang J (2005) Review of injury biomechanics in car-pedestrian collisions. *Int J Veh Saf* 1(2005):100–117
3. Teresinski G, Madro R (2001) Knee joint injuries as a reconstructive factor in car-to-pedestrian accidents. *Forensic Sci Int* 124:74–82
4. EEVC WG17 (2002) Improved test methods to evaluate pedestrian protection afforded by passenger cars. Report, December 1998, updates September 2002
5. Issiki T, Konosu A, Tanahashi M (2007) Development of an FE biofidelic flexible pedestrian leg-form impactor (Flex-GT-prototype) model. Paper number 07-0179, 20th ESV conference, Lyon, France
6. Glasson E, Maistre V, Laurent C (2001) Car front end module structure development regarding pedestrian protection and other mechanical constraints. 2001 SAE world congress, paper number 2001-01-0761, Detroit, Michigan, United States
7. Neal M, Tu J, Jones D (2008) A response surface-based tool for evaluating vehicle performance in the pedestrian leg impact test. 2008 SAE world congress, paper number 2008-01-1244, Detroit, Michigan, United States
8. Neal M (2004) Front structure design procedure for optimal pedestrian leg impact performance. 2004 ASME design engineering technical conferences and computers and information in engineering conference, Salt Lake City, UT, United States, pp 199–207
9. Shuler S, Mooijman F, Nanda A, Surisetty G (2005) Improved energy absorber and vehicle design strategies for pedestrian protection. 2005 SAE world congress, paper number 2005-01-1872, Detroit, Michigan, United States
10. Uikei D, Evans D, Abad S et al (2005) Design exploration of bumper systems using advanced CAE techniques. 2005 SAE world congress, paper number 2005-01-1340, Detroit, Michigan, United States
11. Ishikawa T, Kore H, Furumoto A, Kuroda S (2003) Evaluation of pedestrian protection structures using impactors and full-scale dummy tests. Paper number 271, 18th ESV conference, Nagoya, Japan
12. Konosu A, Issiki T, Tanahashi M, Suzuki H (2007) Development of a biofidelic flexible pedestrian legform impactor type GT (Flex-GT). Paper number 07-0178, 20th ESV conference, Lyon, France
13. Schuster P, Chou C, Prasad P, Jayaraman G (2000) Development and validation of a pedestrian lower limb non-linear 3-D finite element model. 44th Stapp car crash conference, paper number 2000-01-SC21, Atlanta, GA, United States
14. Takahashi Y, Kikuchi Y, Mori F, Konosu A (2003) Advanced FE lower limb model for pedestrians. Paper number 218, 18th ESV conference, Nagoya, Japan
15. Kuwahara S, Hosokawa T, Okada K, Mizuno K (2007) Finite element analysis of pedestrian lower extremity injuries in car-to-pedestrian impacts. 2007 SAE world congress, paper number 2007-01-0755, Detroit, Michigan, United States
16. Yasuki T (2007) Mechanism analysis of pedestrian knee-bending angle by sedan-type vehicle using human FE model. *Int J Crashworth* 12:329–339
17. Deng B, Wang JT, Hahn W (2007) Human model for real-world vehicle-pedestrian impact simulations. In: International symposium of human modeling and simulation in automotive safety, Germany

18. Kerrigan J, Crandall J, Deng B (2007) Pedestrian Kinematic Response to Mid-sized Vehicle Impact. *Int J Veh Saf* 2(3):221–240
19. Untaroiu C, Darvish K, Crandall J, Deng B, Wang JT (2005) A finite element model for the lower limb for simulating pedestrian impacts. *Stapp Car Crash J* 49:157–181
20. Kerrigan J, Bhalla K, Madeley N, Funk J, Bose D, Crandall J (2003) Experiments for establishing pedestrian-impact lower limb injury criteria. 2003 SAE world congress, paper number 2003-01-0895, Detroit, Michigan, United States
21. Ivarsson J, Lessley D, Kerrigan J, Bhalla K, Bose D, Crandall J, Kent R (2004) Dynamic response corridors and injury thresholds of the pedestrian lower extremities. International research council on biomechanics of injury conference (IRCOBI), GRAZ, Austria
22. Glasson E, Maistre V, Laurent C (2001) Car front end module structure development regarding pedestrian protection and other mechanical constraints. 2001 SAE world congress, paper number 2001-01-0761, Detroit, Michigan, United States
23. Dunmore M, Brooks R, Madeley N, McNally D (2006) The effect of leg fracture level and vehicle front-end geometry on pedestrian knee injury and response. *Proc Inst Mech Eng* 220:857–869
24. Martinez L, Guerra L, Ferichola G, Garcia A (2007) Stiffness corridors of the European fleet for pedestrian simulations. 20th ESV conference, paper number 07-0267, Lyon, France
25. Mizuno Y (2003) Summary of IHRA pedestrian safety WG activities (2003)—proposed test methods to evaluate pedestrian protection afforded by passenger cars. 18th ESV conference, paper number 580, Nagoya, Japan

Front Stop Lamps for a Safer Traffic

Ovidiu Antonescu

Abstract Engineering Objective: The paper deals with an innovative idea of placing the stop lamps not only in the rear of the vehicle as usual but in the front of it too. By doing this the traffic safety would increase significantly since everyone involved on it would know that the driver is stopping the vehicle. Especially the pedestrians would benefit of these front brake lights when they are crossing the street. The stop lamps may be placed near to the headlights but they would be difficult to be observed during the night. Thus, a better solution is placing them separately as some turn signals. What does the paper offer that is new in the field in comparison to other works of the author: The paper offers an idea completely new in the automotive filed and it is also new comparing to other works of the author. Conclusion: The innovative idea of placing the stop lamps in the front of the vehicle would offer a safer traffic not only for pedestrians but also for all involved in the traffic.

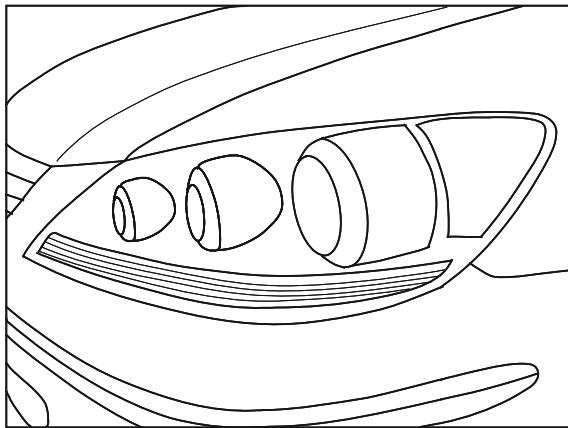
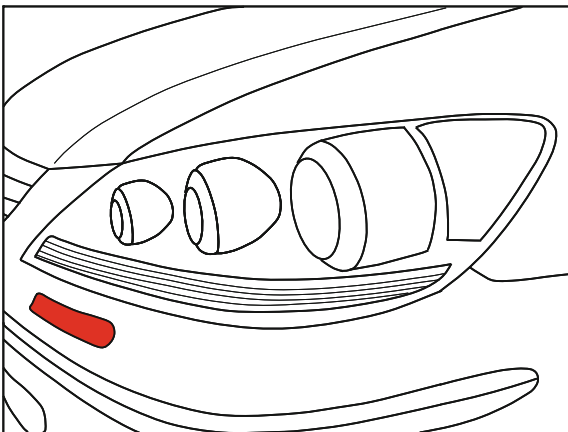
Keywords Front stop lamps • Traffic safety

1 Introduction

There are always solutions to increase the traffic safety. This paper proposes one of them by placing the stop lamps in the front of the vehicle (Fig. 2) as these brake lights are placed in the rear (Fig. 1).

F2012-F03-006

O. Antonescu (✉)
Politehnica University of Bucharest, Bucharest, Romania

Fig. 1 Classic front lighting**Fig. 2** Front lighting with stop lamps

Being important at least as the turn signals, the stop lamps must be visible. A solution is placing them separately from the headlights as some turn signals. As it can be seen in Fig. 2 the front brake lights can be placed in the bumper even if they are not so protected in the case of the front crashing. The low price of them would compensate this disadvantage.

2 A Safer Traffic

Let's suppose that we are pedestrians and we are crossing the street on a zebra and the traffic light is green, of course for us. In the same time a vehicle approaches to the pedestrian crossing, driving straight to us with slow speed and making the impression that it is braking. Now, how do we know the intention of the driver? How can we be sure that the driver is actually stopping the vehicle? Simply,

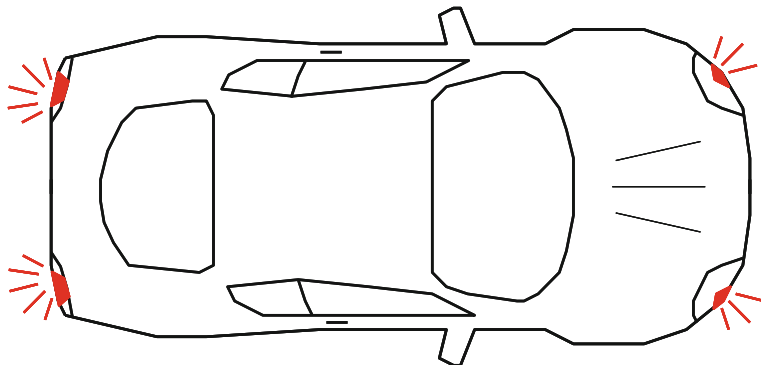


Fig. 3 Innovative brake lighting

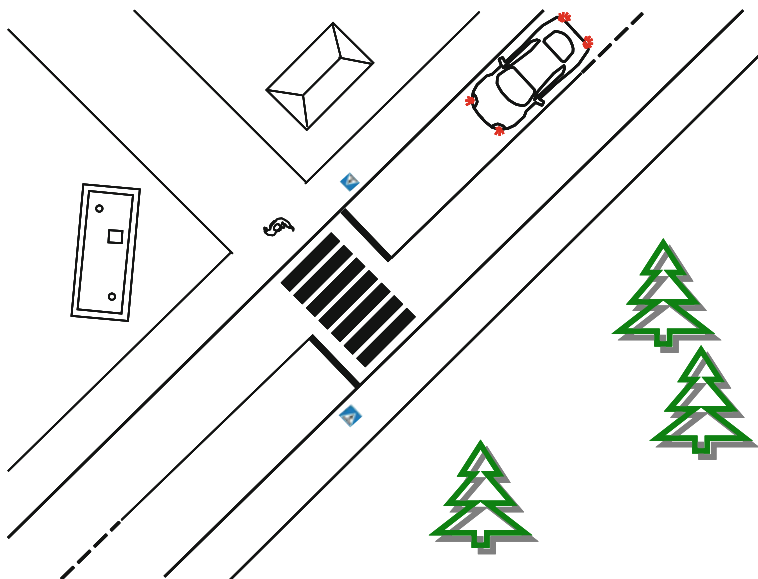


Fig. 4 Crossing a street

by placing two brake lights in the front of the vehicle as it is shown in Fig. 3. Only in this way we will be sure that the driver is pushing the brake pedal.

Let's now reconsider the situation but with a car equipped with these innovative front stop lamps (Fig. 4). In this case the pedestrian knows for sure that the driver is braking the car. We do not know how much the driver pushes the brake pedal but we know how long it takes. Anyway the pedestrian is more confident in crossing the street and so the traffic is now safer.

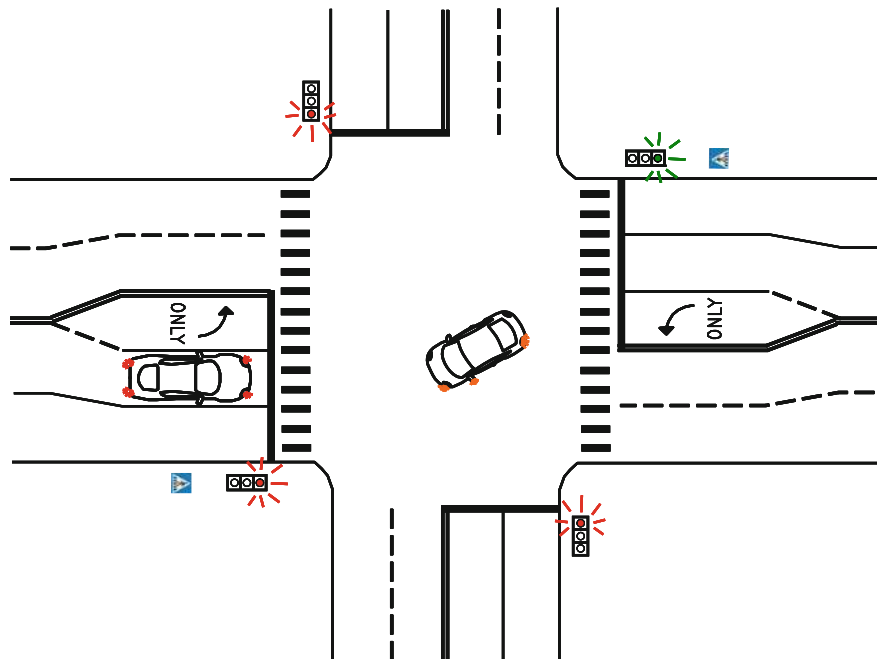


Fig. 5 Turning left

Let's now consider a road intersection (Fig. 5). The driver of the car that is turning left sees that the other driver is actually stopping his vehicle. The same confidence will be felt by the driver that is turning left as it was by the pedestrian.

3 Conclusion

The pedestrians would benefit from the usage of the front stop lamps when they are crossing the street. The stop lamps may be placed near to the headlights but they would be difficult to be observed during the night. Thus, a better solution is placing them separately as some turn signals.

The innovative idea of placing the stop lamps in the front of the vehicle would offer a safer traffic not only for pedestrians but also for all involved in the traffic. Knowing the intention and the acting of the driver are very important concerning the traffic safety.

Study on Headlamp with Spot Light

**Byoungsuk Ahn, Youngsub Oh, Hootaek Cho,
Myunggug Bang and Sunkyoung Park**

Abstract If pedestrian accidents occur in nighttime, the risk of being killed is higher than during daylight. Recognizing pedestrians at night is more difficult than during daylight. New light source, such as HID bulb, and new technology, such as AFLS, have improved a visibility while driving at night; also using sensor, such as night-vision. It is possible to detect a pedestrian; but the driver has to see the display. In this study, Spot light which illuminate the pedestrian directly detected by NIR sensor and image processing is developed and this system help the driver avoid accident by recognizing the presence of the pedestrian early without averting driver's eyes.

Keywords Spot light · Infrared ray · Pedestrian accident · Multi chip LED · Flashing cycle

1 Introduction

In 2009, the number of pedestrian accident occurred by vehicle is 53,518; and 50.4 % of pedestrian accident happened at night.

F2012-F03-007

B. Ahn (✉) · Y. Oh · H. Cho
Hyundai Motors, Seoul, Korea

M. Bang
Hyundai Mobis, Seoul, Korea

S. Park
SL Lighting, Seoul, Korea

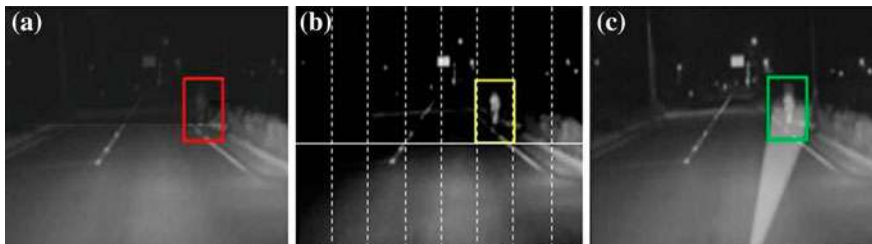


Fig. 1 Configuration of Spot Light system

Especially, the traffic fatality rate is 63.2 % at nighttime; this means that detecting the pedestrian on the road at night is more difficult than during daylight [1].

New light source, such as HID bulb, and new technology, such as AFLS, have improved a visibility while driving at night, but those systems are regulated to prevent from occurring glare to driver who drive the car in front. Therefore, the vehicular headlight cannot sufficiently light up the front, it is difficult to ensure the front visual field, and as result, the driver can miss a pedestrian at night.

In case of vehicle, it is presented by lighting system for example tail lamp, reflex reflector. But In case of pedestrians, they don't have any item or system that present their position at night.

These days, night vision system which detect pedestrians by infrared ray is developed. However, this technology deteriorates driver's observation power because the driver should see the display to recognize the position of pedestrian.

In this study, Spot light which illuminate the pedestrian directly detected by NIR sensor and image processing is developed. This system help the driver avoid accident by recognizing the presence of the pedestrian early.

2 System Configuration

In order to detect pedestrian, infrared rays are used in this system. Visible lights are not good because of glare to other drivers.

Figure 1 shows the concept of the system; as image (a), it is hard to recognize pedestrians if low beam is turned on only. If pedestrian is detected by sensor, such as infrared camera as image (b), the driver can see them directly by using a lighting system (c). The lighting system can be called Spot light.

IR lamp radiates infrared rays to the front of a vehicle, then camera takes infrared image reflected on a lighting target. An image processing unit read the lighting target from an image photographed by the camera and judge whether the lighting target is dangerous or not.

Spot light unit include an LED lamp mounted with a plurality of LEDs dividing a front lighting area of a vehicle to light up the respective areas, and a lamp driving unit controls the spot light unit to turn on the LED lamp lighting up an area where

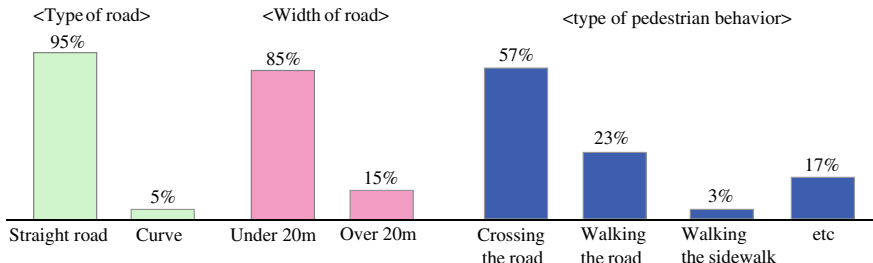


Fig. 2 Status of pedestrian accident

the lighting target is positioned when the image processing unit judges that the lighting target is dangerous.

2.1 Setting Target

In 2009, the rate of pedestrian accidents on the straight road is 95 %. On the other hand, the rate of it on the curve road is 5 % [1]. In addition, the pedestrian road accidents occurred mainly on the road those width is less than 20 m (Fig. 2).

Braking distance can be calculated as a following equation [2]

$$D = \frac{V^2}{254(f + s)} + 0.28t \cdot V$$

D: Braking distance (m)

V: Vehicle speed (km/h)

T: Reaction time (s)

s: inclination (%)

f: road friction coefficient

The friction coefficient is 0.28, which is the value that satisfy all conditions at 80 km/h including wet road; the reaction time is considered 1 s.

According to the above equation, if the vehicle speed is 80 km/h, braking distance is 112 m.

Of course, if recognizing pedestrian early and reducing the vehicle speed sufficiently, it is able to control the vehicle to avoid an accident.

By a comprehensive, Target area, as shown in the Fig. 3, was determined and divided into eight sections. The operating speed is between 30 and 80 km/h.

2.2 Spot Light Module

Figure 4 shows the spot light module. This module has a plurality of LEDs. So each led illuminates the respective divided area. A heat sink is installed on a

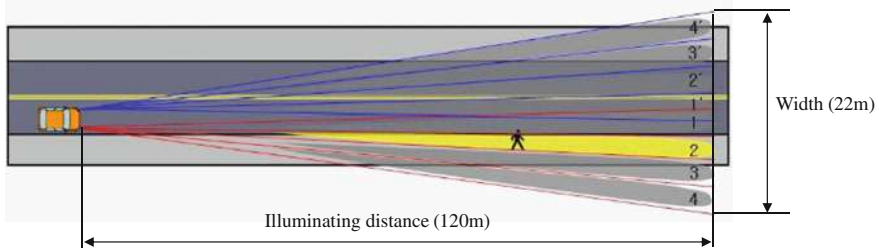
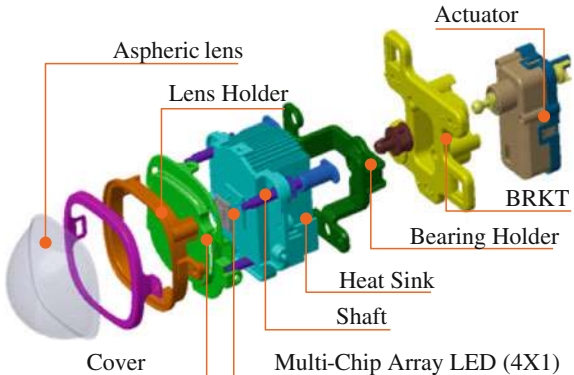


Fig. 3 Setting target area of Spot light

Fig. 4 Spot light module



rear surface of the LED in order to dissipate heat generated from the LED and an aspheric lens provided in the front of the LED to focus or diffuse light emitted from the LED.

The shape of module is similar to the projection module type. The difference is the direction of LED toward the vehicle front and there is no reflector.

The figure below shows simulation images based on the combination of reflector and lens.

The case of (a), the light reflected by a reflector is diffused. So the luminous efficiency of center is low. The case of (b), the light can be condensed by applying the lens but the light reflected by a reflector is diffused (Fig. 5).

So, as the case of (c), the reflector that diffuses the light was removed. There are a little loss because some light from LED cannot be incident on the lens. But desired light pattern was gained.

Spot light module has been optimized as the case of (c) to improves the luminous efficiency and to make a rectangular light pattern.

Figure 6 shows a four-chip LED which is applied on spot light module. Each chip can be controlled individually to illuminate the target area divided into eight sections.

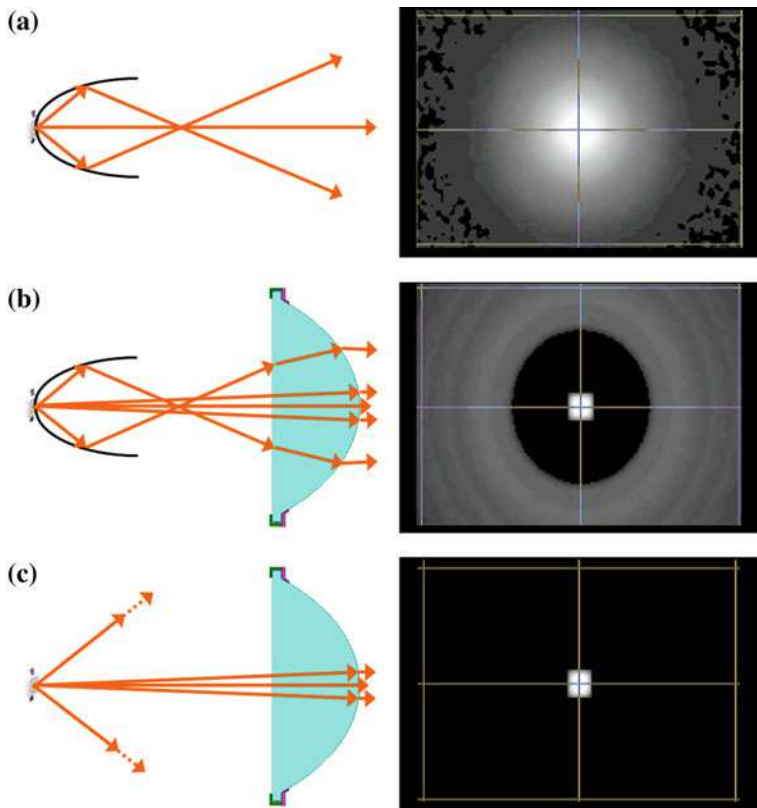


Fig. 5 Image of light pattern by combination of reflector and lens. **a** With reflector, **b** with reflector and lens and **c** Without reflector

In order to detect pedestrians in front 120 m, 72,000 cd the luminous intensity of value is required. In this study, spot light module has the luminous intensity of 85,000 cd value that can recognize pedestrians 130 m in front. Also, according to the equation of braking distance, pedestrian accidents can be prevented at 86 km/h.

Figure 7 shows image of spot light on the road surface. Spot light consists of 4 chips are illuminate the target area determined as Fig. 3.

2.3 Flashing Cycle

Flashing method has been known to draw a driver's attention [3]. In this study, flashing method was applied on spot light to improve the visibility and test was carried out as Fig. 8 to obtain the optimal flashing cycle with 20 subjects.

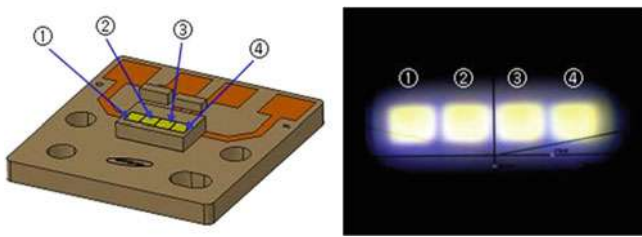


Fig. 6 Multi-chip array LED and light pattern



Fig. 7 Image of spot light on the road surface

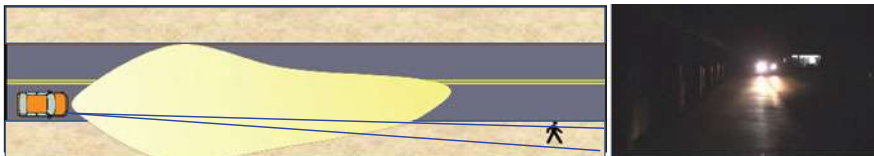


Fig. 8 Blinking cycle impact assessment

The distance between vehicle and pedestrian is 60 m, flashing cycle is 3, 5, 7 Hz. In case of under 3 Hz, it is not illuminate a pedestrian sufficiently while the vehicle was moving fast. On the other hand, it is harmful to human eyes and body if the cycle is over 7 Hz [4].

Figure 9 shows reaction time, visibility and discomfort by flashing cycle. Fast flashing cycle provides faster reaction time and low flashing cycle has a large deviation. Because the interval of turning off the light is so long that drivers cannot see the pedestrian at that time.

Visibility was not affected by flashing cycle. However, some drivers feel an affinity at 5 Hz.

In case of discomfort by flashing cycle, the more discomfort was felt if the faster flashing cycle was applied.

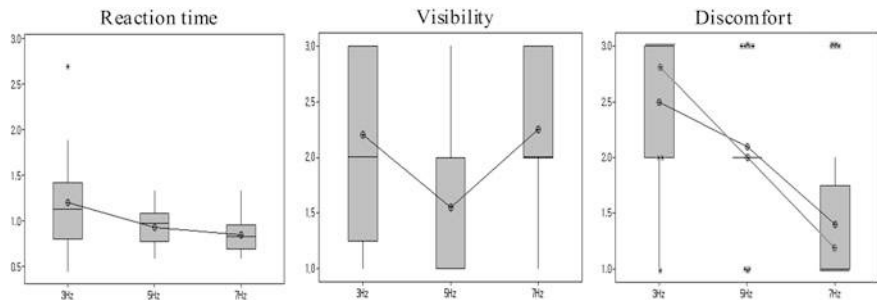


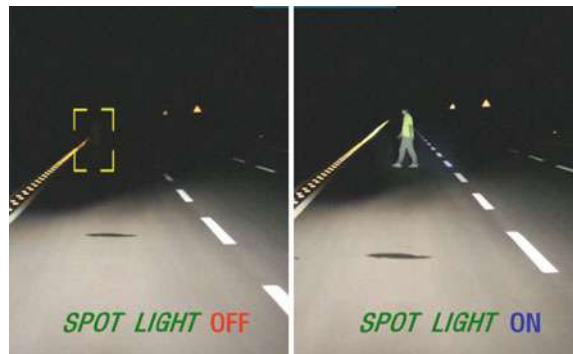
Fig. 9 Driver's reaction time, Visibility, Discomfort by flashing cycle



Fig. 10 Visibility test (walking the sidewalk)

Based on the above test results, finally 5 Hz was applied on spot light system. Further, the driver's visibility is heightened regardless of the vehicle speed if the flashing cycle of the system is changed according to the vehicle speed.

Fig. 11 Visibility test (crossing the road)



3 Test Result

The test was carried out to investigate the effects of spot light. Result may vary depending on the height of the lamp, light source and the color of pedestrian's cloth. However, as shown in Fig. 10, the visibility for pedestrian is greatly improved while spot light is being operated (Fig. 11).

According to test result, the distance recognizing pedestrian is 40 m when low beam is turned on only. On the other hand, the recognizing distance is more than 150 m when Spot light is turned on.

The notable thing is that the driver is able to predict the location of pedestrian. Even if pedestrian is away from the vehicle. The reason is that spot light does not only illuminates him directly but also make beam pattern on the road surface. This means that the result of test is very good compared to the goal 120 m.

In other words, if only low beam is turned on, the time to reach the pedestrian is 1.8 s after recognizing pedestrian at 80 km/h. On the other hand, if spot light is turned on, the time to reach the pedestrian is 6.8 s. This means that a driver gets 5 s to avoid pedestrian accident at 80 km/h when spot light is turned on.

4 Conclusion

In this study, the potential risk area of the vehicle front was set and illuminated if there was a pedestrian in there; though pedestrian recognition performance with infrared images must be supported, Spot light can makes driver find pedestrian quickly than low beam alone at night. In conclusion, it is possible to avoid pedestrian accident by obtaining time and distance.

References

1. Korea National Police Agency (2011) Status for Traffic Accidents 2009
2. Do C (1994) Theory of traffic engineering. Cheong moon gak, Seoul
3. Informal Document No. GRE-53-2 (2004) Evaluation of emergency brake light display (EBLD) system, 53rd GRE agenda item 2.6
4. Informal Document No.9 (2003) Study on the validity of emergency brake light display, 51st GRE agenda item 1.1.2.9

Analysis of Pedestrian Kinematics and Injury Mechanism in Real World Accidents

Daisuke Murakami, Chinmoy Pal, Yoshiko Kawabe
and Tomosaburo Okabe

Abstract Post-impact pedestrian kinematics is complex and depends on various factors such as impact speed, height of the pedestrian, front-end profile of the striking vehicle and pedestrian posture, among others. The aim of this study is to investigate the main factors that determine post-crash pedestrian kinematics. A detailed study of NASS-PCDS (National Automotive Sampling System—Pedestrian Crash Data Study) showed that the vehicle–pedestrian interaction in frontal crashes can be categorized into four types. Pedestrian–vehicle size ratio and the impact speed are the two most influential factors that determine post crash pedestrian kinematics. The findings from the NASS-PCDS study were also confirmed and verified with the help of numerical simulations performed using two modified JAMA human FE models. An adult model (male, 175 cm and 72 kg) and a properly scaled child model (6 years old, 120 cm and 24.5 kg) were effectively utilized to investigate the post-crash kinematics in different conditions.

Keywords FE-analysis · Pedestrian-safety · Accident-analysis · 6-year-old(YO)-child · Postcrash-kinematics

1 Introduction

Even though the motor vehicle occupant fatalities are decreasing in many countries, the overall percentages of pedestrian casualties are increasing compared to that of vehicle occupants. Annual fatalities, for every 1,000,000 people, are 12.3 in

F2012-F03-010

D. Murakami · C. Pal (✉) · Y. Kawabe · T. Okabe
Nissan Motor Company Ltd, Tokyo, Japan

Australia, 15.7 in the EC, 16.4 in the US and 21.8 in Japan. The numbers in developing countries are even higher. Mizuno et al. reported their detailed investigations of pedestrian accident databases from countries including Australia, Germany, Japan and the US (1,605 cases, 9,463 injuries, include 3,305 AIS2+) [1]. According to their report, in one third of those cases, pedestrians are reported to have suffered injuries to their heads and/or lower extremities. Previous studies on pedestrian crash cases pointed out that the vehicle front geometry human height and human posture affect the pedestrian injury mechanism [2]. Further studies [3, 4] targeting child pedestrians' injury distribution pointed out that anthropometry influences impact kinematics. This study focuses on the leading factors affecting post-crash pedestrian movement and the injury mechanisms in relation to impact speed. Human FE model simulations were carried out to reconfirm and endorse the findings and the trends in accident analyses.

2 NASS-PCDS Analysis

The database contains data on 552 pedestrian crashes and 4,499 injuries during 1994–1998. It is not a statistically weighted sample. Statistical inferences of this study are limited in the NASS-PCDS database and do not necessarily represent the overall US pedestrian crash statistics relating to the frequencies of types of pedestrian accidents and the percentage of related injuries. One of the NASS-PCDS variables, 'Vehicle pedestrian interaction (variable 524)', indicates the post-crash pedestrian kinematics. There are 17 codes to describe the types of interaction [4]. Four of those codes are picked out in accordance with frequencies of occurrences. They are categorized as following the four main types (Table 1).

The numbers of cases for each type are indicated in the fourth row of the table, the next two rows show the average pedestrian height, the average impact speed and its standard deviation. On the basis of this basic statistical information, a human FE model simulation, as shown in the last row, was carried out to verify the kinematics for corresponding types of impact. From the simulation results, corresponding to four different (Type A–D) kinematical modes, which is observed in Table 1.

Type A differs from the other three types in the relative velocity after impact. The Type A pedestrian is accelerated in the same direction in which the vehicle is traveling. The pedestrian's body is thrown forward in front of the vehicle.

In the other three types, Types B, C and D, the pedestrians are accelerated by the impact, up to a speed not more than the traveling speed of the vehicle. The torso of the pedestrian travels relatively backward with respect to the front end of the vehicle.

Table 1 Classification of vehicle–pedestrian interaction (Type A–D) in frontal crash

Variable	Type A	Type B	Type C	Type D
	5	1	2	4
Description in NASS-PCDS manual	Thrown straight forward	Carried by vehicle, wrapped position	Carried by vehicle, slid to windshield	Passed over vehicle top
(a): No. of pedestrian (total 275 cases)	35	82	138	20
Average pedestrian height [cm]	158	163	168	172
Average impact speed [km/h]	19.8	21.9	41.0	66.7
(standard dev.)	(12.2)	(11.2)	(19.6)	(10.5)
(b): MAIS 2–	25	67	60	4
(c): MAIS 3+	10	16	78	16
Ratio of MAIS 3+	28.6	19.5	56.5	80.0
(c)/(a) (%)				
FE verification with adult male and 6-year-old child based on JAMA model				

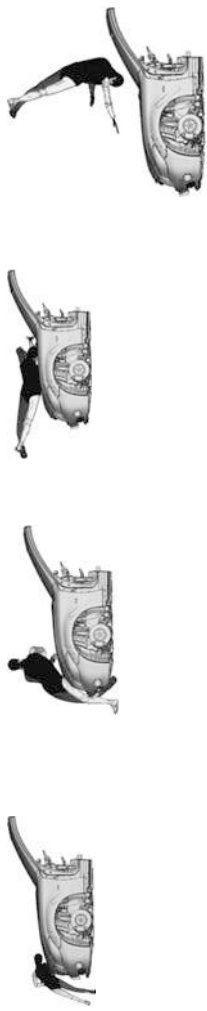
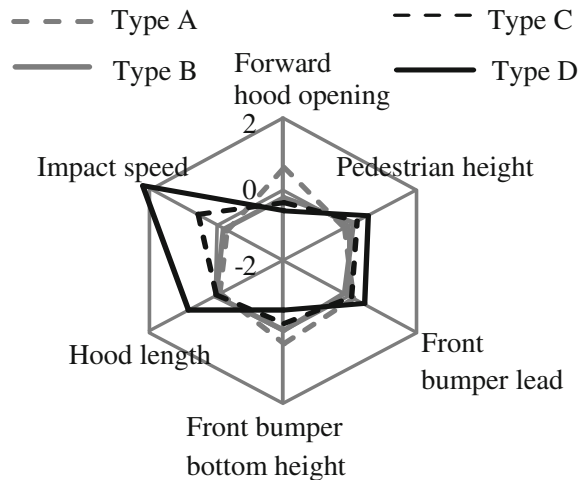


Fig. 1 Components of four types of pedestrian crashes without outliers (refer Fig. 2)



3 Characteristics of Vehicle–Pedestrian Interaction

Six-principal components characterize most of the features of the vehicle–pedestrian interactions as mentioned in [4]. Figure 1 shows the average values for each of the groups of four vehicle–pedestrian interaction types, related to those six principal factors, excluding the outliers (i.e., those data corresponding to higher impact speed $V > 80$ km/h as shown in Fig. 2). It is observed that:

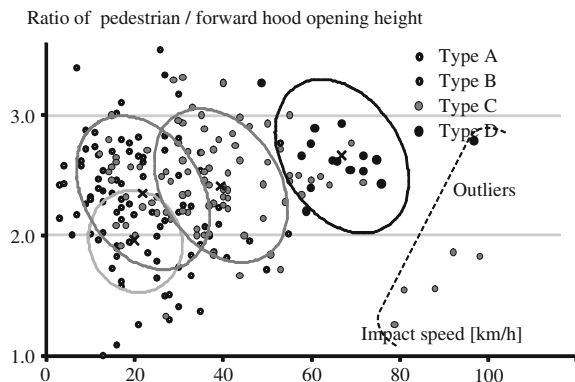
Type D: The polygon shape in the radar chart corresponding to Type D is quite different and is separated from the others. It is more prominent on the ‘Impact speed’ axis. However, note that the occurrence value of Type D is the lowest of the four, i.e., 20 out of 275 as mentioned in Table 1. Hence, the average contains more biases than the others.

Type A: The polygon in the radar chart corresponding to Type A plot gets separated from the other three types on the ‘Forward hood opening’, ‘Front bumper bottom height’ and ‘Pedestrian height’ axes. That means vertical height is the determining factor contributing Type A kinematics which include children.

Type B, C and D: The ‘Impact speed’ axis mostly represents the differences among Types B, C and D. It is to be noted that the three lines cross the ‘Pedestrian height’ axis in the same order and the ‘Front bumper-bottom height’ axis in the reverse order. Hence, the relative values of ‘Pedestrian height’ and ‘Front bumper-bottom height’ are closely coupled and inversely related influencing the post crash kinematics of the pedestrian.

Type B, C and D: The three types are nothing but an extension of a series of similar kinematical movement, distinguished by the amount of movement of the pedestrian moving backwards with respect to the front end of the vehicle. The four factors, ‘Impact speed’, ‘Pedestrian height’, ‘Forward hood opening’ and ‘Front bumper bottom height’ make the differences of the degree of backward movement.

Fig. 2 NASS-PCDS data plotted in impact speed versus height ratio h_p



However, the result of the principal component analysis shows that the ‘Forward hood opening’ and ‘Front bumper bottom height’ are highly dependent, so the first principal component ‘Forward hood opening’ is chosen for further discussion.

The NASS-PCDS cases are plotted and clustered on the graph according to the kinematics types (Fig. 2). The horizontal axis indicates impact speed. The vertical axis shows the relative height ratio h_p of the pedestrian and the forward hood opening height. Four ellipses on the graph indicate typical contour lines (MD = 1) of the equivalent Mahalanobis distance (MD) of each type groups, and the cross marks ‘x’ on those four ellipse centers are the average values of the corresponding groups.

The distributions of the four types show dependency on the impact speed and height ratio. Types A and B share the same impact speed range, $V < 41 \text{ km/h}$, although the height ratio of Type A is generally lower than Type B. With increase of impact speed V and height ratio h_p , ratios of Types B, C and D increase in turn. Impact speed range of $V < 61 \text{ km/h}$ consists of Type A, B and C. Shorter pedestrians tend to be Type A, while taller pedestrians fall into Type C. Type D plots increase their number in the speed range $V > 60 \text{ km/h}$.

Type B, C and D ellipses have slightly negative inclinations. At the same impact speed and hood opening height, the negative inclination indicates that for relatively taller pedestrians (i.e., high h_p) the probability to be included in or falling into the next severe category (i.e., B-to-C or C-to-D) increases compared to that for relatively shorter pedestrians (i.e., low h_p). The same is true for relatively lower hood opening (i.e., high h_p) with the same impact speed and pedestrian height compared to that for relatively higher hood opening (i.e., low h_p).

These plots indicate that, ‘*Impact speed*’, ‘*Pedestrian height*’ and ‘*Front bumper—top height*’ are the three most decisive factors to distinguish or classify the frontal post-crash pedestrian kinematics. As previously mentioned, h_p , the relative height of pedestrian with regard to vehicle front end is one of the main contributing factors that affect post-crash kinematics. Finite element analysis is introduced to show the differences between Type A and B pedestrian kinematics.

Table 2 Overall FE model dimensions and spinal chord model (a, b, c) with response identification (Figs. 3, 4)

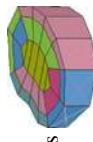
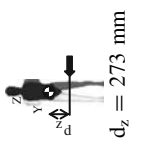
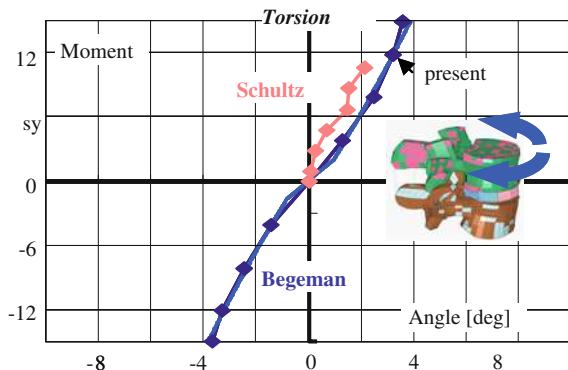
	Adult	Child	Spinal cord modeling (e.g., L3-L4)	
Height	172 cm	120 cm	European 6YO child 50th %ile [7]	Spinal bones joined by different ligaments
Weight	71.9 kg	24.5 kg (range 20–32 kg)		and intervertebral disk
 (a) Ligaments				
 (b) Intervertebral disk				
 (c) Assembly				
IXX	11.8 kg m ²	1.67 kg m ²	All parts scaled properly	Tension, bending, shear, torsion responses are tuned to match component level test results for adult [13] and also overall range of motion [9] which vary with age

Fig. 3 Component level response identification for torsional loading (quasi-static test)



4 FE Analysis of Human Model

The findings from the NASS-PCDS database analysis match previous studies, as is mentioned in the previous section. In this section, we focused on some other aspects of head trajectory and head impact point, with the help of our human FE model. The findings of our study also match the NASS-PCDS database analysis.

An adult male pedestrian model was developed by Japan Automobile Research Inst (JARI) under the supervision of Japan Automobile Manufacturers Association (JAMA) in 2010 [5, 6]. The post-crash pedestrian kinematics, including head trajectory, are already validated with PMHS experiments [5, 12]. In this paper, the head Center Of Gravity (COG) trajectory of the pedestrian FE model is discussed. The adult model was modified in-house to create a 50th percentile 6YO child FE model based on European database of child anthropometry.

In Table 2, overall dimensions are given on the top left side. The adult 50th % ile adult male model is developed in the JAMA human model consortium. All parts of the 6YO child FE model are geometrically scaled according to the European children anthropometry data from this adult model [3, 7].

The weight 24.5 kg of the scaled model is the average of 6YO child weight margin of 20–32 kg. The impact point of the bumper is shown by an arrow. The overall modeling of the L3–L4 spinal chord region is shown in (a) ligaments are modeled by tension-only bar elements, (b) inter-vertebral disk: between two adjacent vertebra 2-layers and in the radial direction 3-layers of solid elements with various sets of material properties to simulate the different bending properties in frontal and lateral directions.

The assembly of L3–L4 is subjected to different types of loads to identify the basic behavior of response of the FE model as reported by JARI report in the JAMA human model consortium to match coupon tests of spinal chord carried out by Begeaman and Schultz [10, 11]. Two main modes of response for pedestrian impact simulation are given in Fig. 3 for torsional behavior and in Fig. 4 for lateral bending behavior which are influential to pedestrian head impact time (HIT) on the hood and the distance the point of impact on the hood is from ground (WAD).

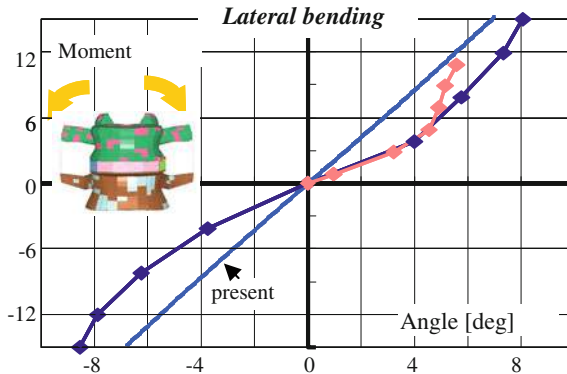


Fig. 4 Component level response identification for lateral bending modes of loading (quasi-static test)

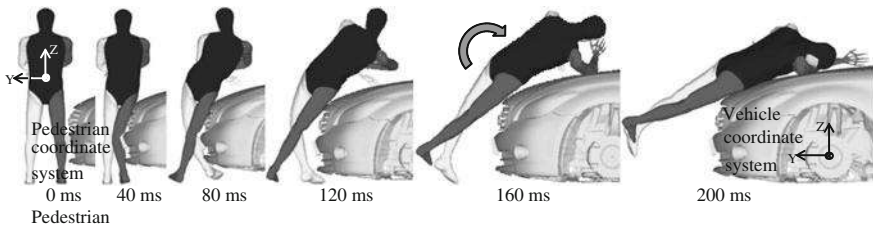


Fig. 5 FE analysis of an adult human (male) verus a sedan crash ($V = 20 \text{ km/h}$)

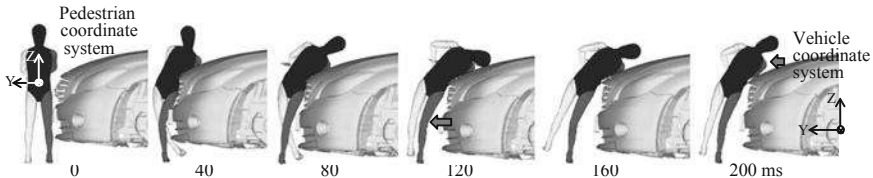


Fig. 6 FE analysis of a child human (6-year-old) versus a sedan crash ($V = 20 \text{ km/h}$)

The graph inside (c) shows the change in range of flexibility with age, with younger children being relatively more flexible than adults.

Adult-male: In Fig. 5, the adult-male human model is hit at his anterior lower leg by the bumper, and falls down to the hood. In the initial phase (0–80 ms), the head moves in the Y-axis direction (the vehicle coordinate system), until his upper femur gets constrained by the front edge of the hood. Then the upper body and the neck moves like a duplex pendulum, rotating around the local X axis of the pedestrian coordinate system as shown in the middle of Fig. 7.

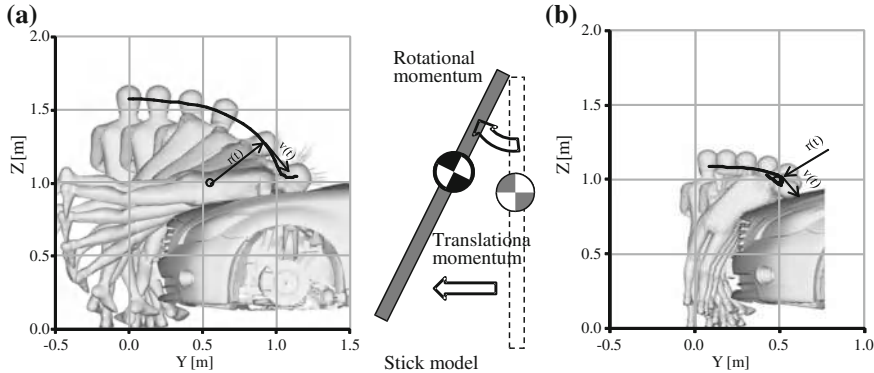


Fig. 7 Superimposed animations of an adult and a child FE models **a** Adult male kinematics (0–280, 40 ms interval) **b** Child kinematics (0–120, 20 ms interval)

6-year-old child: Figure 6 is the 6-year-old child pedestrian model. He was hit right under his COG, and is accelerated in the positive Y direction in the global system, the same as the traveling direction of the vehicle. The pedestrian body is accelerated to a velocity higher than that of the vehicle and his body is gradually thrown forward (160 ms). In this case the upper body of this child pedestrian is lifted up after hitting his abdomen against the front edge of the hood. His head COG trajectory (Fig. 7b) draws an arc centering at the bumper (R1) before his upper body is constrained by the hood. Then his upper body rotates around the front hood edge (R2). After his shoulder contacts the hood (80 ms), the head COG rotates around his neck (R3). At this time (80 ms), his body COG gets accelerated in the positive Y direction and starts to move away from the vehicle.

Figure 8a, b is the time histories of the tangential velocity $v(t)$ of the head COG and the rotational velocity $\theta(t)$, respectively. The rotational velocity $\theta(t)$ is calculated from the tangential velocity $v(t)$ and the curvature radius $r(t)$ of the head COG trajectory.

$$\theta'(t) = v(t)/r(t) \quad (1)$$

The curvature radius $r(t)$ is calculated by the smoothed trajectory of the head COG (Fig. 7). The resultant translational velocity of the head COG (Fig. 8a) of the child FE model hits its highest value when its torso contacts the car front and the head starts to fall down (45 ms). The same for the adult model is much later at 110 ms. The maximum value of the resultant velocity for the child model is slightly lower than that of the adult model. However, the calculated angular velocity (Fig. 8b) for the child and the adult models show quite different patterns. The angular velocity of the adult model (black line) takes its first local maximum 12.9 rad/s at 160 ms when the curvature center of the head COG trajectory comes around its pelvis. The second local maximum at 230 ms (the black dashed line) is the time when the head contacts the hood. The angular velocity of the child model shows a peaky curve. The second largest peak 85.3 rad/s at 80 ms appears when

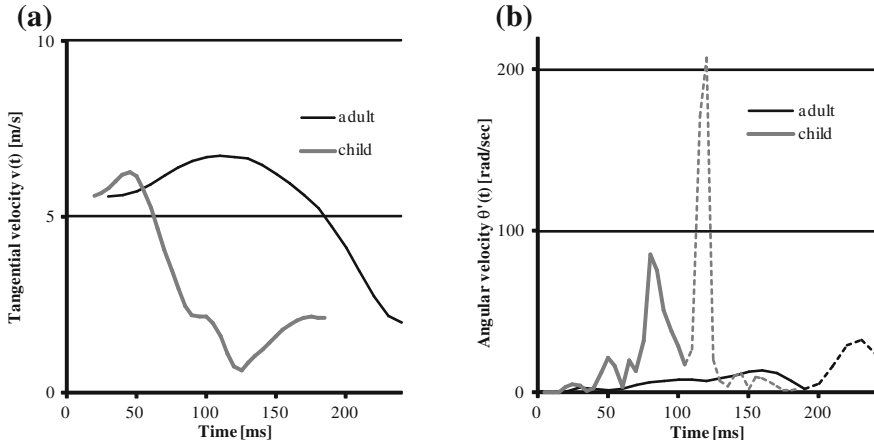


Fig. 8 Head velocity of adult and child FE models (20 km/h without braking) **a** Resultant translational velocity **b** Angular velocity

the child's shoulder is constrained by the hood and the head COG rotates around its neck. The maximum peak at 120 ms appears at the time of the head-hood contact. Contact to the hood bends the head trajectories and minimizes curvature radius. Thus, the highest peak is caused by graphical definition. The following discussion is for the second largest peak.

The tangential velocity $v(t)$ of the adult head COG is 5.9 m/s at the time when the angular velocity takes its secondary peak at 160 ms. The counterpart of the child head COG is 2.9 m/s at 80 ms, less than the half of that of the adult. The angular velocity peak of the head COG is derived from the curvature radius of the trajectory and is dependent on the height ratio.

5 Ground-to-Head-Contact Distance

The measurement of ground to head contact point, i.e., wrap around distance (WAD) from PCDS database is plotted in Fig. 9. The value of ground to head contact point, i.e., wrap around distance (WAD) and the ratio of the WAD/pedestrian height of FE simulation results are plotted for 6YO child pedestrian simultaneously in Fig. 10. In general, the ratio of the WAD/pedestrian height values (children: less than 1.0, adults: greater than 1.0, [8]), agree well with present FE simulations.

Figure 11 show the head COG trajectories of an adult male FE analysis of a crash case with a sedan traveling at 20 and 40 km/h. Comparing the constant velocity cases (black thin lines), the head contact point for the moderate speed (40 km/h) case, locates 220 mm rearward compared to that of the relatively low speed (20 km/h) cases. The difference in head contact point matches the value

Fig. 9 Ground-to-head-contact distance versus impact speed (gray-line with braking, thick-line without braking (adult))

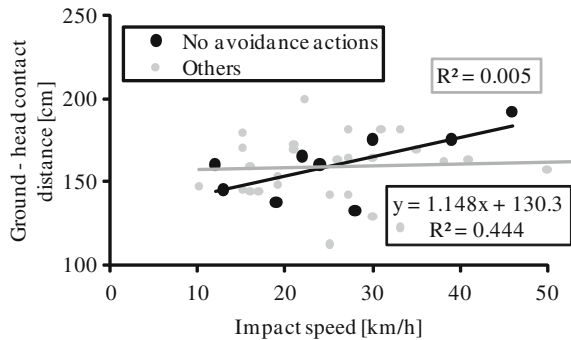
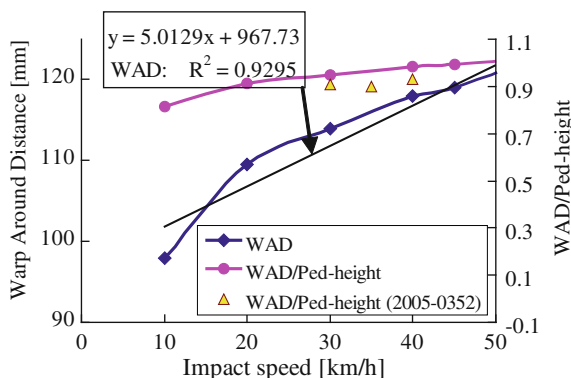


Fig. 10 Warp around distance (WAD), height WAD/pedestrian height versus speed (6YO, hp = 1.5)



derived from the approximated relation as shown in Fig. 9, where 1.148 is the gradient of the ground-to-head-contact distance without braking and steering cases, with respect to the impact speed, as calculated below by Eq. (2).

$$1.148 \times \Delta v = 1.148 \times 20 = 22.9 \text{ [cm]} = 229 \text{ [mm]} \quad (2)$$

In both Fig. 11a, b, the trajectories of deceleration (braking) cases go forward of the vehicle after contacting the hood. In these cases, deceleration switches the pedestrian kinematics from Type C to Type B category, and it may reduce or affect the risk of head-windshield injury in case by case. It is interesting to note that the gradient of WAD with respect to the impact velocity is four times higher for children (5.01) than adults (1.148). It is also very clear that the gradient of WAD at low impact velocity $V = 10\text{--}20 \text{ km/h}$ is stiffer than in the region above $V > 20 \text{ km/h}$ because of the low value of the pedestrian and hood height ratio h_p . This is similar to the tendency as observed in Fig. 2 from PCDS data. Present FE simulations results are well supported by actual accident field data. The three GIDAS cases, closest to our simulation, are chosen from Ref. [8, 2005-0352] and plotted in Fig. 10 as triangular marks estimated from Madymo simulation for comparison.

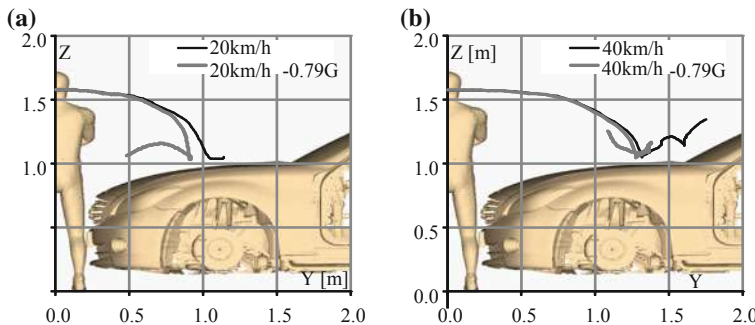
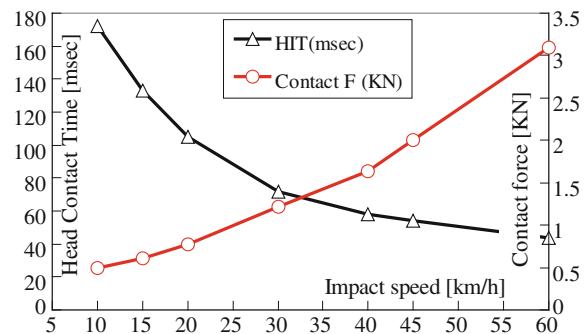


Fig. 11 Head COG trajectory, with/without vehicle deceleration at $V = 20, 40 \text{ km/h}$. **a** Initial velocity 20 km/h, **b** Initial velocity 40 km/h

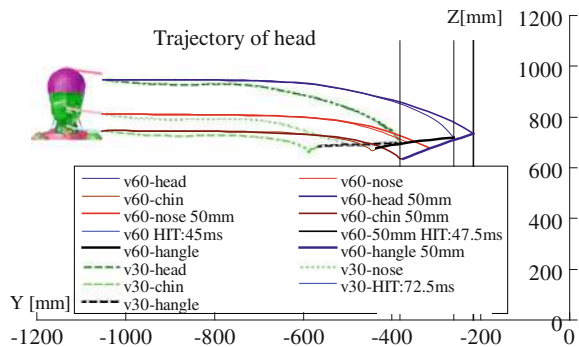
Fig. 12 Head impact time (HIT) and contact force F versus impact speed V (6YO pedestrian hp = 1.5)



They are slightly lower than the present FE model values. This can be well explained by the fact that the 3D detailed FE model based post-crash kinematics simulates more closely the flexible and damped overall dynamic movement of human pedestrians than that of the lumped-mass Madymo model simulation and consequently more likely to match the field accident data with higher accuracy. It should be noted that the order of magnitude and the point of change of the gradient of WAD are dependent on the frontal geometry of the vehicle.

Figure 12 shows the variation of head contact time and contact force F exerted on the head of 6YO child from the hood for different speeds of impact. At lower speed of impact ($V < 20 \text{ km/h}$), the gradient of the “increase of the head contact time” is more than that of the “decrease in head contact force F” with decrease of impact speed. It is partially due to the low tangential velocity and large rotation for 6YO child head at low speed of impact just before contact as explained in the previous section. This is not observed in case of adults. As mentioned in Ref. [8], GIDAS and also the PCDS accident data both indicate that for AIS + 2 injuries, percentage of AIS + 2 head injuries for children (56 %) is almost two times than that of the adult (31 %) even though the overall average speed of impact of head for adult is 10–15 km/h higher than that of the children. Large rotational velocity

Fig. 13 Comparison of head trajectory w.r.t speed
 $V = 60, 30 \text{ km/h}$ and
 $hp = 1.5, 1.55$ for 6YO
pedestrian



with respect to torso just before the head contact with the hood together with low tolerance level of injury are two possible influential factors. However, further investigation is necessary with advanced FE head injury model to study in detail about the minute mechanism of head injury in the future.

Figure 13 shows the comparison of head trajectories for two different speeds of impact ($60, 30 \text{ km/h}$) and the sensitivity of pedestrian height versus hood height ratio hp (1.5 and 1.55, 50 mm difference in height) for a 6YO pedestrian. Three sets of trajectories are plotted corresponding to the target marks fixed to (i) the top of head, (ii) the tip of nose and (iii) the bottom of chin with additional three vertical lines on Y-axis indicating the end points at the time of contact on the hood in vehicle co-ordinate system. The line joining the head, nose and chin positions at the time of impact in Y-Z plane indicates the angle of head impact on hood. With the increase of relative height ratio hp , 1.5–1.55 (i.e., relatively 50 mm taller pedestrian or 50 mm shorter hood opening), the head impact time HIT is increased by 6 % (45–47.5 ms) at $V = 60 \text{ km/h}$ but the head impact angle (v60-hangle-50 mm) is decreased. The change in HIT at $V = 45 \text{ km/h}$ is about 13 % but not plotted in this graph. Again, at low impact speed $V = 30 \text{ km/h}$, the WAD value is reduced by 130 mm but the head impact angle (v30-hangle) is increased, almost horizontal i.e., 90 degrees of rotation of head. As the inertia of the pedestrian upper body about the horizontal plane at the height of hood opening, is proportional to the square of the distance of COG of the upper body (refer Table 2), the time and the distance of flight of head are highly sensitive to hp .

6 Conclusions

This paper systematically discussed the main determining factors of post-crash pedestrian kinematics on the basis of a detailed study on NASS-PCDS. Those cases are categorized into four types (Type A–D) of post-crash pedestrian kinematics. In conclusion, post-crash pedestrian kinematics is determined mainly by impact speed, deceleration due to braking and pedestrian-vehicle height ratio.

These findings were verified and endorsed by a Human FE model. The study is summarized as follows:

Type A: Type A occurs at impact speed $V < 41 \text{ km/h}$. Shorter pedestrian height and higher forward opening height of vehicle lead to Type A kinematics. Shorter pedestrians tend to be thrown forward and are likely to be categorized as Type A. When the impact point is higher than the pedestrian COG, the maximum part of the crash impulse is converted to translational momentum rather than rotational. The translational momentum turns into the positive longitudinal velocity.

Type B: The Type B category shares the lower range of impact speed with Type A, although Type B mainly consists of taller pedestrians. An impact point below pedestrian COG produces rotational momentum, and therefore the proportion of the translational momentum is reduced. The pedestrian moves at a lower velocity than the vehicle, sliding on the hood.

Type C: Type C cases exceed Type B cases at the impact speed of 31–40 km/h. Type C group has a higher ratio of MAIS3 + injuries. Taller pedestrians tend to fall into Type C cases at the same impact speed. Deceleration of the vehicle may reduce the chance or risk of head injury.

Type D: Type D cases occur at the impact speed range higher than 60 km/h. In these cases, after pedestrians' lower extremities contact the frontal area of vehicles, their heads are most likely to directly contact the windshields without their head contacting to the hoods at all.

Head injury: The tangential velocity $v(t)$ and the rotational velocity $\theta'(t)$ are calculated from the trajectory of the head COGs for both the adult and the child FE models. Although the maximum value of the tangential velocity for the child head COG is slightly lower than that of the adult head COG, the maximum value of the rotational velocity for the child head COG is double that of the adult head COG. Relative height of the pedestrian and the vehicle hood edge, as well as the impact speed and braking, determines the head trajectory.

Ground-to-head-contact distance: The continuous distance from the head contact point to the ground surface, measured along the vehicle surface, depends on the impact velocity, pedestrian height and the front hood opening height. Higher impact speed makes the ground-to-head-contact distance longer and consequently leads to higher head-windshield injury risk. FE analysis results quantitatively support the past published literature. The ground-to-head-contact distance dependency on the impact speed is numerically verified by FE analysis. Detailed human FE analysis is essential to reconstruct crash cases correctly and to better articulate hidden information in accident databases. Kinematics of child is different from adults.

Acknowledgments The authors would like to acknowledge the members of users' support group of the ESI Japan, for PAM-CRASH and JARI for the adult human FE model.

References

1. Mizuno Y (2005) Summary of IHRA pedestrian safety WG activities. ESV 19 No. 138
2. Longhitano D et al (2005) Influence of vehicle body type on pedestrian injury distribution. In: SAE world congress
3. Serre T et al (2010) Child pedestrian anthropometry: evaluation of potential impact points during a crash. *Accid Anal Prev* 42(6):1943–1948
4. Kawabe Y (2012) Different factors influencing post-crash pedestrian kinematics. In: SAE world congress 2012-01-0271
5. Takayama S et al (2011) The clarification of individual injury mechanism difference in pedestrian FE model utilizing cadaver scaling and posturing techniques. ESV 22 No. 11-0414
6. Ejima S et al (2003) Modification and validation of human neck model under direct head loading. ESV 18 No. 333
7. Serre T et al (2009) Comparison between new data on children anthropometry and CRS dimensions. ESV 21, paper 09-0484
8. Yang J et al (2005) Correlation of different impact conditions to the injury severity of pedestrian real world accidents. ESV 19 paper 05-0352
9. Caris TL et al (2006) Cervical range of motion data in children. SAE 2006-01-1140
10. Schultz AB et al (1979) Mechanical properties of human lumbar spine motion segments part I. *Trans ASME* 101:79–84
11. Begeman PC et al (1994) Visco-elastic shear response of the cadaver hybrid III lumbar spine. In: SAE world congress 942205
12. Nishimura R et al (2002) Development of the human FEM model for child pedestrian. JSME spring convention, 20025504
13. Martin RB et al (1977) Age and sex-related changes in the structure and strength of the human femoral shaft. *J Biomech* 10:223–231

Development of an On-Board Pedestrian Detection System Using Monocular Camera for Driver Assistance Applications

Pongsathorn Raksincharoensak, Yuichi Sakai, Ikuko Shimizu, Masao Nagai, Dirk Ulbricht and Rolf Adomat

Abstract Recent statistical data of traffic accidents reveals that pedestrian fatalities are a particular priority in Europe and Japan. Many active safety systems for pedestrian protection based on sensor fusion approach such as millimeter wave radar, Laser Imaging Detecting And Ranging (LIDAR) and monocular/stereo camera are proposed. Aiming at large-scale system penetration in automobile markets, low-cost driver assistance system development becomes an important issue, therefore a monocular camera is one of solutions. To realize zero-traffic accident society, the objective of this paper is to develop a driver assistance system for pedestrian collision prevention based on using a monocular camera. As the concept of the system, moving objects on and nearby a crosswalk are interpreted as pedestrians. An on-board camera image processing algorithm is designed to detect the existence of a crosswalk in front of the vehicle. The feature extraction technique used in the algorithm is based on the feature called “cross ratio” of the crosswalk edges and the periodicity of the crosswalk paints. Then, nearby the detected crosswalk position, the region of interest is determined to be used in the moving object detection module. The position and the velocity of the moving object are obtained with the application of optical flow algorithm. Crosswalk image database in real-world traffic in Japan is constructed, and the precision of crosswalk detection is examined by using the database. Optical flow algorithm is applied on the region nearby the detected crosswalk in order to detect moving objects which are inferred as pedestrians. Image-based egomotion estimation is

F2012-F03-013

P. Raksincharoensak (✉) · Y. Sakai · I. Shimizu · M. Nagai
Department of Mechanical Systems Engineering, Tokyo University of Agriculture and Technology, Tokyo, Japan

D. Ulbricht · R. Adomat
Continental, A.D.C. GmbH, Lindau, Germany

used to compensate the error in distance estimation and pedestrian movement. The effectiveness of the proposed system is verified by test drives. The system can perform the detection of crosswalks in urban area in various weather conditions with high detection rate. Pedestrians on crosswalks can also be detected by Optical Flow-based image processing algorithm. The detectable range of the proposed pedestrian detection with crosswalk detection function is 20–25 m in front of vehicle. This approach does not claim to cover 100 % of all pedestrian accidents, but has the advantage of high robustness, low false alarm rate and cost efficient implementation. The feasibility of the proposed camera-based pedestrian detection system is shown in the paper. The validation of the crosswalk detection and pedestrian detection algorithm using real-world driving database will be conducted and demonstrated in the full paper.

Keywords Pedestrian protection • Active safety • Driver assistance system • On-board camera • Image processing • Crosswalk detection

1 Introduction

Statistical data of traffic accidents shown in Fig. 1 reveals that pedestrian fatalities are a particular priority in Europe and Japan. For instance, Figs. 1 and 2 show that pedestrian fatalities account for about 35 % of all road fatalities in Japan [1], about 12 % in US [2] and about 17 % in Europe [3]. Most pedestrian accidents relate to situations when pedestrians are crossing a road, as indicated in Fig. 2 [4]. Advanced driver assistance systems which implement technical solutions for pedestrian protection could help to lower the number of these fatalities. Current approaches make use of stereo cameras, millimeter wave radar and stereo camera sensor fusion or stereo infrared sensors for example (see [5–10]).

In this research we scope on the use of monocular camera and millimeter wave radar. The monocular camera, practically used for several existing functions of driver assistance systems, has potential to be also used for pedestrian classification [11, 12], while the millimeter wave radar can be used to directly measure the distance from the host vehicle to pedestrians for a precise collision risk assessment.

Two approaches of pedestrian detection will be considered. The first approach is based on a sensor fusion technique which combines the information of moving objects from a millimeter wave radar and the crosswalk location information from a monocular camera. The second approach employs an appearance-based pedestrian classification algorithm which leads to a high computational cost in image processing.

To reduce the computational cost of the pedestrian classification algorithm, the authors have presented the effectiveness of the first approach in [13], presenting an alternative approach of the pedestrian detection algorithm based on the assumption that moving objects on a crosswalk can be interpreted as pedestrians. Consequently, the pedestrian classification module is not required in the image

Pedestrian Fatalities around the world	 (2009)[1]	 (2009)[2]	 (2009)[3]
Number of fatalities	1,717	4,092	6,233
% of total traffic fatalities	35%	12%	17%
% of pedestrian Fatalities at night time	69%	69%	46%

[1] ITARDA Information No.83, 2010 May

[2] NHTSA Releases 2009 Pedestrian Fatality/Injury Statistics

[3] European Road Safety Observatory 2009 DaCoTA

Fig. 1 Pedestrian fatalities around the world

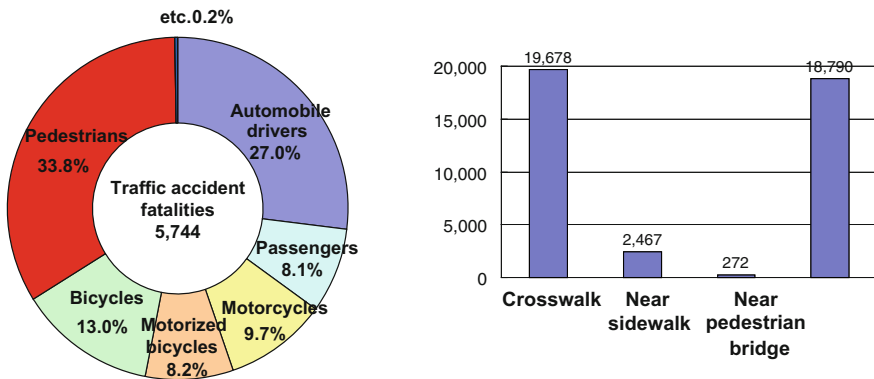


Fig. 2 Detail of pedestrian accidents in Japan from the traffic-accident database in 2007 (The right chart shows situations in which accidents with pedestrians occur.) [4]

processing task, and it is necessary to develop an algorithm to detect the existence of crosswalk in front of the vehicle. This approach does not claim to cover 100 % of all pedestrian accidents, but has the advantage of high robustness, low false alarm rate and cost efficient implementation.

2 Experimental Vehicle

An experimental vehicle equipped with a monocular CMOS camera and a PC for data acquisition and processing is used to investigate the feasibility of the proposed approach. Sensors used in production vehicles are utilized: a monocular CMOS

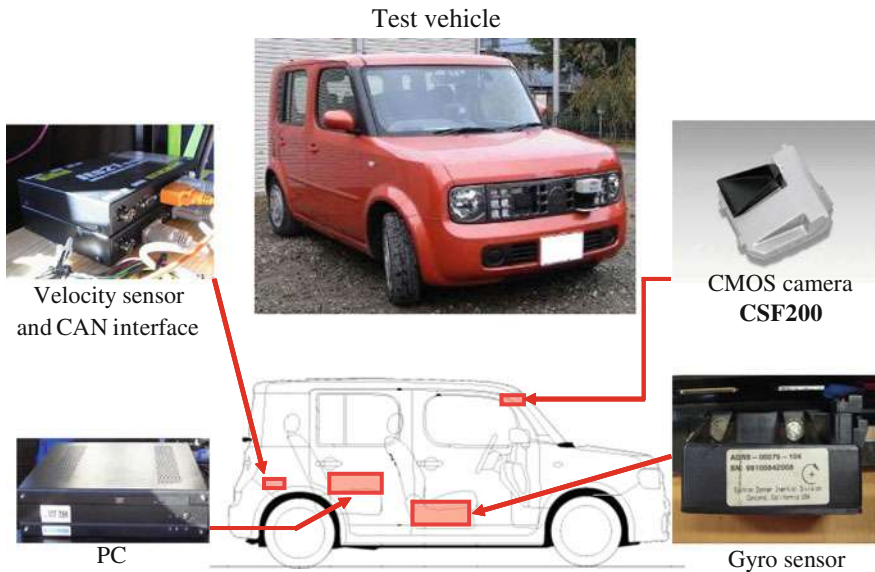


Fig. 3 Experimental vehicle

Fig. 4 Crosswalk and pedestrian image taken by the camera



camera which can be used for the purposes of lane marker detection, traffic sign recognition, or vehicle detection. The sensor and measurement system configuration on the experimental vehicle is shown in Fig. 3.

3 System Design Principle

As the concept of the system, moving objects on and nearby a crosswalk are interpreted as pedestrians. Consequently, the image processing algorithm based on the images captured from the on-board camera is designed to detect the existence

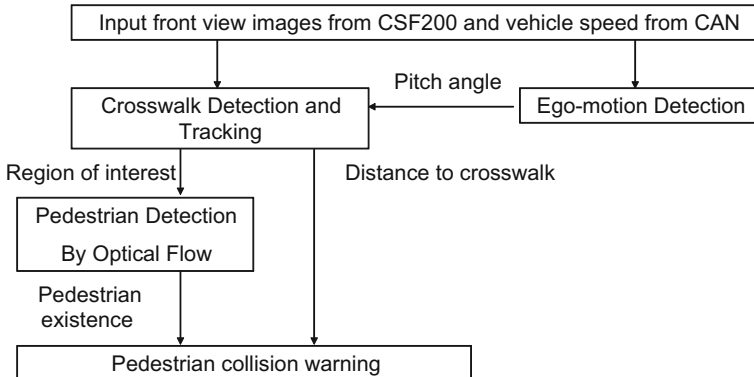


Fig. 5 Schematic diagram of the pedestrian collision warning system

of a crosswalk in front of the vehicle. The feature extraction technique used in the algorithm is based on the value of cross ratio of crosswalk edges and the periodicity of the crosswalk paints. Then, the moving object position and velocity obtained by the optical flow computation are utilized to infer that a pedestrian is on the crosswalk in front of the vehicle. Figure 4 shows an example of image data by the measurement and testing system on the experimental vehicle. A warning can be provided to the driver when there is a potential of a collision. Figure 5 shows the schematic diagram of the pedestrian collision warning system.

4 Crosswalk Detection

To detect a crosswalk, a feature called “cross ratio” of four collinear points is utilized. Since the cross ratio is invariant under the perspective projection, the cross ratio of the crosswalk in 3D space is the same as that of its image (Fig. 6). Here, the cross ratio $[abcd]$ of four points a, b, c, d are calculated as follows [8]:

$$[abcd] = \frac{\overline{ac}}{\overline{bc}} \cdot \frac{\overline{bd}}{\overline{ad}} \quad (1)$$

where, the symbol written as \overline{ab} refers to the distance between the point a and the point b.

The flow diagram of our crossing detection algorithm is shown in Fig. 7. First, to extract boundaries of the white lines on a road, an image captured by the camera is processed by two algorithms: binarization and edge detection. To extract a number of edges from the input image, Canny’s algorithm is employed [9]. Next, an AND operation of the two processing results is calculated in order to reduce the errors influenced by shades on roads. Then, the system classifies the pattern of vertical edge change into two categories: (1) the boundary where the intensity changes from dark to bright, and (2) the one from bright to dark.

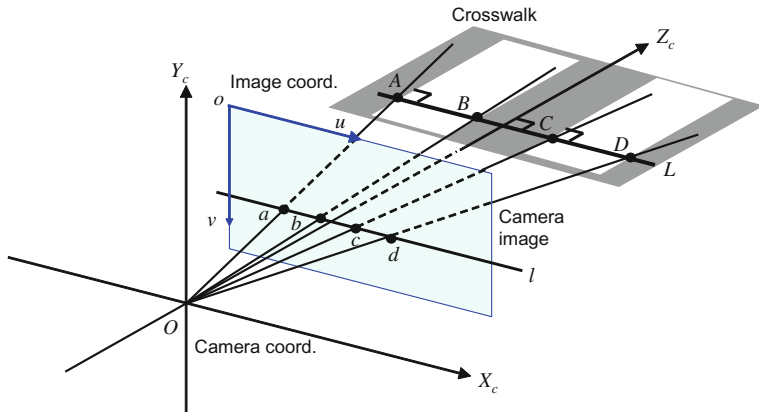


Fig. 6 Description of cross ratio in each coordinate

Finally, we calculate the cross ratios of two pairs of boundaries. Here, it is assumed that the vehicle is driving perpendicular to crosswalk, therefore the algorithm calculates the cross ratio from four points (a, b, c, d in Fig. 6) which have the identical vertical axis level (v) on the image plane. In this step, we reduce the candidates of crosswalk by using the periodicity of the crosswalk by checking the number of boundaries at the identical vertical axis level (v) on the image plane and the width between two edges. Then, the cross ratio [abcd] of four points a, b, c, d are calculated according to the formula in Eq. (1).

According to road traffic regulations in Japan, the value of cross ratio is within the range from 0.203 to 0.309. The crosswalks in Germany are in the range between 0.198 and 0.316. The crosswalk detection is made more robust by the following heuristic. The crosswalk is detected when there are more than three pairs of edge change patterns at the same vertical axis level (v) in the image plane and more than two pairs of edges which are within the range of the cross ratio of crosswalk described above. Moreover, the continuity of the crosswalk detection result at each sampling time is checked with the detection results from six previously-acquired image frames in order to reduce misdetections.

In addition, a tracking algorithm by using the optical flow of four corners of the crosswalk is employed to improve the continuity in the crosswalk detection algorithm. An example of optical flow computation result is shown in Fig. 8.

Urban road image sequences in Japan which include a crosswalk in front of the vehicle are used as a test data set to evaluate the performance of the crosswalk detection algorithm. The detection performance was evaluated by the distance to each crosswalk. The performance indices True Positive and False Negative are used here. True Positive refer to the cases that the system can correctly detect crosswalks, whereas False Negative refer to the cases that the system fails to detect crosswalks where it should detect. The evaluation result is shown in Fig. 9. The system shows high true positive rate over 90 % when the distance to crosswalk is long up to around 20 m.

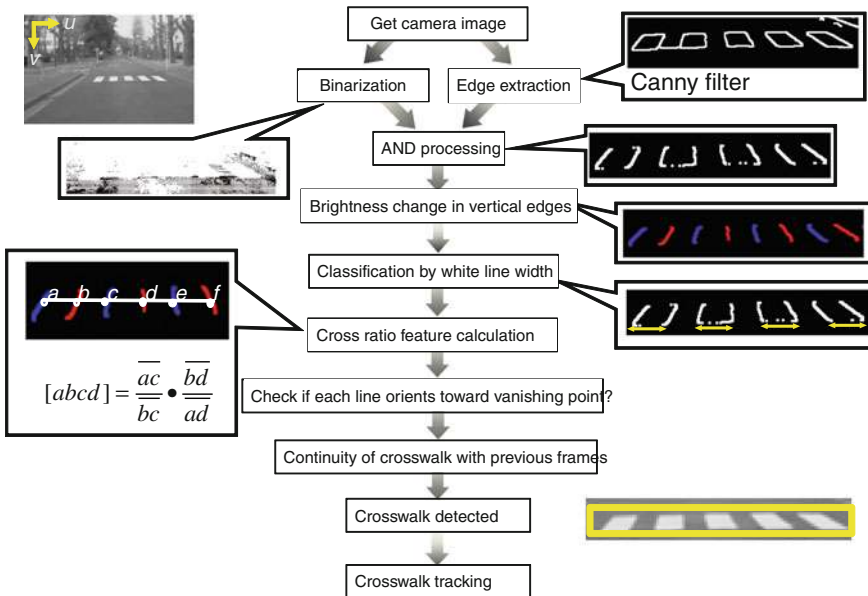


Fig. 7 Process flow for crosswalk detection

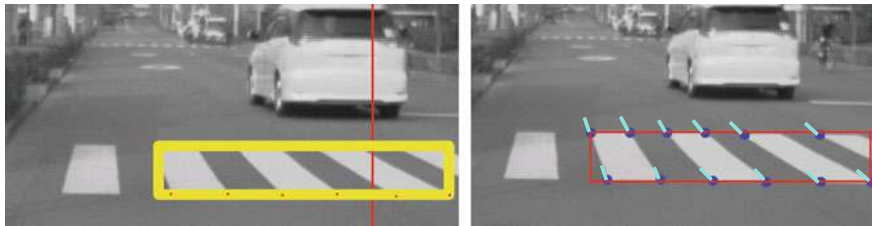


Fig. 8 Optical flow of four corners of crosswalk

5 Optical Flow for Pedestrian Detection

Figure 10a shows the flowchart of the pedestrian detection algorithm based on optical flow. First, the region of interest (ROI) which covers the detected crosswalk are extracted based on the estimated distance to the crosswalk. Then, the optical flow is computed inside the region of interest (ROI) to get the optical flow vectors. Next, the optical flow vectors which deviate from the epipolar lines and the distance between the epipolar lines and the edge of the optical flow vector are larger than a certain value are classified as “Outliers” as shown in Fig. 10b. The outliers which are close together are grouped as moving objects. In the proposed method, the moving objects exist on the crosswalk, so the objects can be inferred as pedestrians. Figure 11 shows an example of optical flow computation result for

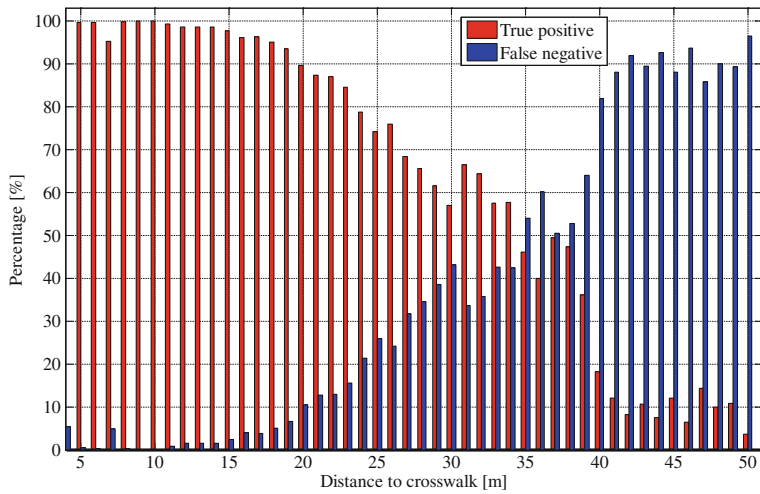


Fig. 9 Crosswalk detection performance by the distance

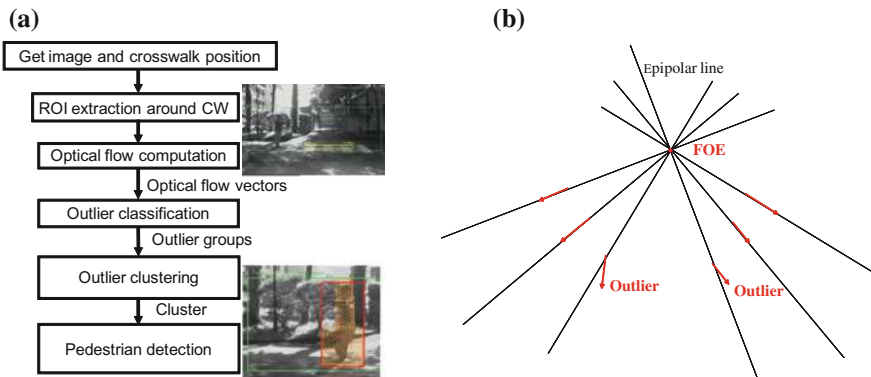


Fig. 10 Flowchart of pedestrian detection by optical flow. **a** Pedestrian detection flowchart. **b** Focus of Expansion (FOE), Epipolar lines and outliers

pedestrian detection. The red arrows show the outlier deviated from the epipolar lines.

Figure 12 shows the pedestrian detection result by the integration of the crosswalk detection and the pedestrian detection system. The crosswalk can be detected at a distance of 19.0 m and the system indicates “CROSSWALK IS DETECTED” message. When the system detects the frontal pedestrian, the message “CROSSWALK OCCUPIED” is indicated.



Fig. 11 Pedestrian detection result by optical flow

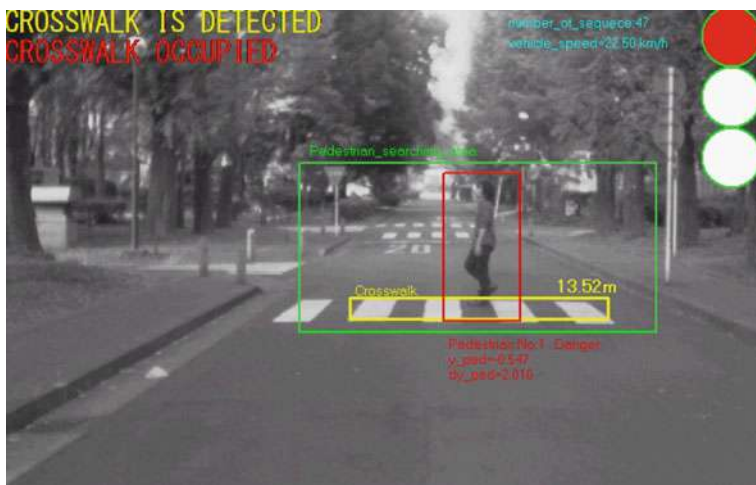


Fig. 12 Detection result of a pedestrian on a crosswalk

6 Conclusions

This paper described an on-board pedestrian detection and collision warning system by using a monocular camera. The design principle proposed here to deal with the pedestrian detection problem is based on the assumption that objects moving along a crosswalk can be inferred as pedestrians under defined circumstances. This principle simplifies the image processing unit computation as it does not require a computationally expensive appearance based pedestrian classification.

method. A key concept of the approach is the detection of a crosswalk by image processing methods based on the cross ratio feature. Moving objects on the crosswalk can be detected with the application of the optical flow feature. The sensor setup on the experimental vehicle for pedestrian detection was presented and experimental results which show that the proposed sensor fusion approach works in practice were given.

- In future, to improve the robustness of the proposed pedestrian detection method, the following investigations will be conducted.
- The investigation of the robustness of the crosswalk detection algorithm against weather conditions.
- The effectiveness of the proposed pedestrian protection system will be analyzed based on statistical data.
- The pedestrian collision risk assessment will be quantitatively conducted for the design of a pedestrian collision warning system.

References

1. ITARDA (2010) Special issue on vehicle to pedestrian accidents. *ITARDA Inf* 83:1–12
2. NHTSA. Traffic safety facts 2009 data. DOT HS 811 394
3. European Road Safety Observatory. Traffic safety basic facts: pedestrians. DaCoTA
4. ITARDA. Pedestrian accidents, ITARDA statistical data, Japan, 2007. http://www8.cao.go.jp/koutu/taisaku/h20kou_haku/pdffiles/honpen/gh1_112.pdf
5. Bishop R (2005) Intelligent vehicle technology and trends. Artech House, Boston, pp 144–150
6. Gandhi T, Trivedi MM (2007) Pedestrian protection systems: issues, survey, and challenges. *IEEE Trans Intell Transp Syst* 28(3):413–423
7. Gavrila DM, Munder S (2007) Multi-cue pedestrian detection and tracking from a moving vehicle. *Int J Comput Vision* 73(1):41–59
8. Coolingh E, Eidehall A, Bengtsson M (2010) Collision warning with full auto brake and pedestrian detection—a practical example of automatic emergency braking. In: Proceedings of IEEE ITSC'10, pp 55–160
9. Henn RW, Grotendieck T, Knoop S, Braeuchle C (2011) Active pedestrian protection by surround sensor technologies. In: Proceedings of 18th world congress on ITS, Florida, USA, 2011
10. Keller CG, Dang T, Fritz H, Joos A, Rabe C, Gavrila DM (2011) Active pedestrian safety by automatic braking and evasive steering. *IEEE Trans Intell Transp Syst* 12(4):1292–1304
11. Viola P, Jones M, Snow D (2003) Detecting pedestrians using patterns of motion and appearance. In: Proceedings of the ICCV'03, vol 2, pp 34–741
12. Munder S, Gavrila DM (2006) An experimental Study on pedestrian classification. *IEEE Trans Pattern Anal Mach Intell* 28(11):1863–1868
13. Raksincharoensak P, Takimoto Y, Muroi H, Shimizu I, Nagai M, Darms M, Adomat R (2009) Development of a pedestrian collision warning system by sensor fusion of monocular camera and millimeter wave radar. In: Proceedings of AAET 2009 symposium (Automatisierungs-, Assistenzsysteme und eingebettete Systeme für Transportmittel), Braunschweig, Germany, pp 1–10

Pedestrian Detection by Neuromorphic Visual Information Processing

Han Woo Joon, Kim Chulsoo and Han Il Song

Abstract There have been many researches being done about pedestrian detection, as pedestrians are exposed to lot of danger on the street according to the fatality statistics. To increase the well-being of the pedestrians there has been many breakthroughs in computer vision researches and its application in actual vehicles. However, the reliability and the complexity of algorithm are still very much in doubt to improve the safety of pedestrian. Most computer vision-based algorithms are complex in nature which will in-turn demand the cost issue for the vehicle manufacturers, while most algorithms' reliability drops significantly in night time (dark surroundings), raining or both conditions. In this work, we try to capture the reliability of our "eyes" and the accuracy of computer vision by implementing neuromorphic visual information processing. Our neuromorphic visual information processing uses basis of result from Hubel and Wiesel's experiment on cat's striate cortex. From the result, we have formed our unique neuromorphic visual information processing which can mimic the response given by the cat's striate cortex to the same input. And since its neuromorphic implementation, it is possible to implement it with relatively simple CMOS technology which would reduce the cost in possible future implementation. The algorithm operates by extracting different directions of orientation features using our neuromorphic visual information processing then neural network is applied to it with a template that resembles upper torso of human body. Our method of orientation feature extraction and the usage of neural network ensure the reliability of our algorithm to perform well under other conditions such as in grey

F2012-F03-017

H. W. Joon (✉) · H. I. Song
Korea Advanced Institute of Science and Technology, Daejeon, Korea

K. Chulsoo
Hyundai Motor Co., Seoul, Korea

surroundings (dusk environment). Current results from data captured in various places in Korea, in London and using the Daimler database shows that our algorithm performs successfully. Those sets of data all varies as the surrounding is different. Especially, the dataset captured in London is with the narrow roads and heavier presence of pedestrians or cyclists. However, despite all this, the detection was successful, as only few changes to parameters could meet the change in the image type. In conclusion, this research has successfully detected pedestrian by using the CMOS neuromorphic approach so as to reduce the cost for implementation whilst improving on the accuracy and reliability of the detection, over 90 % for the video dataset captured during both day and night. Currently there is also an on-going project with Hyundai Motor Co., to implement a hardware that uses our work to detect pedestrians so as to warn them when Hyundai's electric vehicle is near them.

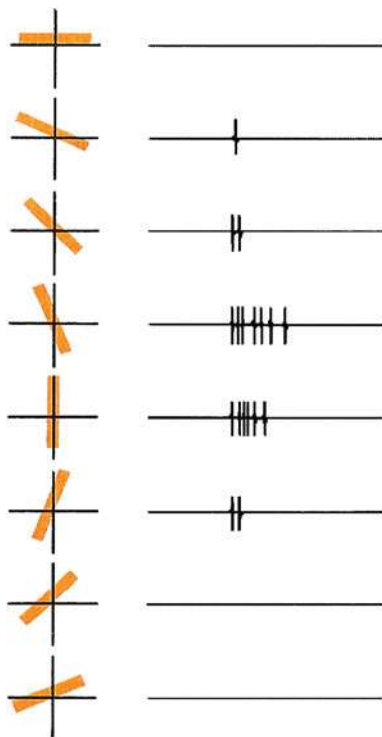
Keywords Pedestrian detection • CMOS • Neuromorphic • Electric vehicle • Neural network

1 Introduction

There have been many researches being done in both academia and industry about pedestrian detection. Pedestrians are exposed to lot of danger on the street as reflected by statistics collected over the years such as, in United States, in 2001, pedestrian fatalities accounted for 12 % of all fatalities [1]. Recently there has been much works done to improve the safety of personnel involved with vehicle such as passengers and pedestrians. Many of vehicle manufacturers offer such system, for example; pedestrian detection to assist in emergency braking should the driver fail to acknowledge the pedestrian in time and head and eye detection to give off alarm should the driver be detected as sleeping. However, these systems have limited impact to improving the safety since the system's reliability comes into question. Pedestrian detection problem, for example, is tackled by using different forms of sensors such as radar, cameras or combination of both [2]. The usage of radar allows the user to detect obstacles that are further away than a visual sensor (camera) can however, in a heavy traffic environment or on busy street of major cities of the world obstruction of other objects will reduce the accuracy and the reliability of the result. Use of visual sensor, however, can detect the pedestrian or any other object using right algorithm.

There have been many works done in using a camera with computer vision algorithm or a combination of camera and radar to improve the accuracy and reliability. Although, conventional computer vision algorithms are effective in their condition of usage [3], they, at most times, lack the robustness of the human vision. We describe here the early vision of bio-inspired implementation of

Fig. 1 Response of the cat's cortex when a rectangular slit of light of different orientations is shown [4]



primary visual cortex, based on the neuron of Hodgkin–Huxley formalism and the visual cortex experimentation of Hubel and Wiesel [4]. In this paper, the elements of neuromorphic processing of visual cortex are proposed with the orientation tuned map of synaptic weights and the spiking neuron, based on the programmable linear MOSFET conductance.

2 Neuromorphic Processing of Visual Information

Although there is not a definite model of visual cortex for the robustness of human vision, Hubel and Wiesel's research on cat's striate cortex confirmed the idea on the functioning of simple cell [4]. It is from this discovery which motivated various theories of object recognition from characters to complex natural images [5].

The motivation for our research was found from the result of the well-known experimentation of simple cell by Hubel and Wiesel as shown in Fig. 1. In this paper, the proposed bio-inspired visual information processing is based on the neuromorphic simple cell using Hodgkin and Huxley formalism, while it can be implemented by analogue-mixed CMOS VLSI circuits. By mimicking the behaviour of simple cell as in Fig. 2, the similar robustness of visual cortex can be



Fig. 2 Simulated neuron behaviour of visual cortex in Fig. 1 by the CMOS neuromorphic neuron

achieved. The simulation result in Fig. 2 shows the consistent outcome as the Hubel and Wiesel's experiment shown in Fig. 1, where the tuned feature orientations are evaluated for the visual stimulus of 50×50 pixels.

The basic neuromorphic system of Fig. 3 is designed to implement the bio-inspired visual signal processing, for the purpose of detecting various object types from human to vehicle, and others. The NN detector template of human object is based on the shape of head-torso, where it allows the flexible postures of head such as side-view or rear view.

The objects in the outdoors can be occasionally obstructed by various reasons. For an example, pedestrians in Fig. 4 are shielded so that it is somewhat occluded, due to the special clothing for the ceremony. The case is taken to evaluate the effect on the neuromorphic processing of half-blocked image. The image for the result of neuromorphic orientations processing shows the object feature behind the textile shield, as presented in the right image of Fig. 4.

In Fig. 4, the more than half of a pedestrian behind is unseen and the road marks of pedestrian crossing are partly obstructed. The right image in Fig. 4 demonstrates the robustness or the wide operation range of neuromorphic processing, enhanced by the combination of orientation processing and image data.

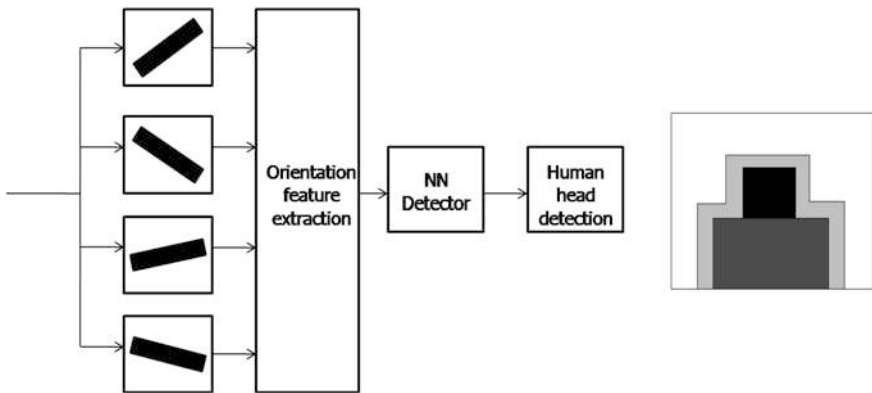


Fig. 3 From left to right neuromorphic vision for human detection, inspired by the visual cortex; the neural network detector of head-torso shape



Fig. 4 From left to right: close-up of pedestrians—heads and torsos are shielded; the image after enhanced neuromorphic orientation processing—heads and torsos are revealed, while the road marks and the person behind the obstruction (cloth textile) become also exposed

The half hidden road marks and obstructed pedestrian are exposed, while the head and torso behind the shield are clearly revealed. The enhanced neuromorphic processing demonstrates the detection of human object using the original head and torso template, regardless of textile shield under the big hat.

It demonstrates the applicability of neuromorphic visual information processing to various uncertain environments, like the half transparent fuzzy or smoky image.

3 Human Object Detection and Pedestrian Detection

The human head, as we know, is comprised of differently directed orientations, regardless of the viewing direction. By using a few different orientation feature extractors mimicking the function of simple cell in the visual cortex, the heads of human object can be represented as the populated area of the output of feature extractors. The upper torso linked to the head also has the pattern of feature

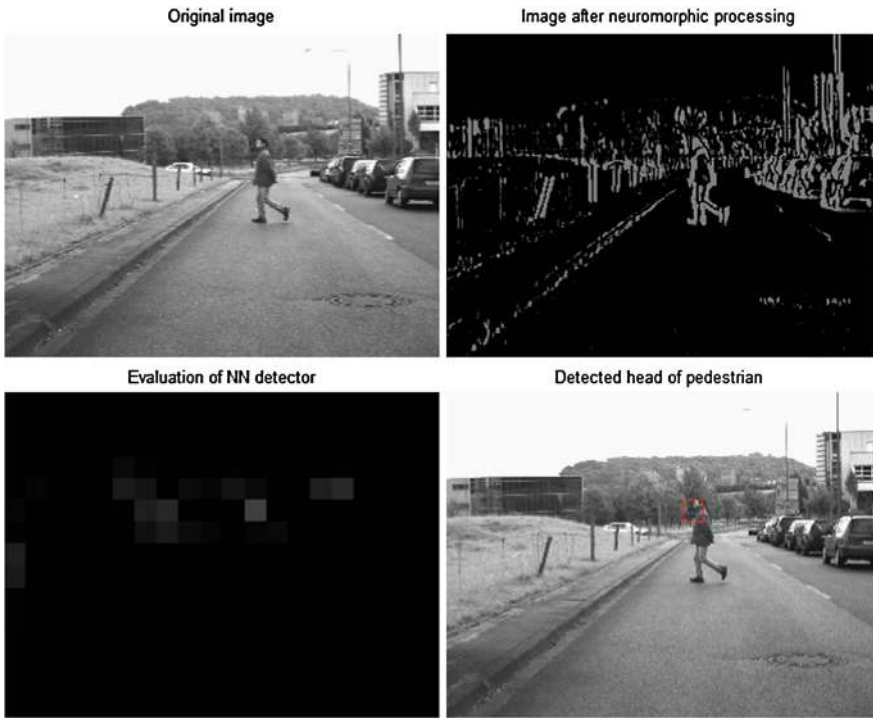


Fig. 5 From top left to clockwise original image; image after neuromorphic processing; detected pedestrian's head located in the original image; probability of detected head area of pedestrian

extractor output. The template of Fig. 3 representing the human figure based on the simulated visual cortex is applied as synaptic weights of neural networks to locate the human head. Though there can be always the quick changes in luminance or human objects, the proposed neuromorphic vision has the robust performance as it is based on the statistics of orientation features, rather than relying on particular exact patterns or colours.

The neuromorphic visual information processing of Fig. 3 is used to detect the pedestrian in the images of Daimler's data set. The images of Fig. 5 illustrate the flow of neuromorphic processing for pedestrian detection. The neuromorphic processing resulted in the head area of relatively as populated by orientations. The detected head location of pedestrian shown in the bottom left image of Fig. 5 is the highlighted patch as an outcome of neural network detector, which is located as a red box in the original image.

In this paper, the purpose of pedestrian detection is to warn the pedestrian about the presence of silent electric vehicle automatically, to avoid the risk of accident. The current electric vehicles like Ray in Fig. 6 are usually equipped with an artificial sound generator, such as the virtual engine sound system (VESS). The VESS is controlled manually, which is switched on or off by the driver as seen



Fig. 6 From *left* to *right* an electric vehicle (Ray from Hyundai Motors Co.); the switch to activate Virtual Engine Sound System



Fig. 7 Video frame of a cyclist; video recorded from vehicle in February 2012, London (UK)

in Fig. 6. Its operation is not controlled by the presence of pedestrians nearby, and the active VESS based on pedestrian detection is desired for more efficiency in safety and the comfort of driving.

For evaluating the robustness to operational environment, the ordinary vehicle-purpose DVR was chosen to prepare the data set from various locations. The image sensor has the resolution of 1280×720 and the frame rate of 30 frames per second.

The image in Fig. 7 is for detecting the cyclist using the pedestrian detection algorithm, because there is no difference in detecting a human object based on head-torso features same system as to the one used to obtain the result of Fig. 5 is used. The image was taken at sunny day time. Though the cyclist is appeared in darker colour and from the back view, the result of neuromorphic processing shows the most high-highlighted area together with the car interior in Fig. 8. The NN detector has the size of 31×64 (width \times height) and the head-torso shape in

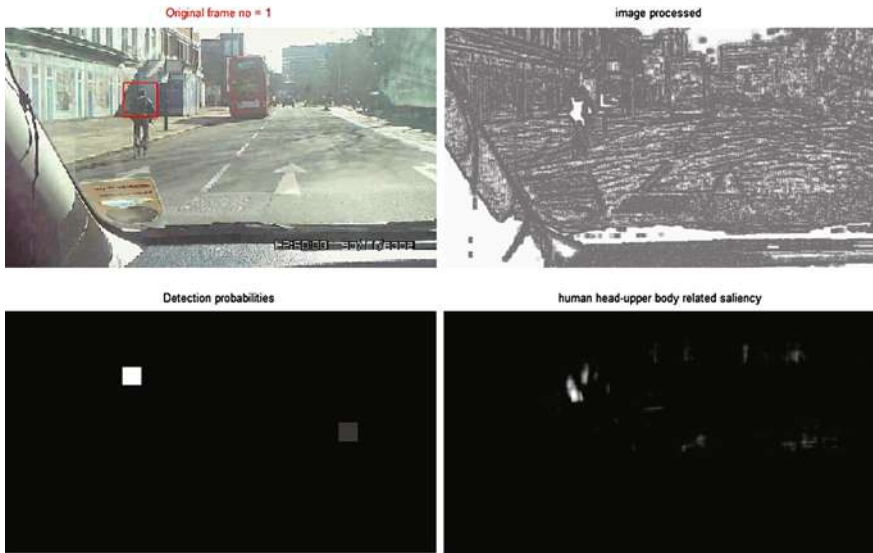


Fig. 8 From *top left* to *clockwise* original image, image after enhanced neuromorphic processing, saliency map related to head-torso, probability of detected head area of human object



Fig. 9 Cropped image of neuromorphic processed for valid view, eliminating the vehicle interior

Fig. 3. The interim result of NN computation, the saliency map still shows the high probability of human object in the front,

As the structure of car interior is fixed and not relevant to pedestrian detection, those area is removed from the subject of evaluation by resetting zeros as in Fig. 9.

The head area of human object is located as a white patch in bottom left image, where the patch is evaluated as the summation of local saliency map and operated by the threshold value. The corresponding location in original image shows the correct detection of cyclist. The distance range of detection is determined by the scale of neuromorphic processed image, to match the NN detector.

The robustness of the neuromorphic pedestrian detection is evident with the successful detection of the pedestrian in night time image, as shown in Fig. 10. The general luminance of the image is quite low and there are lot of light sources



Fig. 10 Night time video frame; video recorded from vehicle in November 2011, Daejeon (Korea)

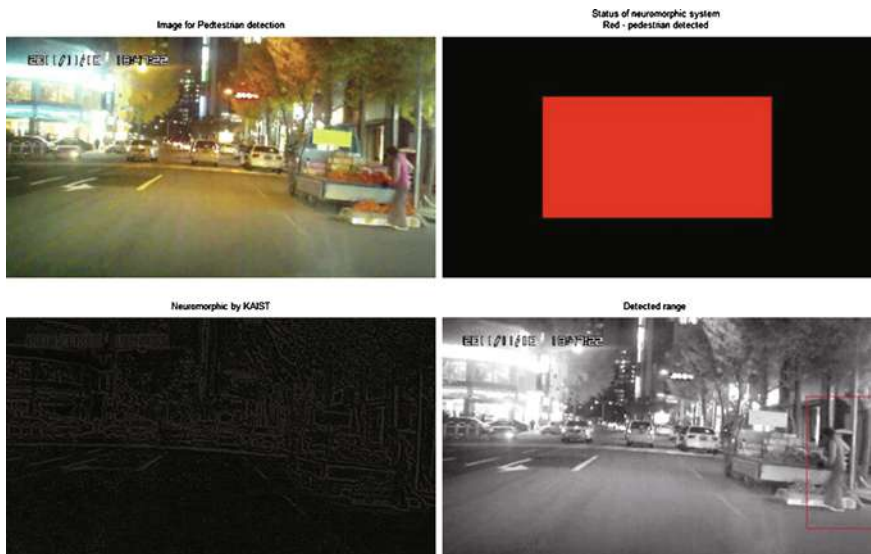


Fig. 11 From *top left* to *clockwise* original image, output to turn on the active VESS, detected pedestrian/human object in a red box, image after neuromorphic processing

captured which will disturb visual processing that are based on luminance. In Fig. 11, the resulting detection is shown in grey image as the algorithm in this paper does not use colour information. The image with a large red box in Fig. 11 represents the pedestrian detection near the vehicle, and is expected to control VESS automatically.

Table 1 Detection rate for images captured in daytime

Day time	Frames including human object	Frames without human object	Total number of frames
Number of frames	18	88	106
Positive detection	15	88	103
Negative detection	3	0	3

Table 2 Detection rate for images captured in night time

Night time	Frames including human object	Frames without human object	Total number of frames
Number of frames	99	5	104
Positive detection	89	2	91
Negative detection	10	3	13

The performance of neuromorphic pedestrian detection is summarized in the Tables 1 and 2, below, showing the experimental results, for the operation in day time and in night time respectively. The result shows the accuracy of over 90 %, where the image sensor has the resolution of 1280×720 and the frame rate of 30 per second. The test locations in day time or night time are of the same location taking same route, though days of test were different.

4 Conclusion

The neuromorphic visual information processing is proposed and evaluated for the pedestrian detection, which shows the performance of over 90 % of detection in simulated test as well as the detection in both day time and night time. The biggest challenge for pedestrian detection or any object detection using visual sensors is the change in luminance over time, where the most of pedestrian detection methods using the ordinary sensor have poor detection rate at night or dusk environment. In this paper, using neuromorphic approach, the improved performance of detection is demonstrated by the successful operation in the night time. It is worth noting that in the night time driving there are still other light sources for human driver such as headlights or etc. The basis for this algorithm came from biological eye and brain to give robustness to the algorithm so that it can be used in different applications without many modifications to the original algorithm. The algorithm is proven to possess such robustness as the human head-torso detection applicable to both pedestrian detection and cyclist detection at the same time. The neuromorphic visual processing demonstrated the advantage of its applicability to various uncertain environment like half-transparent obstacle, in addition to the low cost and reliable implementation in CMOS VLSI based on the earlier test device and simulated evaluation.

Acknowledgments This research work was supported in part by the Ministry of Knowledge and Economy of Korea under the Grant for Next Generation Passenger Electric Vehicle Development, and in part by the National Research Foundation of Korea under the Grant 20110027180F.

References

1. US Department of Transport (2003) Technical report: pedestrian roadway fatalities, April 2003, HS 809 456
2. Gerónimo D, López AM, Sappa AD, Graf T (2010) Survey of pedestrian detection for advanced driver assistance systems. *IEEE Trans Pattern Anal Mach Intell* 32(7):1239–1258
3. Yilmaz A, Javed O, Shah M (2006) Object tracking: a survey. *ACM Comput Surv* 38(13):1–45
4. Hubel DH, Wiesel TN (1959) Receptive fields of single neurons in the cat's striate cortex. *J Physiol* 148:574–591
5. Riesenhuber M, Poggio T (1999) Hierarchical models of object recognition in cortex. *Nat Neurosci* 2:1019–1025

Development of an On-Board Crosswalk Detection for Pedestrian Protection Using a Monocular Camera

**Yuichi Sakai, Pongsathorn Raksincharoensak, Ikuko Shimizu,
Masao Nagai, Dirk Ulbricht and Rolf Adomat**

Abstract Recent, there are many pedestrian accidents in Europe and Japan, and the rate of pedestrian fatalities is higher than the other accidents. These pedestrian accidents usually occur in complex environment such as residential or urban areas where many people exist. Many proposed active safety systems use the sensor fusion approach such as a millimeter wave radar, a LIDAR (Laser Imaging Detecting and Ranging) sensor and a monocular/stereo camera. However, it is difficult for these systems to prevent pedestrian accidents in complex environment. In addition, it is important for such active safety systems to be commercialized at a low cost and be equipped in a simple way, aiming at large-scale system penetration in automobile markets. Therefore, we developed an on-board crosswalk detection system by using a monocular camera and a warning system depending on pedestrian recognition. Crosswalk is located at the position where many people appear and the majority of pedestrian accidents occur. Based on the fact, the proposed system can achieve less false-alarm-rate of pedestrian detection by a combination of crosswalk detection and pedestrian detection. This paper shows the necessity of the crosswalk detection and warning system by the statistical data about pedestrian accidents near crosswalk. An experimental vehicle sensor and equipments used for testing are described. Next, this paper proposes an algorithm of the crosswalk detection and warning system including pedestrian detection with optical flow approach. Finally, this paper shows the feasibility of the system from

F2012-F03-019

Y. Sakai (✉) · P. Raksincharoensak · I. Shimizu ·
Masao Nagai

Department of Mechanical Systems Engineering, Tokyo University of Agriculture and
Technology, Tokyo, Japan

D. Ulbricht · R. Adomat
Continental, A.D.C, GmbH, Lindau, Germany

the relationship between the detection distance and the rate of detection by using many video data captured in city road in Tokyo.

Keywords Pedestrian protection · Active safety · Driver assistance system · On-board camera · Image processing · Crosswalk detection · HMI

1 Introduction

Statistical data of traffic accidents shown in Fig. 1 reveals that pedestrian fatalities are a particular priority in Europe and Japan. For instance, Figs. 1, 2 show that pedestrian fatalities account for about 35 % of all road fatalities in Japan [1], about 12 % in US [2] and about 17 % in Europe [3]. Most pedestrian accidents relate to situations when pedestrians are crossing a road, as indicated in Fig. 2. Advanced driver assistance systems which implement technical solutions for pedestrian protection could help to lower the number of these fatalities. Current approaches make use of stereo cameras, millimeter wave radar and stereo camera sensor fusion or stereo infrared sensors for example (see [4–9]).

In this research we scope on the use of monocular camera and millimeter wave radar. The monocular camera, practically used for several existing functions of driver assistance systems, has potential to be also used for pedestrian classification [10, 11], while the millimeter wave radar can be used to directly measure the distance from the host vehicle to pedestrians for a precise collision risk assessment.

Two approaches of pedestrian detection will be considered. The first approach is based on a sensor fusion technique which combines the information of moving objects from a millimeter wave radar and the crosswalk location information from a monocular camera. The second approach employs an appearance-based pedestrian classification algorithm which leads to a high computational cost in image processing.

To reduce the computational cost of the pedestrian classification algorithm, the authors have presented the effectiveness of the first approach in [12], presenting an alternative approach of the pedestrian detection algorithm based on the assumption that moving objects on a crosswalk can be interpreted as pedestrians. Consequently, the pedestrian classification module is not required in the image processing task, and it is necessary to develop an algorithm to detect the existence of crosswalk in front of the vehicle. This approach does not claim to cover 100 % of all pedestrian accidents, but has the advantage of high robustness, low false alarm rate and cost efficient implementation.

Pedestrian Fatalities around the world	 (2009)[1]	 (2009)[2]	 (2009)[3]
Number of fatalities	1,717	4,092	6,233
% of total traffic fatalities	35%	12%	17%
% of pedestrian Fatalities at night time	69%	69%	46%

[1] ITARDA Information No.83, 2010 May

[2] NHTSA Releases 2009 Pedestrian Fatality/Injury Statistics

[3] European Road Safety Observatory 2009 DaCoTA

Fig. 1 Pedestrian fatalities around the world

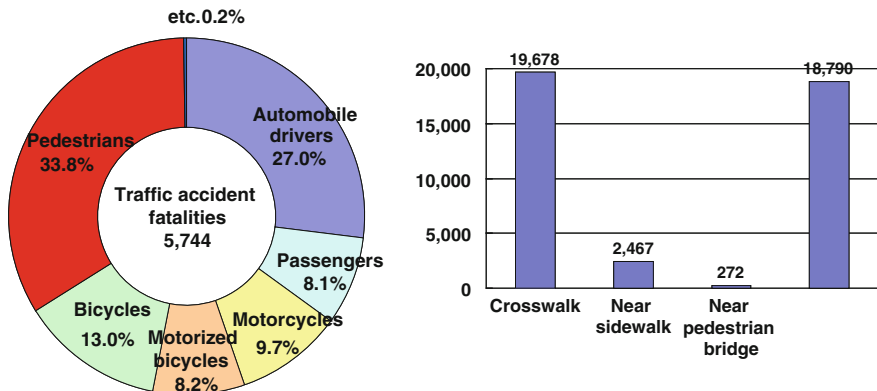


Fig. 2 Detail of pedestrian accidents in Japan from the traffic-accident database in 2007 (The right chart shows situations in which accidents with pedestrians occur.) [2]

2 Experimental Vehicle

An experimental vehicle equipped with a monocular CMOS camera and a PC for data acquisition and processing is used to investigate the feasibility of the proposed approach. Sensors used in production vehicles are utilized: a monocular CMOS camera which can be used for the purposes of lane marker detection, traffic sign recognition, or vehicle detection. The sensor and measurement system configuration on the experimental vehicle is shown in Fig. 3.

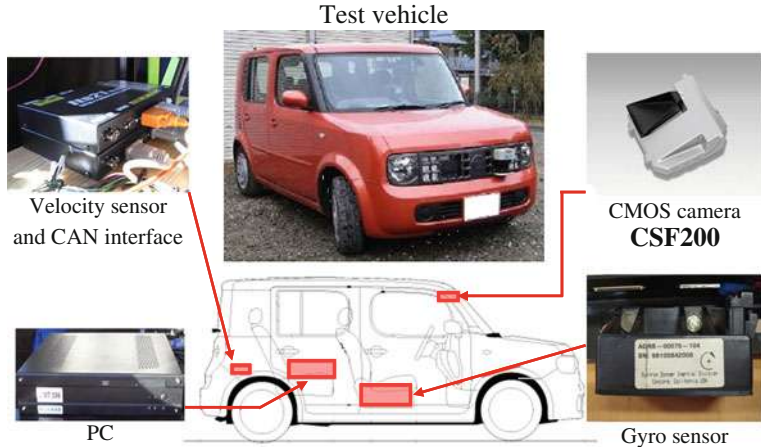


Fig. 3 Experimental vehicle

3 System Design Principle

As the concept of the system, moving objects on and nearby a crosswalk are interpreted as pedestrians. Consequently, the image processing algorithm based on the images captured from the on-board camera is designed to detect the existence of a crosswalk in front of the vehicle. The feature extraction technique used in the algorithm is based on the value of cross ratio of crosswalk edges and the periodicity of the crosswalk paints. Then, the moving object position and velocity obtained by the optical flow computation are utilized to infer that a pedestrian is on the crosswalk in front of the vehicle. Figure 4 shows an example of image data by the measurement and testing system on the experimental vehicle. A warning can be provided to the driver when there is a potential of a collision. Figure 5 shows the schematic diagram of the pedestrian collision warning system.

4 Crosswalk Detection

To detect a crosswalk, a feature called “cross ratio” of four collinear points is utilized. Since the cross ratio is invariant under the perspective projection, the cross ratio of the crosswalk in 3D space is the same as that of its image (Fig. 6). Here, the cross ratio $[abcd]$ of four points a, b, c, d are calculated as follows [8]:

$$[abcd] = \frac{\overline{ac} \cdot \overline{bd}}{\overline{bc} \cdot \overline{ad}} \quad (1)$$

where, the symbol written as \overline{ab} refers to the distance between the point a and the point b .



Fig. 4 Crosswalk and pedestrian image taken by the camera

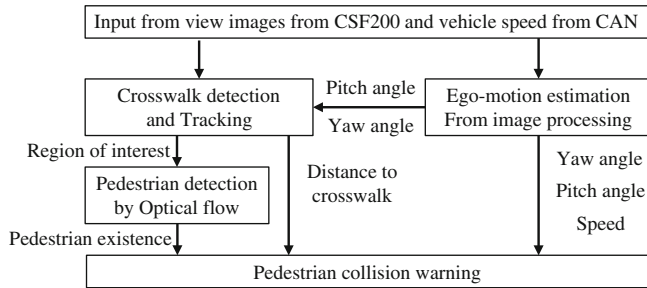


Fig. 5 Schematic diagram of the pedestrian collision warning system

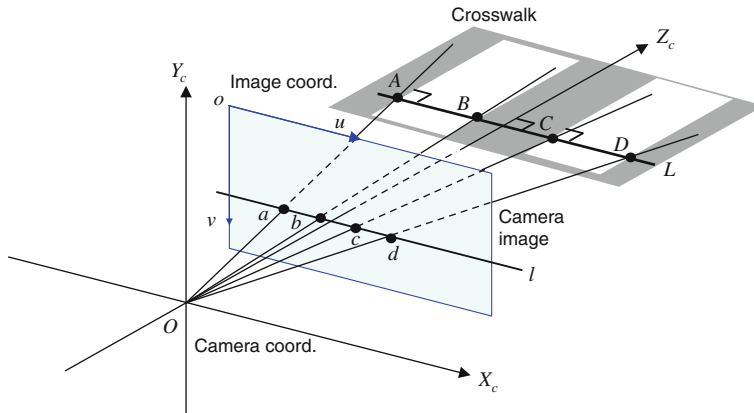


Fig. 6 Description of cross ratio in each coordinate

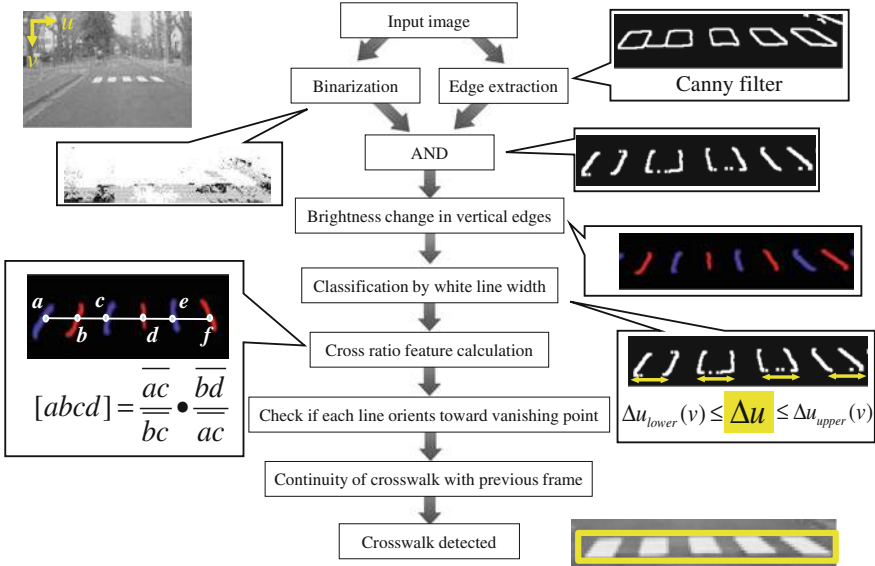


Fig. 7 Process flow for crosswalk detection

The flow diagram of our crossing detection algorithm is shown in Fig. 7. First, to extract boundaries of the white lines on a road, an image captured by the camera is processed by two algorithms: binarization and edge detection. To extract a number of edges from the input image, Canny's algorithm is employed [9]. Next, an AND operation of the two processing results is calculated in order to reduce the errors influenced by shades on roads. Then, the system classifies the pattern of vertical edge change into two categories: (1) the boundary where the intensity changes from dark to bright, and (2) the one from bright to dark.

Finally, we calculate the cross ratios of two pairs of boundaries. Here, it is assumed that the vehicle is driving perpendicular to crosswalk, therefore the algorithm calculates the cross ratio from four points (a, b, c, d in Fig. 6) which have the identical vertical axis level (v) on the image plane. In this step, we reduce the candidates of crosswalk by using the periodicity of the crosswalk by checking the number of boundaries at the identical vertical axis level (v) on the image plane and the width between two edges. Then, the cross ratio $[abcd]$ of four points a, b, c, d are calculated according to the formula in Eq. (1).

According to road traffic regulations in Japan, the value of cross ratio is within the range from 0.203 to 0.309. The crosswalks in Germany are in the range between 0.198 and 0.316. The crosswalk detection is made more robust by the following heuristic. The crosswalk is detected when there are more than three pairs of edge change patterns at the same vertical axis level (v) in the image plane and more than two pairs of edges which are within the range of the cross ratio of crosswalk described above. Moreover, the continuity of the crosswalk detection

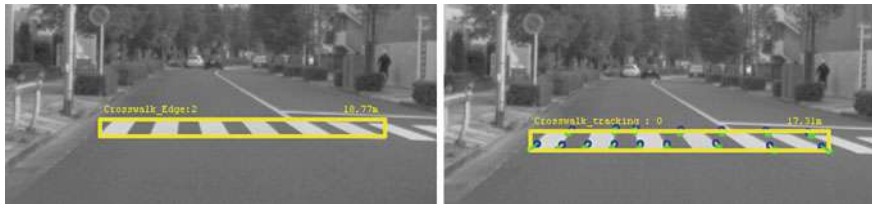


Fig. 8 Optical flow of some corners of crosswalk

result at each sampling time is checked with the detection results from six previously-acquired image frames in order to reduce misdetections.

In addition, a tracking algorithm by using the optical flow of some corners of the crosswalk is employed to improve the continuity in the crosswalk detection algorithm. An example of optical flow computation result is shown in Fig. 8.

5 Optical Flow for Pedestrian Detection

Figure 9a shows the flowchart of the pedestrian detection algorithm based on optical flow. First, the region of interest (ROI) which covers the detected crosswalk are extracted based on the estimated distance to the crosswalk. Then, the optical flow is computed inside the region of interest (ROI) to get the optical flow vectors. Next, the optical flow vectors which deviate from the epipolar lines and the distance between the epipolar lines and the edge of the optical flow vector are larger than a certain value are classified as “Outliers” as shown in Fig. 9b. The outliers which are close together are grouped as moving objects. In the proposed method, the moving objects exist on the crosswalk, so the objects can be inferred as pedestrians. Figure 10 shows an example of optical flow computation result for pedestrian detection. The red arrows show the outlier deviated from the epipolar lines.

Figure 11 shows the pedestrian detection result by the integration of the crosswalk detection and the pedestrian detection system. The crosswalk can be detected at a distance of 20.70 m and the system indicates “Crosswalk Is Detected” message. When the system detects the frontal pedestrian, the display show the message “Crosswalk Occupied”, the traffic sign “Caution crosswalk”, the distance to crosswalk, own vehicle speed and this situation for driver to understand easily.

6 Evaluation of Crosswalk Detection Performance

Urban road image sequences in Japan which include a crosswalk in front of the vehicle are used as a test data set to evaluate the performance of the crosswalk detection algorithm. The detection performance was evaluated by the distance to

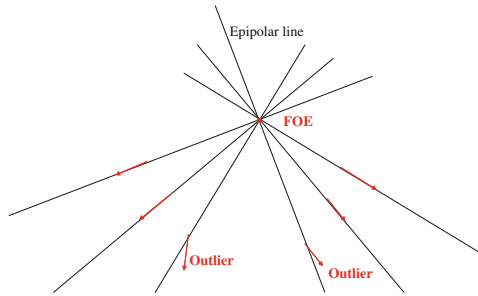
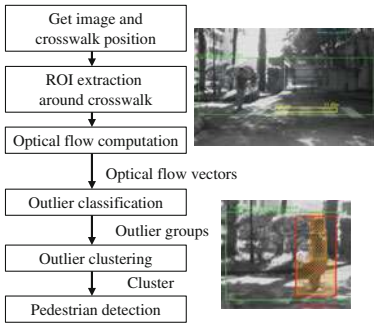


Fig. 9 Flowchart of pedestrian detection by optical flow

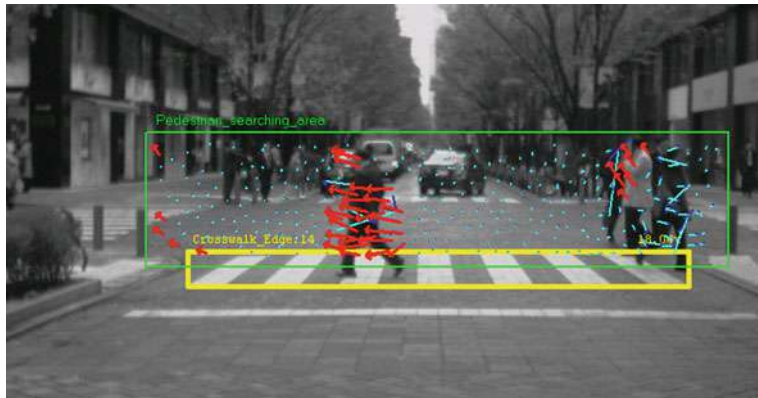


Fig. 10 Pedestrian detection result by optical flow

each crosswalk. The performance indices True Positive and False Negative are used here. True Positive refer to the cases that the system can correctly detect crosswalks, whereas False Negative refer the cases that the system fails to detect crosswalks where it should detect. The evaluation result is shown in Fig. 12. The system shows high true positive rate over 90 % when the distance to crosswalk is long up to around 20 m.

7 Conclusions

This paper described an on-board pedestrian detection and collision warning system by using a monocular camera. The design principle proposed here to deal with the pedestrian detection problem is based on the assumption that objects moving along a crosswalk can be inferred as pedestrians under defined circumstances. This principle simplifies the image processing unit computation as it does

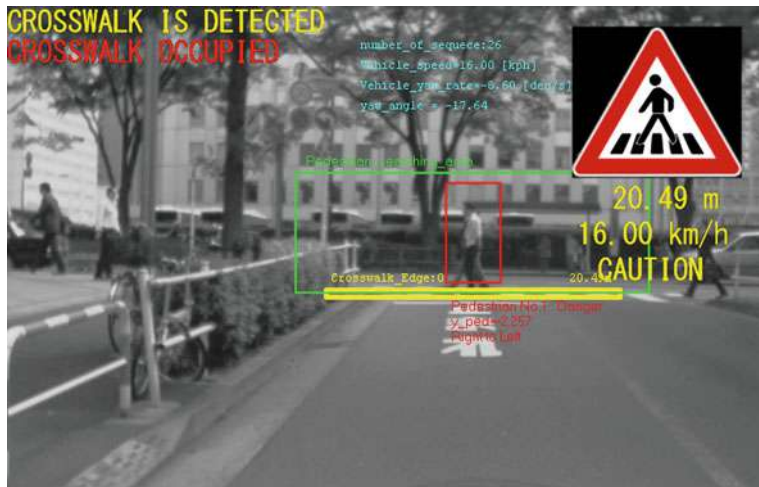


Fig. 11 Detection result of a pedestrian on a crosswalk in city road

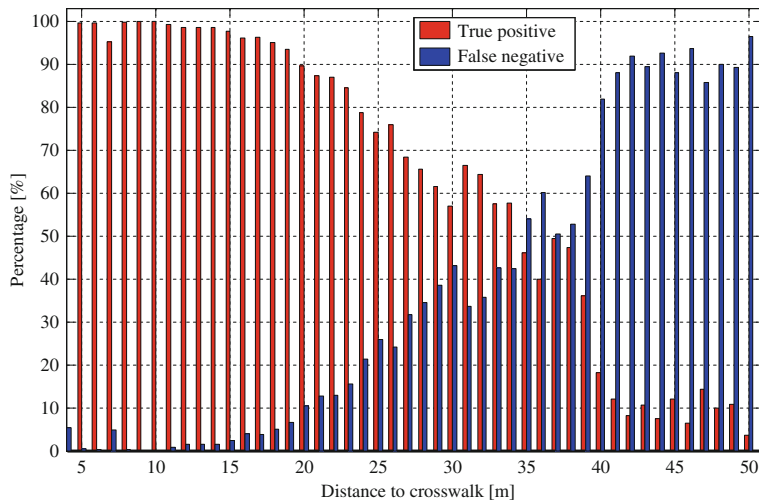


Fig. 12 Crosswalk detection performance by the distance

not require a computationally expensive appearance based pedestrian classification method. A key concept of the approach is the detection of a crosswalk by image processing methods based on the cross ratio feature. Moving objects on the crosswalk can be detected with the application of the optical flow feature. The sensor setup on the experimental vehicle for pedestrian detection was presented and experimental results which show that the proposed sensor fusion approach works in practice were given.

References

1. ITARDA (2010) Special Issue on vehicle to pedestrian accidents. *ITARDA Inform* 83:1–12
2. NHTSA (2009) Traffic safety facts 2009 data. DOT HS 811 394
3. European Road Safety Observatory (2005) Traffic safety basic facts: pedestrians. DaCoTA
4. Bishop R (2005) Intelligent vehicle technology and trends. Artech House: 144–150
5. Gandhi T, Trivedi MM (2007) Pedestrian protection systems: issues, survey, and challenges. *IEEE Trans Intell Trans Syst* 28(3):413–423
6. Gavrila DM, Munder S (2007) Multi-cue pedestrian detection and tracking from a moving vehicle. *Int J Comput Vis* 73(1):41–59
7. Coelingh E, Eidehall A, Bengtsson M (2010) Collision warning with full auto brake and pedestrian detection—a practical example of automatic emergency braking. In: Proceedings of IEEE ITSC'10, 2010, pp 55–160
8. Henn RW, Grotendiek T, Knoop S, Braeuchle C (2011) Active pedestrian protection by surround sensor technologies. In: Proceedings of 18th World Congress on ITS, Florida, USA, 2011
9. Keller CG, Dang T, Fritz H, Joos A, Rabe C, Gavrila DM (2011) Active pedestrian safety by automatic braking and evasive steering. *IEEE Trans Intell Transp Syst* 12(4):1292–1304
10. Viola P, Jones M, Snow D (2003) Detecting pedestrians using patterns of motion and appearance. *Proc ICCV'03* 2:34–741
11. Munder S, Gavrila DM (2006) An experimental study on pedestrian classification. *IEEE Trans Pattern Anal Mach Intell* 28(11):1863–1868
12. Rakhsincharoensak P, Takimoto Y, Muroi H, Shimizu I, Nagai M, Darms M, Adomat R (2009) Development of a pedestrian collision warning system by sensor fusion of monocular camera and millimeter wave radar. In: Proceedings of AAET2009 Symposium (Automatisierungs-, Assistenzsysteme und eingebettete Systeme für Transportmittel). Braunschweig, Germany, pp 1–10

Part IV
Crash Biomechanics

Development and Validation of a Finite Element Model of the Human Thoracic for Rib Fractures Prediction in Automobile Collisions

Zhihua Cai, Fengchong Lan, Jiqing Chen and Fuquan Zhao

Abstract Thoracic trauma is a frequent occurrence in automotive collisions. A finite element human thorax model was developed for predicting thoracic Rib fractures and studying the injury mechanisms of thorax for automotive impact accidents. CT image and MRI image of the human skeleton and internal organs were used to construct the three-dimensional finite element representation of the rib cage and internal organs. The model was created in the finite element code LS-DYNA. The mechanical properties of the biological tissues in this model were based on test data found in the literature. Several experimental studies have been performed to determine the material properties and force-deformation behaviors of the rib tissues under three-point bending or anterior-posterior loading, the full model was validated against post-mortem human subjects (PMHS) impact data responses for both frontal and lateral impact. Good correlation between the model and the cadaver responses were achieved for the force and deflection time-histories these models provide comparative tools for determining the thoracic response to automotive impact injury and can be used to evaluate Rib fractures and determined thoracic injury mechanism and assist with injury prevention in car crash safety research.

Keywords Thorax finite element · Rib fracture · Automotive impact accidents · Thorax injury · Injury analysis

F2012-FO4-001

Z. Cai (✉) · F. Lan · J. Chen

Guangdong Key Laboratory of Automotive Engineering, School of Mechanical and Automotive Engineering South China, University of Technology, Guangzhou, China

F. Zhao

Key Laboratory of Automobile Safety Technology, Geely Automobile Institute Zhejiang, Zhejiang, China

1 Introduction

Thoracic trauma is a frequent occurrence in automotive collisions. Rib fracture is the most frequent type of thoracic injury, followed by the trauma of the pulmonary/lung, heart and liver [1]. Rib fractures are common thoracic injuries that can result in mortality and severe morbidity [2]. As the population continues to age worldwide, rib injury frequency and the associated morbidity and mortality will significantly increase since older drivers are more vulnerable to and more likely to die of chest injuries [3]. To simulate the occupants and pedestrian during the automotive impact accidents, dummies are currently used to represent the occupants and pedestrian. However, current dummies and dummy models lack the detailed information to predict the occupant and pedestrian injuries during a crash, especially rib fractures for the human thorax models, simplified geometry and non strain-rate material properties were used for the rib cage can not to simulate the rib fractures in an automotive crash. Therefore, a detailed finite element human thorax model with proper material properties and the capability to simulate the rib fractures and to better understand the thoracic injuries under frontal and side impacts. In order to better predict rib fractures in automobile collisions, several studies have investigated the biomechanics of human ribs through a range of material and component level tests. Dynamic tension and three-point bending tests on isolated human rib cortical bone coupons have been conducted by researchers in order to quantify the material and failure properties of human ribs [4]. Other studies have investigated the structural response of individual whole ribs in dynamic anterio-posterior loading [5, 6]. The data from these studies provide insight into the tolerance of human ribs and critical data required to locally validate finite element models (FEMs) of the human body. However, the global response and injury tolerance of the human rib cage must be quantified through full scale post-mortem human surrogate (PMHS) testing in order to validate the response of FEMs and anthropomorphic test devices (ATDs), i.e. crash test dummies, used to assess thoracic injury risk in automotive collisions. Therefore it is important to develop a full chest model to evaluate the potential of rib fracture under various impact situations.

The objective of this study was to develop and validate FE models of human thorax. Model and material models were developed in the LS-DYNA code for simulating the mechanical behavior of the biological tissues in the thorax region. The thorax model was validated against PHMS responses in frontal and lateral impacts. Use the model to predict Rib fractures in automobile collisions.

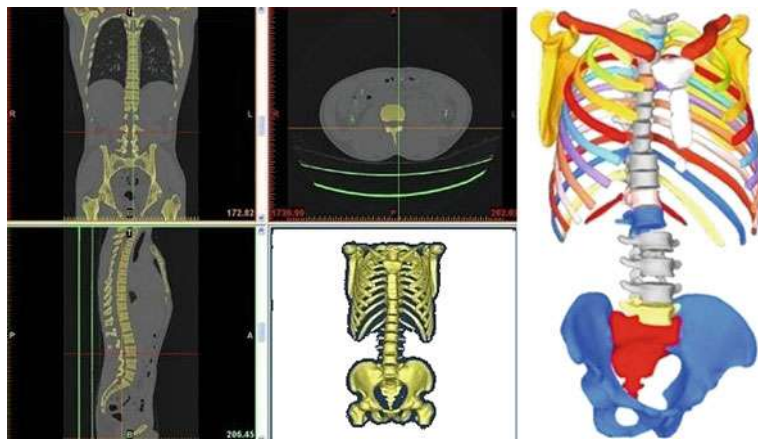


Fig. 1 skeleton geometric model

2 Material and Methods

2.1 Thorax Model Geometry Development

The selected patient data in this study is 35 years old, 170 cm, 65 kg, 50 percentile male with Chinese human characteristics. The geometry has been generated to sufficient accuracy through CT and MRI scans. The slice thickness were $1 + 0.1$ mm. Image resolution was 512×512 , CT image data can accurately distinguish between bone and soft tissues and MRI image data can distinguish between the skin, internal organs and other soft tissues, combined with the two forms of medical imaging data to build a geometric model of the chest. Bones of the body are classified as hard tissues, Established model in IGES format storage chest as shown in Fig. 1.

2.2 Thorax Mesh Development

The rib is composed of two types of bony tissue, the trabecular bone in the middle and cortical bone on the outer surface to reflect the structural composition of the rib fractures. It is necessary to use a fine mesh as shown in Fig. 2a, the outer layer of elements simulating the cortical bone and inner of element simulating the trabecular bone. The sternum was modeled using the cortical bone properties and the cartilage connecting the sternum and the rib as shown in Fig. 2b Since the main application of this model is for thoracic injury studies involving rib fracture injury, the thoracic spine was modeled with great detail. The spine include cortical bone and inner of element simulating the trabecular bone, the disc between in the two spine, the connection between the spine and rib was via rotational joint, As shown

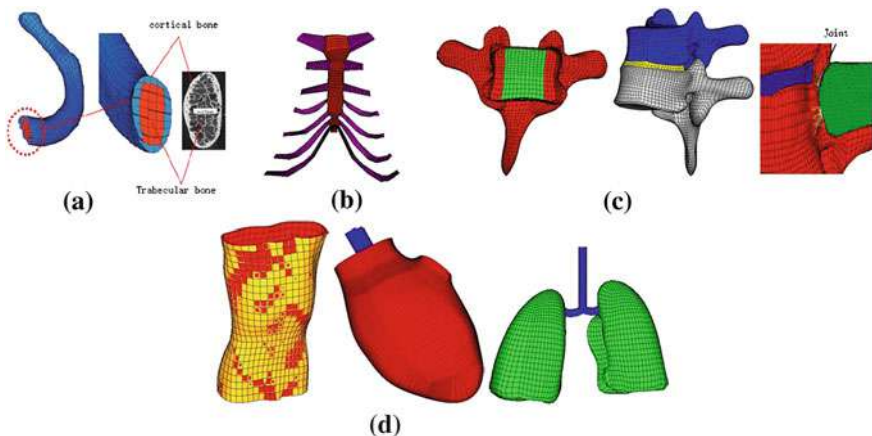


Fig. 2 Thorax organ models. **a** Rib. **b** Sternum and costal cartilage. **c** Spine and disc and connection. **d** Skin and muscles, heart and lung

in Fig. 2c. The rib are connected by the Skin and internal/external intercostals muscles. In this study, the focus of the rib fractures, internal organizations the heart and lung are simplified, as show in Fig. 2d.

The main organizational structure using the 8-node hexahedral element modeling, Skin using shell elements, the material properties were developed in the LS-DYNA code for simulating the mechanical behavior of the biological tissues in the thorax. The model contain about 664889 nodes and 547109 hexahedral element and 886 shells. The model describes the main anatomical characteristics of the skeletal and soft tissues and internal organs as show in Fig. 3.

2.3 Material Models

The material constitutive for all the thorax tissues are either considered as elastic-plastic or linear-elastic and viscoelastic. Hard tissue such as rib, Sternum, Spine were modeled with elastic-plastic solid elements characterized by the power stress-strain law, An elastic-plastic material model (MAT_03) in LS-DYNA was used to simulate skeletal behaviors where rib fracture was defined by specifying a plastic failure strain and initiated by element deletion. Strain rate effects were included in the model with constants from the literature [6, 7]. All material taken from the literature [8–10]. Tables 1, 2 list the material properties for all the tissues modeled in the human chest model.

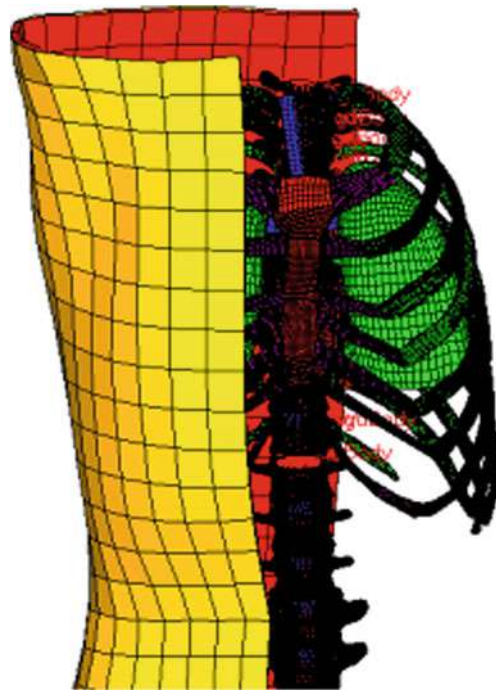


Fig. 3 Thoracic model for front view

Table 1 Hard tissue skeletal material properties

Material	ρ (g/cm ³)	E(GPa)	ν	σ_y (MPa)	E_t (GPa)	β	Cowper-Symonds	Plastic failure strain (%)	
							model		
							C	P	
Cortical bone	2	11.5	0.3	88	1.15	0.1	2.5	7	2
Trabecular bone	1	0.04	0.45	2.2	0.001	0.1	2.5	7	3

Table 2 Soft tissue skeletal material properties

Tissue	material	ρ (kg/m ³)	E (GPa)	ν	(Kpa)	(Kpa)	Bulk (GPa)	β
Disc	elastic	1000	0.0103	0.45				
Costal cartilage	elastic	1600	1.2	0.2				
Skin/ muscle	Viscoelastic	1200		0.49	200	195	2.9	0.1
Heart	Viscoelastic	1000		0.49	67	65	0.74	0.1
Lung	Viscoelastic	600		0.49	67	65	0.74	0.1

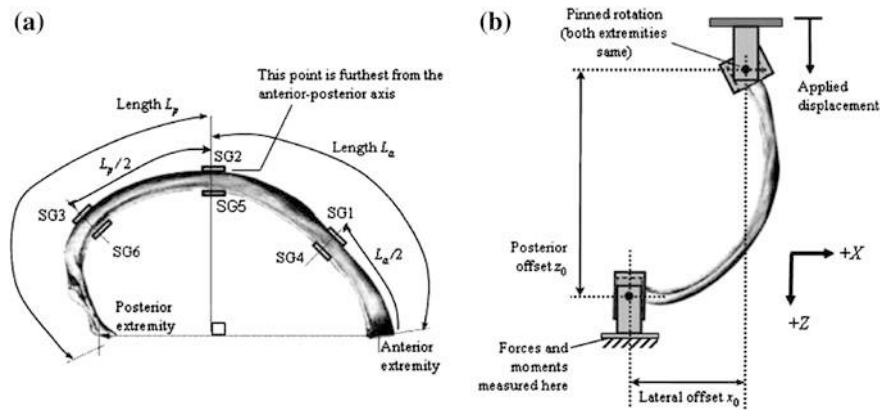


Fig. 4 Experimental set-up showing. **a** Locations of six strain gages on rib bone surfaces and **(b)** loading offsets (Charpail et al. 2005)

3 Model Validation

3.1 The Rib Fractures Validation

Several experimental studies have been performed to determine the material properties and force-deformation behaviors of the rib tissues under three-point bending or tensile loading, in the present study were adapted from the method published by Charpail et.al. (Fig. 4) [11]. Three pairs of uniaxial strain gages (SG) were glued to each rib, one each on the external and internal cortical surfaces, to measure local bone deformations, the pair of ‘‘lateral’’ gages was located at the cross-section furthest from the anterior to posterior axis, the other two gage pairs were located halfway between this pair and the two extremities, and the loaded to rib fracture at either 1,000 mm/s (second rib) or 500 mm/s (fourth and tenth ribs). Time histories of the posterior extremity reaction forces and moments about all three coordinate axes, anterior extremity displacement, and cortical strains were measured in each test.

3.2 Thoracic Model Validation Against Cadaver Data in Frontal Impact

In the early seventies a series of cadaver test was conducted to study thoracic injury due to a frontal impact in the sternum area. Various impact speeds and masses were chosen to impact a stationary seated cadaver’s chest [12, 13]. A 15.24 cm diameter pendulum with 23.4 kg mass was used in the test to strike the cadaver with initial velocities of 6.7 m/s (Test-F22). The forces were measured by a load cell mounted

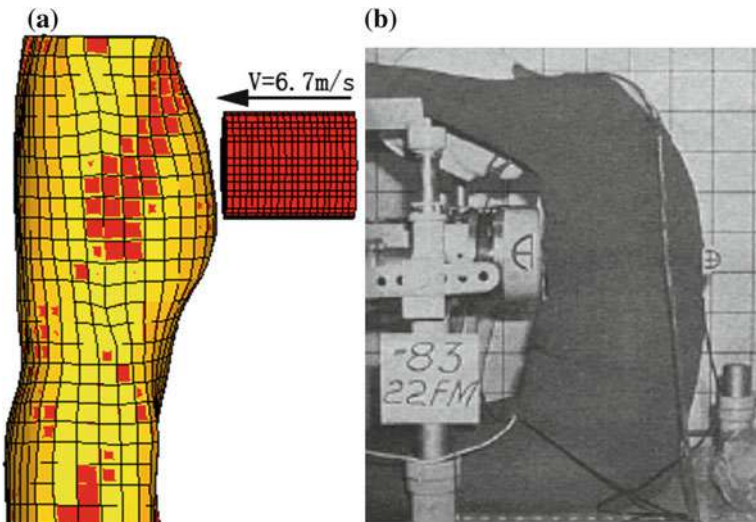


Fig. 5 Front thoracic pendulum impact test. **a** Simulation. **b** Experiment (Kroell et al. 1971)

on the pendulum and the chest deflection of the cadaver specimen was determined from high speed films. Using these data, force–deflection corridors were developed. These corridors provided the basic characteristics of the human thorax structure for frontal impact. In this paper we subjected the model to these impact conditions and compared the model responses to the cadaver test results [14]. A rigid cylinder of 15.24 cm diameter and 23.4 kg mass was positioned at the sternum impact location with an initial velocity 6.7 m/s as shown in Fig. 5. Following the cadaver test conditions, the model was free to move after impact without any constraint. Force–time, deflection–time force–deflection, VC curves were available for thoracic model validation.

3.3 Thoracic Model Validation Against Cadaver Data in Side Impact

The model's side impact response has been validated by pendulum impact tests performed by Chung et al. [15]. On four PMHS using a 50 kg wood impactor of 152.4 mm diameter centered over the 6th rib (Fig. 3). The impact force and chest deflection were measured using a load cell in the impactor and a chest band respectively (Fig. 6).

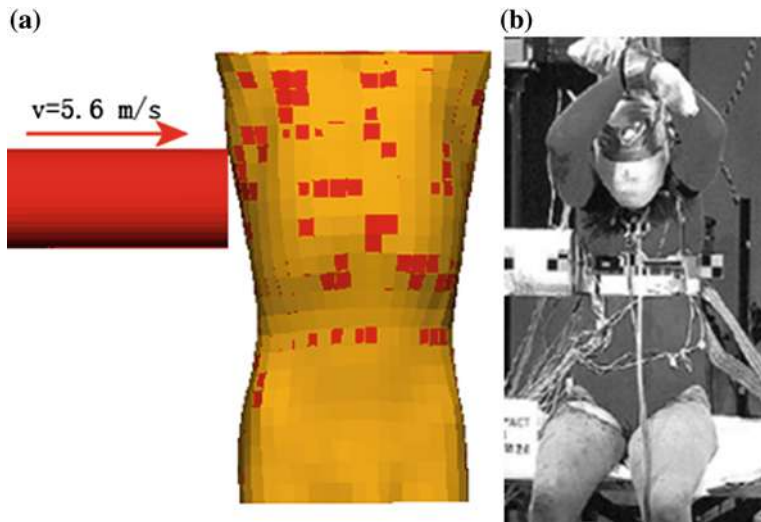


Fig. 6 Side thoracic pendulum impact test. **a** Simulation. **b** Experiment (Chung et al. 1999)

4 Result

4.1 Rib Fractures Under Anterior-Posterior Loads

Figure 7 show the Reaction force and displacement curves measured by experiments and predicted by the FE rib models. Figure 8 shows the Rib fracture locations predicted by FE models of the second rib(a), fourth rib(b) and tenth rib(c), the model predicted rib fracture locations agreed well with that of the test in anterior-posterior dynamic loads. And show the maximum stress in the time of the rib fractures before.

4.2 Model Validation Against Cadaver Data in Frontal Impact

Figures 9, 10 shows the response of the thorax at various times during a frontal pendulum impact and frontal impact simulation to ribs and rib fractures prediction

The frontal pendulum simulation results are shown below (Fig. 11). Figure 11a shows an impact force comparison between model predictions and test result. The model predicted peak force (4250 N) occurred at 12 ms. The model-predicted force-time was also in very good agreement with the test as seen in Fig. 11b, force-deflection response of the model shows a good agreement with the experimental corridor in Fig. 11c.

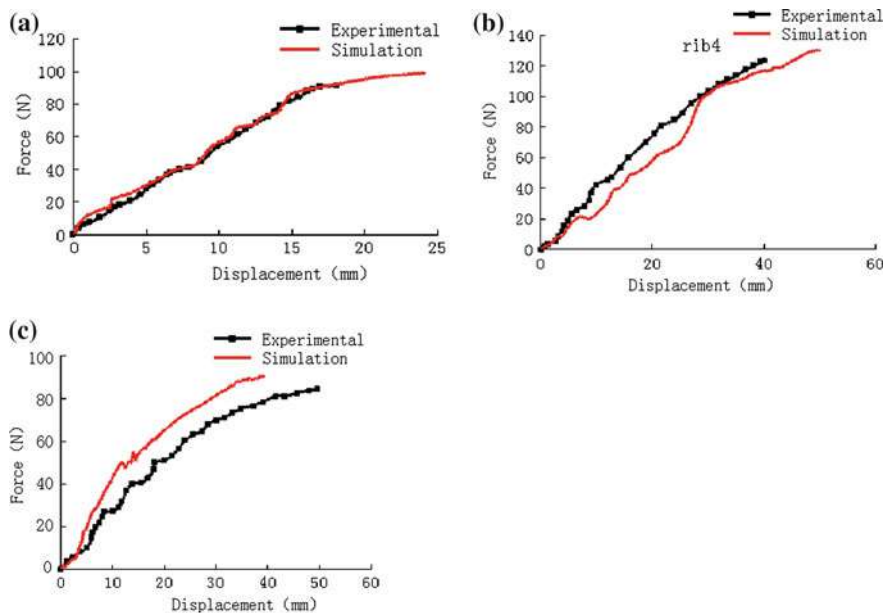
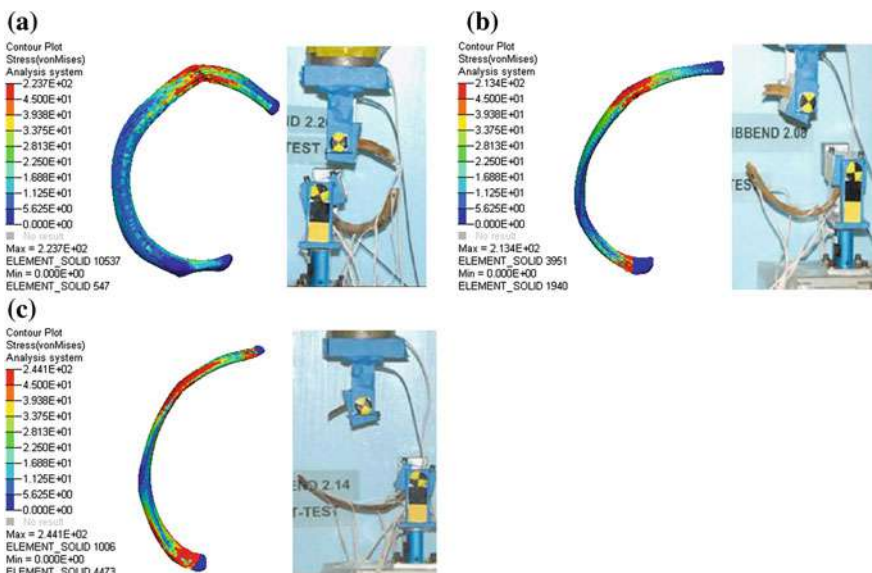


Fig. 7 Force-displacement of the ribs

Fig. 8 Rib fractures predicted by experiments (Charpail et al. 2005). **a** Second rib. **b** Fourth rib. **c** Tenth rib

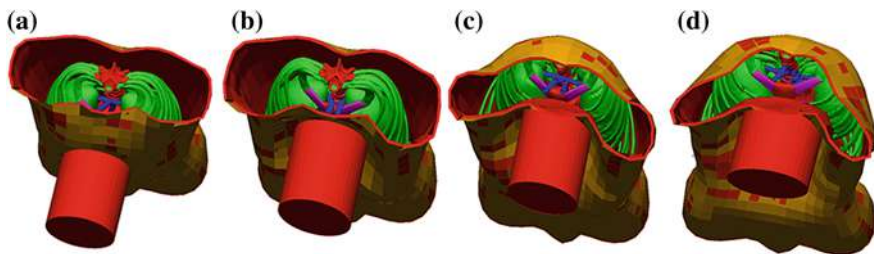


Fig. 9 Front thoracic impact simulation. **a** $t = 0$, **b** $t = 0.015$, **c** $t = 0.030$, **d** $t = 0.045$ ms

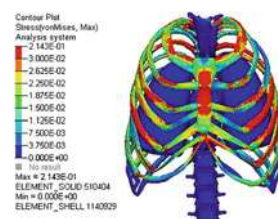


Fig. 10 Side impact rib fractures prediction

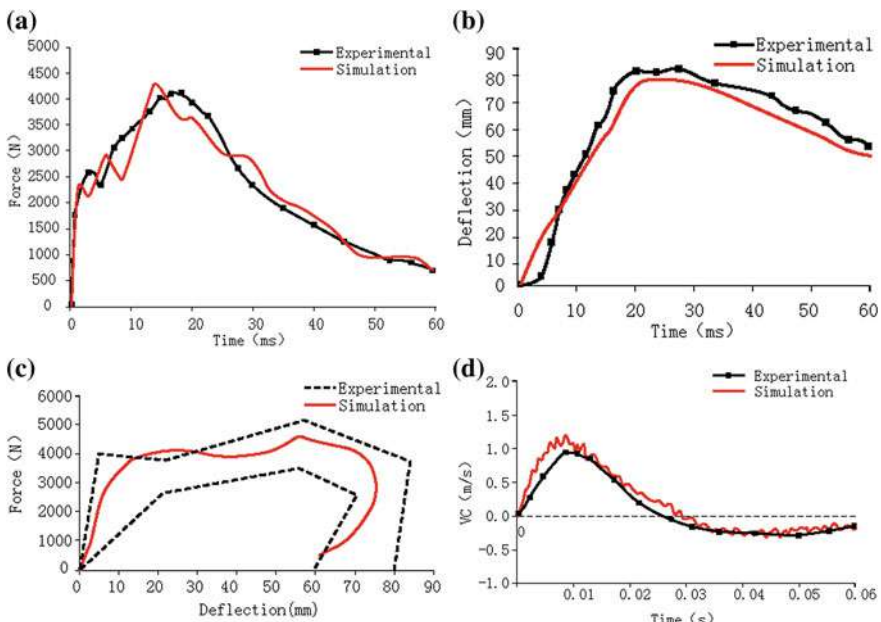


Fig. 11 Front thoracic impact simulation results. **a** Force. **b** Compression. **c** Force-compression. **d** VC

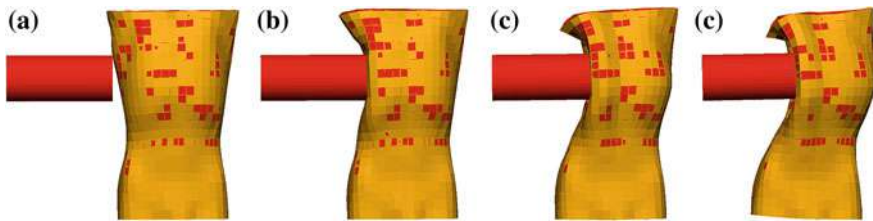


Fig. 12 Chest side crash test simulation

5 Thoracic Side Impact Simulation

Figure 12 shows the response of the thorax at various times during a lateral pendulum impact. Figure 13 shows side impact rib fractures prediction

The side pendulum simulation results are shown below (Fig. 14). Figure 14a shows an impact force comparison between model predictions and test result. The model predicted peak force (3750 N) occurred at 10 ms. The model-predicted force-time was also in very good agreement with the test as seen in Fig. 14b, force-deflection response of the model shows a good agreement with the experimental corridor in Fig. 14c.

5.1 Injury Assessment and Analysis

Some studies revealed that a maximum allowable compression of 75 mm was recommended to limit chest injury to AIS 3 with 25 % probability [16]. Other Studies have shown [17–19] that VC (Viscous Criterion) is most applicable as an indicator of soft tissue injury for velocities of deformation between 3 and 30 m/s., compression criteria is a good predictor of injury for rates of deformation <3 m/s. At these low velocities injury is produced by crushing the tissue and the rate of deformation has little to no effect on injury. At velocities >30 m/s, impact velocity begins to completely govern injury as is seen in blast trauma. Current Impact Standards implement VC threshold of 1 m/s. More than 1 m/s can cause chest injury to AIS 3 with probability 50 %. Figures 10 and 11b show the maximum deformation is 80 > 76 mm, Fractures occurred in second rib and third rib. Figure 13 show the sixty rib fracture, Fig. 11d VC = 1.3 m/s, more than 1 m/s will make internal organs cause AIS 3 with probability 50 %. The results indicate that frontal impact the visceral injury risk is higher, side impact ribs displacement smaller but the fracture risk is higher.

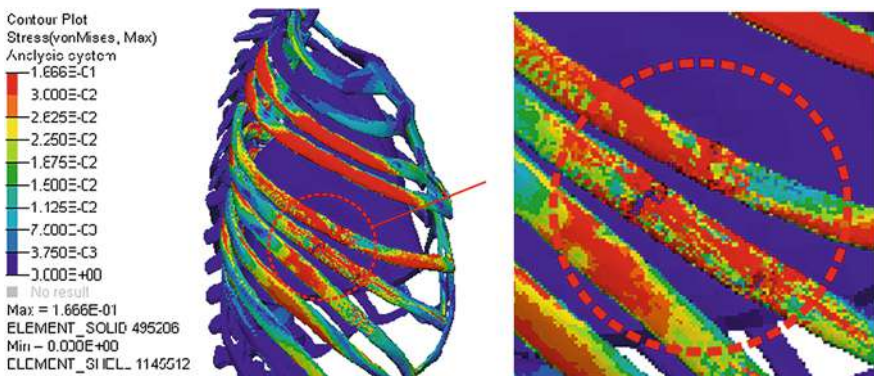


Fig. 13 Side impact rib fractures prediction

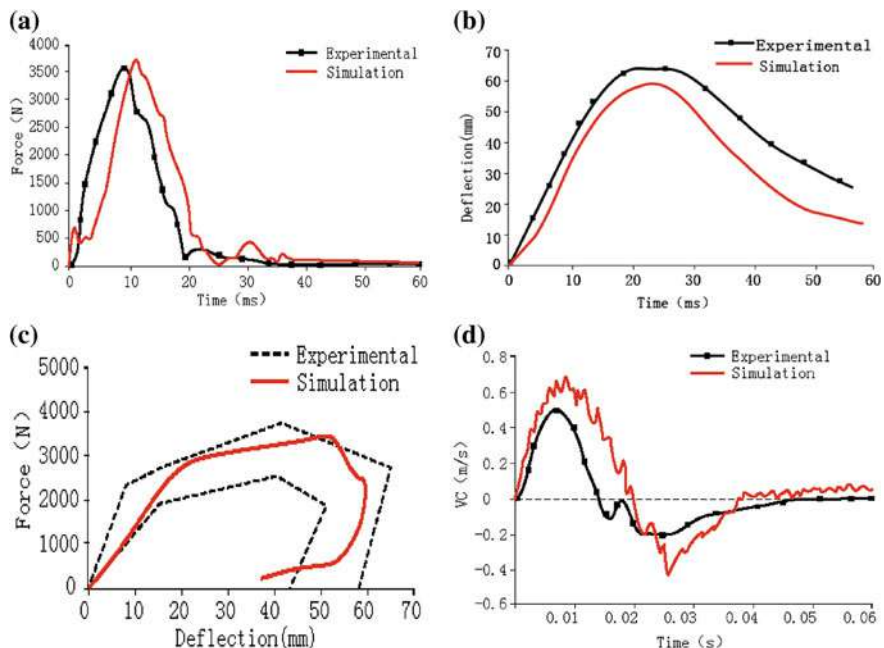


Fig. 14 Side thoracic simulation results. **a** Force. **b** Compression. **c** Force-compression. **d**. VC

6 Conclusions

A detailed finite element model of the human thorax was developed for impact injury studies. The model has realistic geometric and material representation of the rib cage, heart and lungs. The mechanical properties of the biological tissues in this model were based on test data found in the literature. The full model was

validated against PMHS (post-mortem human subjects) impact data responses for both frontal and lateral impact. The response of the model to various pendulum tests agrees with experimental data, Good correlation between the model and the cadaver responses were achieved for the force, chest compression and VC of both simulations compared well with the experiments with slight differences attributed to the initial impact position. Further development is currently underway to include important shoulder ligaments and the abdomen model to accurately human body model. These models provide comparative tools for determining the thoracic response to automotive impact injury and can be used to evaluate Rib fractures and determined thoracic injury mechanism and assist with injury prevention in car crash safety research.

References

1. Cavanaugh JM (1993) The biomechanics of thoracic trauma. In: Nahum AM, Melvin JW (eds) Accidental injury-biomechanics and prevention[M], Springer, New York
2. Wang S (2001) Personal communication, quarterly CIREN meeting [R]. National Highway Traffic Safety Administration, Washington DC
3. Yoganandan N, Pintar FA (1998) Biomechanics of human thoracic ribs [J]. J Biomech Eng 120:100–104
4. Kenper AR, Kennedy EA (2011) Reducing chest injuries in automobile collisions: rib fracture timing and implication for thoracic injury criteria. [J] Ann Biomed Eng 39(8):2141(11)
5. Charpail E, Trosseille X, Petit P, Laporte S (2005) Characterization of PMHS ribs: a new test methodology [J]. Stapp Car Crash J 49:183–198
6. Li Z, Kindig MW, Kerrigan JR, Untaroiu CD, Subit D, Crandall JR, Kent RW (2010) Rib fractures under anterior-posterior dynamic loads: experimental and finite-element study[J]. J Biomech 43(2):228–234
7. Choi HY, Lee IH (1999) Advanced finite element modeling of the human body for occupant safety simulation. EuroPam
8. Ruan J, El-Jawahri R, Raed E et al. (2003) Analysis of human thoracic impact responses and injuries in cadaver impacts using a full human body finite element model [J]. Stapp Car Crash J 47:299–321
9. Kemper AR, McNally C, Kennedy EA, Manoogian SJ, Rath AL, Ng TP, Stitzel JD, Smith EP, Duma SM (2007) Material properties of human rib cortical bone from dynamic tension coupon testing[J]. Stapp Car Crash J 49:199–230
10. Kemper AR, McNally C, Pullins CA, Freeman LJ, Duma S (2007) The biomechanics of human ribs: material and structural properties from dynamic tension and bending tests[J]. Stapp Car Crash J 51:235–273
11. Charpail E, Trosseille X, Petit P, Laporte S, Lavaste F (2005) Characterization of PMHS ribs: a new test methodology [J]. Stapp Car Crash J 49:183–198
12. Kroell CK, Schneider DC, Nahum AM Impact tolerance and response of the human thorax, in biomechanics of impact injury and injury tolerances of the thorax-shoulder complex, SAE paper no. 710851
13. Kroell CK, Schneider DC, Nahum AM “Impact tolerance and response of the human thorax II”, in biomechanics of impact injury and injury tolerances of the thorax-shoulder complex, SAE publication PT-45, SAE paper no. 741187

14. Deng YC, Kong W, Ho H (1999) Development of a finite element human thorax model for impact injury studies, SAE international congress and exposition detroit, Michigan, SAE paper 1999-01-0715
15. Chung J, John M (1999) Cavanaugh, thoracic injury mechanisms and biomechanical responses in lateral velocity pulse impacts[C]. 43rd Stapp Car Crash Conf
16. Nahum AM, Melvin JW (2002) Accidental injury biomechanics and prevention [M], 2nd edn. Springer, New York
17. Viano DC, Lau IV (1988) A viscous tolerance criterion for soft tissue injury assessment [J]. *J Biomech* 21:387–399
18. Viano DC, King AI, Melvin JW, Weber K (1989) Injury biomechanics research: an essential element in the prevention of trauma [J]. *J Biomech* 22(5):403–417
19. Viano DC, Lau IV, Asbury C, King AI, Begeman P (1989) Biomechanics of the Human Chest, Abdomen, and Pelvis in lateral impact[R], Proceedings of the 33rd association for the advancement of automotive medicine

Part V

Crash Pre-judge Technology/Traffic Accident Analysis and Reconstruction

A Study on Injury Prediction Method and Influential Factors in Side Impact Crashes Using Accident Data

Hiroshi Kuniyuki

Abstract In order to reduce casualties in traffic accidents, more analyses are required from the engineering and medical science viewpoints when investigating traffic accidents. A key technology in this respect is injury prediction, which reduces the response time of the emergency rescue teams through automatic collision notification, and evaluates the injury mechanisms and risks. In this study, research questions are clarified by studying the factors that influence side impact crashes in traffic accidents in Japan, and determining significant factors that reduce accident casualties by constructing an injury prediction method. In this study, statistical accident analysis is applied to a combination of data obtained from the Institute for the Traffic Accident Research and Data Analysis (ITARDA) in-depth accident investigation database (Micro Data) and ITARDA Macro Data which is the official database for traffic accidents that occur throughout Japan. First, 73 nearside and 108 farside crashes are selected from Micro Data. Second, an object variable and 22 explanatory variables from the accident information are selected and categorized. The object variable is the maximum of AIS (MAIS). Third, an ordinal logistic regression analysis is performed to construct the injury prediction models using these variables. Finally, a comparison of the obtained results with Macro Data validates these models, and the outlier cases show extraordinary accidents. The results show that the significant factors are delta-V, damage grade, and striking vehicle weight for nearside crashes; and delta-V, vehicle category, lap zone-vertical, and seat belt use for farside crashes. Thus, these two types of crashes have different factors. The MAIS predictive accuracy rate is approximately 75, and the judgment rate of fatal and serious injuries (MAIS 3+) is approximately 90 %. The prediction models can correspond to Macro Data. The accident conditions

F2012-F05-003

H. Kuniyuki (✉)

Institute for Traffic Accident Research and Data Analysis (ITARDA), Tokyo, Japan

arising from ± 1 MAIS residual exhibit several characteristics. Eight cases with a large degree of error in nearside crashes involved five cases of SUV or truck side impact crashes with serious chest injuries. In farside crashes, 12 cases with a large degree of error included four unbelted drivers with serious head or neck injuries. These cases indicate that these extraordinary accidents have additional factors that influence injuries. At present, there is no published research on the side impact prediction method using Japanese Micro Data and Macro Data. In the United States, several injury prediction methodologies have been studied. However, only a few studies refer to accidents with residuals. In conclusion, this study shows the results of the proposed injury prediction methods and significant factors in side impact crashes by using data on traffic accidents in Japan. These prediction models can correspond to documented accident data. Furthermore, the residual analysis conducted indicates characteristic accident factors such as SUV side impacts for nearside crashes and unbelted drivers for farside crashes. Further investigations into these outlier accidents would prove beneficial in reducing traffic accident casualties in Japan.

Keywords Safety • Injury prediction • Statistical accident analysis • Logistic regression • Side impact crash

1 Introduction

Traffic accident casualties in Japan have decreased over the past decade; however, a relatively large number of traffic accident casualties still occur in Japan, with 4,612 fatalities occurring within 24 h and 859,105 casualties occurring in 2011. These data represented a reduction of around 5 % from the previous year; however, the rate of decrease has slowed down over the past few years. The Japanese government has set a new target for traffic accidents, 3,000 fatalities or fewer and 700,000 casualties or fewer by 2015, with the aim of achieving the safest road traffic in the world. To achieve these targets, more contributory aspects for traffic accidents need to be identified and studied, and more effective countermeasures are needed.

For passive safety technology, effective restraint systems, such as air bag system, have been developed and have helped reduce casualties. To further reduce casualties, studies on the state of vehicles involved in the impacts and the injuries sustained by the occupants of these vehicles are required, from the engineering and medical science viewpoints. A key technology in this respect is injury prediction, which reduces the response time of the emergency rescue teams through automatic collision notification, and evaluates the injury mechanisms and risks.

Typically, occupant injury prediction studies are based on National Automotive Sampling System/Crashworthiness Data System (NASS/CDS) using logistic regression models. Malliaris et al. indicated several predictors such as delta-V, seat

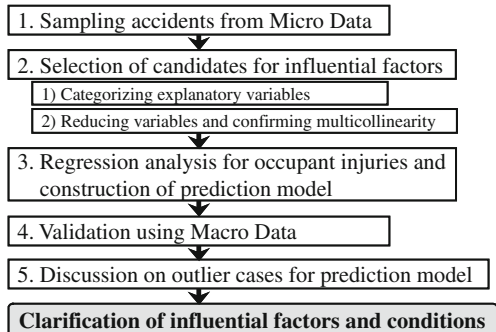
belt use, and crash direction [1]. Augenstein et al. constructed algorithms for practical application, a few of which are being applied to vehicles in the United States [2, 3]. In Japan, studies have been conducted using accident data [4, 5] and simulations [6, 7]. These studies show numerous predictors with many viewpoints. However, very few studies have been conducted on factors influencing vehicle occupant injury using the findings of in-depth accident investigations in Japan.

The author examines the injury prediction method and influential factors in frontal collisions using Japanese accident data [8]. The previous study identified the significant factors and created an injury prediction model for frontal collisions. Furthermore, the findings of extraordinary accidents to reduce casualties can be found in the outlier analysis. This study investigates side impact crashes using the same method and helps establish injury prediction models, and clarifies influential factors in side impact crashes in Japan. Ordinal logistic regression analysis is applied to the Institute for Traffic Accident Research and Data Analysis (ITARDA) in-depth accident investigation database (Micro Data). Furthermore, this model is verified by comparing with ITARDA Macro Data which is the database for all traffic accidents that occur throughout Japan, because Micro Data have sampling limitations. Finally, residual analysis indicates some extraordinary accidents in side impact crashes in Japan. The crash types are classified as nearside and farside crashes from the driver's perspective.

2 Methodology

2.1 Flow of the Study

Figure 1 shows the flow of the study used to clarify factors influencing traffic accident casualties. First, sampling accidents from Micro Data are conducted. Second, candidates for the influential factors are selected by categorizing explanatory variables, reducing variables, and confirming multicollinearity. Third, ordinal logistic regression analysis is used to construct an injury prediction model using these factors. In this model, all explanatory variables are significant. Fourth, validation performed using Macro Data shows the significance of this model for side impact crashes. Finally, outlier cases for the prediction model show extraordinary accidents. This process yields unknown important factors that have not been evaluated. The above steps clarify the influential factors and extraordinary accident conditions.

Fig. 1 Flow of the study

2.2 Object Data Sources

Micro Data were used to develop the models. Object data sources were 2000–2010 accidents, involving small and regular passenger vehicles, Kei car (light vehicles with an engine displacement of 660 cc or less), and Kei trucks (light trucks with an engine displacement of 660 cc or less). Both Kei car and Kei truck are standards unique to Japan. Nearside crashes have an impact direction of Collision Deformation Classification (CDC) codes 02R, 03R, or 04R. Farside impact crashes have an impact direction of CDC codes 08L, 09L, or 10L. The number of sampled nearside crashes is 73 drivers without missing principal values, and the number of sampled farside crashes is 108 drivers. About 65 of these accidents were the result of intersecting collisions, while single vehicle accidents accounted for 3 %.

2.3 Ordinal Logistic Regression Modeling

The maximum of AIS (MAIS) is considered as an object variable. AIS is an ordinal scale variable that has six categories of abbreviated injury scale. Explanatory variables do not necessarily follow normal distributions; therefore, an ordinal logistic regression model is applied in this study. The ordinal logistic regression equation is given as follows:

$$\text{logit}(P(Y \leq Y_j)) = \log \frac{P(Y \leq Y_j)}{1 - P(Y \leq Y_j)} = a_j - \sum_{i=1}^l b_i x_i \quad (1)$$

where Y is the MAIS category, $P(Y \leq Y_j)$ is the probability of MAIS $\leq Y_j$, and l is the number of explanatory variables. a_j are the threshold values for the Y_j categories, x_i are the explanatory variables, b_i are regression coefficients for x_i . a_j and b_i are calculated using the maximum likelihood method. The estimated MAIS category is the largest probability of MAIS. The statistical analysis software SPSS Ver.19 (IBM) is used in this analysis.

Table 1 Explanatory variables and their categories

Factors	Variable type ^(a)	Categories
Vehicle category	C(3)	Kei car ^(b) /Kei truck ^(c) / Small or Regular vehicle
Vehicle registration year	OS(4)	$\leq 1994/1995-1999/$ 2000-2004/ ≥ 2005
Vehicle curb weight, kg	OS(3)	$<900/< 1300/\geq 1300$
Collision object	C(4)	Regular vehicle/SUV/Heavy vehicle/ Structure
Striking vehicle curb weight, kg	C(2)	$<3500/\geq 3500$
Multiple impact	C(2)	Yes/No
Rollover	C(2)	Yes/No
Damage grade	C(2)	Small or Medium/Large
Lap zone-horizontal, CDC code	C(3)	F/P,Y,D/B,Z
Lap zone-vertical, CDC code	C(2)	A,G,H/E,L,M,W
Extent of damage code	OS(3)	1/2-3/4-9
Delta-V, km/h	Q	
EBS ^(d) , km/h	Q	
Impact speed, km/h	Q	
Striking vehicle impact speed, km/h	Q	
Seat belt use	C(2)	Belted/Unbelted
Steering air bag deployment (A/Bag)	C(2)	Yes/No (including no air bag)
Occupant gender	C(2)	Male/Female
Occupant age, yrs	OS(3)	$\leq 29/30-54/\geq 55$
Occupant height, cm	OS(3)	$<155/< 170/\geq 170$
Occupant weight, kg	OS(3)	$<50/< 70/\geq 70$
Occupant BMI	OS(3)	$<19/< 25/\geq 25$

^(a) C Categorical variable (number of categories)

OS Ordinal scale variable (number of categories)

Q Quantitative variable

^(b) Light vehicle with an engine displacement of 660 cc or less

^(c) Light truck with an engine displacement of 660 cc or less

^(d) EBS Equivalent barrier speed

2.4 Selection of Variables and Categorizing

Explanatory variables are considered on the basis of the different viewpoints mentioned in previous studies and investigated in Micro Data. Some of these variables have very little information; therefore, 22 explanatory variables are taken into consideration. As a logistic regression model is based on the premise of linear relation between the variables and their log odds ratios [9], the log odds ratios of the variables are ascertained. The odds ratios are calculated between MAIS 3+ and MAIS <3. These explanatory variables are then categorized into few groups

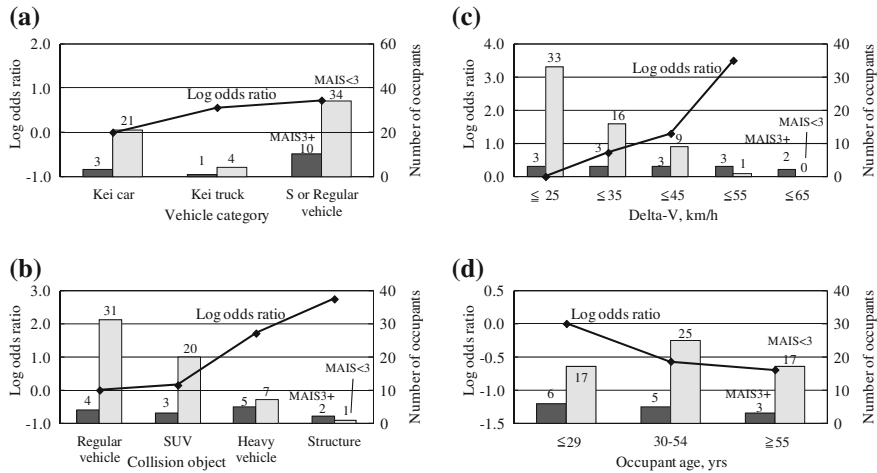


Fig. 2 Log odds ratio of variables and number of occupants for nearside crashes. **a** Vehicle category. **b** Collision object. **c** Delta-V. **d** Occupant age

because the samples of accidents are few. Table 1 shows the explanatory variables and their defined categories.

Figure 2 shows the log odds ratio and number of occupants in MAIS 3+ and MAIS <3 for explanatory variables in nearside crashes. Figure 3 shows the same in farside crashes. Vehicle registration year, vehicle curb weight, extent of crash damage (CDC code), and some occupant attributes including body mass index (BMI) are set as ordinal scale variables [8]. The vehicle impact speed, delta-V, equivalent barrier speed (EBS), and striking vehicle impact speed are set as quantitative variables because they have linear log odds ratios in small divisions. Other variables are set as categorical variables as shown in Table 1.

2.5 Influential Factors and Prediction Model

Prior to performing the regression analysis, variables that are not obviously significant or have multicollinearity are excluded using Pearson's product-moment correlation coefficients and Spearman's rank correlation coefficients. The standard of exclusion is a p value for MAIS >0.5 and a multicollinearity coefficient >0.5. Ordinal logistic regression analysis is performed using these constricted factors. The selection of variables is performed using a backward selection method based on the Wald test. Any variable whose p value is >0.05 is excluded, while an equation whose Akaike's information criterion (AIC) is smaller is selected. The AIC is defined as follows:

$$AIC = -2 \log L + 2(k + l - 1) \quad (2)$$

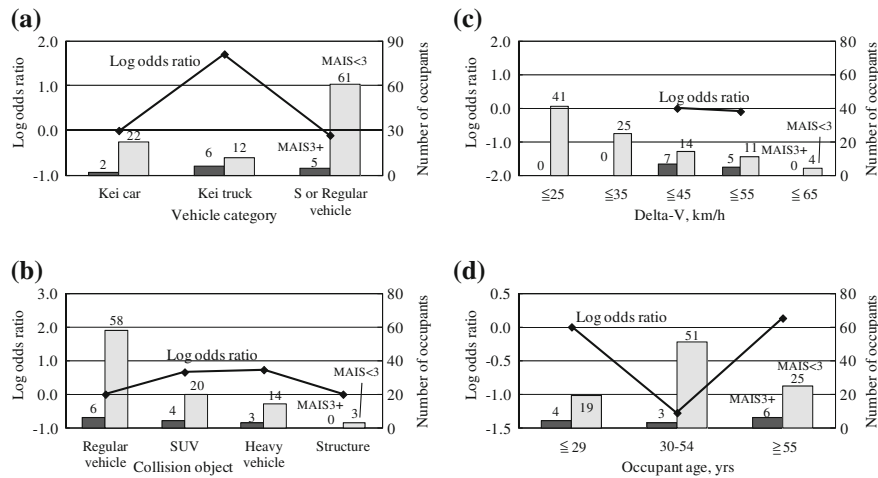


Fig. 3 Log odds ratio of variables and number of occupants for farside crashes. **a** Vehicle category. **b** Collision object. **c** Delta-V. **d** Occupant age

where L is the maximum likelihood, k is the number of object variables' categories (6 in this case), and l is the number of explanatory variables.

2.5.1 Nearside Crashes

EBS and striking vehicle impact speed are excluded because they have multicollinearity with delta-V. EBS has the highest value of Pearson's product-moment correlation coefficient, r , for MAIS ($r = 0.523, p < 0.001$) among the three variables; however, delta-V ($r = 0.507, p < 0.001$) is selected because its coefficient is almost the same as that of EBS and delta-V is easier to obtain during a crash. Vehicle category is excluded because the p value is high ($p = 0.994$) and has multicollinearity with vehicle weight ($r = 0.837, p < 0.001$) using Spearman's rank correlation coefficients. In addition, occupant height has multicollinearity with gender ($r = 0.628, p < 0.001$) and occupant weight ($r = 0.511, p < 0.001$), and occupant weight has multicollinearity with BMI ($r = 0.662, p < 0.001$); therefore, occupant height and weight are excluded. Ordinal logistic regression analysis is performed using the remaining 17 variables for nearside crashes.

2.5.2 Farside Crashes

EBS is excluded because it has multicollinearity with delta-V. Delta-V is selected because its coefficient ($r = 0.412, p < 0.001$) is higher than that of EBS. The striking vehicle impact speed does not have multicollinearity with delta-V, and is

Table 2 Regression results for nearside crashes

Factors		Coefficients	S.E.	p-value
Intercept	MAIS = 1	0.997	1.099	0.364
	MAIS = 2	2.165	1.232	0.056
	MAIS = 3	2.959	1.169	0.011
	MAIS = 4	4.203	1.262	0.001
	MAIS = 5	–	–	–
Delta-V		0.075	0.024	0.001
Damage grade	Small or Medium	–1.593	0.607	0.009
	Large	–	–	–
Striking vehicle	<3500 kg	–1.344	0.662	0.042
curb weight	≥3500 kg	–	–	–

$AIC = 116.6$, $\chi^2 = 34.85$

Nagelkerke $R^2 = 0.431$

correlated to MAIS ($r = 0.213$, $p = 0.03$). Vehicle weight is excluded because it has multicollinearity with vehicle category ($r = 0.716$, $p < 0.001$) and its correlation coefficient is lower than that of the vehicle category. In addition, striking vehicle weight is excluded because it has multicollinearity with lap zone-vertical ($r = 0.507$, $p < 0.001$) and its correlation coefficient is lower than that of the striking vehicle weight. Furthermore, occupant height and weight are excluded for the same reason mentioned in nearside crashes. Ordinal logistic regression analysis is performed using the remaining 17 variables for farside crashes.

3 Results

3.1 Nearside Crashes

The significant factors ($p < 0.05$) are delta-V, damage grade, striking vehicle weight, and steering air bag deployment (A/Bag) for nearside crashes. In this analysis, the coefficient for A/Bag is negative. A negative coefficient means that a case without A/Bag presents a lower risk factor than that with A/Bag. This effect cannot be explained from previous studies. Moreover, the AIC is lower when it is not using A/Bag than when it is using A/Bag; therefore, the A/Bag variable is excluded in the final prediction model for nearside crashes. In addition, because the variable of seat belt use is adopted in other studies [2, 4], this variable is added in the regression model. However, it is not much significant ($p = 0.862$). Therefore, seat belt use factor is not considered in the final prediction model. Table 2 shows the final results of ordinal logistic regression analysis for nearside crashes, and Table 3 shows the comparison between the predicted MAIS and observed MAIS for nearside crashes. The MAIS predictive accuracy rate is 73 and the judgment rate of fatal and serious injuries (MAIS 3+) is 88 %. Thus, the prediction model for nearside crashes shows good results.

Table 3 Predicted MAIS for nearside crashes

Observed MAIS	Predicted MAIS						Total
	1	2	3	4	5	6	
1	47	1	0	0	1	0	49
2	8	2	0	0	0	0	10
3	2	1	0	2	0	0	5
4	3	1	0	1	0	0	5
5	1	0	0	0	3	0	4
6	0	0	0	0	0	0	0
Total	61	5	0	3	4	0	73

Predictive accuracy 0.726, Judgment rate of fatal and serious injuries: 0.877

Sensitivity for MAIS 3+ 0.429, Specificity for MAIS 3+: 0.983

3.2 Farside Crashes

The significant factors ($p < 0.05$) are delta-V, vehicle category, and lap zone-vertical for farside crashes. Similar to nearside crashes, when the variable of seat belt use is added in the regression model, the p value becomes 0.139 and its *AIC* does not decrease; however, residuals between the predicted MAIS and observed MAIS are improved. Therefore, the variable of seat belt use must be added to the regression model. In this model, the p value of lap zone-vertical worsens to some extent ($p = 0.078$); however, the regression model is still totally optimum. Table 4 shows the results of ordinal logistic regression analysis for farside crashes, and Table 5 shows the comparison between the predicted MAIS and observed MAIS for farside crashes. The MAIS predictive accuracy rate is 79 and the judgment rate of fatal and serious injuries (MAIS 3+) is 88 %. Thus, the prediction model for farside crashes also shows good results.

4 Validation of the Prediction Models

4.1 Comparison with Macro Data

To validate the prediction models with documented accidents, the predicted results for the respective significant factors are compared with Macro Data. In Macro Data, the accidents used for comparison are intersecting collisions with right side or left side impacts occurring between 2000 and 2010. The rates of fatalities and serious injuries for drivers are analyzed by cross tabulations for the respective significant factors. These rates are defined as follows:

$$\text{Rate of fatalities} = \frac{\text{Number of fatalities}}{\text{Number of casualties}} \quad (3)$$

Table 4 Regression results for farside crashes

Factors		Coefficients	S.E.	p-value
Intercept	MAIS = 1	4.424	0.886	<0.001
	MAIS = 2	5.415	0.956	<0.001
	MAIS = 3	6.705	1.078	<0.001
	MAIS = 4	7.370	1.171	<0.001
	MAIS = 5	8.680	1.498	<0.001
Delta-V		0.066	0.020	0.001
Vehicle category	Kei car	-0.010	0.649	0.988
	Kei truck	1.323	0.623	0.034
	Small or Regular vehicle	-	-	-
Lap zone -vertical	A,G,H	1.008	0.573	0.078
	E,M,L,W	-	-	-
Seat belt use	Unbelted	0.846	0.572	0.139
	Belted	-	-	-

AIC = 141.3, χ^2 = 31.59

Nagelkerke R^2 = 0.316

Table 5 Predicted MAIS for farside crashes

Observed MAIS	Predicted MAIS						Total
	1	2	3	4	5	6	
1	83	0	1	0	0	0	84
2	9	0	2	0	0	0	11
3	7	0	1	0	0	0	8
4	2	0	0	0	0	0	2
5	1	0	0	0	1	0	2
6	0	0	1	0	0	0	1
Total	102	0	5	0	1	0	108

Predictive accuracy 0.787, Judgment rate of fatal and serious injuries: 0.880

Sensitivity for MAIS 3+: 0.231, Specificity for MAIS 3+: 0.968

$$\text{Rate of serious injuries} = \frac{\text{Number of serious injuries}}{\text{Number of casualties}} \quad (4)$$

In Japanese Macro Data, delta-V is not analyzed but *Pseudo* delta-V, defined in Table 6, is recorded for every 5 km/h increase in speed. Two consecutive steps (± 5 km/h) from 10 to 50 km/h are added for comparison with the predicted rates. In the comparison, it is assumed that fatalities have MAIS of 5+ and serious injuries have MAIS of 3–4, because MAIS of 5+ has 43 % cumulative fatalities in Micro Data. Furthermore, vehicles with lap zone-vertical codes of “A,” “G,” or “H,” which have upper side deformation such as to the roof, are assumed to have a large damage grade because the lap zone-vertical data are not recorded in Japanese Macro Data. Vehicles without these codes are assumed to have a small or medium

Table 6 Definition of *Pseudo delta-V*

Type of accidents	Definition ^(a)
Intersecting collision	$Pseudo\ delta - V_1 = \frac{M_2}{M_1 + M_2} \times V_2$
Structure collision	$Pseudo\ delta - V_1 = V_1$

^(a) where V Vehicle hazard recognition speed

M Vehicle curb weight

Subscript 1 Calculated(struck) vehicle

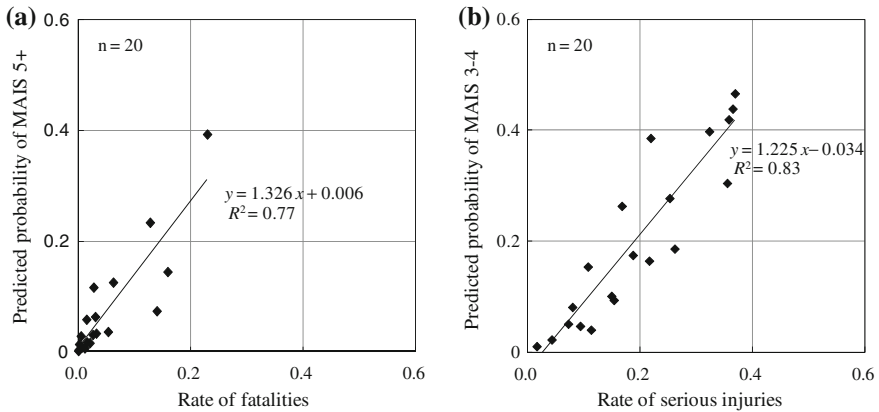
2 Striking vehicle

damage grade, whereas categories that have less than 40 casualties or zero fatality are excluded in the comparison.

Figure 4 shows the comparison for nearside crashes between the rate of fatalities in Macro Data and the predicted probability of MAIS 5+ and that between the rate of serious injuries in Macro Data and the predicted probability of MAIS 3–4. Figure 5 shows the same comparison for farside crashes. These data have strong correlation. Therefore, the injury prediction models can be used to evaluate occupant injuries in side impact crashes in Japan. However, the fatality rate for farside crashes has a slower inclination and a lower correlation than that for other crashes. One of the reasons is that there are few samples of fatalities in farside crashes. In addition, there are two groups that have different tendencies, as shown in Fig. 5a. This is an issue that needs further investigation.

4.2 Injury Risks by Influential Factors

The prediction models in this study evaluate injury risks by using influential factors and are compared with Macro Data for the respective conditions. In this comparison, the predicted probability of MAIS 3+ is compared with the rate of fatalities and serious injuries, which is the number of fatalities and serious injuries divided by the number of casualties. Figures 6 and 7 show comparisons for nearside and farside crashes. These prediction models can generally correspond with documented accident data. In these figures, large damage grade impacts have twice the risk of fatalities as compared with small or medium damage grade impacts in nearside crashes. Nearside crashes are twice as severe as farside crashes in terms of fatalities and serious injuries. Regarding the striking vehicle weight for nearside crashes and the vehicle category for farside crashes, these factors show the same tendencies between the predicted lines and Macro Data in Figs. 6 and 7; however, their values are different to some extent. The p values of these two factors are lower than those of other factors. As a result, these factors cause large errors in the prediction models. This is because these factors depend on the specified samples and few samples are available. This is one of the important issues of Japanese Micro Data.



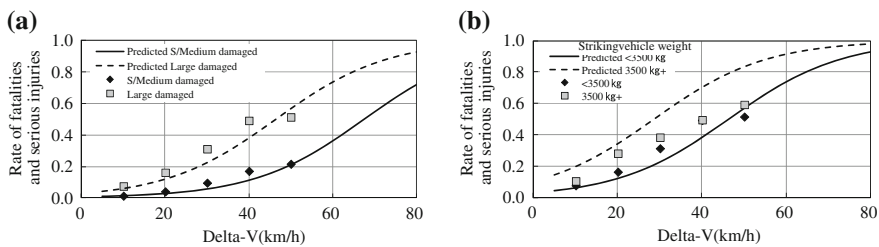


Fig. 6 Injury prediction for influential factors in nearside crashes. **a** Damage grade for striking vehicle weight <3,500 kg. **b** Striking vehicle weight for large damage

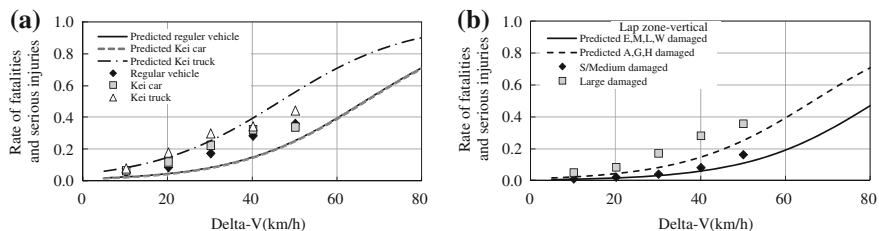


Fig. 7 Injury prediction for influential factors in farside crashes. **a** Vehicle category for belted drivers with A, G, or H lap zone-vertical. **b** Lap zone-vertical for belted drivers in regular vehicles

Table 7 Accident cases with large residual for nearside crashes

Residual	Accident characteristics	Number of casualties
Underestimated	SUV or truck collision with chest injury	5
	Belted driver with abdomen injury	1
	Unbelted driver with B-lap zone impact	1
Overestimated	Minivan without large deformation	1
Total		8

For nearside crashes, there are five underestimated SUV or truck collisions that resulted in chest injury. SUV side impact crashes are one of the extraordinary accident types in the United States. Although the size of SUVs in Japan is smaller than that in the United States, SUV side impact crashes are one of the extraordinary accident types in Japan, too. The factor of SUV is considered in the first regression model but it is not selected, and further study is required. For farside crashes, there are four unbelted drivers with head, neck, or chest injury. Seat belt use is one of the significant factors in the prediction model of farside crashes; however, its evaluated effect is insufficient. Further investigations into these outlier cases are needed.

On the other hand, there are no single vehicle accidents in the outlier cases. This shows that these prediction models can evaluate single vehicle accidents. However, more samples of single vehicle accidents are needed to confirm the accuracy of the models.

Table 8 Accident cases with large residual for farside crashes

Residual	Accident characteristics	Number of casualties
Underestimated	Unbelted driver with head, neck, or chest injury	4
	Multiple impact (with frontal impact)	2
	Belted female driver with abdomen injury	2
	Heavy vehicle collision	1
	Unknown	2
Overestimated	Belted young driver	1
Total		12

6 Conclusions

This study presents injury prediction method and detailed factors that influence nearside crashes and farside crashes using data on traffic accidents in Japan. Ordinal logistic regression analysis using Micro Data is used to construct the injury prediction models and illustrate significant factors. Japanese Macro Data is used to validate these models. Furthermore, the residual analysis indicates characteristic accident factors that could not be evaluated by the models. The conclusions of this study are as follows:

- (1) The significant factors are delta-V, damage grade, and striking vehicle weight for nearside crashes; and delta-V, vehicle category, lap zone-vertical, and seat belt use for farside crashes. Thus, these two types of crashes have different factors.
- (2) The prediction models using the above factors show good results, and the MAIS predictive accuracy rate is approximately 75 and the judgment rate of fatal and serious injuries (MAIS 3+) is approximately 90 %. Furthermore, the models can correspond to Macro Data, which show data for documented accidents.
- (3) The residual analysis indicates characteristic accident factors such as SUV side impacts for nearside crashes and unbelted drivers for farside crashes. These factors are found to be influential. Further investigation into these outlier accidents would prove beneficial in reducing traffic accident casualties in Japan.

References

1. Malliaris AC et al (1997) Relationship between crash casualties and crash attributes. SAE Technical Paper, No 970393
2. Jeffrey A et al. (2001) Development and validation of the URGENCY algorithm to predict compelling injuries. Proceeding of the 17th ESV conference, no. 352

3. Jeffrey A et al. (2003) Methodology for the development and validation of injury predicting algorithms. Proceeding of the 18th ESV conference, no. 467
4. Suguru Y et al. (2011) Estimation of injury risk using Japanese accident data (second report). Proceeding of the JSAE annual congress (Spring), no. 78–11, pp 5–8
5. Shigeru T et al. (2009) A new methodology for predicting injury severity based on Japanese traffic accident data. Proceeding of the JSAE annual congress (Spring), no. 29–09, pp 1–4
6. Yusuke M et al. (2010) Prediction method of injured body parts on virtual accident database in frontal collision constructed from multi-body dynamics simulations. Proceeding of the JSAE annual congress (Spring), no. 78–10, pp 27–30
7. Maika K et al. (2011) Occupant injury prediction based on frontal collision accident simulations using a human model—consideration of age and gender. Proceeding of the JSAE annual congress (Spring), no. 78–11, pp 15–18
8. Kuniyuki H (2012) A study on injury prediction method and influential factors in frontal collision using accident data. Trans JSAE 43(2):261–267
9. Takahashi Y (1995) Introduction to logistic and proportional hazard models for doctors. Nihon Igakukan, Tokyo

Research on Vehicle Transportation Safety Risk Assessment and Control

Jie Yang and Xinpeng Tang

Abstract Introduce the theory of vehicle transportation security risk assessment and control, and apply it in the automobile unit (division)'s vehicle transportation support tasks. The paper is introduced in fuzzy analytic hierarchy process (FAHP) and fuzzy comprehensive evaluation (FCE) to obtain the comprehensive priority of the risk factors and the risk level of the entire system, and accordingly give the risk control measures, finally verified by an example, indicate the effectiveness and feasibility of this method for the transportation security management forecast and decision making.

Keywords Vehicle transportation safety · Risk assessment · FAHP · FCE · Control measures

1 Introduction

With the increasing of vehicle ownership in China, there are greater hazard in vehicle transport safety, accidents occur frequently. In the army, the transportation support tasks at all levels are heavy, with complex environment, difficult conditions, plus drivers team placed quickly. These lead to more transportation safety risk factors, the safety management is extremely difficult. According to statistics,

F2012-F05-004

J. Yang (✉) · X. Tang
School of Mechanical Science and Engineering, Huazhong University of Science and Technology, Wuhan, China

the number of accidents caused by military vehicle transportation is more than 60 % of the total every year. Preventing vehicle accident is the top priority of the military safety works, so it becomes the urgent matter to improve ways and means of vehicle safety management. Along with the time development and the progress of science and technology, new security measures appear more and more, however, not all safety measures lead to increased safety [1]. Risk management is a comprehensive management functions to assess and address the risks faced by an organization [2]. The use of risk assessment and control can predict the risk factors in the transport process comprehensively, grasp of the safety risk level accurately, and formulate target-oriented risk control measures in accordance with the assessment result, thus effectively reduce the occurrence of risk event, improve the security of vehicle transport.

Safety risk assessment and control, means that after taking comprehensive prediction and assessment of system risk, according to the results, take targeted restrictive measures on the system risks and countermeasures to control risks incident [3]. Vehicle transportation safety risk assessment and control, means to combine the risk management and road transport security theory, based on the risk identification, make a qualitative or quantitative assessment of transportation safety risk, and formulate appropriate safety measures with risk control theory. The goal includes: minimizing risk of pre-accidents events, minimizing risk transport accidents, minimizing transport accidents effects, minimizing effects of transport catastrophes [4].

Common strategic methods of risk control includes: risk avoidance, risk reduction, risk transfer and risk acceptance. Technical method includes: remove, replace, mitigate, isolation, process control, protection and discipline [5]. Vehicle transportation safety risk control measures roughly divide into two classes: One is to prevent the accidents, such as the vehicle examines annually, another is to mitigate the injuries after the accident, such as the use of seat belts [6].

Implementing vehicle transportation safety risk assessment and control, should first set up a specialized organization, make them clear the duties and basic procedures, then according to the actual task, analyse the risk factors, implement risk assessment, formulate corresponding risk control scheme by the assessment results analysis, and perfect in the process of implementing the control scheme, in order to control over the security risks of the whole task process.

This paper selects the fuzzy comprehensive evaluation methods based on the fuzzy analytic hierarchy process to determine the weight. The method concentrates reflection the respective advantages of AHP and FCE, not only overcomes the limitations of the traditional risk assessment methods to quantify the risk factors difficultly, but also solves the problem that there is partial more uncertainty in the process of assessment, and it carries out a clear analysis difficultly when using other methods. Risk control takes target control mode in management control learn, that is a tracking control way, implemented by the operating procedures “setting the overall objective—the decomposition of objective—implementation and achievement of objective—the feedback objective achievement” [7]. Finally, the paper combines with an example, obtains the comprehensive sort of a

transportation task safety risk sub-factors relative to the overall goal, comes to the comprehensive security risk rating score of the task, and gives the appropriate risk control report.

2 Instruction of the Assessment Method

2.1 Setting up the Assessment Index System

A risk management system is a detailed and systematic process to identify risks and understand the likelihood and potential consequences of [8]. Transportation support tasks taken up by automobile unit (division) responsible, not only include general daily transport, but also include important transport task such as combat exercises, the large-scale persons and goods transport and etc. And the risks are often with the characteristics of the difficult environment, complex condition, quantity of personnel and vehicles participating, so the risk factors involved in the tasks are also very complex. The establishment of a risk index system should fully consider all the risk factors affecting transportation safety, and systematically classify risk factors, screen out the typical indicators which can represent the various components of the transportation security system. The indicators selected should not only follow the law of traffic accidents, but also grasp the key points of the task itself, it is necessary to be able to reflect on a part of the risk factors, but also to guarantee the independence of the indicators.

In accordance with the principles above and the actual military transport safety, automobile unit (division) transportation safety risk assessment index system can be established as the construction below (as shown in Table 1).

2.2 Based on FAHP to Determine the Weight

After establishing the index hierarchy, it also determined the affiliation of risk indicators factors. Following from the above hierarchy and expert advice, use the method of constructing fuzzy consistent matrix to obtain the weight of the factors at all indicators layers. Now introduce the concept of the fuzzy consistent matrix [9] firstly:

Definition 1: Set matrix $R = (r_{ij})_{n \times n}$, if meet $0 \leq r_{ij} \leq 1$, $(i, j = 1, 2, \dots, n)$, it says R is a fuzzy matrix.

Definition 2: Set fuzzy matrix $R = (r_{ij})_{n \times n}$, if meet $r_{ij} + r_{ji} = 1$, $(i, j = 1, 2, \dots, n)$, it says fuzzy matrix R is a fuzzy complementary matrix.

Definition 3: Set fuzzy matrix $R = (r_{ij})_{n \times n}$, if i, j, k meet $r_{ij} = r_{ik} - r_{kj} + 0.5$, it says fuzzy matrix R is a fuzzy consistent matrix.

Table 1 Military vehicle transportation security risk assessment index system

The first level index layer	The second level index layer
Driver (U_1)	Physical condition (U_{11}), psychological quality (U_{12}), professional ethics and attitude discipline (U_{13}), driving technical experience (U_{14})
Vehicle technology condition (U_2)	Handling stability (U_{21}), braking performance (U_{22}), wheels and tires (U_{23}), light signal (U_{24}), assembly components reliability (U_{25})
Environmental condition (U_3)	Road conditions (U_{31}), traffic environment (U_{32}), weather and climate conditions (U_{33}), task itself (U_{34}), time period (U_{35})
Organization and management (U_4)	Timeliness of safety education (U_{41}), task program establishment and implement (U_{42}), tool and Spare parts equipped with (U_{43}), maintenance and safety checks (U_{44}), medical and maintenance support on the way (U_{45})
Others (U_5)	Other traffic participants' behaviour (U_{51}), natural geological disasters (U_{52})

Table 2 0.1–0.9 scale meaning table

Scale	Meaning	Explanation
0.5	Equally important	Compared to two factors, both are equally important
0.6	Slightly important	Compared to two factors, the former than the latter slightly
0.7	Obviously important	Compared to two factors, the former than the latter extremely important
0.8	Strongly important	Compared to two factors, the former than the latter strongly
0.9	Extremely important	Compared to two factors, the former than the latter is extremely important
0.1–0.4	Contrary to the above	Contrary to the above

- (1) Structure the fuzzy complementary matrix. Combined with expert advice, by the comparison between each two factors, construct fuzzy complementary matrix $R = (a_{ij})_{n \times n}$. It indicates the relative importance between this layer related factors for relative upper index. Quantitative description for the importance of the each two factors comparison shows such as 0.1–0.9 scale meaning table (as shown in Table 2).
- (2) Get fuzzy consistent matrix. Check out whether the fuzzy complementary matrix constructed has the consistency from definition 3, if not, get the fuzzy consistent matrix by the following methods: First sum the fuzzy complementary matrix as per row, written for $r_i = \sum_{k=1}^n a_{ik}$, ($i = 1, 2, \dots, n$), and make the following mathematical transformation $r_{ij} = \frac{r_i - r_j}{2n} + 0.5$, thus established matrix $R = (r_{ij})_{n \times n}$ is fuzzy consistent.
- (3) Calculate all levels factors weights. Take the line and normalization method to fuzzy consistent matrix $R = (r_{ij})_{n \times n}$ to calculate all levels factors

weights $W = (w_1, w_2, \dots, w_n)$, where the weights meet

$$w_i = \frac{\sum_{j=1}^n r_{ij} - 1 + \frac{n}{2}}{n(n-1)}, (i = 1, 2, \dots, n), n \text{ is the order of } R.$$

- (4) Calculate integrated sort weights of the level factors relative to the target layer. Calculate from target layer to bottom layer, the importance of comparing all the factors in same layer relative to the target layer is used by integrated sort weight. If the sort weights of the factors b_1, b_2, \dots, b_m in the first layer relative to the target layer is $w_{b_1}, w_{b_2}, \dots, w_{b_m}$, and the sort weights of the factors c_1, c_2, \dots, c_n in the second layer relative to the factor b_i is $w_{c_1}, w_{c_2}, \dots, w_{c_n}$, When c_i and b_j are not linked, $w_{c_{ij}}$ is 0. The integrated sort weight of the factor c_i in the second layer relative to the target layer is $W_i^T = \sum_{i=1}^n w_{b_i} \cdot w_{c_{ij}}$, in which $j = 1, 2, \dots, n$. Repeating the process to the bottom, can obtain the security risks integrated sort weight of all sub-factors relative to target layer.

2.3 Fuzzy Comprehensive Evaluation Method [10] to Conduct Comprehensive Assessment

- (1) Establish the Factors Set. Accordance with the hierarchy of the index system, establish the security risk factor sets in the first layer $U = \{U_1, U_2, \dots, U_m\}$, divide factors set U into m sub-factor sets $U_i = (U_{i1}, U_{i2}, U_{i3}, \dots, U_{ij})$, in which $i = 1, 2, \dots, m; j = 1, 2, \dots, t$.
- (2) Establish the Comments Set. In accordance with the degree of influence risk factors, transportation security risk rating is divided into {High, higher, generally, lower}, with $V = (v_1, v_2, v_3, v_4)$ to represent.
- (3) Evaluation of Factor Sets in the Second Level
- I. Single factor evaluation. Regard sub-factor U_{ij} to the comments set V as a fuzzy mapping, it can determine the fuzzy membership of single sub-factor U_{ij} attach to each comment, thus get the fuzzy evaluation vector of sub-factor U_{ij} on V : $r_{ij} = (r_{ij1}, r_{ij2}, r_{ij3}, r_{ij4})$
 - II. Construct sub-factors set evaluation matrix. According to the fuzzy evaluation vector of the sub-factors U_{ij} , it can determine the fuzzy evaluation membership degree matrix of

$$U_i$$

$$R_i = (R_{i1}, R_{i2}, \dots, R_{im})^T = \begin{pmatrix} r_{i11} & r_{i12} & r_{i13} & r_{i14} \\ r_{i21} & r_{i22} & r_{i23} & r_{i24} \\ \dots & \dots & \dots & \dots \\ r_{im1} & r_{im2} & r_{im3} & r_{im4} \end{pmatrix}$$

- III. Determine the sub-factor weight. Second-level factors weight is represented by $W_i = (w_{i1}, w_{i2}, \dots, w_{ij})$. It can be established by FAHP.
- IV. Establish a single-level fuzzy evaluation model. According to the fuzzy theory, get the evaluation result of U_i using fuzzy synthetic relationship operations: $C_i = W_i \circ R_i = (c_{i1}, c_{i2}, \dots, c_{i4})$, in which “ \circ ” is fuzzy synthetic relationship operator. Fuzzy synthetic relationship operator generally includes three types: main factors determine type $M(\wedge, \vee)$ or $M(\vee, \wedge)$, main factors of outstanding $M(\vee, \cdot)$, weighted average type $M(\cdot, +)$. The operator is generally selected according to the actual situation.
- V. Comprehensive evaluation of the overall goal. Regard every factor set U_i as a factor, use C_i as its single factor evaluation, it can obtain a fuzzy mapping from factors set U to V , that is the fuzzy evaluation matrix of U relative to V , $R = (C_1, C_2, C_3, \dots, C_s)^T$, combining with the sub-factors weight of $U:W = (w_1, w_2, \dots, w_s)$. Then it could obtain the fuzzy comprehensive evaluation vector of overall goal $C = W \circ R = (c_1, c_2, \dots, c_4)$. This approach can be used for three or even more advanced fuzzy comprehensive evaluation.

3 An Application Example

A border regiment plans to transport winter goods and materials for directly under border station. The time is the whole day on October 7, ** years. Transportation line: Regiment headquarters—X border station. Task: Transport several all kinds of materials 48 tons and 18 rotation officers and soldiers. Dispatched vehicles: Ten (One command vehicle, eight 6t truck, one passenger car). The other personnel: main drive, co-pilot a total of 12, 4 led cadres. Road conditions: 360 km (National highway about 180 km, Gobi simple road about 100 km, mountain road about 80 km). Environment condition: The winding mountain road, early winter cold climate, accompanied by the mountains of snow, cold, windy weather, complex situation. In order to ensure that the whole transportation task are completed safely and smoothly, league organizations relevant leaders and business personnel to carry out security risk assessment in the assessment index system on the basis of Table 1, and make the risk control scheme according to the assessment results.

3.1 Using FAHP to Obtain All Levels of Factors Weights and the Integrated Sort Weight

By the expert survey and FAHP above, calculate the factor weights of each level and its integrated sort weight on target layer. The result is shown in Table 3.

Table 3 Factor weights and its integrated sort weight

First level index layer	Weight w_i	Secondary index layer	Weight w_{ij}	Integrated sort weight	Integrated sort
Driver	0.2125	Physical condition	0.2567	0.0545	4
		Psychological quality	0.2433	0.0517	5
		Professional ethics and attitude discipline	0.2700	0.0574	3
		Driving technical experience	0.2300	0.0489	7
Vehicle technology condition	0.1875	Handling stability	0.2250	0.0422	12
		Braking performance	0.2125	0.0398	15
		Wheels and tires	0.2000	0.0375	16
		Light signal	0.1750	0.0328	19
		Assembly components reliability	0.1875	0.0352	17
Environmental condition	0.2250	Road conditions	0.2150	0.0484	8
		Traffic environment	0.1900	0.0428	10
		Weather and climate conditions	0.2275	0.0512	6
		Task itself	0.1775	0.0399	14
Organization and management	0.2000	Time period	0.1900	0.0428	10
		Timeliness of safety education	0.2125	0.0425	11
		Task program establishment and implement	0.2250	0.0450	9
		Tool and spare parts equipped with	0.1750	0.0350	18
		Maintenance and safety checks	0.2000	0.0400	13
		Medical and maintenance support on the way	0.1875	0.0375	16
Others	0.1750	Medical and maintenance support on the way	0.5200	0.0910	1
		Natural geological disasters	0.4800	0.0840	2

3.2 Fuzzy Comprehensive Evaluation

Invite ten experts to collect the survey comments, obtain the fuzzy evaluation matrix of the sub-factors sets on secondary index layer U_i to reviews V . Select $M(\cdot, +)$ type, that is weighted average type fuzzy synthetic relationship operator to do evaluate plan of the various sub-factors set on secondary index layer:

$$C_1 = W_1 \circ R_1 = (0.1040, 0.2337, 0.3487, 0.3137),$$

$$C_2 = (0.0438, 0.1100, 0.3313, 0.5150),$$

$$C_3 = (0.1113, 0.3770, 0.2938, 0.2180),$$

Table 4 Safety risk reviews set score table

Goal scoring (a perfect 100 points)	Fuzzy reviews set	Index reviews set
≥ 80	High	
70 – 80	Higher	$V = \{\text{high, higher, general, lower}\}$
60 – 70	General	
40 – 60	Lower	

$$C_4 = (0.2375, 0.2125, 0.2750, 0.2750).$$

$$C_5 = (0, 0.052, 0.2520, 0.6960),$$

Now we can know the fuzzy comprehensive evaluation matrix of overall goal U is $R = (C_1, C_2, C_3, C_4, C_5)^T$, ultimately the overall risk evaluation result got is $C = W \circ R = (0.1029, 0.2067, 0.3014, 0.3891)$.

4 Results Analysis and Risk Control

4.1 Results Analysis

The results above shows that, the proportion of the transportation task comprehensive security risk accounts for the “high”, “high”, “Normal”, “lower” is 10.29, 20.67, 30.14, 38.91 %. Now contrasting to the safety risk reviews set score table (Table 4), take $V = \{90, 80, 65, 50\}$, the risk composite score

$$k = \sum_{i=1}^4 c_i v_i = 64.8430, \text{ so the security risk level of the transport task is “general”}.$$

Similarly, the risk level of the main risk factors to affect the overall security risk is: “driver” in general, “vehicle technical condition” in lower, “environmental conditions” in general, “organization and management” in general, “others” in lower.

From the sort of individual security risk factors relative to the overall impact, we can see that the risk fact should be caused enough attention of policymakers, such as “Other traffic participants’ behaviour”, “natural geological disasters”, “professional ethics and attitude discipline” and etc.

4.2 Risk Control

According to the integrated sort of factor risk, combining with risk control theory, formulate appropriate risk control measures in order. And make the risk control

Table 5 Transportation tasks security risk control report

Order number	Risk factor	Risk control measure
1	Other traffic participants' behaviour	Strict safety education and driving organization
2	Natural geological disasters	Perfect plan, strengthen investigation, strict driving organization
3	Professional ethics and attitude discipline	Adjust drivers, strict safety education and management
4	Physical condition	Adjust drivers, health care
5	Psychological quality	Adjust drivers, psychological counselling
6	Weather and climate conditions	Grasp meteorological information anytime, perfect plan, strengthen safety guidance and driving organization
7	Driving technical experience	Strictly select drivers, strengthen safety guidance
8	Road conditions	Strengthen safety guidance and driving organization
9	Task program establishment and implement	Review and check the scheme seriously, improve anytime
10	Time period	Avoid danger period, arrange rest time scientifically
11	Traffic environment	Strengthen safety guidance and key sections organization
12	Timeliness of safety education	Strengthen implement, tracking guide organization
13	Handling stability	Strengthen specific technical guidance
14	Maintenance and safety checks	Strict accountability, strengthen the work coordination
15	Task itself	Clear responsibility, strengthen the organization and inspection
16	Braking performance	Strengthening technical guidance, take auxiliary measures
17	Medical and maintenance support on the way	Clear responsibility, strengthen coordination
18	Wheels and tires	Strengthening safety guidance, perfect plan
19	Assembly components reliability	Strictly select and check for vehicles
20	Tool and spare parts equipped with	Strengthen supervision and check, full consideration
21	Light signal	Strict maintenance and inspection

measures enacted itemized list in chronological order, ultimately form the transportation tasks security risk control report (as shown in Table 5).

5 Conclusions

The use of FAHP to determine the weight of the transport safety risk factors, overcomes the disadvantages of the traditional AHP, and determines importance order of risk factors more comprehensively and reasonably. The example shows

that, this method used for comprehensive assessment of the vehicle transportation safety risk factors, can determine the priority of the risk factors, and also can obtain the risk level of the whole system combined with the risk factors scores. The assessment results draw closer to the people's way of thinking and the actual qualitative assessment, and the decision-making information provided are more broad and accurate. Consequently provide a better basis for the development of risk control measures. The use of vehicle transportation security risk assessment and control, could predict the risk factors during the vehicle transport more intuitive and assess accurately, establish the risk control measures more targeted, provide a good method means for army to prevent vehicle accident. This method also applies to the safety management of professional vehicle transportation enterprises.

References

1. Røsjø B (2003) The RISIT research programme—risk and safety in the transport sector. The Research Council of Norway, Oslo
2. Xinli L (2006) Risk management. Peking University Press, Beijing
3. Lin B (2007) Safety system engineering. China Labor Social Security Press, Beijing
4. Szymanek A (2010) “Defence-in-depth” strategy in transport risk management. TST 2010, CCIS 104:51–58
5. Guohua C (2007) Risk engineering. National Defense Industry Press, Beijing
6. Hong T (2006) Risk control and road traffic safety. Chin Mark 26:84–85
7. Dong Du (2006) Management control learn. Tsinghua University Press, Beijing
8. Work Cover Corporation (2003) Road freight transport industry occupational health and safety. Work Cover Corporation of South Australia, Adelaide
9. Feng K (2008) The fuzzy multiple attribute decision theory, methods and the application. China's Agricultural Science and Technology Press, Beijing
10. Xiaoqiu S (2004) Fuzzy mathematical theory and method. China's Mining Industry Press, Xuzhou

Development of an Integrated Test Bed and Virtual Laboratory for Safety Performance Prediction in Active Safety Systems

**Thomas Helmer, Thomas Kühbeck, Christian Gruber
and Ronald Kates**

Abstract This paper describes recent progress toward achieving representative and reliable active safety performance assessment of advanced driver assistance systems (ADAS). Because ADAS act within a complex, dynamic traffic environment, reliable evaluation of their safety benefits poses methodological challenges. For a proposed ADAS, its expected contribution to reduction of mortality and injuries as well as false positives should be predicted. To meet these challenges, our approach incorporates identification of target scenarios; calibration and validation of stochastic behavior and accident injury models; stochastic (Monte-Carlo) simulation of target scenarios in varied traffic contexts with/without ADAS; and integration of supporting and corroborating field and laboratory analyses. These include a new controlled, high-throughput approach to sensor testing and algorithm validation in camera-based ADAS using a virtual graphical test bed, which supports systematic identification of critical external conditions that could modify performance or lead to a failure mode. The methodologies introduced here are designed to ensure validity of all key links in the assessment chain, not limited to those aspects that can be assessed in a single test.

Keywords Active safety · Effectiveness · Evaluation · Testing · Methodology

F2012-F05-005

T. Helmer (✉) · T. Kühbeck · C. Gruber
BMW AG, Munich, Germany

R. Kates
REK Consulting, Otterfing, Germany

1 Introduction

Improved automobile sensor and inter-vehicle communication technologies are spurring the conception and development of novel advanced driver assistance systems (ADAS) that are believed to have a positive impact on safety. However, deploying ADAS based purely on “engineering intuition” (without prior impact assessment) is neither risk-free nor cost-effective: Risks are associated with false positive interventions, for example; long observation periods required to accumulate performance statistics result in a severe feedback lag to the development and optimization process. Thus, in order to design assistance systems that will most effectively reduce the number of accidents and their severity, there is an urgent need for reliable safety performance assessment during development, prior to deployment.

In addition to automobile manufacturers and suppliers, public policy and opinion makers as well as regulatory agencies are key stakeholders in safety assessment. Assessment techniques likely to be accepted by all stakeholders should provide targeted, quantified safety performance prediction: In this context, a *target* corresponds to a specific traffic situation or accident scenario, for example, “pedestrian collisions involving a mid-block dash by the pedestrian”. *Quantification* refers here to an objective metric: for example, the expected reduction in the MAIS2+ (maximum of the abbreviated injury scale) injuries to pedestrians. Further components of overall safety performance include estimated frequency of false-positives (i.e., unnecessary triggering), classified according to severity of their side-effects. Stochastic (non-deterministic) influences on the effectiveness of safety devices are well known in the field of passive safety assessment. In active safety assessment, stochastic influences introduce new complexities, because ADAS work by modifying the pre-crash chain of events. Thus, their effects are “filtered” by stochastic response functions (e.g., driver response characteristics, influence of surrounding traffic). Moreover, sensors are also subject to uncertainties and stochastic influences. Thus, detection quality and ultimately safety performance (including false positives) can depend sensitively on specifications for sensors, system activation logic, etc. Assessment methodologies that can reliably quantify the effects of sensor quality and parameter variations on performance are thus needed for parameter optimization.

This paper describes recent progress toward achieving representative and reliable active safety performance assessment of ADAS. The key challenge is that ADAS are actors within a complex, dynamic traffic environment. To meet this challenge, our approach includes identification of target scenarios; calibration and validation of stochastic behavior and accident injury models, a virtual graphical algorithm testing environment; stochastic (Monte-Carlo) simulation of target scenarios in varied traffic contexts with/without ADAS; and integration of supporting and corroborating “classical” analyses.

2 Requirements for Active Safety Assessment in ADAS

2.1 Identification of ADAS Target Scenarios

Safety performance analysis of novel ADAS requires identification of target accident scenarios that could be positively affected by a proposed ADAS. This stage usually involves an assessment of the priority of the target scenarios based on summary statistics from existing accident data bases such as the German In-Depth Accident Study (GIDAS) [1–6]. (As the number of proposed ADAS increases, this step should include assessments of “competing” safety systems that address similar targets). This level of accident data base analysis is preliminary in that it provides little or no information on the potential of proposed ADAS for actually preventing or mitigating the accident in question, nor does it begin to address the risks associated with false positives.

In order to be useful for detailed safety performance assessment, preliminary analysis should include generation of plausible hypotheses concerning how (by what specific mechanisms) a proposed ADAS would avoid or mitigate accidents in target scenarios. In practice, the hypothesis generation stage may need to be revisited, since detailed assessment may reveal that the original targets are not efficiently addressed by the proposed ADAS, or that adverse effects outweigh the benefits.

2.2 Safety Performance Metrics

2.2.1 Injury Reduction

Quantification of ADAS safety benefits in a target scenario requires comparison of an objective safety performance metric “with vs. without” the system. An ideal metric should reflect injury and mortality reduction *in the field*, not just under lab conditions. To this end, one applies the law of conditional probabilities: Suppose we can estimate the influence of an ADAS on probabilities and detailed characteristics of accidents in the field (see below). By estimating the dependence of injury severity probabilities (MAIS, injury severity score: ISS) conditioned on accident characteristics and “convoluting” (folding) these probabilities, one can quantify expected injury reduction in the field.

Several complementary approaches are available for estimating the dependence of injury severity probabilities on accident characteristics. One method is to construct multivariate logistic regression models (or more advanced multivariate statistical models) using existing accident databases [7–10]. The generalizability of models based on a particular country—Germany, in the case of GIDAS—is of course a separate issue that goes beyond the scope of this paper. Another approach used in our group is referred to here as “co-simulation”: A representative sample

of pre-crash time series including all relevant characteristics of the vehicles and humans involved is generated (see below). These characteristics are input to a high-resolution crash simulator, which can then quantify key severity indicators such as the head injury criterion (HIC), chest acceleration/extension, neck forces, etc. on virtual dummies [11]. ADAS benefits of course include not only decreases in injury severity by mitigation but also crashes that are entirely avoided by the ADAS [4].

2.2.2 Specificity or Number Needed to Treat

It is noteworthy that some active safety interventions such as automatic braking or swerving could induce severe adverse effects, such as a loss of controllability, either for the original driver or for upstream vehicles. Moreover, even *controllable* interventions or warnings are associated with mildly adverse effects in terms of user acceptance if they are clearly superfluous. Considering that ADAS can only be effective if they are activated, and activation usually depends on user acceptance, there is a feedback loop from false positives to overall effectiveness. Hence, further components of overall performance usually involve classification and quantification of expected false-positives (unnecessary triggering) according to severity of adverse effects as well. A useful statistic borrowed from medicine is the “number needed to treat” (NNT), defined here as the number of system actions needed to prevent one “adverse outcome”. This statistic may be computed separately for each type of system action (warnings, interventions) and with respect to any metric component such as injuries at some severity level (e.g., MAIS 3+), total collisions, etc. If one can associate a “cost” with each kind of system action and a “benefit” with each prevented adverse outcome, then it is possible to compute and optimize an overall safety performance metric.

3 Assessment Techniques

3.1 Stochastic Modeling Techniques and Traffic

This section gives an overview of an approach to safety performance assessment and optimization of ADAS using stochastic or “Monte-Carlo” simulation [6, 12]. Simulative safety performance assessment of ADAS requires first of all reconstruction or modeling of all important processes—including physiological, psychological, and physical phenomena—that contribute to accident risk and that can be influenced by an ADAS within a target scenario. Second, estimation of specificity (e.g., by NNT statistics as described above) also requires modeling and simulation of all situations in which the system might be triggered, whether or not an accident would have occurred. These situations generally occur far more

frequently than the accidents we would like to prevent! Hence, the function of ADAS in the entire range of relevant traffic contexts must be modeled, not just the function in the small subset of situations that have led to accidents as recorded in known databases.

As a general strategy for evaluating proposed safety systems, it is useful to think in terms of a virtual experiment: We thus define one or more “base” or reference cases which describe the scenario in question without the proposed safety system and design a virtual experiment to assess a difference with the system. The quality of simulation-based assessment will depend on simulation *fidelity*, i.e., how well and with what degree of depth and complexity these processes and their interactions are modeled—particularly the possible partial and global failure modes. Human misjudgment is always involved. When one quantifies the frequency of human errors, it almost seems surprising how few accidents occur. The reason is of course that inherent redundancies (such as risk perception and corrective emergency actions by one of the actors) usually compensate for partial failures. As a first step toward validation of simulation fidelity, simulation results in the reference case (“without the system”) can be compared with the “gold standard” of empirical data or field measurements. The safety benefits of any ADAS will depend on how well the system influences or interacts with all of these processes (e.g., by adding redundancy) to reduce the probability of global failures and/or mitigate their consequences.

Design of ADAS and prediction of ADAS safety performance must take into account the stochastic nature of the processes to be modeled. In order to minimize NNT, one must avoid false positive responses, i.e., triggering the system for the vast majority of situations where no accident would have occurred. In statistical terms, ADAS, sensor and detection logic should be designed for extremely high specificity. However, in most scenarios, intrinsic variance due to human actions implies that the occurrence of an accident (“point of no return”) cannot be predicted with certainty until the time to collision (TTC) is only a few hundred milliseconds, even if all sensors are ideal. In other words specificity is subject to intrinsic, time-dependent limitations. System actions usually need to be carried out at a larger TTC to be effective, implying residual uncertainty. In fact, when developing system action strategies, one usually has a trade-off between timing of strategies and adverse effects of false positives.

Consider for example three strategies to avoid a rear-end collision: (1) automatic swerving; (2) automatic strong braking; (3) warning with enhanced brake assist.

- (1) *Automatic swerving* could often avoid rear-end collisions even at TTC of ~ 500 ms, but false positive swerving interventions are highly damaging.
- (2) While *automatic braking* raises controllability issues, the damage of a false alarm is likely to be less severe than in automatic swerving; however, at freeway speeds, effective automatic braking must occur prior to the TTC at which the driver could still theoretically avoid collision by swerving.

- (3) A warning with enhanced brake assist is far less damaging than the other alternatives in case of false positives. However, to be effective, a rear-end collision warning should occur early, prior to the TTC at which the driver can still theoretically avoid collision by a lane change. The residual uncertainty (and thus the need for stochastic modeling) is thus quite substantial considering the possible variations in driver reactions and responses.

Additional uncertainties result from the technological capabilities of sensors, and there is usually a trade-off between specificity and latency of sensor logic, for example, in object classification. Hence, sensor modeling also has important stochastic aspects. Moreover, driver decisions and actions in an acutely dangerous situation are likely to be triggered or influenced by assistance functions and interact with their effectiveness. These processes are non-deterministic as well. Summarizing, optimization of ADAS almost always involves strategic decision algorithms under uncertainty, which must properly consider benefits, risks, and constraints. A key feature of almost all relevant accident processes is thus the element of variation within a sample or population. In safety research, it is usually inadequate to assume an average value for a critical quantity such as a reaction time, because accidents are rare events. Hence, the cases in which a safety system will be utilized tend to involve the “tails” of all probability distributions; for example, pedestrians who severely underestimate the time required to cross the street or the speed of an approaching vehicle are relatively rare, but they represent a substantial proportion of those suffering collisions. For this reason, any method that seeks to predict the performance of a safety system must provide some systematic way of sampling representative events from relevant distributions.

3.2 Generation of Representative Samples for Analysis

There are currently two main approaches to generation of representative samples for safety benefit analysis of ADAS in target scenarios. One common approach is to identify relevant accidents for the target scenario in databases such as GIDAS [1, 13], reconstruct the scenario immediately preceding each real accident, and then attempt to simulate the effect that a safety system would have provided. There are several limitations to the use of reconstructed databases: First, this method provides no information on the rate of false positives or on “NNT” statistics, since it does not generate a representative sample of situations in which the system would be triggered (including situations in which no accident would have occurred). Second, a database containing exactly one particular pre-crash reconstruction for each accident is not suitable for optimization of ADAS system performance. The reason is that the precise details of the pre-crash phase are subject to uncertainties. System effectiveness in alternative reconstructions of similar a posteriori probability could be lower than expected from optimization on the limited reconstruction set. In addition to these limitations, the use of known

reconstructions does not eliminate the need to take into account the stochastic nature of the response to warnings and interventions.

A second method used in our group (referred to here as “Monte-Carlo simulation”) is to simulate the scenario as a process in which situations are repeatedly generated according to an appropriate exposure model. In a small minority of situations, an accident would occur in the absence of ADAS. In order to evaluate a proposed system, we perform virtual experiments as described above without the ADAS in question or with the system in various configurations. By the virtual experiment technique, we can determine effectiveness as well as NNT (or false positive rates) for each configuration. The technique is best explained by a specific illustration:

3.3 Pedestrian Protection: An Illustration of Stochastic Modeling

The act of a pedestrian crossing a street requires consideration of several distinct entities, each described by a complex, dynamically evolving state: pedestrians, individual drivers, and vehicle dynamics. Each of these entities in turn is characterized by multiple attributes and is subject to various influencing factors that could be specified as part of the scenario. The pedestrian’s strategies, decisions, observation behavior, walking/running speed, reactions to threats, etc. may be influenced by age, gender, physiology, sobriety (or lack thereof!), fatigue, etc. His immediate ability to perceive a threat could be further influenced by vehicle visibility, alertness, ability to perceive approaching vehicles or estimate speeds and gaps in traffic, road characteristics, traffic management, and so forth. All of these variables can affect accident probability. The speed of crossing and the agility of the pedestrian in an emergency are further variables that could influence accident probability.

Traffic flow and road characteristics (including infrastructure) can also affect both accident probability and accident severity in direct and indirect ways: For example, the pedestrian’s “tactical” decision to cross the road at a particular point and his gap acceptance behavior could be influenced by the waiting time in dense traffic and by his perception of danger; greater traffic flow speeds are associated with higher visibility requirements, longer stopping distances, and potentially more severe impacts. Infrastructure such as lighting or crosswalks clearly has an important influence: If a pedestrian has the choice of a sufficiently nearby crosswalk, he will be less likely to attempt a crossing at a dangerous position. Even the timing of traffic signals can have an effect, e.g., some pedestrians may become impatient and not wait for green if the red phase is too long [14].

In view of these requirements, we have developed a virtual evaluation technique based on stochastic (“Monte-Carlo”) simulations for modeling pedestrian crossing behavior. In a typical optimization of a safety system, one is interested in

relatively small differences in effectiveness (accident numbers, MAIS characteristics, etc.) among different system configurations, so that it is typical to simulate millions of crossings for each set of parameters considered. In this stochastic simulation approach, all relevant natural and induced processes are modeled as a sequence of states subject to both deterministic interactions and stochastic (random) influences. One considers a virtual sample of pedestrians with varying characteristics, drawn from a realistic population, who attempt to cross a stream of traffic. Driver and vehicle characteristics, vehicle trajectories, and traffic characteristics are also drawn from a virtual sample, as well as key environmental variables.

After generating the context and drawing parameters describing the situation, the simulation program models the crossing process in parallel from the pedestrian's point of view and the driver's point of view. In the case of the pedestrian, the modeled processes include the decision as to when to cross and whether to run or walk, the trajectory taken, observation and monitoring of traffic during crossing, perception/detection of threats, and possible responses.

The driver is determined as a result of the pedestrian's choice of when to cross. In some cases, the gap is so large that essentially no interaction occurs. In the case of the driver, the modeled processes include initial speed choice, the trajectory taken, perception of potential conflicts and reactions to these conflicts. In any particular crossing, the trajectories are followed until the pedestrian successfully reaches the other side or the driver stops the vehicle or there is a collision.

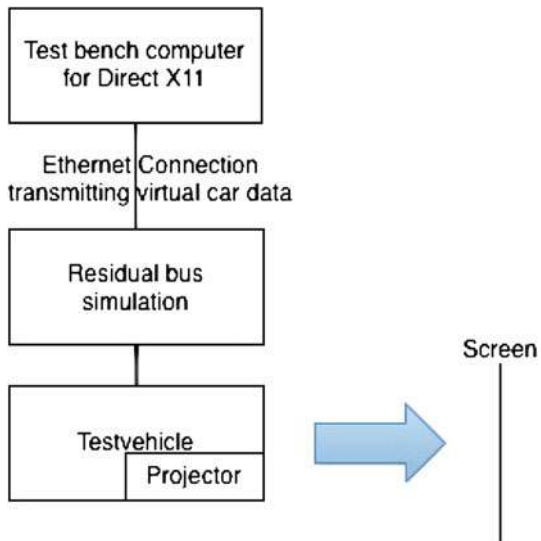
Perception processes for both the driver and the pedestrian take into account the visual orientation and the probability of objects being located within the central field of view, as well as the rate of change of angular size on the retina. All reaction processes (drivers and pedestrians) are modeled according to the OODA paradigm (observe, orient, decide, act) of Green and others [15–18].

After each crossing, any concomitant variables of interest are compiled for subsequent statistical analysis. For example, since the TTC value is continuously updated during a simulated crossing, one can record the TTC at the first moment of braking for all drivers in collisions.

3.4 Controlled, High-Throughput Algorithm Testing and Validation

Present and future ADAS such as preventive pedestrian protection or city collision mitigation utilize various sensor types and algorithms to acquire and assess information about their surrounding environment. As explained earlier, realistically quantified sensor and algorithm characteristics are key inputs to performance assessment, particularly when Monte-Carlo simulation is used. An example is the latency probability function for camera-based object identification. Field testing of ADAS algorithms is usually very time-consuming; due to practical limits on the

Fig. 1 Schematic system description



number and spectrum of test scenarios, representative sampling of field effectiveness is hardly possible. Moreover, in field testing, the validation effort increases dramatically with system complexity, as failures can be attributable to any component part, and performance can also depend on exogenous details. It is often very difficult to reproduce the conditions that led to a failure and isolate the cause. As suggested by [19] testing every possible scenario in a real-system leads to a state explosion. Therefore, the focus should be on testing the system regarding a set of given important scenarios that it has to cope with.

This section describes a new controlled, high-throughput approach to algorithm testing and validation in camera-based ADAS using a virtual graphical test bed. A key feature of this test bed is utilization of graphical simulation producing a virtual environment for the test system [20]. Keeping the virtual exogenous variables, e.g. lighting, weather, scene complexity, and track conditions constant allows the environment to generate reproducible scenarios for objective algorithm evaluation and thus supports systematic identification of critical external conditions that could modify performance or lead to a failure mode.

The method is illustrated in Fig. 1 as applied to a preventive pedestrian protection algorithm. The stationary test bench consists of a high-definition projector producing images based on a computer games engine to simulate vehicles and pedestrians. Combining this data with “virtual” car data leads to authentic system reactions.

As one example of the application, suppose we need to evaluate algorithm performance and distinguish algorithmic weaknesses. We can proceed as follows: The dynamics of traffic participants (such as vehicles and pedestrians in the example of pedestrian protection) can be specified using Monte-Carlo Simulation as discussed above to generate a representative sample of virtual situations

pertaining to a chosen scenario. A for the camera ideal picture (containing a static list of objects) recorded and analyzed by the camera system guarantees fault-free object detection, leading to a targeted and comprehensive algorithm test that is isolated from the object detection problem. Due to the sheer mass of combinations, the system will probe unusual or unanticipated situations that would not have been seen by a field test.

As a second example of the application, an important aspect of Monte-Carlo simulation as explained above is modeling of camera system and algorithm behavior. Now, this system modeling often involves a certain level of abstraction, at least at the beginning, which may or may not accurately reflect the true system behavior under all circumstances. Using the virtual sample, the controlled, high-throughput virtual graphical test bed also provides a comparison of the abstract simulated system behavior model with the virtual system behavior under a comprehensive range and variety of pedestrian and vehicle trajectories. In this way, the system can discover unanticipated discrepancies, and the simulation model can be refined if required to produce a more reliable estimate of system effectiveness.

Once the sensor model has been tested under ideal conditions (fault-free object detection), the high-throughput virtual graphics testing environment can also be utilized in sensitivity studies with respect to key input determinants such as road characteristics, traffic flow, obstacles, complexity, weather conditions, illumination, some of which could impact fault-free object detection. In combination with Monte-Carlo simulation, the “gold standard” of collisions that would have occurred without the assistance system is known from simulation. Thus, the virtual environment can produce a large, informative, and reproducible sample of situations resulting in true positives (“hits”) as well as false positives and “near misses” to provide an objective evaluation of the underlying algorithm. Moreover, to the extent that performance deficits (e.g., slow object identification) can be associated with particular input determinants (e.g. scene complexity or multiple target scenarios), the method supports optimization of the visual detection system.

3.5 Incorporation of Classical Testing Methods

The stochastic methods described above are designed to be combined with “classical” testing methods, particularly

- experiments on test tracks;
- driving simulator studies;
- large observational studies in real traffic (field operational tests, FOT).

Test tracks are primarily used for testing and evaluation of functions within a vehicle [21]. Real vehicles (including their dynamics) are tested under full experimental control [22] in realistic environments under a range of different conditions (e.g., road classes, weather) [21, 23]. However, test track experiments are limited by certain practical constraints: The most important requirement,

particularly in safety-critical functions, is that an experiment should not endanger the participants (test drivers or other experimental subjects) [24]. This requirement—as well as the practical difficulty of constructing complex traffic situations—limits the range and variety of scenarios that can be tested. The resulting challenge of building complex yet safe scenarios on a test track and the limited realism due to absent surrounding traffic leads to the conclusion that “overall functionality and performance [cannot] be evaluated on basis of a limited number of tests” [25]; hence, overall effectiveness cannot be assessed on a test track [26].

As mentioned above, the safety effects of ADAS are “filtered” by stochastic response functions that include driver response characteristics, which can thus be at least as important for active safety performance as vehicle characteristics [27]. The considerable variability of human behavior [28] is best assessed via relevant behavioral studies (or subject experiments). In the Monte-Carlo paradigm, behavioral results (classified by situation) are encapsulated in appropriate probability models [29]. One approach offering advantages in usability, ergonomics, and acceptance [21] is driving simulator experiments. With different setups (from static to full six axis motion) [21, 22, 24], they provide high reproducibility [21, 27, 30] together with good experimental control [23]. They allow situations too risky for field tests (for example, emergency braking or swerving, driver response under severe distraction, critical failures) to be studied under risk-free conditions.

In addition to the complexity and effort necessary for a driving simulator study [23], disadvantages include limited realism in driving dynamics as well as behavioral artifacts due to an artificial environment. These limitations can result in systematic shifts in the distribution of driver response characteristics compared to real traffic [21, 23, 30]. In view of these disadvantages and the limited number of situations [31], a reliable overall assessment of effectiveness of an ADAS usually cannot be generated by simulator studies alone [32]. However, within the Monte-Carlo approach of encapsulated probability distribution models, these disadvantages can be substantially overcome. One re-calibrates the distributions by comparison with available real vehicle data to obtain models approximating driver response distributions of real traffic. Thus, driving simulator studies allow extraction of valuable data on human behavior under a range of circumstances, data that would be difficult or impossible to obtain elsewhere.

Observational studies in traffic, known as naturalistic driving studies (NDS) or field operational tests (FOT), have a decisive advantage, in that they include realistic surroundings and unbiased human behavior [23] under field conditions. Clearly, FOT are only applicable to functions that are already rather highly developed [25] and safe for testing in traffic. It has been observed that studies [33–36] based on this method up to now have tended to be quite costly and time-consuming [22], but for automobile safety, testing costs should not be of primary concern. The main issue is that of experimental design and control: specific situations can hardly be triggered or reproduced [24, 23], and systematic variation of conditions is difficult or impossible to achieve [23]. Thus, a sampling design to estimate true positive system response rates of safety functions [24] is not possible. Moreover, although FOTs are capable of assessing the effects of active safety systems in traffic in the sense of an overall

effectiveness (e.g. [37]), they are usually not feasible as an optimization tool during the development process due to long study time required and the resulting severe feedback lag to the development and optimization process.

Nonetheless, FOT results, including data on exposition [28], are an important basis for the modeling of human behavior during the assessment process. In a testing environment that includes stochastic simulation of virtual scenarios, FOT results still can play a decisive role in validation of the virtual models at the core of Monte-Carlo simulation. They offer an additional level of testing and calibration to reinforce laboratory and simulation results. Finally, they may provide a unique opportunity to observe unexpected behavioral patterns, given adequate sample size and driving time [22].

4 Conclusions

Because ADAS act within a complex, dynamic traffic environment, reliable evaluation of their safety benefits requires us to address severe methodological challenges. Essential steps begin with identification of target scenarios and a detailed understanding of which processes within the complex interactions of drivers, other road users, and traffic may fail, leading to accidents. Plausible mechanisms for accident avoidance or mitigation by a proposed ADAS need to be formulated and modeled as influences on these processes in detail. Process models should include all situations in which ADAS might be triggered—including non-accident situations.

Ideally, a “gold standard” to quantify ADAS safety benefits would be direct estimation of mortality and injury reduction from accident statistics and direct measurement of false-positive counts in the field. However, estimation of ADAS safety benefits from accident statistics requires long observation periods and is confounded by multiple parallel influences on these statistics; false-positive rates need to be measured not just once, but for each algorithmic threshold setting. Hence, a methodology is required that can predict mortality and injury reduction as well as false positives.

Since accidents are rare events often involving several individually unlikely failures, prediction and optimization of ADAS safety performance must take into account the stochastic nature of the processes involved—for example by Monte Carlo simulation, as described above in the case of pedestrian safety. All relevant natural and induced processes are modeled as a sequence of states subject to both deterministic and stochastic (random) influences and interactions. If we regard simulations as virtual controlled experiments, then the benefits and possible negative effects (false positives) of ADAS emerge by statistical analysis similar to that carried out with real accident data, with the advantage that statistical power is limited only by the number of cases simulated, and confounders can be controlled. The main challenge is to formulate and calibrate process models (including all relevant features of the probability distributions) and to take into account the

specific effects of ADAS within these models and for each target scenario. As seen in the case of pedestrian safety, models of each link in a chain of sub-processes are required.

The quality of predictions as a whole depends on the quality of each “sub-process” model. The more individual process elements that are tested, the greater the overall reliability of the process models and hence of stochastic simulation. Laboratory tests are used to calibrate models of key sub-processes with high fidelity (validity). In the case of vehicle algorithms, a particularly important sub-process is the ADAS algorithm itself. A source of uncertainty that is difficult to model is the reliability of software in a complex operating environment. Specific process tests such as algorithms in the loop can serve to demonstrate the reliability in a real-world situation. Novel methods for algorithm validation as described above use a virtual graphical test bed capable of controlling and varying the virtual exogenous variables and generating reproducible scenarios. Single laboratory tests considered here include hardware in the loop test facilities, behavioral and/or technical testing of subsystems/vehicle (e.g., driving simulation, test track, test rigs), and methods based on real traffic testing (e.g., controlled studies, field operational tests).

Safety assessment thus involves a collection of testing techniques, each of which will estimate the effects of a system on a particular subset of processes contributing to the likelihood and severity of an accident. Each testing technique has a characteristic range of validity for the processes that it probes. For complex active safety problems, it is unlikely that a single laboratory test can be designed to cover the entire chain of processes with adequate validity in order to estimate field effectiveness. If we define a “key process” here as one that sensitively determines the outcome, then any key process whose test has low validity will disproportionately compromise the validity of the assessment chain. The methodologies introduced here are designed to ensure validity of all key links in the assessment chain, not limited to those aspects that can be assessed in a single test. Ideally, quantification of safety impact for an active safety system would provide an estimate including all traffic contexts in which the system is designed to operate. The methodologies described here represent an important step in this direction; however, exposure studies, statistical accident analyses, and/or behavioral studies will usually be required in order to identify the most representative scenarios and the key human and technical processes. By combining these techniques, we can obtain refined estimates that can come increasingly close to the true field performance.

References

1. GIDAS German In-Depth Accident Study. http://www.gidas.org/files/GIDAS_eng.pdf
2. Ebner A, Samaha RR, Scullion P, Helmer T (2010) Methodology for the assessment and evaluation of active safety systems using scenarios: application to preventive pedestrian

- protection. In: Proceedings of the international research council on biomechanics of injury (IRCOBI), pp 155–168
3. Ebner A, Samaha RR, Scullion P, Helmer T (2010) Methodology for the development and evaluation of active safety systems using reference scenarios. In: Proceedings of the 17th ITS world congress
 4. Ebner A, Helmer T, Huber W (2009) Bewertung von Aktiver Sicherheit—Definitionen, Referenzsituationen und Messkriterien. 1. Automobiltechnisches Kolloquium; München, 16. und 17. April 2009, Technische Universität München-Garching, VDI Wissensforum GmbH, Düsseldorf
 5. Ebner A, Helmer T, Samaha RR, Scullion P (2011) Identifying and analyzing reference scenarios for the development and evaluation of active safety: application to preventive pedestrian safety. *Int J Intell Transp Syst Res* 9(3):128–138
 6. Helmer T, Ebner A, Huber W (2009) Präventiver Fußgängerschutz—Anforderungen und Bewertung. 18. Aachener Kolloquium Fahrzeug- und Motorenmechanik
 7. Helmer T, Scullion P, Samaha RR, Ebner A, Kates R (2010) Predicting the injury severity of pedestrians in frontal car crashes based on empirical, in-depth accident data. In: Proceedings of the 17th ITS world congress
 8. Helmer T, Scullion P, Samaha RR, Ebner A, Kates R (2011) Predicting the injury severity of pedestrians in frontal vehicle crashes based on empirical, in-depth accident data. *Int J Intell Transp Syst Res* 9(3):139–151
 9. Helmer T, Samaha RR, Scullion P, Ebner A, Kates R (2010) Injury risk to specific body regions of pedestrians in frontal car crashes modeled by empirical, in-depth accident data. In: Proceedings of the 54th stapp car crash conference
 10. Helmer T, Samaha RR, Scullion P, Ebner A, Kates R (2010) Kinematical, physiological, and vehicle-related influences on pedestrian injury severity in frontal car crashes: multivariate analysis and cross-validation. In: Proceedings of the international research council on biomechanics of injury (IRCOBI), pp 181–198
 11. Gruber C, Wimmer P, Marbler-Gores H, Sinz W (2012) Integrale Sicherheit. Durchgängige Methode zur numerischen Simulation. Grazer Symposium Virtuelles Fahrzeug
 12. Kates R, Jung O, Helmer T, Ebner A, Gruber C, Kompass K (2010) Virtual optimization of pedestrian protection systems in intelligent vehicles by stochastic simulation techniques. Erprobung und Simulation in der Fahrzeugentwicklung
 13. Erbsmehl C (2009) Simulation of real crashes as a method for estimating the potential benefits of advanced safety technologies. In: Proceedings of the 21st international technical conference on the enhanced safety of vehicles (ESV 2009), Nr. 09-0162
 14. Asaba M, Saito T (1998) A study on pedestrian signal phase indication system. In: Ninth international conference on road transport information and control, 21–23 April 1998, London, pp 182–185
 15. Green M (2000) “How long does it take to stop?” Methodological analysis of driver perception-brake times. *Transp Human Factors* 2(3):195–216
 16. Hick WE (1952) On the rate of gain of information. *Q J Exp Psychol* 4:11–26
 17. Lerner N (1993) Brake perception-reaction times of older and younger drivers. In: Proceedings of the human factors and ergonomics society annual meeting, vol. 37, pp 206–210
 18. Olson PL, Sivak M (1986) Perception-response time to unexpected roadway hazards. *Hum Factors J Hum Factors Ergonomics Soc* 28:91–96
 19. Cardell-Oliver R, Glover T (1998) A framework for the test and verification of real-time systems. In: IEEE colloquium on real-time systems, p 5/1–5/4
 20. Fitzpatrick CJ (2012) A configurable 3D graphical simulation of traffic incidents for testing active and passive safety systems in BMW vehicles. Staffordshire University
 21. Bock T (2009) Handbuch Fahrerassistenzsysteme, Bewertung von Fahrerassistenzsystemen mittels der Vehicle in the Loop-Simulation. Vieweg + Teubner Verlag/GWV Fachverlage GmbH, Wiesbaden, pp 76–83

22. Lietz H, Petzold T, Henning M et al (2008) Methodische und technische Aspekte einer Naturalistic Driving Study. FAT Schriftenreihe 229 BASt, FE 82.0351/2008, Forschungsvereinigung Automobiltechnik E.V. (FAT)
23. Breuer J (2009) Handbuch Fahrerassistenzsysteme, Bewertungsverfahren von Fahrerassistenzsystemen. Vieweg + Teubner Verlag/GWV Fachverlage GmbH, Wiesbaden, pp 55–68
24. Bock T (2008) Vehicle in the loop: test- und Simulationsumgebung für Fahrerassistenzsysteme. Dissertation, Technische Universität, München
25. Fach M, Ockel D (2009) Evaluation methods for the effectiveness of active safety systems with respect to real world accident analysis. In: 21st international technical conference on the enhanced safety of vehicles (ESV 2009), Nr. 09-0311
26. Van Auken RM, Zellner JW, Chiang DP, Kelly J, Silberling JY, Dai R, Broen PC, Kirsch AM, Sugimoto Y (2011) Advanced crash avoidance technologies (ACAT) program—final report of the Honda-DRI team, volume I: executive summary and technical report. DOT HS 811 454A. Dynamic Research Inc./National Highway Traffic Safety Administration
27. Breuer J (2002) Objektive Bewertung der Aktiven Sicherheit von Fahrzeugen: Kritische Betrachtung. VDA Technischer Kongreß 2002—Sicherheit durch Elektronik. VDA—Verband der Automobilindustrie, Frankfurt a. Main, pp 105–113
28. Burgett A, Srinivasan G, Ranganathan R (2008) A methodology for estimating potential safety benefits for pre-production driver assistance systems (DOT HS 810 945)
29. Carsten OMJ, Nilsson L (2001) Safety assessment of driver assistance systems. Delft: Eur J Transp Infrastruct Res S225–S243
30. Fastenmeier W, Gstalter H, Zahn P (2001) Prospektive Risikopotentialabschätzung am Beispiel der Spurwechsel-Assistenz. Der Fahrer im 21. Jahrhundert, Nr. 1613 der Reihe VDI-Berichte. VDI Verlag, Düsseldorf
31. Kusano KD, Gabler HC (2011) Potential effectiveness of integrated forward collision warning, per-collision brake assist, and automated pre-collision braking systems in real-world, rear-end collisions. In: Proceedings of the 22st international technical conference on the enhanced safety of vehicles (ESV 2011), Nr. 11-0364
32. Gründl M (2005) Fehler und Fehlverhalten als Ursache von Verkehrsunfällen und Konsequenzen für das Unfallvermeidungspotential und die Gestaltung von Fahrerassistenzsystemen. Dissertation, Universität Regensburg
33. Antin J, Lee S, Hankey J, Dingus T (2011) Design of the in-vehicle driving behavior and crash risk study: in support of the SHRP 2 naturalistic driving study. SHRP2 report S2-S05-RR-1, Virginia Tech Transportation Institute
34. Benmimoun M, Benmimoun A (2010) Large-scale FOT for analyzing the impacts of advanced driver assistance systems. In: Proceedings of the 17th ITS world congress
35. Dingus TA, Klauer SG, Neale VL et al (2006) The 100-car naturalistic driving study, phase II—results of the 100-car field experiment. Nr. DOT HS 810 593. Department of Transportation, National Highway Traffic Safety Administration, Washington
36. Sayer JR et al (2011) Integrated vehicle-based safety systems light-vehicle field operational test key findings report. DOT HS 811 416, The University of Michigan: Transportation Research Institute
37. Digges KH, Nicholson RM, Rouse EJ (1985) The technical basis for the center high mounted stoplamp. SAE Technical Paper (851240)

Finite Element Analysis of Cervical Spinal Nerve Tissue Tolerance to Whiplash Injury: A Preliminary Study

**Chaoyang Chen, Bo Cheng, Chuanhua Huang, Binhuai Jiang,
Dawei Chen and Xin Tao**

Abstract Research and/or Engineering Questions/Objective Whiplash can occur in frontal, side and rear car collisions but most complaints occur in rear collision by another vehicle. Whiplash can produce acute and chronic neck pain, headache, paresthesia, or even paralysis. The facet capsule, intervertebral discs, cervical ligaments, and cervical spinal nerves can be injured during whiplash. Injury to the nerve can result in more severe clinical symptoms, including motor, sensory, and sphincter disturbance. But the accelerations that can cause nerve injury are unknown. The aim of this study was to assess the threshold chest acceleration that causes cervical spinal nerve injury using finite element (FE) methods. **Methodology** Multi-slice CT images with 1.2 mm slice distance of a de-identified adult male were used to construct the three-dimensional FE model of cervical spine components using Mimics software. FE components include the head, neck, upper thorax, ligament, intervertebral disks, ligaments, and muscle fascias. The elements in the FE model components were reconstructed for a better quality using ANSA and Hypermesh software. Acceleration curves obtained from volunteer rear impact tests were input into the FE model and run using LS-DYNA. The FE model was validated by comparing the head movement corridor with volunteer data. Strain on the cervical spinal nerve was used to determine the injury probability based on our neurophysiology and biomechanical *in vivo* experimental data. **Results** Mimics

F2012-F05-006

C. Chen (✉) · B. Jiang
Department of Biomedical Engineering, Wayne State University, Detroit, MI, USA

B. Cheng · X. Tao
State Key Laboratory of Automotive Safety and Energy, Tsinghua University, Beijing, China

C. Huang · D. Chen
Goldstone FE Consultation Ltd, Detroit, MI, USA

software provided an effective and rapid approach to build a FE model. An increase of chest acceleration caused an increase of the strain of the spinal nerve. The maximum stretch speed of the spinal nerves was showed to be 199 ± 23 mm/sec from the simulation of rear impact. 7 Gs chest acceleration produced a maximum 24 % strain of the spinal nerve resulting in a 40 % probability of spinal nerve injury. The highest strain was found to be in the 3rd cervical spinal nerve. Increased acceleration in the shoulder more than 7 Gs did not cause further increase of nerve strain in the simulation. *Limitations of this study* The limitation of this study is that only the cervical spine, head and upper shoulder model was used in the computer simulation. It will be better if the whole vehicle and whole body FE model was constructed for our research. In addition, muscle biofidelities were not simulated in this model. *What does the paper offer that is new in the field in comparison to other works of the author* Currently, most research uses ANSYS software to construct FE models, which is a tedious procedure. Mimics, ANSA, and HyperMesh software combined applications provided a new and rapid approach to build a human FE model, yet the element quality can be better controlled. This paper first reported a research of spinal nerve tolerance to whiplash injury using FE analysis methods. *Conclusion* Mimics, ANSA, and HyperMesh software combined applications provided a new and rapid approach to build a human FE model, yet the element quality can be better controlled. Our neck finite element model was the first FE model developed to study the spinal nerve tolerance to whiplash injury. The model validation was performed at the global level by tracking the head kinematics. The simulation results corresponded to clinical scenarios and volunteer testing outcomes. Our simulation demonstrated that 6 Gs chest accelerations with no headrest may cause 25 % probability of cervical spinal nerve injury. Increased chest acceleration to 9, or 10 Gs did not cause further increase of spinal nerve maximum strain, or injury probability. A higher strain was frequently found in the C3 spinal nerve under different chest accelerations.

Keywords Rear impact · Whiplash · Nerve injury · Finite element analysis

1 Introduction

Neck whiplash can occur in frontal, side and rear car collisions but most complaints occur after a rear-end collision by another vehicle. Whiplash occurs when the head lags behind the accelerated torso, producing relative acceleration between the head and thorax during motor vehicle collisions. Whiplash can produce acute and chronic neck pain, headache, dizziness, vertigo, paresthesia, or even paralysis. The structures most likely to be injured during whiplash are the facet capsule, the intervertebral discs, the cervical ligaments, and cervical spinal nerves, and spinal cord [1]. But injury to the

nerve can result in more severe clinical symptoms, including motor, sensory, and sphincter disturbance. However what accelerations cause nerve injury is unknown.

Anthropomorphic dummies and computer modelling approaches have been used to investigate human injury mechanisms and tolerances on cervical spine musculoskeletal system [2]. But these anthropomorphic dummies provide no information about the spinal nerve and spinal cord injuries and might not simulate the nerve injury. The need for accurate modelling to analyze injury from automobile accident has led engineers to be interested in finding new and better methods for injury biomechanics research and designing of protection devices. Currently, computational finite element analysis (FEA) is a method that is cost-effective and provides accurate analysis outcomes and has been extensively used in the industry and bio-engineering research. Once developed, a computer FEA model does not require the destruction of human tissues, crash test dummies, or automobiles. With computer modelling, tests could be repeated with alteration of only a single variable, allowing for the application of the scientific method to automotive safety engineering [3]. Therefore, we hypothesized that the computer modelling may be the only readily approach to assess human nerve tissue injury and tolerance.

Overstretching of the nerve tissues leads to nerve dysfunction [4, 5]. The hypothesis of this study is that noxious whiplash movement of the cervical spine leads the spinal nerve to be mechanically stretched. However, the accelerations that can cause nerve injuries in whiplash has not yet been studied, and the purpose of this study was to develop a neck finite element model that can be used to understand the lowest injury strain of the spinal nerves under the dynamic conditions of whiplash. The model validation was checked by comparing global responses with published volunteer data under the whiplash loading conditions. The acceleration thresholds causing nerve tissue injury will then be calculated and evaluated based on published nerve injury criteria.

It is well known that building a accurate human FE model is time-consuming and tedious. With the emergence of new MRI and CT techniques, as well as advanced software such as Materialise's Mimics 14.0, it is possible to build human FE models quickly and efficiently.

The specific aims of this study are: (1) to establish three-dimensional finite element model of human cervical spine using Mimics 14.0, and to determine if Mimics can be used to effectively build an FE model; (2) to validate this model under whiplash loading conditions by comparing its global responses with published validated data; (3) to evaluate the strain distribution of the spinal nerve under whiplash conditions; (4) to determine the lowest strain on the spinal nerve that can cause nerve injury.

2 Materials and Methods

Establishment of finite element models: Computed tomography (CT) images of a de-identified adult male were used to construct the three-dimensional, geometrical surface model of each vertebra using Mimics 14.0 (Materialise Inc., Leuven, Belgium).

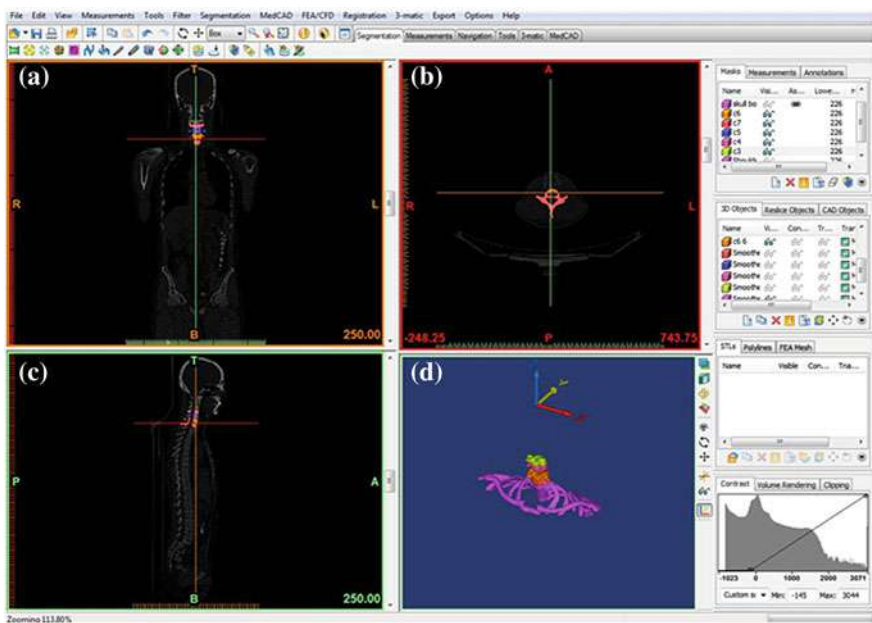


Fig. 1 The interface for 3-D geometry re-construction. **a** Anterior-posterior (AP) view (*frontal plane*) of the cervical spine components, **b** bird view (*transverse plane*) of a vertebral body, **c** lateral view (*midsagittal plane*) of the cervical spine, **d** 3-dimensional view of the built components

Multi-slice helical CT images with 1.25-mm distance between slices were imported into Mimics software by directly reading the consecutive CT Dicom format images of human cervical spine. The following procedures were performed: defining bone or soft tissue image threshold, withdrawing each outline using “Segmentation” function, partitioning each edge of layer picture using “Draw or “Erase” function, and editing selectively (Fig. 1). The parts were meshed and output into Nastran file format using “3-matic 5.1” function for further processing.

C1-T1 intervertebral bodies with all anatomic components and intervertebral disks were reconstructed individually using Hypermesh and ANSA software. The spinal cord and spinal nerve were then incorporated into the model. A realistic and accurate 3-D finite element model of the cervical spine was thus established. The model was composed of the head (H), the seven cervical vertebrae (C1–C7), the first thoracic vertebra (T1) and shoulder, the intervertebral discs and the relevant soft-tissue components of the spinal column (Fig. 2a). The anterior longitudinal ligaments (ALL), posterior longitudinal ligaments (PLL), ligamentum flavum (LF), intertransverse ligaments (ITL) and muscles were built into the model as shown in Fig. 2b.

The cervical 3-D geometry model of each vertebral body was then converted into the Nastran file format. The Nastran files were then imported into FEA pre-processing software Hypermesh (Altair Inc, Troy, MI, USA) to re-mesh the vertebral bone elements for quality control. The file was then saved into LS-DYNA file format

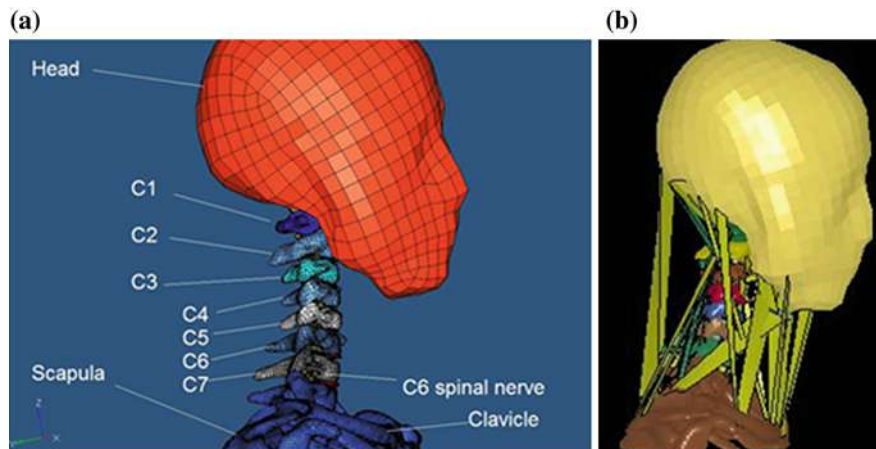


Fig. 2 **a** FE model of bone components and the spinal nerve. The spinal cord is covered by bone hence it is invisible in this picture. The muscles and ligaments are not shown in this figure. **b** The anterior longitudinal ligaments (ALL), posterior longitudinal ligaments (PLL), ligamentum flavum (LF), intertransverse ligaments (ITL) and muscle fascias

(Key file). The elements of the model were tetrahedral element. The model file was then imported into ANSA software (version 13, BETA CAE Systems USA Inc., Farmington Hills, MI, USA) to convert all elements into hexahedral element.

Each element size was controlled to be greater than 0.4 mm in order to reduce computer calculation time. Since each element with side length less than 0.4 mm increased the calculation time by 40 % approximately. After model elements were resized the file was saved as Key file (LS-DYNA) format. The dole was then loaded into Hypermesh, all components loaded into the Hypermesh were assigned with mechanical properties (Young's modulus) as showed in Table 1.

Loading conditions and constraints: Horizontal kinematic chest acceleration data was extracted from Meyer's rear-impact volunteer's experiment (Fig. 3b) [6]. The volunteer's chest acceleration curve was applied to the FE model at T1 vertebral body and the shoulder to simulate the rear collision conditions.

Calculations for the finite element model were performed using LS-DYNA's solver (Livermore Software Technology Corporation, Livermore, CA, USA). The first calculation was performed with chest acceleration loaded with Meyer's chest acceleration curve. The resultant "d3plot" file was opened by LS-DYNA pre-post processing function to track nodal movement during whiplash. Head kinematic responses were tracked and compared to Meyer's volunteer's head kinematics (acceleration) to determine model validation. After the model was validated through this procedure, different curves with increased acceleration (G) values (Fig. 4) were applied to the chest to determine the consequent strain produced in the spinal nerves in response to increased acceleration to the shoulder.

Strain data on the spinal nerves were obtained using LS-DYNA LSTC Pre-post processing function. Specific elements were selected to track strain distribution.

Table 1 Material properties used for various components in the model [4, 5, 12]

Components	Young's modulus (Mpa)	Density (Kg/mm ³)	Poisson's ratio
Bone	10000	1.83E-06	0.29
Disk	34	1.83E-06	0.4
ALL	30	1.20E-06	0.3
PLL	20	1.20E-06	0.3
Muscles	5	6.00E-07	0.4
Nerve	0.06	1.00E-07	0.5

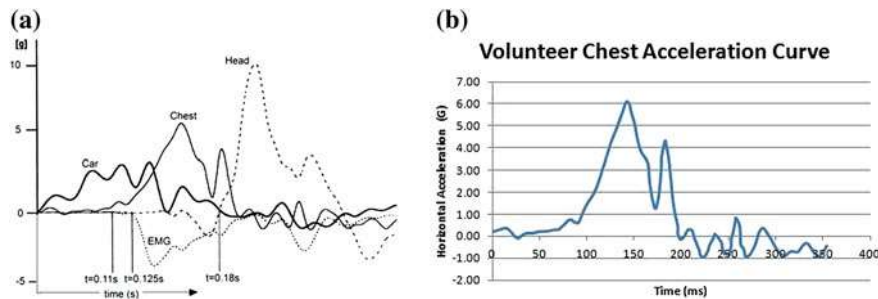


Fig. 3 **a** Acceleration curves of car, chest and head kinematics recorded by Meyer et al. [6] during a rear impact volunteer test. Impact velocity was 13.5 kph and delta V was 7.5 kph. **b** Chest acceleration curve that was loaded into our FE model as horizontal Y orientation acceleration

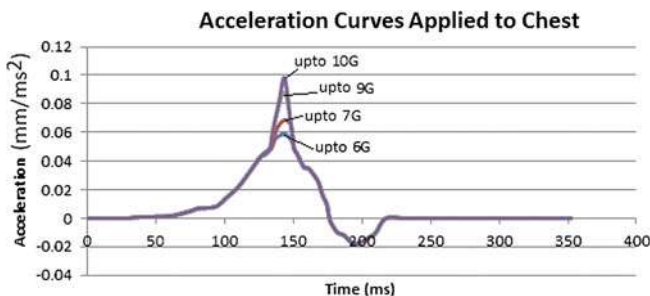


Fig. 4 Increased acceleration curves that were applied to the chest in this study. These curves were modified from Meyer's chest acceleration curve

The outcome files were saved into Microsoft CSV format. These files were opened with Microsoft Excel for further data processing.

Determination of spinal nerve tolerance to injury: Nerve injury criteria were obtained from the published papers to determine the threshold acceleration at the shoulder that causes nerve injury. The injury criteria was based on the probability of nerve conduction impairs from injury (Fig. 5) [7]. Figure 5 demonstrates the probability of nerve dysfunction caused by various strains under different nerve

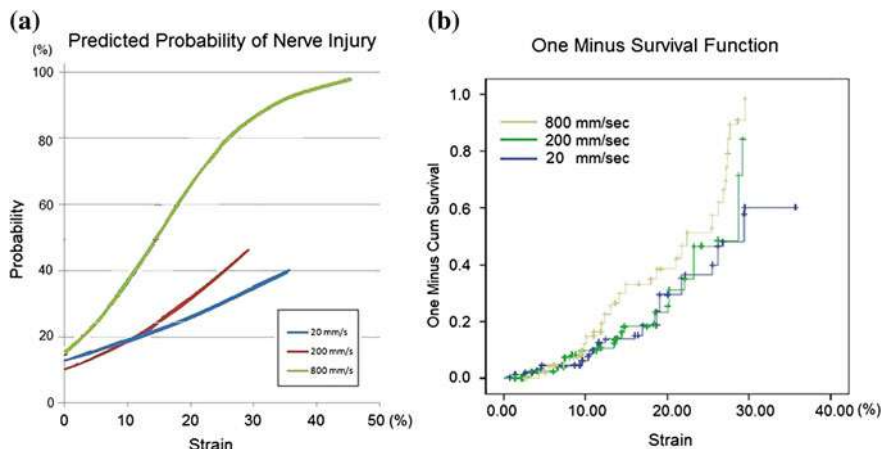


Fig. 5 **a** Predicted probability of nerve dysfunction by binary logistic regression analysis with cut-off set at -44.19% ($\text{Mean} \pm 2\text{SD}$) ($\text{Mean} = -0.86\%$, $\text{SD} = 21.66$) of component action potential (CAP) amplitude decrease. 5.63% strain (in 800 mm/s group), 15.38% strain (200 mm/s group), and 18.73% strain (20 mm/s group) caused 25% probability of nerve injury respectively. **b** Survival analysis (Kaplan) showed 800 mm/s group had the highest probability of failed nerve function [7]

stretch speed including 20 mm/sec, 200 mm/sec, and 800 mm/sec rates. In this series of tests, nerve conduction functional loss to 44.19% was defined as injury criteria. It was found that 5.63% strain under 800 mm/s nerve stretch speed, 15.38% strain under 200 mm/s stretch speed, and 18.73% strain under 20 mm/s stretch speed caused 25% probability of nerve injury respectively (Fig. 5a) [7]. In addition, there was partial recovery of nerve function at lower strains (less than 10% strain) and lower stretch speed (less than 20 mm/sec).

3 Results

Modelling The results shows that based on thin layer CT scanning technique, Mimics in combination with Hypermesh can reserve geometric features and make accurate three-dimensional finite element models quickly and efficiently. However the size of automatic-generated elements could be smaller than 0.3 mm . The small size of elements can significantly increase the calculation running time when using LS-DYNA software. Hence manual adjustment of element size was performed using ANSA software. The results demonstrated that ANSA could efficiently resize the element of selected anatomic components.

Global responses Global kinematic responses from the model demonstrated a whiplash movement of neck as found in Meyer's volunteer's tests. The head moved backward, then moved forward as in a whiplash (Fig. 6). The headrest was not simulated in this study.

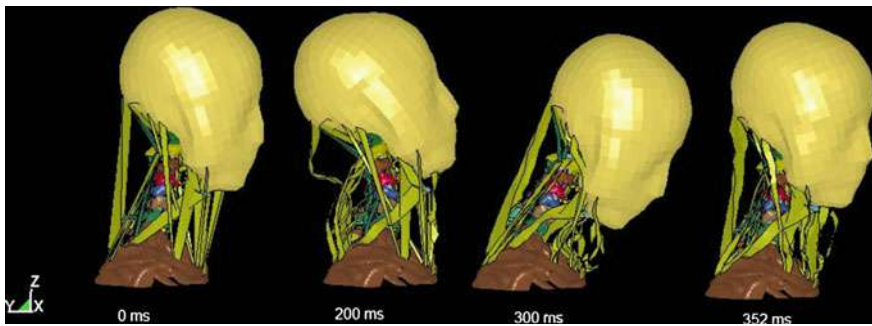


Fig. 6 Head and neck kinematic movement from whiplash simulation

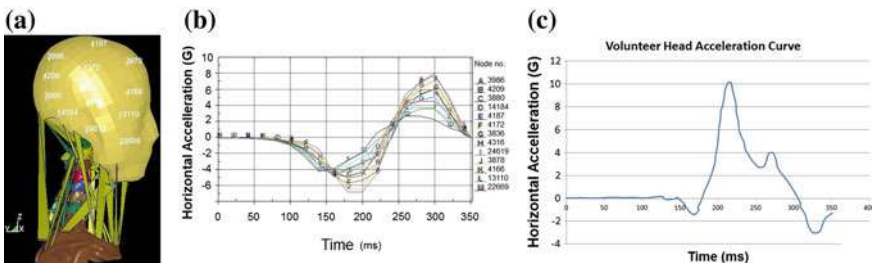


Fig. 7 a Nodal points selected for tracking head acceleration during whiplash. b Acceleration curves of selected nodes movement during whiplash simulation that were compared with volunteer head acceleration curve for model validation. c Volunteer head acceleration curve with head restrain measured by Meyer et al. [6]

The simulation outcomes demonstrated similar trends of head kinematic movement during whiplash simulation (Fig. 7a). Most of the response points from the FE model had the same trend of acceleration (Fig. 7b) as found in Meyer's [6] experimental acceleration curve (Fig. 7c). However, there were differences in the moment of peak values and the negative peak value between 120 and 170 ms. The difference could be resulted from head restraint contact about 140 ms from the start of impact in Meyer's volunteer tests [6]. The peak value of horizontal acceleration of the head from the FE model was smaller than that of the head kinematic data recorded from the volunteer in Meyer's experiment. Using HyperView (Altair Inc, Troy, MI, USA), the strain change contour was viewed directly (Fig. 8). The elements at C1-C7 levels were selected to track strain change of the spinal nerves.

Strain rate of the spinal nerves Using LS-DYNA's pre-post processing function, the strain rate was measured by displacement versus time. The maximum strain rate was identified to be 199 ± 23 mm/sec in this simulation.

Spinal nerve strain change over the time This whiplash computer simulation demonstrated that acceleration on the chest produced up to 32 % of the maximum

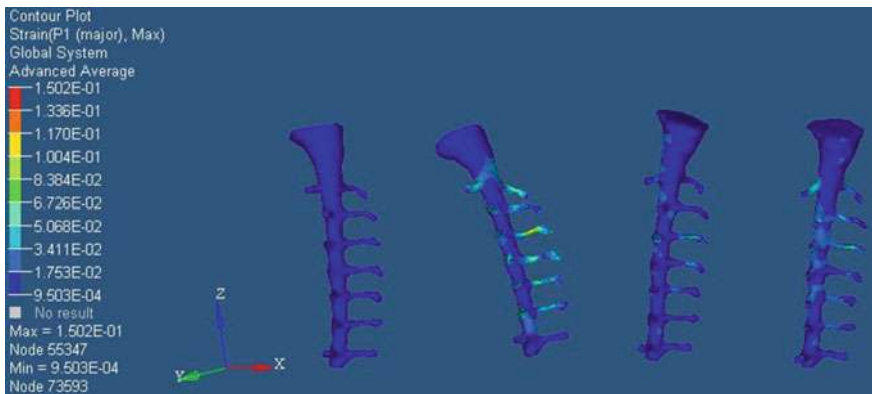


Fig. 8 View of strain distribution on the spinal nerves and spinal cord using Hyperview

principal strain on the spinal nerves. From the time point of 0 to 180 ms during rear impact, higher chest acceleration caused the spinal nerves to be stretched to higher strains. The highest strain was found in the C3 spinal nerve when 7 Gs acceleration was applied to the chest, in which the spinal nerves were demonstrated to be stretched up to a 32 % strain. Increase of acceleration beyond 7 Gs did not increase strain of the nerve. 10 Gs acceleration did not produce higher strain of the nerve more than 30 % before the intervertebral disk failed. The C3 spinal nerve appeared to be the most frequent nerve to be stretched to the highest strain when exposed to various accelerations (Figs. 9 and 10).

Determination of spinal nerve injury Based on our in vivo nerve injury neurophysiologic studies, the threshold causing 25 % probability of nerve injury was 15.38 % strain under 200 mm/s stretch speed was considered to cause and 18.73 % strain under 20 mm/s stretch speed [7]. This simulation demonstrated that C3 nerve can be stretched up to 24 % strain, the probability of nerve injury was predicted to be up to 40 %. The strains of other cervical spinal nerves were less than 15 %, hence the injury probability of other spinal nerves was predicted to be less than 25 %.

4 Discussion

Whiplash-associated disorders such as neck pain have been reported as one of the most common injuries involved in motor vehicle accidents. In the surveys conducted by US and British Columbia insurance institutes, neck injuries make up to 40–71 % of the injury claims [8]. Whiplash-associated disorder (WAD) has an annual incidence of 3.8 per thousand in the US [9]. Among US insurance claims, neck sprains make up 40 % of claimants. 61 % of injury claims reimbursed by the Insurance Corporation of British Columbia were WAD [8]. The majority of reported WAD are AIS 1 (600,000 of 700,000 in 1992–1993) (Table 2), with an

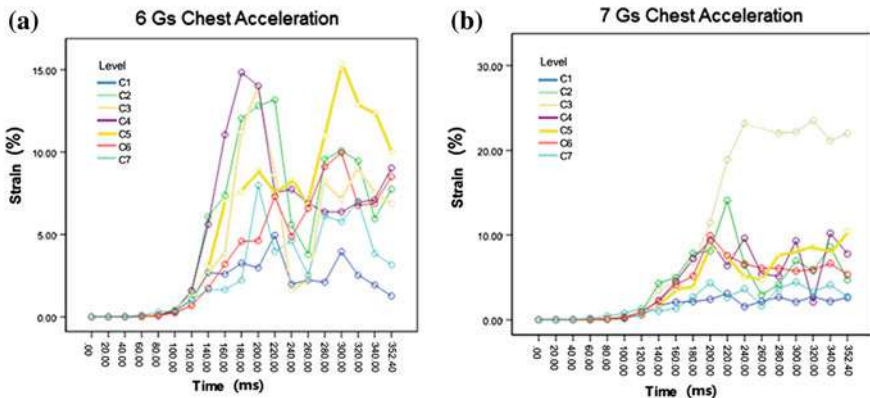


Fig. 9 Distribution of strain on different level of spinal nerves. C1 = 1st cervical nerve, C7 = 7th cervical nerve. **a.** Applying 6 Gs ($6 \times 9.8 \text{ m/s}^2$) acceleration to the chest resulted in up to 15 % maximum principal strain on the spinal nerves (C4 and C5 spinal nerves). C4 spinal nerve was stretched to 15 % strain, while 13–15 % strains were distributed at C2, C3, and C5 spinal nerves. **b.** Distribution of strain on different levels of the spinal nerves when 7 Gs acceleration was applied to the chest. 7 Gs ($7 \times 9.8 \text{ m/s}^2$) acceleration of the chest produced up to 24 % maximum principal strain on the C3 spinal nerve, 13.7 % strain on C4, 10 % strain on C2

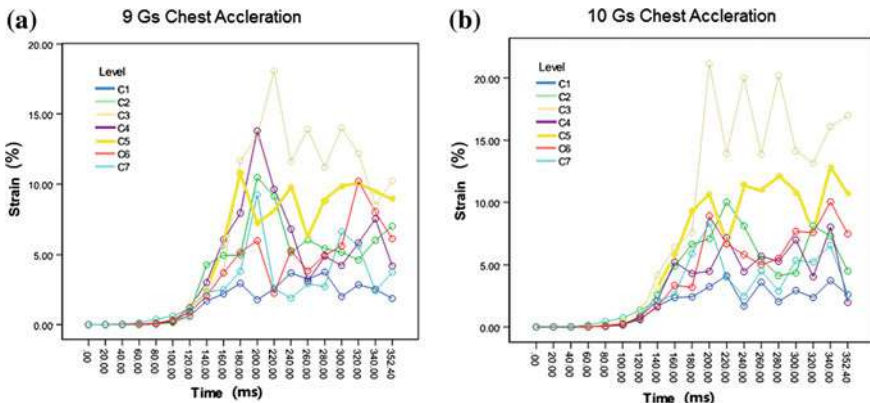


Fig. 10 **a** Distribution of strain on different level of the spinal nerves when 9 Gs acceleration was applied to the chest. The C3 was stretched to 17 % strain, and the C4 spinal nerve was stretched to 13.7 %, strain of other spinal nerves were less than 12 %. **b** Distribution of strain on different level of the spinal nerves when 10 Gs acceleration was applied to the chest. The C3 was stretch to up to 21.6 % strain. C5 was stretch to up to 12 % of strain. Other spinal nerves were stretched to the strain no more than 10 %

estimated annual cost of \$3.9 billion [10]. As most of whiplash-relevant motor vehicle accidents happened at low or moderate speed, whiplash patients typically do not experience bone fracture as evidenced by X-ray and MRI imaging. The whiplash symptoms are most likely caused by soft tissue injury. Several

Table 2 Whiplash-associated disease AIS classification (Spitzer et al. [8])

0	No complaint about the neck; no physical signs
1	Neck complaint—pain, stiffness, or tenderness only
2	Neck complaint with musculoskeletal signs including decrease range of motion and point weakness
3	Neck complaint with neurological signs including decrease or absent deep tendon reflexes, weakness, and sensory deficits
4	Neck complaint with fracture or dislocation

anatomical structures were proposed as potential injury sites, including facet joints, intervertebral discs, muscles and ligaments, spinal nerve and dorsal root ganglion (DRG). Injury to the nerve tissues can result in more severe clinical symptoms, including motor, sensory, and sphincter disturbance. However the acceleration thresholds that can cause nerve injury is unknown. It is impossible to test human or animal spinal nerve strain and stress directly. The only feasible approach is to use mathematic computer simulation methods. In this study, FE analysis computer simulation methods were used to investigate the spinal nerve tolerance to whiplash injury from rear impact based on our previous biomechanical and neurophysiologic research outcomes [4, 5, 7]. The reason we investigated the rear impact is because that rear collisions cause pain in the neck almost twice as frequently as frontal collisions [11].

Modelling It is well known that using ANSYS or other industrial software to construct geometric accurate human body FE model is a tedious and time consuming procedure. Mimics is a software specially developed for medical image processing. Using Mimics for the segmentation of 3 dimensional medical images from CT or MRI will be create highly accurate 3D models in igs format and can further be converted into FEA packages (such as ANSA, Hypermesh) for geometry meshing. It is found in this study that Mimics 14.0 is a expedient software to build human FE models with accurate anatomic features. Combined Mimics, ANSA, and HyperMesh software for applications provided a new and rapid approach to build a human FE model, yet the element quality can be better controlled.

By optimizing the size of the elements, the computer calculation running time was reduced. The size of the automatically generated finite elements from Mimics could be smaller than 0.4 mm. When the size of the element length is smaller than 0.4 mm, the results become increasingly accurate, but smaller elements can significantly increase computer calculation running time. Only with further advancements in computation power can the elements become smaller and more precise. In this study, all elements were resized to be bigger than 0.4 mm in element side length using ANSA software.

Because many numerical simulation studies have shown that hexahedral element mesh is better than tetrahedral element mesh because hexahedral elements can increase the analysis accuracy and simulate element mechanical properties better than tetrahedral elements for viscoelastic materials [12]. Hence all the tetrahedral elements of this numeric FE model were converted into hexahedral elements. These processes were accomplished automatically using ANSA software.

Validation This model was validated by comparing the head kinematic response with published head global kinematic responses from volunteer rear impact tests. Although the simulation responses of the head could not perfectly match the experimental observations, the model reasonably demonstrated the basic responding features under whiplash. The negative peak head acceleration value was smaller than Meyer's volunteer negative peak value (Fig. 7b,c), this could be resulted from the effects of head restraint used in Meyer's volunteer tests. The volunteer's head contacted the headrest at the 140 ms, which stopped the head moving backward further. While in our FE simulation, there was not a headrest, hence the head moved more backward than volunteer's head. Simulation with a headrest will be considered in our future studies. In addition, to make a better model, further optimizations of the model are required, which will be included in our future studies, such as muscle biofidelity.

Simulation outcomes Our simulation outcomes matched the clinical findings. In this FE simulation, it was found that exposure to various impact accelerations, the C3 nerve was the most frequently spinal nerve stretched to a higher strain than other spinal nerves, indicative of higher probability of C3 nerve injury. Clinically, Lord et al. [13] reported that the third occipital nerve headache is a common condition in patients with chronic neck pain and headache lasting for 3 months after whiplash. The third occipital nerve consists of the C3 spinal nerve majorly and C2 spinal nerve partially. Among 100 patients with chronic neck pain and headache lasting more than 3 months, the prevalence of the third occipital nerve headache was as high as 53 % (95 % CI 37–68 %). Pain was relieved by C3 nerve root block treatment. The long-lasting pain and effective nerve block treatment indicated that the third occipital nerve headache is the neuropathic pain from C3 spinal nerve injury.

Nerve injury criteria Nerve injury criteria was based on our in vivo testing outcomes. Under 200 mm/s stretch speed, the strain threshold to cause 25 % probability of nerve injury was 15.38 % strain; under 20 mm/s stretch speed strain threshold to cause 25 % probability of nerve injury was 18.73 % strain [7].

Spinal nerve injury prediction This FE simulation demonstrated that 6 Gs chest acceleration cause several spinal nerves (C3, C4, C2, C5) stretched to 10 % strain. Based on nerve injury criteria, these nerves were predicted to be exposed to 25 % probability of nerve injury during rear impact. Since C3 spinal nerve could be stretched to 32 % strain, C3 nerve injury probability could be as high as 50 %. Increased chest acceleration to 9 or 10 Gs did not cause further increase of spinal nerve maximum strain.

Comparisons between volunteer tests and simulation Human volunteer tests showed that 2–6 Gs rear impact can cause minor neck pain for a short time period [14], but 2.8–8.6 Gs impact acceleration was also reported not to cause symptom in other volunteer tests [15, 16]. The increase of acceleration appeared not to increase neck pain severity (Table 3) [17]. Our simulation outcomes demonstrated that 6 Gs chest acceleration may stretch the cervical spinal nerve to have 25 % injury probability. Neck pain can come from other soft tissues, such as muscles, facet joint capsules, and ligaments, in addition to the nerve tissues. In this study,

Table 3 Volunteer testing outcomes

Study	Impact velocity (km/h)	Impact direction	Measured head acceleration (G)	Change in struck vehicle velocity (km/h) (ΔV)	Results	Head restraint
Szabo and Welch [19]	16	Rear	10.1–13.7		Minimal (< 1 day) or no symptoms	Yes
McConnell [20]	7–16		4.3		Minimal or no symptoms	No
Ono and Kanno [21]	2.0–4.3	Rear and front			No symptom	
Scott [14]	2.0	Rear	2.0–6.0		Neck pain for 1 day	Yes
Siegmund [22]	7.5–9.4	Rear and frontal		6.1–7.63	No Symptom	No
West [16]	2.9	Rear	1.5–18.6		Minor symptoms at highest forces	No
Geigl [23]		Rear		6.0–12.0	No symptoms	Yes
Rosenbluth [15]	3.0–13	Rear	2.8–8.6		No	No
Matsushita [24] La		Rear & F & Rear	1.4–6.3 5.8–10.9		Minor symptoms for 2–4 days in a few volunteers	Yes
McConnell [25]					Few had symptoms lasting for hours to days	
Dubois [26]	2.4–14	Rear		0.29–1.91	Absolute no injury	
Castro [17]	16–26.4	Rear	1.0–10.0		Few had pain for a few days	Yes
Brault [27]	4.9–10	Rear		4–8	Neck pain >2 days	Yes
Howard [28]		Rear	3.0–6.0		Neck pain for 3 days	Yes

only nerve injury tolerance was studied, which may not completely explain the neck pain in volunteer tests or clinical pain scenario, thus, in our future studies, soft tissue injury tolerance also needs to be investigated.

The limitation of this study is that only cervical spine and upper shoulder were composed for computer simulation. In addition, muscle biofidelities were not simulated in this model. Hence in our future studies, muscle biofidelities and dynamic response [18] will be considered and built into the FE model for analysis. The whole vehicle and whole body FE models will also be constructed for a better simulation.

5 Conclusion

Mimics, ANSA, and HyperMesh software combined applications provided a new and rapid approach to build a human FE model, yet the element quality can be better controlled. Our neck finite element model was the first FE model developed to study the spinal nerve tolerance to whiplash injury. The model validation was performed at the global level by tracking the head kinematics. The simulation results matched clinical scenarios and volunteer testing outcomes. The simulation outcomes demonstrated that chest accelerations of 6 Gs may be the threshold for cervical spinal nerve injury under 25 % probability of injury. 7 Gs chest acceleration may cause 50 % probability of the C3 spinal nerve injury. Increased chest acceleration to 9 or 10 Gs did not cause further increase of spinal nerve maximum strain. A higher strain was frequently found in the C3 spinal nerve under different accelerations of rear impacts.

Acknowledgments This research was supported by an Opening Fund of State Key Laboratory of Automotive Safety and Energy of Tsinghua University, Beijing, China (KF11011).

References

1. Martin D (1998) The acute traumatic central cord syndrome. In: Gunzburg R (ed) Whiplash injury: current concepts in prevention, diagnosis, and treatment of the cervical whiplash syndrome, 1st edn. Lippincott Williams & Wilkins, Philadelphia, pp 129–133
2. Ferrari R (1999) The whiplash encyclopedia: the facts and myths of whiplash, 1st edn. In: Robert F (ed) Aspen Publishers Inc, Gaithersburg, pp 449–470
3. Hedenstierna S, Halldin P (2008) How does a three-dimensional continuum muscle model affect the kinematics and muscle strains of a finite element neck model compared to a discrete muscle model in rear-end, frontal, and lateral impacts. Spine (Phila Pa 1976) 33(8):E236–245
4. Singh A, Lu Y, Chen C, Cavanaugh JM (2006) Mechanical properties of spinal nerve roots subjected to tension at different strain rates. J Biomech 39(9):1669–1676
5. Singh A, Kallakuri S, Chen C, Cavanaugh JM (2009) Structural and functional changes in nerve roots due to tension at various strains and strain rates: an in vivo study. J Neurotrauma 26(4):627–640

6. Meyer S (1998) The minimal collision velocity for whiplash. In: Gunzburg R (ed) Whiplash injury: current concepts in prevention, diagnosis, and treatment of the cervical whiplash syndrome, 1st edn. Lippincott Williams & Wilkins, Philadelphia, pp 107–109
7. Chen C, Virk GS, Yaldo J, Guruprakash GK, Kallakuri S, Cavanaugh JM (2011) The effects of strain and displacement rate on spinal nerve injury and recovery. In: Proceedings of annual meeting of orthopaedic Research Society, San Francisco, California, pp 1274
8. Spitzer WO, Skovron ML, Salmi LR, Cassidy JD, Duranceau J, Suissa S, Zeiss E (1995) Scientific monograph of the quebec task force on whiplash-associated disorders: redefining “whiplash” and its management. *Spine (Phila Pa 1976)* 20(8 Suppl):pp. 1S–73S
9. Barnsley L, Lord SM, Wallis BJ, Bogduk N (1994) Lack of effect of intraarticular corticosteroids for chronic pain in the cervical zygapophyseal joints. *N Engl J Med* 330(15):1047–1050
10. Winkelstein BA, Nightingale RW, Richardson WJ, Myers BS (2000) The cervical facet capsule and its role in whiplash injury: a biomechanical investigation. *Spine (Phila Pa 1976)* 25(10):1238–1246
11. Deans GT, Magalliard JN, Kerr M, Rutherford WH (1987) Neck sprain—a major cause of disability following car accidents. *Injury* 18(1):10–12
12. Zhang JG, Wang F, Zhou R, Xue Q (2011) A three-dimensional finite element model of the cervical spine: an investigation of whiplash injury. *Med Biol Eng Comput* 49(2):193–201
13. Lord SM, Barnsley L, Wallis BJ, Bogduk N (1994) Third occipital nerve headache: a prevalence study. *J Neurol Neurosurg Psychiatry* 57(10):1187–1190
14. Scott MW, M.W., Guzman HM, Howard RP, Bomar JB, Smith HL (1993) Comparison of human and ATD head kinematics during low-speed rear-end impacts. In: Proceedings of the thirty seventh stapp car crash conference, Warrendale, PA, SAE Paper# 930094
15. Rosenbluth W, Hicks L (1994) Evaluating low-speed rear-end impact severity and resultant occupant stress parameters. *J Forensic Sci* 39(6):1393–1424
16. West DH, Gough JP, Harper G (1993) Low speed rear-end collision testing using human subjects. *Accid Reconstr J* 5:22–26
17. Castro WH, Schilgen M, Meyer S, Peuker C, Wortler K (1997) Do “whiplash injuries” occur in low-speed rear impacts? *Eur Spine J* 6(6):366–375
18. Kumar S, Narayan Y, Amell T (2002) An electromyographic study of low-velocity rear-end impacts. *Spine (Phila Pa 1976)* 27(10):1044–1055
19. Szabo T, Welcher J, Anderson R (1994) Human occupant kinematic response to low speed rear-end impacts. In: Proceedings of the thirty eighth stapp car crash conference, Warrendale, Pennsylvania, SAE paper # 930094
20. McConnell W, Howard RP, Guzman HM, Bomar JB, Raddin JH, Benedict JV (1993) Analysis of human test subject kinematic responses to low velocity rear end impacts. In: Proceedings of the thirty seventh stapp car crash conference, Warrendale, PA, SAE Paper# 930889
21. Ono K, Kanno M (1996) Influences of the physical parameters on the risk to neck injuries in low impact speed rear-end collisions. *Accid Anal Prev* 28(4):493–499
22. Siegmund G, Williamson PB (1993) Speed change (Δv) of amusement park bumper cars. In: Proceedings of the Canadian multidisciplinary road safety conference VIII, Saskatoon, Saskatchewan, June 14–16, 1993, pp 299–308
23. Geigl B, Steffan H, Leinzinger P, Roll P, Muhlbauer M, Bauer G (1994) The movement of head and cervical spine during rearend impact. In: Proceedings of International IRCOBI conference on the biomechanics of impacts, Lyon, France 1994, pp 127–137
24. Matsushita T, Sato TB, Hirabayashi K, Fujimura S, Asazuma T, Takatori T (1994) X-Ray study of the human neck motion due to head inertia loading. In: Proceedings of the thirty eighth stapp car crash conference, Warrendale, PA, SAE Paper# 942208
25. McConnell W, Howard RP, Poppel JV, Krause R, Guzman HM, Bomar JB, Raddin JH, Benedict JV, Hatsell CP (1995) Human head and neck kinematics after low velocity rear-end impacts: understanding whiplash. In: Proceedings of the thirty nine stapp car crash conference, Warrendale, PA, 1995, SAE Paper# 952724

26. DuBois R, McNally BF, DiGregorio JS, Phillips GJ (1996) Low velocity car-to-bus test impacts. *Accid Reconstr J* 8:44–51
27. Brault JR, Wheeler JB, Siegmund GP, Brault EJ (1998) Clinical response of human subjects to rear-end automobile collisions. *Arch Phys Med Rehabil* 79(1):72–80
28. Howard RP, Bowles AP, Guzman HM, Krenrich SW (1998) Head, neck, and mandible dynamics generated by ‘whiplash’. *Accid Anal Prev* 30(4):525–534

A Rear View Camera Based Tailgate Warning System

Chong Sun, Guanglinx Ma, Manoj Dwivedi, Yi Zeng and Xubo Song

Abstract On-vehicle rear view cameras have been widely in the market. Main purpose of rear view camera is to provide the driver with a good view to rear scenes, especially the blind spot areas. Rear view camera is automatically turned on when reverse gear is engaged and turned off when vehicle moves forward. In general, a rear view camera is only used in back-over and parking manoeuvres. In most of driving scenarios, a vehicle moves forward and the rear view camera stays idle and not used. In this paper, rear-end pre-crash safety system utilizing on-vehicle rear view camera is presented. The system detects vehicles approaching from behind and calculate TTC (time to collision) of approaching vehicle to host vehicle. Based on the calculated TTC, if the system judges that there is high possibility of collision, the system can give a warning to approaching vehicle by flashing hazard light. In addition, the system can also issue a warning to the driver of host vehicle and automatically take some actions to minimize injury caused by collision. For example, pre-tensing seat belt, move headrests forward etc.

Keywords Active safety · Rear pre-crash · Vehicle detection · Tailgate warning · Intelligent vehicle · Rear view camera

F2012-F05-007

C. Sun (✉) · G. Ma · Y. Zeng · X. Song

Advanced Product Development, Delphi (China) Technical Centre, Shanghai, China

M. Dwivedi

Algorithm Development Group—Safety and Forewarn, Delphi Electronics & Safety, Bangalore, India

1 Introduction

Pre-crash safety systems using radar and vision detecting technology have been commercialized in the market. While the primary focus of these systems has been for frontal collisions, rear-end collisions actually have a higher proportion of the traffic accident injuries.

According to accident analysis of crashes in Japan [1], rear-end collisions account for only 4 % of fatalities, but approximately 50 % of injuries. In addition, a high proportion (77 %) of rear-end collisions result in neck injury, most of which can be categorized as whiplash injury. The primary cause of rear-end collisions is driver's poor attention to which caused by distraction ahead when driving, approximately 14 % of accidents occur when the driver is looking forward but make's misjudgement by carelessness.

In this paper, a new pre-crash safety system for rear-end collisions is explained. It was developed to help alert drivers of vehicles approaching from behind, and also to reduce whiplash injury. This new system uses existing rear view camera installed in the rear bumper to detect a vehicle approaching closely from behind during front driving. If it judged that there is high risk of collision, the hazard lights would flash to warn the driver of the approaching vehicle and the headrests are automatically moved forward, thereby reducing the risk of whiplash injury.

2 General Overview

The paper describes both day time vehicle detection and night time bright spot detection algorithms. The algorithms are different since a common algorithm cannot provide desired performance as the way vehicles are seen during day and night are different. The glare due to bright spots during night time also inhibits identification of vehicle boundaries and separating the nearby vehicles. The current approach uses a separate camera setting for day time and another camera setting for night time. During night time the camera has much lower exposure setting so that no other light is seen except the bright spots due to vehicles and street lights. A day-night detection algorithm is developed to identify whether the vehicle is being driven during day time or night time and switches the algorithm appropriately.

3 Day Time Detection

In this chapter, the method to detect vehicles from one frame in daytime scenario is discussed. After the detection process, vehicle position and size on image are known.

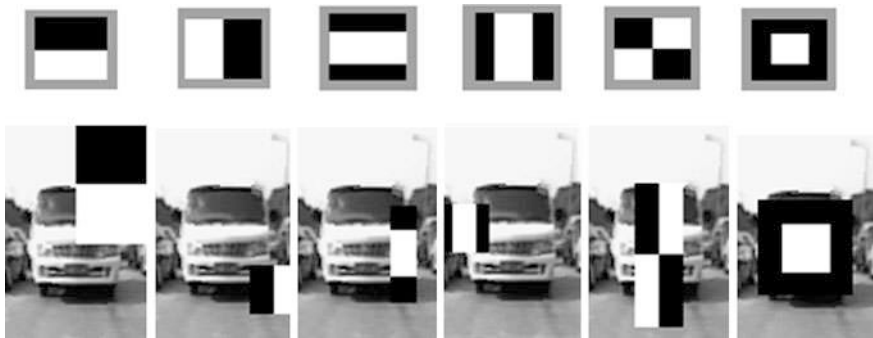


Fig. 1 Basic features

Our method, which is quite similar to [2], can be divided into 4 parts: feature extraction, feature selection for weak classifiers, strong classifier training by Ada boost, and combining classifiers into cascaded ones.

3.1 Feature Extraction

The features used in our method are known as Haar-like rectangle features, as the vehicle appearance is roughly symmetrical. Of course, before feature extraction on every sample image, training samples or sub-images should be interpreted by integral image [2]. Every Haar-like feature can be defined $asf(d_x, d_y, scale_x, scale_y, t_p)$. Where d_x, d_y are the coordinates of bottom right of the rectangle feature, $scale_x$ is the width of rectangle, $scale_y$ is the height of rectangle, t_p represents which type of basic feature it is. Figure 1 shows the six type of basic features used in our system.

By scaled and shift on the sub-image, thousands of features will come into being from 4 type of basic features. The number of extracted feature depends on the size of sub-image, scale factor and shift step.

3.2 Feature Selection for Weak Classifier

This section will describe how to select best features (classifiers) from thousands of extracted features, in order to obtain lowest error according to given weighted sample pool. As week classifier is the one whose classification capability is slightly higher than random guess, many models can be used to train weak classifier.

A linear week classifier which is combined by single features is designed in our method. It can be indicated as

$$h(x) = s(x - b) \quad (1)$$

Where x is the feature value of samples, $s = \{1, -1\}$, if $h(x) > 0$, the sample has been classified as positive sample, otherwise, has been classified as negative ones. Every feature f_i learns all weighted samples, and then a proper value b_i can be selected for individual feature, with lowest classification error ϵ_i . The optimal feature or weak classifier is the h_{op} with

$$\epsilon_{op} = \min(\epsilon_0 \dots \epsilon_n) \quad (2)$$

3.3 AdaBoosting

The next step of selecting weak classifier is to combine several weak classifiers into a strong classifier with significant detection rates. Most common algorithm to achieve this includes Adaptive Boosting (AdaBoost) which formulated by Yoav Freund and Robert Schapire [3], Support Vector Machines (SVM) which was invented by Vladimir Vapnik. The algorithm we choose here is AdaBoost, which has great generalization and low computational costs [4]. The detail process of AdaBoosting method is described as follow. A clear target true positive rate (fpr_{target}), false negative rate (fnr_{target}) and maximum number of weak classifiers shall be determined in advance. The classification capability of strong classifier gradually increases during the above boosting process, as soon as the process end, the capability reaches the expecting level.

3.4 Cascade Classifier

If we train only one strong classifier which can achieve a quite low false positive rate and false negative rate, it may generate a large number of week classifiers. This will result in slow detection speeds, especially when the classification task is not an easy one. A cascade of strong classifier is one of the most popular methods to solve this issue; its schematic is showing in Fig. 2. Only sub-images passed through all strong classifiers (all stages) will be considered as positive sample.

For a real-time detection application, this structure allows us to balance a detection rate and detection speed by selecting proper number of stages and proper false negative rate and false positive rate for every stage. As shown in Fig. 2, any samples which are rejected by early stage, have no chance to go into next stages. So it is necessary to set a low false negative rate for every stage. On the other hand, any samples which been passed in early stage by mistake, has chance to be rejected in next stages, so a high false positive rate for one stage can be acceptable in purpose of increase detection speed.

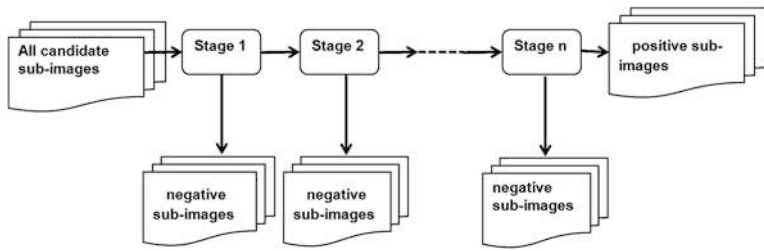


Fig. 2 Cascade schematic

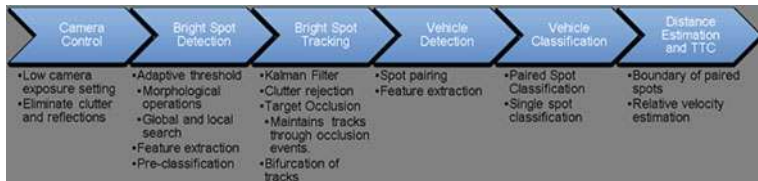


Fig. 3 Nighttime algorithm blocks

The false positive rate of the cascade classifier is lower than any of the single classifiers performing alone.

$$fnr_{final} = fnr_1 * fnr_2 * fnr_3 * \dots * fnr_n \quad (3)$$

Generally, an efficient cascade of classifier becomes more and more powerful, stage by stage. The early and relatively weak stage is responsible to reject most of negative samples very quickly, which looks quite different from vehicle. The latter stages focus on distinguishing challenge samples, at most situation, with lots of processing time.

4 Night Time Detection

The night time tailgate warning algorithm looks for bright spots belong to vehicle headlights for vehicle detection and classification. Incidentally, the vehicle headlights are the brightest objects during night time. The major blocks of the night time tailgate algorithm are show as Fig. 3.

The “Camera Control” block sets the camera to a low exposure setting so that only the brightest spots are visible in the image and glare due to vehicle lights are reduced. The camera control reduces the clutter and reflections in the image and except vehicle lights and street lights no other lights are visible.

The “Bright Spot Detection” block detects the bright spots in the image. A predefined region of interest (ROI) is used to focus on the area of interest and decrease required processing power and background influence. A histogram based

adaptive threshold selection method then generates a binary image. The potential bright spots are then detected using contour tracing algorithm designed to achieve fast morphological image processing. The various features of these bright spots are also extracted.

The “Bright Spot Tracking” block tracks the bright spot over multiple frames and calculates its trajectory. The tracking algorithm uses Kalman filter on image plane. The tracker eliminates all inconsistent targets and ensures consistent detection of all objects of interest.

The “Vehicle Detection” block identifies the potential vehicle spot pairs based on their size, shape and location and calculates similarity parameters. The key parameters used in the block for spot pairing are similarity in vertical position, distance between spots, size similarity and position in the image. The spots are not paired in case there is any bright spot in between.

The key parts of “Vehicle Classification” block are paired spot classification, fog light identification and single spot classification.

The paired spot classification checks overall similarity between spots based on previous history. The method compares overall similarity along with pair age and number of saturated pixels and confirms the spots as vehicle light pair. The classification uses the spot similarity index and pair history in case a bright spot is shared between multiple pairs (potentially multiple vehicles in nearby lanes).

The fog light identification method checks if two very bright spots are exactly one over other and the spot below has smaller or same size as the spot in top. If identified, the spot below is marked as fog light spot and is not used for pairing. The identification also helps in pairing in case one light has clearly separated low beam and fog light and other has fused low beam and fog light.

The single spot classification applies for bright spots that have features similar to vehicle with fused light spots and they are not paired with any other spot. They are commonly seen in oncoming vehicles with high beam ON. These bright spots are likely to have high number of saturated pixels. Also the spot shape is likely to be more in horizontal direction compared to vertical direction.

The single spot classification method also takes care of continued classification during spot bifurcation by observing sudden change in bright spot size and creation of a new bright spot adjacent to existing spot. The classification is transferred from original single spot to a paired spot involving original spot and new spot.

The distance estimation is done using the boundaries of the paired spot or using the width of the fused vehicle spot. The boundaries are calculated using only the saturated pixels of the image so that the distance estimation has less effect due to halo of the spots.

The calculation of the time to collision (TTC) is based on distance estimation and relative velocity of the following vehicle in ego lane. The host velocity cannot be used here since a collision can occur even if host vehicle is stationary (compared to a forward camera application for vehicle detection where collision can occur only if host velocity is greater than velocity of leading vehicle).

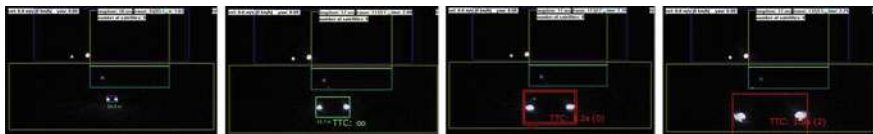


Fig. 4 Vehicle classification–Low Beam ON

A warning is issued if TTC value is less than threshold and following vehicle is at very near distance. The currently implemented warning is flashing of brake lights. The active headrest can also be pushed ahead in case of detection of potential rear collision (not implemented).

4.1 Test Results

The algorithm was tested on various night time videos. The testing was done for correct vehicle spot pairing and classification and correct classification for fused vehicle spots. The distance estimation and TTC are checked and false alarms are noted.

A consistent algorithm performance is observed in test scenario (for both ego lane and side lanes)

- True detection number: 944
- False detection rate: 1.09 %
- Miss detection rate: 0.00 %

4.2 Observations

In case an oncoming vehicle switches ON high beam when it is very near, a false TTC alarm is possible due to sudden change in spot size. For oncoming vehicles in side lanes, the detection gets lost when vehicle is about to overtake. The following scenario shows the performance for following vehicle with low beam ON (Fig. 4).

The following scenario shows the performance for following vehicle with high beam ON (Fig. 5).

5 Lane Assignment & Tracking

In order to filter out some false detection and estimate the interesting information which can't be measured directly, such as target's velocity and yaw rate, a tracking process is applied here.

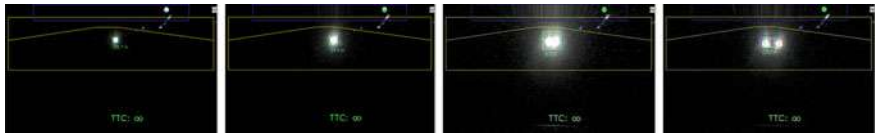


Fig. 5 Vehicle classification–High Beam ON

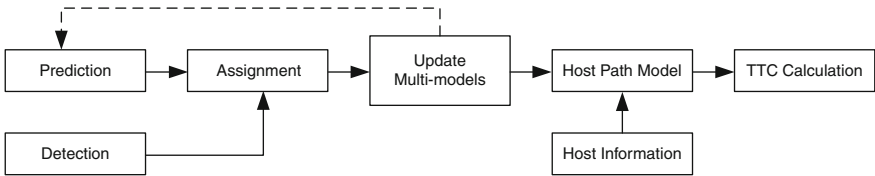


Fig. 6 Vehicle tracking and lane assignment algorithm

As shown in Fig. 6, in each frame, except for the first frame, every detection result should find out the corresponding detection result in previous frame, if there is any. Here a nearest neighbor method is adopted to run fast enough on low powerful hardware. Then the detection location of one target in sequential two frames are put into an extended Kalman filter, and two motion models, which can switch automatically based on the property of target, are adopted to cover different target's maneuvering characteristic.

After the tracking process, a threaten assessment module is going to judge every tracked target, and one main function is lane assignment. In there, the host path model is first estimated with the host trajectory as well as updated yaw rate and steering angle count, following the Kalman filter based fusion framework. Then the distance between the tracked target and the host path is calculated according to the path model and target's trajectory information coming from the tracker. At last, the closest in path vehicle will be selected, and its TTC information is one main criterion for warning.

6 Experiments and Results

6.1 Data Set for Vehicles

We selected 8,000 candidates for ego vehicle data and 16,000 candidates for side (left & right) vehicle data. The distance from target vehicle to host vehicle is at the range of 5 ~ 20 meters. Figure 7 shows some examples.

	Left	Ego	Right
Small			
Mid			
Large			

Fig. 7 Ego vehicle & side vehicle candidates

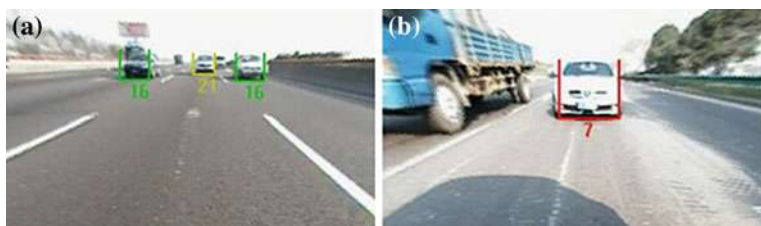


Fig. 8 Vehicle detection on the images from a rear-view camera

6.2 Vehicle Detection Performance

This section presents some results drawn from videos of real road environments. In a 125 min sample video of 26,900 frames, we totally have 34,994 target vehicles which were approximately 5–20 m behind. The 125 min sample video consists of 40 min in downtown, 50 min in urban and 35 min in freeway /highway.

The target vehicles were detected resulting in a miss detection rate of 0.3943 % and a false positive rate per image of 1.52 %. Figure 8 shows the results of vehicle detection on the images from a rear-view camera. Figure 9 shows the composition of miss detection and false positive detection.

Figure 10 shows the analysis result of miss detection according to road condition. Freeway & highway have less miss detection rate than other road conditions. Urban has higher miss detection rate because of one snow scenario in which one following vehicle missed, and that vehicle keeps there for a very long time.

Figure 11 shows the analysis result of miss detection according to weather condition. In challenge condition, the detection distance behind the host vehicle

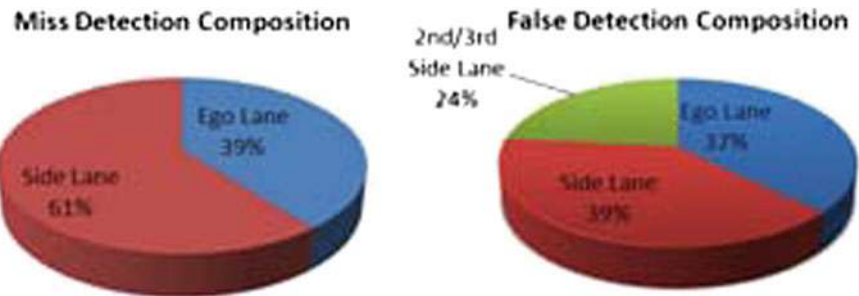


Fig. 9 Composition of miss detection and false positive detection

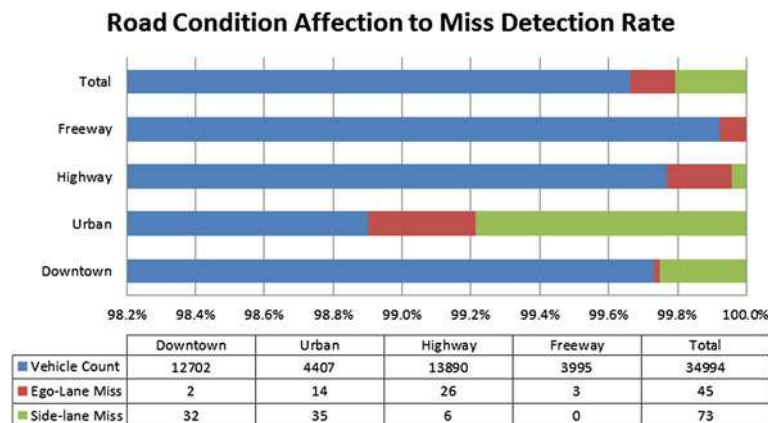


Fig. 10 Miss detection analysis according to road condition

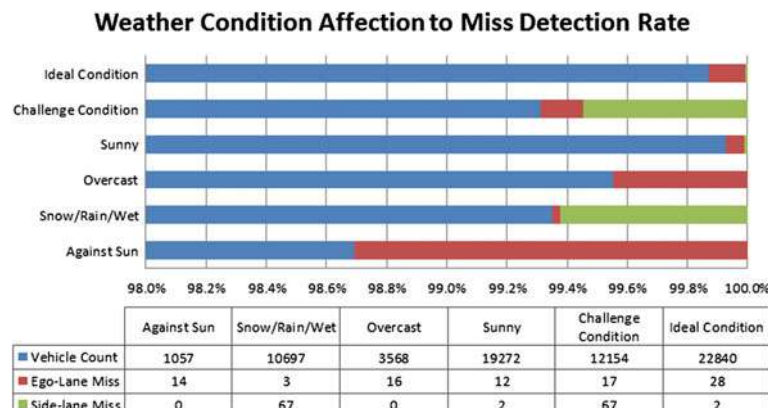
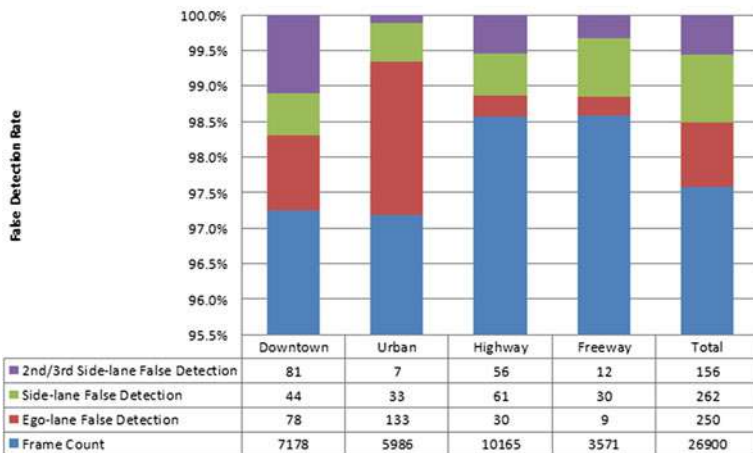


Fig. 11 Miss detection analysis according to weather condition

(a) Road Condition Affection to False Detection Rate



(b) Weather Condition Affection to False Detection Rate

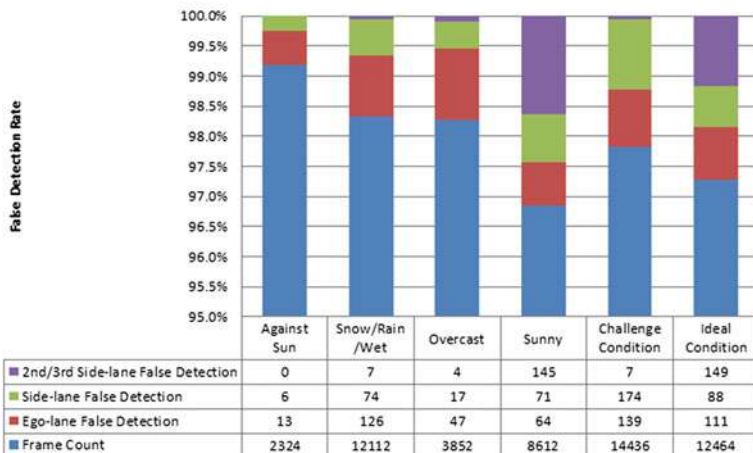


Fig. 12 False detection analysis according to road condition (a) and weather condition (b)

became shorter than in ideal condition. In condition against sun, miss detection rate became much higher because of the large bright spot at the centre of image.

Figure 12a shows the analysis result of false detection according to road condition. Freeway & highway have less false detection rate than other road conditions. In downtown false detection rate became higher because of one scenario in which many challenging objects are beside the road.

Figure 12b shows the analysis result of false detection according to weather condition. False detection rate is not affected by weather condition a lot. In some scenarios, high false detection rate is due to rich image information at the border of ROI.

6.3 TGW Warning Evaluation

This section presents the result of TGW warning occurrence. We still use the same sample videos which have duration time of 125 min as section B.

In the totally 125 min scenarios, only 1 positive warning occurred and there was no false warning occurred. The false vehicle detection in section B didn't lead to a false warning.

7 Summary/Conclusions

In this paper we presented robust a real time online vehicle detection algorithm applied by AdaBoost learning scheme in combination with LDA feature. A novel lane assignment and TTC calculation algorithm is also presented. In addition, a bright spots detection algorithm in combination of online camera exposure control enables detection of vehicle in night also is very robust in spite of high illumination of head lamps of approaching vehicle directly to our camera. A novel day-night detection algorithm is also presented which detected day and night automatically and apply the corresponding vehicle detection algorithm based on the detected scenario.

The proposed algorithm can detect vehicles from 5 meter up to 20 meter behind the host vehicle. Detection rate of the system is 98 % in ego lane and 95 % in side-lane respectively. False alarm rate is less than 2 %.

Main limitation of this system is the detection range. Our aim is to utilize already available on vehicle fisheye rear view camera to do vehicle detection. With 124° wide horizontal field of view, the image is distorted a lot and consequently detection range is limited up to 20 m. However, 20 m detection range still meets the requirement of our application as most to rear-end collision is occurred in low speed [2].

References

1. Matsubayashi K, Yamada Y, Iyoda M, Koike S, Kawasaki T, Tokuda M, Development of rear pre-crash safety system for rear-end collisions. Toyota Motor Corporation Japan, Paper Number 07-0146
2. Viola P, Jones MJ (2004) Robust real-time face detection. Int J Comput Vis 57(2):137–154
3. Freund Y, Shapire R (1995) A decision-theoretic generalization of on-line learning and an application to boosting. In: Proceedings of the second European conference on computational learning theory, 1995
4. Nunn C, Kummert A (2009) An improved AdaBoost learning scheme using LDA Features for object recognition. In: Proceedings of the 12th international IEEE conference on intelligent transportation systems, 2009

Part VI

**Driving Action Perception and Safety
Assistance System**

On Electric Vehicle Alert for Detection and Emergency Response

Juan J. Garcia, Yannick Blecon and M. J. Dalmau

Abstract Research and/or Engineering Questions/Objective This paper summarises the activities to be carried out within the project recently approved by the European Commission to develop effective warning systems to be implemented in electric vehicles particularly to protect vulnerable pedestrians such as visually impaired people and the elderly. The project, entitled eVADER from ‘Electric vehicle alert for detection and emergency response’, is currently sponsored by the EC with grant no. 285,095 and it combines the efforts of an international consortium made up of Universities, Research Institutes, Tier-one suppliers and OEM’s. One of the important objectives of the project is to recognise that recent studies suggest that vehicles, driven in electric mode, either hybrid or pure electric vehicles, are considerably quiet and, thus, that they constitute a safety hazard for pedestrians and bicyclists in traffic. It is claimed that such vehicles are not acoustically perceived due to the power unit being exchanged from a combustion engine to electric motors; something that essentially cuts away all power unit noise and leaves tyre/road noise, the latter of which is the same as for similar-sized vehicles with combustion engines. Actions have been taken by the US and Japanese governments as well as within international bodies such as UN/ECE and ISO, with the expected outcome that “minimum noise” of vehicles shall be measured with a standard method and legal limit values for such “minimum noise” shall be established. **Methodology** Recent findings reported in NHTSA Technical Report (September 2009) suggest that pedestrian and cyclist crashes involving both electric vehicle (EV) and Internal Combustion Engine (ICE) driven vehicles commonly occurred on roadways, in zones with low speed, with higher incidence rates for EV and Hybrid EV (HEV) or EV when compared with internal

F2012-F07-002

J. J. Garcia (✉) · Y. Blecon · M. J. Dalmau
Applus+ IDIADA, Tarragona, Spain

combustion driven vehicles (ICE). The study showed that for vehicles moving slowly or stopping, backing up or entering or leaving a parking place the HEV was about two times more likely to be involved in a pedestrian accident than ICE vehicles. Similar trend was also found for cyclists, particularly at intersections. Accordingly, special concern is given to noise at speeds below 20 km/h for which the problem is expected to be the worst and where not enough data is available. *Results* eVADER will investigate the interior and exterior soundscape of electric vehicle for safe operation, considering driver's feedback, feasible pedestrian reactions, driver and pedestrian warning systems and pedestrian safety. The project will also analyse innovative methods to improve the acoustic detectability of electric vehicles in urban scenarios. The project will define solutions to warn vulnerable users of a nearby moving vehicle while providing means for heightening the awareness of drivers in critical situations. Among other's some of the most important areas covered by eVADER will be: (1) Optimum warning signals definition to induce correct driver reaction for safe operation. (2) Adaptation of the warning signals to the real in-service vibro-acoustic environment. (3) Optimum warning signals definition for pedestrians in close-to-accident situations. (4) Adaptation of the warning signals to real urban and exterior noise. (5) Integration of the generation of acoustic warning signals with in-vehicle intelligent systems data such as external microphones, vehicle speed (CAN) or Advance Driver Assistance (ADAS) systems. (6) Use of in-vehicle complementary information to improve directivity, timing, intensity, modulation and frequency characteristics of the warning signal, depending on real close-to accident scenario. (7) Optimum warning signals maintaining the quietness of residents. *Limitations of this study* The project is quite ambitious because it must combine, psychoacoustic knowledge, electro-acoustic design of highly directive acoustic sources, state-of-the-art ADAS systems and other in-vehicle intelligent systems and integrate all of them to build up a clever warning system that will detect pedestrians and will act selectively when any of them are in a close-to-accident situation. This will guarantee that this warning system will not increase the noise pollution in cities. *What does the paper offer that is new in the field including in comparison to other work by the authors?* The concept of integrating ADAS and in-vehicle intelligent safety systems with a sophisticated and highly directional acoustic source is a novel concept not presented before. *Conclusions* The project analyses innovative methods to improve the acoustic detectability of electric vehicles in urban scenarios. The project also defines solutions to warn vulnerable users of a nearby moving electrical vehicles while providing means for heightening the awareness of drivers in critical situations.

Keywords Electric • Pedestrian • Detection • Warning

1 Expected Growth of Electric Vehicles

It seems that the world's vehicle fleet is rapidly changing. Electric (EV) and hybrid vehicles with electric drive (HEV) are becoming more and more popular and frequent. Also among heavy vehicles for urban use, such as busses and delivery trucks, hybrid vehicles are gaining in popularity. A leading businessman and analyst, Mr Ulrik Gripe, President of Ener1 in Europe, recently predicted that in the next 20–30 years "all cars will be electrified somehow" [AD 2010]. An indication of this trend is the Japanese government's announcement that its goal is that in 2020 at least 50 % of all cars sold should be electrified [1].

2 Problems Related to the Acoustic Perception of Electric Vehicles

Driving in electric mode means that the propulsion will be much quieter than for today's quietest cars and trucks, although the electric power units are not silent. This is a break-through in urban noise reduction, with a potential to significantly reduce noise emission at intersections, in congested traffic and in other cases where speeds are low. However, due to tyre/road noise being unaffected, the overall effect of a fully electrified vehicle fleet will be approximately 4 dB(A) lower noise at the most favourable location before and after an intersection and 2 dB(A) as an average, according to calculations [1]. With simultaneous tyre/road noise reductions, which are likely to happen, the overall noise reducing effect will be higher. But how do we make use of the improvement potential, which may mean not only higher quality of life but also less health problems due to emissions pollution in urban areas?

As an example, an inquiry made by INRETS in France (National Institute for Research on Transportation and Security) shows that one-third of French population is annoyed by this kind of noise [1]. This conclusion can easily be extrapolated to the whole European population. Therefore, electric vehicles provide a great opportunity of improving the daily life of city inhabitants. At least for speeds lower than 50 km/h, which is a usual speed limit in cities streets, engine is the dominant noise source in cars. Electrification of cars will thus be an efficient way of reducing noise level in cities. On the other hand, one can expect that such quiet cars may be dangerous, especially for the visually impaired (VI) people who can no longer see and would in addition not hear an approaching electric vehicle any longer while they intend to cross a road. This is also true for non-visually impaired people, as many of us are used to use their ears only to get some information about their environment. Of particular importance, children and the elderly are also target groups.

This is the reason why some vehicle manufacturers of electric vehicles equip their cars with loudspeakers emitting continuous sounds, thus increasing the

exterior noise of the vehicle. The generalization of such a solution would ruin one of the major electric cars advantages of electric cars, as mentioned above. There is a clear need to develop a solution to find a compromise between the need for a less noisy environment in cities and a high level of safety for pedestrians when interacting with EV.

Recent research work suggests that vehicles, driven in electric mode, either hybrid or pure electric vehicles, emit such weak noise that they are a safety hazard for pedestrians and cyclists in traffic. Additionally, a special informal group “Quiet Road Transport Vehicles (QRTV)” to deal with this “problem” was established within the UN/ECE/WP29/GRB in 2010 [QRTV-1, 2010]. Similar national groups have been established both in USA and in Japan [JASIC, 2009-2].

Similar research was conducted by the University of California, Riverside in 2008 and noticed similar facts as previously discussed. The experiment conducted consisted of making audio recordings of an HEV and ICE vehicle, approaching from different direction at 8 km/h. While the ICE car was heard 11 m away, the HEV was only identified within 3.4 m, thus leaving only 2 s reaction time for the pedestrian/cyclist. Further testing showed that overall an HEV needs to be 74 % closer than a conventional car [1–3].

A different study from Western Michigan University also confirmed that HEVs and ICE vehicles are equally safe at speeds higher than 32 km/h due to the noises generated by the tires and the wind. Furthermore, Hybrid vehicles were tested when leaving a stoplight, and as it was shown, no dangers were posed to the pedestrians [4, 5].

Yet another study by the U.S. National Highway Traffic Safety Administration conducted in 2009, found that an HEV is two times more likely to get involved in an accident at low speeds than a conventional ICE vehicle, in the scenario of the vehicle slowing, stopping, backing up or parking. The study also showed that the incidence rate in pedestrian and cyclist crashes is also greater for HEVs to conventional vehicles [6].

In September 2010, Volvo cars and a Swedish energy company, Vattenfall, issued the first results of the Volvo V70 demonstration program. Before the field trial, the test drivers mentioned that they were particularly concerned for the pedestrian safety due to the quietness of the vehicle. After the testing, most of them changed their opinion and stated that it was not as big of a problem as they thought it would be, however they had to be more careful and take additional care while driving due to others being unaware of their position.

3 Evader Proposing Solutions

It is known that to facilitate wide spread customer acceptance and use of fully electric vehicles (FEV), eVADER will look for solutions to the absence of engine noise in this type of vehicles. eVADER will make an in-depth assessment regarding interior and exterior acoustic characteristics of these types of vehicles

during normal operation in order to create valid solutions for car makers. eVADER will take into account already existing or in-development existing pedestrian protection systems (active safety) been the first project with a holistic view to provide a solution integrating the following aspect for Vulnerable Road Users (VRU) safety:

- Definition of relevant and realistic traffic situations in close-to accident scenarios involving VRU.
- Psycho-acoustics and weighting of acoustic perceptibility of EV and HEV in close-to-accident situations for VRU.
- Reliability in VRU identification and spatial localization by in-vehicle detection systems.
- Integration of in-vehicle intelligent systems (including ADAS) with external (for VRU) and internal (for drivers) warning signals to minimise the risk of accident with VRU. These warning signals can combine both acoustic and visual signals.
- Use of the optimised acoustic source directivity to optimise VRU warning information and minimising urban noise pollution and resident's annoyance. This improved directivity of the interior and exterior warning sound can be based on physical orientation of the acoustic source or by electronic control of an array of simpler sources.

eVADER will provide innovative approaches and technologies to improve safety in urban and inter-urban environments by identifying close-to-accident patterns that will activate an 'intelligent and customized' acoustic warning signal to warn pedestrians in general and specially vulnerable road users such as VI people, cyclists, the elderly and children, thus reducing EV-pedestrian crashes. This will be achieved guaranteeing the best compromise between safety and minimum acoustic intrusion in the environment in order to minimize the negative effect on the quietness of residential and urban areas.

eVADER will also study the integration of automatic breaking to the extent of recommended implementation strategy, i.e. at what point it should be trigger in the event of near accident situation when audible warning has not been effective. Therefore the project will look for recommendations and strategies/scenarios but not aim at a real implementation. Since there are other projects running involving pedestrian detection and automated braking, eVADER will organise some joint workshop where the results can be shown and the participants will be able to cross-feed ideas and brainstorm on connecting the acoustic warning with the automated braking strategy. One of the already identified projects is AsPeCSS, co. no. 285106 under negotiation, for pedestrian protection. Communication with this project is guaranteed as IDIADA is also project coordinator.

3.1 Concept

The eVADER project will develop a methodology that will integrate acoustic and in-vehicle intelligent systems to generate an intelligent and targeted reaction of the electric vehicle in any situation with an imminent risk of a vulnerable road user crash.

eVADER will provide innovative approaches and technologies to improve safety in urban and inter-urban environments by identifying close-to-accident patterns that will activate an ‘intelligent and customized’ acoustic warning signal to warn pedestrians in general and specially vulnerable road users such as VI people, cyclists, the elderly and children, thus reducing EV-pedestrian crashes. This will be achieved guaranteeing the best compromise between safety and minimum acoustic intrusion in the environment in order to minimize the negative effect on the quietness of residential and urban areas.

3.2 Project Objectives

It is known that to facilitate wide spread customer acceptance and use of fully electric vehicles (FEV) a series of potentially critical safety issues specifically need to be addressed. Some of these issues are related to the consequences of electrification with respect to the safety requirements (high voltages, hazardous substances, etc). Another important issue is the absence of engine noise in these types of vehicles which will require an in-depth assessment regarding interior and exterior acoustic characteristics of these types of vehicles during normal operation.

We have to emphasize that the main limitations of the current Vehicle Sound Pedestrian (VSP) [7] are associated to their acoustic omni-directionality and lack of integration of currently available intelligent vehicle active systems. These first generation systems are normally activated at low vehicle speeds producing an exterior sound which is independent on other environmental conditions such as the position of the pedestrian, the background noise and other inputs that might affect safety.

The main objectives of eVADER are:

- (1) to investigate the acoustic perception of FEV which require solutions to warn vulnerable road users of the presence of nearby moving vehicles. and
- (2) integrate those findings with providing solutions for improving the awareness of drivers in critical situations. eVADER solutions will also integrate existing pedestrian protection systems, such as ADAS, and other in-vehicle intelligent systems with the acoustic warning system. This will require the investigation of different technologies and solutions to explore different levels of effectiveness and acceptability feasible with FEV.

Thus, this project will provide innovative approaches and technologies to improve safety in urban and inter-urban environments by identifying close-to-accident patterns that will activate an ‘intelligent and customized’ acoustic warning signal to warn pedestrians in general and specially vulnerable road users such as VI people, cyclists, the elderly and children, thus reducing EV-pedestrian crashes. This objective must be achieved guaranteeing the best compromise between safety and minimum acoustic intrusion in the environment in order to minimize the negative effect on the quietness of residential and urban areas.

3.3 eVADER Key Innovations Will Be

- To develop a comprehensive knowledge of sound criteria and exterior noise of EV with especial emphasis on driver’s feedback and pedestrian safety.
- To achieve a high level of pedestrian safety in terms of the additional risk associated to the low exterior noise of EV.
- Integration in-vehicle intelligent systems safe in terms of the additional risk associated to the low exterior noise of EV.
- Integration of in-vehicle intelligent systems data with warning signals generation algorithms for close-to-accident pedestrian safety.

3.4 eVADER Technical Objectives

The following specific technical developments shall be covered in order to carry out the project objectives define above.

- (1) Develop an in-depth understanding of the perceptibility of EV by VRU and the effects of urban background effects and other psychological aspects affecting acoustic awareness.
- (2) Reliable identification of vulnerable road users and the integration of the identification systems with current driver assistance systems.
- (3) Acoustic radiators with high directivity and orientability to point at a point or small volume in space around the close-to-accident pedestrian.
- (4) Integration of the acoustic warning system with in-vehicle intelligent systems data such as external microphones, vehicle speed (CAN data) or ADAS system.
- (5) Adaptation to urban background noise.
- (6) An experimental/demonstration vehicle will be equipped with those systems that will foreshadow the *second generation VSP*. We have to emphasize that the main limitations of the current VSP are associated to their acoustic omnidirectionality and lack of integration of currently available intelligent vehicle active systems. These first generation systems are normally activated at low

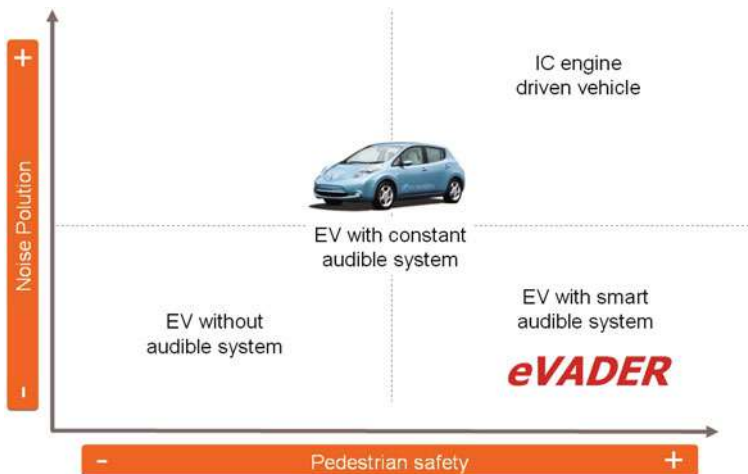


Fig. 1 The objective of eVADER in the noise pollution—pedestrian safety compromise

vehicle speeds producing an exterior sound which is independent on other environmental conditions such as the position of the pedestrian, the background noise and other inputs that might affect safety.

Figure 1 shows the positioning of the second generation VSP system developed in eVADER with respect to the VSP currently used in EV. Note that the second generation VSP systems will achieve a better compromise between noise pollution and pedestrian safety than current systems implemented in EV.

Figure 2 shows the fundamentals ideas and system integration involved in this proposal, maintaining the quietness of residents. The concept depicted in this figure should be valid for forward as well as for backwards manoeuvres.

4 Relevant Topics Addressed by the Proposal

This project is conceived under the requirements presented inside the Work Programme FP7-SST-2011-RTD-1 and aims at answering the call topic *GC.SST.2011.7-1. Specific safety issues of electric vehicles*.

This part of the program defines the baseline regarding where does the project work start (Table 1).

The key objective of the eVADER project is to provide next generation scientific and technological solutions for the detectability of electric (and other low-noise) vehicles, with the aim to improve the road safety of VRU by minimizing close-to-accident risks. The envisaged approach is to realise this through creating an intelligent, selective and targeted acoustic environment, maximizing safety and minimizing noise annoyance. This objective fully answers the priority topic of the

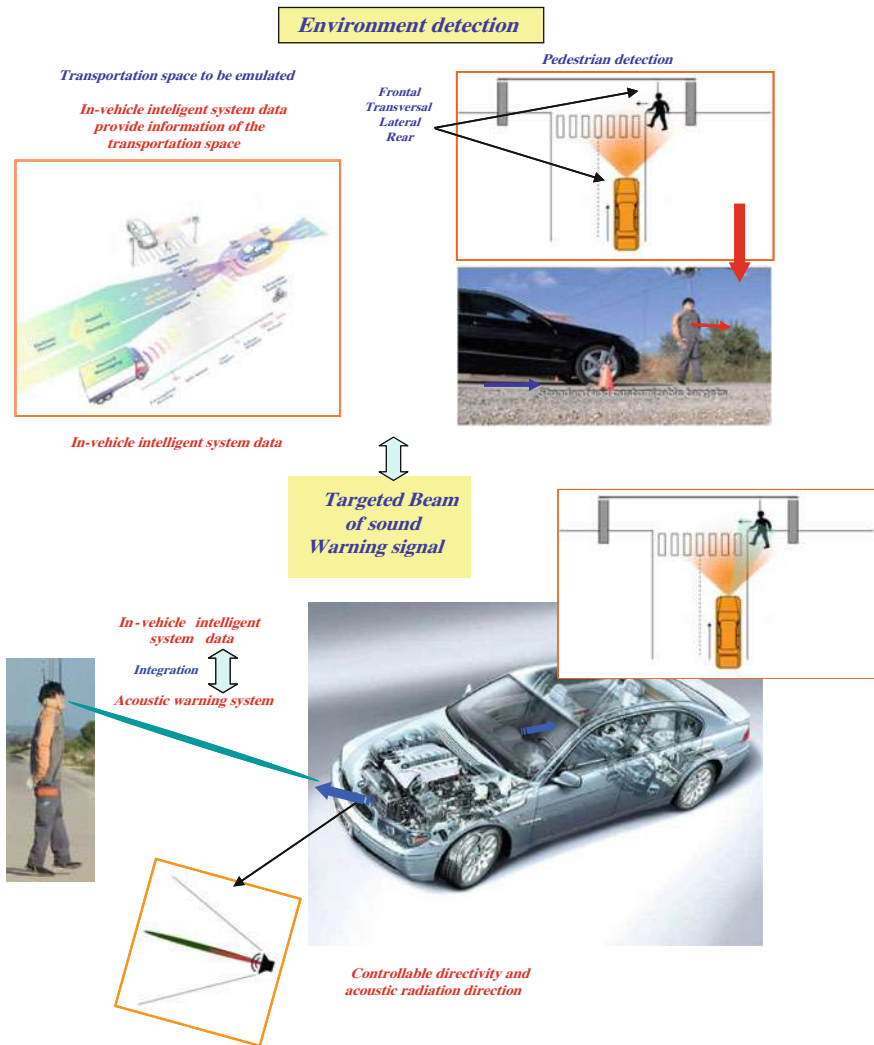


Fig. 2 Concept implementation scheme (equivalent for forward and backwards vehicle manoeuvres)

call GC.SST.2011.7-1: “The second subtopic should produce systems and technologies capable of giving effective warning to vulnerable users at a sufficient distance while maintaining the advantages of electric technologies in terms of improving the current road noise environment”.

Table 2 summarises the answers of eVADER to the call as stated in the work programme and, therefore, constitutes the baseline against which the project will measure its progress and the results the project aims to achieve.

Table 1 Work programme extract

GC.SST.2011.7-1. Specific safety issues of electric vehicles

To facilitate widespread customer acceptance and use of Fully Electric Vehicles (FEVs), a series of potentially-critical safety issues specifically need to be addressed. Therefore, analysis of the consequences of electrification with respect to safety requirements has to be made. In particular, the presence of high voltages and potentially hazardous chemicals necessitate the definition of specific design, usage and rescue guidelines, *while the absence of engine noise requires in-depth assessment regarding interior and exterior acoustic characteristics during normal operation*

Activities will focus on

- (a) Safe handling, rescue and maintenance including solutions to ensure safe plug-in/recharging during normal operation, prevention of misuse/abuse, and protection against fire and electric shocks during maintenance and repair or in the event of a crash including rescue and towing operations in the post crash phase
- (b) *Acoustic perception of the FEV, requiring solutions to warn vulnerable road users of the presence of a nearby moving vehicle while providing a means for heightening the awareness of drivers in critical situations. Including the application/adaptation of existing pedestrian protection systems (active safety) to the raised needs*

Different technologies and solutions shall be explored and assessed also from the perspective of overall effectiveness and acceptability, the objective being to develop FEVs which are optimised in terms of both, energy efficiency and safety, a fundamental requirement to enable FEVs to become mass products in the future

Innovative EV specific safety technologies and solutions should *eliminate the risk that these new vehicles be perceived as less safe than their current equivalents*, thus the safety and energy efficiency of EV use should contribute to more customer acceptance of EVs

Given the specificity of these subtopics, small, focused projects are encouraged in particular. The work should be complementary to the objective GC-ICT-2011.6.8 ‘ICT for fully electric vehicles’

Expected impact

The expected impact of the first subtopic should be technologies and procedures that avoid additional casualties to the current level due to electrocution risks. The second subtopic should *produce systems and technologies capable of giving effective warning to vulnerable users at a sufficient distance while maintaining the advantages of electric technologies in terms of improving the current road noise environment*

The criteria and performance or research indicators will be based on the achievement of the following objectives:

- (1) To develop an in-depth understanding of the perceptibility of EV by VRU and the effects of urban background effects and other psychological aspects affecting acoustic awareness.
- (2) Reliable identification of vulnerable road users and the integration of the identification systems with current driver assistance systems.
- (3) Acoustic radiators with high directivity and orientability to point at a point or small volume in space around the close-to-accident pedestrian.
- (4) Integration of the acoustic warning system with in-vehicle intelligent systems data such as external microphones, vehicle speed (CAN data) or ADAS system.

Table 2 Answers to the call text

Call expectations	eVADER answers
To facilitate widespread customer acceptance and use of Fully Electric Vehicles (FEVs), a series of potentially-critical safety issues specifically need to be addressed. Therefore, analysis of the consequences of electrification with respect to safety requirements has to be made. In particular, <i>the absence of engine noise requires in-depth assessment regarding interior and exterior acoustic characteristics during normal operation</i>	eVADER focuses on acoustics perception of the FEV. eVADER system is an intelligent safety system that helps the driver and vulnerable road user, vulnerable road users (mainly VI people, the elderly and children) to avoid accidents
Activities will focus on: (b) Acoustic perception of the FEV, requiring solutions to warn vulnerable road users of the presence of a nearby moving vehicle while providing a means for heightening the awareness of drivers in critical situations. Including the application/adaptation of existing pedestrian protection systems (active safety) to the raised needs	eVADER will investigate the psychoacoustic principles that determine and optimise the acoustic perception of warning signals produced by FEV. This will be applicable to both VRU and drivers. The optimum warning signals will be then produced and managed an intelligent algorithm that will use environmental information to decide when and how the warning signal must be produced. The combination of acoustic and visual warnings will be explored to understand their interactions
FEVs which are <i>optimised in terms of... safety</i> ... to enable FEVs to become mass products in the future ... <i>eliminate the risk that these new vehicles be perceived as less safe than their current equivalents...</i>	eVADER will allow FEV to combine all the advantages inherent to electrification with a high level of pedestrian safety specially optimised for vulnerable road users eVADER solutions will provide drivers and pedestrian with smart information about their close-to-accident scenario assisting in the decision about the correct action to be taken while limiting acoustic intrusion in the environment
... should contribute to more customer acceptance of EVs	Customers will be able to assess that the integration of eVADER technological results in EV will make them safer and comparable to ICE driven vehicles. Drivers off FEV will not suffer any additional stress associated to their vehicles not being perceived by vulnerable road users
The work should be complementary to the objective GC-ICT-2011.6.8 'ICT for fully electric vehicles'	eVADER is in alignment with GC-ICT-2011.6.8 'ICT for fully electric vehicles' in the target concerning Functional Safety in which it is stated that " <i>Research will also address adaptation and improvement of in-vehicle active safety for FEVs, integrated driver-vehicle—infrastructure safety, protection of vulnerable road users</i>

- (5) Adaptation to urban background noise.
- (6) An experimental/demonstration vehicle will be equipped with those systems that will foreshadow the second generation VSP. We have to emphasize that the main limitations of the current VSP are associated to their acoustic omnidirectionality and lack of integration of currently available intelligent vehicle active systems. These first generation systems are normally activated at low vehicle speeds producing an exterior sound which is independent on other environmental conditions such as the position of the pedestrian, the background noise and other inputs that might affect safety.

This criteria and performance indicator of the above objectives will be based on and measured by means of:

- (1) Patents granted
- (2) Technical and scientific publications
- (3) Qualitative assessment based on peer review
- (4) Experimental tests that prove that the improvement has been achieved (objective and subjective tests)
- (5) Implementation of the new acoustic warning systems in a test vehicle and experimental validation (objective and subjective assessment of the results achieved).

5 Contribution of the Project in Objective GC.SST.2011.7-1

The key objective of the eVADER project is to provide next generation scientific and technological solutions for the detectability of electric (and other low-noise) vehicles, with the aim to improve the road safety of VRU by minimizing close-to-accident risks. The envisaged approach is to realize this through creating an intelligent, selective and targeted acoustic environment, maximizing safety and minimizing noise annoyance. This objective fully answers the priority topic of the call GC.SST.2011.7-1: “The second subtopic should produce systems and technologies capable of giving effective warning to vulnerable users at a sufficient distance while maintaining the advantages of electric technologies in terms of improving the current road noise environment”.

References

1. Yoshinaga H, Namikawa Y (2009) Predicting noise reduction by electrification of automobiles, InterNoise09
2. Are hybrid cars too quiet to be safe for pedestrians? Scientific American; hybrid cars are harder to hear. University of California, Riverside, 28 Apr 2008
3. Nuckols B (2007-10-03). Blind people: hybrid cars pose hazard. USA Today
4. Electric cars and noise: the sound of silence. The Economist, 7 May 2009

5. Kerber S, Fastl H (2009) Prediction of perceptibility of vehicle exterior noise in background noise, Sarah Simpson (August 2009)
6. Incidence of pedestrian and bicyclist crashes by hybrid electric passenger vehicles. National Highway Traffic Safety Administration. Sept 2009
7. Tabata T, Konet H, Kanuda T (2010) Development of Nissan approaching vehicle sound for pedestrians. In: The 25th world battery, hybrid and fuel cell electric vehicle symposium and exhibition, EVS-25 Shenzhen, China, 5–9 Nov 2010

On-Demand Driver Vigilance Enhancement Without Drowsiness Detection

Shane Chang

Abstract When drowsiness detection is unreliable or absent, conventional on-demand driver vigilance enhancement approaches become ineffective. We propose a new, detector-free method to provide an alert signal to a driver in this case. Its unique triggering mechanism is based upon our hypothesis that as one becomes sleepy, his pain threshold lowers and an otherwise below-threshold stimulation becomes painful. We use the pain illusion phenomenon to construct a user-tailored innocuous thermal alert signal, to be triggered only by a host's own declining vigilance state, to produce a noxious response. This response will serve to arrest and eventually raise the host's arousal, when noxious sensation would disappear completely, automatically. In this paper, we present the design rationale, prototype instrumentation and preliminary findings from testing this hypothesis.

Keywords Vigilance • Arousal • Pain illusion • Driver safety

1 Introduction

It is well known that sleep debt and circadian rhythm collectively impact a person's arousal state, or vigilance, continuously [1, 2]. In the driving context, vigilance is defined as a composite of visual perception, decision-making and subsequent motor control in response to a specific stimulus. As such it has a

F2012-F07-003

S. Chang (✉)
Honda Research Institute, California, CA, USA

response-time dimension and an orthogonal error axis. During the wake period it follows a rhythmic rise to peak at about 2 ~ 3 h after waking up, a trough after lunch, to be followed by another peak after dinner, then a nadir post sleep onset. Actual measurements have validated the rhythmicity in this vigilance model [3–5].

For moving vehicle control it is critical to know when a driver's vigilance is on the decline. This real-time requirement calls for detecting minute changes in vigilance constantly. Technologies in use typically rely on detection of certain marker events either directly from the driver or from theoretically corresponding behavior changes such as steering control relative to roadways. Direct methods rely on sensing, for instance, of pupil diameter change patterns, eyelid closure interval or blink rate, all of which purportedly reveal a person's internal state concerning arousal and attention [6]. In the pupil diameter case, when a certain high frequency change is detected, it is deemed that the driver is at the subtle onset of a particularly acute drowsy period, when interventions can be deployed most effectively [7]. Collectively all existing measurement techniques depend on data statistics to overcome inter-subject variability. A personalized contiguous vigilance sensor with fine resolution and high specificity remains illusive.

Once a major drowsy episode (most beneficially at its onset) is detected, tools for intervention are called upon to inject stimulus into the environment to draw the subject's attention, hopefully resulting in raised arousal and consequently elevated vigilance. Their mileage vary, however. An audio warning signal may be drown out immediately by environmental sounds, and a vibro-tactile style stimulus may be ignored after repeated use, or be confused with a vehicle's behavior on a rough road or tire malfunction. More importantly our body's adaptive mechanisms may further erode the effectiveness of such external intervention. To be functional, an injected stimulus has to remain novel in order to leverage brain's attentional mechanisms for enhancing vigilance [8, 9]. There lies the efficacy question: what's novel to one person may not be novel to another; in one situation a novel stimulus may become part of a background noise in another; and what's novel at the moment may not be so moments later. The novelty aspect of any external stimulus faces even more challenges in today's environment, where we are submerged in constant stimulation. It is difficult to design a unique signal that stands out in all settings.

In contrast, our body places very high priority to endogenously generated signals. One of such high-priority attention-grabber is pain. At the onset of an acute pain experience, for instance, we respond rapidly amidst all other activities to deal with it immediately. As a result, our arousal level would usually be elevated following the stimulation, if we were in a resting state. If the onset appeared while we were busy with a collection of activities, our attention would be reset afterwards with our priorities sorted again, bringing our mind back to the proper task on hand, such as controlling the vehicle in motion.

In this paper, we present the design and initial test of a unique technique, using a novel pain proxy as a driver vigilance enhancement agent. The construction of the agent with persistent high saliency, its delivery trigger and related background will be detailed in the next section. In the experiments section we illustrate

methods for testing the efficacy of this new technique. We present initial findings from our experiments and preliminary analysis of confounding issues in the results and discussion section. On-going activities and future prospects of this approach conclude this paper.

2 Background

The theory of pain as a sensation started in the ancient times. Initially encapsulating spiritual qualities, scholastic work evolved it from being philosophical to metaphysical to mechanical, reaching a perception model of the nervous system over many hundreds of years.

Modern medicine brought new understanding to the pain pathways and their mediating mechanisms. Research results from biology, neurophysiology and anesthesiology all point to the fact that the two types of pain perceptions, acute and chronic, possess their own control hierarchies. Reactions to pain experiences are governed further by an emotional dimension, and vary greatly from person to person, depending on age, gender, genetic makeup, stress profile, and many other factors. At molecular and cellular levels, high-threshold nociceptors are activated by intense mechanical, thermal, or chemical stimuli and feed this information to nociceptive neurons in the spinal cord, which project via the thalamus to the insula region and other cortical areas generating the sensory and emotional qualities of pain for the whole subject person. Simultaneously these spinal cord pathways are subject to descending inhibitory and facilitatory influences from the brainstem [10]. Functional imaging research suggests that the insula is involved in two types of salience: an interoceptive information processing hub that links interoception with emotional salience to generate a subjective representation of the body (this involves the anterior insular cortex with the pregenual anterior cingulate cortex and the anterior and posterior mid-cingulate cortices); and a general salience system concerned with environmental monitoring, response selection, and skeletomotor body orientation that involves all of the insular cortex and the mid-cingulate cortex [11].

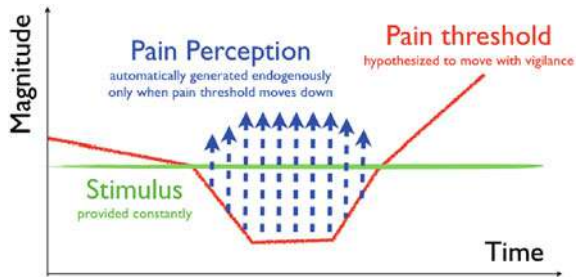
Normally, activity in low-threshold afferents is carried by independent peripheral and central pathways and only generates innocuous sensations without emotion, through the same central switching regulator in the insula. The right anterior insula regulates the interaction between the salience of the selective attention created to achieve a task (the dorsal attention system) and the salience of arousal created to keep focused upon the relevant part of the environment (ventral attention system). This regulation of salience is critical during challenging tasks where attention might fatigue to result in careless mistakes. On the other hand, if there is too much arousal, anxiety will diminish performance [12].

Innocuous sensations, such as a thermal sensation generated from touching a table surface, hence suffer the fate of being filtered out in a busy environment when many dissimilar stimuli are present. Noxious signals, from touching a hot

stove top, on the other hand travels more directly to the insula where proper dispatch takes place to engage relevant brain regions responsible for the generation of avoidance behaviors to move the hand immediately. There is a continuum between innocuous and noxious for a sensation type. For example, at 37 °C an object would feel warm to a hand. As it heats up beyond 42 °C, a threshold that triggers the release of a different set of neural transmitters to activate their corresponding receptors, it becomes noxious (heat pain), commanding more of our attention [13]. If this warning is ignored arousal will further go up and anxiety may set in, before tissue damage ensue. Similarly a decreasing temperature initially at 22 °C will be cool to the touch; after dropping below a certain point it will produce a noxious sensation (cold pain) to initiate another behavior in order to avoid tissue injury.

Pain, a noxious experience, is perceived through a two-step mechanism: first a threshold for the brain to take notice of its presence, and then a higher threshold called tolerance for the body to initiate last minute reactive behavior. Studies in pain medicine have shown that pain threshold is different from pain tolerance. More specifically, there is no strict correlation between pain tolerance and pain threshold, and pain tolerance is more closely related to clinical pain than is the pain threshold and no significant difference between individuals was found for pain threshold [14]. Recent literature reports sleep deprivation produces hyperalgesic changes in pain tolerance in healthy subjects [15]. Hypersensitivity is a pathological condition in which an innocuous stimulus is perceived noxiously. Opioidergic and serotonergic processes as mediating mechanisms of these hyperalgesic changes have been studied to show clear correlation between accumulation of sleep debt, reduced pain threshold and amplified perception [16]. It is postulated in recent research from anesthesiology that neuronal networks evolved to regulate naturally occurring sleep preferentially modulate traits that define states of sedation and anesthesia. Collectively different neural transmitters in various brain regions orchestrate to give arousal and the pain center plays a key role in keeping everything in balance [17].

Inspired by these related discoveries in neuroscience, sleep and pain medicine and motivated by the desire to address shortcomings in drowsiness detection, we present a new approach to driver vigilance enhancement. We hypothesize that as a subject's sleep debt accrue over a day, the accumulating stress would lower the pain threshold. As a result, an otherwise innocuous signal would produce a noxious response, subjectively, calling for more attention from the host when presented. Compared with other non-noxious stimulation, it would greatly increase arousal level, in the driving case, to enhance vigilance in the driver. Moreover, as the driver's pain threshold moves back up again, the sensation would become an innocuous one, in the presence of the same signal. This process framework is illustrated in Fig. 1. The challenges for testing this hypothesis mainly lie in two fronts: the construction of a personalizable innocuous stimulus that activates noxious signal response, and the development of associated triggering mechanism that does not rely on external sensing of a person's vigilance level. In the following

Fig. 1 The framework

section we outline the design of the signal, its triggering mechanism, and the experimental setup to test their effectiveness.

3 Experimental Design

3.1 Inocuous Pain Sensation

Thermal pain is clearly an easy signal to generate. In fact it is a standard tool in pain research to trigger pain responses in patients for identification and treatment of diseases.

To avoid inflicting real pain and its associated consequences, we employ a variant construct called the thermal pain illusion, where a spatially interlaced simultaneous presentation of innocuously warm and cool signals elicits pain response (the interlaced bars of alternating colors in Fig. 2b illustrate a typical arrangement). This phenomenon was first confirmed by Thunberg over a 100 years ago [18] with its underlying mechanisms closely scrutinized only recently [19]. Experiments show that by spatially arranging the placement of interlaced contact areas and changing temperature profiles in the two channels one can produce in a subject a range of sensations from the thermal neutral to warm to cold to thermal pain [20–22], at times engaging distinct regions of the brain for pain processing, even when in fact all individual temperature settings remain exclusively inside a thermally innocuous range [23–25].

It is this elicited strong response (thermal grill illusion, or TGI) through the pain pathways and their regulating mechanisms, without actually having the associated tissue damage an equivalent thermal pain signal would trigger, that we seek to implement in our framework. We call the stimulus-generating instrument the Thunberg Thermal Grill (or TTG). In the remain part of this paper, we assume the driver will be holding on to a unique steering wheel constantly, with even pressure, and the TTG signals are given on concentric, interlaced rings of cold/warm channels, as illustrated in Fig. 2a. Each ring is made of copper tubing with an outside diameter of 5, with 2 mm thermal insulation on both sides. The pictured prototype has 16 rings, each of which is supplied by one of the two temperature

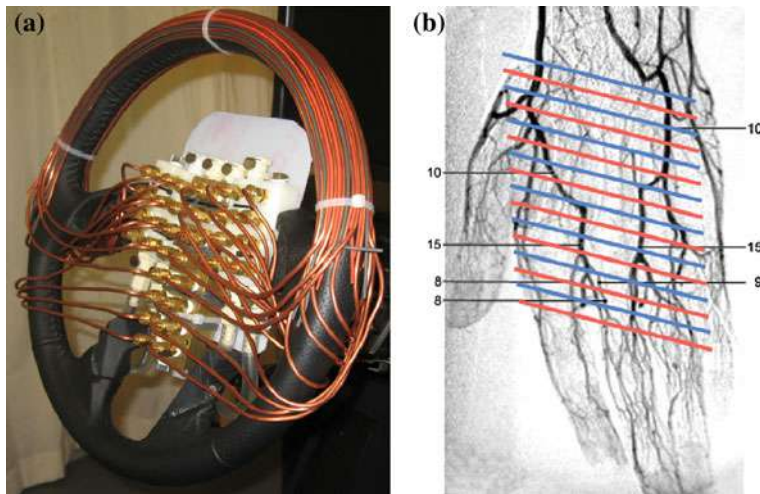


Fig. 2 Prototype TTG steering wheel (a) and hand position relative to the thermal grill layout (b). The red colored bars indicate warm channels, and blue cold ones

controlled water circulators. Thermocouples are used to measure the actual temperature test subjects come in contact with directly.

3.2 Tgi Triggering Mechanism and Pain-Threshold Detection Protocols

As is shown in Fig. 1 the pain-threshold controls the trigger. Using our hypothesis, we postulate that in the constant presence of a just-below-threshold, pre-determined TTG configuration (green colored stimulus) a subject will have two distinct perceptions, with one being painful, or TGI (upward blue dotted arrows), when the pain threshold falls down below the stimulus, and the other being just thermal, innocuous when the pain threshold is above it.

Following a temperature profile, a continuous varying set of stimuli is presented to a subject. To determine each person's pain threshold, we instruct a person to hold onto the TTG wheel, and upon perceiving TGI to press a button. The channel temperature combination is then recorded in a matrix along with the temperature gap between the TTG wheel channels as a marker.

In this paper we present three temperature profile protocols, as illustrated in Figure 3, with both channels starting at the same temperature. In protocol A, one channel is held at its initial setting of 40, while the other channel gradually cools to 20 °C. In B, one channel is held at its initial setting of 20, while the other channel heats to 40 °C. In C, both channels start at 33, with one heating to 40, while the other cooling down to 20 °C in synchrony. Throughout our tests, lab ambient

temperature was kept at 23 ± 1 °C and subject wore normal office clothing. Each subject is to be tested twice in the same day, one at 10, and the other at 1:00 am to capture pain threshold settings at the theoretical peak and nadir of vigilance. Repeated tests are spaced sufficiently apart to avoid accumulating sleep restriction effects. Subjects were asked to refrain from caffeine intake during test days.

4 Results and Discussions

As illustrated in Fig. 3 (bottom row), the temperature gap increases over time. In protocol A, subject initially experienced a warm steering wheel, followed by a short period when strong cold sensation would emerge, before detecting TGI. In protocol B, initial experience was predominantly cold at 20 (relative to subject's hands at 32 °C), with it slowly receding to produce a warm sensation before perceiving TGI. Protocol C has a more subtle transition as it starts near 32 °C, the hand's temperature.

A common observation was as soon as the gap exceeded 16 °C, subjects started to report TGI superimposed by either cold or hot sensation. While the TGI onset is rather subtle, at the end of each protocol, when the temperatures in the TTG wheel reached 20 and 40 °C respectively, pain illusion was strong and persistent. So clear so that in certain instances it grabbed some subjects attention back from watching a movie, presumably upon noticing the pain illusion saliency. It is suspected that for these subjects the settings of the TTG wheel at that time may have reached pain tolerance levels, far surpassing their pain thresholds.

Inter-subject variability was immediately apparent, in distinguishing temperature settings that trigger warm-to-hot sensations (before heat pain), TGI and pain illusion. They vary for the same subject as well. For example, after reaching TGI and pain illusion clearly at marker 20/40 °C, when we reversed the temperature profile, the “exit” marker at which TGI would vanish at different temperature settings from its corresponding “entry” marker. Such confounds refocused our attention on the design of the experiments, including protocols and instrumentation.

The first confound has to do with the requirement that subject's hands are to hold on to the TTG wheel at the two and ten o'clock positions constantly during a test. This requirement turns out to be hard to enforce in a driving simulator setting when hands move relative to the steering wheel as one drives. The resulting variable mechanosensory input from this type of hand motion generated sufficiently high amplitude activation signals to mask the more subtle, slowly appearing TGI beyond the pain threshold in question. In addition to distorting thermal sensation prior to TGI onset, the tactile input from the TTG wheel created various distractions to subjects that prevented them from noting subtle onset of pain thresholds while the temperatures continued to change. Taking a lesson from pain medicine research, where a thermode is affixed to a subject's skin surface with tape to ensure constant contact pressure, and taking into account of latest

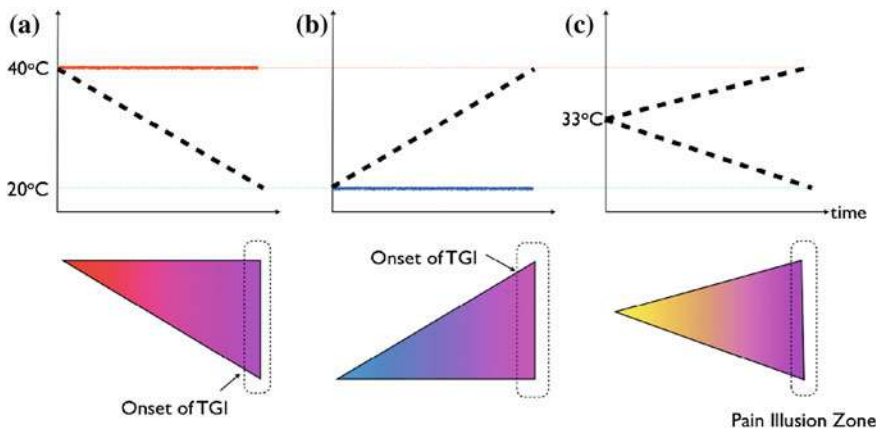


Fig. 3 Three protocols (top row) and three sensation profiles (bottom row), by approaching pain illusion from thermally. **a** The warm side, **b** The cold side, **c** The neutral side. Solid dash lines show changing temperature. Total experiment time is 30 min

research reports on reference values of mechanical and thermal pain from a pain-free population [26] we will modify our test protocol in the future to address this confound.

Another confound has to do with thermal energy transfer between the TTG wheel and the hands in contact. Over the test period, a ± 3 °C change in palm temperature was observed, effectively changing the designed approaching angle to a pain threshold in three different protocols.

In A, hands tend to be warmer before having pain illusion, with a larger marker temperature gap than in B, which tended to have an earlier onset. This could be due to cutaneous warming effect on vigilance, as it was observed to promote sleep onset with sufficient thermal energy transfer [27]. We further postulate that thermal impact on peripheral nociceptors was creating a subtle movement in pain threshold, similar to that when heat injury occurs pain threshold moves down immediately to amplify pain sensation. Our situation is more complex in that the constantly changing holding pressure from the hands distorts thermal inputs to the insula, creating a traffic jam there, making unwanted engagement of other somatosensory pathways.

To completely remedy the above situation we plan to develop a new protocol to employ discrete, rapid on/off delivery of thermal pulses for much shorter intervals, spaced with resting period to minimize thermal transfer effects. In addition to being able to compare with brain activation mapping results from functional MRI studies of noxious and thermal stimulation [25] the new protocols will have the advantage for randomized delivery of pulses for control. A potential side effect in using pulsed stimulation is temporal summation in pain perception. High frequency, repeated application of short pain stimulus reduces sensation over time quickly [28] but over the long run produces hypersensitivity, particularly if the stimulus is of a noxious kind [29]. Although the individual TTG channel

temperature is innocuous, when combined to form an illusion of pain, it's not clear it will cause temporal summation-like adaptation. Adequate intervals between pulses may lessen this side effect by arresting unwanted drift in basal threshold.

Chronic short sleeping subjects may present a new set of challenges in our study. According to a recent review [30] chronic sleep restriction introduces a whole collection of maladaptive modification to our immune, endocrine, cardiovascular and pain algesia, masking the component of pain threshold movements that we hypothesize to be vigilance related. With listed ill effects including lapses of attention, slowed working memory, reduced cognitive throughput, depressed mood and preservation of thought, unscreened subjects bring to our test their own unique stressors. More specific sleep debt assay is needed to truly test for cause and effect between vigilance decline and lowered threshold in pain perception.

Subject screening will also help address the most complex issue we did not tackle thus far: pain phenotyping. Results from research show that there is a genetic link to pain sensitivity, even though currently studies focus on pain tolerance amplification, not pain threshold [31, 32]. Although it is not clear for pain illusion stimulation at this time, it is known that in certain subjects, experiencing centrally-induced pain will develop injury-like changes that is typical of nerve injury response. We understand that after nerve injury maladaptive changes can occur in injured sensory neurons and along the entire nociceptive pathway, which may lead to spontaneous pain or pain hypersensitivity. The resulting neuropathic pain syndromes present themselves as a complex combination of negative and positive symptoms that vary enormously from individual to individual. This variation depends on a diversity of underlying pathophysiological changes resulting from the convergence of etiological, genotypic, and environmental factors. We need to understand them completely in order to delineate potential side effects from applying TGI as vigilance enhancing agents.

Over all, we have a lot to do going forward, on the human body side as well as on the instrument side. Control protocols will also have to incorporate new features to handle temperature change rates, stimulation duration, baseline temperature effects among others.

5 Future Research

In the environment we live in today, our sensory load is full almost all the time causing frequent fatigue and vigilance decline. In this paper, we presented the construction of a unique, high saliency alert signal and the theory behind the development effort towards employing it to elevate a driver's arousal endogenously. Our autonomous triggering mechanism leverages the supposed interaction between drowsiness and pain threshold to eliminate the dependence on a dedicated drowsiness detector. In our research we identified multitude of confounding factors that require reexamination in our test protocol. By incorporating a randomized, pulsed delivery of low thermal energy stimuli, our future experiments are aimed at

teasing out the subtle movements in pain threshold first. Then by incorporating better understanding of the whole somatosensory regulation network we target to design an in-vehicle test over drowsiness inducing driving, to see if indeed a sub-threshold innocuous alert signal can trigger noxious response when a driver becomes drowsy. We remain hopeful that once tested, this framework of autonomously alerting drivers only when their body needs it can fundamentally reduce safety system complexity in future vehicles.

References

1. Borbély AA (1982) Two process model of sleep regulation. *Hum Neurobiol* 1(3):195–204
2. Van Dongen HPA, Dinges DF (2000) Circadian rhythms in fatigue, alertness and performance. In: Kryger MH, Roth T, Dement WC (eds.) *Principles and practice of sleep medicine*. WB Saunders Company, Philadelphia, pp 391–399
3. Carskadon MA et al (1986) Guidelines for the multiple sleep latency test (MSLT): a standard measure of sleepiness. *Sleep* 9(4):519–524
4. Dorrian J, Rogers NL, Dinges DF (2005) Psychomotor vigilance performance: neurocognitive assay sensitive to sleep loss, in scientificcommon,
5. Rajaraman S et al. (2012) A new metric for quantifying performance impairment on the psychomotor vigilance test, *J Sleep Res*
6. Abe T et al (2011) Detecting deteriorated vigilance using percentage of eyelid closure time during behavioral maintenance of wakefulness tests. *Int J Psychophysiol* 82(3):269–274
7. Shirakata T, Tanida K (2010) Detect the imperceptible drowsiness. *SAE Int J Passeng Cars-Electr Electr Syst* 3(1):98–108
8. McAlonan K et al (2006) Attentional modulation of thalamic reticular neurons. *J Neurosci* 26(16):4444–4450
9. Crick F (1984) Function of the thalamic reticular complex: the searchlight hypothesis. *PNAS* 81(14):4586–4590
10. Craig AD (2003) Pain mechanisms: labeled lines versus convergence in central processing. *Annu Rev Neurosci* 26:1–30
11. Taylor KS (2009) at al. Two systems of resting state connectivity between the insula and cingulate cortex. *Hum Brain Mapp* 30(9):2731–2745
12. Eckert MA et al (2009) At the heart of the ventral attention system: the right anterior insula. *Hum Brain Mapp* 30(8):2530–2541
13. Dhaka A et al (2006) TRP ion channels and temperature sensation. *Annu Rev Neurosci* 29:135–161
14. Gelfand S (1964) The relationship of experimental pain tolerance to pain threshold. *Can J Psychology/Revue Canadienne de Psychologie* 18(1):36–42
15. Onen HS et al (2001) The effects of total sleep deprivation, selective sleep interruption and sleep recovery on pain tolerance thresholds in healthy subjects. *J Sleep Res* 10(1):35–42
16. Kundermann B et al (2004) The effect of sleep deprivation on pain. *Pain Res Manag* 9(1):25–32
17. Lydic R, Baghdoyan HA (2005) Sleep, Anesthesiology, and the neurobiology of arousal state control. *Anesthesiology* 103:1268–1295
18. Thunberg T (1896) Förnimmelserne vid till samma ställe lokaliserad, samtidigt pågående kold-och värmereaktion. *Uppsala Läkfören Förh* 1:489–495
19. Craig AD, Bushnell MC (1994) The thermal grill illusion: unmasking the burn of cold pain. *Science* 265(5169):252–255
20. Green BG (2002) Synthetic heat at mild temperatures. *Somatosens Mot Res* 19(2):130–138

21. Bouhassira D et al (2005) Investigation of the paradoxical painful sensation ('illusion of pain') produced by a thermal grill. *Pain* 114:160–167
22. Li X et al (2009) The importance of stimulus parameters for the experience of the thermal grill illusion. *Neurophysiologie Clinique/Clinical Neurophysiol* 39:275–282
23. Peltz E et al (2011) Functional connectivity of the human insular cortex during noxious and innocuous thermal stimulation. *NeuroImage* 54:1324–1335
24. Lindstedt F et al (2011) Evidence for thalamic involvement in the thermal Grill Illusion: an fMRI study. *PLoS ONE* 6(11):e27075
25. Tseng MT et al (2010) Distinct and shared cerebral activations in processing innocuous versus noxious contact heat revealed by functional magnetic resonance imaging. *Hum Brain Mapp* 31:743–757
26. Neziri AY et al (2011) Reference values of mechanical and thermal pain tests in a pain-free population. *Eur J Pain* 15:376–383
27. Raymann RJE et al (2005) Cutaneous warming promotes sleep onset. *Am J Physiol Regul Integr Comp Physiol* 288:R1589–R1597
28. Vierck CJ et al (1997) Characteristics of temporal summation of second pain sensations elicited by brief contact of glabrous skin by a preheated thermode. *J Neurophysiol* 78:992–1002
29. Woolf CJ et al (2000) Neuronal plasticity: increasing the gain in pain. *Science* 288(5472):1765–1768
30. Banks S, Dinges DF (2007) Behavioral and physiological consequences of sleep restriction in humans. *J Clin Sleep Med* 3(5):519–528
31. Lindstedt F et al (2011) Perception of thermal pain and the thermal grill illusion is associated with polymorphisms in the serotonin transporter gene. *PLoS ONE* 6(3):e17752
32. von Hehn CA, Baron R, Woolf CJ (2012) Deconstructing the neuropathic pain phenotype to reveal neural mechanisms. *Neuron* 73(4):638–652

Pre-Crash Performance of Collision Mitigation and Avoidance Systems: Results from the Assess Project

**Andrés Aparicio, Sébastien Baurès, Jordi Bargalló,
Carmen Rodarius, John Vissers, Oliver Bartels, Patrick Seiniger,
Paul Lemmen, Thomas Unselt, Maminirina Ranovona,
Tatsuhiro Okawa and Swen Schaub**

Abstract Integrated vehicle safety systems that combine elements from primary and secondary safety have a high potential to improve vehicle safety, due to their ability to influence crash conditions and/or to adapt to these crash conditions. So far no standard evaluation procedures have been developed and implemented. The main goal of the ASSESS project is to develop harmonized and standardized assessment procedures for related collision mitigation and avoidance systems. Procedures are developed for: (1) Driver behavior evaluation (2) Pre-crash system performance evaluation (3) Crash performance evaluation (4) Socio-economic assessment. This paper presents the activities related to the “Pre-Crash evaluation”. The objective is to provide a tool box for the specific evaluation of the

F2012-F07-006

A. Aparicio (✉) · S. Baurès · J. Bargalló
Applus IDIADA Group, Santa Oliva, Spain

C. Rodarius · J. Vissers
TNO, Helmond, The Netherlands

O. Bartels · P. Seiniger
Bundesanstalt für Straßenwesen (BASt), Bergisch Gladbach, Germany

P. Lemmen
Humanetics Europe GmbH, Delft, The Netherlands

T. Unselt
Daimler AG, Stuttgart, Germany

M. Ranovona · T. Okawa
Toyota Motor Europe NV/SA, Brussels, Belgium

S. Schaub
TRW Automotive GmbH, Alfdorf, Germany

pre-crash performance of collision mitigation and avoidance systems and their contribution to the overall system performance.

Keywords Active safety • Autonomous emergency braking • Assessment

1 Introduction

In order to have a wide spread impact on safety, a test procedure for driving assistance systems has to be directly linked to the effectiveness of these systems. The paper describes how the complete test procedure has been developed, including the derivation of ‘Test scenarios’ from ‘Accident scenarios’, the development of a ‘Test target’ representing a full 3D vehicle suitable for ‘car to car’ testing and the definition of the most relevant ‘Key performance indicators’. Unlike other approaches, the ASSESS test procedures do not only test full autonomous braking but also incorporate driver reaction. Hence, also warning functions can be evaluated.

This test procedure was evaluated in three different test laboratories, each using a different methodology to move the so called target vehicle. Challenges faced in each test setup will be discussed. Besides the definition of the test procedure, an important result is also the definition of appropriate accuracies, needed to achieve a high reproducibility, repeatability and robustness.

2 Scenarios

Based on available accident data within the consortium (including GIDAS, STATS—19 and national data from different countries), four groups of accident scenarios and parameters have been identified:

- Rear-end collisions in longitudinal traffic
- Intersection with cross-traffic accidents
- Collisions with oncoming traffic
- Cut-in maneuvers in longitudinal and oncoming traffic.

All these accident scenarios have been prioritized and for the most relevant ones adequate test scenarios have been derived. However, intersections and oncoming traffic, as well as cut-in with oncoming traffic cannot be addressed by systems currently available in the market and/or to appear in the next years. For this reason, the actually executed test maneuvers were reduced to rear-end collisions in longitudinal traffic. A detailed description is given in [1–3] and [4].

It is important to distinguish accident scenarios and test scenarios. Accident scenarios describe those real life situations that are most relevant and typical real traffic accidents, while test scenarios name the abstract conversion of the accident scenarios into a standardized, repeatable, reproducible test laboratory situation. The final test scenarios are:

- Stationary Target Vehicle (TV, the test target) approached by the Subject Vehicle (SV, the vehicle under test) at constant speed (50 and 80 km/h).
- Slow TV (10 constant speed) approached by faster SV (50 km/h constant speed).
- TV and SV driving at constant speed (50 km/h, with initial heading distance of 14 m) and TV braking (with 4 and 7 m/s² deceleration).

The runs were carried out usually with an overlap of 100, but some of them were also performed with an overlap of 50 %. There were also scenarios defined with a TV driving at 20 and an approaching SV at 100 km/h. Since there is not enough data for statistical analysis, these scenarios are also not considered further here.

2.1 Test Method Requirements

The objective is to improve road safety. Therefore, the procedure must deliver results that match the behavior of the vehicle under test with the real world. The test method presented here is intended for both consumer tests (such as Euro NCAP), as well as for vehicle technical standards (such UN ECE). The primary goal is to be able to determine test results that are objective, reproducible and repeatable.

Moreover, there are other boundary conditions. For example, it is necessary to keep the test time and test costs under control. It also must be possible to test the behavior of the vehicle with a black box approach, without access to internal parameters or specifications of the manufacturer (although certain vehicles present some issues, as they need to be reset when the AEB is activated repeatedly). And finally, tests and results have to be transmitted to the consumers in a comprehensive but understandable way.

2.2 Consideration of Driver Behavior

In order to take into account the behavior of the driver during emergency braking, ASSESS implemented several activities for determining driver reaction time [5]. A sample of real drivers was requested to drive in rear-end accident scenarios in driving simulators in order to derive these parameters.

From these tests, a constant force rate of 300 N/s up to a maximum brake pedal force of 360 N was defined as average driver's action over the brake pedal and a driver's reaction time of 1.2 s to visual and/or audible warning. The transferability of these results to other vehicles cannot be guaranteed. However, the value of the reaction time is consistent with [6].

2.3 Braking and Warning Times

The mechanics of the braking process—particularly with regard to emergency braking systems—is derived from the report from Winner [7]. The common measurement for assessing the risk situation is the so called Time-to-collision (TTC). This is the time that would remain until the collision point, assuming a uniform motion of the SV and TV:

$$TTC = \frac{\text{relative distance}}{\text{relative speed}} \quad (1)$$

In order to better understand accident avoidance, several kinematics calculations can be implemented with this value. Some remarks follow.

- For an initial situation with full overlap of two vehicles and a vehicle width of 2 m in a imminent rear-end condition, the minimum escape time is approximately 0.6 s. The vehicle response delay can be considered by adding 0.1 s. These times are not reached by ordinary drivers in general. Winner [7] gives values of 1–1.6 s for normal evasive actions.
- Suitable warning times should then be placed so that the driver can still avoid the accident and that the warning is not triggered too early. It should be noted that (already relatively rare) false alerts, adversely affects the confidence of the driver into the system ([8], p. 7). A warning should be triggered so that the accident can be avoided with the usual response time and delay (1 s driver reaction + the time of the evasive maneuver).
- The appropriate time for an autonomous braking intervention can also be derived with similar concepts, but is much more limited by legal constraints (the Vienna Convention, product liability issues) and other associated technical difficulties (recognition reliability). For example, systems only initiate a full intervention when the accident is not avoidable [9].

2.4 Derivation of key performance indicators

The measurements during the tests are mainly accelerations, velocities and positions of the SV and TV. Additionally, the trigger time of additional safety feature, e.g. reversible belt pretensioners was recorded, see also [10]. For the evaluation of individual vehicles and the statistical analysis of reproducibility and repeatability of the test procedure, however, discrete parameters are required:

- The TTC value at the time of the first warning defines the warning behavior of the SV.
- The start of braking maneuver is represented by the TTC at the time when the SV exceeds the threshold of 0.1 m/s^2 .

- The speed reduction is the difference of the initial closing speed of the vehicles when TTC is 3 s and the closing speed at impact. Closing speed refers here to relative speed between SV and TV.

Based on these characteristics, a total of more than 300 experiments have been statistically analyzed to obtain a statement about the validity.

2.5 Validation Criteria

Realism of the test procedure

An autonomous braking intervention can be expected when the safety system detects with relatively high degree of certainty an unavoidable collision. For reasons of product safety and liability this requires a high level of confidence [11].

A warning to the driver will certainly require a lower confidence threshold, but for reasons of product acceptance, the vehicle manufacturer has an interest in keeping the number of false warnings as small as possible. Thus, timing for warning was selected as validation criterion for transferability of the results to reality.

Repeatability

Repeatability can be validated if results within a test house have a small scatter. For this, a classical mean analysis is not possible, since the real expected value is not known. The repeatability is therefore considered initially to be sufficient if the standard deviation is significantly smaller than 10 % of the mean value. A deeper analysis will be prepared by project partners at the end of the ASSESS project.

Reproducibility

As part of the ASSESS project, the defined test procedures have been implemented in three different test houses with very different test tools. If it is possible to show that the results (warning time points, braking points in time, speed reduction) between the three testing institutes are comparable, the reproducibility of the test method can be validated.

3 Test tools

3.1 Measurement and control

The test vehicles were equipped with different measurement equipment to accurately determine the position and velocity. These were differential GPS combined with inertial platforms (BAST, IDIADA) and high-precision in-door position sensor (TNO). When needed, data obtained in SV and TV could be synchronized by the use of GPS time signal.



Fig. 1 ASSESSOR target

Relative position of the vehicles (longitudinal and lateral) was controlled by human drivers (BASt), by robots (IDIADA) or by a guided system (TNO).

The contact between SV and TV (to determine impact point in time, if occurred) was determined by contact sensors (BASt, IDIADA) or direct position determination (TNO).

The detection of the acoustic warning signal was done with microphones and frequency filters. These allowed the real-time detection of the warning and the triggering of the driver reaction.

The driver reaction (1.2 s after the driver warning) was applied in all test houses with a brake robot which actuated over the brake pedal.

3.2 Test Targets

ASSESSOR test target

The test target developed within the ASSESS project is the ASSESSOR [12]. It has an internal radar reflector made of metallic foil and its radar-reflecting characteristics represent a typical compact car [1] (Fig. 1).

This target object is able to withstand impacts up to 80 km/h—depending on the mass of the propulsion system—with good levels of crash forgivingness.

ADAC test target

The ADAC-target is optimized for good detectability and is commercially available. In combination with the ADAC propulsion system, it is able to withstand impacts up to 50 km/h relative speeds, without any significant damage to the SV (see Fig. 5).

Reference vehicle

In order to validate the test targets, a VW Passat (model year 2011) was used as a reference. Several approaching tests were executed. For safety reasons, the tests were terminated when the warning signal was issued. The validation process compared the warning times obtained with the different targets.



Fig. 2 BAST MARVIN kart with the ASSESSOR rear-end part

3.3 Propulsion Systems

Remote Kart System (BAST)

BAST has developed its own propulsion system for test targets. It is based in a kart concept and its name is MARVIN (Motorized Autonomous Research Vehicle for INnovations). Top speed is over 80 km/h, with a maximum deceleration of 7 m/s^2 . The total mass is 250 kg including the test target (ASSESSOR). The speed of the kart is controlled by a closed-loop controller on-board and braking and steering by a remote control commanded by an operator outside the vehicle. During the tests, the system withstood impacts up to 50 km/h without significant damage to the SV. A detailed description is given in ([13] and [14]) (Fig. 2).

The tests implemented for this analysis were done in the proving grounds of the RWTH Aachen in Aldenhoven and in an air base rented by BASt. The controllability of the system is 0.5 km/h and $\pm 30 \text{ cm}$ in position.

Rabbit vehicle (IDIADA)

IDIADA used a rabbit vehicle concept, which consists of a car carrying a test target held from a crane. IDIADA used the full ASSESSOR. This is mounted on a trolley, which is initially connected with an electromagnet to a crane. In case of collision, the solenoid and the whole target are released. The trolley is shielded with radar absorbing material, in order to do not interfere with the radar system of the SV. In both vehicles, a complete set of driving robots are used to precisely control the trajectories and relative positions of both vehicles. The running speed of the rabbit vehicle can be specified very precisely. A lateral offset of a few centimeters can be achieved (Fig. 3).

VeHIL (TNO)

The test laboratory VeHIL (Vehicle Hardware in the Loop) consists of a chassis dynamometer where the SV is mounted and a support system (trolley) on which the TV is mounted (rail guided or robotic vehicles). VehIL works with the



Fig. 3 IDIADA rabbit vehicle

principle of relative motions, which means that instead of having both, SV and TV moving, the SV is stationary, although driving on the chassis dynamometer, and the TV moves relatively towards the SV. The dynamometer is adjustable so that the braking performance matches the vehicle's performance on real roads. The system is located in a hall with inside dimensions of 200×40 m. The speed of the test vehicle is processed real time by a simulation unit and translated to the real world situation. From there, this unit feeds back all necessary information to the pre-crash test system (PCTS) resulting in an adaptation of the TV's speed according to the actions taken by the car on the roller bench. As part of the ASSESS project the PCTS was implemented. This allowed tests with relative speeds up to 80 km/h and tests up to $TTC = 0$ s (Fig. 4).

Principal advantages of this test system are the high repeatability of the system, the independence to weather influences and the use of relative movements that allow also safe testing of high speeds. For high relative speeds, the system can be adjusted with dampers or crash tubes that absorb part of the impact, thus reducing the impact severity for SV and TV and allowing testing also at high relative speeds with only small risk of damage to the TV and SV.

Rail system (ADAC)

The motion system consists of a running trailer made up of rails. These rails carry a sled which holds the test target. When the target is impacted, it can slide over the rails. Static tests were always performed with the rail system, but without any towing vehicle (Fig. 5).

The ADAC test system can be moved with a maximum speed of 80 and a maximum impact speed of 50 km/h. The test system can be decelerated up to 6.5 m/s^2 . The speed of the towing vehicle can be adjusted by experienced drivers with 1 km/h accuracy. A lateral offset of approximately ± 30 cm is reached. The main limitation of this test setup is that it does not allow tests involving lane

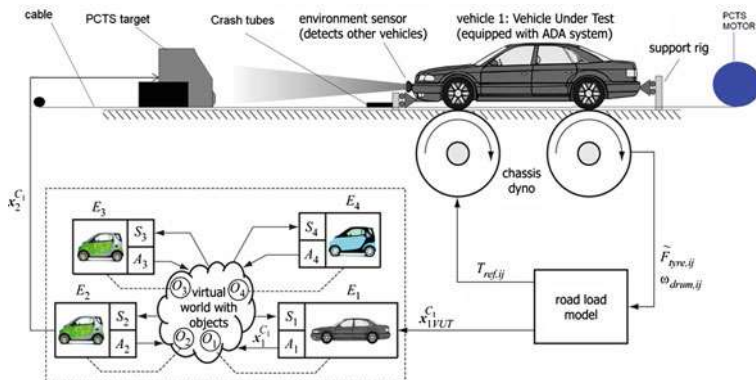


Fig. 4 VeHIL test bench

Fig. 5 ADAC rail system and test target (Source ADAC)



changes or with a certain overlap, because there could be an radar interference from the rail system.

3.4 Test Vehicles

Various SV were available to evaluate the proposed test procedures in the test labs. The two vehicles that were tested in all the test institutes use only radar sensors in various configurations. A detailed description of system properties is given in the next (Table 1).

An overview of the tested combinations (TV and SV) is presented in the next (Table 2).

Table 1 Properties of the tested vehicles

	A vehicle	Vehicle B
System	Radar-based system. Autonomous braking if a collision is unavoidable, brake assist different thresholds depending on the detected target object	
Warning	Optical and acoustic warning at $TTC = 2.6$ s	Visual and audible warning when $TTC 2\text{--}3$ s
Autonomous actions	If no reaction by the driver after a warning by the driver, two-stage automatic braking at $TTC = 1.6$ (partial braking), $TTC = 0.6$ s (full braking)	If no reaction by the driver, different levels of autonomous braking. Delays and thresholds unpublished.
Sensors	Short-range radar (0.2–30 m), medium-range radar (60 m), long-range radar (200 m), camera	Long-range radar (range >150 m)

4 Results

4.1 Overall Results

The following plot shows an example of the measurements obtained in several test runs (Fig. 6).

An overview of the results for selected scenarios is shown in the next table (full analysis in [14] (Table 3)).

4.2 Applicability to Reality

The considerations in [7] and in Sect. 2.5 can be further developed in order to define an optimum area of feasibility where a warning can lead to avoidance of the accident (either by evasion or braking action initiated by the driver). This area is marked in green in the graph below. Additionally, the measurement results of warning times (TTC) are plotted as function of differential speed (Fig. 7).

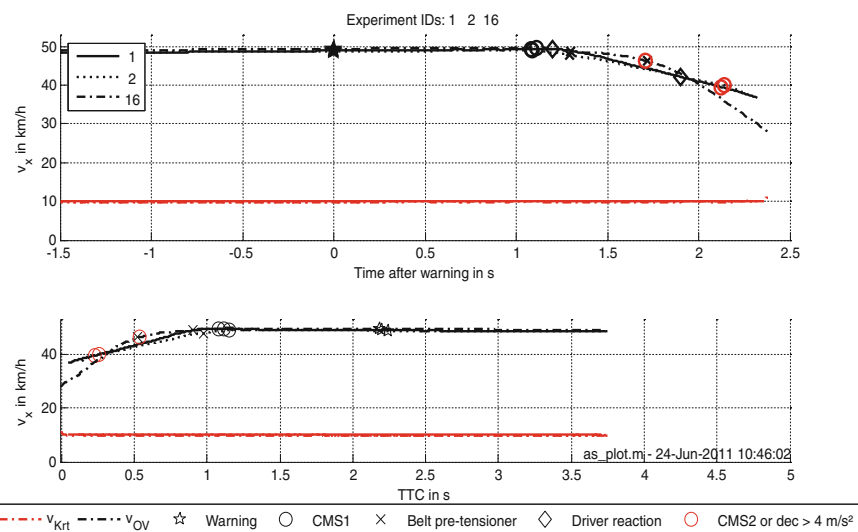
The vast majority of warnings (both vehicles, all targets) is within the expected range (as defined in [15]). In the case of the moving TV, in 88 % of the runs a warning was initiated. In the stationary case, the rate is significantly lower. This is consistent with the experience that the identification of a stationary target is much challenging, particularly for systems using only radar sensors [16]. The warnings obtained with a real vehicle are comparable to the warnings on the target objects.

Additionally, it is found that braking takes place at the earliest at a TTC of about 1 s. The accident at this time in practice is no longer avoidable [7].

The measurement results obtained with the developed test procedures cover correctly the real vehicle performance and the expected values. This validates the

Table 2 Properties of the tested vehicles

No	Target	Propulsión system	Vehicle	Driver reaction
1	ASSESSOR	MARVIN Kart	A	Yes/No
2	ASSESSOR	MARVIN Kart	B	Yes/No
3	ASSESSOR	VeHIL	A	Yes/No
4	ASSESSOR	VeHIL	B	Yes/No
5	ASSESSOR	Rabbit vehicle	A	Yes/No
6	ASSESSOR	Rabbit Vehicle	B	Yes/No
7	ADAC	Trailer	A	No
8	VW Passat	—	A	No

**Fig. 6** Plot of three measurements: vehicle A at 50 and MARVIN at 10 km/h, with no driver reaction, reaction after 1.2, and reaction after 1.7 s, shown values are for warning, braking and pre-tensioners**Table 3** Mean values of parameters for selected scenarios (separated by vehicle)

Scenario	No of tests		Speed reduction		TTC at warning		TTC at braking	
	A	B	A	B	A	B	A	B
50–10 wo reaction	42	24	16,36	10,48	2,17	2,79	1,14	0,80
50–10 with 1,2 s reaction	21	19	38,77	19,13	2,11	2,82	1,05	0,66
50–0 wo reaction	17	25	12,81	6,37	2,08	0,00	1,08	0,60
50–0 with 1,2 s reaction	13	8	28,66	7,92	2,03	0,13	0,87	0,60
80–0 wo reaction	1	0	0,00	0,00	1,05	0,00	0,00	0,00
80–0 with 1,2 s reaction	2	0	27,47	0,00	1,92	0,00	0,81	0,00
Total	96	76						

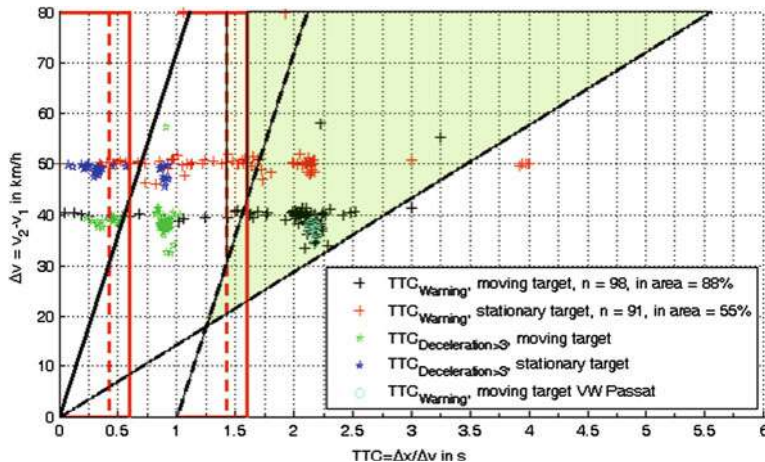


Fig. 7 Range of expected warnings compared to measured warnings

test method including stationary and moving TV and the use of autonomous actions of the vehicles and driver reactions.

4.3 Repeatability and Reproducibility

An overview of the results of various test houses and vehicles is presented in the next figures (Fig. 8).

The results with a moving TV (scenario: SV 50, TV 10 km/h, no driver's reaction, no offset) show a good comparability for warning and braking time for all test houses with vehicle A. The scatter, both within the test institute (= repeatability), and among different testing bodies (= reproducibility) are small and this applies also to the reduction in speed.

The speed reduction in the VeHIL and ADAC system is slightly higher than with MARVIN and rabbit vehicles. Possible explanations for this are:

- The ‘better’ results were obtained at a later stage in the project—and it was already known that a calibration of the radar from vehicle A should be made after each attempt.
- It is also known that the ASSESSOR begins to flutter slightly in crosswinds. This flutter does not occur naturally in a hall (VeHIL) and is not observed for the ADAC test target (Fig. 9).

The repeatability of the measurements with stationary TV is shown in the next figure. Results were less repeatable for vehicle B. Since this is not the case for all test institutes and not for vehicle A, it is assumed that this is not influenced by

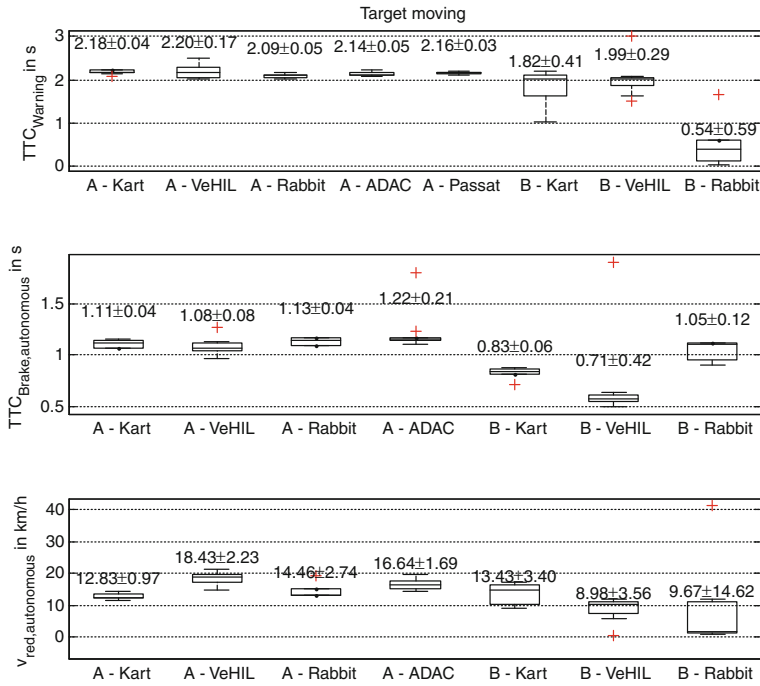


Fig. 8 Results of a moving target with the mean and standard deviation (not simulated driver's reaction)

the motion system. More likely is, that the ASSESSOR target was difficult to detect by vehicle B under some circumstances (Fig. 10).

4.4 Influence of Driver Reaction in Repeatability and Reproducibility

It has been checked that in order to have a repeatable and reproducible simulation of the driver's reaction, it is important to implement a good control of the actuator and limit elasticities of the connection (Fig. 11).

Despite the difficulties to implement a repeatable driver reaction, the consortium concludes that a simulated driver's reaction is important for the assessment of the safety effect, as it also allows the evaluation of brake assistance. An alternative approach is described in [[17], page 26], but it relies in the tuning of the force control based on the vehicle specific performance.

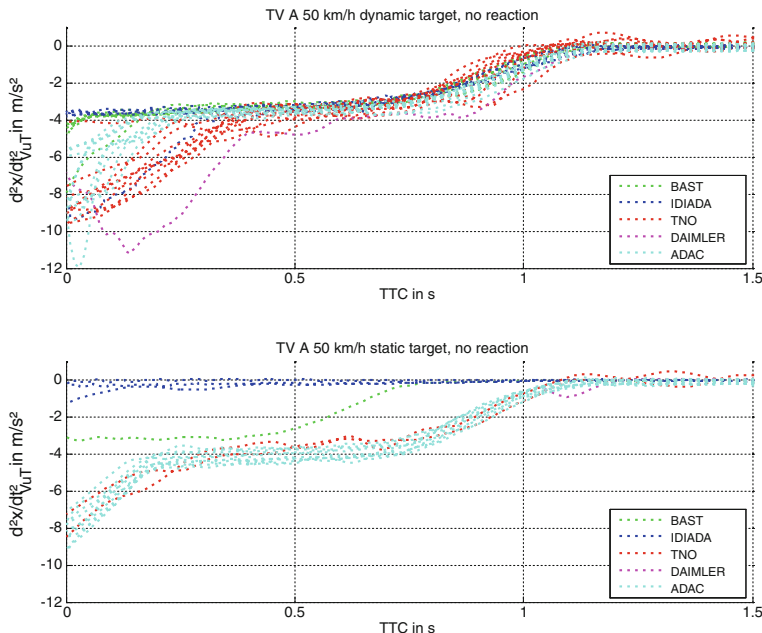


Fig. 9 Deceleration as a function of TTC for vehicle A, separated by test institutes (for comparison, tests executed by Daimler are also included)

5 Conclusions

5.1 Validation of the test procedure

The presented results show that the proposed test method is suitable for the assessment of the performance of a pre-crash braking system when facing a moving target at constant speed. The measurement of the performance against a stationary TV turned out to be more difficult. However, by using an improved test target more consistent results are expected.

One of the key factors affecting the test results seems to be the target object itself, especially because a good balance between robust detectability for different sensing technologies (e.g. radar, video, etc.), flexible usage for all defined scenarios, as well as crashability up to high Δv without damage to the SV.

On the other side, different propulsion systems and laboratory set-ups were used comparatively. The results proof, that the proposed assessment methodology can work with various laboratory set-ups and therefore is well suited for widespread application. Furthermore, the study shows that it is very important to implement driver reaction, in order to observe the full benefit of the integrated safety system.

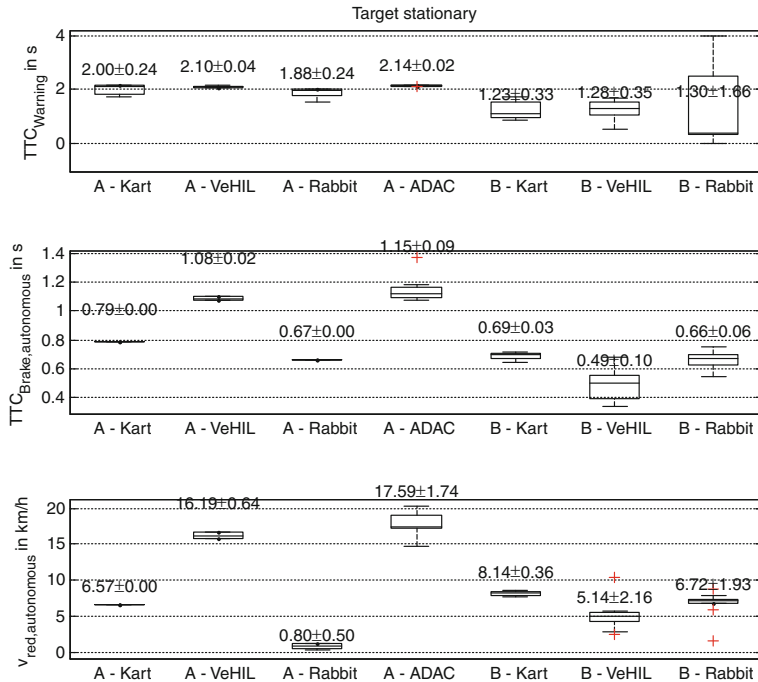


Fig. 10 Results for stationary target with the mean and standard deviation (not simulated driver's reaction)

5.2 Test Requirements

For the test scenarios with a constant speed TV, variables to control are:

- Speed of the TV
- Speed of the SV (including brake system operations/simulated driver's reaction)
- Relative distance (longitudinal and lateral) and heading angle between SV and TV
- Brake pedal control, in order to simulate driver reaction

Speed value of the TV and SV could easily be controlled within the range of ± 1 km/h.

The measured TTC values between the test institutes are well comparable. The achieved accuracies (s.d. of about 2 %) are considered to be sufficient.

Scatter in the measured speed reduction is about an order of magnitude, depending on the test institute. These comparatively high variances indicate that the final measured speed reduction is highly sensitive to all test parameters. It has to be noted that for the tests for one vehicle the scatter was significantly lower than for the other vehicle, where also different stages of ASSESSOR were used. After further improvements to the target, this point should be evaluated again.

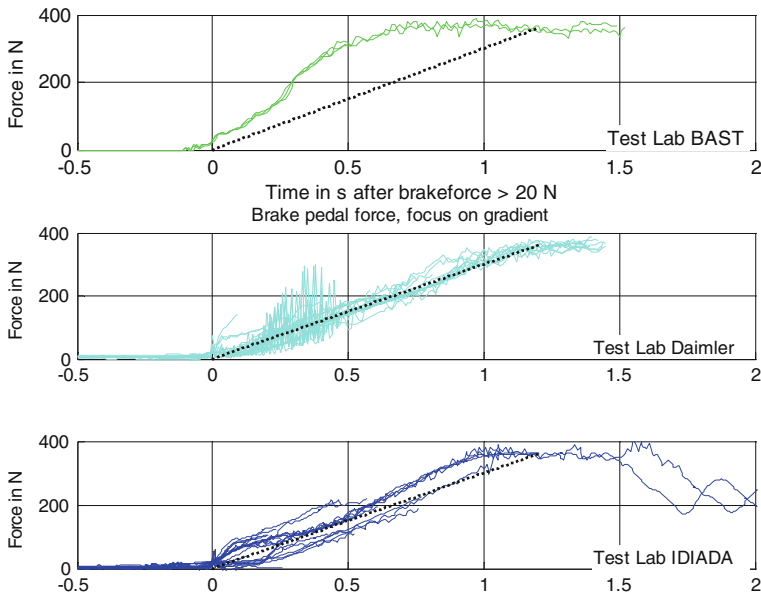


Fig. 11 Brake force during the tests with driver reaction

The maximum lateral alignment during the experiments was in the range of a few cm (TNO VeHIL, IDIADA rabbit vehicle) or in the area ± 30 cm (BASt Kart, ADAC motor system). However, no significant difference in results between these two groups can be determined. The influence of the lateral distance (if they are in the range ± 30 cm) is therefore negligible.

This is consistent with the theoretical analysis of expected system performance for 50 overlap and 100 % overlap: since the point of no return for steering evasion only moves 150 ms in time, robust AEB systems should not change their braking strategy for offset situations. This will certainly be different for low overlap (e.g. 5 %).

In principle, the speeds should be kept constant prior to the start for a few seconds. In the ASSESS experiments, a period of at least 3 s was proposed.

These are the suggested repeatability values:

- Speed ± 1 km/h
- Lateral distance ± 30 cm
- Beginning of the test $\gg > 3$ s TTC.

Acknowledgments This paper summarizes the latest results corresponding to the pre-crash performance of the European project ASSESS (Assessment of Integrated Vehicle Safety Systems for improved vehicle safety, EC grant agreement no. 233942).

References

1. Bartels O, Langner T, Aparicio A, Rodarius C, Lemmen P (2010) ASSESS D4.1—action plan pre-crash evaluation. Bergisch Gladbach
2. McCarthy M, Fagerlind H, Heinig I, Langner T, Heinrich S, Sulzberger L, Schaub S (2009) ASSESS D1.1—preliminary test scenarios. Crowthorne
3. Wisch M, Fagerlind H, McCarthy M, Roynard M, Hulshof W, Boissou J-F, Schaub S, Heinig I, Viström M (2010) ASSESS D1.2—specifications for scenario definitions. Bergisch Gladbach
4. Wisch M, Fagerlind H, McCarthy M, Roynard M, Hulshof W, Boissou J-F, Schaub S, Heinig I, Viström M (2010) Analysis of accident data for test scenario definition in the ASSESS project. ESAR Conference, Hannover
5. Ranovona M, Tsuchida J, Chin E, Unselt T, Munoz O, Aparicio A (2011) ASSESS D3.2—report on the experimental study results of the evaluation of behavioral aspects. Brussels
6. Hoffmann J (2008) Das Darmstädter Verfahren (EVITA) zum Testen und Bewerten von Frontalkollisionsgegenmaßnahmen. Fortschrittsberichte VDI, Reihe 12, Band 693. VDI Verlag, Düsseldorf
7. Winner H (2012) *Frontalkollisionsschutzsysteme*. In: Winner H, Hakuli S, Wolf G (Hrsg): Handbuch Fahrerassistenzsysteme, S. 522ff. 2. Auflage. Verlag Vieweg + Teubner, Wiesbaden
8. Mages M (2009) *Top-Down-Funktionsentwicklung eines Einbiege- und Kreuzenassistenten*. Fortschrittsberichte VDI, Reihe 12, Band 694. VDI Verlag, Düsseldorf
9. Breuer J, Faulhaber A, Frank P, Gleissner S (2007) Real world safety benefits of brake assistance systems. 20st. ESV conference, Lyon
10. Mages M, Seyffert M, Class U (2012) Benefit of reversible belt pre-pretensioning for different pre-crash scenarios—reduction of occupant displacement and the effect on injury, Airbag 2010, Karlsruhe
11. Gelau C, Gasser T, Seeck A (2012) Fahrerassistenz und Verkehrssicherheit. In: Winner H, Hakuli S, Wolf G (Hrsg) Handbuch Fahrerassistenzsysteme, S. 24ff. 2. Auflage. Verlag Vieweg + Teubner, Wiesbaden
12. Schöner HP, Hurich W, Haaf D (2011) Selbstfahrendes soft crash target zur Erprobung von Fahrerassistenzsystemen. Konferenz AAET, Braunschweig
13. Seiniger P, Bartels O, Wisch M, Langner T (2011) Development of a target propulsion system for ASSESS. 22nd ESV conference, Washington
14. Rodarius C, Seiniger P, Baurès S, Waagmeester K, Aparicio A, Vissers J, Ranovona M ASSESS D4.3—pre-crash evaluation final status. Publishing pending
15. Seiniger P, Bartels O, Rodarius C, Vissers J, Unselt T, Aparicio A, Baurès S (2012) Ein validiertes Testverfahren für Notbremssysteme—Ergebnisse des ASSESS-Projekts. 5. Tagung Fahrerassistenz, München, 16.5.2012
16. Henle L, Regensburger U, Danner B, Hentschel E, Hämmерling C (2009) Fahrerassistenzsysteme. ATZ Sonderheft "Die neue E-Klasse von Mercedes-Benz", 01/2009
17. Breuer J (2012) Vorausschauende Längsschutzsysteme: Praxisrelevanz und Bewertungsverfahren. 14. VDA Technischer Kongress, Stuttgart

Optical Self Diagnostics for Camera Based Driver Assistance

HadjHamma Tadjine, Dehghani Anoushirvan,
Dick Eugen and Karsten Schulze

Abstract An increasing number of vehicles are equipped with cameras. As perception sensors, they scan the surrounding field and supply the Advanced Driver Assistance Systems (ADAS) for building up an environmental model through the use of computer vision techniques. While they are performing well under good weather conditions their efficiency suffers under adverse environmental influences such as rain, fog and occlusion through dirt. As a consequence, the vision based ADAS has procured poor quality information, and the model also becomes faulty. This paper deals with methods to estimate information quality of cameras in order to warn the assistance system of possible wrong working conditions. In particular, situations of soiling or occlusion of the windshield or camera lens, as well as foggy weather are taken into account in this paper. In the issue of occlusion total, fractional and transparent effectuations have to be recognized and distinguished. Therefore this paper proposes an approach based on edge analysis of consecutive frames and presents initial experimental results of the implementation. In the field of Fog Detection a method based on the Logarithmic Image Processing Model is described and the results are shown.

Keywords Self-optical diagnostic · Camera · Fog detection · Occlusion

F2012-F07-008

H. Tadjine (✉) · D. Anoushirvan · D. Eugen · K. Schulze
IAV GmbH, Berlin, Germany

1 Introduction

Through use of camera-based driver assistance systems versatile possibilities have evolved to support the driver. Both in-vehicle multipurpose cameras and exterior fish-eye parking cameras help to extend the drivers perception in various situations. Detecting pedestrians, road signs, other vehicles or generate bird's eye view are just a few to mention. Likewise, the human optical perception, the ability to see is constricted by visibility conditions. Unfortunately in the real world there are plenty of situations and influences which can degrade camera sight, such as adverse weather conditions, lens occlusions through ice or dirt, blurring effects through water or translucent occlusions, cracks in the lens or windshield.

Furthermore, there can be other failures caused by sensor defects or disruption during data transfer. To avoid malfunction of the ADAS it is therefore necessary to detect all kinds of failures and degradations of image quality and warn or deactivate affected modules. So the ADAS can be transferred to a fail-safe level and therefore the vehicle safety is increased. For this reason IAV is working on a self-diagnostics module which provides camera-based ADAS with extensive image quality information regarding the current condition. In the field of image degradation due to bad weather many approaches for detection or restoration have been introduced. Grmer et al. [1–3] deal with the phenomenon of raindrops on the windshield and how to register and eliminate them. Gallen et al. [4–6] focus on the effects of fog during day and night time. Other attempts i.e. reflectance measurement of road surface are made in [7]. The main goal of the self-diagnostics module is to tackle the most frequent disrupting situations out of a single stand-alone function.

This paper deals with the general architecture of an optical self-diagnostics module. An approach for occlusion detection of exterior camera systems is introduced and experimental results are discussed.

An attempt for fog detection through use of an in vehicle monocular camera is also discussed and presented.

2 Architecture of the Self Diagnostics Module

2.1 Feature Scanning

The module is intended as an additional function for the camera-based ADAS which feeds its surrounding with image quality information. Therefore, existing diagnostic functions out of every single assistance system can be separated and included centrally into a dedicated module.

For the different camera systems, interior and exterior, the module has to be adaptively designed. To ensure this flexibility it is merged out of multiple applications which handle one or two situations (see Fig. 1a). This structure enables an

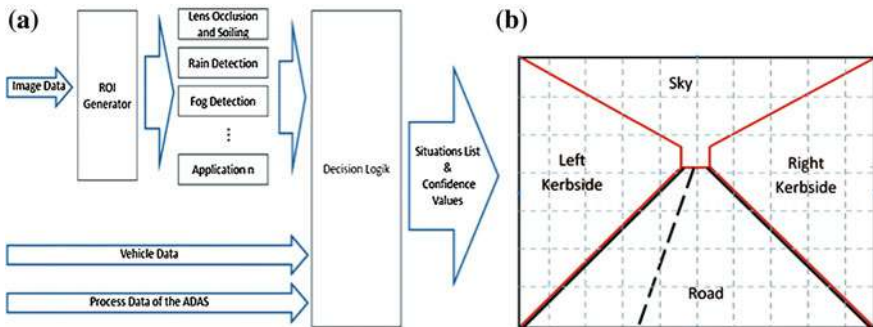


Fig. 1 Module architecture. **a** Modular structure **b** ROIs in blocks or expectable scene

effective and appropriate calculation for different scenarios to be expected. Thus it is possible to activate single applications based on external sensor data (i.e. temperature) or for example driver commands. As a single sub-module is activated, it scans the recent video sequence for the required features and displays the results. Attached to these, an additional confidence value is submitted which indicates the reliability.

2.2 ROIs Generator

Not every feature is present in the whole image. Hence to reduce runtime, a region of interest generator supplies the applications with the particular part of the frame, so that the sub-module scans only the interesting regions. Possible subdivisions can be seen in the Fig. 1b.

2.3 Module Interface

To enhance the reliability of the diagnostic module an internal and an external data is gained and analysed. External information can be vehicle data provided by CAN or other Bus system. As an example the use of vehicle velocity, exterior temperature or light sensors can be interesting. As internal information, results of camera-based ADAS can be analyzed and used as validation for the estimated situation. For example, the status of blindness can be overridden by detected objects. After scanning the sequences for particular features its confidence value is calculated and forwarded by means of a data bus system. So the output consists of the detected situation and its probability measurement.

2.4 Required Detections

For ADAS there are basically six aspects of situations to be taken in consideration.

- Lens occlusion or soiling
- Weather condition
- Environmental situation
- Optical faults
- Sensor faults
- Visibility distance.

2.5 Lens Occlusion or Soiling

One of the most important and highly frequent occurring failures for exterior cameras is the occlusion or soiling of the lens. The substance either solid or fluid covering the lens, is detaining the light rays to pass through the objective and hitting the photo sensor of the camera. As a consequence the resulting image becomes faulty and influences the interpretation of the environment. This problem can affect the whole image in the total case or can partially occur if only some fractions are soiled.

Another differentiation is the level of translucency. Soiling and occlusion can be fully opaque, and then there will be no usable information on the affected region. The other situation would be transparent, where the objects on the image can be fully recognizable or completely blurred. An approach for the problem of lens occlusion and soiling is addressed in [Sect. 3](#).

2.6 Weather Conditions

Both, interior and exterior cameras can suffer from adverse weather conditions. Important phenomena are summarised as follows:

- Rain/Snow
- Fog
- Fogging of optical components
- Icing.

But also consequences of weather phenomena have to be considered:

- Wet lane
- Snowy roads
- Road glare/saturation.

In all of these aforementioned situations the weather is influencing the sight of the camera and has to be detected. In this paper the problem of fog is addressed particularly.

2.7 Environmental Situations

Not only the weather could affect the quality of the captured image but also the current surrounding environment plays a decisive role for the correct interpretation of the actual situation. Even though the camera components are fully available, the sight could be constricted through different given situations such as:

- Day- or Night-time
- Passing through road tunnels
- Bridge passages
- Inner-city roads or Highways.

This information enables the ADAS to adapt to the current situation and activate appropriate functions or vice versa.

2.8 Optical Faults

Occurring defects on the optical components of the camera correspond to the most severe failures. They can appear as:

- Dust on the lens
- Loose lens
- Interior fogging
- Cracks or stone impacts on the lens.

In each case, it is usually required to, if possible, repair the defect or to replace the whole component. Additionally the camera system has to be calibrated after every physical service. Hence the detection of optical failures has to comply with a high reliability to avoid False Positives.

2.9 Sensor Defects

Similar to the previous section, any failures on the photo sensor entail cost-intensive consequences. Possible causes are:

- Blooming
- Smear

- Picture Element defects ("Black or White Dots")
- Thermal Noise.

2.10 Visibility distance

As an extra requirement the estimated visibility distance has to be displayed. Based on the meteorological definition that the most distant black object with a remaining local contrast of 5 % is determined as visible it is possible to estimate the visibility conditions. As a whole, the previous named aspects are merged to a situations list and submitted by the diagnostics module. As previously, an additional confidence measure is attached to the actual statement.

2.11 Lens Occlusion and Soiling Detection

With the problem of soiling and occlusion of the lens in particular, there is concern for exterior cameras. Nevertheless the algorithm can also be applied for interior cameras to activate the windshield wipers. In general soiling and occlusion occur as a static and locally fixed phenomenon which can be further subdivided into:

- total
- partial
- transparent.

In case of total and partial occlusion a layer of material is covering the lens. The image data is falsified and usually no objects can be detected through the layer. If the substance is opaque the recognition of this soiling is straight forward. A greyscale image $I(u; v)$ is divided into defined regions of interest. Therefore a sliding window w with size $w \times h$ is swapped. The mean value of the window μ_w is calculated as follows:

$$\mu_{w(u,v)} = \frac{1}{w.h} \sum_{i=1}^h \sum_{j=1}^w I(u+i, v+j) \quad (1)$$

and the window σ_w is calculated as:

$$\sigma_w = \frac{1}{w.h} \sum_{i=1}^h \sum_{j=1}^w [\mu_w - I(u+i, v+j)]^2 \quad (2)$$

A temporal analysis of each ROI shows that μ and σ of the affected regions remain the same over a series of consecutive frames. For the case of transparent occlusion the values for μ now can differ. While an opaque occlusion is blocking the whole amount of light rays transparent substances enable a partial passage. Depending on the material and its thickness the rays can be diffracted and the

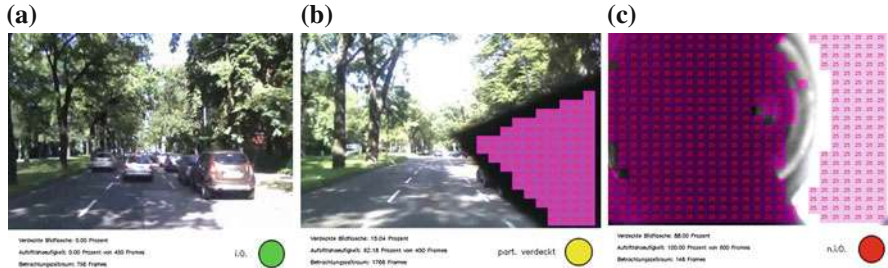


Fig. 2 Results of the occlusion detection. **a** Clear sight **b** partially occluded **c** totally occluded

image becomes blurry. Although the parts are still occluded objects can sometimes be detected. For recognizing such transparent soiling it is necessary to take a frequency test. In a temporal observation it can be shown that soiled regions mostly have a lower frequency spectrum than the free counterparts. Consequently, for the detection it is also possible to evaluate each ROI over a series of frames and determine a threshold as classifier.

Since the boundaries of the occlusions are static the analysis contributes to a reliable detection. Therefore the vertical and horizontal gradients for each ROI are calculated and compared to the gradients of the previous frames. Of course for the whole lens occlusion and soiling detection the vehicles velocity has to exceed a determined threshold.

2.12 Experimental Results of Occlusion

In Fig. 2 the first experimental results can be seen. As depicted, the single frames are subdivided into blocks for which the features are calculated and compared to the previous block values. If a threshold is being crossed the respective ROI is coloured magenta (see Fig. 2b and c). In the next step, the marked regions are counted and the image is classified as free, partially or fully occluded.

2.13 Fog Detection

Fog appears when the temperature around the saturated air crosses the dew temperature of the water vapour. The water condensates into tiny droplets which hover in the air. This aerosol diffracts, attenuates and absorbs the light to some extent so that the remaining beam is alleviated. For the humans optical perception, as well as for the camera, this causes a reduction of contrast and so a resulting reduction of visibility.

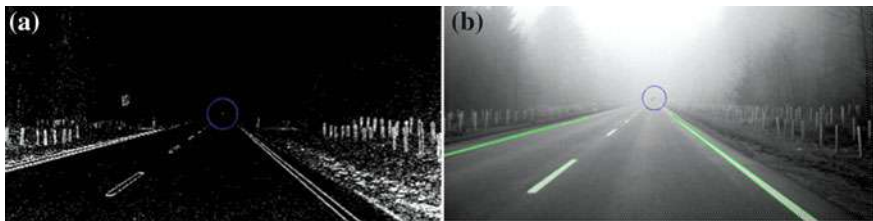


Fig. 3 Contrast mapping

Out of a meteorological definition an object counts as visible if it has at least a local contrast of 5 %. For a visibility measurement an image has to be transformed into a depiction where the pixels with a contrast greater than the threshold are painted (see Fig. 3a). As can be seen in Fig. 3b through presence of fog in the circular area around the inflection point shows no information.

This means that by definition the parts of the image can be counted as not visible. Hence, this paper proposes a method to analyse the contrast around the vanishing or inflection point of a picture to derive the presence of fog. The principle of the approach is structured as follows:

2.14 Vanishing Point Estimation

The vanishing point in an image is the direction of the most distant point in the world coordinate system. Theoretically the visibility distance in this point is ∞ . It can either be assumed as fixed or estimated by means of computer vision techniques. Through use of calibration data of the camera like focal length, camera height, camera pitch angle, camera yaw angle as well as the principle point of the sensor the expected inflection point can be determined.

However, tests showed that through alternating vehicle loading this point can deviate. For the vehicle pitch angle a deviation of 1.5–1.8° of arc is possible. This represents up to 40 pixels for the camera used in the tests. On that account it is necessary to do pitch angle compensation in advance to the current fog detection.

The estimation is basically implemented equivalent to [8]. The authors describe a double-stage method which enables robust vanishing point detection. In the first stage a data-driven estimation is based on line segments that are weighted by means of defined criterion and extrapolated to their intersection point.

The entity of all intersections is then averaged by their weight and undergoes a temporal filtering before it is fed back as new vanishing point. Additionally a confidence value is delivered. Due to this and the recent estimation in the second stage a Kalman filter is used to assess the current pitch and yaw angle. For the approach in this paper, the first stage is sufficient because only the current inflection point is needed. Results of the vanishing point estimation can be seen in Fig. 3b.

2.15 Contrast Calculation

For the computation of the local contrasts the Logarithmic Image Processing Model (LIP) is used. This model is based on the human brightness perception (described by the Weber's Law and Fechner's Law) and reflects characteristics like brightness scale inversion, saturation characteristics and psychophysical contrast notion [9].

The contrast in this model is calculated as follows: For a given Image $I(u, v)$ with the grey values $g \in (0, \dots, q)$ the contrast between two neighbouring points is:

$$C_{(u,v),(u',v')} = \frac{q|I(u, v) - I(u', v')|}{q - \min(I(u, v), I(u', v'))} \quad (3)$$

To evaluate a contrast at a particular point it is now necessary to involve the surrounding pixels. Therefore a neighbourhood has to be defined. Out of the possibilities of 2-, 4- or 8-pixel neighbourhood in the tests, the 2-pixel neighbourhood proved to be sufficient and of course is less computation timeconsuming than the other alternatives. The resulting contrast is then calculated by the equation:

$$C_{u,v} = \frac{1}{n} * (\blacksquare_{(i=1,\dots,n)} C_{(u,v),(u',v')}) \quad (4)$$

Where \blacksquare is defined as addition of two grey tone functions

$$I(u, v) \blacksquare I(u', v') = I(u, v) + I(u', v') - \frac{I(u, v)I(u', v')}{q} \quad (5)$$

and* is the scalar multiplication with a positive real number :

$$a * I(u, v) = q - q\left(1 - \frac{I(u, v)}{q}\right)^a \quad (6)$$

Where n represents the number of neighbouring points.

An important detail to mention is: Before the calculations, a Grey Scale Inversion has to be performed. In our case this means that q is the darkest black and respectively 0 the saturating light intensity. Further details can be seen in [9]. In this approach the contrast for a predefined region of the incoming image is calculated and mapped. Also all pixels with a value beneath the 5 %-threshold are set equal to zero. As a result, all pixels which are, by definition, visible can be seen in the contrast mapping.

The current Fog Detection is an adaptive window which is set concentric to the position of the vanishing point on top of the contrast mapping. The idea is to iteratively increase the size of the window as long as the contrast values which are enclosed are still zero. To save computation time the contrast map is here implemented as an Integral Image [10].



Fig. 4 Results of the fog detection

The size of the window is then a measure for the resulting visibility distance. Unfortunately, with a monocular camera the determination of the scene depth is non-trivial. Hence the flat world hypothesis has to be applied. Then out of the calibration parameter and triangulation, simple distance estimation can be realised. An approach for a stereo camera can be seen in Hautire et al. [11].

2.16 Classification

In a last part, the measure for the visibility distance we obtained from the contrast calculation has to be evaluated and the situation has to be classified. As previously mentioned, every pixel which is greater than zero on the contrast map depicts a visible point in the world coordinate system. With the assumption of a distance equal to 1 in the inflection point this means a contrast value greater 5 % in this area is in accordance to a 1 visibility distance. In this case, the resulting window size would remain zero.

The calculated value derived from the window size is temporally filtered and the fog severity is than determined as:

- clear sight
- minimal fog
- mid-level fog
- dense fog.

2.17 Experimental results of fog detection

The first promising results of the Fog Detection can be seen in Fig. 4. The Circle in the middle of the frame represents the part of the image where no objects are visible to the camera. Note that through the assumption of a flat world any vehicles running ahead can disrupt the estimation. Due to this, the object detection of the ADAS during the tests was used to avoid this malfunction. Detected objects in front of the ego vehicle either caused the algorithm to stop or the scanning window was shifted aside so that the classification could still remain enabled. For a solution without a given object detection additional free space detection has to be implemented.

3 Conclusion

This paper describes a module that provides extensive quality information for captured traffic scenes through use of vehicle cameras. This information can be used to increase the reliability of the ADAS and so raise the security of passengers

and pedestrians. Implementations of first sub-modules were proposed and have to be further developed and improved. As a perspective the other named modules have to be added and tested in future development.

References

1. Grmer S, Kummert A, Park S-B, Egbert P (2009) Vision-based rain sensing with an in-vehicle camera. In: IEEE intelligent vehicles symposium
2. Nashashibi F, Charette Rd, Lia A (2010) Detection of unfocused raindrops on a windscreen using low level image processing. Proceedings of the 11th international conference control, automation, robotics and vision
3. Kurihata H, Takahashi T, Ide I, Mekada Y, Murase H, Tamatsu Y, Miyahara T (2005) Rainy weather recognition from in-vehicle camera images for driver assistance. In: IEEE intelligent vehicles symposium
4. Gallen R, Cord A, Hautire N, Aubert D (2011) Towards night fog detection through use of in-vehicle multipurpose cameras. In: IEEE Intelligent vehicles symposium
5. Hautire N, Tarel J-P, Aubert D (2007) Towards fog-free in-vehicle vision systems through contrast restoration. IEEE conference on computer vision and pattern recognition
6. Hautire, N, Aubert D (2005) Contrast restoration of foggy images through use of onboard cameras. Proceedings of the 8th international IEEE conference on intelligent transportation systems
7. Roser M, Lenz P (2010) Camera-based bidirectional reflectance measurement for road surface reflectivity classification. In: IEEE intelligent vehicles symposium
8. Suttorp T, Bücher T (2006) Robust vanishing point estimation for driver assistance. Proceedings of the 9th international IEEE conference on intelligent transportation systems (ITSC 2006)
9. Pinoli J-C (1979) The logarithmic image processing model: connections with human brightness perception and contrast estimators. *J Math Imaging Vis* 57(2)
10. ViolaP, Jones MJ (2004) Robust real-time face detection. *Int J Comput Vis* 57(2)
11. Hautire N, Labayrade R, Aubert D (2005) Estimation of the visibility distance by stereo vision: a generic approach. In: Conference on machine vision applications

Object Detection and Classification Using a Rear In-Vehicle Fisheye Camera

HadjHamma Tadjine, Markus Hess
and Schulze Karsten

Abstract In the USA from 2014 the implementation of fisheye rear cameras will begin to become more widespread due to upcoming federal legislation. By adding Intelligence to such cameras, IAV GmbH has developed and performed a variety of reversing functions such as Pedestrian Detection and General Object detection. Such implementations will permit the OEM to introduce systems to help reduce the 6,000 or so reversing accidents involving children that currently take place each year in the USA alone. Pedestrian detection is a key problem in computer vision, with several applications including surveillance and automotive safety. Much of the progress of the past few years has been driven by the availability of challenging public datasets. Advanced vehicles equipped with camera vision based advanced driver assistance systems (ADAS) increase rapidly. IAV GmbH is now in Advanced Development for adding intelligent Driver Assistant Functions for fisheye rear mounted cameras. A real time vision-based system for driver assistance on-board vehicles is developed. Safety and ease-of-use of vehicles are the two central themes in this line of work. This paper focuses on the safety aspect and presents a prototype system for the detection of the most vulnerable traffic participants: pedestrian using a fisheye mounted camera. This paper proposes a robust rear-view camera based moving object detection algorithm for backup aid and parking assist applications. A single fish-eye camera is used in order to get much larger FOV (field of view) for object detection. The dataset contains richly annotated video, recorded directly from a vehicle, with challenging images of fisheye camera. IAV GmbH also benchmark several promising detection systems, providing an overview of state-of-the art performance and a direct, unbiased

F2012-F07-009

H. Tadjine (✉) · M. Hess · S. Karsten
IAV GmbH, Munich , Germany

comparison of existing methods. Finally, by analysing common failure cases, IAV GmbH helps identify future research directions for the field.

Keywords Pedestrian detection • Fisheye camera • HOG • SVM • Adaboost

1 Introduction

The protection of pedestrians represents one of the major current challenges when developing modern automobiles. Pedestrian detection has been a deeply investigated field in vision community. Object detection in images and videos has received a lot of attention in the computer vision and pattern recognition communities in recent years. Currently, it is a challenging problem with many potential applications. Object detection is an important element of various computer vision areas. The basic goal is to find an object of a predefined class in static images or video frames. By extracting certain image features, this task can be sometimes handled, such as edges, colour regions, textures, contours, etc. Afterwards, some heuristics is applied to find configurations and/or combinations of those features characteristics of the object that one wants to detect. But, for complex objects, such as pedestrians, it is hard to find features and heuristics that will handle the huge variety of instances of the object class [1].

Thus, pedestrian detection in cluttered environment is an open problem. The major difficulties lie in [2]:

- Different appearance of the same pedestrian caused by the diversity of the size, colour and style of pedestrian clothing.
- Pedestrian is a non-rigid object. The complexity of the model due to the variety of pedestrian shape and size of a pedestrian.
- Clutter background. Complexity of background formed by vehicles, trees, wire poles, and billboards.

Performance of pedestrian detection depends on the properties of extracted features and the classifier used. In this paper the attention on pedestrian detection based fished camera in parking situation is presented. The advantage is due to the most important field of view (Fig. 1). This work presents a new concept of system capable of extracting pedestrians behind of the ego-vehicle from colour captured by a mega pixel fisheye single camera mounted on the rear of the vehicle. It is more important to integrate a camera with a fisheye lens on the back side of a vehicle to see the rear area from a wider view, which is more convenient to the drivers when they drive the vehicle in reverse. During parking, the rear camera, integrated into the tailgate handle, provides wide-angle images of the area behind the vehicle. Precise distances of the detected pedestrian are displayed on the image, and become dynamic to illustrate the trajectory at the moment when the driver begins the manoeuvre. During riskier manoeuvres, when the driver has

Fig. 1 Camera based driver assistance system

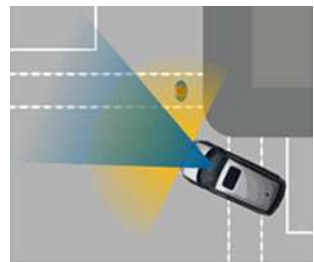
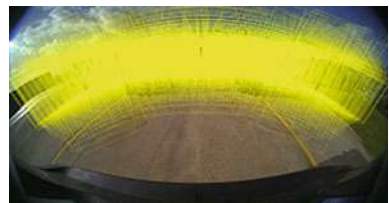


Fig. 2 ROI's generation using fisheye camera



limited visibility, the cameras display the area to the front of the vehicle even if visibility is obstructed. The system monitors cars, bicycles and pedestrians passing in front of the vehicle, displaying the wide-angle image on a screen for the driver.

The forward/Rear obstacle detection subsystem is a wide angle camera (mounted on the front Bumper) based assistance function. The actual subsystem will detect both moving and stationary obstacles at least 8 meters ahead of the vehicle during benign daytime conditions. While under conditions which do not match the benign daytime definition, there may be degradation in detection range. One of the advantages of the current proposed system is that, the current proposed system do not corrects the images before performing the pedestrian detection. The simplest technique to obtain initial object location hypotheses is the sliding window technique, where detector windows at various scales and locations are shifted over the image. The computational costs are often too high to allow for real-time processing [3, 4].

Significant speedups can be obtained by either coupling the sliding window approach with a classifier cascade of increasing complexity [5–7] or by restricting the search space based on known camera geometry and prior information about the target object class. For the proposed approach a modified sliding windows is proposed as seen in the Figs. 2 and 3.

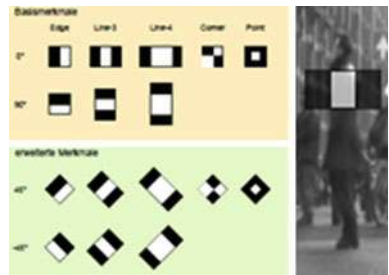
2 Feature Extraction

The choice of features is the most critical decision when designing a detector, and finding good features is still largely an empirical process with few theoretical guidelines (Fig. 4).

Fig. 3 Hypothesis based sliding windows



Fig. 4 Haar like features



3 Haar Like Features

Each feature is represented by a template (shape of the feature); it's coordinate relative to the search window origin and the size of the feature. A subset of the features prototypes used is shown in the following figure.

Each feature is composed of two or three “black” and “white” rectangles joined together. The Haar-like features value is calculated as a weighted sum of two components: the pixel gray level values sum over the black rectangle and the sum over the whole feature area (all black and white areas). The weights of these two components are of opposite signs and for normalization purpose; their absolute values are inversely proportional to the areas. Hundreds of features are used in a real and robust classifier. Therefore, the direct computation of pixel sums over multiple rectangles would make the detection task very slow and not suitable for real-time applications. An efficient method for computing the sums quickly is introduced. The integral image, Summed Area Table (SAT), is computed over the whole image as discussed in Zhu et al. [8].

4 Histogram of Oriented Gradient

The basic idea is that local object appearance and shape can often be characterized rather well by the distribution of local intensity gradients or edge directions, even without precise knowledge of the corresponding gradient or edge positions. In practice this is implemented by dividing the image window into small spatial

regions (cells.), for each cell accumulating a local 1-D histogram of gradient directions or edge orientations over the pixels of the cell. The combined histogram entries form the representation. For better invariance to illumination, shadowing, etc., it is also useful to contrast-normalize the local responses before using them. This can be done by accumulating a measure of local histogram “energy” over somewhat larger spatial regions (blocks) and using the results to normalize all of the cells in the block. The use of orientation histograms has many precursors, but it only reached maturity when combined with local spatial histogramming and normalization in Lowe’s Scale Invariant Feature Transformation (SIFT) approach to wide baseline image matching as seen in Dalal and Triggs [4], in which it provides the underlying image patch descriptor for matching scale invariant key points. This method captures edge or gradient structure that is very characteristic of local shape and it does so in a local representation with an easily controllable degree of invariance to local geometric and photometric transformations: translations or rotations make little difference if they are much smaller than the local spatial or orientation bin size.

5 Local Binary Patterns

In the Local Binary patterns (LBP) approach for texture classification, the occurrences of the LBP codes in an image are collected into a histogram. The classification is then performed by computing simple histogram similarities. However, considering a similar approach for image representation results in a loss of spatial information and therefore one should codify the texture information while retaining also their locations. One way to achieve this goal is to use the LBP texture descriptors to build several local descriptions of the pedestrian and combine them into a global description [9].

6 Edge Orientation Histograms (EOH)

The basic idea is to build a histogram with the directions of the gradients of the edges (borders or contours). It is possible to detect edges in an image but it in this case the detection of the angles is the most important topics [10].

7 Colour Self Similarity

Colour information is such a feature enjoying popularity in image classification] but is nevertheless rarely used in detection. Furthermore, second order image statistics, especially co-occurrence histograms, are gaining popularity, pushing

feature spaces to extremely high dimensions [5, 6]. The second order statistics of colours is proposed as additional feature. Colour by itself is of limited use, because colours vary across the entire spectrum both for people (respectively their clothing) and for the background, and because of the essentially unsolved colour constancy problem. However, people do exhibit some structure. Colours are locally similar the skin colour of a specific person is similar on their two arms and face, and the same is true for most people's clothing. Therefore, we encode colour self-similarities within the descriptor window, i.e. similarities between colours in different sub-regions. The normalised RGB is used as colour space, including $4 \times 4 \times 4$ histograms in normalised RGB.

8 Classification

There exist many classification techniques that can be applied to object detection. Some of the commonly applied classification techniques are support vector machine (SVM) [3, 11] and AdaBoost [12–14].

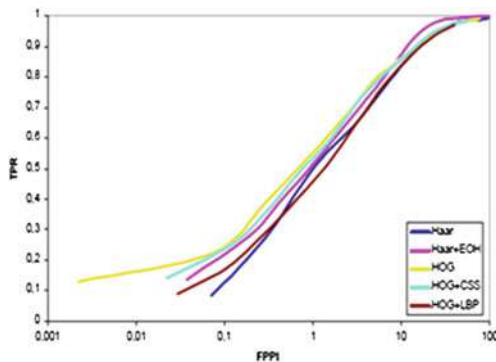
9 Support Vector Machines

Support vector machines is one of the popular large margin classifiers used [15] which has a very promising generalization capacity. Due to space limit, we omit details of SVM. Refer to [15] for details. In our experiments, SVM classifiers with three different kernel functions, linear, quadratic and RBF kernels are compared with the features calculated from previous section.

10 Adaboost

AdaBoost is one of the first practical and efficient algorithms for ensemble learning [8]. The training procedure of AdaBoost is a greedy algorithm, which constructs an additive combination of weak classifiers such that the exponential loss is minimized. Here x is the labelled training examples and y is its label; $f(x)$ is the final decision function which outputs the decided class label. AdaBoost iteratively combines a number of weak classifiers to form a strong classifier. Weak classifier is defined as a classifier with accuracy on the training set greater than average. The final strong classifier $H(\bullet)$ can be defined as, where w is a weight coefficient; (\bullet) is a weak learner and n is the number of weak classifiers. At each new round, AdaBoost selects a new hypothesis $h(\bullet)$ that best classifies training samples with minimal classification error. Each training sample receives a weight that determines its probability of being selected for a training set [16]. If a training sample is correctly

Fig. 5 Positive rate detection depending on false detection based on different approaches (*TPR* True Positive Rate and *FPI* False Positives per Image)



classified, then its probability of being used again in a subsequent component classifier is reduced. Conversely, if the pattern is misclassified, then its probability of being used again is increased. In this way, the algorithm focuses more on the misclassified samples after each round of boosting.

11 Tests and Evaluation

Special dataset was collected using a fisheye camera under different weather, street and driving conditions. This dataset consists of three training sets and two test sets. Each training set contains 3,800 pedestrian examples and 4,000 non-pedestrian examples. All samples are scaled to size 16×32 pixels. For boosted cascade of covariance features, a set of over complete rectangular covariance filters and subsample the over complete set is generated in order to keep a manageable set for the training phase. It contains approximately 1,200 covariance filters. Since, the resolution of the test samples is quite small, the border of each test sample by one pixel is extended. To shift the pedestrian in the test sample to the centre an extra margin is used and which increases a flexibility of the boosted classifier. During classification, we count the number of the positively classified windows and use this number to test whether the test sample is pedestrian or non-pedestrian.

The covariance features is trained with various combination of SVM as discussed in Joachims [17]. The covariance descriptors for all regions are concentrated into a combined feature vector and the SVM classifier is trained using this feature vector. Our preliminary experiments show region of size 7×7 pixels, shifted at a step size of 2 pixels over the entire input image of size 16×32 to be optimal for the used datasets (total feature length of 2,520). For the HOG features, a cell size of 3×3 pixels with a block size of 2×2 cells is used, descriptor stride of 2 pixels and 18 orientation bins of signed gradients to train SVM classifiers.

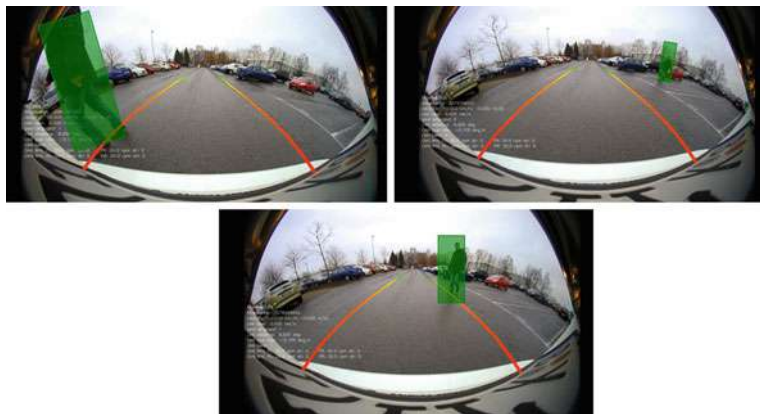
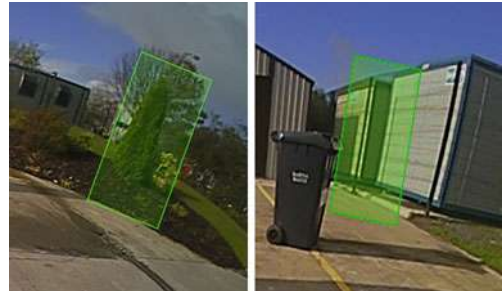


Fig. 6 Pedestrian detection

Fig. 7 False detection



The boosted cascade is trained with more non pedestrian samples, i.e., by making use of cascade structure, manually are increased the non-pedestrian training sample size from a set of non-pedestrian images.

To compare and evaluate the performance of the detectors, a bootstrapping technique to HOG is applied using covariance features. Bootstrapping is applied iteratively; new non-pedestrian samples are generated. The improvement of training HOG feature using bootstrapping technique over initial classifier is up to 8 % increase in detection rate at 3,4 % false positives rate while the improvement is slightly lower in covariance features. However, this performance gain comes at a higher computation cost during training phase as training samples are now much more complex. A comparison of the best performing results for different feature types are shown in Fig. 5. In all experiments, nonlinear SVMs improve performance significantly over the linear one. However, this comes at the cost of a much higher computation time. From the Fig. 6 it can see that the proposal approach could detect perfectly pedestrian. Figure 7 presents some false detection.

12 Conclusion

This paper has presented a fast and robust pedestrian detection technique using fisheye camera used by parking assist Systems. From the experimental results on datasets used in this context, the proposed system has shown to give high detection performance at a low false positive rate.

On this dataset, previous methods reported have significantly higher miss rates at almost all the false positive rates per window. On-going work includes the search of new features for human detection. How to optimally design a cascaded classifier may also be a future topic. To further accelerate the detection, we have also introduced a faster strategy—two-layer boosting with heterogeneous features—to exploit the efficiency of the Haar feature and the discriminative power of the covariance feature. The proposed detector runs faster than the original covariance feature detector. The performance of the proposed approach will be also evaluated using other pedestrian dataset generated from VGA camera.

References

1. Dollar P, Wojek C, Schiele B, Perona P (2009) Pedestrian detection: a benchmark. In: CVPR. pp 1–80
2. Tadjine HH, Hess M, Montag M (2011) Vehicle detection in close-up range with a fisheye camera. In: FAST-zero'11—first international symposium on future active safety technology toward zero-traffic-accident. Tokyo, Japan. Sept 5–9
3. Mikolajczyk K, Schmid C, Zisserman A (2004) Human detection based on a probabilistic assembly of robust part detectors. Proceedings of the European conference computer vision, Prague, CZ, vol 1, pp 69–81
4. Dalal N, Triggs B (2005) Histograms of oriented gradients for human detection. Proceedings of the IEEE conference computer vision and pattern recognition, San Diego, CA, vol 1, pp 886–893
5. Papageorgiou C, Poggio T (2000) A trainable system for object detection. Int J Comput Vis 38(1):15–33
6. Viola P, Jones MJ, Snow D (2003) Detecting pedestrians using patterns of motion and appearance. In: Proceedings of the IEEE international conference computer vision
7. Wu Y, Yu T (2006) A field model for human detection and tracking. IEEE Trans Pattern Anal Mach Intell 28(5):753–765
8. Zhu Q, Avidan S, Yeh M, Cheng K-T (2006) Fast human detection using a cascade of histograms of oriented gradients. In: Proceedings of the IEEE conference computer vision pattern recognition, New York, vol 2, pp 1491–1498
9. Gavrila DM, Munder S (2007) Multi-cue pedestrian detection and tracking from a moving vehicle. Int J Comput Vis 73(1):41–59
10. Amit Y, Geman D, Fan X (2004) A coarse-to-fine strategy for multiclass shape detection. IEEE Trans Pattern Anal Mach Intell 26(12):1606–1621
11. Munder S, Gavrila DM (2006) An experimental study on pedestrian classification. IEEE Trans Pattern Anal Mach Intell 28(11):1863–1868
12. Viola P, Jones MJ (2004) Robust real-time face detection. Int J Comput Vis 57(2):137–154
13. Paisitkriangkrai S, Shen C, Zhang J (2008) Fast pedestrian detection using a cascade of boosted covariance features. IEEE Trans Circuits Sys Video Technol 18:8

14. Mori G, Ren X, Efros A, Malik J (2004) Recovering human body configurations: combining segmentation and recognition. In: Proceedings of the IEEE conference computer vision pattern recognition, Washington, DC, vol 2, pp 326–333
15. Sabz Meydani P, Mori G (2007) Detecting pedestrians by learning shapelet features. In: Proceedings of the IEEE conference computer vision pattern recognition
16. Laptev I (2006) Improvements of object detection using boosted histograms. Proceedings of the BMVC, Edinburgh, UK, pp 949–958
17. Joachims T (1999) Making large-scale SVM learning practical. Advances in Kernel methods—support vector learning. MIT Press, USA

Abnormal Driving Behavior Detection Using a Linear Non-Gaussian Acyclic Model for Causal Discovery

Zujie Zhang, Yuta Inoue, Kazushi Ikeda, Tomohiro Shibata,
Takashi Bandou and Takayuki Miyahara

Abstract This paper proposed a causal discovery method for driving behavior signals representing explicit driving actions to gain a better understanding in driving actions and to apply them to improve advanced driver assistance systems. The first- and second-order statistics have only correlation information and hence they cannot tell anything on causality. In other words, causality appears in higher-order statistics. To utilize such information, we apply a linear non-Gaussian acyclic model (LiNGAM) that assumes non-Gaussian observation noise to the driving actions. Non-Gaussian assumption makes it possible to use ICA to estimate the mixing matrix of observed variables. The mixing matrix can transform to a triangular matrix that expresses causality. This method is called ICA-LiNGAM. ICA-LiNGAM can extract causality in time-series of vectors. Driving actions are time-series of vectors that play an essential role in the safe driving. To obtain driving data, we carried out experiments in which subjects drove a freeway without any instruction except for its route. In our method, both instantaneous and lagged causal influences have been considered by using the Structural Vector Autoregression (SVAR) to the continuous time series data. SVAR model is a generalization of LiNGAM model so the assumption of independence and non-Gaussianity is ensured for ICA-LiNGAM analysis. The conventional LiNGAM can be regarded as a special case of SVAR when the autoregressive order is zero. In the experiment ICA-LiNGAM worked well with SVAR model and the analysis result showed a clear causal relationship between lagged variables of driving

F2012-F07-010

Z. Zhang (✉) · Y. Inoue · K. Ikeda · T. Shibata
Nara Institute of Science and Technology, Nara, Japan

T. Bandou · T. Miyahara
DENSO CORPORATION, Kariya, Japan

action signals. The experiment shows that ICA-LiNGAM can find out both the obvious and latent causal relations between driving behaviors.

Keywords Driver behavior signal processing • Causal inference • Linear non-Gaussian acyclic model • Independent component analysis

1 Introduction

The role of human factors is an important component in the system of safe operation of vehicles, and has been paid attentions for both the design of equipment and various applications. However, driver's behaviors are influenced by their environmental, psychological and vehicle design factors and hence are difficult to analyze. Moreover, they strongly depend on the drivers' personality and customs. Hence, modeling driving behaviors is a desirable but difficult task.

For the task, recent car-related technologies such as sensor technology, telecommunication network and energy control are promising tools. In fact, they have contributed to improve advanced driver assistance systems (ADASs). However, although such ADASs recover a car and its driver from a dangerous situation to a safer one, they cannot prevent the car from going to a dangerous situation in advance. One of the reasons is that driving actions have strong but unknown causality and cannot be determined whether they are dangerous or not. Hence, the understanding of driving behaviors will help an ADAS predict the car's situation.

The driving behaviors such as throttle and brake are not independent of each other but related. Although the Principle Component Analysis (PCA) or other methods can measure the behaviors' correlation, they cannot extract the causality in the behaviors. Recently, some methods for causal inference have been developed in the machine-learning community.

In this paper, we applied a linear non-Gaussian acyclic model (LiNGAM) [1], one of the causal-inference methods, to driving data and showed the method can extract causality through our computer experiments.

A LiNGAM is a method for causal inference, assuming that observation noises (or disturbance variables) obey non-Gaussian distributions. Thanks to this property, independent components are extracted by ICA methods [2, 3] and so are dependencies in variables. The ICA-LiNGAM is an estimation method of causality using these properties [4].

One extended method of the LiNGAM is the Structural Vector Autoregression (SVAR) model [5]. The SVAR model can treat both instantaneous and lagged causal influences. In fact, some of the causality in driving data are largely lagged. For example, a blinker is activated a few seconds before a steering is turned.

The driving data were collected under unconstrained conditions [6]. In the measured signals, the throttle position, the break pressure and the steering angle

were used for our analysis, where each signal was segmented into several lagged-signals based on the SVAR model. The ICA-LiNGAM was then applied for causal discovery, which produced a Direct Acyclic Graph (DAG) expressing the causal relations.

2 Materials and Methods

2.1 Experiments for Driving Data

In the experiment, we measured the velocity of the vehicle, the distance from the preceding vehicle, the position of the throttle, the M/C pressure of the brake, the steering angle, the front view, the driver's face, and so on [6]. The subject was a male driver experiencing more than 25 years and drove in all the experiments. He made a round-trip in a suburb, during morning with good weather conditions. We collected 129 sub-sequences in the outgoing portion of the trip and 134 in the incoming portion. In this work, we used the throttle position (A), the brake pressure (B) and the steering angles (S) among the measured signals because these variables express intentional operations of the driver.

2.2 Preprocessing by SVAR

To reduce the time-scale of dependency, we applied the SVAR [5] to the data vectors in advance that can treat both instantaneous and lagged causal influences. In fact, some of the causal influences in driving data are largely lagged. For example, a blinker is activated a few seconds before a steering is turned.

The SVAR is an extension of LiNGAM [1]. The LiNGAM is a kind of Structural Equation Models (SEM) and extracts a causality from given time series variables $x_i(t)$, $i = 1, \dots, T$, assuming that the generating process is recursive [7] or a Directed Acyclic Graph (DAG) in a graphical model [8, 9], that the process is linear, that is

$$x_i = \sum_{k(j) < k(i)} b_{ij} x_j + e_i + c_i \quad (1)$$

where c_i is a constant term and e_i is a disturbance term, and that the disturbances obey non-Gaussian distributions where they are independent of each other, $p(e_1, \dots, e_m) = \prod_i p_i(e_i)$.

The model (1) can be rewritten in the matrix form as

$$\mathbf{x} = \mathbf{B}\mathbf{x} + \mathbf{e} \quad (2)$$

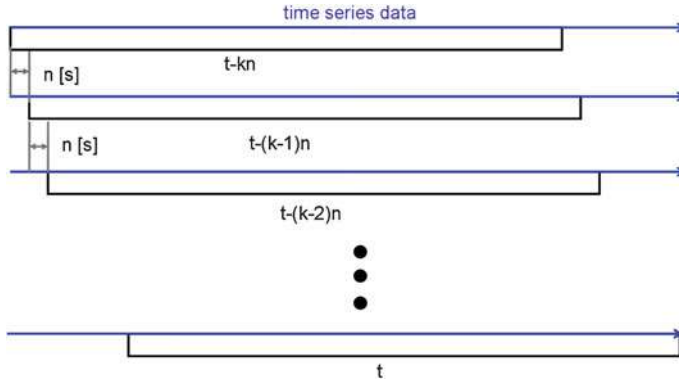


Fig. 1 Lagged signals

where $\mathbf{B} = \{b_{ij}\}$ is the adjacency matrix representing a DAG. An element b_{ij} represents the causal connection strength from a variable x_j to x_i . Due to the acyclic assumption, matrix \mathbf{B} can be permuted to be a strict lower triangular matrix [7].

The SVAR has not only the instantaneous signal but also lagged signals, that is,

$$\mathbf{x}(t) = \sum_{\tau=0}^k \mathbf{B}_\tau \mathbf{x}(t - \tau) + \mathbf{e}(t) \quad (3)$$

Where k is the number of time-delays used, which is referred to as the order of the AR model. When $k = 0$, model (3) is simply the LiNGAM. When $k > 0$, this model is an ordinary autoregressive model.

In this study, we applied the SVAR model to driving data analysis as a pre-processing. In other words, the SVAR model removed the causality of the same signals (A, B, S) in time (Figs. 1 and 2).

In Fig. 1, kn [seconds] means the lagged time period τ in SVAR model (4), and n is chosen properly according to the sample rate of the data. Figure 2 shows the lagged signals for all explicit driving action after pre-processing, where the arrows express causality between nodes. Note that the thin arrows are naturally expected (the causality in the same signal) while the thick arrows are examples of expected causality to be found by our algorithm.

As a result of preprocessing, the residual of the SVAR,

$$\mathbf{x}(t) - \sum_{\tau=0}^k \mathbf{B}_\tau \mathbf{x}(t - \tau), \quad (4)$$

is expected to have only instantaneous information and to be applicable to the ordinary causality analysis.

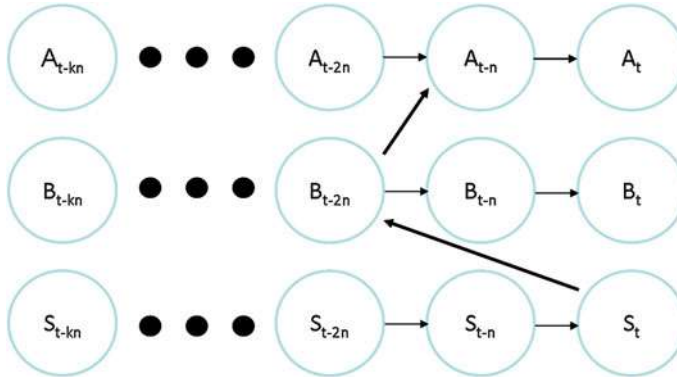


Fig. 2 All lagged signals

2.3 ICA-LiNGAM

The model (2) is rewritten as

$$\mathbf{x} = (\mathbf{I} - \mathbf{B})^{-1} \mathbf{e} = \mathbf{A}\mathbf{e}, \quad (5)$$

meaning that the observation vector \mathbf{x} is an instantaneous mixture of the disturbance vector \mathbf{e} . Hence, we can determine the adjacency matrix \mathbf{B} by calculating the mixture matrix \mathbf{A} , which can be done by an Independent Component Analysis (ICA) method [2].

ICA algorithms decompose mixed signals to independent components using the higher-order statistics of signals. Because Gaussian distributions have only up to second-order statistics, we need the assumption of non-Gaussian.

In this paper, the ICA-LiNGAM refers to the method that estimates \mathbf{A} by the FastICA [3] and calculates \mathbf{B} using (5) after an appropriate procedure of permutation and normalization.

3 Results

By applying the data in 2.1 to the SVAR in 2.2 and the ICA-LiNGAM in 2.3, DAGs that expressed causality among the signals A, B and S were given. In Fig. 3, each number followed by a character A, B or S represents the lagged time, i.e., A1 means variable $A(t - 1)$, and the number on each edge is the strength of the causality.

To show the results more clearly, Table 1 shows the causal relationship among the same mode (A, B or S) given by the LiNGAM with $n = 1, 2, 3$, and $k = 3, 4, 5, 6$. In the table, a node (B0 in the first row, for example) causes its right node (B1), and it is red if it follows the time order and blue if it shows the reverse order of time.

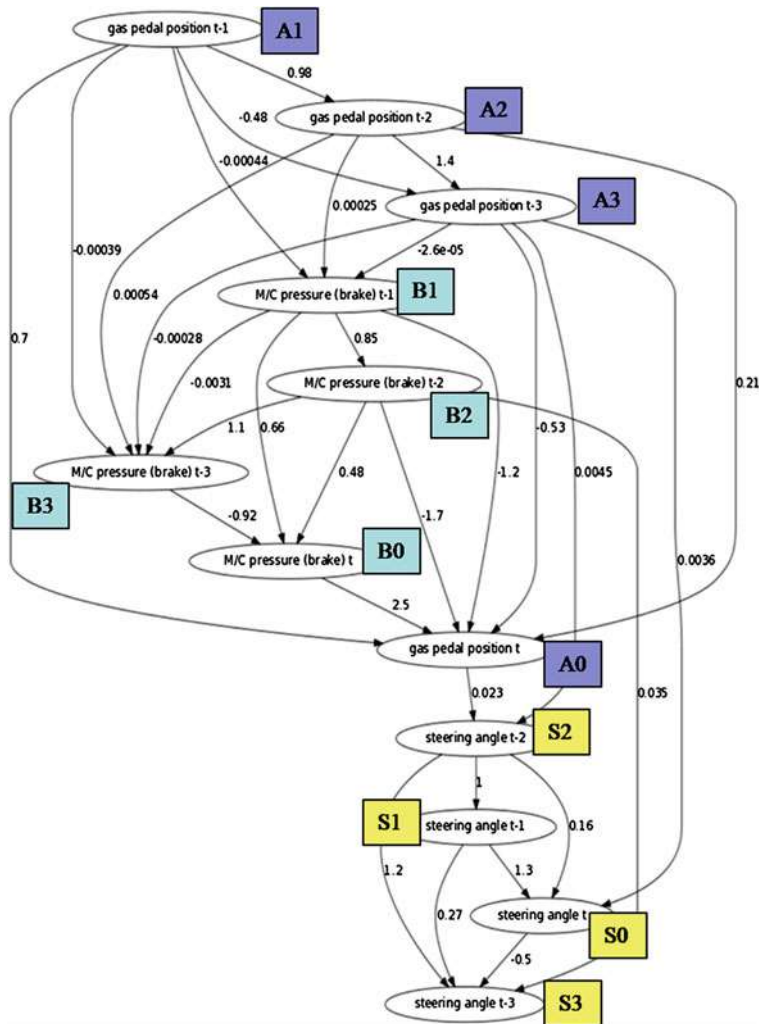


Fig. 3 ICA-LiNGAM experimental data

4 Discussions

Appearing reverse-order sequences in time was also discussed in [1]. This phenomenon often happens in the LiNGAM due to the similarity of the forward and backward sequences. Actually, we can regard both cases as natural causality that A0 causes A1 and that A1 causes A0 by changing our viewpoint.

The results strongly depend on the parameters n and k . For a constant k , a small n led to different causal sequences of A and S from a large n . Because n determines the part of driving actions to be analyzed, a small n extracts only minor details of

Table 1 Grid discovery for ICA-LiNGAM

n1,k3: [B0 B1 B2 B3	, A0 A1 A2 A3	, S1 S0 S2 S3]
n2,k3: [B0 B3 B2 B1	, A3 A2 A1 A0	, S0 S1 S2 S3]
n3,k3: [B0 B3 B2 B1	, A3 A2 A1 A0	, S0 S1 S2 S3]
n1,k4: [B0 B1 B2 B3 B4	, A0 A1 A2 A3 A4	, S2 S1 S0 S3 S4]
n2,k4: [B0 B4 B3 B2 B1	, A4 A3 A2 A1 A0	, S0 S1 S2 S3 S4]
n3,k4: [B0 B1 B2 B3 B4	, A4 A3 A2 A1 A0	, S0 S1 S2 S3 S4]
n1,k5: [B0 B1 B2 B3 B4 B5	, A0 A1 A2 A3 A4 A5	, S3 S4 S2 S1 S0 S5]
n2,k5: [B0 B5 B4 B3 B2 B1	, A5 A4 A3 A2 A1 A0	, S0 S1 S2 S3 S4 S5]
n3,k5: [B0 B1 B2 B4 B4 B5	, A5 A4 A3 A2 A1 A0	, S0 S1 S2 S3 S4 S5]
n1,k6: [B0 B1 B2 B3 B4 B5 B6 , A0 A1 A2 A3 A4 A5 A6 , S2 S1 S0 S5 S4 S3 S6]			
n2,k6: [B6 B0 B1 B2 B3 B4 B5 , A6 A5 A4 A3 A2 A1 A0 , S0 S1 S2 S3 S4 S5 S6]			
n3,k6: [B0 B1 B2 B3 B4 B5 B6 , A6 A5 A4 A3 A2 A1 A0 , S0 S1 S2 S3 S4 S5 S6]			

the actions and cannot find a global structure. As k increases, the number of nodes also increases that makes our analysis difficult. In fact, we can find no special meaning in a huge DAG because it is too complicated. The parameters should be chosen appropriately and more intensive experiments are necessary.

One problem of our method, the ICA-LiNGAM is lack of global optimality. In our simulation, we chose appropriate initial values using prior knowledge and heuristics. However, this is not applicable to less informative cases in the future. An alternative is the direct estimation method for LiNGAM model (DirectLiNGAM) that uses exogenous variables [10]. The Direct LiNGAM is guaranteed its convergence with fixed steps.

5 Conclusions

We presented a causal discovery method based on a linear non-Gaussian acyclic model and applied it to real driving data. To make it applicable, we introduced a preprocessing method called the SVAR that reduces dependency of signals in time. The results showed this method is effective to extract causality in the data but time-order is not necessarily determined.

References

- Shimizu S, Shimizu S, Hoyer PO, Hyvärinen A, Kerminen AJ (2006) A linear non-gaussian acyclic model for causal discovery. *J Mach Learn Res* 7:2003–2030
- Hyvärinen A, Oja E (2000) Independent component analysis: algorithms and applications. *Neural Netw* 13(4–5):411–430

3. Hyvärinen A, Karhunen J, Oja E (2001) Independent component analysis. John Wiley & Sons, New York
4. Shimizu S, Hyvärinen A, Kano Y, Hoyer PO (2005) Discovery of non-gaussian linear causal models using ICA. In: Proceeding of the 21st conference on uncertainty in artificial intelligence (UAI-2005), 2005, pp 526–533
5. Hyvärinen A, Zhang K, Shimizu S, Hoyer PO (2010) Estimation of a structural vector autoregression model using non-gaussianity. *J Mach Learn Res* 11(May):1709–1731
6. Mima H, Ikeda K, Shibata T, Fukaya N, Hitomi K, Bando T (2009) Estimation of driving phase by modeling brake pressure signals. In: Proceedings of international conference on neural information processing (ICONIP), Bangkok, Thailand, LNCS 5863, Springer, 2009, pp 468–475
7. Bollen KA (1989) Structural equations with latent variables. John Wiley & Sons, New York
8. Pearl J (2000) Causality: model, reasoning, and inference. Cambridge University Press, Cambridge
9. Spirtes P, Glymour C, Scheines R (2001) Causation, prediction, and search. The MIT Press, USA
10. Shimizu S, Inazumi T, Sogawa Y, Hyvärinen A, Kawahara Y, Washio T, Hoyer PO, Bollen K (2011) Direct LiNGAM: a direct method for learning a linear non-gaussian structural equation model. *J Mach Learn Res* 12: 1225–1248

euroFOT: Field Operational Test and Impact Assessment of Advanced Driver Assistance Systems: Final Results

Mohamed Benmimoun, Andreas Pütz, Adrian Zlocki
and Lutz Eckstein

Abstract Within the first European large scale field operational test euroFOT the effects of eight different Advanced Driver Assistance Systems (ADAS) were investigated. About 1,000 vehicles equipped with different ADAS were used. The Institute of Automotive Engineering (ika) of the RWTH Aachen University analysed the effects of ACC usage in combination with FCW under normal driving conditions of 100 passenger cars. The results of the data analysis show positive effects on traffic safety and fuel consumption. In addition, the complete process chain from the data collection to the analysis was defined and conducted at the ika.

Keywords Advanced driver assistance systems · Driver behaviour · Active safety · Impact assessment · Field operational test

1 Introduction

One of the main challenges of road transport is the reduction of fatalities. The worldwide number of fatalities exceeds more 1.2 million per year [1]. To identify possible approaches to improve traffic safety various initiatives were launched in Europe within the last years. One of these approaches is the wide deployment of Advanced Driver Assistance Systems (ADAS).

F2012-F07-012

M. Benmimoun (✉) · A. Pütz · A. Zlocki · L. Eckstein
Institut für Kraftfahrzeuge (ika), RWTH Aachen University, Aachen, Germany

These systems are designed to support drivers in their daily driving routine by increasing driving comfort, safety and efficiency with regard to traffic flow as well as fuel consumption. In addition to different studies [2] Field Operational Tests (FOT) were conducted within the last few years that aim to investigate short- and long-term effects of ADAS under normal driving conditions. The first large-scale FOT for investigating effects of ADAS was started within the seventh framework program of the European Commission. Objective of the euroFOT project was to assess the impacts of eight different ADAS with regard to driver acceptance, traffic safety and efficiency as well as fuel consumption. All tested functions are in production and are integrated as such in the vehicles. Overall, about 1,000 vehicles were used for data collection in the project.

This paper presents the results of the conducted analysis of the collected data of 100 passenger cars equipped with an Adaptive Cruise Control (ACC) and a Forward Collision Warning (FCW) function.

2 State of the Art

Field operational tests belong to experiments under realistic settings and are an important method to assess the impact of ADAS because of low controlling factors. This allows investigating the naturalistic driving behaviour under real driving conditions which is highly important for the assessment of ADAS. Based on the collected data the analysis answers predefined research questions to assess the impact. To gather a sufficient amount of data, an experiment duration of several months is necessary.

In the U.S. large-scale FOTs are used as an evaluation method since 1996 [3]. In addition to FOTs of Intelligent Speed Adaptation Systems (ISA) [4], Forwards Collision Warning (FCW) [5], Lane Departure Warning (LDW) [6], Adaptive Cruise Control (ACC) [7], and naturalistic driving studies were conducted [8].

Also in Europe a growing number of large-scale FOTs can be observed. First activities were started on a national level and afterwards extended to cooperative projects between different partners in the European Union (e.g. euroFOT). The following table highlights some of the conducted FOTs in Europe and the US (Fig. 1).

The first large-scale FOTs were carried out in Sweden (1999) [4] and Great Britain (2000) [9] and focused on the safety potential of Intelligent Speed Adaptation (ISA). On European level the TeleFOT [10] started at the same time as the euroFOT project.

3 Methodology

In the following, the analysis approach for the ACC and FCW used in euroFOT is presented. To that end, first the defined experimental design of both systems is described and afterwards the data analysis approach of the collected data is given.

	Tested Systems	Number of vehicles	Number of participants	Duration [Months]	Mileage [km]
NHTSA ICC FOT (1996 – 1998)	ICC	10	108	13	108,000
VOLVO IVI FOT (2001 – 2004)	ACC, CWS, AdvBS	100	> 1000	> 24	16,300,000
ACAS FOT (2003 – 2004)	ACC, FCW	14	66	9	158,000
Mack IVI FOT (2004 – 2005)	LDW	22	31	12	1,400,000
IVBSS FOT (2008 – 2010)	FCW, LDW, CSW, LCM	26	108	10	1,394,000
ISA Sweden (1999 – 2002)	ISA	5000	10,000	12	75,000,000
ISA GB (2001 – 2008)	ISA	20	20	5	570,000
The assisted driver (2006 – 2007)	ACC, LDW	20	20	5	n.a.
SeMiFOT (2008 – 2009)	ACC, FCW, LDW, BLIS	14	39	6	171,440
euroFOT (2008 – 2012)	ACC, CSW, FCW, LDW, SRS, BLIS, FEA, IW	971	1038	12	34,868,000
TeleFOT (2008 – 2012)	NAV, SL, SA, SC, GD, TI, eCall, FCW, ACC, LKA, LDW	n.a.	2986	12	n.a.

AdvBS: Advanced Braking System, CWS: Collision Warning System, CSW: Curve Speed Warning, GD: Green Driving, FEA: Fuel Efficiency Advisor, IW: Impairment Warning, ICC: Intelligent Cruise Control, ISA: Intelligent Speed Adaptation, LCM: Lane Change Merge, LKA: Lane Keeping Assist, NAV: Navigation System, SA: Speed Alert, SC: Speed Camera, SL: Speed Limiter, SRS: Speed Regulation System, TI: Traffic Information

Fig. 1 Overview of FOTs in Europe and the US

3.1 Experimental Design

The participants of the FOT are non-professional drivers that were recruited by different car dealerships in Germany. They were contacted by the dealerships after buying a vehicle of the specific manufacturer equipped with ACC and FCW. To collect all relevant data (CAN data and GPS data) data loggers were installed in all 100 vehicles. The data loggers are able to record, temporarily store and transmit the data afterwards to a centralised server system. Overall, about 100 CAN signals were recorded. In addition to dynamic measures (velocity, acceleration, yaw rate, steering angle, wheel speed etc.) status information of different systems were considered (e.g. state of turn indicator, wiper, ADAS). To avoid modifications of the customers' vehicles and influences to the driving behaviour no additional data sources like video systems were used.

For the impact assessment it is necessary to assess also trips without the influence of the system as a reference (baseline) besides trips with activated system (treatment). The comparison of the collected data in both phases (baseline/treatment) forms the basis for the assessment of the systems' impact. Based on

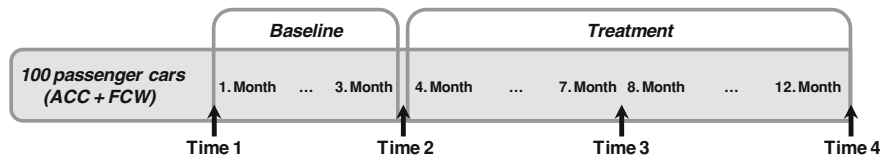


Fig. 2 Experimental design for the vehicle fleet of 100 passenger cars

these research questions hypotheses to be tested (e.g. ACC decreases the number of incidents) have been defined. By means of the hypotheses the required signals and data sources for data collection have been identified.

The experimental duration of the FOT for the vehicle fleet of 100 passenger cars was twelve months of which the first three months served as a baseline. During this baseline period the ADAS were not available and the naturalistic driving behaviour of the participants was analysed. In the following treatment period the systems were activated and the drivers were free to use the systems as desired. Neither further instructions were given to the drivers nor were they accompanied by a supervisor. Drivers used the vehicles in their daily routine (e.g. way to work). The experimental design for the 100 passenger cars is shown in Fig. 2.

In addition to the selection of relevant driving scenarios (e.g. incidents, lane change manoeuvres) different indicators are necessary for the impact analysis. Especially for the hypothesis testing the so called performance indicators (e.g. number of harsh braking events, average speed) are required for the statistical analysis. Moreover, so called situational variables such as weather conditions or road type are relevant for the hypothesis testing in order to ensure that the comparison of baseline and treatment is done under similar circumstances to avoid influences from external effects.

Furthermore subjective data is collected by means of four time-based (Time 1 to Time 4) questionnaires to analyse the effect on user acceptance. The first two questionnaires (Time 1 and 2, see Fig. 2) were spread during the baseline phase. The remaining questionnaires (Time 3 and 4) were distributed at half-time and at the end of the treatment phase.

3.2 Data Analysis

The required signals were recorded with defined sampling rate. By means of the installed data loggers the collected data were transmitted wirelessly to the centralised server system at the ika (see Fig. 3). After the successful transmission of the data to the server (within the data management) the data processing is conducted. Firstly, the data quality analysis includes the assessment of missing data parts and plausibility checks of the recorded signals. In a second step, the gathered data was enriched with map attributes (e.g. road type, speed limits) from

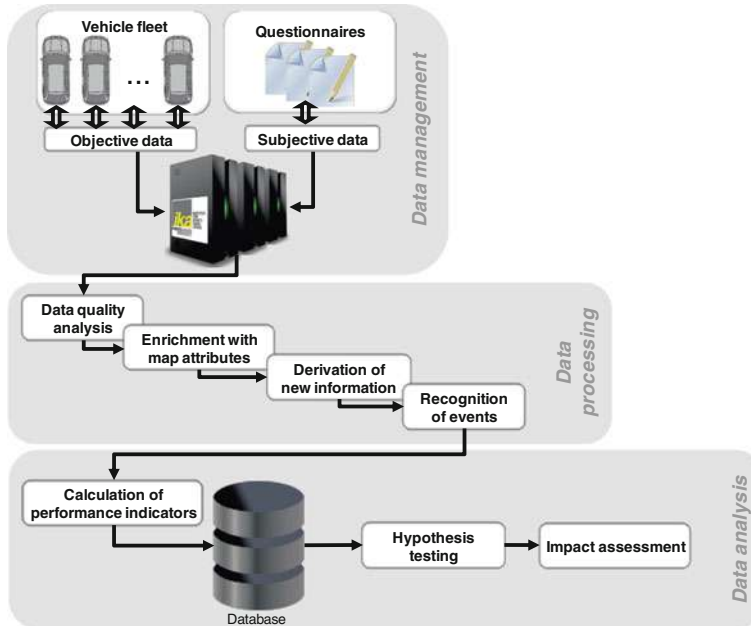


Fig. 3 Processing steps between data collection and impact assessment

a digital map based on the recorded GPS information. Afterwards, additional information (e.g. time-headway, Time-to-Collision (TTC), average speed) was calculated from the collected data. Finally, situational variables and relevant driving events were identified by means of an automated recognition process [11].

The data analysis starts with the calculation of the performance indicators that are necessary for the hypothesis testing. Afterwards, the processed data was stored on a database, which served as a basis for the data analysis. The results of the hypothesis testing were used as input for the impact assessment.

The processing of the raw data led to an increase in the data amount due to the enrichment and derivation process. Overall, about 1 TB of data is available for the impact assessment, see Fig. 4.

4 Results of the Impact Assessment

The magnitude and the experimental set-up of the conducted FOT allow detailed insights into various aspects of the daily use of ACC and FCW by normal customers. In the following some of the main outcomes of the conducted statistical analysis are presented. Thereby, the analysis focuses on changes in traffic safety, driver behaviour and environment while driving on motorways.

	<i>Mileage [km]</i>	<i>Number of drivers</i>	<i>Number of trips</i>	<i>Data amount</i>
Raw data	1,954,329	98	144,280	493 GB*
Data processing	1,954,329	98	144,280	990 GB
Impact assessment				
<i>Baseline</i>	233,071	84	6048	100 GB
<i>Treatment</i>	747,296	84	18,268	293 GB

* compressed

Fig. 4 Overview of data amount

4.1 Safety

The combination of ACC and FCW show a positive impact on driving safety. While there was no decrease in average speed (an indicator previously linked to increase in safety [12]), the average time-headway (THW) shows an increase of about 16 % (see Fig. 1) and leads therefore to larger/greater safety margins. Due to the predefined settings of the ACC time-headway the number of (intended or unintended) close approaching manoeuvres is highly reduced and prevents therefore critical driving situations. The analysis of critical time-headways (<0.5 s) reveals a reduction of 73 % on motorways. As a consequence of the safer distance behaviour the frequency of harsh braking manoeuvres is lower when driving with active ACC. Two out of three harsh braking events (67 %) can be avoided by the use of ACC. Like for the harsh braking events the number of incidents is lower when using ACC and FCW. The incidents based on vehicle kinematics show more than 80 % reduction. Details on the incident definition can be found in [13] (Fig. 5).

Explanations for the increase in average time-headway and the reduction of critical time-headways, harsh braking events and incidents can be found in the selectable ACC settings that can never be lower than the legally prescribed value which is not always considered by drivers in their normal driving behaviour. Resulting from the increase in average time-headway the reaction time to avoid (unintended) close approaching events is higher. If the driving situation exceeds the braking capacities of the ACC because of a highly decelerating vehicle in front, the presented warnings (by the ACC and FCW) give the driver appropriate time to react on the driving situation. It could be shown in the analysis that this effect can be mainly attributed to the ACC by comparing situations where only one of the functions was active (Fig. 6).

In phases of active ACC (independent on the FCW status) a significant decrease of harsh braking events was observed. In case of deactivated ACC and activated FCW no such effect could be shown. To specify the contribution of each individual function the change in issued FCW warnings was investigated. To that end, it can be seen in Fig. 7 that the highest reduction during the treatment period was found

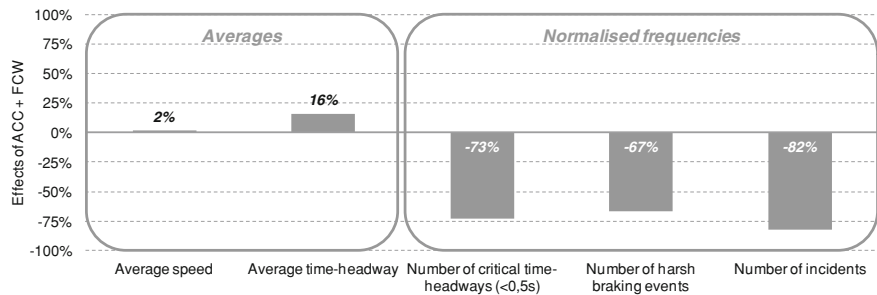


Fig. 5 Overview of safety indicators for driving with active ACC and FCW on motorways

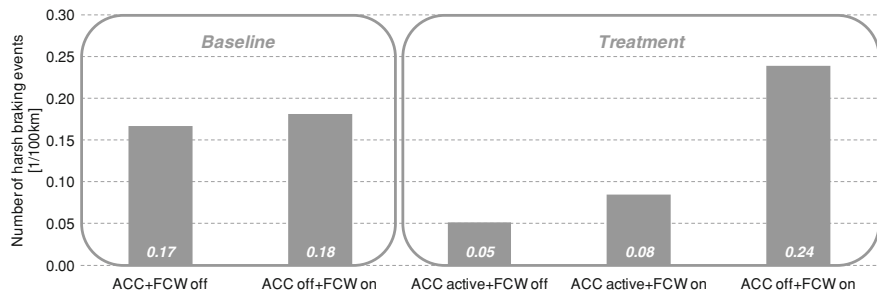


Fig. 6 Number of harsh braking events within different experimental phases

in phases when the ACC was active. The number of warnings was significantly decreased by about 80 %.

4.2 User Behaviour

ACC related changes in the driving behaviour can be deduced from the same performance indicators that are associated with safety. Those are mainly based on objective data and indicate especially a safe distance behaviour which leads to safety benefits. Additionally, the questionnaire data indicates that the expectations of drivers to the ACC are fulfilled, i.e. the scores on satisfaction and usefulness that drivers gave before gaining access to the systems match those given during and after the trial. In Fig. 8 it can be seen that the acceptance rating on the Van der Laan scale (scaling from -2 to +2) shows low variation.

The acceptance is based on the average of the questionnaire items related to satisfaction and usefulness. In terms of usage, drivers mainly use ACC on motorways. Here, the proportion of kilometres driven with active ACC reaches almost 50 %. The increase in the usage frequency can be confirmed by evaluating the travel time and distance with and without active ACC. Comparing the first

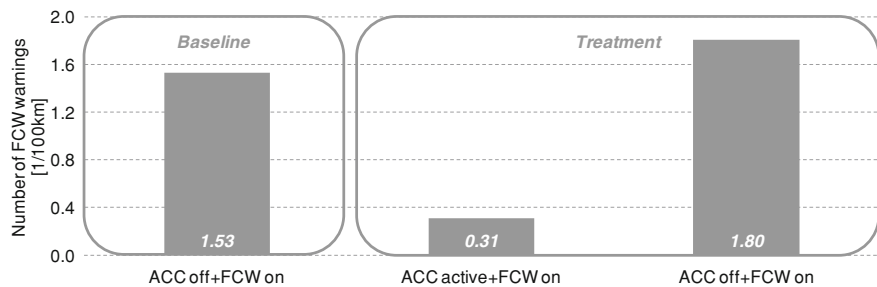


Fig. 7 Number of FCW warnings in different experimental phases

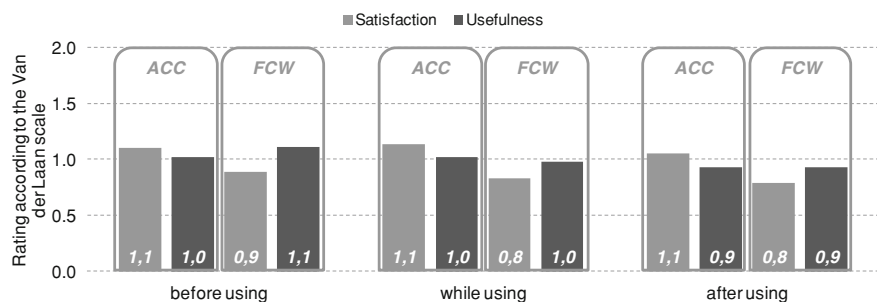


Fig. 8 Acceptance rating for ACC and FCW

months to the last months of the FOT there is a significant increase of ACC usage in terms of travel time with active ACC (31 %) and frequency of ACC activations (53 %). The drivers seem to get used to the positive perception of the ACC and use the system longer and more often over time even though they do not indicate a change in their usage behaviour within the questionnaires. This increased use of ACC is in line with the perceived increase of safety and comfort which is self-reported by the drivers. In contrast, self-reported ratings on trust do not change over time and thus do not reflect the positive perception related to safety and comfort. Confidence which is a sub-criterion of trust even decreased thus expressing that the drivers had higher expectations than the system could fulfil.

The majority of the drivers (close to 70 %) perceive the FCW as safety increasing and most helpful on motorways in normal traffic conditions. The ratings on satisfaction and usefulness remain high throughout the study, but are in general slightly lower than those of ACC. The slight decrease in the ratings can be interpreted by high expectations of the drivers at the project start. In addition, drivers are not uniformly positive to the investigated FCW's audio-visual interface. Some reported that they perceive the timing of the warnings as to early and therefore annoying. This can be attributed to varying individual comfort zones in

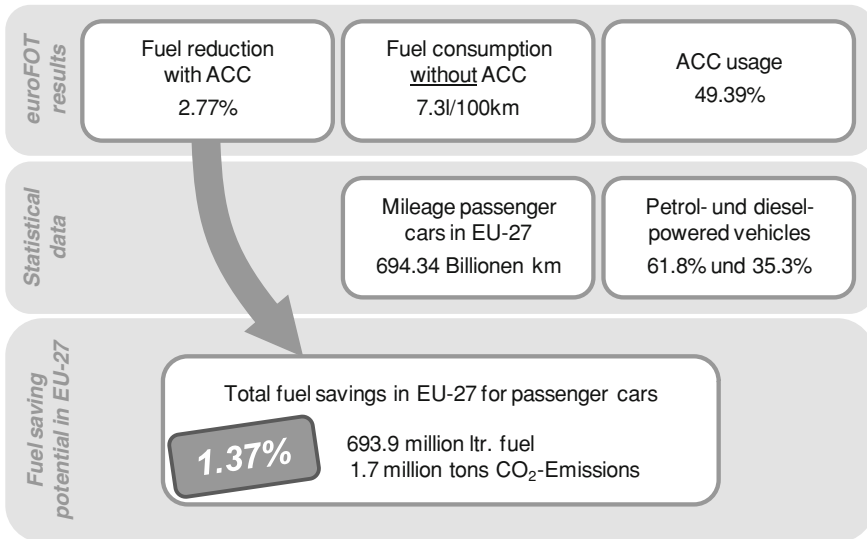


Fig. 9 Fuel saving potential of ACC for driving on motorways

terms of following distances and reinforces the need for investigating new and creative ways of offering individual adaptations possibilities. Acceptance is a key parameter for the effectiveness of ADAS since unsatisfied drivers tend to switch off the system and therefore no benefit can be achieved.

4.3 Fuel Consumption

Based on a lower variation in speed when driving with active ACC, it is hypothesised that there are also positive effects on environment in terms of fuel consumption and CO₂ emission. The analysis of the fuel consumption shows a significant reduction of 2.77 % while driving on motorways. This system related change in fuel consumption and the measured average fuel consumption of 7.3 l/100 km is combined with the usage rate of 49.4 % that is reached during the FOT on motorways and projected to the EU-27 level (see Fig. 9).

For the European passenger car fleet which consists of approximately 62 % petrol and 35 % diesel powered vehicles the overall fuel saving potential of 1.37 % accounts for almost 700 million litres of fuel every year and 1.7 million tons of CO₂ based on the average fuel consumption that is evaluated with the objective data. The statistical data on the total mileage of passenger cars and the fleet composition can be found in [14] and [15].

5 Conclusions and Recommendations

During the euroFOT project data of about 1,000 vehicles was collected. With the help of the gathered data the impact of eight different ADAS was evaluated. The analysis of the effects of ACC and FCW usage showed positive effects on traffic safety, driver behaviour and driver acceptance as well as fuel consumption.

The relevant factor for the reduction in harsh braking events, incidents etc. can be attributed to changed distance behaviour. The analysis shows that the average time-headway was increased at about 16 %. In addition to the usage rate of 50 % the analysis of acceptance rating revealed a positive perception of the ACC and FCW. Furthermore, a reduction in fuel consumption of 2.8 % was observed which results in less CO₂ emissions.

Based on the gathered insights with regards to how drivers use the systems valuable input for the various stakeholders (suppliers, vehicle manufacturers, and research institutes) for improving system design and promoting product development is provided. Moreover the positive results are a powerful tool to raise public awareness about the potential of ADAS. These will provide further impulses for consideration of ADAS in the customer's purchase decision. By means of increased penetration rates a major contribution for improving traffic safety can be achieved.

References

1. NN (2012) 2nd Global Status Report On Road Safety. Weltgesundheitsorganisation (WHO)
2. NN (2010) Was leisten Fahrerassistenzsysteme?. Deutscher Verkehrssicherheitsrat e.V., Bonn
3. Koziol J, Inman V, Carter M et al (1999) Evaluation of the intelligent cruise control system volume I—study results. US Department of Transportation National, Oct 1999
4. NN (2002) Results of the world's largest ISA trial. Swedish National Road Administration
5. Sayer JR, LeBlanc D, Bogard S et al (2011) Integrated vehicle-based safety systems field operational test final program report. US Department of Transportation National, June 2011
6. Alkim T, Bootsma G, Looman P (2007) Roads to the future—the assisted driver. Rijkswaterstaat, Roads to the Future, April 2007
7. Sayer J, LeBlanc D, Bogard S et al (2005) Automotive collision avoidance system field operational test, Report: Methodology and Results. US Department of Transportation, Aug 2005
8. Neale LV, Dingus TA, Klauer SG, Sudweeks J (2005) An overview of the 100-car naturalistic study and findings. In: 19th international technical conference on the enhanced safety of vehicles (ESV), June 2005
9. Lai F, Chorlton K, Carsten O (2007) ISA-UK—overall field trial results. University of Leeds, Feb 2007
10. Will D, Zlocki A, Eckstein L (2012) Detailed FOT for the analysis of effects between nomadic devices and ADAS. Transport Research Arena
11. Benmimoun M, Fahrenkrog F, Benmimoun A (2010) Automatisierte Situationserkennung zur Bewertung des Potentials von Fahrerassistenzsystemen im Rahmen des Feldversuchs euroFOT. VDI/VW-Gemeinschaftstagung Fahrerassistenz und Integrierte Sicherheit, Wolfsburg
12. Nilsson G (1981) The effects of speed limits on traffic accidents in Sweden. In: International symposium on the effects of speed limits on traffic crashes and fuel consumption proceedings, 1981

13. Benmimoun M et al (2011) Incident detection based on vehicle CAN-data within the large scale field operational test "euroFOT". In: 22nd enhanced safety of vehicles conference, Washington, 2011
14. NN (2010) EU energy and transport, Statistical pocketbook 2010. Europäische Kommission
15. NN (2011) The automobile industry, Pocket Guide 2011. European Automobile Manufacturers' Association (ACEA), Brussels

A New Risk Evaluation Index for Rear-End Collisions Considering Drivers' Risk Perception

Hui Zhang, ShaoBo Qiu, Hongjian Li and Bin Liu

Abstract Rear-end collision is a main type of traffic accidents. In this study, we divided collision risks of car-following cases into three types, potential risk, obvious risk, and driver's subjective risk perception. We designed different experiments to examine performance and parameters of six collision risk judgment indices which have been proposed (e.g. TTC, THW) in the paper under these three types of collision risks. On that basis, we developed a new risk index and called it as "Driver Risk Perception".

Keywords Rear-end collisions · Risk judgment indices · Risk perception · Driver · Safety

1 Introduction

Vehicle collision avoidance technology is an important research area of vehicle safety. From the results of traffic accident analysis, rear-end collision is one of the main types. In order to decrease the number of rear-end collisions, lots of automobile factories focus on development of rear-end collision avoidance system. Collision avoidance system usually uses relative distance, relative speed, or relative deceleration as factors of indices to judge levels of collision risk. TTC is the main risk index used in FAW's systems, but when relative speed is so small, it can not correctly evaluate risk.

F2012-F07-023

H. Zhang (✉) · S. Qiu · H. Li · B. Liu
R&D Center, FAW, Changchun, China

Drivers judge and operate vehicle on the basis of their perception of external surroundings. It means that considering drivers' risk perception is necessary for accomplishing collision avoidance function. Risk perception is psychological metrics, what vehicle parameters will have directly relationship with drivers' risk perception is an important issue.

In this study, we divided drivers' risk perception into three types, potential risk, obvious risk, and driver's subjective risk perception. Potential risk means that relative velocity between following vehicle and preceding vehicle is zero; obvious risk means that the collision risk owing to deceleration of the preceding vehicle; driver's subjective risk perception means that the collision risk owing to acceleration of the following vehicle. First, we analyzed the parameters of six collision risk judgment indices (e.g., time to collision (TTC), time headway (THW) and so on) under different types of drivers' risk perception by using a simple computer car-following simulation. Then, we developed a new index based on the result from the first step, and it is called as "Driver Risk Perception (DRP)". We compared the DRP with TTC. The results indicated that DRP can evaluate each type risk.

2 Indices Analysis

2.1 Definition of Indices

- (1) Time Headway (THW) is an index describing predicted time of following vehicle with current velocity up to the current position of preceding vehicle.
- (2) Time to Collision (TTC) is an index representing predicted time to collision with preceding vehicle on an assumption that current relative velocity is maintained [1].
- (3) $1/TTC$ is the inverse of TTC depicting time rate of change of visual angle to preceding vehicle that is equivalent to driver's braking behavior [2].
- (4) KdB is defined based on assumption that acceleration and deceleration of preceding vehicle is equivalent with varied area of preceding vehicle reflected into driver's eye. When relative distance between following vehicle and preceding vehicle is 100 m and relative velocity is -0.1 km/h , KdB is 0 dB [3].
- (5) Risk Perception (RP) is a combined equation of $1/TTC$ and inverse of THW [4].
- (6) Margin-To-Collision (MTC) is an index defined by a ratio of the summation of relative distance and stopping distance of preceding vehicle divided by stopping distance of following vehicle. The index also represents the possibility of collision in a case where preceding vehicle and following vehicle decelerate abruptly at the same time (the abrupt deceleration is assumed to be 0.7 [G] ($= 6.9 \text{ [m/s}^2]$) [5] (Tables 1 and 2).

2.2 Experiment Method

In this experiment, we designed a simple car-following simulation by Matlab to analyze performance of each index under different type of risk conditions (potential risk, obvious risk, and driver's subjective risk perception). The detail of experiment is shown below:

(1) Potential risk condition

The velocities of following vehicle and preceding vehicle were constant velocity, 80 km/h. The relative distance between following vehicle and preceding vehicle was 30 m. The relative velocity between following vehicle and preceding vehicle was 0 km/h. There is a potential risk in this condition. Specifically, when the preceding vehicle decelerates abruptly, the following vehicle (absolute velocity is 80 km/h) can not stops at the back of preceding vehicle because relative distance (30 m) is not enough for stop distance of following vehicle, that is to say, the collision cannot be avoided.

(2) Obvious risk condition

The velocity of following vehicle was 80 km/h. The velocity of preceding vehicle was set at 60 km/h. The velocity of preceding vehicle was set at 60, 80, 100 km/h. The initial relative distance between following vehicle and preceding vehicle was 30 m. In this condition, the velocity of preceding vehicle is smaller than the velocity of following vehicle, so that the following vehicle was closing constantly to preceding vehicle until it crashed into the preceding vehicle and stopped.

(3) Driver's subjective risk perception

The velocity of following vehicle was set at 60, 80, 100 km/h. The velocity of preceding vehicle was set at 40 km/h. The initial relative distance between following vehicle and preceding vehicle was 30 m. In this condition, the following vehicle was closing to preceding vehicle until it crashed into the preceding vehicle and stopped.

2.3 Experiment Results

(1) Potential risk condition

Figure 1 shows the performance of each index under potential risk condition. According to analysis of results, we found that only THW (= 2.7), RP (= 0.37), MTC (= 4.33) can evaluate potential collision risk, while TTC, 1/TTC, KdB can

Table 1 Interpretation of parameter used in indices

	Parameter	Unit
V _p	Velocity of preceding vehicle	km/h
V _f	Velocity of following vehicle	km/h
a _p	Acceleration of preceding vehicle	m/s ²
a _f	Acceleration of following vehicle	m/s ²
V _r	Relative velocity(= V _f -V _p)	km/h
a _r	Relative acceleration (= a _f -a _p)	m
P _p	Position of preceding vehicle	m
P _f	Position of following vehicle	m
D	Relative distance(= P _f -P _p)	
μ	Friction factor (= 0.7)	

Table 2 Equation of each index

Index	Equation
THW	THW = D/V _f
TTC	TTC = D/V _r
TTC ⁻¹	TTC ⁻¹ = V _r /D = 1/dt(dθ/θ) = 1/dt(ln D)
KdB	KdB = 10log ₁₀ -2V _r /D ³ _{5×10⁻⁸}
RP	RF = 5/TTC + 1/THW
MTC	MTC = (D + V _p ² /19.6 × μ)/(V _f ² /19.6 × μ)

not. Analyzing the parameters of THW, RP, MTC, we found that equations of them include the velocity of the following vehicle.

(2) Obvious risk condition

Figure 2 shows results of each index when changing the velocity of preceding vehicle. The results indicated that except THW, other indices can evaluate the collision risk under obvious risk condition. To compare the range of variation owing to different velocity of preceding vehicle, we found that the variation of the value of TTC and MTC are obvious than other indices.

(3) Driver's subjective risk perception

Figure 3 shows results of each index under driver's subjective risk perception condition. The results indicated that each index can evaluate the collision risk owing to the variation of velocity of the following vehicle. Changing the velocity of following vehicle, the relative velocity is also varied, so that the indices which equations include relative velocity are varied following by variation of the velocity of following vehicle. However, comparing with the results of obvious risk condition, the variations of RP and MTC in the results of driver's subjective risk perception condition are significant, while the variations of TTC, 1/TTC, KdB are not evident.

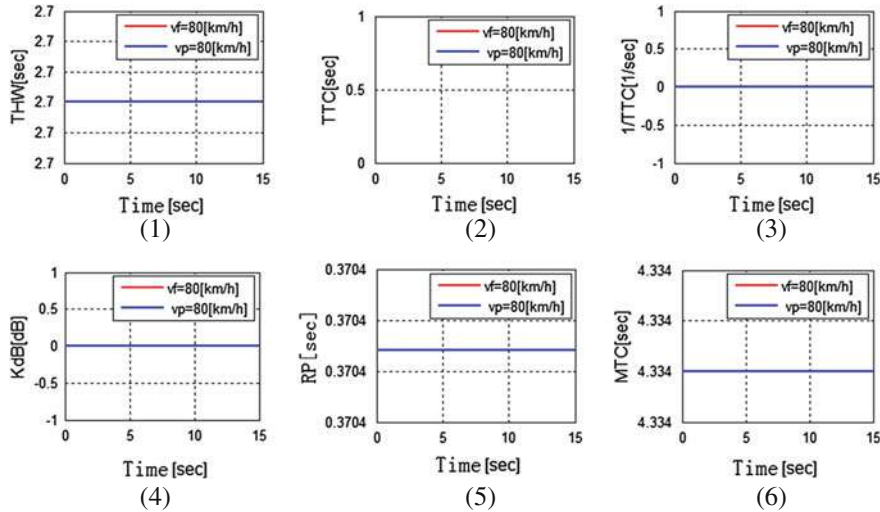


Fig. 1 Results under potential risk condition

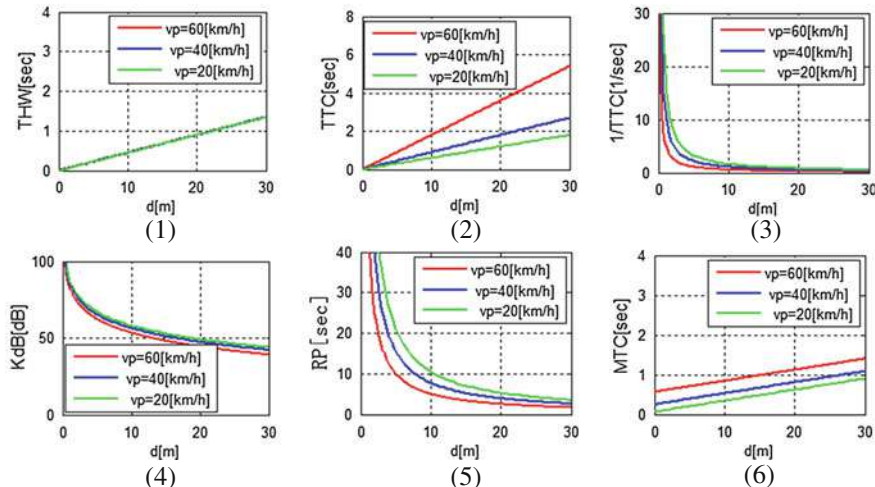


Fig. 2 Results under obvious risk condition

3 A New Index of Driver Risk Perception

3.1 Index Definition

According to analysis the performance of indices under different risk conditions (potential risk, obvious risk, and driver's subjective risk perception), we found that most indices use relative distance, relative velocity to evaluate collision risk, e.g.

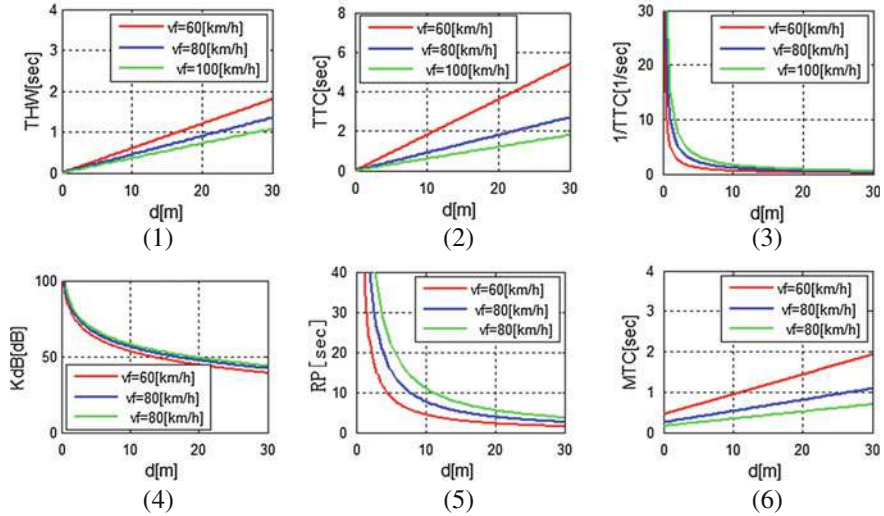


Fig. 3 Results under driver's subjective risk perception

TTC, 1/TTC, KdB, when relative velocity becomes zero, they cannot evaluate the difference of collision risk of long and short relative distance, in other words, they cannot evaluate potential risk. However, the indices which using the velocity of the following vehicle in their equations can evaluate potential risk, e.g. THW, RP, MTC. It indicated that the velocity of the following vehicle is effective to evaluate potential risk in car-following case.

When changing the velocity of following vehicle, all indices are useful to evaluate the obvious risk and the driver's risk perception. When changing the velocity of preceding vehicle, the THW lost its efficacy, the indices which including relative velocity are useful to evaluate the obvious risk and the driver's risk perception. It indicated that the magnitude of velocity of preceding vehicle affects risk level. In addition, considering from the view of optic flow, the risk perception will become stronger not only because of acceleration of following vehicle [4], but also as a result of deceleration of preceding vehicle.

RP includes the velocity of following vehicle, however it not consider influence of velocity of the preceding vehicle to drivers' risk perception.

MTC includes velocities of the following vehicle and the preceding vehicle, however this index is calculated not by the current decelerations, but the assumed abrupt decelerations.

On the basis of the view mentioned above, we developed a new index which is combination of velocity of the following vehicle, relative deceleration of the following vehicle and the preceding vehicle, and 1/TTC, we called it as Driver Risk Perception (DRP). Velocity of the following vehicle and relative acceleration of the following vehicle and preceding vehicle express the driver's risk perception due to optic flow, and 1/TTC shows driver's braking action. The equation is shown below:

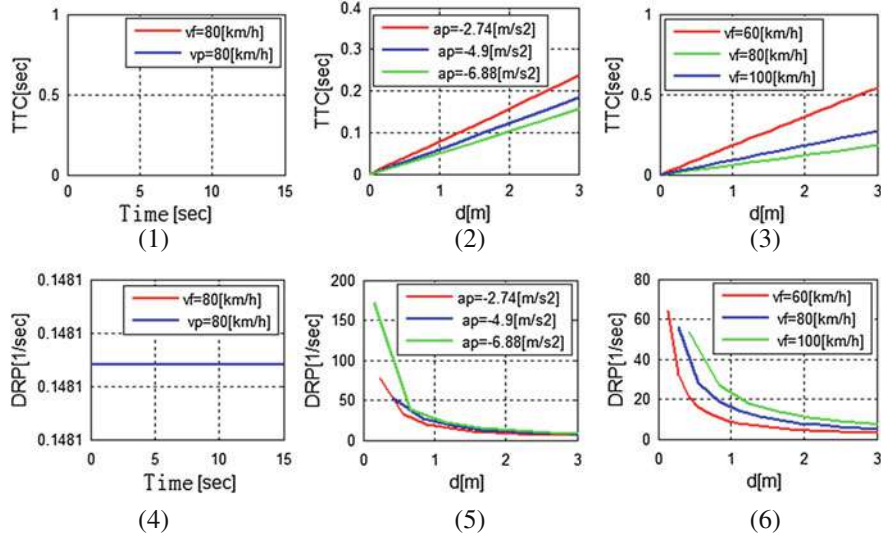


Fig. 4 Comparison of DRP and TTC under different risk conditions. x-axis of (1) and (4) means simulation time. x-axis of (2), (3), (5), (6) shows the distance before crash

$$DRP = \frac{Vr + \alpha Vf + \beta ar}{D} \quad (1)$$

$$\alpha = 0.2; \beta = 1.6$$

3.2 Comparison with Other Indices

In Sect. 2, we analyzed the performance of indices under three types risk conditions (potential risk, obvious risk, and driver's risk perception). In this section, we compared the performance of DRP with conventional index of TTC under those risk conditions.

Figure 4 shows results from comparison of DRP and TTC under three type risk conditions introduced above. The results indicated that DRP can evaluate every risk condition. Moreover, DRP can also evaluate different decelerations of preceding vehicle with different limit values.

4 Conclusion

In this study, we divided risk into three types, potential risk, obvious risk, and driver's subjective risk perception. We designed different experiments to examine performance and parameters of each risk index under three types risk conditions

mentioned above. We found that (1) the index which including speed of following vehicle is better for evaluating potential risk than others; (2) the index which including relative velocity is better for evaluating obvious risk and driver's subjective risk perception; (3) the magnitude of velocity of preceding vehicle also affects intensity of obvious risk. On that basis, we developed a new risk index, and it is called as "Driver Risk Perception (DRP)". We compared DRP with TTC, the results shows DRP is better than TTC in evaluation of collision risk of car-following case.

References

1. Lee DN (1976) A theory of visual control of braking based on information about time-to-collision. *Perception* 5(4):437–459
2. The Vision Society of Japan (2000) Handbook of visual information processing. Asakura Shoten Co., Ltd., Tokyo
3. Tsuru N et al (2006) Emergency evaluation by approaching in longitudinal direction (fourth report). No.116-06, p 7–10
4. Takayuki K et al (2008) Identification of visual cues and quantification of drivers' perception of proximity risk to the lead vehicle in car-following situations. *JMSTL* 1(2):170–180
5. Kitajima S et al (2007) Analysis of mechanism of rear-end collision accident by drive video recorders -analysis of driver's deceleration action using margin to collision (MTC) and investigation of possibility of applying to collision prevention- (in Japanese with English summary). *Trans Soc Autom Eng Jpn* 38(4):191–196

Study on the Highway Vehicle Collision Avoidance and Warning System

Yuncheng Wang, Xie Fei, Jianhua Wang and Xu Hao

Abstract This paper discusses an automotive collision avoidance and warning system based on millimeter-wave radar. With the theory and application research of proactive early-warning and avoidance control, we have established the avoidance control strategy and algorithm. This system can identify the dangerous targets and automatically determine whether the vehicle is in a dangerous condition. According to the level of risk status, it will take appropriate measures such as alarming, decelerating or even automatically braking to reduce the likelihood of rear-end accidents and improve the driving safety on the highway.

Keywords Collision avoidance · Highway · Target detection · Safety distance · Control strategy

1 Introduction

With the continuous development of modern traffic and automotive industry in recent years, the highway construction has developed rapidly. However, the traffic accidents occur more frequently than ever. On the highway, when encounters inclement weather, poor road conditions, traffic congestions or driver fatigue, the car would be prone to occur rear-end collisions, head-on collisions or even serial

F2012-F07-025

Y. Wang (✉) · X. Fei · J. Wang · X. Hao
State Key Laboratory of Automotive Simulation and Control, Jilin University,
Changchun, China

collision accidents. According to the statistics of traffic accidents, two-car rear-end collision accidents account for 65 % and 80 % of traffic accidents could be attributed to drivers' delayed response. Mercedes-Benz had done analysis of various types of accidents, and concluded that if the drivers could respond 0.5 s earlier they would avoid 60 % of rear-end collisions. Besides, 40 % of the side impacts and 30 % of frontal collisions can also be prevented. If they could have more time in advance to take measures, the vast majority of traffic accidents would be effectively prevented [1, 2]. Therefore, the vehicle active anti-collision warning system really has a great significance for the driving safety and it will achieve a broad market prospect.

2 System Components

Vehicle active anti-collision warning system belongs to the context of active safety technology, and it is an auxiliary device to help drivers automatically avoid a car collision [3]. When moving, the vehicle can automatically discover other cars, pedestrians or obstacles which may cause a dangerous threat to the vehicle within the field of vision. When the system has predicted the coming danger, it can remind the driver or automatically control the vehicle to avoid collision accidents. The vehicle active anti-collision warning system has been shown in Fig. 1, including the following sections.

2.1 Information Collection System

Information collection system consists of many sensors that used to obtain the host car speed, the target car speed, relative distance, road conditions and other information. Foremost among those sensors is the target detection device—radar, which now has three major categories widely used by us: ultrasound, optical and electromagnetic. The millimeter-wave radar is the most representative one within the electromagnetic category. The vehicle active anti-collision warning system described in this paper is based on millimeter-wave radar.

2.2 Data Processing System

After having received signals from target detection devices and vehicle sensors, the data processing system would analyze the collected date, and identify or classify the risk of targets. Then, according to the different levels of the dangerous conditions, the system would select the corresponding control strategies and let the appropriate actuators work.

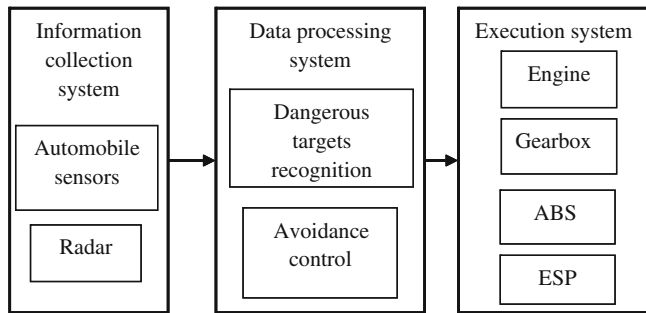


Fig. 1 Vehicle active anti-collision warning system function diagram

2.3 Execution System

The execution system is used to receive control commands produced by the data processing system, then make appropriate actions to achieve the desired effect, and finally complete the corresponding collision avoidance action. Execution System includes the alarm device, deceleration mechanism and brake mechanism. The alarm equipment is installed on the operation panel. The deceleration function is achieved by the control of engine and gears. The brake mechanism includes brake system, ABS and ESP.

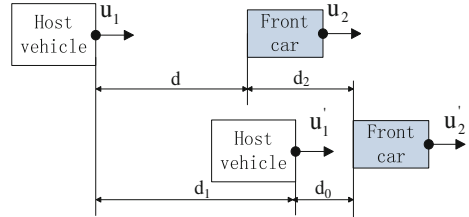
3 Dangerous Targets Recognition and Avoidance Control Strategy

3.1 Safety Distance Model

The total braking distance can be acquired by analyzing the vehicle braking process. Thus, basing on the vehicle safety, the vehicle safety distance model can be established, which helps the driver keep safety distance between vehicles. This paper has analyzed the sports schemes of the front vehicle and the following vehicle when driving [4, 5], and as it is shown in Fig. 2.

The speed of the following vehicle is u_1 , and u_2 represents the front vehicle's speed. The safety distance between the head of the following vehicle and the rear of the front vehicle is d . After t seconds, the speed of the following vehicle will be reduced to u_1' , and cover the distance of d_1 . Simultaneously, the speed of the front vehicle will be reduced to u_2' , and cover d_2 . At this time, the distance between the two vehicles will change to d_0 , which represents the minimum safety distance that should be reserved to guarantee that the two vehicles are out of danger, and we usually set d_0 as 2–5 m. The four distances presented above meet the following equation:

Fig. 2 Moving vehicles spacing diagram



$$d = d_1 - d_2 + d_0 \quad (1)$$

The letter d is used to represent the vehicle safety distance. It varies and means different critical distances in accordance with different situations. We can acquire four different distances according to the safety distance model: Lock-in Target distance D_t , Safety Critical distance D_s , Danger Critical distance D_d and Limited Critical distance D_L . In this paper D_{rel} and V_{rel} respectively represent the actual relative distance and relative speed between the target and the host vehicle.

3.2 Targets Recognition and Classification

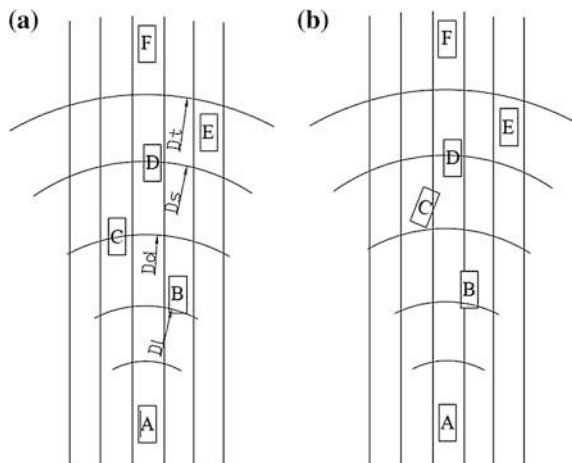
It is critical to identify the threatening targets by analyzing numerous targets information which includes relative distance, relative angle and relative velocity between host vehicle and other targets detected by the radar. The process of targets recognition and classification includes the following two steps. Firstly the lateral spacing distance can be acquired by analyzing the distance and angle between the target and the host vehicle, using it to decide whether the target is in the same lane with the host vehicle. Then, judging by comparing the relative distance, it can decide which type it belongs to within the safety distance model. The targets recognition principle is shown in Fig. 3. In Fig. 3a there appears four targets in the radar's scanning coverage except target F. In this situation, target D is the most dangerous one and we should set it as an important object of judgment. In Fig. 3b as you can see, when target B goes across lane or target C merges lane, there will be three targets that should be judged. And according to the distance priority level, target B is most dangerous. Target E is not dangerous for its lane is far from the host vehicle's lane. From the above analyzing, we should set the targets which are driving in front of the host vehicle in the same lane as threatening targets and set the targets in the adjacent lane as potential threatening targets. The targets apart from the host vehicle's lane are non-threatening targets.

The millimeter wave radar is located in the middle of the host vehicle. Usually the detection range of distance, angle and velocity respectively is 150 m, ± 10 and ± 150 km/h. The width of the lane is a and the width of the vehicle is b . In Fig. 4 if the corresponding parameter of target B is $T_b(R_b, \theta_b, v_{rb})$, the determination criterion for the threatening level can be acquired, as shown in Chart 1.

target type \ target condition	Left targets ($\theta_i < 0$)	Right targets ($\theta_i > 0$)
threatening targets	$R_i \sin(-\theta_i) \leq \frac{a}{2}$	$R_i \sin \theta_i \leq \frac{a}{2}$
potential threatening targets	$\frac{a}{2} < R_i \sin(-\theta_i) \leq a - \frac{b}{2}$	$\frac{a}{2} < R_i \sin \theta_i \leq a - \frac{b}{2}$
non- threatening targets	$R_i \sin(-\theta_i) > a - \frac{b}{2}$	$R_i \sin \theta_i > a - \frac{b}{2}$

Chart 1 The decision condition of the targets' threatening level

Fig. 3 Vehicle driving environment simulation diagram. (a) driving environment 1 (b) driving environment 2

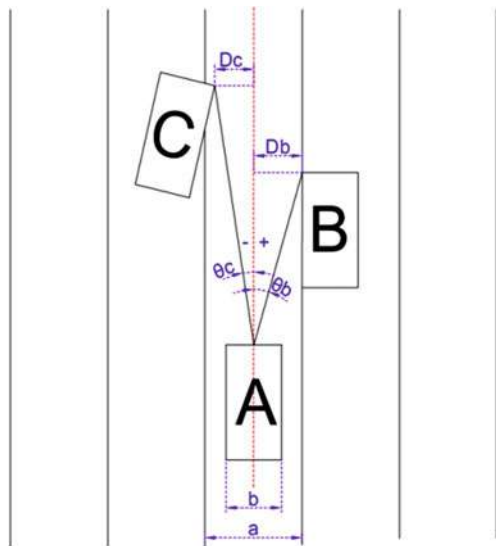


3.3 Avoidance Control Strategy

The avoidance control strategy is designed to avoid traffic accident as the car runs in some driving conditions. The work pattern of the vehicle active anti-collision warning system is decided by the control strategy. Two main control strategies are formulated according to the recognition of the dangerous targets and the difference of different drivers—tend-to-comfort and tend-to-safety.

The road condition is commonly good, and the traffic density is low on the highway. Especially, the drivers who have good driving skill or drive the commercial vehicles should pay attention to both traffic safety and traffic efficiency. So the tend-to-comfort control strategy is put forward. It takes Safety Critical distance, Danger Critical distance and Limited Critical distance as the demarcation points. The specific demarcations are as follows:

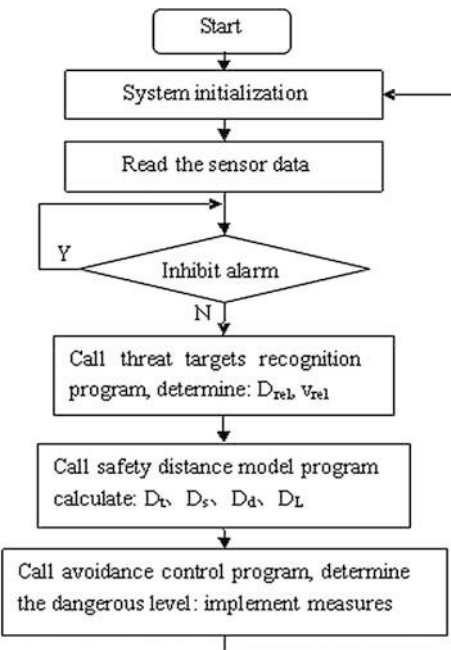
Fig. 4 Targets recognition principle diagram



- (1) When the real relative distance between the car and the threat targets detected by the millimeter wave radar is more than the Safety Critical distance, driving the car is safe, and then the safety control strategy is implemented.
- (2) When the relative distance is between the Safety Critical distance and the Danger Critical distance, the system would remind the drivers to drive carefully with low frequency warning sound of drops. This is alarm control strategy.
- (3) When the distance of threat targets is less than the Danger Critical distance, the threat targets become dangerous ones. The system would remind the drivers to drive slowly with high frequency warning sound of drops and then the car will automatically slows down. This is deceleration control strategy.
- (4) When the relative distance of threat targets is less than the Limited Critical distance, the accident is unavoidable. The system would remind the drivers of emergency braking with high frequency warning sound of drops and then the car will automatically fast increase the braking force until the car is out of danger. This is brake control strategy.

The tend-to-safety control strategy can help the drivers with less experience and common driving skills to keep enough safety distance. This strategy takes the Lock-in Target distance, Safety Critical distance and Danger Critical distance as the demarcation points. The corresponding control strategy can be inferred similarly.

Fig. 5 The main program flow chart



3.4 Avoidance Control Algorithm Process

In order to visualize the working principle of the Vehicle active anti-collision warning system and describe the control process of the avoid controller, here we have designed the control process of the system, including the system main process and avoid control process [6]. Both of them are shown in Figs. 5 and 6. The control logic corresponds to the tend-to- comfort control strategy. And this control algorithm process is formulated on the basis of control strategy.

In the following chart D_r represents for the safe distance between vehicles prescribed by the highway. S_0 , S_1 , S_2 , S_3 are the execution measures correspond to different judgments. They are corresponding to the four control strategies in proper sequence: safety control strategy, alarm control strategy, deceleration control strategy and brake control strategy.

4 Simulation and the Result Analysis

By using MATLAB/Simulink we can set up the vehicle model, targets model, safety distance model and the avoidance controller model. The simulation analysis is used for several typical riding conditions. The simulation results are shown in

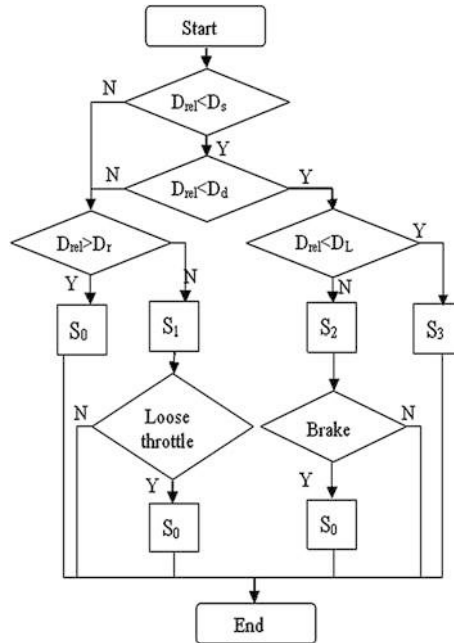


Fig. 6 Avoid control program flow chart

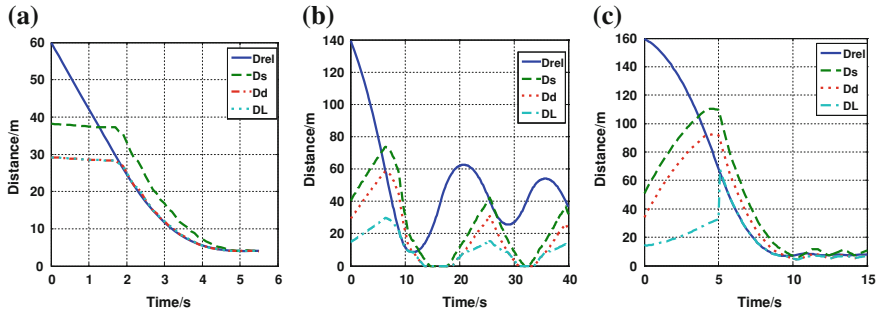


Fig. 7 Simulation results of three conditions (a) static targets (b) low-speed targets (c) deceleration targets

Fig. 7a–c respectively represent for riding conditions of static targets, low-speed targets and deceleration targets.

During all the three working conditions, the drivers don't need to handle the vehicle. By comparing the results of actual distance D_{rel} with D_s , D_d and D_L , we conclude that the actual distance is almost in the safe range, and is lower than safe distance only in some short time, but not lower than limited distance, so the host vehicle can get rid of the dangerous conditions and make sure the collision accident won't appear.

5 Conclusion

Considering the composition of the vehicle active anti-collision warning system, this paper focused on the study of avoidance control. It has formulated the dangerous targets recognition algorithm, and divided the targets into non-threatening targets, potential threatening targets and threatening targets. Two avoidance control strategies of tend-to-comfort and tend-to-safety have been put forward. According to the corresponding control strategy we have built the algorithm and flow. All of these have formed the foundation for the development of vehicle active anti-collision warning system. The model of the system has been set up and the results of simulation demonstrate that the control strategy is reasonable and the control algorithm is efficient. The system has good instantaneity and accuracy, and it can effectively avoid rear-end accidents on the highway. This study also has a certain instructive significance to develop the vehicle anti-collision system products.

References

1. Wang CD, Halajian S (1997) Processing methods enhance collision-warning systems. *Microwaves & RF* 36(3):72–82
2. Woll JD (1995) VORAD collision warning radar (C). In: Proceedings of the radar conference. Record of the IEEE 1995 international, 8–11 May 1995, pp 369–372
3. Seiler P, Song B, Hedrick JK (1998) Development of a collision avoidance system. *Development* (4):17–22
4. WangJunLei (2005) Research and development of the highway rear-end collision warning system (D). Chang-an university
5. McLaughlin SB (2008) Analytic assessment of collision avoidance systems and driver dynamic performance in rear-end crashes and near-crashes (D). Virginia Polytechnic Institute and State University
6. Jansson J, Gustafsson F, Ekmark J (2002) Decision making for collision avoidance systems (Z). SAE 2002 world congress & exhibition

Effectiveness Assessment of Human-Machine Interface in Driver Assistance System

**Bo Li, Weiguo Liu, Xiaolin Zhang, Zhijie Pan
and Fuquan Zhao**

Abstract In the recent years, with the development of Driver Assistance System such as Lane Departure Warning System and Forward Collision Warning System, how to design more effective Human-Machine-Interface to provide warning information, gets more and more attention. The purpose of this study is to introduce a quantitative test method for effectiveness assessment of Human-Machine-Interface for Driver Assistance system (DAS) in a simulated driving environment, and to assess different kinds of Human-Machine-Interfaces by proposed test method. In this paper, a large number of driver volunteer experiments in different scenarios and test conditions based on a driving simulator linked with the Human-Machine-Interface have been done, to assess the effects of visual warning methods, auditory warning methods, tactile warning methods and any combination of these three methods. In the experiments, the graphic type and text type of the visual warning, the buzzer type and human-voice type of the auditory warning, and the tactile warning are regulated. With proposed test method, the driver's reaction time and comprehension time (the time of understanding warning meaning) are assessed.

Keywords Human-machine interface · Driver assistance system · Driver reaction time · Driver comprehension time · Warning methods

F2012-F07-027

B. Li (✉) · W. Liu · Z. Pan · F. Zhao
Zhejiang Geely Automobile Research Institute Co., Ltd, Beijing, China

B. Li · X. Zhang
Tokyo Institute of Technology Precision and Intelligence Laboratory, Yokohama, Japan

1 Introduction

Driver Assistance System concluding lots of Active Safety functions such as Lane Departure Warning system (LDW) and Forward Collision Warning system (FCW) is one of the most important vehicle systems, In terms of necessity, popularization and regulation.

- *Necessity* Each year, China has a large number of traffic accidents. With the popularity of passive safety technology and traffic knowledge, since 2002 the total amount of traffic accidents has decreased. But, in recent years, the downward trend of accidents has slowed down, because it is close to the limits of the passive safety technology. So, the new innovation Active Safety technology become necessary for China market. Figure 1 shows the traffic accidents data from 2001 to 2009 in China [1].
- *Popularization* With the effectiveness has been proved, Active Safety functions get more and more attention. For example, Volvo released City-Safety Package and Human-Safety Package in 2009, and got good market feedback. In the near future, Driver Assistance systems and Active Safety functions will be rapidly gaining popularity,
- *Regulation* With test procedure of Autonomous Emergence Braking, Lane Departure Warning and other functions promulgated by the Euro-NCAP and US-NCAP, the promotion of Active Safety technology will grow faster.

The design of Human-Machine-Interface (HMI) for Driver Assistance System, especially for Active Safety functions is one of the most important factors to affect the performance. If the system has a good designed HMI, driver can save the reaction time and comprehension time (the time of understanding warning meaning), that is very valuable to prevent the collision happens. The total reaction time (include reaction time and comprehension time) of normal drivers is generally 1.64 to 2.2 s [2]. Therefore, for a Forward Collision Warning system, the TTC (Time to Collision) for activating warnings is generally 1.8 to 3.0 s, that is a very short time for driver to do the reactions such as braking and steering.

NHTSA's report [3] gave lots of meaningful recommendations for the design of crash warning systems such as FCW and LDW, but no details about the assessment or evaluation for the usability of HMI. Mikael Ljung and others introduced a test method to assess HMI performance quantitatively [4], but without considering comprehension time.

An effectiveness assessment method could both measure pure reaction time (no including the time of understanding) and comprehension time, is provided in this paper. In order to prove the advantage of the method, a test result using provided method is presented.

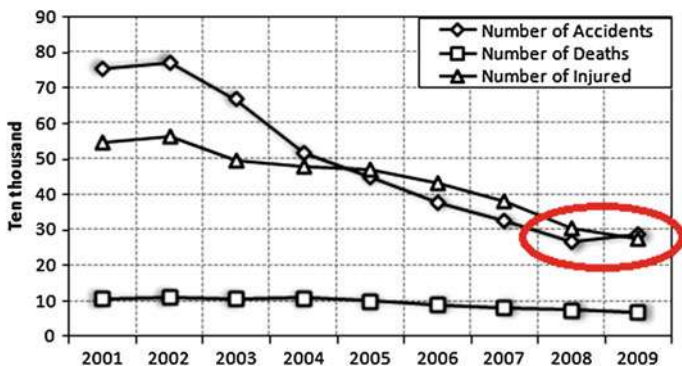


Fig. 1 Traffic accidents data from 2001 to 2009 in China

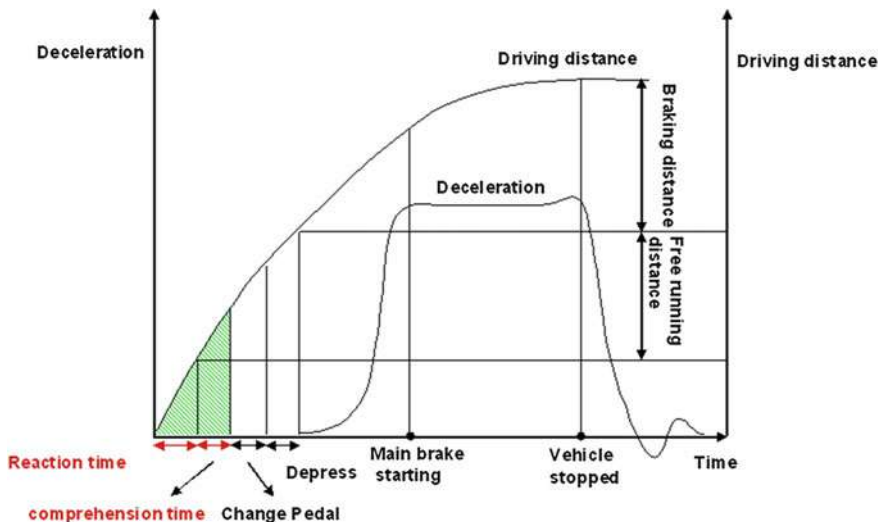


Fig. 2 The relationship between reaction time, comprehension time and braking distance

2 Methodology and Equipment

2.1 Methodology

As shown in Fig. 2, reaction time and comprehension time are important factors for the braking distance in an emergency brake. Reaction time and comprehension time are defined as follows.

- *Reaction time* From the timing that warning information of system is activated, to the timing that driver feels the warning information.
- *Comprehension time* From the timing that driver feels the warning information, to the timing that driver understands the warning information.

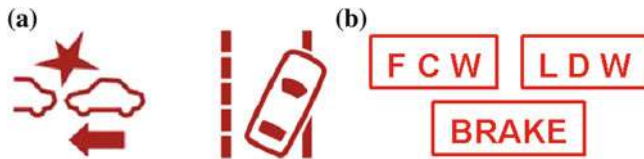


Fig. 3 Contents of warning, **a** Graphic display, **b** Text display

Reaction time is relative to the physical type of warning information. For example, different physical types can be used as visual warning, auditory warning, tactile warning and any combination of these three methods. Comprehension time is relative to contents of warning information. For example, different contents as graphic display, text information display, buzzer warning, and human-voice warning, as shown in Fig. 3.

In this study, first the total response time (include reaction time and comprehension time) is measured. For this measurement, the warning activated timing and the pedal or steering changed timing should be recorded by test equipment. The total response time is shown as Formula 1. Second, the reaction time is measured. For measurement of reaction time, the warning activated timing and the driver react timing (before understanding the meaning of warning information, but already feel the warning) should be recorded by test equipment. The reaction time is shown as Formula 2. Therefore, comprehension time could be calculated by Formula 3.

$$T_{total\ response} = T_{pedal\ or\ steering\ change} - T_{warning\ activated} \quad (1)$$

$$T_{reaction} = T_{driver\ react} - T_{warning\ activated} \quad (2)$$

$$T_{comprehension} = T_{total\ response} - T_{reaction} \quad (3)$$

In this study, 10 samples of reaction time and comprehension time, are collected for each warning type. Therefore, expected value and variance data are used to show the performance of each different warning type, as Formula 4.

$$\begin{aligned} E(T_{reaction}) &= \sum_{i=1}^{10} \frac{t_{ri}}{10} \\ E(T_{comprehension}) &= \sum_{i=1}^{10} \frac{t_{ci}}{10} \\ V(T_{reaction}) &= \sum_{i=1}^{10} \left(t_{ri} - \sum_{i=1}^{10} \frac{t_{ri}}{10} \right)^2 \\ V(T_{comprehension}) &= \sum_{i=1}^{10} \left(t_{ci} - \sum_{i=1}^{10} \frac{t_{ci}}{10} \right)^2 \end{aligned} \quad (4)$$

2.2 Equipment

In order to automatically and accurately record the warning activated timing, pedal or steering changed timing, and driver react timing, the test equipment should fulfill requirements such as:

- *Warning activated timing* To record the warning activated timing, a module that can send out warning information and record timing, should be implemented.
- *Pedal or steering changed timing* To record pedal or steering changed timing, a module that can get pedal position and steering angle and/or angle rate, should be implemented.
- *Driver react timing* To record driver react timing, two types experiment can be used. First method is using image processing device to detect driver face or eyes motion, and analysis motion information to recognize whether driver is realizing the warning is activated. Second method is design a special experiment for driver reaction time. The experiment environment should be simulated as normal driving situation, can ensure authenticity of driver reaction. In this test, driver's task is not to drive the vehicle or understand the meaning of warning information, but to react and response as soon as possible to any visual and/or auditory and/or tactile warning. For the first method, experiment can record the timing of driver eyes and/or face's motion changing, but can't certify the timing is the driver react timing. Compare to that, second method can exactly record the timing of driver react. There for the second method is used to record the driver react timing.

In this study, the experiment equipment for assessment is designed. This equipment consists of the following components, as shown in Fig. 4.

- *Vehicle Dynamic Model* This module has responsibility for simulating the vehicle dynamic features.
- *Control Cabinet & E-Move Motion* The two components are the actuator to simulate the vehicle motion by the order from Vehicle Dynamic Model.
- *Active safety Function controller and Sub-Controller* The active safety functions such as FCW or LDW, are implemented in this two modules. It can be implemented by the software logics using C/C++, simulink or other language, or hardware ECU such as HIL (Hardware in Loop).
- *Input HMI* Input HMI is the input device for driver to operate the vehicle or simulator, such as brake pedal, gas pedal, steering wheel, shift lever and other devices. The input signals will be sent to Vehicle Dynamic Model module.
- *Output HMI* This output HMI is original HMI for the driving simulator, for example a real integrated cluster. This module should provide the normal original information for the driver.
- *Sensor Model* This module is the simulation of sensor performance for the Active Safety functions. This module could be a ideal sensor model with no noise or errors for measurement accuracy, but also could be a real sensor model with noise and errors.

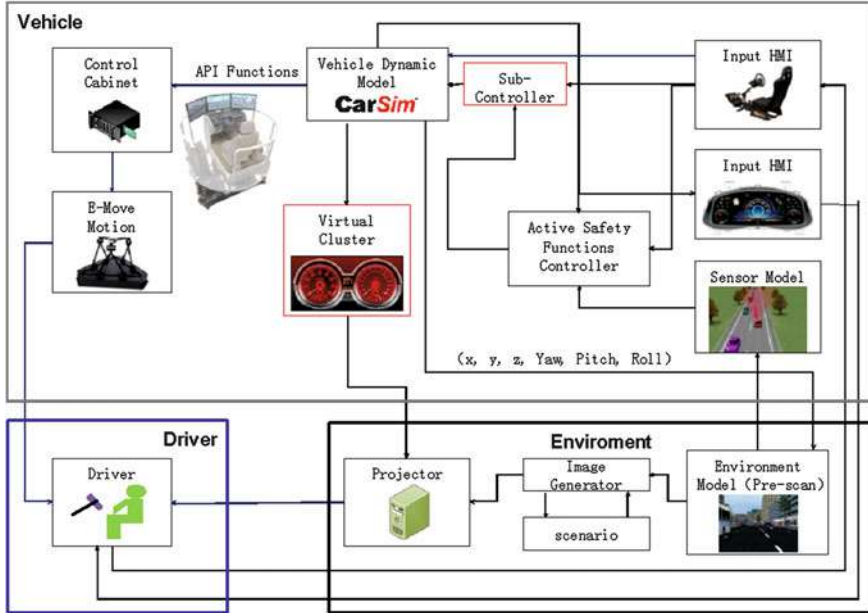


Fig. 4 The system structure for assessment equipment

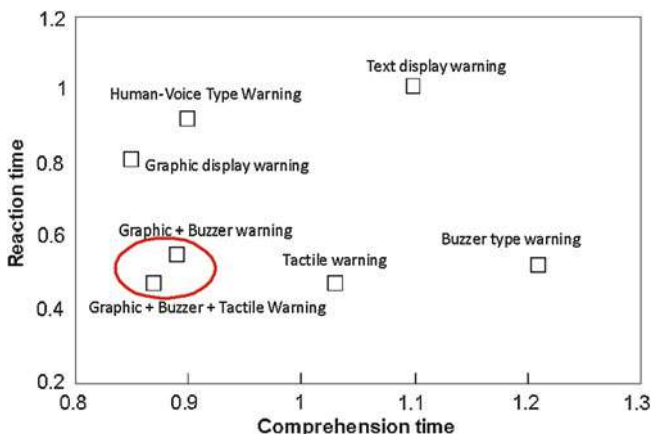
- *Environment Model* The road and structure is built in this module. Vehicle Dynamic Model provides ego-vehicle motion information (include x, y, z, yaw, pitch, roll) to this module, and environment model will calculate the ego-vehicle position.
- *Scenario and Image Generator* Scenario module provides the motion information of other vehicles in the environment. Image generator create the image that driver should see from driving position, from the information provided by environment model and scenario module.
 - *Projector* Projector is the display module to show the image to driver.
 - *Driver* Who give the driving order to vehicle or simulator.
 - *Virtual Cluster* Virtual Cluster provides HMI information that the original output HMI can't provide to the driver. For example, in this study, various types of warning information from the active safety system is provided by this module.

3 Result

In this study, the graphic type and text type of the visual warning, the buzzer type and human-voice type of the auditory warning, and the tactile warning are assessed by the above method. And the result is as Table 1 shown.

Table 1 The test result of different type warning information

	Average of reaction time	Variance of reaction time	Average of comprehension time	Variance of comprehension time
Graphic display warning	0.81	0.15	0.85	0.16
Text display warning	1.01	0.22	1.1	0.11
Buzzer type warning	0.52	0.12	1.21	0.24
Human-voice type Warning	0.92	0.13	0.9	0.12
Tactile warning	0.47	0.12	1.03	0.2
Graphic + Buzzer warning	0.55	0.11	0.89	0.11
Graphic + Buzzer + Tactile warning	0.47	0.15	0.87	0.12

**Fig. 5** The test result of different type warning information

As shown in Fig. 5, “Graphic + Buzzer” type warning and “Graphic + Buzzer + Tactile” type warning have the best performance in both reaction time and comprehension time.

4 Conclusion

In this study, an effectiveness assessment method could both measure reaction time and comprehension time, has been presented. And use the test method, the effectiveness of different types of warning information has been assessed. “Graphic + Buzzer” type warning and “Graphic + Buzzer + Tactile” type warning should be recommended for the HMI design of the driver assist system or active safety system.

References

1. Zhao S (2009) Road traffic accidents in China. IATSS Res 33(2):125–127
2. McGehee DV (2000) Driver reaction time in crash avoidance research validation of a driving simulator study on a test track. In: Proceedings of the human factors and ergonomics society annual meeting July 2000 vol. 44 no. 203-320-3-323
3. Campbell JL (2007) Crash warning system interfaces: human factors insights and lessons learned. National Technical Information Service, Springfield, Virginia 22161
4. Jung M (2007) Influence of study design on results in HMI testing for active safety. Enhanced safety vehicles (ESV) Conference (2007)No.07-0383-O

Part VII

Vehicle Controls on Handing and Stability

Sliding Mode Control for All-Wheel Steering of Four-Axle Vehicle

Kaifeng Zheng and Sizhong Chen

Abstract The four-wheel steering (4WS) has been studied for a long time. And many control algorithms, such as proportional control, optimal control, sliding-mode control and H_2/H_∞ control, have been applied to it. However, few works expand those control algorithms to four-axle vehicle. The traditional four-axle vehicle can be steerable in the first and the second axle, which is called double-front-axle-steering (DFAS) vehicle. By adding Electro-hydraulic Power Steering System to the third and the forth axles, the DFAS vehicle becomes an all-wheel steering (AWS) vehicle. Some control algorithms could apply to it to control the steering angles of the third and the forth axle like the application to 4WS vehicle to control the rear wheel steer. In fact, due to the large size and high center of mass, reducing steer radius and enhancing stability through all-wheel steering is more important than the application in two-axle vehicle. In the paper, a sliding mode controller (SMC) to control the steering angles of the third axle and forth axle is proposed for a four-axle vehicle to improve handling and stability. In order to design the SMC, a linear all-wheel steering model of four-axle vehicle is established firstly, which considers the tire cornering stiffness perturbation and the crosswind disturbance. The yaw rate and sideslip angle are considered as two important state variables for this model. Then a reference model which contains an ideal yaw rate and zero-sideslip angle is developed. Finally, the switching function of the SMC is chosen based on the error of state variable between the all-wheel steering model and the reference model. The SMC aims to make the all-wheel steering model track the reference model through controlling the steering angles of the third and the fourth axle. Unfortunately, in this control strategy, adverse-phase

F2012-F08-001

K. Zheng (✉) · S. Chen

School of Mechanical Engineering, Beijing Institution of Technology,
Beijing 100081, China

steering appears between the third and the fourth axle, causing serious tire wear problem. So a modified sliding mode controller is given, which is a compromise between controller performance and tire wear. In order to investigate the effect of the modified controller, two typical tests, double lane change test and crosswind disturbance test, are carried out through numerical simulation. The controller built in Matlab/Simulink, and a high precision four-axle vehicle mode developed in TruckSim make two tests easily to accomplish co-simulation of driver-controller-vehicle close-loop system. The simulation results show that the modified SMC has robustness to vehicle parameter perturbation and insensitivity to crosswind disturbance. Moreover, all-wheel steering four-axle vehicle has better handling performance and stability compared with traditional DFAS vehicle.

Keywords Sliding mode control · Four-axle vehicle · All-wheel steering

1 Introduction

In the past years, many control strategies, such as proportional control, optimal control, sliding mode control and H_2/H_∞ were proposed to improve the two-axle vehicle's lateral stability. Furukawa [1] summarized those control strategies and pointed out their effectiveness and limits. However, few works expand those control algorithms to multi-axle vehicle, especially for four-axle vehicles. Huh [2] proposed a proportional backward control for three-axle vehicle. Lane change simulation under 18 DOF nonlinear vehicle model demonstrated the advantage of the proposed control law. An [3] proposed an optimal control for three-axle vehicle, where the sideslip angle and yaw rate were controlled to improve the maneuverability by independent control of the steering angles of the six wheels. A numerical simulation and a scaled-down vehicle experiment showed its good effective. Qu [4] proposed a SMC for three-axle vehicle. The SMC tried to make the steering characteristics of uncertain vehicle mode follow the characteristics of the reference mode, even exiting outer disturbance and uncertain parameters. Kerem [5] extended 4WS idea to an n-axle vehicle and attempted to determine the best steering strategy. It is found that few controllers are designed for four-axle vehicle, and many of them do not consider parameter perturbations and external disturbances. Moreover, many of them aim at reducing turning radius at low velocity, and do not work at high velocity. However, for familiar DFAS four-axle vehicle, which demands both maneuverability and stability, all-wheel steering is an effective method to improve the stability.

In the paper, a sliding mode controller to control the steering angle of the third axle and forth axle is proposed for four-axle vehicle to improve handling and stability.

2 Vehicle Model

Two degrees of freedom (2DOF) vehicle model is considered in this paper, shown in Fig. 1. L_i ($i = 1, 2, 3, 4$) represents the distances between the i th axle and the center of gravity. It is important to keep in mind that an axle located behind the vehicle center of gravity is located by a negatively signed distance [6]. In here, L_3 and L_4 are negative.

Considering the tire cornering stiffness perturbations and crosswind disturbance, a linearized equation of motion of all-wheel steer vehicle becomes

$$\begin{cases} mu(\dot{\beta} + r) = -\beta \sum K_{zi} - \frac{\sum L_i K_{zi}}{u} r + \sum K_{zi} \delta_i + F_d \\ I_z \dot{r} = -\beta \sum L_i K_{zi} - \frac{\sum L_i^2 K_{zi}}{u} r + \sum L_i K_{zi} \delta_i + L_d F_d \end{cases} \quad (1)$$

where m is vehicle mass, I_z is yaw inertia, u is the forward velocity, δ_i is steering angle of i th axle, β is the sideslip angle at CG, r is the yaw rate, $K_{zi} = K_{z0i} + \Delta K_{zi}$, K_{z0i} is defined as the nominal value of i th axle cornering stiffness, ΔK_{zi} is defined as the perturbation value of i th axle, F_d is assumed to be the external disturbance force impacting on the vehicle, and L_d is the distance from the CG to the point where F_d acts on vehicle.

For traditional DFAS vehicle, we can set $\delta_2 = k\delta_1$. Then the vehicle model can be written as

$$\dot{\mathbf{X}} = (\mathbf{A}_0 + \Delta \mathbf{A})\mathbf{X} + (\mathbf{B}_{u0} + \Delta \mathbf{B}_u)\mathbf{U} + (\mathbf{B}_{w0} + \Delta \mathbf{B}_w)\delta_1 + \mathbf{B}_d F_d \quad (2)$$

where

$$\begin{aligned} \mathbf{A}_0 &= \begin{bmatrix} \frac{-\sum K_{z0i}}{mu} & \frac{-\sum L_i K_{z0i}}{mu^2} - 1 \\ \frac{-\sum L_i K_{z0i}}{I_z} & \frac{-\sum L_i^2 K_{z0i}}{I_z u} \end{bmatrix}, \mathbf{X} = \begin{bmatrix} \beta \\ r \end{bmatrix}, \mathbf{U} = \begin{bmatrix} \delta_3 \\ \delta_4 \end{bmatrix}, \\ \Delta \mathbf{A} &= \begin{bmatrix} \frac{-\sum \Delta K_{zi}}{mu} & \frac{-\sum L_i \Delta K_{zi}}{mu^2} \\ \frac{-\sum L_i \Delta K_{zi}}{I_z} & \frac{-\sum L_i^2 \Delta K_{zi}}{I_z u} \end{bmatrix}, \mathbf{B}_d = \begin{bmatrix} \frac{1}{mu} \\ \frac{L_d}{I_z} \end{bmatrix} \\ \mathbf{B}_{w0} &= \begin{bmatrix} \frac{K_{z01} + kK_{z02}}{mu} \\ \frac{L_1 K_{z01} + kL_2 K_{z02}}{I_z} \end{bmatrix}, \Delta \mathbf{B}_w = \begin{bmatrix} \frac{\Delta K_{z1} + k\Delta K_{z2}}{mu} \\ \frac{L_1 \Delta K_{z1} + kL_2 \Delta K_{z2}}{I_z} \end{bmatrix}, \mathbf{B}_{u0} = \begin{bmatrix} \frac{K_{z03}}{mu} & \frac{K_{z04}}{mu} \\ \frac{L_3 K_{z03}}{I_z} & \frac{L_4 K_{z04}}{I_z} \end{bmatrix}, \\ \Delta \mathbf{B}_u &= \begin{bmatrix} \frac{\Delta K_{z3}}{mu} & \frac{\Delta K_{z4}}{mu} \\ \frac{L_3 \Delta K_{z3}}{I_z} & \frac{L_4 \Delta K_{z4}}{I_z} \end{bmatrix} \end{aligned}$$

Due to \mathbf{B}_{u0} is full rank and reciprocal matrix, the vehicle model satisfies matching condition. It means that there are matrices \mathbf{M}_x , \mathbf{M}_u , \mathbf{M}_w and \mathbf{M}_d which made Equation (3) tenable.

$$\Delta \mathbf{A} = \mathbf{B}_{u0} \mathbf{M}_x, \quad \Delta \mathbf{B}_u = \mathbf{B}_{u0} \mathbf{M}_u, \quad \Delta \mathbf{B}_w = \mathbf{B}_{u0} \mathbf{M}_w, \quad \mathbf{B}_d = \mathbf{B}_{u0} \mathbf{M}_d \quad (3)$$

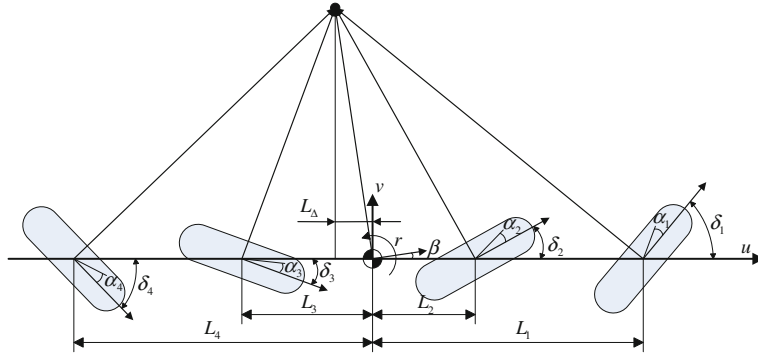


Fig. 1 2DOF vehicle model

The physical meaning of a matching condition is that the system uncertainty and control action are on a same channel. So by taking appropriate control effect, it is possible to offset directly or weaken influence of uncertainty.

Then, the vehicle model can be written as

$$\dot{\mathbf{X}} = \mathbf{A}_0 \mathbf{X} + \mathbf{B}_{u0} [\mathbf{U} + \mathbf{d}(\mathbf{x}, t)] + \mathbf{B}_{w0} \delta_1 \quad (4)$$

where $\mathbf{d}(\mathbf{x}, t) = \mathbf{M}_x \mathbf{X} + \mathbf{M}_u \mathbf{U} + \mathbf{M}_w \delta_1 + \mathbf{M}_d F_d$ is the total uncertainty of the system.

3 The Reference Model

The ideal steering state for AWS is [7]: its steering sensitivity (steady-state gain of yaw rate) is always consistent with the traditional DFAS vehicle. In other words, it is to keep the driver feel no great change compared with that of old vehicle, while its sideslip angle at CG is always zero value as far as possible (in order to keep no sideslip during cornering). According to above requirement, the reference model can be established as follows

$$\dot{\mathbf{X}}_d = \mathbf{A}_d \mathbf{X}_d + \mathbf{B}_d \delta_1 \quad (5)$$

where

$$\mathbf{A}_d = \begin{bmatrix} -1/\tau_\beta & 0 \\ 0 & -1/\tau_r \end{bmatrix}, \mathbf{B}_d = \begin{bmatrix} k_{\beta d}/\tau_\beta \\ k_{rd}/\tau_r \end{bmatrix}, \mathbf{X}_d = \begin{bmatrix} \beta_d \\ r_d \end{bmatrix}$$

where β_d , r_d represent sideslip angle and yaw rate of the reference model respectively, scale factor k_{rd} is taken as the steady-state gain of yaw rate of DFAS

vehicle with same structural parameters, $k_{\beta d} = 0$, τ_β , τ_r are lag time constants of the first-order inertia link to sideslip angle and yaw rate respectively. Here $\tau_\beta = \tau_r = 0.2s$.

4 Sliding Mode Controller Design

We define the state tracking error between the actual state and the reference model \mathbf{e} as

$$\mathbf{e} = \mathbf{X} - \mathbf{X}_d = \begin{bmatrix} e_1 \\ e_2 \end{bmatrix} = \begin{bmatrix} \beta - \beta_d \\ r - r_d \end{bmatrix} \quad (6)$$

Then, the derivative of tracking error \mathbf{e} is

$$\begin{aligned} \dot{\mathbf{e}} &= \dot{\mathbf{X}} - \dot{\mathbf{X}}_d \\ &= \mathbf{A}_0 \mathbf{X} + \mathbf{B}_{u0} [\mathbf{U} + \mathbf{d}(\mathbf{x}, \mathbf{t})] + \mathbf{B}_{w0} \delta_1 - \mathbf{A}_d \mathbf{X}_d - \mathbf{B}_d \delta_1 \\ &= \mathbf{A}_0 \mathbf{e} + (\mathbf{A}_0 - \mathbf{A}_d) \mathbf{X}_d + \mathbf{B}_{u0} [\mathbf{U} + \mathbf{d}(\mathbf{x}, \mathbf{t})] + (\mathbf{B}_{w0} - \mathbf{B}_d) \delta_1 \end{aligned} \quad (7)$$

Here, we need to construct a switching function as follows

$$\mathbf{S} = \begin{bmatrix} s_1 \\ s_2 \end{bmatrix} = \mathbf{C} \mathbf{e} = \begin{bmatrix} 1 & c_1 \\ 1 & c_2 \end{bmatrix} \begin{bmatrix} e_1 \\ e_2 \end{bmatrix} \quad (8)$$

where c_1 and c_2 are positive undetermined parameters.

The derivative of switching function is

$$\dot{\mathbf{S}} = \mathbf{C} \dot{\mathbf{e}} = \mathbf{C} [\mathbf{A}_0 \mathbf{e} + (\mathbf{A}_0 - \mathbf{A}_d) \mathbf{X}_d] + \mathbf{C} [\mathbf{B}_{u0} [\mathbf{U} + \mathbf{d}(\mathbf{x}, \mathbf{t})] + (\mathbf{B}_{w0} - \mathbf{B}_d) \delta_1] \quad (9)$$

Let $\dot{\mathbf{S}} = \mathbf{0}$ and $\mathbf{d}(\mathbf{x}, \mathbf{t}) = \mathbf{0}$, we can get the equivalent control.

$$\mathbf{U}_{eq} = -(\mathbf{C} \mathbf{B}_{u0})^{-1} \mathbf{C} [\mathbf{A}_0 \mathbf{e} + (\mathbf{A}_0 - \mathbf{A}_d) \mathbf{X}_d + (\mathbf{B}_{w0} - \mathbf{B}_d) \delta_1] \quad (10)$$

The equivalent control just works for nominal vehicle model, but it cannot restrain parameter perturbations and external disturbances. In order to has robust ability, a robust control with a constant reaching law is given

$$\mathbf{U}_{rob} = -(\mathbf{C} \mathbf{B}_{u0})^{-1} \mathbf{G} \text{sgn}(\mathbf{S}) = -(\mathbf{C} \mathbf{B}_{u0})^{-1} \begin{bmatrix} g_1 & 0 \\ 0 & g_2 \end{bmatrix} \begin{bmatrix} \text{sgn}(s_1) \\ \text{sgn}(s_2) \end{bmatrix} \quad (11)$$

where g_1 and g_2 are undetermined parameters.

So, the controller is

$$\mathbf{U} = \mathbf{U}_{eq} + \mathbf{U}_{rob} \quad (12)$$

Substituting Eq. (12) into (10) we obtain

$$\dot{\mathbf{S}} = -\mathbf{G} \text{sgn}(\mathbf{S}) + \mathbf{C} \mathbf{B}_{u0} \mathbf{d}(\mathbf{x}, \mathbf{t}) \quad (13)$$

In addition, in order to decouple the sliding, assuming

$$\mathbf{CB}_{\mathbf{u}0} = \begin{bmatrix} 1 & c_1 \\ 1 & c_2 \end{bmatrix} \begin{bmatrix} \frac{K_{203}}{mu} & \frac{K_{204}}{mu} \\ \frac{L_3 K_{203}}{I_z} & \frac{L_4 K_{204}}{I_z} \end{bmatrix} = \begin{bmatrix} \rho_1 & 0 \\ 0 & -\rho_2 \end{bmatrix} \quad (14)$$

where

$$\begin{aligned} c_1 &= \frac{-I_z}{mu L_4} > 0, & c_2 &= \frac{-I_z}{mu L_3} > 0, & \rho_1 &= \frac{K_3}{mu} \left(1 - \frac{L_3}{L_4} \right) > 0, \\ \rho_2 &= \frac{K_4}{mu} \left(\frac{L_4}{L_3} - 1 \right) > 0 \end{aligned} \quad (15)$$

Constructing a Lyapunov function $V_T = \mathbf{S}^T \mathbf{S}/2$, then the time derivative of V_T can be obtained

$$\begin{aligned} \dot{V}_T &= \mathbf{S}^T \dot{\mathbf{S}} = \mathbf{S}^T [-\mathbf{G}\text{sgn}(\mathbf{S}) + \mathbf{CB}_{\mathbf{u}0} \mathbf{d}(\mathbf{x}, t)] \\ &= -[s_1 \ s_2] \begin{bmatrix} g_1 & 0 \\ 0 & g_2 \end{bmatrix} \begin{bmatrix} \text{sgn}(s_1) \\ \text{sgn}(s_2) \end{bmatrix} + [s_1 \ s_2] \begin{bmatrix} \rho_1 & 0 \\ 0 & -\rho_2 \end{bmatrix} \begin{bmatrix} d_1(x, t) \\ d_2(x, t) \end{bmatrix} \quad (16) \\ &= -g_1 |s_1| - g_2 |s_2| + \rho_1 s_1 d_1(x, t) - \rho_2 s_2 d_2(x, t) \\ &\leq -|s_1|(g_1 - \rho_1 |d_1(x, t)|) - |s_2|(g_2 - \rho_2 |d_2(x, t)|) \end{aligned}$$

Equation (16) indicates that the control system can be guaranteed to be asymptotically stable (because the derivative of Lyapunov function V_T is no more than 0) if we choose two parameters g_1 and g_2 satisfying Eq. (17).

$$\begin{cases} |d_1(x, t)| \leq g_1 / \rho_1 \\ |d_2(x, t)| \leq g_2 / \rho_2 \end{cases} \quad (17)$$

In addition, in order to reduce the chattering, the $\text{sgn}(\bullet)$ function is substituted by a saturation function.

$$\text{sat}(s_i) = \begin{cases} 1 & s_i > 1 \\ s_i & |s_i| \leq 1 \\ -1 & s_i < -1 \end{cases}, \quad i = 1, 2 \quad (18)$$

5 The Modified Controller

Unlike the two-axle vehicle, the sliding model controller designed for all-wheel steering of four-axle vehicle cannot be applied directly because of the adverse-phase steering angle inputs to the third and fourth axle. The simple step steer simulation under linear 2DOF mode illustrates this problem. Vehicle starts step steer at 0.1 s with a constant velocity 65 km/h and steering angle of the first axle

Table 1 Vehicle and control parameters

Parameters	Value
m	11000 kg
I_z	3048.1 kg m ²
K_i ($i = 1, 2, 3, 4$)	260000 N rad ⁻¹
L_1	1.8 m
L_2	0.5 m
L_3	-0.85 m
L_4	-2.2 m
k	0.9
g_1	10
g_2	10

input 3°. The parameters of four-axle vehicle are shown in Table 1. The results are shown in Figs. 2, 3 and 4.

It can be seen from the Figs. 2a and 3a that the controller got from Eq. (12) can make the sideslip zero and keep the yaw rate tracking the yaw rate of DFAS vehicle. However, Fig. 3a illustrates that it brings about the adverse-phase steering inputs to the third and fourth axle which will result in serious tire wear. Moreover, large adverse-phase steering angle will reduce stability and bring driver bad handling feeling. So a modified controller is proposed as follows

$$\mathbf{U}' = \frac{1}{2} \begin{bmatrix} k & k \\ 1 & 1 \end{bmatrix} \mathbf{U} \quad (19)$$

For the modified controller, the same step steer simulation is carried out. And results are also shown in Figs. 2, 3 and 4. It is shown in Fig. 2b that although the sideslip angle is not zero, it is a very small. Correspondingly, in Fig. 3b, the yaw rate does not track the DFAS vehicle, but it is not so far than the reference. Those prove the modified controller almost does not deteriorate the performance. The adverse-phase steering turns into a same-phase steering shown in Fig. 3b with small value.

6 Co-simulation and Results

In order to investigate the effect of the modified controller, double lane change test and crosswind disturbance test are carried out [8]. The modified controller is built in Matlab/Simulink. And a high precision vehicle model is developed in TruckSim where we choose the “Military: Armored combat vehicle, 8 × 8(ii–ii)” and adopt the default driver model. The real velocity, the steering angle of first axle, the sideslip angle and the yaw rate computed from the vehicle model are considered as the feedback inputs for the controller. Then the steering angles of 3rd axle and 4th

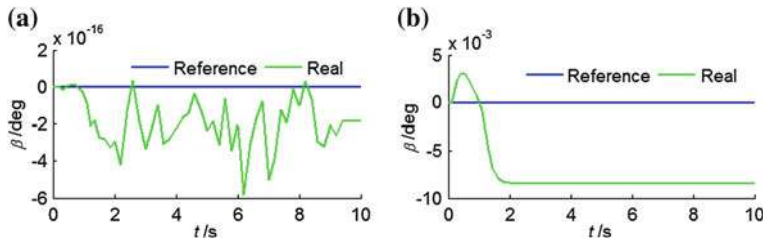


Fig. 2 The sideslip angle. a Eq. (12), b Eq. (19)

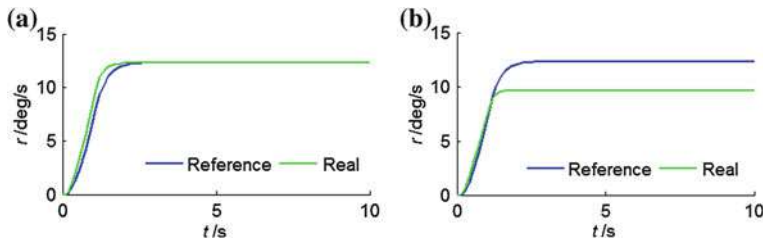


Fig. 3 The yaw rate. a Eq. (12), b Eq. (19)

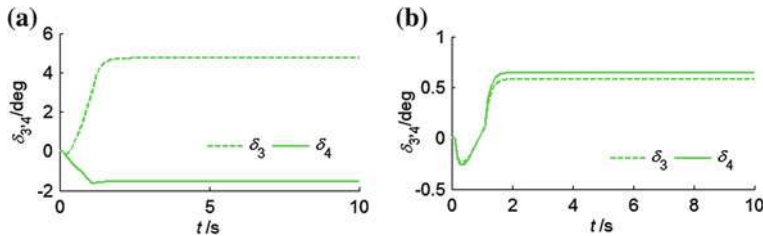


Fig. 4 The steer angles of 3rd and 4th axle. a Eq. (12), b Eq. (19)

axle are outputted by the controller. Though this co-simulation, two types of tests of driver-controller-vehicle close-loop system can be easily accomplished.

6.1 Double Lane Change Test

“Double Lane Change @ 65 km/h” procedure containing a preview driver mode and a given double lane change road is adopted for double lane change test. Here, two road surface conditions were prepared: dry road (tire-road friction coefficient $\mu = 0.85$) and wet road ($\mu = 0.3$). Vehicle velocity is 65 km/h. The results are shown in Figs. 5, 6, 7, 8, and 9.

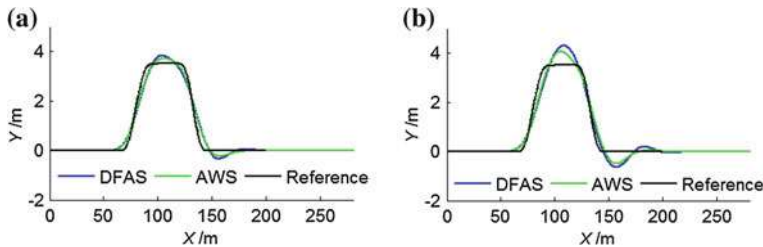


Fig. 5 Vehicle trajectory. **a** $\mu = 0.85$, **b** $\mu = 0.3$

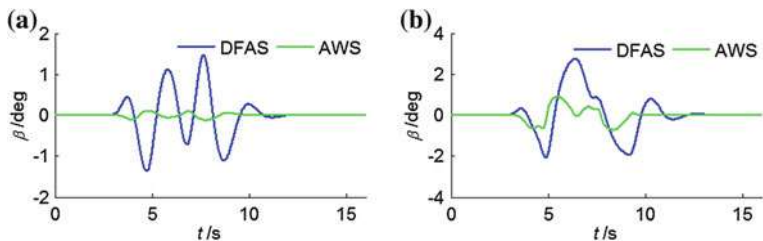


Fig. 6 The sideslip angle. **a** $\mu = 0.85$, **b** $\mu = 0.3$

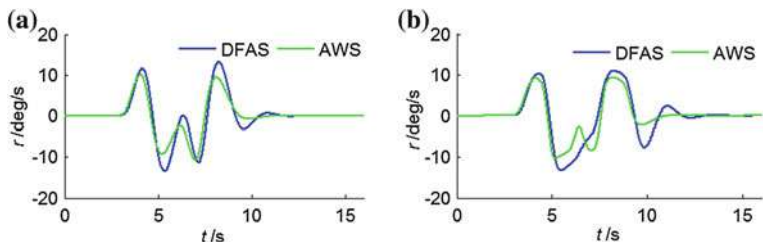


Fig. 7 The yaw rate. **a** $\mu = 0.85$, **b** $\mu = 0.3$

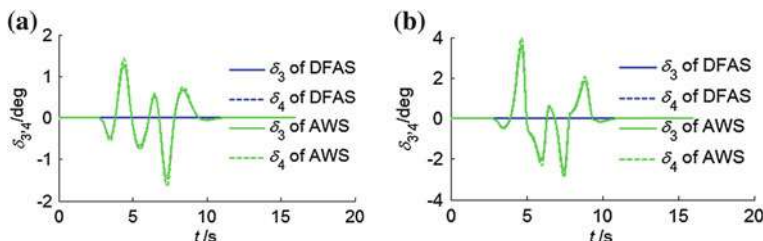


Fig. 8 The steer angles of 3rd axle and 4th axle. **a** $\mu = 0.85$, **b** $\mu = 0.3$

It can be seen from Fig. 5, whether on dry road or wet road, AWS vehicle has smaller lateral offset than DFAS vehicle. However, compared to the reference trajectory, the real trajectory on wet road has larger lateral offset than that on dry

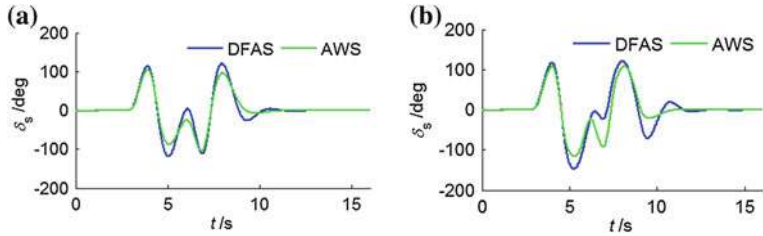
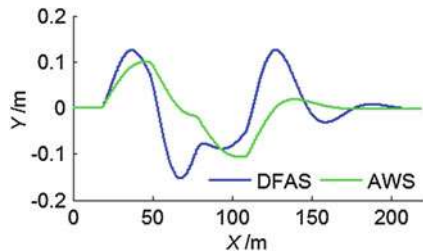


Fig. 9 The steering wheel angle. **a** $\mu = 0.85$, **b** $\mu = 0.3$

Fig. 10 Vehicle trajectory

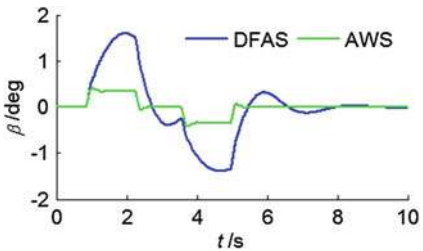
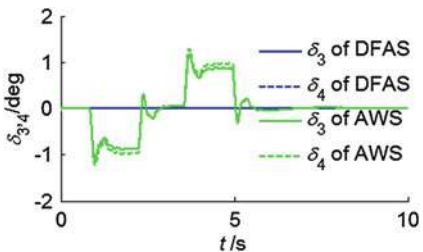
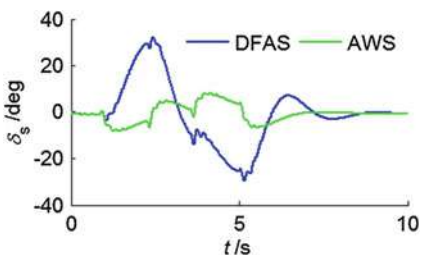


road. This illustrates that although the driver tries to cover this test, the reduced lateral force of tire makes it difficult to accomplish. Comparing the sideslip angle (Fig. 6) and the yaw rate (Fig. 7), driver inclines the AWS vehicle because of its smaller sideslip angle and nearly unchanged yaw rate whether on dry road or wet road. Figure 8 shows the steering angle of 3rd axle and 4th axle which come from the modified controller outputs. The max steering angle is 1.5° on dry road, and 4° on wet road. This is an acceptable value at the high velocity 65 km/h. In Fig. 9 the steering wheel angle indicates the AWS vehicle reduces the driver's work. In summary, the double lane change test under two road surface conditions shows that the modified controller has good robustness in the tire cornering stiffness perturbation, and improves handling and stability.

6.2 Crosswind Disturbance Test

Like double lane change test, we adopt default crosswind test procedure which has “No Offset w/1 s. Preview” driver path follower, the default vehicle velocity 80 km/h and the default wind velocity 100 km/h. Driver tries to keep a straight line to pass through a left crosswind disturbance firstly then a right crosswind disturbance. The simulation results are shown in Figs. 10, 11, 12 and 13.

Figure 10 shows that the vehicle trajectory of AWS vehicle with modified sliding mode controller has the smaller lateral offset than the DFAS vehicle. In Fig. 11, the max sideslip angle of DFAS vehicle is 1.7° , but just 0.5° of AWS vehicle. The smaller lateral offset and sideslip angle show the modified controller

Fig. 11 The sideslip angle**Fig. 12** Steer angle of 3rd axle and 4th axle**Fig. 13** The steering wheel angle

has better performance in rejection of crosswind disturbance. The max steering angle of 3rd axle and 4th axle is 1.2° shown in Fig. 12, which imply its few energy input. At last, the smaller steering wheel angle of AWS vehicle shows the reducing of driver's work.

7 Conclusion

A sliding mode controller to control the steering angles of the third axle and forth axle is proposed for a four-axle vehicle to improve handling and stability. In order to avoid the adverse-phase steering angle input for the third and fourth axle, a modified controller is given which is a compromise between the control performance and the tire wear. Then the effectiveness of the modified controller is verified though double lane test and crosswind disturbance test. The simulation results show that the modified SMC has robustness to vehicle parameter perturbations and insensitivity to crosswind disturbance. Moreover, it could enhance the

handling performance and stability of all-wheel steering four-axle vehicle compared with traditional DFAS vehicle.

Acknowledgments The author would like to thank Fan Lu who contributed timed and ideas to this paper.

References

1. Furukawa Y, Abe M (1997) Advanced chassis control systems for vehicle handling and active safety. *Veh Syst Dyn* 28:59–86
2. Huh K, Kim J, Hong J (2000) Handling and driving characteristics for six-wheeled vehicles. In: IMechE, pp 159–170
3. An SJ, Yi K, Jung G et al (2008) Desired yaw rate and steering control method during cornering for a six-wheeled vehicle. *Int J Automot Technol* 9(2):173–181
4. Qu Q, Zu JW (2008) On steering control of commercial three-axle vehicle. *J Dyn Syst Meas Control*, 130/021010-1021010-11
5. Kerem B, Samim Unlusoy Y (2008) Steering strategies for multi-axle vehicles. *Int J Heavy Veh Syst* 25(2/3/4):208–236
6. Williams DE (2011) Generalised multi-axle vehicle handling. *Veh Syst Dyn iFirst*, pp 1–18
7. Du F, Li J, Li L et al (2010) Robust control study for four-wheel active steering vehicle. In: 2010 international conference on electrical and control engineering, pp 1830–1833
8. Hiraoka T, Nishihara O, Kumamoto H (2004) Model-following sliding mode control for active four-wheel steering vehicle. *Rev Automot Eng* 25:305–313

Vehicle Control Via Real-Time Flow Modeling and Flow Manipulation

Hiroshi Tokutake, Taro Tsukada and Eiji Itakura

Abstract A vehicle control method that uses flow manipulation for gust response suppression was developed. A separation enhancement control technique that uses air injection is proposed. The yaw moment values for various aerodynamic side slip angles of a scale model car were measured. The results show that the proposed system reduces the yaw moment caused by a crosswind disturbance by 20 %. Additionally, the effective condition of air injection was examined using a fundamental wind tunnel test. Furthermore, a real-time modeling method is proposed for the flow condition around the car. A simple flow modeling method that uses a complex velocity potential is introduced, and the experimental results are compared with the theoretical results and discussed.

Keywords Flow modeling • Disturbance response • Flow manipulation • Air injection • Wind tunnel test

Nomenclature

S	frontal projected area m^2
U	mainstream velocity m/s
n	yaw moment Nm
l_{wb}	wheel base length m
β_w	aerodynamic sideslip angle deg
C_n	yaw moment coefficient $n/(0.5 \rho U^2 S l_{wb})$
C_p	pressure coefficient

F2012-F08-003

H. Tokutake · T. Tsukada (✉)
Kanazawa University, Kanazawa, Japan

E. Itakura
Toyota Motor Corporation, Toyota, Japan

- St* Strouhal number based on the wheel base length
Re Reynolds number based on the wheel base and mainstream velocity

1 Introduction

Sophisticated body shapes with low drag, which represent a growing trend for recent fuel-efficient cars, have unsteady motion caused by their aerodynamic yaw moment. It has been reported that a well-rounded front shape increases the sensitivity of the yawing moment to cross winds [1]. Such unavoidable characteristics require a high workload of the driver, and the car's dynamics should be compensated by active control. There are several control methods for car dynamics that use the frictional force of the tires [2, 3]. However, fuel-efficient cars use narrow tires [4]. Consequently, it is difficult to generate a sufficiently large control moment to suppress the gust responses. Therefore, we propose the use of a flow manipulation method to enhance the separation on the body surface and generate a large control moment. Control methods that use a control surface attached to the body have been reported [5]. In contrast, our method uses air injection, which has the advantage of not changing the body shape.

Many flow manipulation methods have been proposed [5–7]. These flow manipulation methods have mainly been aimed at increasing the aerodynamic performance and suppressing the separation. The flow condition changes drastically when separation occurs [8]. Usually, a wing's performance is deteriorated as a result of the separation. However, the present method enhances the separation to generate a large yawing moment. Furthermore, the basic algorithm for the real-time modeling of the flow condition is provided here.

This paper proposes a separation enhancement control structure that uses air injection. In addition, a real-time modeling concept is introduced. Then, a wind tunnel model equipped with a micro-air jet is constructed. Finally, the proposed method is validated using wind tunnel testing.

2 Method

2.1 Flow Manipulation

In the present method, the flow condition around a car is controlled using a flow manipulator. Information about the flow condition around the car is useful for determining the most effective control input. The flow condition around the car

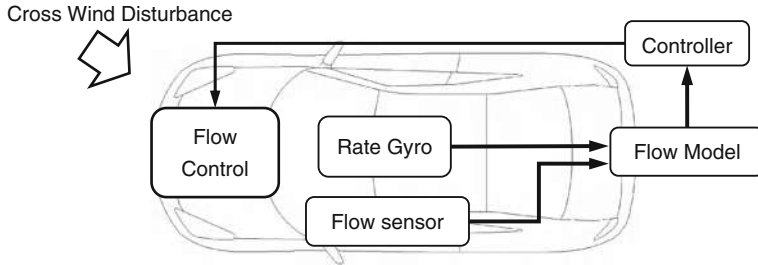


Fig. 1 Structure of the proposed control method

depends on the gust disturbances and car dynamics. Therefore, the car is equipped with motion and flow condition sensors, and the measured values are used to construct a flow model in real-time. The estimated flow condition is provided to the controller, and the control devices are actuated (Fig. 1). There are several techniques for controlling the flow behavior around a car. We used air injection devices to enhance the flow separation. Consequently, large aerodynamics forces are generated. In this paper, the performance of the proposed air injection method is validated using fundamental experiments.

2.2 Real-Time Modeling

The proposed control method requires a precise flow model. The flow model that is used should precisely define all of the flow dynamics to determine the optimal input for flow manipulation. Usually, the flow dynamics can be solved numerically when the boundary condition is defined. However, it is impossible to define the boundary condition of an actual car under an unknown gust input. Therefore, an asymptotic method that uses the measured flow condition and car motion is proposed (Fig. 2). In this method, the measured values are used to improve the boundary condition of the simple fluid dynamics model. The procedures are as follows.

- (i) The initial boundary condition is defined.
- (ii) The car motion is measured.
- (iii) The measured car motion is input to the flow model, and the flow condition is calculated.
- (iv) The flow conditions at several points on the body surface are measured and compared with the estimated value from the flow model.
- (v) The estimation error of the flow condition is used to update the boundary condition.
- (vi) Return to step (ii).

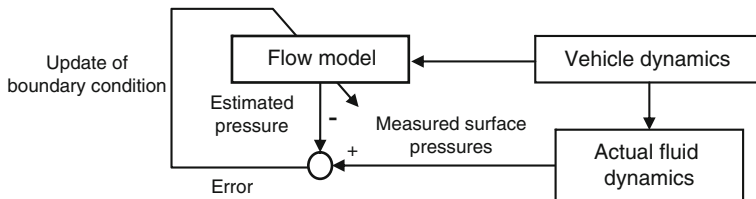


Fig. 2 Structure of the proposed real-time modeling method

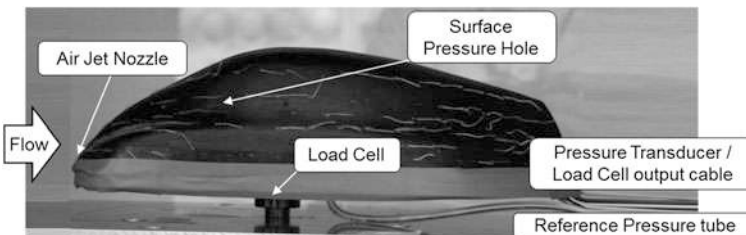


Fig. 3 Wind tunnel model and hole assignment

3 Experimental Apparatus

3.1 Wind Tunnel Test of Scale Model Car and Two-Dimensional Wing Model

The experiments were performed using an NPL wind tunnel with a closed test section of $600 \times 200 \times 200$ mm in the streamwise, horizontal, and vertical directions, respectively. The mainstream velocity was measured using a pitot tube with an accuracy of 5 %. The used surface pressure transducers have an accuracy of 5 %F-S. The full scale ranges from -62 to 62 Pa. The used load cell has an accuracy of 1.5 %F-S. The full scale is 0.098 Nm.

A 1/20 scale model car with a typical low drag shape was used (Figs. 3 and 4). It was mounted on the load cell and set in the test section at various side slip angles, allowing the aerodynamic forces to be measured. There was a hole on the model surface to measure the static pressure. The differential pressure between this pressure hole and the static pressure of the pitot tube was measured. The hole for the air injection was placed on the front surface of the scale model. The injection was controlled using a solenoid valve at the injection hole. When the valve was opened, the flow rate of the injection was $4.7 \times 10^{-4} \text{ m}^3/\text{s}$. The Reynolds numbers of the experiments ranged from 8×10^4 to 2×10^5 .

A two-dimensional wing model was also tested. The airfoil was the same as the cross-section of the car model at the pressure hole. The injection hole was placed at the leading edge (Fig. 5).

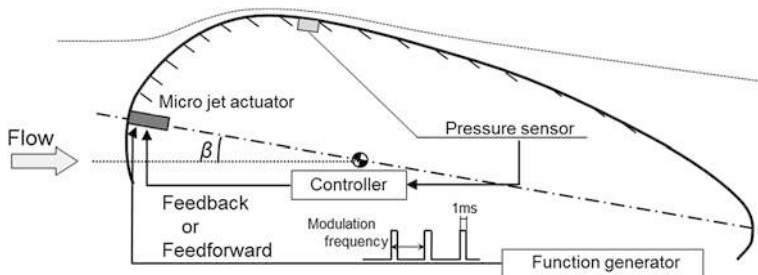


Fig. 4 Block diagram of air injection control

Fig. 5 Two-dimensional wing model

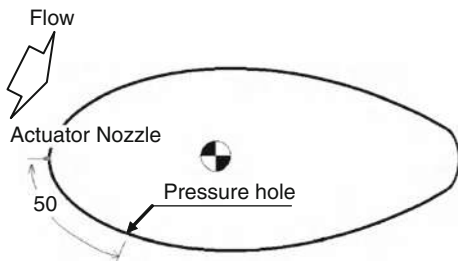
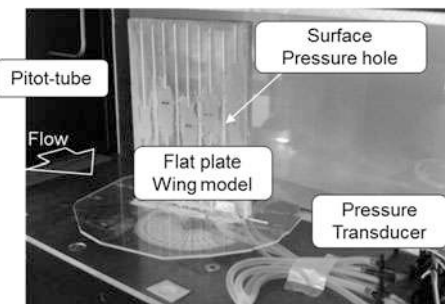


Fig. 6 Experiment with flat plate



3.2 Basic Experiment for Real-time Modeling

A wind tunnel test using a flat plate was performed to validate the real-time modeling (Fig. 6). The code length and span of the plate were 105 and 160 mm, respectively. The static pressures on the plate surface with various side slip angles were measured. The mainstream velocity was 5 m/s.

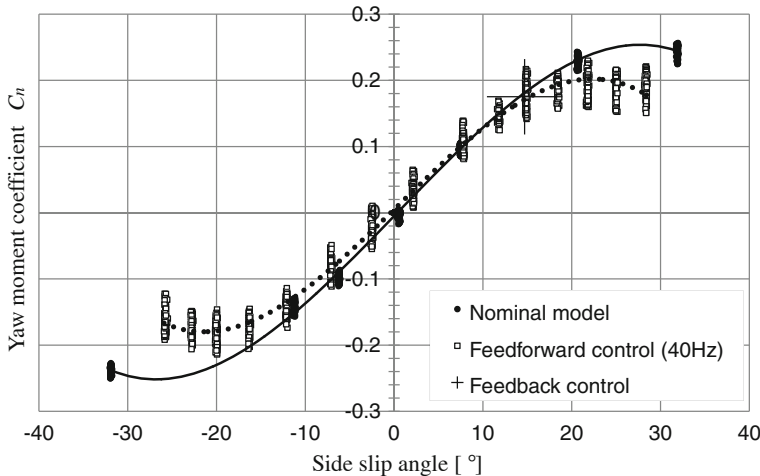


Fig. 7 Yaw moment coefficient with aerodynamic side slip angle

4 Results

4.1 Flow Manipulation Experiment using Scale Model Car

The aerodynamic forces were measured using various side slip angles. Air injection was operated as a feed forward input. The valve was opened for 1 ms at a frequency of 40 Hz, that is, $St = 0.44$. Figure 7 shows the yaw moment coefficients subject to the sideslip angle, and the dotted line is the approximate curve. The yaw moment coefficients without air injection are also plotted, and the solid line is the approximate curve. It can be seen that the yaw moment coefficient is decreased by the air injection. This decrease in the yaw moment is especially evident at a large side slip angle. At a side slip angle of 25° , the yaw moment coefficient is decreased by 20 %. However, the effect of the flow manipulation is weak at a small side slip angle.

Next, the air injection was operated as a feedback control. The scale model car was set at a side slip angle of 15° . The pressure at the static pressure hole was measured, and when the measured value crossed p_{th} moving downward, the valve was opened for 1 ms, where p_{th} is equal to 97 % of the average pressure at a side slip angle of 15° . The flow condition around the car was controlled continuously using this feedback control. The measured yaw moment coefficient with the feedback control is plotted in Fig. 7. The amount of the decrease in the yaw moment by the feedback control is approximately the same as that by the feed forward input.

The yaw moment of the two-dimensional wing was measured with various feed forward inputs. The valve was opened for 1 ms with a frequency of 0–120 Hz, which corresponded to an St of 0–1.8, where $St = fl/U$, f is the frequency of the input, l is a cord length of 150 mm, and U is a mainstream velocity of 10 m/s. The results are

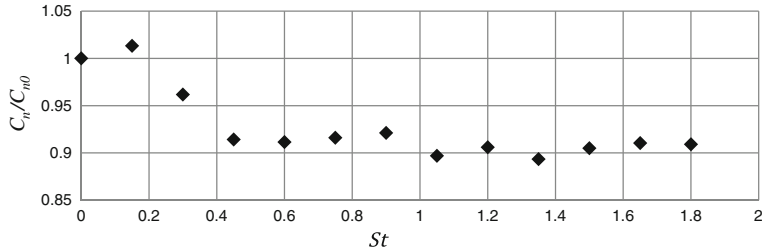


Fig. 8 Normalized yaw moment coefficient of two-dimensional wing

shown in Fig. 8. The yaw moment coefficient is normalized with dividing by C_{n0} , which is the yaw moment coefficient at $S_t = 0$. The flow rate increases as S_t becomes larger. Consequently, the input disturbance to the flow increases. However, the yaw moment coefficient is approximately constant when S_t is larger than 0.44, which is the frequency of the feed forward control of the previous experiment. This result indicates that the effect of the air injection depends on the frequency rather than the flow rate, and an optimal frequency exists.

4.2 Gust Response Simulations with Flow Manipulation

In order to demonstrate the proposed method, the car dynamics with a gust input were simulated using a two-wheel vehicle model with a mass of 900 kg, moment of inertia about the Z-axis of 1,200 kgm^2 , distance from the center of gravity to the front axle of 1.1 m, distance from the center of gravity to the rear axle of 1.2 m, cornering stiffness of 30 kN/rad, and side force coefficient of 0.96. These characteristics represent a typical lightweight automobile. The forward velocity of the car is 25 m/s, and a side wind disturbance of 15 m/s is input from 0 to 1 s. The nominal yaw moment coefficient is assumed to be 0.30. Additionally, it is assumed that the proposed air injection method decreases the yaw moment coefficient by 20 %. This is approximately the same performance as the wind tunnel test results using the scale model car. Figure 9 shows the simulated car responses to the gust input with and without the proposed method. Obviously, the lateral displacement of the nominal model is larger than that with the proposed method. The difference is 50 cm, 4 s after from the gust input. This difference becomes important during actual driving.

4.3 Real-Time Modeling

A real-time modeling method was proposed in the previous section. This method requires a numerical model to calculate the flow condition around the vehicle at every sampling time. A precise numerical method that requires a long calculation

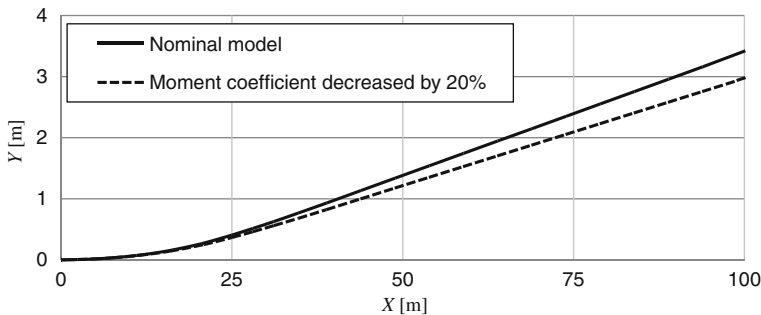


Fig. 9 Simulations of vehicle motion with cross wind disturbance

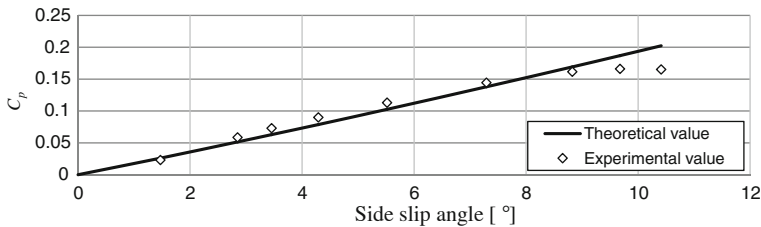


Fig. 10 Pressure of flat plate wing

time such as Navier–Stokes equations cannot be applied to the real-time modeling. Therefore, we propose a simple flow modeling method that uses the complex velocity potential [9]. This can treat the unsteady flow. As a first step of the research, the results of the wind tunnel test and the proposed method are compared. Figure 10 shows the pressure coefficients at the pressure hole at 80 % of the chord length from the leading edge on the leeward surface. It can be said that they agree well. Next, a real-time calculation will be performed using this flow model.

5 Conclusions

A vehicle control method that uses flow manipulation was proposed. In this method, the flow condition is modeled in real-time and provided to the controller to determine the appropriate control input. The structure of the control method was proposed, and basic experiments were performed. The aerodynamic forces of a scale car model equipped with air injection were measured. The results indicated that the proposed flow manipulation device had sufficient performance to suppress the gust response of the car motion. The yaw moment coefficient was decreased by 20 % by the proposed flow manipulation method. Additionally, the results of a wind tunnel test using a two-dimensional wing showed the appropriate control

condition for the air injection. The effective frequency of the air injection was revealed.

The fundamental procedure for modeling the flow condition in real-time was shown. The flow model was improved iteratively by comparing the estimated flow condition and measured value. A simple calculation method for the flow dynamics based on the potential flow was proposed, and the calculated value agreed with the experimental results. This calculation method could be applied to the proposed control system because the calculation load is very low.

References

1. Hucho W-H (1998) Aerodynamics of road vehicles 4th edn. Society of Automotive Engineers, Warrendale, pp 246, 248–249
2. PYihand J (2005) Modification of vehicle handling characteristics via steer-by-wire. IEEE Control Syst Soc 13(6):965–976
3. Huchtkoetter H, Gassmann T (2004) Vehicle dynamics and torque management devices. SAE, SAE Technical Paper 2004-01-1058
4. Jack E (2011) Automotive technology: a systems approach 5th edn. NATEF, Clifton Park, p 1311
5. Vos R, De Breuker R (2007) Morphing wing flight control via post buckled precompressed piezoelectric actuators. J Aircraft 44(4): 1060–1068
6. Filippone A (2009) Inverted jet spoilers for aerodynamic control. J Aircraft 46(7):1240–1252
7. Joslin RD, Miller DN (2004) Fundamentals and applications of modern flow control. AIAA, Reston
8. Simpson RL (1989) Turbulent boundary-layer separation. Annu Rev Fluid Mech 21:205–232
9. Okumura K, Tokutake H (2012) The flapping aircraft dynamics with wing deformation under gust input. In: Proceedings of the 28th congress of the international council of the aeronautical sciences 2012 (Accepted)

Road Test for Interaction Between Differential Lock and Driving Control System

Jian Zhao, Bing Zhu, Jing Li, Jian Wu and Hui Lu

Abstract Driving control system which is composed of TC + AMT (Torque Converter + Automatic Mechanical Transmission) and TCS (Traction Control System) could improve vehicle's performance of starting, accelerating and climbing on bad adhesion road. The similar improvement could also be achieved by a differential lock. They share overlap control field so that conflicts might exist. In this paper, a short-time four-wheel drive vehicle equipped with driving control system and differential locks is tested on icy road and split-mu road, which is covered by ice on one side and dry asphalt road on the other side. Road tests are carried out by turning on or off TCS and cooperating with differentials locked or unlocked separately. The TC and AMT are used during all tests. The results show that the proper cooperation of AMT, TCS and differential locks provides improved start-up performance on slippery road. However, if shifting up to 3rd gear is expected on split-mu road, manual differential locks are under qualified, while the TCS is more flexible and should be adopted.

Keywords Road test · Driving control system · Differential lock · Interaction and coordination

F2012-F08-005

J. Zhao (✉) · B. Zhu · J. Li · J. Wu · H. Lu

College of Automotive Engineering and State Key Laboratory of Automotive Simulation and Control, Jilin University, Changchun, China

1 Introduction

As all components of drive line contribute to the torque transmit from engine to driven wheels, researches on interaction and cooperation of different driveline components are concerned in order to improve driving performance of vehicles [1–4]. Recently, driving control system which is composed of TC + AMT (Torque Converter + Automatic Mechanical Transmission) and TCS (Traction Control System) is researched [5, 6]. In this system, engine, automatic shifting gearbox and active braking control on driven wheels are coordinated to improve operation convenience, fuel economy as well as driving performance.

Particularly, the traction control system limits the slip ratio of driven tires within the optimal region by applying active brakes onto slipping driven wheels together with engine torque reduction. Therefore, an improvement of both longitudinal and lateral tire forces can be achieved and the vehicle driving performance of starting, accelerating and climbing on bad adhesion road will be enhanced consequently [6].

As the traction control can partially restrict the speed difference between driven wheels on one axle, the function is called electronic differential lock control [7]. However, mechanical differential locks are always equipped on off-road vehicles, and they provide the similar functions and work more reliably at off-road driving under lower gears. Thus, conflicts might exist as they share overlap control field. If one of them could be replaced by the other one, only one of them is necessary. Otherwise, the potential conflicts have to be considered to maximize the advantages of each subsystem. Therefore, it is necessary to analyze the interaction between them and find of the necessity of their coordination before above mentioned driving control system is equipped on an off-road vehicle.

In this paper, a short-time four-wheel drive vehicle equipped with driving control system and differential locks is researched. Each axle of the vehicle is equipped with a differential lock. The vehicle is reconfigured with a driving control system developed by the group the authors working in. The driving control system is composed of a set of TC + AMT and a TCS control system. The TC + AMT is used to achieve automatic gear shifting and smooth start-up, and active braking are utilized in this system to accomplish traction control. The engine torque control is required by both gear-shifting and traction control. A priority based algorithm and CAN network is adopted to coordinate gear shifting control and traction control.

The vehicle was tested on icy road and split-mu road, which is covered by ice on one side and dry asphalt road on the other side. Various sets of test maneuvers were carried out by turning on or off TCS and cooperating with differentials locked or unlocked separately. The TC and AMT were used during all tests.

2 Tested Vehicle and Procedures

2.1 Tested Vehicle

The configuration of the tested vehicle is shown in Fig. 1. The tested vehicle is a light off-road vehicle with short-time four-wheel drive. Each of the driven axles is equipped with a differential lock. The original vehicle was equipped with an electronic control diesel engine and manual gearbox. It was modified by a set of driving control system. The dry friction clutch and manual gearbox were replaced by TC + AMT, and the engine torque is adjusted by the accelerator regulation. Furthermore, a set of TCS system actuating accelerator and wheel brakes was added. As both of AMT system and TCS use transmission rotational speed as inputs and engine accelerator as actuator, a coordination controller is utilized to eliminate their conflicts. A priority based algorithm is designed for this purpose and data transfer between the two systems is achieved by CAN Bus. When excessive slippery on driven wheels occurs, the traction control function will be triggered. Once the TCS is triggered, up-shifting is prohibited by the coordination controller. Furthermore, brake control in TCS is only activated below the 3rd gear to ensure the stability of the vehicle. Once the AMT shifts to 4th gear, the TCS is only work at engine control mode.

In order to monitor and record the tests, a set of test system composed of dSPACE AutoBox and PC is utilized. The system is also used in driving system development. Signals such as accelerator position, gears, wheel brake pressure, yaw rate and steering wheel angle is recorded. Furthermore, control signals from controllers are also recorded by the system.

2.2 Test Procedures

The vehicle was tested on a uniform low-mu road and a split-mu road. The uniform low-mu is an icy road which coefficient is approximate uniform and constant at a small value. The split-mu road is covered by ice on one side and dry asphalt road on the other side. Thus, there is significant difference between the coefficients of each side. There exists a slope of 5 % for the test road, which increases the possibility of slipping of driven wheels.

Tests were carried out as 4WD mode, and differentials were locked or unlocked as necessary. The driving system was allowed to shift up to the 3rd gear, while the TCS was turned on or off in different tests. To eliminate the influence from the driver, he was required to press the accelerator pedal fully in some tests. In the other tests, the accelerator pedal was controlled by the driver normally, and it was required to be pressed as making sure the vehicle could accelerate as fast as possible. The driver was allowed to regulate the steering wheel when side slip of the vehicle appeared.

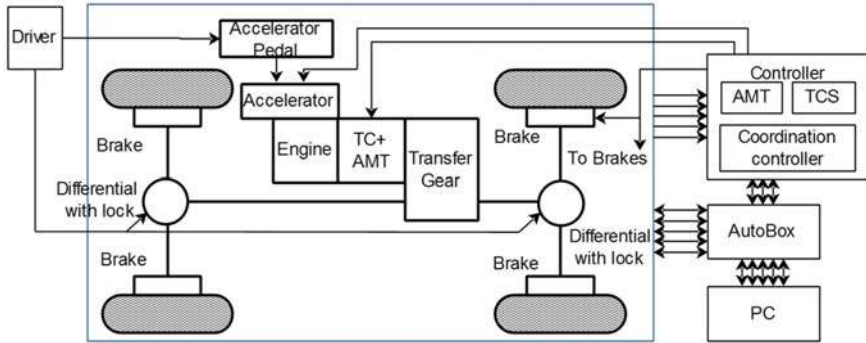


Fig. 1 Configuration of tested vehicle

3 Tests on Icy Road

Curves in Fig. 2 show the test results when the vehicle was driving on the icy road with the differentials locked and TCS turned off. The top left curves show the velocity of vehicle and linear speeds of four driven wheels. In the legend, v is the velocity of the vehicle and v_{fl} , v_{fr} , v_{rl} and v_{rr} are the linear speeds of front left, front rear, rear left and rear right wheel separately.

The top right figure shows two different curves, and its left y-axis illustrates the yaw rate of the vehicle and the right one illustrates the steering wheel angle applied by the driver. The bottom left figure contains the curves of position of accelerator and control flags. In the legend, k_D is the position of accelerator pedal applied by the driver and k_E is the position of the engine accelerator which was regulated by the controller. The measurements of k_D and k_E are illustrated on the left y-axis. F_{Gear} is the Gears and F_{TCS} is the flag of TCS being on or off. Their measurements are illustrated on the right y-axis. The bottom right figure shows brake pressure of four wheels, and p_{fl} , p_{fr} , p_{rl} and p_{rr} are the brake pressure of front left, front rear, rear left and rear right wheel separately. It demonstrates the brake control applied by controller when TCS was triggered. All of the other results curves are of the same definition.

The results show that with only differentials locked, all of the driven wheels slipped along with the increasing value of accelerator and triggered the up-shifting of gearbox. Further wheel slippery appeared after the gearbox shifting to 2nd gear. Finally, the vehicle cannot start up. Furthermore, the vehicle yawed with the peak value of yaw rate over 0.1 rad/s and steering wheel regulated by driver was necessary.

The test results when the vehicle was driving on icy road with the differentials locked and TCS turned on were shown in Fig. 3. And the accelerator pedal was fully pressed. It is seen that both engine control and brake control were engaged and the slippery of all wheels was reduced significantly. It took 9.8 s for the vehicle reaching the speed of 20 km/h. The average acceleration is 0.57 m/s^2 .

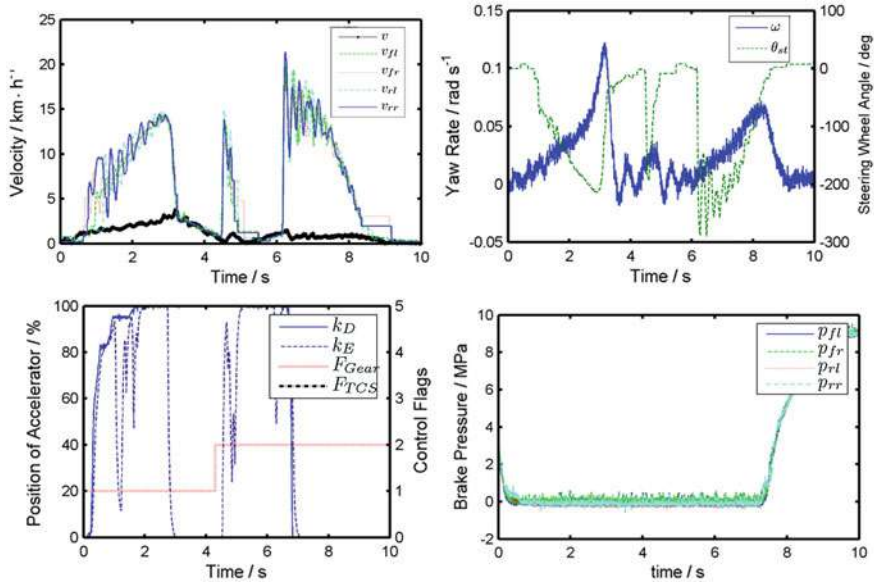


Fig. 2 Test results on icy road with differentials locked and TCS off, full acceleration

Furthermore, the value of yaw rate was also reduced and not much steering regulation was needed.

Figure 4 shows the test results when the differentials were locked and TCS was turned off, while the accelerator pedal is controlled by the driver. As the driver maintained the pedal at a small value, the wheels were not slip. But the acceleration of the vehicle was also reduced. It took the vehicle 18 s reaching the speed 20 km/h and the average acceleration is 0.31 m/s².

4 Tests on Split-Mu Road

Curves in Fig. 5 show the test results when driving on the split-mu road with the differentials locked, TCS turned off and fully accelerating. It is shown that slippery didn't occur as one side wheels were driving one the dry asphalt road. However, the difference between the driven forces on tires of both sides resulted in a severe side slipping of the vehicle and the test was forced to termination. It is also concluded that tests for both differentials locked and TCS on split-mu road is not necessary as the driven wheels won't slip and TCS won't be triggered.

Figure 6 shows the results on testing with the differentials unlocked, TCS on and fully accelerating. It is seen that both of engine control and brake control were engaged and the wheels brake worked as electronic differential control. The wheels slippery were reduced and the acceleration of the vehicle was increased

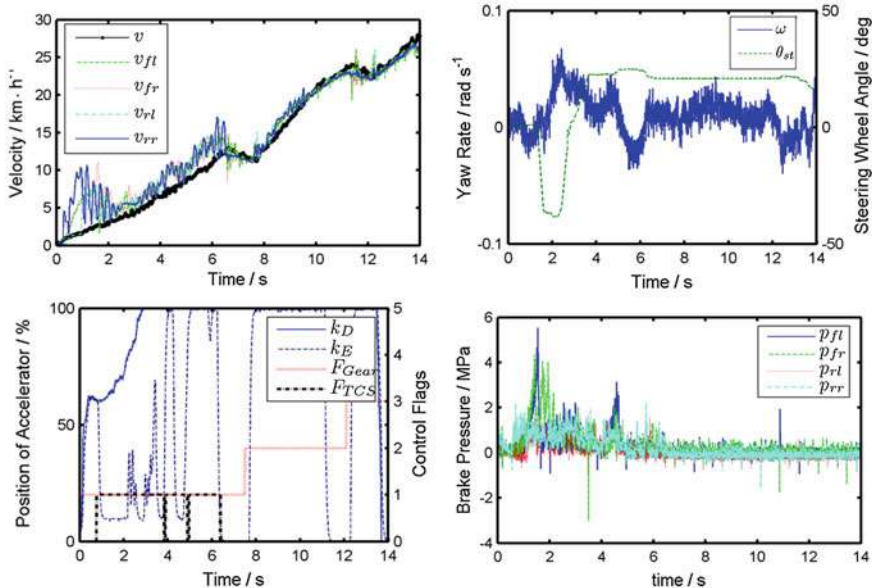


Fig. 3 Test results on icy road with differentials locked and TCS on, full acceleration

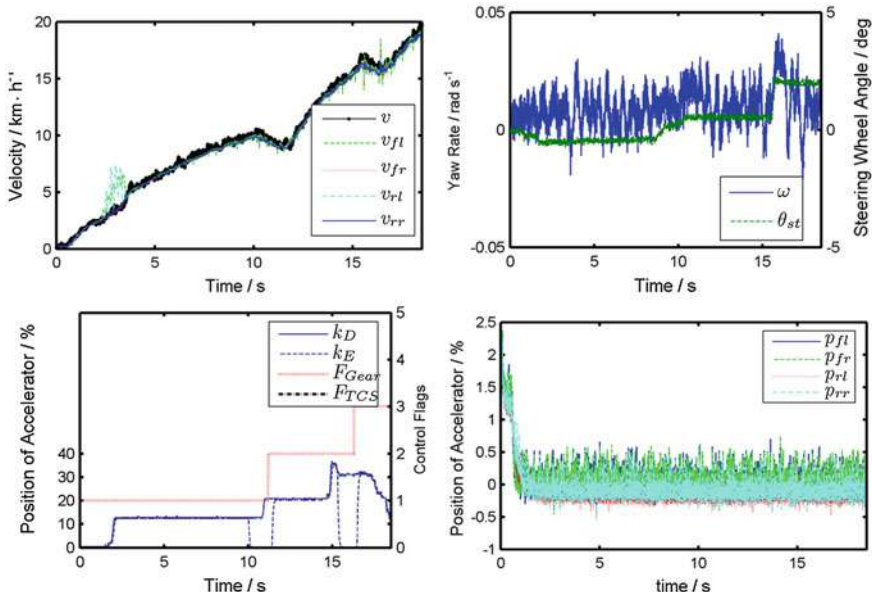


Fig. 4 Test results on icy road with differentials locked and TCS off, normal acceleration

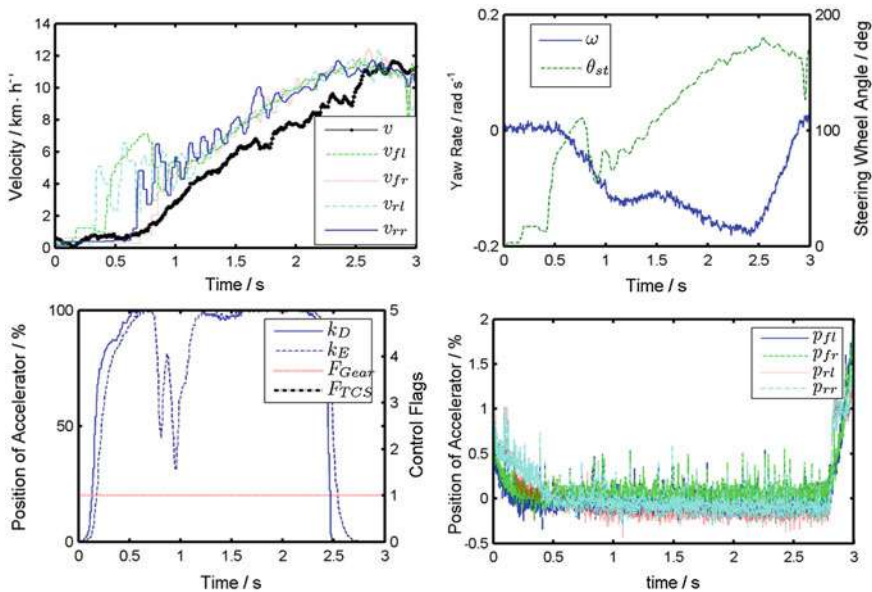


Fig. 5 Test results on split-mu road with differentials locked and TCS off, full acceleration

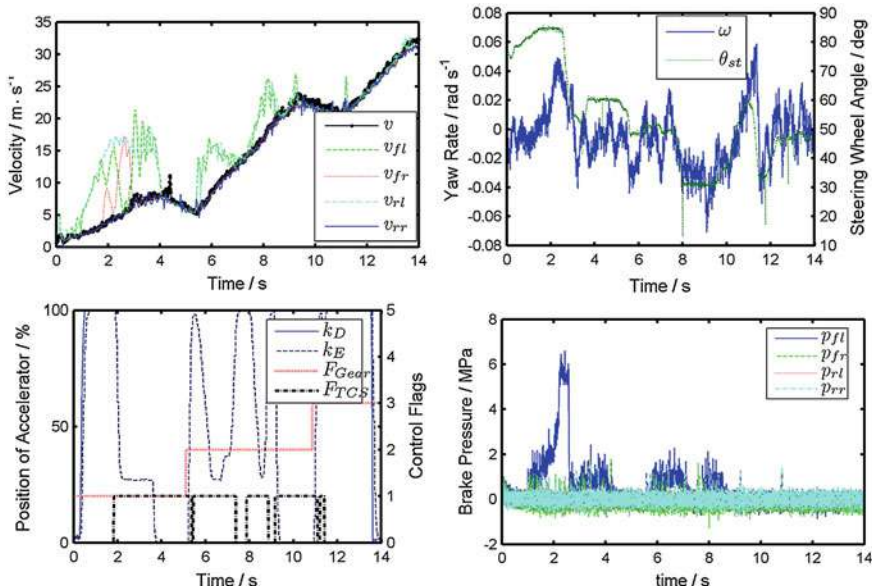


Fig. 6 Test results on split-mu road with differentials unlocked and TCS on, full acceleration

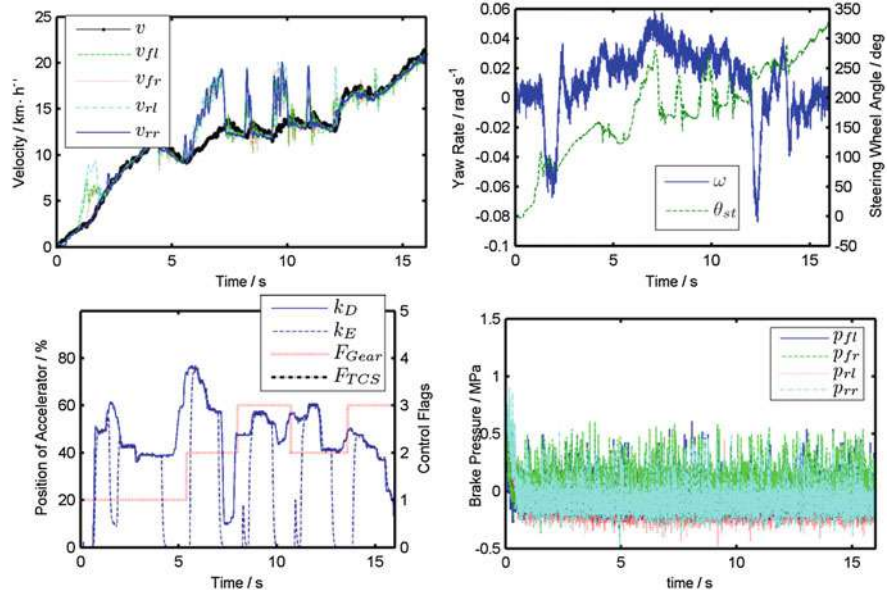


Fig. 7 Test results on icy road with differentials locked and TCS off, normal acceleration

without excessive side slipping. It reached 20 km/h at 8.5 s and 30 km/h at 13.2 s. The average acceleration is 0.63 m/s².

Figure 7 shows the results on testing with the differentials locked and TCS function switched off. The driver didn't press down the pedal completely but regulated it to ensure its startup as big as possible. It is seen that the driven wheels didn't slip, and the vehicle still had the tendency of side slipping. The driver had to reduce the value of accelerator pedal position together with steering wheel adjustment to maintain the stability of the vehicle. Therefore, the vehicle started up, but the acceleration was affected negatively. It reached 20 km/h at 15.4 s and the average acceleration is 0.36 m/s².

5 Conclusion

In this paper, road tests were carried out for a short-time 4WD vehicle equipped with driving control system and differential locks on icy road and split-mu road. The results show that: 1. With differentials locked and TCS turned off, acceleration would be improved. However, it is also harmful to handling stability severely. 2. Driving performance could be further improved with both TCS on and differentials locked on icy road. It provides a better compromise between acceleration and stability in the case of TCS on and differentials locked. 3. The electronic

differential lock function of TCS works well on split-mu road. The acceleration is increased with low yaw rate. 4. The vehicle could start up under driver's control with differentials locked on both roads, but TCS works better.

It is concluded that the cooperation of AMT, TCS and differential locks provides improved start-up performance on smooth road. However, if up-shifting to 3rd gear is expected on split-mu road, manual differential locks are under qualified and TCS should be adopted. In future work, combination technique of driving system mentioned in this paper and automatic differential locks should be developed.

Acknowledgments This project was supported in part by the National Science Foundation of China for Young Scholars (51105169) and Jilin Provincial Research Foundation for Young Scholars, China (201101028).

References

1. Jawad B, Hachem N, Cizmic S, et al (2001) Traction control applications in engine control. SAE paper 2001-01-3464
2. Kunii R, Iwazaki A, Sekiya S, et al (2005) Development of direct electromagnetic clutch system. SAE Paper 2005-01-0551
3. Smithson R, Miller D, Allen D (2004) Scalability for an alternative rolling traction CVT. SAE Paper 2004-01-0355
4. Gao Y, Li J, Zhao J, et al (2009) Full-time four wheel drive vehicle traction integrated control strategy. J Jilin Univ(Engineering and Technology Edition) 39(2):296–299
5. Yuan S, Li Y, Li J (2008) Research on traction control system based on electronic control diesel engine, TC + AMT and Brake. J Jilin Univ (Engineering and Technology Edition) 20(3):807–810
6. Li J, Lu H, Zhao J, et al (2011) Matching test of driving force control modes for automatic transmission vehicle on ice road. J Jilin Univ(Engineering and Technology Edition), Vol. 41, Sup. 2. 2011, 41(9): 30–35
7. He Y (2008) Research on the control strategy of LSD by Brake. Wuhan University of Technology, Wuhan

Evaluation of the Effectiveness of Active Safety Systems in Vans with Respect to Real World Accident Analysis

Francisco Javier Páez Ayuso, Arturo Furones Crespo, Francisco Aparicio Izquierdo and Blanca Arenas Ramírez

Abstract This paper belongs to “F08: Vehicle Controls on Handling and Stability” topic. It is aimed to assess the potential influence of three active safety systems—the Antilock Brake System (ABS), the Brake Assist System (BAS) and the Electronic Stability Programme (ESP)—in collisions with vans involved, through the analysis of fatal real world accidents occurred in Spain. The methodology follows during this study is based on a retrospective accident analysis of the technical reports of the Spanish Traffic Directorate (DGT). A detailed database has been compiled by the INSIA—UPM accident analysis department, comprising 254 fatal accidents with vans involved, occurred in rural roads during 2009 and 2010. In case of fatal accidents, these reports prepared by the Spanish Traffic Police show a high quality data. This information has been analysed to identify major accidents and causes of accidents (HFF method), in order to identify reference accident scenarios, which take into account the active safety systems proposed. A sample of these accidents, selected from the most representative scenarios, has been re-analyzed and re-evaluated considering the assumed effect of each specific active safety system. Although the performance of active safety systems explains basically their behaviour in test conditions, they are not sufficient to assess their success in each real world situation. Active Safety systems interact with the driver, the vehicle and the environment. A full forecast of their potential is only possible by modelling the driver-vehicle-system-environment. This methodology has already been applied by authors to evaluate the effectiveness of active safety systems in case of pedestrian accidents. This study continues the same research line based on real world accidents analysis, applied to accidents involving vans. The findings show that a

F2012-F08-006

F. J. Páez Ayuso (✉) · A. Furones Crespo · F. Aparicio Izquierdo · B. Arenas Ramírez
University Institute of Automobile Research (INSIA), Technical University of Madrid
(UPM), Espanha, Spain

number of the collisions could have been avoided by implementing these systems. Even though comprising a small number of cases, it is an invaluable resource for monitoring real world performance of active safety systems.

Keywords Vans • Light goods vehicle • Real world accidents • Active safety systems • Effectiveness

1 Introduction

In order to assess the safety performance of vans it is necessary to be able to identify these vehicles data relating to accident involvement. Many EU Member States do not collect information on goods vehicles of this size and many use different definitions of smaller goods vehicles that could not be made to fit the European definitions. The type of vehicle “van” as considered in this paper includes two categories:

- Category 1 (C1): N1, vehicles designed and constructed for the carriage of goods and having a maximum mass not exceeding 3.5 tonnes (extracted from 2007/46/EC [4]). This definition is consistent with “Light Goods Vehicle, LGV” or “Light Commercial Vehicle, LCV”.
- Category 2 (C2): car-derived LGV, a variant of a passenger car design that has been adapted to carry goods.

There is relatively limited data in Europe on van crashes. In-depth work has been carried out in Britain [2] and Germany [3] and these investigations indicate what while vehicles do not necessarily have a higher crash rate than other motor vehicles, crashes tend to occur in predominantly urban environments.

The growing problem of accidents in the transport of goods in light vehicles has been undertaken in some studies in Europe. In this regard, stresses the project IMPROVER [1], which shows that the country of the EU-25 with the highest number of fatalities in accidents involving LGV's is Spain, followed by Poland, Italy and France (data from 2002).

This paper summarises a study performed by the Accidentology and Vehicle Dynamics Unit of INSIA with the aim of the evaluation of the potential of accident reduction which could be achieved by incorporating different active safety systems to the Spanish van fleet.

2 Methodology

The methodology was established to carry out a retrospective in-depth analysis of Accident Reports. These reports came from two different sources, the Spanish Traffic Police and the Spanish Traffic Directorate (DGT), and contained detailed

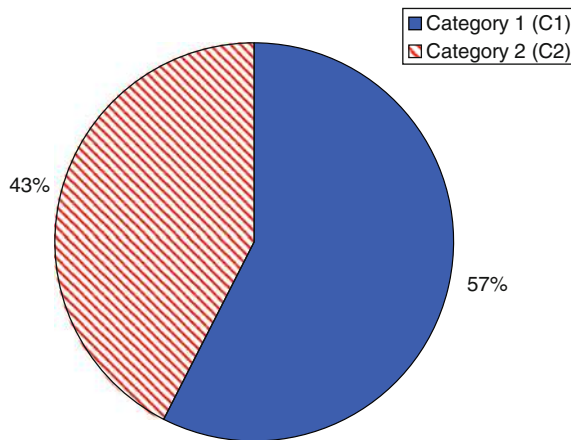


Fig. 1 Distribution of vans involved in studied accidents by category

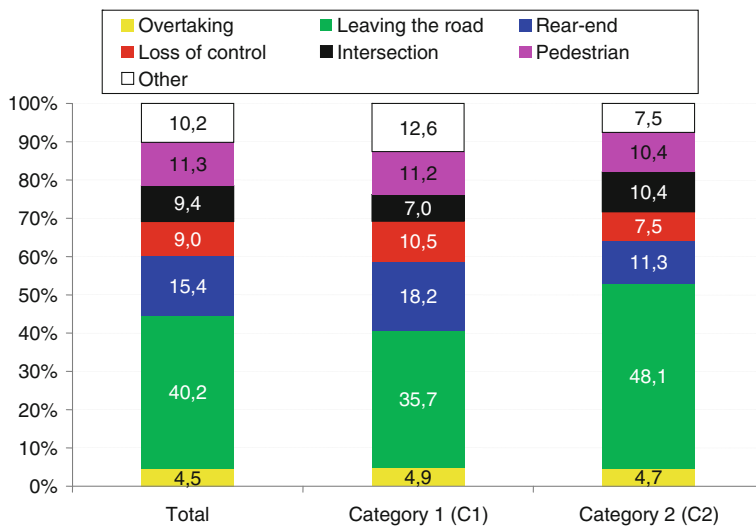


Fig. 2 Distribution of vans involved in studied accidents by crash configuration and by category

information about real-world fatal accidents involving vans and occurred in Spanish rural roads between 2009 and 2010.

All available information and data investigated have been analyzed in depth and were used to simulate the accident. The scene was first recreated through detailed sketches, to scale, with the geometry, measurements, marks, traces, collision point and rest positions. The corresponding vehicle parameters were then loaded.

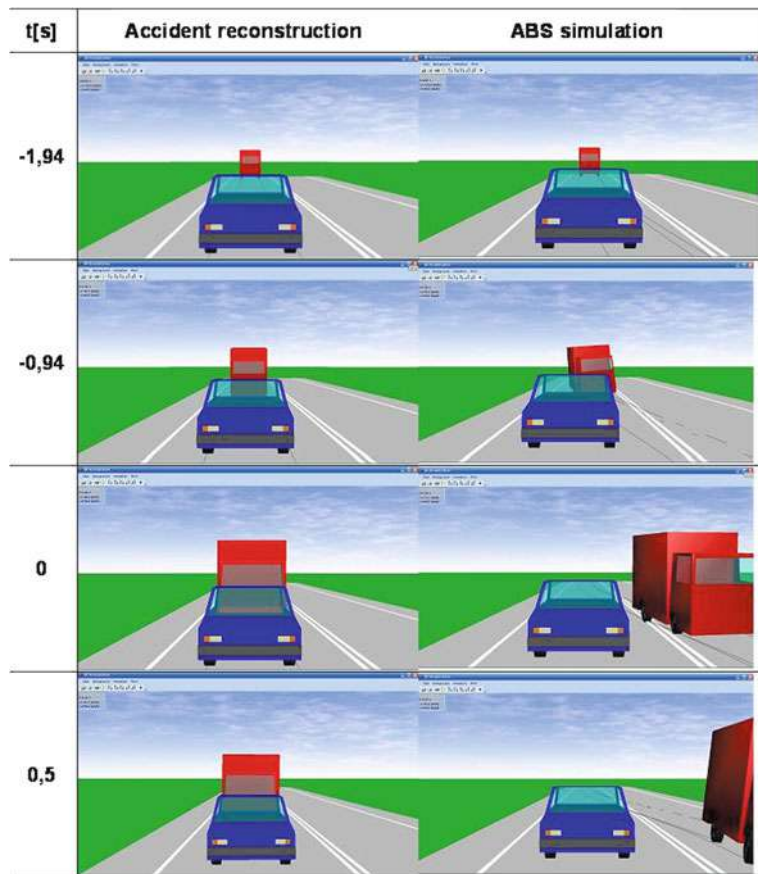


Fig. 3 Time-line comparison between the real accident reconstruction and the ABS simulation

An operational method of accident causation analysis is necessary to reach the definition of more appropriate measures, involving notably electronic safety functions, possibly able at preventing it. Along this objective, the Human Functional Failures (HFF) method [5] has been applied to the investigated accidents. It presents several operational grids of analysis along the accident process production, in line with theoretical models, which offer a means of progressing in the conceptions regarding the human role in accident generation.

Every single case has been virtual simulated twice using the PC-Crash® software: the first is a reconstruction of the real accident and the second is a simulation in which the operation of the active systems –ABS, BAS and ESP- is emulated modifying the collision parameters and its potential consequences. A common simulation procedure with simplified hypotheses about the driver's reactions and the active systems operation was previously adopted, considering the functional criteria of these systems:

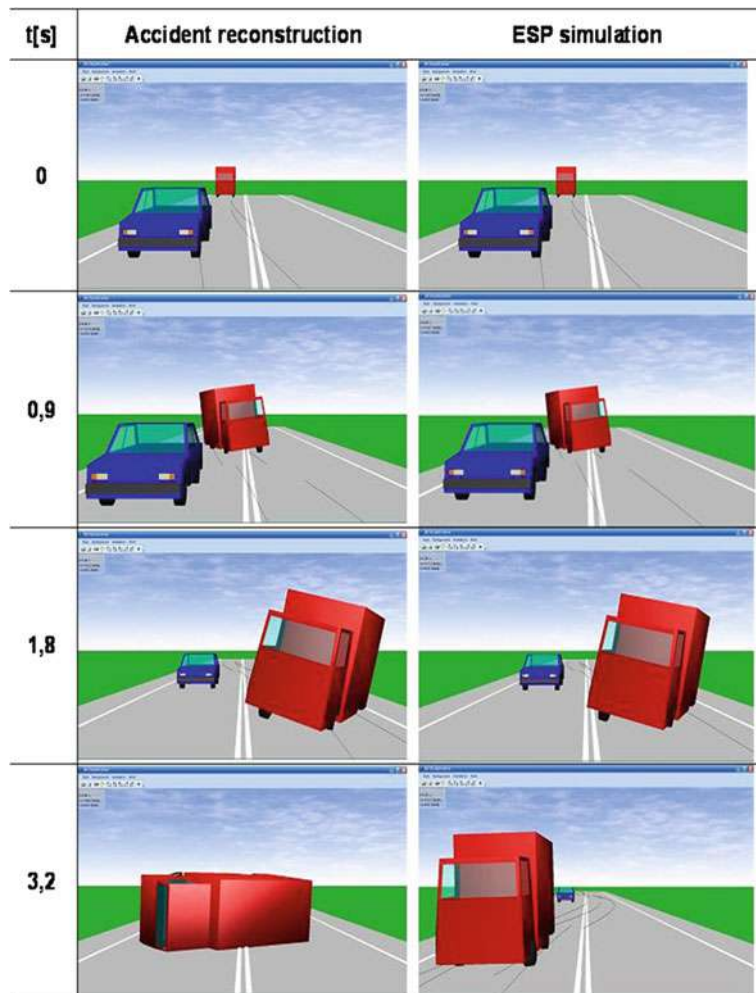


Fig. 4 Time-line comparison between the real accident reconstruction and the ESP simulation

Table 1 Potential effectiveness (%) of the ABS, ABS + BAS and ESP systems in vans involved in real accidents by category

%	Category 1 (C1)	Category 2 (C2)	Total
ABS	14,7	12,3	13,9
ABS + BAS	23,8	13,2	19,9
ESP	16,8	19,8	17,7

- The Antilock Brake System (ABS) is an automobile safety system that allows the wheels on vehicle to continue interacting with the road surface as directed by driver steering inputs while braking, preventing the wheels from locking up.

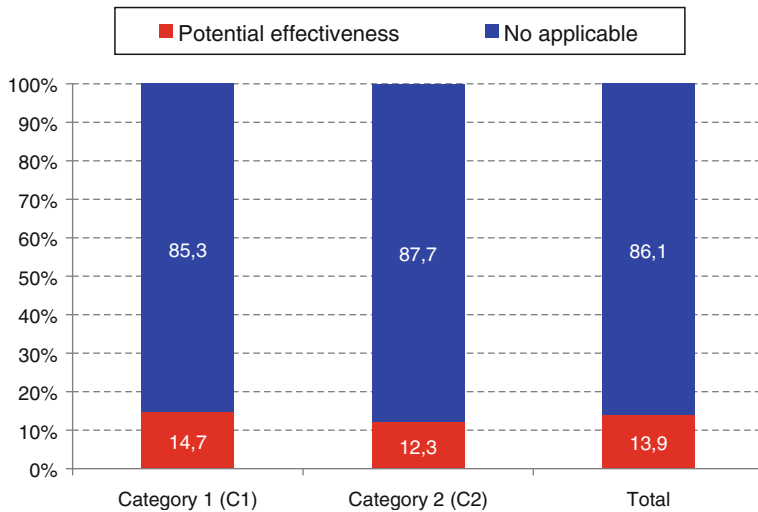


Fig. 5 Potential effectiveness of the ABS system in vans involved in real accidents

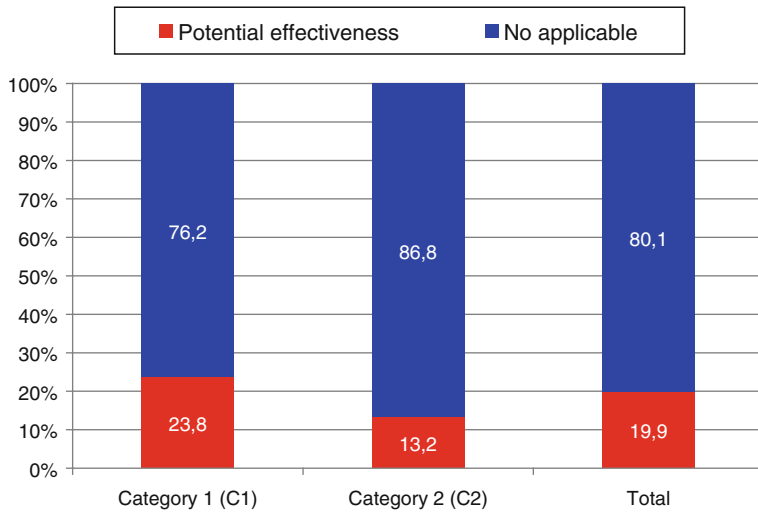


Fig. 6 Potential effectiveness of the ABS + BAS system in vans involved in real accidents

The ABS generally offers improved vehicle control and decreases stopping distances on dry and slippery surfaces for many drivers.

- The Brake Assist System (BAS) combined with the Antilock Brake System (ABS), measures the speed and force of brake application to determine whether the driver is attempting an emergency stop. If such an emergency is determined, the system applies additional brake pressure to allow the driver to take full advantage of the Antilock Brake System (ABS) which prevents wheel lock up.

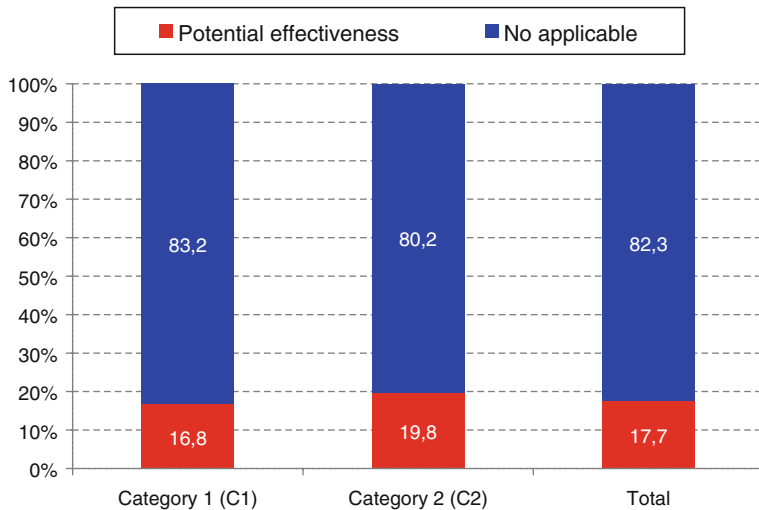


Fig. 7 Potential effectiveness of the ESP system in vans involved in real accidents

- The Electronic Stability Program (ESP) is a technology that improves the vehicle stability by detecting and reducing the loss of traction. When it detects loss of steering control, it automatically applies the brakes to drive the vehicle where the driver intends to go and it also reduces the engine power until the control is regained.

3 Results

According to the van categories as defined previously, the Fig. 1 shows the distribution of vans involved in the real-world fatal crashes by category.

By modifying the parameters that affect the van behaviour according to the ABS, BAS and ESP characteristics, a second set of virtual simulations for all the cases has been obtained. These active systems have been simulated in the case of the crash configuration could be improved by them. The distribution of the accidents by crash configuration and by category is drawn in Fig. 2.

Both real reconstructions and ABS/BAS/ESP-simulation outputs were compared by pairs. Examples of such comparison are presented in Figs. 3 and 4 which illustrate some key sequences. The Possible Perception Point (PPP) is the same for both cases as also is the reaction time of the driver.

Figure 3 simulates a rear-end collision and the braking system of the involved van does not contain ABS system. During the real situation and when the driver applies an emergency braking action the wheel is locked up; after that, the vehicle

does not react to steering wheel inputs. When the ABS is simulated, the vehicle develops combined manoeuvres (braking and steering) and the collision avoidance action is possible.

Figure 4 simulates a van overtaking another moving vehicle and driving along the same lane. The real van does not include an ESP system. During the real situation and when the driver tries to return to his lane after the overtaking manoeuvre, the van rolls over onto its side due to the inadequate velocity. When the ESP is simulated, it helps the driver and the vehicle finishes the manoeuvre.

Finally, the potential effectiveness of the analysed systems in vans involved in accidents is shown in the Table 1 and in Figs. 5, 6 and 7.

4 Conclusions

For many years numerous studies have conducted to estimate the effectiveness of safety systems for vehicles. However, the most of these ones has been focused on passenger cars and clear gaps were detected in the case of specific studies on vans.

Multi-disciplinary approaches such as this study make the identification of critical parameters easier and simplify the development of practical solutions by quantifying their potential impact on future actions to improve van safety. Using this methodology, a database comprising 254 fatal accidents with vans involved was created, including information of the vehicle, and scene. Reconstructions of these accidents were performed using advanced techniques to accurately estimate multiple parameters from the collision, the pre- and post-impact phases.

The gathered information has been used for the evaluation of the effectiveness of the Antilock Brake System (ABS), the Brake Assist System (BAS) and the Electronic Stability Programme (ESP). The performance of these systems has been simulated in reconstructions, so it was possible to analyse their capacity for the avoidance of the analysed accidents. The evaluated active systems proved to be efficient for avoiding the accidents in a percentage of the studied cases.

The implementation of active safety systems in all new vehicles will lead to achieve reductions in van-involved accidents or to decrease their severity. So, it is recommended to influence on the generalization of ABS, BAS and ESP as standard equipment in all new vans.

Finally and in order to assess the safety performance of vans it is necessary to be able to identify these vehicles data relating to accident involvement, vehicle registration and vehicle usage. It would improve any future evaluations of van safety performance or help to monitor the effects of any policy decisions.

Acknowledgments This research was partially supported by the Ministry of Public Works and Transport (FURGOSEG: “Desarrollo y aplicación de una metodología integrada para el estudio de los accidentes de tráfico con implicación de furgonetas”, P24/08) and the Community of Madrid (SEGVAUTO: “SEGuridad de Vehículos AUTomóviles”). The authors would like to thank the experts of the Spanish Traffic Police and the Spanish Traffic Directorate (DGT) for their contribution.

References

1. Hohnscheid D, KJ and others (2006) Impact assessment of measures concerning the improvement of road safety of light goods vehicles (LGV). Final report of Subproject 2, IMPROVER Project, 2006
2. Lenard J, Frampton R, Kirk A, Morris A, Newton R, Thomas P and Fay P (2000) An overview of accidents and safety priorities for light goods vehicles. IMechE paper, 2000
3. Niewohner W; Berg FA, Froncz M (2001) Accidents with vans and box-type trucks (Transporters); Results from official statistics and real-life crash analyses. In: Proceedings of enhanced safety in vehicles (ESV) Conference, 2001
4. The European Parliament and the Council of the European Union (2007) Directive 2007/46/EC on establishing a framework for the approval of motor vehicles and their trailers, and of systems, components and separate technical units intended for such vehicles. Official J EU, L 263, Sept 2007
5. Van Elslande P, Fouquet K (2007) (INRETS) Analyzing human functional failures in road accidents. D5.1. from Project No. 027763—TRACE, 2007

High Accuracy Yaw Rate Sensor for Preventive Safety System

Masamoto Kawaguchi, Naoki Fujimoto, Takashi Katsumata and
Masaaki Tanaka

Abstract With a recent growing awareness of vehicle safety, the need for preventive safety systems is also increasing. This has promoted the practical use of new preventive safety systems, notably Adaptive Cruise Control (ACC) and Lane Keeping Assist (LKA) and the compulsory installation of existing preventive safety systems such as Electronic Stability Control (ESC) in all vehicles. In ESC and other preventive safety systems, tracking of actual vehicle behavior is important, and the yaw rate sensor is a key sensor necessary to keep track of the behavior. The need for high-accuracy yaw rate sensors has been increasing day by day in the context of the practical use of new preventive safety systems and the need for upgrading existing preventive safety systems. We have already implemented the capacitive accelerometer for air bags that features an element configuration using a general-purpose single-crystal SOI wafer, and a stacked structure comprising a sensor chip and a circuit chip. This time we have successfully developed a high-accuracy yaw rate sensor by applying the technology of the capacitive accelerometer. (1) Optimization of the sensor element configuration (using a frame structure to reduce leakage vibrations). (2) Flip-chip bonding of the sensor chip and the circuit chip using a cross layout to achieve both the reduction of heat deformation/parasitic capacity and the avoidance of interference between resonance frequencies. Utilizing the above two techniques has enabled us to achieve the high accuracy of the yaw rate sensor. As a result, we have developed a yaw rate sensor with a zero-point accuracy of $\pm 3^\circ/\text{s}$ (actual value: $\pm 0.5^\circ/\text{s}$) in the $\pm 100^\circ/\text{s}$ range.

F2012-F08-008

M. Kawaguchi (✉) · N. Fujimoto · T. Katsumata · M. Tanaka
Denso Corporation, Kariya, Japan

Keywords ESC · Yaw rate sensor · Flip chip · SOI · Safety system · Capacitive sensor

1 Introduction

Vehicle safety systems are broadly classified into two types: the passive safety system designed to reduce injury at the time of an accident, and the preventive safety system designed to ensure vehicle stability before an accident occurs and to assist in avoiding an accident. With a recent growing awareness of vehicle safety, the need for preventive safety systems is also increasing. This has promoted the practical use of new preventive safety systems, notably Adaptive Cruise Control (ACC) and Lane Keeping Assist (LKA) and the compulsory installation of existing preventive safety systems such as Electronic Stability Control (ESC) in all vehicles. Figure 1 illustrates the overview of the ESC system, a major preventive safety system.

The ESC system is designed to prevent a vehicle from drifting out of its lane (failing to turn) or from spinning (turning too much) against driver's intention, such as "to turn along a curve". In the system, the torque brake control of each wheel is optimized to prevent a vehicle from drifting or spinning by comparing driver's intention, which is estimated based on the data from the steering angle sensor, the wheel speed sensor, and the accelerometer, to the actual vehicle behavior detected based on the output from the yaw rate sensor and other sensors.

In ESC and other preventive safety systems, tracking of actual vehicle behavior is important, and the yaw rate sensor is a key sensor necessary to keep track of the behavior. The need for high-accuracy yaw rate sensors has been increasing day by day in the context of the practical use of new preventive safety systems and the need for upgrading existing preventive safety systems.

In recent years, the capacitive accelerometer [1, 2] and the yaw rate sensor [3, 4] have been studied actively in the MEMS field. The reason is that compared to the piezoresistive and piezoelectric accelerometers, the capacitive accelerometer has high sensitivity, excellent DC detection capability, and good temperature characteristics, and allows easy self-testing. The yaw rate sensor, which is used for vehicle control, is also required to be highly accurate as preventive safety systems become more sophisticated. In this context, efforts have been made to achieve a thick structure using SOI [5–7], the *Si-glass anodic bonding technique* [8], and the trench refill process [9] and to achieve high accuracy by improving the anchor structure to reduce impacts of thermal stress and packaging stress [10, 11].

We have implemented the capacitive accelerometer for air bags with a stacked structure comprising an SOI based sensor chip and a circuit chip as shown in Fig. 2 [12–14]. Here we applied the same technique to achieve high accuracy, a challenging issue on the yaw rate sensor.

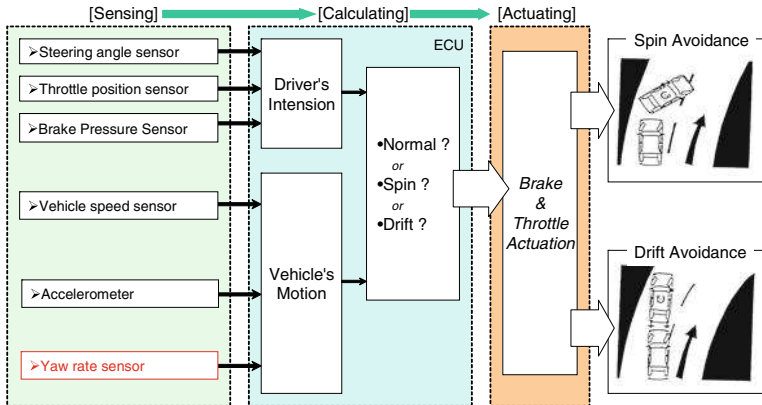
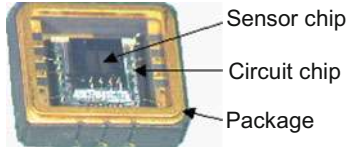


Fig. 1 Concept of the ESC system

Fig. 2 Accelerometer



The key points of developing a high-accuracy yaw rate sensor are the sensor element design and the package design.

2 Sensor Element Design

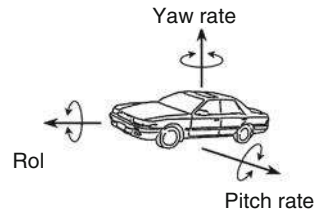
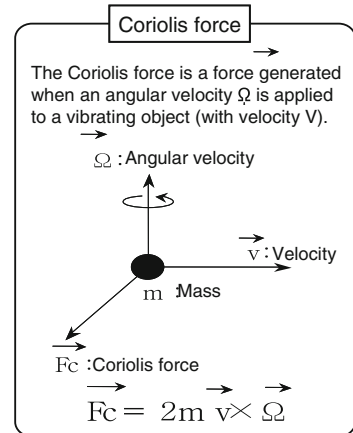
As shown in Fig. 3, a vehicle position is expressed by the rotational angles around three axes: forward/backward, left/right, and up/down. The angular velocity around each axis is called roll rate, pitch rate and yaw rate. Thus a yaw rate sensor detects the angular velocity of lateral rotation of a vehicle.

Figure 4 shows the detection principle of the vibration type yaw rate sensor, which is based on the Coriolis force. The Coriolis force acts on the mass of an object M that moves with velocity V in a plane rotating at an angular velocity Ω , and is expressed by the following equation:

$$F_c = 2MV \times \Omega \quad (1)$$

Equation (1) also indicates that the direction of the Coriolis force is perpendicular to both the velocity vector V and the angular velocity vector Ω .

Figure 5 shows a comparison of operational behaviors between an accelerometer and a yaw rate sensor.

Fig. 3 Vehicle rotations**Fig. 4** Detection principle of the yaw rate sensor

Both accelerometer and yaw rate sensor can be described by a two dimensional spring-mass model. A Yaw rate sensor is more complex with two springs and masses which are connected to each other by a coupling spring compared to an accelerometer with only one mass and spring. In an accelerometer, the masses stay still while no acceleration is applied, whereas in a yaw rate sensor, the two masses are oscillated in opposite phase at a constant frequency all the time even while no angular velocity is applied. When an angular velocity is applied, the Coriolis force makes the two masses oscillate in opposite phase in a direction orthogonal to the driving direction. This oscillation is detected as a capacity change. The reason why a MEMS gyroscopic sensor comprises two masses is to distinguish an acceleration-induced oscillation from a Coriolis force-induced oscillation. When acceleration is applied, the two masses move in phase compared to the opposite phase for the Coriolis force, and thus allows to cancel the noise from acceleration.

Figure 6 shows the functional configuration of the yaw rate sensor element. The function of the sensor element is broadly divided into four parts.

The first part is the driving electrode that generates a driving force for driving the masses at a constant frequency all the time.

The second part is the drive monitor electrode that detects the driving force generated by the driving electrode as a capacity change in the driving direction.

The third part is the detecting electrode that detects a capacity change proportional to the Coriolis force.

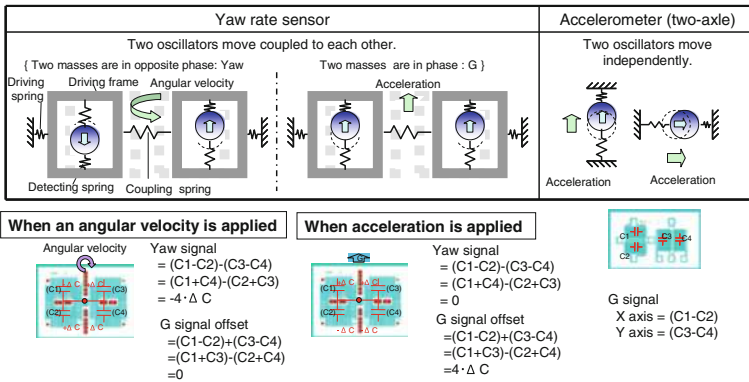


Fig. 5 Comparison between the accelerometer and the yaw rate sensor

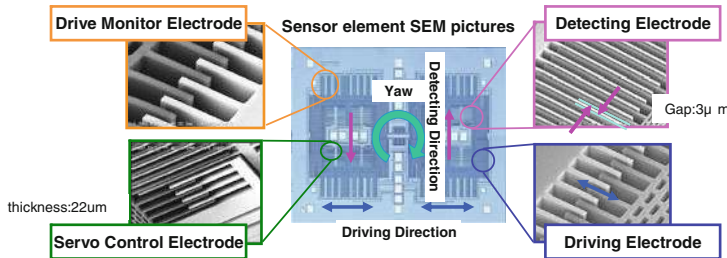


Fig. 6 Functional configuration of the yaw rate sensor element

The fourth part is the servo control electrode that uses electrostatic attraction to suppress displacement in the detecting direction.

A yaw rate sensor detects a tiny amount of capacity changes compared to an accelerometer. For example, when an acceleration of 1G is applied to the accelerometer, the masses are displaced by 100 Å (10 nm) and the capacity is changed by 4 fF. On the other hand, when an angular velocity of 10°/s is applied to the yaw rate sensor, the masses are displaced by 0.8 Å (0.08 nm) and the capacity is changed by 0.2 fF (20 aF). It is compulsory to vibrate the two masses precisely to detect this tiny amount of capacity change accurately. Inhibiting factors for the precise vibration include interference between the sensor driving frequency and any other resonance frequency, impacts of air viscosity, and dimensional deviations of the oscillators due to fabrication errors. Any of these factors may cause the two masses not to vibrate in a straight line properly. This is called leakage vibration. Separating the driving frequency from other resonance frequencies (especially the rotational resonance frequency) is the most important among many ways to suppress leakage vibration.

Figure 7 shows the simulation results of the sensor element. In a mass structure similar to that of the accelerometer (H-shaped structure), the ratio of the rotational

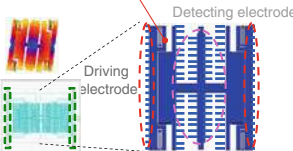
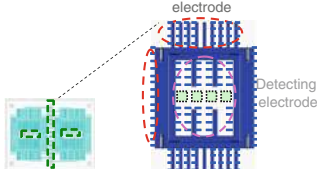
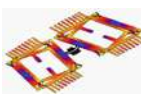
Item	H-shaped structure	Frame type structure
Sensor element	In the open area of the mass, resonance occurs at low frequency. 	
	Open type (H-shaped)	Frame type (square-shaped)
Ratio between structural resonance frequencies	(the ratio of the rotational resonance frequency to the driving resonance frequency) : 1.4 	(the ratio of the rotational resonance frequency to the driving resonance frequency) : 3.7 

Fig. 7 Analysis results of the sensor element

resonance frequency to the driving frequency is tend to be small (1.4 for the structure shown in Fig. 7). We therefore applied a frame type structure to increase the ratio of the rotational resonance frequency to the driving frequency.

Figure 8 shows the results of the structural simulation to optimize the dimension of the frame structure.

The frame width was optimized to be 100 μm based on the ratio of the rotational resonance frequency to the driving resonance frequency, and chip size constraints. As a result, we were able to increase the ratio of the rotational resonance frequency to driving resonance frequency to 3.7.

3 Package Design

As shown in Fig. 9, the accelerometer has a circuit chip and a sensor chip stacked in the ceramic package and electrically connected by Au wires. Thus, when the Au wires swing, the parasitic capacity values between the wires change resulting in lower accuracy.

In addition, the accuracy of a capacitive sensor tends to be affected by temperature change. In other words, the distance between detection electrodes may change by structural deformation caused by thermal stress on the sensor chip lowering the accuracy of the sensor.

Here flip-chip (FC) bonding with Au bumps was applied to reduce the amount of change in the parasitic capacity values between the wires caused by swinging as well as the amount of structural deformation caused by temperature change. In FC bonding, the parasitic capacity values do not fluctuate since rigid Au bumps are used for electrical connection. This bonding technique, however, had hardly been applied to MEMS sensors because it would cause large heat deformation.

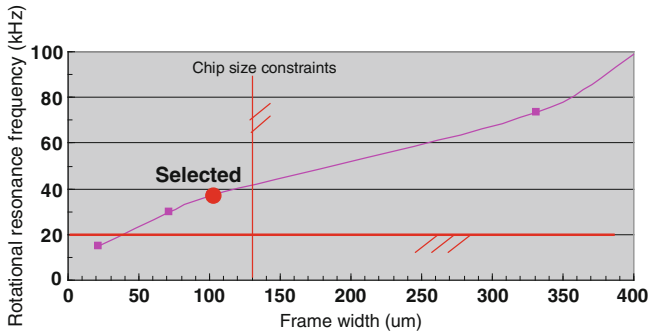


Fig. 8 Analysis results of the frame structure

	Accelerometer	Yaw rate sensor
Structure	 Wiring length Stress propagation	 Short wiring
Electrical connection between the chips	Wire bonding	FC bonding
Sensor accuracy	Low, chip back side stress	High, no chip back side stress
Sensor sensitivity	Low, large wiring capacity	High, extremely low wiring capacity

Fig. 9 Overview of the package structure

Therefore, we tried to optimize the sensor configuration to suppress heat deformation. First, the effect on capacity depending on the warpage of the sensor chip was studied as shown in Fig. 10. As a result it was found that the capacity changed only when the sensor chip was warped diagonally.

Next, the bonding layout was optimized from the point of view of reducing this diagonal deformation. As a result, it was found that bonding the sensor chip using a cross layout as shown in Fig. 11 could suppress the amount of diagonal warpage of the chip. Compared to the normal bonding layout (two parallels), the amount of warpage was reduced by one-third. Thus, both the reduction of heat deformation/parasitic capacity and the avoidance of interference between resonance frequencies were achieved.

FC bonding also connects 20 bumps collectively and requires maintaining the bondability of each bump and accommodating variations in the positions and heights of the bumps. These requirements were achieved by separating the function of the bumps on the sensor chip side from the function of the bumps on the circuit chip side. For the bumps on the sensor chip side, loads and ultrasonic

		Capacity change		
		$Y = (S21 + S22) - (S11 + S12)$		
Warpage direction of the chip	Diagonal	Vertical	Lateral	
Yaw capacity change	$Y = (B + B) - (A + A) = 2B - 2A$	$Y = (C + C) - (C + C) = 0$	$Y = (D + D) - (D + D) = 0$	

Fig. 10 Impacts of heat deformation of the sensor chip

Pad layout	Cross	Two parallels
Deformation image		
Warpage amount	1/3	1

Fig. 11 Analysis results of FC bonding layouts

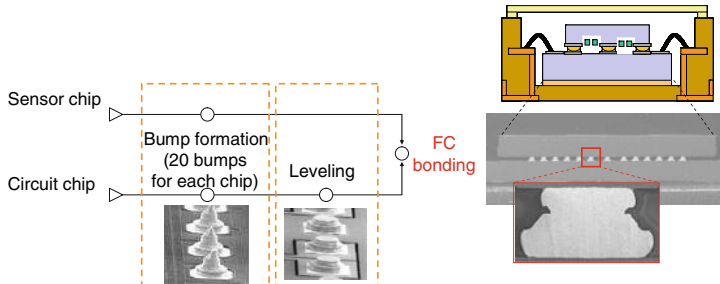


Fig. 12 Overview of FC bonding and cross-section of the bonded area

vibrations are applied in the same manner as wire bonding to form new surfaces through plastic flow and ensure bondability. For the bumps on the circuit chip side, leveling is conducted to ensure bondability and uniform height, allowing the accommodation of positional and height variations. Figure 12 shows the overview of FC bonding and the cross-section of the bonded area.

Fig. 13 Zero-point temperature characteristic (initial)

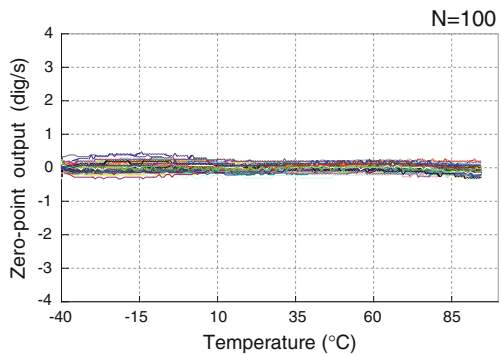


Fig. 14 Thermal shock test result

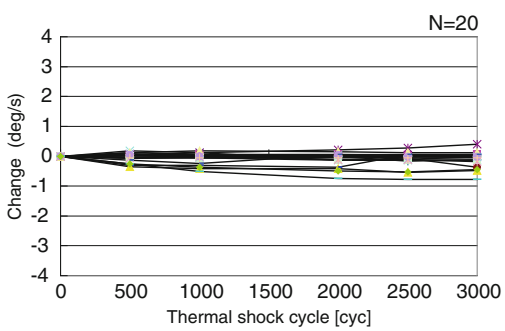
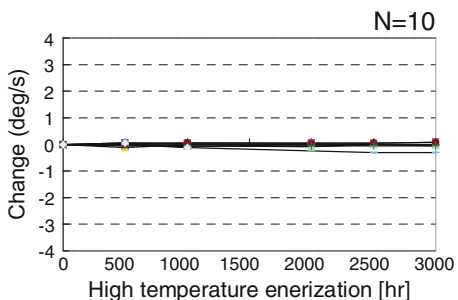


Fig. 15 High temperature energization test result



4 Evaluation Results

Figure 13 shows the zero-point temperature characteristic of the sensor (initial). Optimizing the sensor element configuration and bonding the sensor chip using a cross layout has enabled us to achieve the zero-point temperature characteristic with $\pm 3^\circ/\text{s}$ (actual value: $\pm 0.5^\circ/\text{s}$).

The results of thermal shock testing and high temperature energization testing are shown in Figs. 14 and 15, respectively. After 3000 cycles of thermal shock

from -40 to 105 °C, yaw rate sensors showed little change in the zero-point temperature characteristic. In addition, after 3000 h energization at a high temperature of 95 °C, yaw rate sensors showed little change in the zero-point temperature characteristic either.

5 Conclusion

Here we developed a high-accuracy yaw rate sensor. High accuracy was achieved by optimizing the sensor element configuration (using a frame structure to reduce leakage vibrations), and by flip-chip bonding of the sensor chip and the circuit chip using a cross layout to allow both the reduction of heat deformation/parasitic capacity and the avoidance of interference between resonance frequencies. The developed yaw rate sensor has a zero-point accuracy of ± 3 °/s (actual value: ± 0.5 °/s) in the ± 100 °/s range.

Based on the above techniques, we plan to develop sensors with wider dynamic ranges in the future.

References

1. Offenberg M, Munzel H, Schubert D, Schatz O, Larmer F, Muller E, Maihofer B, Marek J (1996) Accelerometer in surface micromachining for airbag applications with high signal/noise ratio. SAE1996, 960758
2. Analog Dialogue, vol 33, no 1, January, 1999. Dual axis, low g , fully integrated accelerometers
3. Kim S, Lee B, Lee J, Chun K (2001) A gyroscope array with linked-beam structure. In: MEMS, pp 30–33
4. Palaniapan M, Howe RT, Yasaitis J (2003) Performance comparison of integrated Z-axis frame microgyroscopes. In: MEMS, pp 482–485
5. Johnson JD, Zarabadi SR, Christenson JC, Noll TA, Single crystal silicon low-G accelerometer. SAE2002-01-1080
6. Prikhodko IP, Zотов SA, Trusov AA, Shkel AM, Sub-degree-per-hour silicon MEMS rate sensor with 1 million Q-factor. Th1C.002, Transducers11
7. Yang P, Peng C, Zhang H, Liu S, Fang D, Xia S, A high sensitivity SOI electric-field sensor with novel comb-shaped microelectrodes, Th3P.009, Transducers11
8. Chae J, Kulah H, Najafi K (2002) A hybrid silicon-on-glass lateral micro-accelerometer with CMOS readout circuitry. In: MEMS, pp 623–626
9. Chae J, Kulah H, Najafi K (2003) An in-plane high-sensitivity, low-noise micro-G silicon accelerometer. In: MEMS, O_6_1, pp 466–469
10. Lapadatu D, Habibi S, Reppen B, Salomonsen G, Kvisterøy T (2001) Dual-axes capacitive inclinometer/low- g accelerometer for automotive applications. In: MEMS, pp 34–37
11. Hammond J, McNeil A, August R, Koury D, Inertial transducer design for manufacturability and performance at Motorola. 1D3.3, Transducers' 03
12. Kramer T, Foltin W, Goto K, Sakai M (2004) Development of sensing technology for preventive safety system. F2004I055, FISITA2004

13. Isobe Y, Muto H, Fukada T, Fujino S (2006) Super-slim automotive accelerometer applied MEMS technology. F2006V144, FISITA2006
14. Yoshida T (2010) MEMS practical use technology for automotive sensor. In: Transactions of the 27th sensor symposium on sensors, micromachines and application system, pp 7–10
15. Higurashi E (2008) Flip chip bonding technology to realize highly functional MEMS. Trans Jpn Inst Electron Packag 11(6):456–460

The Exploration and Improvement of Steering Heavy for Heavy Dumper

Jian Chen

Abstract The heavy phenomenon about the steering system for 6×4 dumpers is presented. Checking computations steering system parameter on theory, it can find out the steering system performance cannot be improved effectively according to the theory parameters. At the same time, the comparative analysis is carried out with the same type of dumpers which are reflected fairly good on the marketplace. The main reason is found out about the steering heavy on the dumpers. It carries out an optimization on the dumper's system parameters. The test results show that the steering performance of the dumpers is improved obviously, and better than the same type of competitor's dumpers. Heavy vehicles is generally used to power steering system at home and abroad, however, in the actual operation process, steering system often appear to heavy phenomenon, especially heavy dump trucks, and because of the severe overloading, steering heavy show particularly outstanding phenomenon. Steering heavy will cause the vehicle steering difficult, add to the driver fatigue, influence the safe driving, reduce automobile driving smooth and stability, and directly affect the driver's personal safety, so it must be ruled out [1].

Keywords Dumper · Steering system · Power steering · Steering heavy · Test and verification

F-2012-F08-009

J. Chen (✉)
Commercial Vehicle Research Institute, Anhui Jianghuai Automobile Co. Ltd, Hefei, China

1 Background

For heavy vehicle, power steering system directly affect the automobile steering control and driver portability force evenness, or even influence the vehicle steering stability, also will affect the force and service life of the steering system parts.

A heavy dump on the market, because of its use of the environment is bad, and overload is very serious, appeared to heavy phenomenon. It Mainly shows that steering wheel rotation is heavy in the vehicle, locks phenomena when turning, and steering wheel have shock vibration feeling, Sometimes light and heavy, steering wheel's return is poor, or even disappear, etc. It means that the power steering system cannot completely meet some severe conditions requests, for example, severe overloading and mountainous area. It impacts on the car's steering stability and driving safety. Based on this, according to the steering system, this paper gives contrasting with competing product, checking theory calculation, and connecting with the verification test method of steering system optimization design.

2 The Matching Design and Calculation of the Steering System

2.1 The Choice of the Power Steering Gear Specifications

2.1.1 Power Steering Gear Cylinder Size Selection

According to the design specification requirements of the dump: in total quality 40 t, front axle load value: $G = 6,300 \text{ kg}$.

If power steering gear diameter is too small, power steering hydraulic system easy to produce the fault; too big, waste materials and increase costs.

According to “automotive design” requirement:

- front axle load $G \leq 5,500 \text{ kg}$, choose $d = \Phi 100$ cylinder size of steering gear;
- front axle load $G > 5,500 \text{ kg}$,

$$\frac{d^2}{10000} = \frac{G}{5500} \quad (1)$$

When $G = 6,300 \text{ kg}$, according to the formula (1) $d = \Phi 107 \text{ mm}$, actual using cylinder for $\Phi 110 \text{ mm}$ diameter, the output torque $M = 5,560,000 \text{ N}\cdot\text{mm}$.

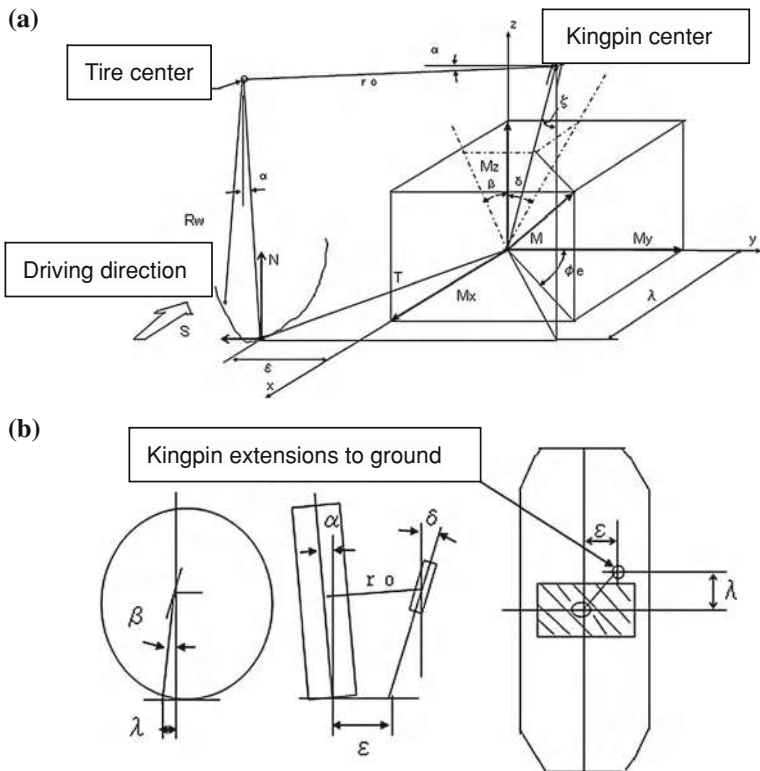


Fig. 1 Steering mechanism structural schemes (a) Overall force and structure parameters (b) Major structure parameters about kingpin

2.1.2 Steering Moment Calculation

For overloaded vehicles, the force between tire and the ground will form the great static torque around master pin when turning, now according to actual force condition to analyze the dump, steering mechanism structure force state see Fig. 1, the need parameter value for calculating torque and the calculation results as is shown in Table 1.

$$\text{among, } \lambda = (Rw \cos \alpha + ro \sin \alpha) \sin \beta \quad (2)$$

$$\varepsilon = ro \cos \alpha - Rw \sin \alpha - (Rw \cos \alpha + ro \sin \alpha) \sin \delta \quad (3)$$

According to the type (2) (3) calculated $\lambda = 18.4$ mm, $\varepsilon = 18.4$ mm, Generation into the formula (4)

$$T = \sqrt{\lambda^2 + \varepsilon^2} = 33.1\text{mm} \quad (4)$$

Table 1 The calculated parameters to torque and results

Parameter name	Parameters meaning	Value
N(N)	Front axle weight $\times 0.5$, which is unilateral tire load	30870
$\varepsilon(\text{mm})$	From the ground tire sales center to take place around the axle tyres distance	27.5
$\lambda(\text{mm})$	From the ground tire sales center to take place before and after the shaft tire distance	18.4
$\Phi e1(^{\circ})$	Inner angle with wheel steering	34
$\Phi e2(^{\circ})$	Outer angle with wheel steering	44
μ	Road surface friction coefficient	0.8
$Rw(\text{mm})$	Tire radius when fully loaded	526
$r_o(\text{mm})$	Length of steering knuckle arm	101
$\alpha(^{\circ})$	Wheel camber Angle	1
$\beta(^{\circ})$	Kingpin caster	2
$\zeta(^{\circ})$	Kingpin inclination Angle	7
S(N)	With the weight of the tire \times road surface friction coefficient ($N \times \mu$)	24696
$M1(\text{N}\cdot\text{mm})$	The inner Kingpin torque	1015465
$M2(\text{N}\cdot\text{mm})$	The outer Kingpin torque	991505
$Mr(\text{N}\cdot\text{mm})$	The output torque of steering gear	1739789

$$\zeta = \tan^{-1} \sqrt{(\tan \delta)^2 + (\tan \beta)^2} = 7.27^{\circ} \quad (5)$$

Will type (2) to (5) generation into, type (6), and (7) may be calculated inside and outside sales wheel torque.

$$M1 = N \sin \zeta \cdot \sin \Phi e1(\varepsilon + Rw \sin \zeta \cos \Phi e1) + TS \cos \zeta = 1015465 \text{ N} \cdot \text{mm} \quad (6)$$

$$M2 = N \sin \zeta \cdot \sin \Phi e2(\varepsilon + Rw \sin \zeta \cos \Phi e2) + TS \cos \zeta = 991505 \text{ N} \cdot \text{mm} \quad (7)$$

At the same time according to the steering gear pitman arm length is 280 mm, steering arm length is 323 mm, bending and horizontal bars arm length 186.3 mm can calculate the output torque to steering gear.

$$Mr = (M1 \times 186.3 / 186.3 + M2 \times 186.3 / 186.3) / 323 \times 280 = 1739789 \text{ N} \cdot \text{mm}$$

Obviously $M > Mr$, So the choice of power steering gear meet theory design requirements.

2.1.3 Static Properties of Power Steering Gear

Static properties of power steering gear is to evaluate the main characteristics of power steering gear index, usually with input and output hydraulic torque relations between the curve said [2]. According to $\Phi 110$ mm diameter cylinder of steering gear and meet the requirements of the theoretical calculation to torque, selected

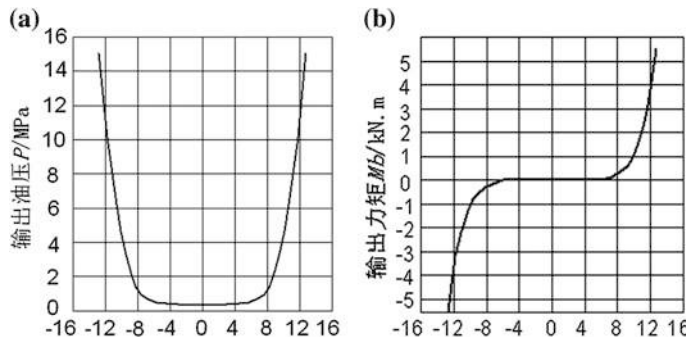


Fig. 2 Power steering gear static characteristic curve (a) Input torque Ma/NM(b) Output torque Ma/NM

rated pressure for 15 MPa of integral power steering gear, the steering gear static characteristic test curve and don't consider steering gear efficiency loss of output torque respectively as shown in Fig. 2a, b shown.

From the above for steering gear cylinder size, turned to the selection of torque theoretical calculation, and static characteristic test curve and steering output torque curves can be seen, the choice of power steering gear can meet the requirements of the design theory.

2.2 Matching Parameter Selection of Steering Pump

Power steering pump is hydraulic power steering power car pump, also can saying is the heart of power steering system. For large trucks for, hydraulic steering system parameter selection is especially important. Into the pump parameter selection is not reasonable, can not be with the choice of steering gear parameters matching, and will lead to abnormal work into the pump or work fault, not only increase the car turned to resistance, will cause serious steering system of other fault, the influence of the car to stability and driving safety.

With reference to the competing goods dump a turn the steering pump choice of parameters, and the parameters of check calculation.

2.2.1 The Maximum Pressure into the Pump

Considering the steering pump the oil from the mouth to mouth inlet between the products of the line loss, in the selection of the pump to maximum pressure, should make into the pump, the maximum pressure meet formula (8):

$$P_p = P_1 + \Delta p \quad (8)$$

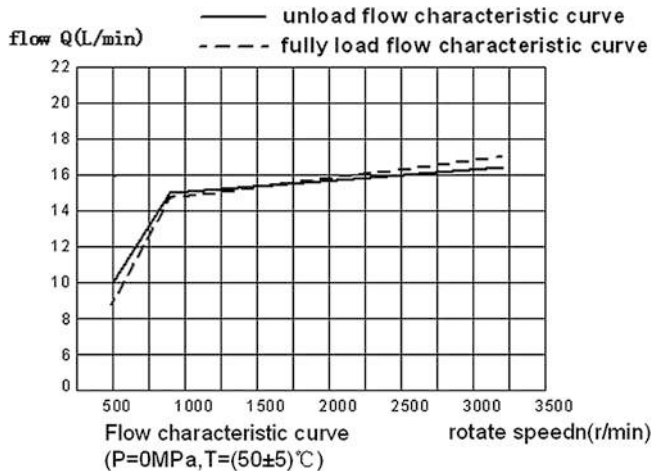


Fig. 3 Steering pump work flow characteristic curve

among: p_1 Steering the maximum pressure, value 15 MPa.

ΔP Line loss. Market experience shows that: in the steering gear pressure meet use requirements of the situation, general into the pump pressure than the highest steering highest higher pressure (0.5–1.0) MPa, the only way to give full play to the advantages of the two, because the pipeline layout is longer, the pressure loss is opposite bigger, this value 1.0 MPa.

P_P Into the pump, the maximum pressure of oil inlet for $15 + 1$ MPa.

2.2.2 Control Flow with Steering Pump Q_p

Generally take quartile $Q_p \geq (1.05\text{--}1.15) Q_{\max}$, Q_{\max} the maximum flow for steering gear, and the value take 15 L/min, the value 18 L/min $> (1.05\text{--}1.15) Q_{\max}$, meet the requirements and steering gear.

General turned to the flow rate of the pump of oil pump work with increasing speed increase. The oil pump rotation speed requirements in 900–1000 r/min the following linear increase in rotational speed limit is not obvious increase above flow. This can guarantee to sensitivity, prevent the steering wheel swing. Choice of steering pump flow characteristic curve as shown in Fig. 3 work.

2.2.3 The Steering Pump Nominal Emissions

Low speed (to pump rotation speed in 1,200 r/min the following) into the pump output flow and the relationship between the discharge for:

$$Q = q_t \times n \quad (9)$$

among: q , The pump nominal emissions, 20 ml/r

n The idle to pump rotation, 500 r/min

From the formula can get, $Q = 500 \text{ r/min} \times 20\text{ml/r} = 10 \text{ L/min}$

If into the pump emissions too small, easy to appear when the idle to heavy; Displacement is too large, the system is easy to fever, influence fuel economy.

According to the calculation above, heavy dump selected steering gear specifications, power steering pump and can meet the requirements of normal use conditions.

3 The Exploration and Improvement of Steering Heavy

Theoretical calculation and analysis, into the pump can meet steering requests, but from the market feedback to see, and can't meet the actual market demand, in the overload situation, still has turned to heavy phenomenon. For this we and competing goods similar models are compared and analyzed.

3.1 Competing Truck Compared and Analyzed

3.1.1 Angle Ratio and Force Transmission Ratio Comparative Analysis

For steering heavy phenomenon, reference to the market on the better competing goods equivalent models, the steering system of the main properties were analyzed. Steering system of the main properties including: the efficiency of the steering system, steering system and transmission ratio of the horns of the force transmission ratio, steering gear transmission of transmission characteristics, the deputy gap of steering system stiffness and steering wheel rotation of the total laps [3]. In this, the main analysis steering mechanism of influencing the steering system of the horns of the transmission ratio and force transmission ratio, and combined with competing goods vehicles are compared and analyzed. The form of transmission mechanism decorate as shown in Fig. 4.

Among them, i: steering gear transmission ratio; rk1: a bridge to bend arm long; re1: for steering pitman arm long; Front axle steering transmission Angle ratio: iw1 = rk1/re1; Front axle corresponding steering system Angle ratio: iw0 = iw × iw1.

Through the Tables 2 and 3 calculation contrast, can see, the equipments of steering Angle ratio relative competing goods to explain in the same force cases, than competing goods vehicles to manipulate light, light by over 10 %. And the actual, the competing goods models on the market responded well, did not appear to heavy phenomenon, the analysis results and the practical situations do not

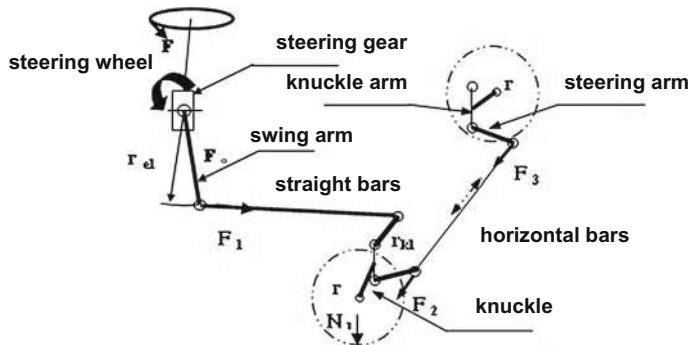


Fig. 4 Transmission's form arrangement

Table 2 The parameters of competing dump compared with the certain dump

Parameter	Pitman arm r_{e1}	Bent arm r_{k1}	Steering angle transmission i_w
Competing dump	290	290	26.2
Certain dump	280	323	26.2

conform to, need to the steering system parameter selection and matching performance further analysis.

3.1.2 Steering a Comparative Analysis of the Main Parameters

The dump when overload front axle charge more than 9.5 tons, shaft badly exceed the charge, and competing goods vehicles using the steering gear, its configuration parameters such as shown in Table 4.

Competing dumper by 17 Mpa car steering gear inlet pressure, and the larger output torque, which can effectively reduce the role of the forces on the steering wheel, alleviate the driver fatigue strength, but such a high inlet pressure, the steering gear itself and the reliability of the inlet pipeline the demand is higher, so the equipments need to choose a higher parameters can improve the configuration market competitiveness of products.

3.1.3 Steering Pump Performance Parameters of the Comparative Analysis

According to competing goods used for the steering gear tip truck to pump matching parameters, see Table 5. Main will turn to the maximum pressure pump, the control flow and speed range increased.

Table 3 The parameter calculation results and comparison about the competing dump compared with the certain dump

Parameter	Front axle steering transmission mechanism transmission	Steering system angle transmission
Competing dump	i_{w1}	1.0
Certain dump	i_{w1}	1.1

Table 4 Steering gear performance parameters of the competing dump

Applicable front axle load/Kg	Angle ratio	Total turns of steering gaer	Highest hydraulic/ MPa	Oil pump flow/(L/min)	Output torque / (N·m)
6,000–10,000	26.2	6.2	17	16–20	7621

Table 5 Steering pump performance parameters comparison

Parameters	Nominal displacement	Maximum pressure	Control flow	Speed range
Rectification before	20 ml/r	15 + 1 MPa	15–17 L/min	500–3,200 r/min
After rectification	20 ml/r	17 + 1 MPa	16–20 L/min	500–3,900 r/min

3.1.4 Comparative Analysis of the Steering Pipeline System Arrangement

- (1) the dump pipeline layout power steering is shorter, and power steering tank smaller, cause the system radiating performance is poor; Into the pump in the serious overloading the conditions of use, front axle load is too big, adding to the steering pump oil in temperature, pump internal parts appear ablation, adhesion, damage phenomenon, mainly is the blade ablation, makes steering pump power provide inadequate.
- (2) power steering tank position irrational collocation, regulated than the oil tank mouth inlet mouth in regulated pump vertical direction will also lower. Hydraulic steering pump vane pump for, since the ability to absorb is poorer, improve the oil tank position, make the oil tank a mouth position to pump a certain height above, can make the tank to pump oil supply pressure to increase, make the oil tank inside the power steering fluid are more likely to enter into the pump, won't appear occasionally suck empty and air into the cause lack of oil phenomenon.

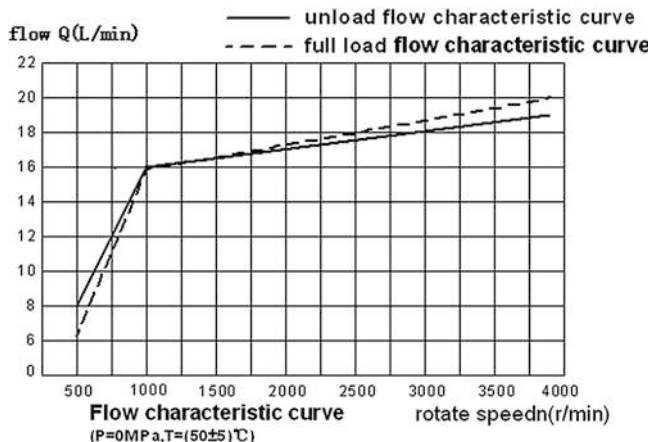


Fig. 5 Steering pump work flow characteristic curve

3.2 Steering System Improvement Measure and Optimization Design

3.2.1 The Specifications of the Steering Gear Selection

In the full understanding market mainstream configuration and the view of the dump the phenomenon of severe overloading, will $\Phi 110$ mm diameter cylinder of steering gear up to $\Phi 117$ mm diameter cylinder. Steering gear performance parameter selection see Table 4.

3.2.2 The Specifications of the Steering Pump Selection

Due to the power steering system performance parameters matching not reasonable and produce output pressure slants small, which could provide direction machine drive to pressure problems front axle, selection and competing goods vehicles of the same model of power steering pump, improve the steering pump maximum working pressure and flow. Figure 5 to improve the steering pump flow after work characteristic curve, and Fig. 3 contrast can see, into the pump work flow have increased significantly.

3.2.3 The Optimization Design of the Piping System

- (1) for regulated position is not reasonable decorate oil tank, the oil tank regulated mouth regulated inlet higher pump mouth more than 30 mm, in order to improve the steering pump self-priming capacity and inlet efficiency.

Table 6 Test data of steering portability

Test data	Rectification before		Competing dump		After rectification	
	Left	Right	Left	Right	Left	Right
Steering wheel torque Mmax (N·m)	7.5	8.3	6.9	6.8	4.8	4.6
Steering wheel force Fmax (N)	33.3	36.9	27.6	27.3	19.1	18.5
Steering wheel reactive role W (J)	112.71		109.92		78.59	
Steering wheel average friction torque Msw (N·m)	2.78		2.21		1.73	
Steering wheel average friction Fsw (N)	12.36		8.84		6.91	

- (2) increase steering gear return pipe road length, improve the overall system to pipe cooling capacity.
- (3) to effectively by oil tank capacity 1.9 L increased to 2.5 L, and competing goods keeps consistent, further enhance the heat capacity and improve sealing performance oil tank, oil tank lid fall off easily to solve problems such as early damage and filter, avoid power steering the oil by pollution, and cause into the pump early wear phenomenon the frequent occurrence.

4 Vehicle Test

4.1 Portability Test of Steering

To test the portability can be through the vehicle and the road test bench test, for the road test, general have in situ to test and double new line test two kinds, in GB/T 6323.5 to the double new line test regulated, mainly USES the in situ to test and double new line test methods, test according to the picture on the ground in the car present double new line to 10 km/h of the speed of the road, and the five kinds of index test evaluation, and the specific see GB/T 6323.5 test specification.

In view of the above results, the reference to competing goods type parameters to ascend, and after rectification of the condition and the competing goods car test comparative analysis.

Table 6 for rectification and competing goods before and after tip truck from five aspects to the portability of the test data comparison. According to the data, it is known that the rectification before, this dump five indexes are higher than the competing goods vehicles; After rectification, performance index was significantly better than before the reform, and competing goods vehicles than to superior performance, turned to the portability obviously improved.

The test results show that: the choice of power steering gear model, we should consider and supporting into the pump are applicable, supporting the steering pump pressure of work must meet the requirements of power steering gear. If the match into the pump pressure below the power steering gear requirements, should consider to choose larger type of power steering gear, increase cylinder diameter size in order to meet the requirements of the output torque.

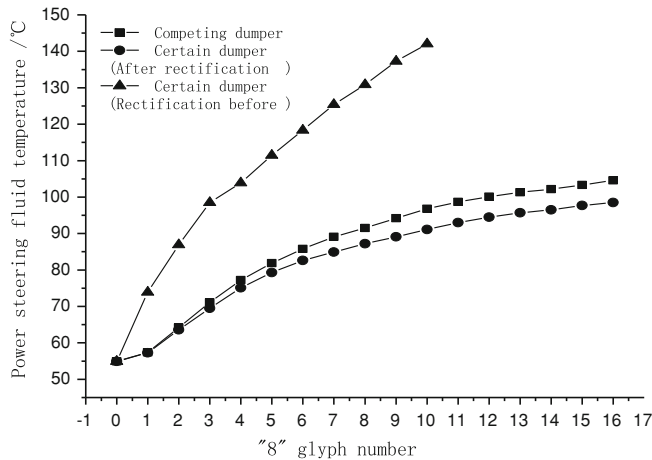


Fig. 6 Steering system oil temperature contrast

4.2 Steering System Temperature

Figure 6 steering system temperature and competing goods the same models before and after rectification contrast can be seen in the, in the environment temperature close, vehicle initial temperature, load and axle charge the same situation, this dump in continuous 10 “8” glyph (namely double new line, the image is called “8” glyph) measurement process, after rectification of power steering system than before the temperature change significantly rectification, the highest temperature reduced nearly 40 °C; At the same time in 10–16 “8” glyph measurement process, found that steering system smaller temperature rise, final temperature of 98.5 °C, while competing goods dump is 104.6 °C, obviously lower than competing goods vehicles.

Figure 7 intuitive reflects a dump after rectification and competing goods vehicles steering system in front and back “8” glyph test and measurement of the temperature change rule, by comparison is not difficult to find, temperature rise significantly better than competing goods vehicles.

Figure 8 for competing dumper with the temperature reduction time comparison. The chart shows, in the steering system by 90 °C temperature dropped to 60 °C in the process, competing goods need to dump the 1,040 s, and the equipments need 750 s.

Through the above three temperature of the evaluation index, can draw the conclusion that the dump steering system temperature after rectification, cooling system improved performance, certainly will greatly improve the life of the steering system, at the same time, the whole line of the hydraulic supply, flow has the positive impact on the supply.

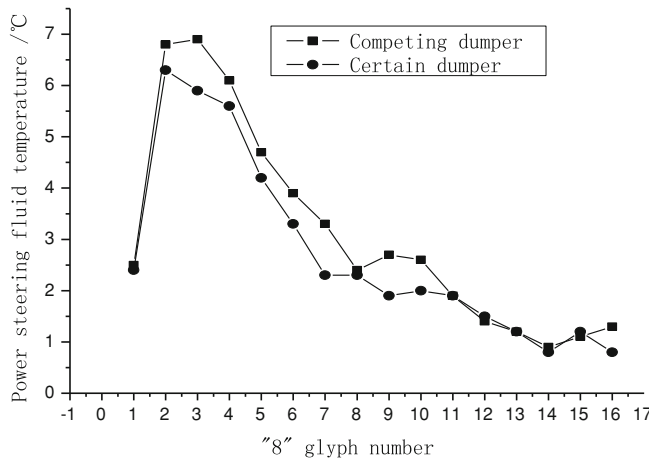


Fig. 7 Steering system comparison with raising temperature

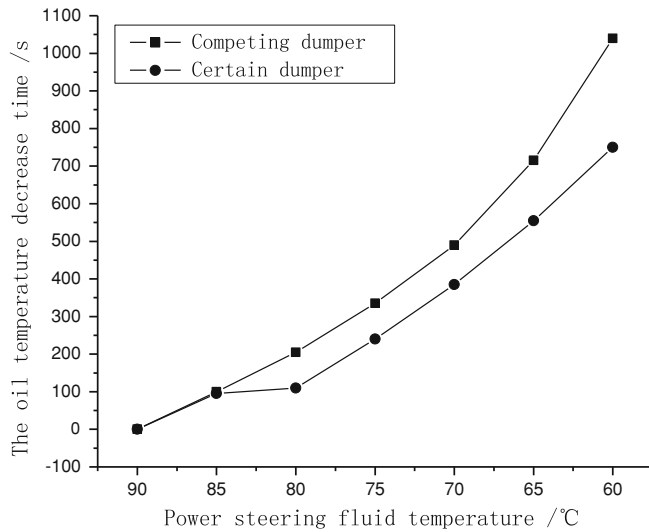


Fig. 8 Steering system comparison with reduced temperature

5 Conclusion

According to the market to reflect the heavy phenomenon, combined with the same competing type steering transmission mechanism stress analysis. At the same time and the competing goods vehicles in the steering system parameter selection and configuration on the contrast analysis, led to the dump to explore into the main reason for the heavy, and to reopen the steering system parameters selection, and

improve the system configuration. Finally, the steering system temperature, turned to the portability and competing goods data type is compared, and the results show that the corrective measures can effectively reduce the temperature steering system, at the same time to light performance obviously ascension.

Late in the oil market will turn to effective volume increased to 2.5 by 1.9 L, extended power steering pipeline, change big cylinder size steering gear, and at the same time by changing matching into the pump and a series of measures, and after long-term market test and verify, the effect is remarkable.

At the same time according to the market experience shows that users in the use of the vehicle need to pay attention to: is prohibited in the downhill slide down when, not because the engine work will make hydraulic pump stop working, and lose steering function, cause too much resistance to difficult; A sharp turn, should be timely change into the lower gear, make the engine speed not less than 800 r/min, in order to ensure that the power steering the normal work of the system.

This article mainly aims at heavy dumper on the market by the severe over-loading analysis, to use bad working conditions, overloaded serious other heavy car has a reference.

References

1. Chen Y, Zhang J, Wu B-B General malfunction and removing methods of front axle steering system. Commun Sci Technol Heilongjiang 2001(4):56–57
2. Huang C-S, Wu B-L, Ying G-Z (2005) Analysis of truck steering system. Des Calcul Res 2005(5):19–23
3. Wang J (2006) Configuration analyzing and modern designing methods of steering-system of heavy-duty vehicle. Wu Han University of Technology master's degree thesis

Sidewise Adaptive Single-Track Vehicle Model for ESC

Zhenfu Chen, Georg Roll, Alfred Eckert and Peter Rieth

Abstract Electronic Stability Control (ESC) typically compares the reference yaw rate (desired yaw rate) and the measured yaw rate (actual yaw rate) and then makes the required interventions. The reference yaw rate will normally be calculated with a symmetric vehicle reference model. But many vehicles have different dynamics for left and right curve driving. In this case the symmetric vehicle reference model will acquire large problems to gain the correct reference yaw rate. Recently, Continental has developed a new procedure to identify the asymmetry of the vehicle dynamics and to apply the sidewise adaptive parameters for calculation of the reference yaw rate. The vehicle dynamics and the handling performances are normally described with a mathematical vehicle model and dependent on many vehicle parameters. To simplify the computation complexity, Continental has selected the quasi linear single-track model as the vehicle reference model. For this single-track vehicle model only some important vehicle parameters are used, which have direct influence on the vehicle behaviour such as oversteering or understeering. Vehicles in their initial state from series production normally have symmetric dynamics. Some of these parameters can be measured directly and the others can be identified with appropriate driving manoeuvres and methods. For the real usage of vehicles the parameters may be very different from the initial ones and the vehicles may have strong asymmetric dynamics. In such cases, the single-track model with constant parameters may cause too many wrong or too late required interventions. To improve the ESC performances for such reasons Continental has developed a new sidewise adaptive single-track vehicle model. The most important parameter for the single-track model is the tire-side stiffness of the rear axle. During driving the vehicle dynamics will be monitored

F2012-F08-012

Z. Chen (✉) · G. Roll · A. Eckert · P. Rieth
Chassis and Safety, Continental, Frankfurt, Germany

permanently. Under certain conditions the tire-side stiffness will be continually calculated online for two different driving directions. These newly identified parameters will then be verified, limited and transmitted to the former ones. In this way the parameters will be permanently updated online so that the ESC has always the correct parameters for the actual driving situation. Practice has already shown that using this sidewise adaptive single-track model the reference yaw rate can be calculated more precisely. The ESC performance is improved significantly especially for vehicles with asymmetric characteristics. The number of faulty and unnecessary ESC interventions is largely reduced. This procedure can be applied to all passenger cars and light trucks with an ESC system.

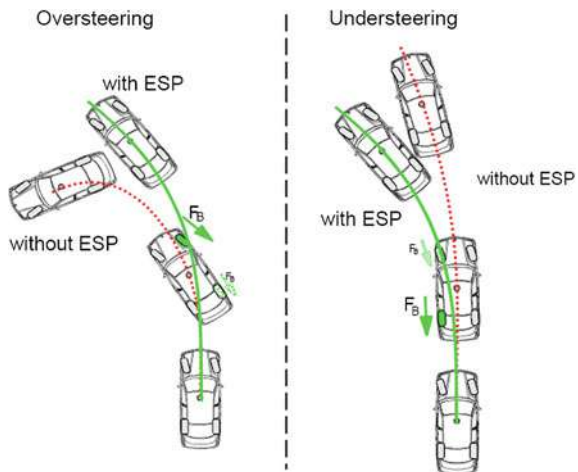
Keywords Electronic stability control · Reference yaw rate · Single-track model · Asymmetric vehicle behaviour · Online parameter identification and adaption

1 Introduction

For improving the active safety of road traffic, ESC has been widely used [1]. Based upon current estimates regarding the effectiveness of ESC systems, investigations in the USA have confirmed that a standard ESC fitment for all vehicles could save thousands of lives every year, providing potentially the greatest safety benefits produced by any safety device since the introduction of seat belts. Therefore in the USA, ESC is already mandatory for new cars and Europe has followed with a similar regulation. ESC is undoubtedly the most powerful safety system to fulfil this requirement. As one of the most important ESC-System suppliers, Continental has developed and produced ESC-Systems for nearly 20 years. In this field Continental has gathered considerable valuable experience and the ESC functionality of Continental systems has always been improved and expanded, for example today's ESC is becoming the basis for all higher vehicle dynamics and safety control systems, such as Advanced Driver Assistance Systems (ADAS), especially the Emergency Brake and Steer Assist (EBA/ESA).

The most important part of the ESC system from Continental is the Active Yaw Control (AYC) [2], which continuously compares the actual vehicle behaviour with the expected vehicle behaviour (Fig. 1). If the difference between the actual vehicle yaw rate, which is measured directly with suitable sensors, and the expected yaw rate (reference yaw rate) exceeds certain thresholds for a defined duration, an ESC intervention will be initiated. In an oversteering situation (the measured yaw rate is larger than the reference yaw rate) the ESC intervention will create an additional torque around the vertical axis, so that the actual vehicle yaw rate will be reduced. Otherwise the ESC will initiate an intervention to enlarge the actual vehicle yaw rate in an understeering situation. In both cases the ESC intervention will always try to create such an extra torque around the vertical axis

Fig. 1 Overview of the active yaw control



to force the vehicle yaw rate to follow the reference yaw rate, which is normally calculated with an appropriate reference vehicle model (Fig. 2). As most important inputs for calculating the reference vehicle model we normally use the steering angle at the steering wheel or the steering angles of the front wheels, and the vehicle velocity or the reference velocity. The output is the reference yaw rate or the desired yaw rate. In order to guarantee optimal control performance, the reference yaw rate must absolutely correspond with the behaviour of the stable car in every driving situation.

So the correct reference yaw rate is the essential precondition for optimal ESC control. For this reason Continental has made substantial investigations and developments for creating the reference vehicle model and identifying suitable vehicle parameters.

Unfortunately the vehicle parameters can vary in a wide range for different curve directions and driving manoeuvres. Therefore, it is extremely important to operate with well suited parameters in the respective situation. In order to fulfil this demand, Continental developed a new mechanism for online identification and adaption of the important vehicle parameters as discussed in the following.

2 Quasi Linear Single-Track Model

The key requirement for the reference vehicle model is that the calculated reference yaw rate should be identical with the actual real vehicle yaw rate in normal driving situations, where a normal driver can master the vehicle easily and an ESC-Intervention is unwanted. According to many scientific investigations, most vehicles have linear characteristics for the handling performances in normal driving situations [3].

Fig. 2 Inputs and output of the vehicle reference model

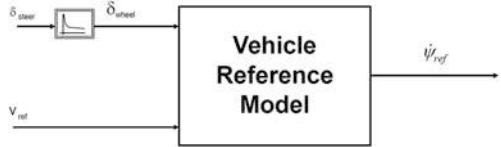
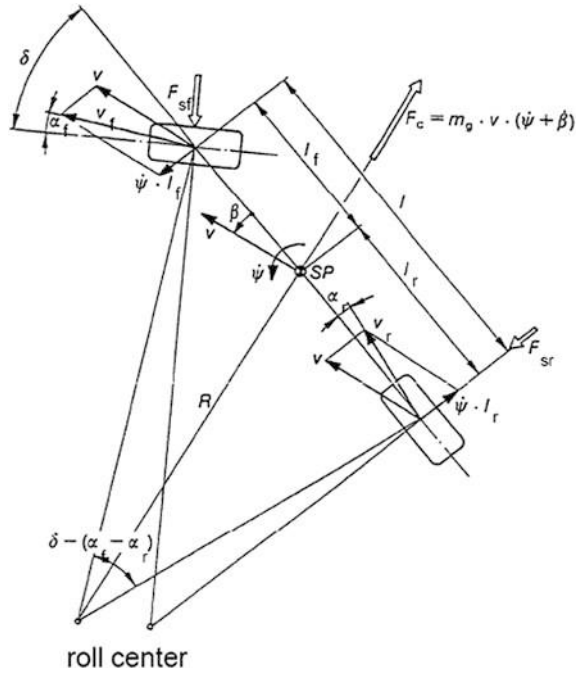


Fig. 3 Single track model with variables and angles



The vehicle behaviour can be described with a so-called single-track model (Fig. 3). The basic motion equations can be derived from the torque balance and the side-force balance as following:

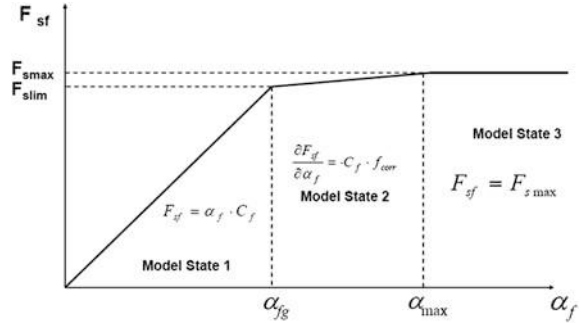
$$\sum T = 0 \rightarrow I_Z \cdot \psi̇ = F_{sf} \cdot l_f - F_{sr} \cdot l_r \quad (1)$$

$$\sum F_s = 0 \rightarrow m \cdot a_y = F_{sf} + F_{sr} \quad (2)$$

In Eqs. (1) and (2) I_Z is the vehicle inertia around the yaw axis, $\psi̇$ is the yaw acceleration, F_{sf} and F_{sr} are the tire side-force of the front and rear axle, l_f and l_r are the distances from the Centre of Mass to the front and rear axle, m is the vehicle mass and a_y is the lateral acceleration.

In the linear range we have made some necessary assumptions and simplifications for the basic motion equations: the tire side force is proportional to the tire side-slip angle, the front wheel steering angle δ and the vehicle side-slip angle β

Fig. 4 Vehicle reference model for side force with three mode states



are small and the influence of the longitudinal forces on the lateral dynamic is insignificant. So we have following relationships:

$$\alpha_f = \delta - \beta - \frac{\psi \cdot l_f}{v} \quad ; \quad \alpha_r = -\beta + \frac{\psi \cdot l_r}{v} \quad (3)$$

where v is the vehicle velocity

$$F_{sr} = \alpha_r \cdot C_r \quad ; \quad F_{sf} = \alpha_f \cdot C_f \quad (4)$$

$$a_y = v \cdot (\beta + \psi) \quad (5)$$

In Eq. (4) C_f and C_r represent the tire side-force stiffness of the front and rear axle. If we put Eqs. (3), (4) and (5) in Eqs. (1) and (2) and rewrite the basic equations, then we will obtain the vehicle motion equations for the linear single-track model as following:

$$mv \cdot \beta + (C_r + C_f)\beta - (-m \cdot v^2 + C_r \cdot l_r - C_f \cdot l_f) \frac{\psi}{v} = C_f \cdot \delta \quad (6)$$

$$I_z \cdot \psi - (C_r \cdot l_r - C_f \cdot l_f)\beta + (C_f \cdot l_f^2 + C_r \cdot l_r^2) \frac{\psi}{v} = C_f l_f \cdot \delta \quad (7)$$

In consideration of the physical limitation of different road surface conditions and under guarantee of the physical and numerical stability of the reference vehicle model, the possible maximal side-force $F_{sf,max}$ of the front axle should be limited to the theoretically maximal friction force $F_{zf} \cdot \mu_{\max}$ of this axle for the current road surface with an uncertainty factor f of approx. 1.1 as shown in Fig. 4:

$$|F_{sf}| \leq F_{sf,max} = f \cdot F_{zf} \cdot \mu_{\max} \quad (8)$$

In this way the characteristic line of the side force on the front axle is divided into three states. The model state 1 is taken for small tire side-slip angles with $\alpha_f < \alpha_{fg}$ where the side-force is assumed to be proportional to the side-slip angle until the theoretical maximal friction force $F_{sf,\max} = F_{zf} \cdot \mu_{\max}$ will be reached. So the reference vehicle model is linear in this state. The model state 3 describes the

saturation zone for very large tire side-slip angles with $\alpha_f > \alpha_{\max}$ where the possible maximal side-force $F_{sf,\max}$ is reached and the side-force does not increase any longer. The model state 2 is the transition area between model state 1 and model state 3, where the increase gradient for the side-force F_{sf} is very small. The static friction coefficient μ_{\max} of the road surface will be estimated online by an advanced vehicle state estimator. Through solution of the above differential Eqs. (6) and (7) and in consideration of the limitation of Eq. (8), the theoretical reference yaw rate ψ_{ref} will be calculated continually for given input signals front wheel steering angle δ and vehicle velocity v . In practice, the actual real vehicle yaw rate ψ_{meas} will be measured directly by the yaw rate sensor. The ESC system calculates the control strategy usually according to the difference between the reference yaw rate ψ_{ref} and the measured yaw rate ψ_{meas} .

3 Identification of the Initial Vehicle Parameters

For the correct calculation of the reference yaw rate according to Eqs. (6) and (7), many vehicle parameters are necessary. The more precise these parameters are determined, the higher the ESC performance will be. For the ESC application development, generally an initial vehicle (a prototype vehicle) will be used. In this case some of the parameters of the initial vehicle can be determined directly with good reliability. These are the vehicle mass m , the distance from the centre of mass to the front axle l_f and the distance from the centre of mass to the rear axle l_r . The three remaining parameters: vehicle mass inertia I_z around the yaw axis, the tire side-force stiffness of the front and rear axle C_f and C_r must be estimated with suitable procedures. Continental utilizes the offline identification method to determinate these parameters with the initial vehicle. For this purpose we have to modify the basic vehicle motion Eqs. (6) and (7) in the way that the unknown variable β and its derivation $\dot{\beta}$ will be eliminated. Thus a new yaw motion equation for the linear single-track model is as follows:

$$I_z \cdot \psi + \left(\frac{C_f \cdot C_r \cdot l^2}{C_f + C_r} \right) \frac{\psi}{v} + \left(\frac{C_r \cdot l_r - C_f \cdot l_f}{C_f + C_r} \right) m \cdot a_y = \left(\frac{C_f \cdot C_r \cdot l}{C_f + C_r} \right) \cdot \delta \quad (9)$$

For the identification of the three remaining parameters in Eq. (9) some experiments must be designed for efficiently generating informative data. Therefore we have specified a set of special driving situations for the identification and verification of the vehicle parameters.

There are following general requirements for driving situations:

The road surface should be dry, level and smooth.

The vehicle dynamics must remain in the linear zone, therefore the maximal lateral acceleration should not exceed 0.4 g.

The vehicle should provide sufficient dynamic stimulation. Therefore the steering angle input must be quick and large enough.

The experiments should include as many typical handling test driving situations as possible, such as steering angle step, ramp, sinusoidal input, steady constant circle driving etc.

The vehicle velocity should cover a very large range from approx. 30 kph until 120 kph, this should vary very slowly during the test procedure to avoid the influence of the longitudinal dynamics on the yaw motion.

Using the measured data of these variables δ , a_y , v , and ψ , the initial parameters I_Z , C_f and C_r for the prototype vehicle will be identified in the time domain. For this purpose the method of least squares is applied. That means the squares of the difference between the measured yaw rate ψ_{meas} and the estimated model yaw rate ψ according to Eq. (9) should be minimized for the whole experiment data.

4 Adaptation of the Vehicle Parameters

The initial parameters from the offline identification are very well suited for the initial prototype vehicle. But in the normal usage of the series vehicles the vehicle parameters may be very different from these initial parameters. In this case, if the reference vehicle model operates further on with the constant initial parameters, the reference yaw rate may be wrong and faulty ESC interventions cannot be avoided. To investigate the possible influence of the parameter changes on the vehicle behaviour efficiently, the most powerful way is to analyze the term understeer gradient U , which is one of the main measures for characterizing steady-state cornering behaviour and is defined as following:

$$U = \frac{d(\delta - \delta_0)}{da_y} = \frac{(C_r \cdot l_r - C_f \cdot l_f)}{C_r \cdot C_f \cdot l} \cdot m \quad (10)$$

According to the definition, the vehicle is understeering, if the understeer gradient U is positive. Otherwise the vehicle is oversteering, if the understeer gradient U is negative. If the understeer gradient U is equal to zero, then the vehicle is neutral. The value and the sign of the understeer gradient U is a function of four independent vehicle parameters: vehicle mass m , the position of the centre of mass l_f or l_r then C_f and C_r . The vehicle mass inertia I_Z has absolutely no influence on the understeer gradient U . The change of the vehicle mass can only affect the value of U , but not its sign. The change of the remaining parameters may affect both the value and the sign of U . For this reason the change of these three parameters should be identified online and updated in an intelligent way for the reference vehicle model, which should be easy, quick, reliable and effective. In Eq. (10) it is easy to notice, that the change of l_r and C_f can be approximately represented by a corresponding change in C_r for achieving the same value of U .

For example, an increase of l_r has nearly the same effect on U as an increase in C_r and an increase of C_f is similar for U as a decrease in C_r . With these considerations we definitely only need to update C_r to represent the influence of the changes of all possible parameters on the vehicle behaviour, and also the reference vehicle model. Therefore we let all other parameters except from C_r remain constant and always have the initial values. The possible deviations to their initial values for these parameters will be detected with the relative change of the new identified tire side-force stiffness of the rear axle C_{r_new} to its initial value C_{r0} . For the online identification of the new C_{r_new} we have to use the Eq. (9) and solve the equation for C_r

$$C_{r_new} = \frac{ml_f \frac{a_y}{v\psi} - \frac{I_r\psi}{v\psi}}{\frac{l_r^2}{v^2} - \frac{l_r\delta}{v\psi} + \frac{ml_f \frac{a_y}{v\psi}}{C_f} + \frac{I_r\psi}{C_f v\psi}} \quad (11)$$

The relative change ΔC_{r_adapt} of C_r to its initial value C_{r0} can be expressed as following.

$$\Delta C_{r_adapt} = \frac{C_{rnew}}{C_{r0}} = \frac{K_{Z1} \cdot a_y - K_{Z2} \cdot \psi}{a_y + K_{N1} \frac{\psi}{v} - K_{N2} \cdot \delta + K_{N3} \cdot \psi} \quad (12)$$

Here we have put all constant terms together and simplified the expression with 5 new constants K_{Z1} , K_{Z2} , K_{N1} , K_{N2} and K_{N3} , which are only dependent on the initial vehicle parameters. Theoretically, we can obtain a new value for ΔC_{r_adapt} each loop in the time domain, if the divisor term in Eq. (12) is not zero. But in practice we have already taken numerous measurements to ensure that the online estimated new C_{r_new} for the ESC system is always usable and valid. First we have to select the efficient driving situations for the online identification of the new C_{r_new} . The criteria are similar as for the offline parameter identification: quasi steady curve driving, lateral vehicle dynamics are in linear zone. Therefore the actual driving situation will be observed permanently. If the conditions are fulfilled, the data will be measured and a new identification cycle for C_{r_new} will be started.

During this identification cycle as many valid new values as possible for C_{r_new} should be calculated. After this, the mean value from each identification cycle will be calculated. This new mean value will then be taken over to the former one with a low pass filter. In this way the tire side-force stiffness of the rear axle C_r will be continually adapted online. The reference vehicle model applies this adapted C_r for the calculation of the reference yaw rate for ESC. Another further measurement is to save the updated new C_r in the EEPROM, if it is necessary, so that this value can directly be used by the ESC at the beginning of next new engine start.

5 Asymmetry of the Vehicle Behaviour and Sidewise Adaption

Up to now, ESC developers have always assumed that vehicle lateral dynamics are symmetrical. That means the same inputs will result in the same vehicle behaviour both for left curve and for right curve driving. For such vehicles we only need one set of parameters for the reference vehicle model. For most vehicles with minute asymmetry, the ESC performance will be good enough by using the same parameter set for all driving situations, so long the vehicle dynamic asymmetry lies in a certain tolerance range.

Unfortunately we have noticed some vehicles in practice which show extremely strong asymmetric driving dynamics properties. This asymmetry can be verified by constant steady circle driving as shown in Fig. 5. With the same vehicle velocity and the same constant steering angle the vehicle traces two circles with very different radii R_{left} , R_{right} for left and right directions. If the symmetric reference vehicle mode is applied in the ESC for such a vehicle, the reference circle radius R_{ref} of the ESC must be between R_{left} and R_{right} . The same vehicle could be detected to be oversteering for left curves and understeering for right curves, even when the vehicle is in a stable, normal driving situation. Then faulty ESC interventions may take place, what is absolutely unacceptable for a safety control system. To avoid faulty ESC interventions and to improve the ESC performance Continental has recently developed a new sidewise adaptive single-track vehicle model, which monitors the vehicle lateral dynamics permanently. If a strong asymmetry for the vehicle is detected and verified, the vehicle reference model will use different parameters for different driving situations. For this purpose the tire side-force stiffness of the rear axle C_r will be online identified separately for left and right driving situations according to Eq. (12). If the estimated relative changes $\Delta C_{r_adapt_left}$ and $\Delta C_{r_adapt_right}$ are so different that the allowed threshold has been exceeded, a strong asymmetry is assumed for this vehicle and the sidewise adaption for the parameter C_r will be started. If a left curve driving is detected and all other conditions for the parameter identification are fulfilled, the measured data will be used for the calculation of a new average relative change $\Delta C_{r_adapt_left}$ for this identification cycle. This identified new value will be limited to boundaries between 80 and 120 % of the initial values of the parameter C_r . After this a new tire side-force stiffness of the rear axle $C_{r_new_left}$ for the left driving situations will be updated through a suitable low pass filter and then applied to the single-track vehicle model. In the same way the new tire side-force stiffness of the rear axle $C_{r_new_right}$ for the right driving situations is identified and adapted. There are also some vehicles which have very different characteristics for different driving manoeuvres such as powered driving, braking and trailing throttle. For such vehicles we can classify all driving situations according to two driving directions and three driving manoeuvres to six categories. For each category the tire side-force stiffness of the rear axle will be identified online and adapted. So the new side wise adaptive single-track vehicle model can have up to

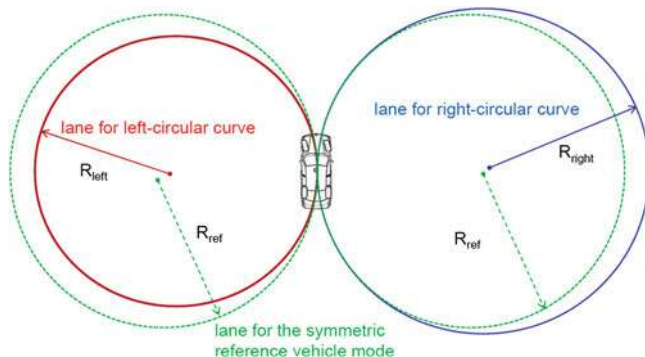


Fig. 5 Typical situation for a vehicle with asymmetric dynamics for *left* and *right* curves

six different $C_{r,new,i}$ and always select the correct parameters for the actual driving situation.

6 Conclusions

The key component of the ESC-System from Continental is the AYC, which uses a reference vehicle model for the calculation of the reference yaw rate and compares this with the actual vehicle yaw rate. If the difference between them exceeds certain thresholds for a defined duration an ESC intervention will be initiated. Therefore the quality and efficiency of the ESC performance are directly dependent on how exact and useful the calculated reference yaw rate is. For a good and reliable ESC control, Continental has selected a quasi linear single-track reference vehicle model with the maximal limitation of the tire side-force at the front axle according to the estimated actual static road friction coefficient. Such a reference vehicle model uses very few vehicle parameters and can simplify the computational complexities of the reference yaw rate significantly. At the same time the front tire side-force limitation ensures the physical and numerical stability of the reference vehicle model. For the determination of the requested vehicle parameters, Continental has developed some powerful procedures to identify and to adapt these parameters, which should be qualified optimally for the actual vehicle state and the current driving situation. The first step is to select a representative prototype vehicle for the determination of the initial parameters. The initial vehicle mass and the position of the centre of mass which is expressed by the distance from the centre of mass to the front axle or to the rear axle can be measured directly. For the determination of three remaining parameters: vehicle mass inertia I_Z around the yaw axis, the tire side-force stiffness of the front axle C_f and rear axle C_r , the offline identification method is applied. For this purpose a set of efficient driving manoeuvres is specified, so that the estimated initial parameters

with the measured data are a good compromise for all typical driving situations. For consideration of the vehicle state changes, a procedure for the online identification and adaption of the most important parameter axle C_r was developed.

According to this procedure, all other initial values always remain constant, the parameter C_r will be monitored permanently and calculated continuously during curve driving, if the requested conditions for the online identifications are fulfilled. For some vehicles the driving situations can be classified into two driving directions or further into three driving manoeuvres, powered driving, braking and trailing throttle, so that together up to six detailed categories can be considered. For each category the tire side-force stiffness of the rear axle will be identified online and adapted. In this way the possible asymmetry in the lateral dynamics or different characteristics for different driving manoeuvres is taken into account by the updated parameter C_{r_new} . Therefore, by applying such a sidewise adaption of vehicle parameters, the reference vehicle model always has the correct parameter for the actual driving situation and the current manoeuvre. The quality of the reference yaw rate is improved largely. The number of possible faulty ESC interventions is reduced significantly. The ESC control becomes more efficient and comfortable.

The most significant point of this paper, is that Continental does not switch over to a far more complex two-track vehicle model but continues with the simple single-track model, the different driving manoeuvres can be taken into consideration just by simply using different values for only one parameter, the side-stiffness C_r of the rear axle.

This sidewise adaptive single-track vehicle model can be applied to all passenger cars and light trucks for an ESC system.

References

1. 黄炳华; 陈祯福, ESC的最新事件和发展趋势[J] 汽车工程 2008年第1期?>1 - 9
2. Fennel H, Gutwein R, Kohl A, Latarnik M, Roll G (1998) Das modulare Regler- und Regelkonzept beim ESP von ITT Automotive“[J], 7. Aachener Kolloquium Fahrzeug- und Motortechnik, 5–7. Oktober, 1998, Aachen S. 409–431
3. Mitschke M, Wallentowitz H (2004) Dynamik der Kraftfahrzeuge. Springer, Berlin

Dynamic Stability Control Strategy Development for an In-Wheel Motorized Electric Vehicle

Jianwu Zhang, Yan-e Zhao, Xiqiang Guan and Tongli Lu

Abstract As a type of distributed propulsion technology for new energy vehicles in recent future, in-wheel motorized four-wheel drive systems are increasingly seen in small sized battery energy stored and plug-in hybrid electric vehicles. For integration of the steer and traction controls the vehicle dynamics model is developed in Matlab/Simulink environment, in which the electric vehicle is simplified to be the symmetric half model of two degrees of freedom and the terrain mechanics model counting for side adhesion effect is adopted. Feedforward regulation and feedback correction control algorithms are applied and the vehicle steering angle, drive velocity, yaw rate and sideslip angle are treated as input variables in the control system. Both numerical simulations and experiments are performed for validation of the present method. It is demonstrated by comparison of the test results with the numerical predictions that the present control strategy is fairly good in efficiency for improving handling stability of the in-wheel motorized electric vehicles.

Keywords Electric vehicle (EV) · Direct yaw-moment control (DYC) · Active front steering · Optimal SQP method · Sliding mode control

F2012-F08-013

J. Zhang (✉) · Y. Zhao · X. Guan · T. Lu
School of Mechanical Engineering, Shanghai Jiao Tong University, Shanghai, China

1 Introduction

Electric vehicles (EVs) are commonly recognized to provide one of the best solutions to automobile emission and oil shortage issues. An innovation configuration for electric vehicles is all-wheel-drive EVs, in which each wheel is driven individually by a motor. The in-wheel motors transmit powers by a set of transmission systems directly to the wheels, known as electric wheels [1]. In such a configuration, the traction force of each individual wheel can be controlled by alternation of the torque of the corresponding wheel motor [2]. The unequal independent wheel motor control may allow the vehicle dynamic stability improvement, that is, the vehicle cornering and handling stability may be enhanced in junctional and bisectional road conditions. In addition, independent driven wheels provides another steering control input, i.e. the torque steering. This means that, the vehicle yaw rate can be controlled by this direct yaw-moment control (DYC).

However, the control system becomes very complicated in motorized vehicles. For the case of yaw stability control, the objective is to make the EV follow the desired yaw rate while keeping the sideslip angle minimum. The main difficulty in the design is due to the strong nonlinearity and uncertainty in the problem [3]. In recent years, a number of researches have been published, dealing with a good vehicle dynamic stability by controlling a unique variable: either yaw rate or slip angle. However, for a desired vehicle dynamic response, both the two variables must be applied [4]. Therefore, integrated control systems have been proposed, where the steering and brake controls are cooperated to improve the vehicle dynamic stability and handling performance. Nevertheless, it is difficult and in many cases impossible to solve this problem by using classical linear method. Several authors have proposed different methods to achieve the specified control performance. Shino et al. propose a control system based on optimal control theories to improve the handling and stability of electric vehicles by direct yaw moment generated from the driving or braking forces [5]. Peng and Hori develop a dynamic feedback control algorithm based on the dynamics of the vehicle, which strives optimally distribute the tractive efforts between the two wheels for better performance [6]. Wang et al. adopt the a simple robust servo-controller Robust Model Matching Controller (R-MMC) [7]. In fact, the vehicle yaw stability is involved with a lot of uncertainties nonlinearities. Although several control methods have already been proposed, their controllers are dependent on some immeasurable parameters such as vehicle velocity, slip angle or cornering stiffness [8].

The sliding mode control (SMC) method has the advantages of robustness and good performance in controlling the non-linear systems. A sliding mode control method is proposed to improve vehicle yaw stability by the integrated yaw moment control and active front steering (AFS) and optimal traction-force distribution control method. Computer simulations and experiments are performed with cornering maneuver and single lane change maneuver separately to verify the effectiveness and validation of the yaw stability controller.

2 Vehicle Modeling for Controller Design

Neglecting the influence of aerodynamic effect, rolling resistance, steering mechanism and suspension system, the motion equations governing the lateral and the yaw motions of the electric vehicle can be expressed as follows

$$mv(\dot{\beta} + \gamma) = F_{y1} + F_{y2} + F_{y3} + F_{y4} \quad (1)$$

$$I_z\dot{\gamma} = l_f(F_{y1} + F_{y2}) - l_r(F_{y3} + F_{y4}) + M_z \quad (2)$$

$$M_z = \frac{d}{2}(F_{x2} - F_{x1} + F_{x4} - F_{x3}) \quad (3)$$

where, m is the vehicle mass, F_{xi} ($i = 1, 2, 3, 4$) and F_{yi} ($i = 1, 2, 3, 4$) are longitudinal force and lateral force of the i th wheel, l_f and l_r are the distances from the vehicle center of gravity to the front and the rear axles respectively, d is wheel base, γ is the yaw rate, v is vehicle velocity and v_x, v_y are the lateral velocity and the longitudinal velocity of the vehicle respectively, β is the vehicle body sideslip angle, $\beta = \arctan(v_y/v_x)$.

The latest semi-empirical tire model, Magic Formula model due to Pacejka, is used in this study for its convenience and accuracy. The coefficients in the formula depend on the type of tire and road conditions, and its values have been validated with actual tire test data. The sideslip angles of each tire are calculated as follows:

$$\alpha_1 = \alpha_2 = \beta + \frac{l_f\gamma}{v} - \delta, \quad \alpha_3 = \alpha_4 = \beta - \frac{l_r\gamma}{v} \quad (4)$$

where, δ is steering angle of the front wheel.

Furthermore, since the dynamic response of modern motor drives are much faster than wheel dynamics and considering the dominant poles of the closed loop system, an electric motor and its drive can be simply modeled as [1]

$$G(s) = \frac{T}{T^*} = \frac{1}{1 + 2\xi s + 2\xi^2 s^2} \quad (5)$$

3 Design of Yaw Stability Controller

3.1 Global Model of the Controller

In order to improve handling and stability of the vehicle, the sideslip angle and the yaw rate of the vehicle are controlled to trace their desired values. The direct yaw

moment generated by the longitudinal forces is employed as the control input to make actual responses approach to the desired values.

In the linear tire model, the lateral force F_{yi} is simply calculated as the product of the sideslip angle α of the tire and its equivalent cornering stiffness C_i

$$F_{yi} = C_i \alpha_i \quad (6)$$

From Eqs. (1)–(6), the following expressions can be obtained as

$$\dot{\beta} = a_{11}\beta + a_{12}\gamma + e_1\delta_f \quad (7)$$

$$\dot{\gamma} = a_{21}\beta + a_{22}\gamma + b_2M + e_2\delta_f \quad (8)$$

where, coefficients in Eqs. (7) and (8) are defined as follows

$$a_{11} = \frac{2(C_f + C_r)}{mv_x}, \quad a_{12} = \frac{2(l_f C_f - l_r C_r)}{mv_x^2} - 1, \quad a_{21} = -\frac{2(l_f C_f - l_r C_r)}{I_z}, \quad a_{22} = \frac{2(l_f^2 C_f + l_r^2 C_r)}{I_z v_x},$$

$$b_2 = \frac{1}{I_z}, \quad e_1 = \frac{2C_f}{mv_x}, \quad e_2 = \frac{2l_f C_f}{I_z}$$

It can be seen from Eqs. (7) and (8) that yaw moment can be controlled by adjusting the longitude force of each wheel. Therefore, the controller contains a reference block, an active front steering control block, a direct yaw rate controller and a dynamic force distribution controller.

3.2 Reference Model of Yaw Rate γ_d and β_d

According to the control objective, the steady state value of vehicle sideslip angle with respect to arbitrary front steering angle may be determined to be zero.

$$\beta_d = 0 \quad (9)$$

The desired value of the yaw rate can be determined by considering a vehicle moving with a constant forward speed while negotiating a steady state cornering maneuver. Constant radius turn of a vehicle, being referred to as the neutral steer behavior, could be achieved when the yaw rate is given by the following relationship

$$\gamma_d = \frac{v_x}{l_f + l_r} \delta \quad (10)$$

It is noted that in accordance to the above definition, the error between the actual and desired yaw rate is a measure of the vehicle steerability. Minimization of this term leads the vehicle to neutral steering behavior. In most cases, a stronger steerability is needed because of the great under steer tendency of most vehicles.

Although this is a good behavior for the vehicles driving on low friction roads, the controller based on the above definition of γ_d can influence the vehicle stability particularly at high speeds. Therefore, the value of γ_d can be modified in terms of the longitudinal speeds as

$$\gamma_d = \frac{v_x}{(l_f + l_r)(1 + k_{us}v_x^2)} \delta \quad (11)$$

where k_{us} is the positive constant and its increase leads the vehicle to an understeering behavior and a more severe stability.

3.3 Active Front Steering Controller

Road friction and vehicle inertia and state parameters such as mass and velocity vary with driving and road conditions. In order to provide robustness with respect to vehicle system parameter uncertainties and improve disturbance rejection, the SMC methodology is used to design the active steering controllers. The basic idea of the SMC is to choose a suitable sliding surface in state space and select a feedback control law that drives the system trajectories to reach and stay on the sliding surface, in spite of the presence of model inaccuracy and external disturbances. Once the system trajectories are on the sliding surface, the closed-loop dynamics are completely governed by the equations that define the surface. This means the dynamics of the closed-loop system is independent of system parameter variations and hence robustness is achieved [9]. In the case of AFS controller, the difference between the actual and reference yaw rate defines the tracking error, whose derivative can be written as

$$\dot{e} = \dot{\gamma} - \dot{\gamma}_d \quad (12)$$

Then the sliding surface $s = 0$ can be defined as

$$s = e \quad (13)$$

The sliding surface can be simply chosen to be the surface of the tracking error. The system dynamics in the sliding mode may be presented as follows

$$\dot{s} + \lambda s = 0 \quad (14)$$

where, λ is a positive constant.

The conditions in Eqs. (13) and (14) state that the system trajectories reach the sliding surface and remain on the surface, respectively. Substitution of Eq. (8) into Eq. (14) results in

$$a_{21}\beta + a_{22}\gamma + e_2\delta_f - \dot{\gamma}_d + \lambda(\gamma - \gamma_d) = 0 \quad (15)$$

The best approximation of a continuous control law can then be written in the following form as

$$u_0 = \delta_f = \frac{1}{e_2} [-a_{21}\beta - a_{22}\gamma + \dot{\gamma}_d - \lambda(\gamma - \gamma_d)] \quad (16)$$

In order to satisfy Eq. (16), regardless of the presence of uncertainty and disturbances on system dynamics, a term discontinuous across the surface $s = 0$ can be added to u_0 and forms the following switching control law

$$u = u_0 - l\text{sgn}(s) \quad (17)$$

where, sgn is the sign function and l is the controller design parameter that determines the speed at which the system approaches the sliding surface. This control gain must be chosen large enough to guarantee the following sliding condition

$$\frac{1}{2} \frac{d}{dt} s^2 = s\dot{s} \leq -\eta|s| \quad (18)$$

where, η is a strictly positive constant.

In addition, the presence of the discontinuous term in the above control law always leads to control chattering, which is highly undesirable as it may involve extremely high control effort and excite unmodeled high-frequency dynamics. Thus, to eliminate this effect, the sgn function in Eq. (17) is replaced by the saturation function, which is used to approximate the continuous control action within a boundary layer around the sliding surface. The saturation function is defined below

$$\text{sat}(x) = \begin{cases} x & \text{if } |x| \leq 1 \\ \text{sgn}(x) & \text{if } |x| > 1 \end{cases} \quad (19)$$

Accordingly, the final control law becomes:

$$u = \delta_f = \frac{1}{e_2} [-a_{21}\beta - a_{22}\gamma + \dot{\gamma}_d - \lambda(\gamma - \gamma_d)] - l\text{sat}(s/\varepsilon) \quad (20)$$

where, ε is the boundary layer thickness.

This control input is the steer angle at the front wheels, hence the corrective steer angle is the difference between the SMC output and the steer input from the driver and given as

$$\Delta\delta_f = \delta_f - \delta_{fd} \quad (21)$$

where δ_{fd} is the steer angle at the front wheels demanded by the driver.

3.4 Yaw Moment Controller

The sideslip angle and the yaw rate are chosen to be the main control variables of the stability controller. When the EV is in stable state, the desired sideslip angle is near to zero and the yaw rate is the first step delay response of the front wheel steering. Apply Laplace transformation to Eqs. (7) and (8), the transfer functions from steering angle to the side slip angle and the yaw rate can be written in the following forms respectively

$$\frac{\beta}{\delta}(s) = G_B(v) \frac{1 + T_B(v)s}{1 + \frac{Q(v)}{P(v)}s + \frac{1}{P(v)}s^2} \quad (22)$$

$$\frac{\gamma}{\delta}(s) = G_R(v) \frac{1}{1 + T_e(v)s} \quad (23)$$

where, GR, GB, Te, TB, Q, P are determined by the related EV parameters respectively.

It can be seen from Eqs. (1)and (2) that β and γ have a couple relationship to some extent. The side slip angle and the yaw rate will be deviate from the desired value if only a unique variable is controlled. Therefore, both variables have to be controlled for a desired vehicle response. Suppose the sliding face is defined as follows

$$S = c\beta + \dot{\beta} = 0 \quad (c > 0) \quad (24)$$

where, c is the control parameter. According to the arriving condition $\dot{S} + kS = 0$ ($k > 0$), the following equation can be obtained

$$\ddot{\beta} = -(k + c)\dot{\beta} - kc\beta \quad (25)$$

Substituting Eqs. (24) and (25) into Eq. (2), the yaw rate can be expressed as follows

$$\dot{\gamma} = \left(\frac{F_{y1} + F_{y2} + F_{y3} + F_{y4}}{mv_x} \right)' + (k + c)\dot{\beta} + kc\beta \quad (26)$$

Therefore, the function of external yaw moment by controlling both of the sideslip angle and the yaw rate can be written in the following form as

$$\begin{aligned} M_z = & -[(F_{y1} + F_{y2})l_f - (F_{y3} + F_{y4})l_r] + I_z \left(\frac{F_{y1} + F_{y2} + F_{y3} + F_{y4}}{mv_x} \right)' + (c + k)I_z\dot{\beta} \\ & + ckI_z\beta \end{aligned} \quad (27)$$

3.5 Dynamic Force Distribution Controller

For the yaw rate controller, active yaw moment can be generated according to the yaw tracking error as mentioned above. However, the generated yaw moment control can not be used as the control inputs for the four driving motors directly [10]. Therefore, the dynamic force distribution control is needed.

The inputs of the force distribution controller are yaw moment and driving force. The force commands for four motors are given and need to be calculated by the controller. However, there is a redundancy problem because of the longitudinal forces of the four motor wheels. Therefore, an optimal sequential quadratic programming method (SQPM) is used to resolve that redundancy and to realize dynamic optimal traction force-distribution control.

Suppose the four tires are all in adhesion state, yaw moment M_z can be given by the following equation

$$M_z(t) = \begin{pmatrix} -\frac{d}{2} & \frac{d}{2} & -\frac{d}{2} & \frac{d}{2} \end{pmatrix} \cdot (F_{x1}(t) \quad F_{x2}(t) \quad F_{x3}(t) \quad F_{x4}(t))^T \quad (28)$$

Since the traction force can be a function of longitudinal tire slip ratio, Eq. (28) can be expressed as

$$M_z(t) = D \cdot f(\lambda(t))^T \quad (29)$$

where, $f(\lambda(t)) = (f(\lambda_1(t)), f(\lambda_2(t)), f(\lambda_3(t)), f(\lambda_4(t)))$; $D = \begin{pmatrix} -\frac{d}{2}, \frac{d}{2}, -\frac{d}{2}, \frac{d}{2} \end{pmatrix}$; $\lambda_i(t)$ is the ratio of the i th tyre.

According to Eq. (29), $\lambda(t)$ can be given by dynamic inverse mapping in the following form as

$$\lambda(t) = Q(M_z(t), \lambda(t-T), M_z(t-T), \dots, \lambda(t-kT), M_z(t-kT), \dots) \quad (30)$$

where Q is a special function. T is the sampling time.

SQP method is used to resolve Eq. (30) and calculate the optimal slip ratio for every tire by the following form as

$$\underset{\lambda(t)}{\text{Min}} (\|W_1(\lambda(t) - \lambda_d)\|_2 + \|W_2(\lambda(t) - \lambda(t-T))\|_2) \quad (31)$$

where, λ_d is the desired optimal slip ratio which is determined by road condition estimation. W_1 and W_2 are weight matrices, which are determined by experiments.

Resolving Eq. (31), the dynamic inverse mapping obtained as follows can be used as the dynamic optimal traction force distribution control law

$$\lambda(t) = \tau_u \lambda(t-T) + \tau_v M_z(t) \quad (32)$$

where τ_u is the time delay coefficient and τ_v is the proportional coefficient.

Table 1 Vehicle inertia and dynamic parameters

M (kg)	I_z (kg m^2)	l_f (m)	l_r (m)	D (m)	C_f (N/rad)	C_r (N/rad)
1535	2630	1.2	1.34	1.45	-26681	-36711

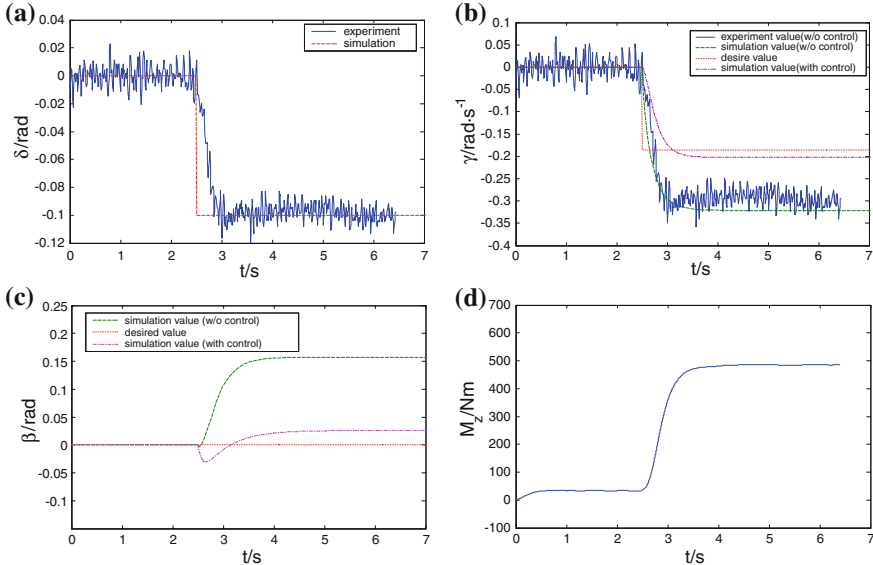


Fig. 1 Comparison of the simulation and the experiments values at J-turn. **a** Steering input angle, **b** yaw rate response, **c** side slip angle response, **d** external yaw moment

4 Results and Discussion

Computer simulations are carried out to confirm the effectiveness of the control system designed in this study. To illustrate the performance characteristics of the proposed control system, a base vehicle without control system has been considered as the competitor vehicle. All simulations are conducted under the condition that the road friction coefficient is 0.8 and the vehicle speed is 10 m/s. Parameters of the vehicle model are tabulated in Table 1. The results of simulation are explained in the following sections.

4.1 J-Turn Simulation and Experiment

In J-turn simulation, after the vehicle runs straightly at constant speed of 10 m/s for 2.5 s, the front steering angle pattern as shown in Fig. 1a with the maximum steering angle is 0.1 rad, is input into the vehicle by the driver. Figure 1b-d illustrate the simulation results of dry road condition with respect to the given

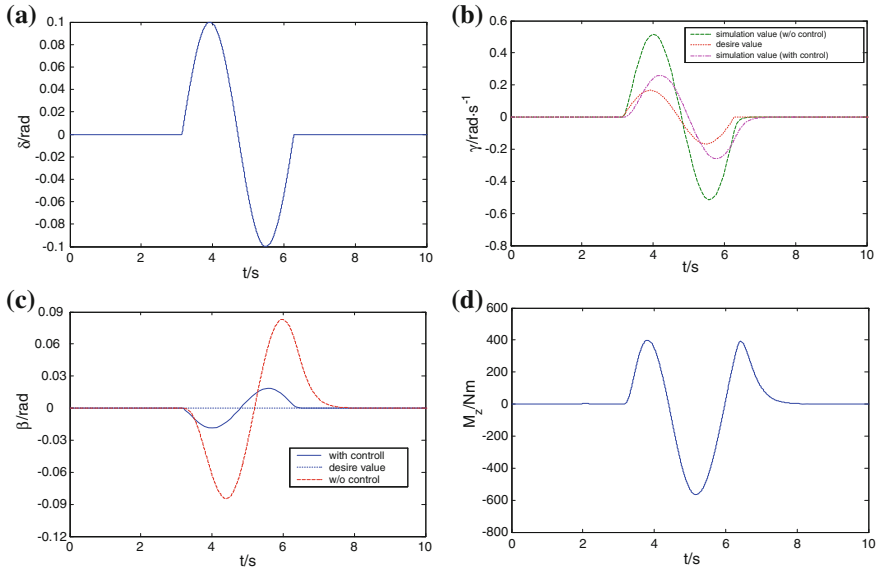


Fig. 2 Lane-change simulation. **a** Steering input angle, **b** yaw rate response, **c** side slip angle response, **d** external yaw moment

steering angle input. Figure 1b is the response of yaw rate. It can be seen that the simulated yaw rate response curve of the uncontrolled vehicle can trace the curve of the experiment, which indicated that the model is correct. Nevertheless, the yaw rate derivates from the desired value seriously and the vehicle is unstable. After applying the designed controller, the yaw rate response can almost exactly trace the desired value. Figure 1c is the response of vehicle body sideslip angle. Only simulation results are given to the sideslip angle because of the cost of the unique sensor measuring the sideslip in real vehicle. From the curves in Fig. 1c, it also can be seen that the sideslip angle is also reduced significantly comparing with the response of uncontrolled vehicle. Figure 1d is the external yaw moment generated by the different distributed torque of the designed controller. The results indicate that the stability of the electric vehicle is improved significantly by applying the controller.

4.2 Lane Change Simulation

Lane change is another important experiment to examine the maneuver stability of the vehicle. Only simulation results are given here because of the limitation of the experiment conditions. The vehicle is simulated to run at a constant speed of 10 m/s before a lane change maneuver is input by the driver, as shown in Fig. 2a. Figure 2b, c illustrate the time history of the yaw rate and the sideslip angle

response in the case of dry road condition. It can be found that the yaw rate researches to 0.5 rad/s without control. At the same time, the EV body sideslip angle is 0.08 rad. It indicates that the EV is in unstable condition. After applying the stability control strategy, the maximum yaw rate is reduced to 0.21 rad/s, which is much closed to the desired value 0.18 rad/s. At the same time, the maximum sideslip angle is reduced significantly to 0.02 rad, which is near to the desired value zero. It shows significantly that the designed controller can provide satisfactory level of tracing performance according to the desired value. Figure 2d is the external yaw moment generated by the different distributed torque of the designed controller. All these show that the designed controller can provide satisfactory level of tracing performance according to the desired values. The improvement of the yaw rate as well as the sideslip response in this study means that vehicle handling can also be improved significantly.

5 Conclusion

A novel drive-assist stability system for four-in-wheel motor drive electric vehicles is proposed in this paper. The system adjusts the output torque of each motor to meet the requirement of the drive demand and the road conditions. The control system integrates the direct yaw-moment and the active front steering control based on the sliding mode control theory. Computer simulations and experiments are performed with cornering and single lane change maneuver separately at the high speed. The results show that the presented method can effectively control sideslip angle and yaw rate of electric vehicle simultaneously and achieves multi-objective control of sideslip angle and yaw rate of vehicle. The designed controller significantly enhances the cornering stability and handling performance.

References

1. Tahami F, Kazemi R, Farhanghi S (2003) A novel driver assist stability system for all-wheel-drive electric vehicles. *IEEE Trans Veh Technol* 52(3):683–692
2. Goodarzi A, Esmailzadeh E (2007) Design of a VDC system for all-wheel independent drive vehicles. *IEEE/ASME Trans Mechatron* 12(6):632–639
3. Song JH, Kim HS, Kim BS (2007) Vehicle longitudinal and lateral stability enhancement using a TCS and yaw motion controller. *Int J Automot Technol* 8(1):49–57
4. Zhang Y, Yin C, Zhang J (2006) Vehicle dynamic control algorithm and its implementation on control prototyping system. *Int J Automot Technol* 7(2):167–172
5. Motoki Shino MN (2003) Independent wheel torque control of small-scale electric vehicle for handling and stability improvement. *JSAE Rev* 24:449–456
6. He P, Hori Y (2006) Optimum traction force distribution for stability improvement of 4WD EV in critical driving condition. In: 9th IEEE international workshop on advanced motion control

7. Jianyong W, Houjun T, Li S et al (2007) Improvement of vehicle handling and stability by integrated control of four wheel steering and direct yaw moment. In: Control conference
8. Yihu W, Dandan S, Zhixiang H et al (2007) A fuzzy control method to improve vehicle yaw stability based on integrated yaw moment control and active front steering. In: International conference on mechatronics and automation
9. Junjie He DAC, Levesley MC, Manning WJ (2004) Integrated active steering and variable torque distribution control for improving vehicle handling and stability. SAE paper 2004-01-1071
10. He P, Hori Y (2007) Experimental evaluation of dynamic force distribution method for EV motion control. In: Power conversion conference—Nagoya

A Study of Cornering Braking Control Strategy Based on Road Identification

Xiqiang Guan, Yao Li, Tengyue Ba and Jianwu Zhang

Abstract Identification of road friction is a prerequisite to optimize vehicle cornering braking control strategy. A maximum aligning moment method is proposed to estimate road friction coefficient using the sensors equipped with the steering system. Based on the hardware and the control logic of anti-lock braking system (ABS), an enhanced stability braking system (ESBS) is designed to improve the performance during cornering braking. Simulation and experimental results show that the estimation algorithm can identify changes of road conditions precisely and the control strategy improves braking efficiency and lateral stability of the vehicle, and thus has a high value of practical application.

Keywords Road identification · Brush tire model · Cornering braking · Slip ratio · Turning radius

1 Introduction

The principle of Anti-lock braking system (ABS) is to control the slip ratio of each wheel near the corresponding slip ratio of the maximum adhesion coefficient (s_{μ}), as a result of which the vehicle will obtain maximum braking force and good lateral stability. However, s_{μ} is not a constant, which may change with the variety of road conditions [1]. Burckhardt formula [2] depicts the relationship between

F2012-F08-014

X. Guan (✉) · Y. Li · T. Ba · J. Zhang
School of Mechanical Engineering, Shanghai Jiao Tong University, Shanghai, China

slip ratio and the adhesion coefficient of some typical roads, and the dry asphalt road, wet asphalt road and ice or snow covered road are about 0.15, 0.1 and less than 0.05, respectively, so road identification is helpful for ABS to make the best use of the adhesion between tires and road.

Besides, because of the longitudinal and lateral load transfer, the braking force and lateral force of each wheel vary greatly during cornering braking. This phenomenon may yield a large yaw moment which is possible to reduce the lateral stability of the vehicle and increase the opportunity of an accident. In order to improve the performance of ABS, it is necessary to design a control strategy to maintain the lateral stability of a vehicle during cornering braking.

In recent years, so many papers, in allusion to the identification of road friction and cornering braking control strategy, have been published. Mauer [3] proposed a method for road identification by taking advantage of brake pressure, slip ratio and brake deceleration, however, an acceleration transducer was needed according to the method, which not only increased costs, but also caused a larger error. Ahn [4] and Hsu [5] proposed to establish a nonlinear observer to estimate road friction, but it is hard to estimate the value of road friction promptly and accurately when the road condition changes continually. Li [6] proposed a cornering braking control strategy based on fuzzy control, but this approach needed to add a lot of extra sensors to measure vehicle states, which largely increased the cost of development.

In this paper, a maximum aligning moment method is proposed to estimate road friction coefficient based on tire lateral characteristics. Utilizing the control logic of ABS, an enhanced stability braking system (ESBS) is developed to improve braking performance during cornering. Compared with ESP, the ESBS has a potential cost advantage, because except the hardware equipped with ABS, only a gyro is added to ESBS to obtain the information of yaw rate.

2 Tire Model

Tire is the direct contact part between vehicle and road, so the road friction coefficient should be estimated accurately on the premise of building a simple and precise tire model.

2.1 Brush Tire Model

Brush Tire Model (BTM) [7] is the function of tire slip angle α and friction coefficient μ . Generally the Brush Tire Model equation can be expressed as:

$$F_y = \begin{cases} -3\mu F_z \gamma \{1 - |\gamma| + \frac{1}{3}(\gamma)^2\}, & \text{if } |\alpha| \leq \alpha_{sl} \\ -\mu F_z \text{sgn}(\alpha), & \text{otherwise} \end{cases} \quad (1)$$

Fig. 1 Single-tire bench tests



$$M_z = \begin{cases} \frac{l}{2} \mu F_z \gamma (1 - |\gamma|)^3, & \text{if } |\alpha| \leq \alpha_{sl} \\ 0, & \text{otherwise} \end{cases} \quad (2)$$

Where $\gamma = (C_{zf} \tan(\alpha)) / (3\mu F_z)$, F_z is tire vertical load, C_{zf} is cornering stiffness, l is tire contact length, α_{sl} is the slip angle when slippage occurs. $\alpha_{sl} = \tan^{-1}(1/\theta_y)$.

2.2 Tire Model Validation

In order to validate the accuracy of tire model, especially the tire lateral properties, a series of single-tire bench tests (as shown in Fig. 1) were carried out, and the test results were compared with Magic Formula Tire Model (MFTM) [7].

In the test, wheel speed is about 18 km/h, and tire pressure is 220 kPa. Figure 2 shows the relationship between tire lateral forces, aligning moment and tire slip angle. By comparing the results between simulation and tests, it can be found that the MFTM is better than BTM, but the tire lateral properties can also be reflected by BTM accurately. In addition, by comparing tire lateral force and aligning moment under same vertical load condition, it can be seen that the tire slip angle corresponding to maximum aligning moment is less than that corresponding to maximum lateral force. In other words, aligning moment reaches the maximum earlier than lateral force. So it illustrates that if the information about aligning moment can be used in estimation model, then the condition between wheel and road may be estimated earlier when steering angle is small.

3 Model Estimation

3.1 Algebraic Relation Between Maximum Aligning Moment and Wheel-Road Friction

Through the above analysis, it is beneficial for fast convergence of estimate results if the tire aligning moment could be measured. However, the tire aligning moment M_z is difficult to be measured directly by sensors. The finding by analysis is that

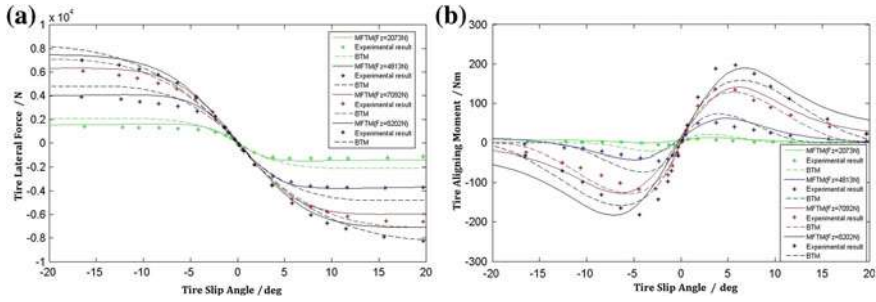


Fig. 2 Lateral force/aligning moment to tire slip angle under different vertical load condition. **a** Lateral force to tire slip angle. **b** Aligning moment to tire slip angle

the aligning moment of whole steering system M_a [8] can be calculated when the steering moment is measureable. More importantly, there exists a simple algebraic relation between M_a and μ when the BTM is taken into consideration. And the aligning moment M_a can be expressed as:

$$M_a = (-F_{yf}\xi_c + M_{zf}) \quad (3)$$

where F_{yf} is vertical load of front axle, ξ_c is caster trail, M_{zf} is whole aligning moment of front axle.

Considering the total load of front axle, the lateral offset of load has no effect on calculation. Using the Eqs. (1) and (2), the Eq. (3) can be derived as below:

$$\begin{aligned} M_a &= [3\mu F_{zf}\gamma\{1 - |\gamma| + \frac{1}{3}(\gamma)^2\}\xi_c + \frac{l}{2}\mu F_{zf}\gamma(1 - |\gamma|)^3] \\ &= \mu F_{zf}sign(\gamma)[\{1 - (1 - |\gamma|)^3\}\xi_c + \frac{l}{2}|\gamma|(1 - |\gamma|)^3] \end{aligned} \quad (4)$$

In order to compute the maximum aligning moment, the above Eq. (4) is taken its partial respect to $|\gamma|$, and can be written as below:

$$\frac{\partial M_a}{\partial |\gamma|} = \mu F_{zf}sign(\gamma)(1 - |\gamma|)^2\left(\frac{l}{2}(1 - 4|\gamma|) + 3\xi_c\right) \quad (5)$$

By calculating, aligning moment M_a reaches the peak when $|\gamma|$ is:

$$|\gamma| = \frac{1}{4}\left(1 + \frac{6\xi_c}{l}\right) \quad (6)$$

Substituting Eq. (6) into the previous Eq. (4):

$$M_{aMax} = \mu F_{zf}sign(\gamma) \cdot f(\xi_c, l) \quad (7)$$

$$\text{Where } f(\xi_c, l) = \frac{(1+6\xi_c)(27l^3+134l^2\xi_c-156l\xi_c^2+72\xi_c^3)}{512l^3}$$

Hence,

$$\mu = \frac{M_{a\text{Max}}}{f(\xi_c, l)F_z \text{sign}(\gamma)} \quad (8)$$

It can be seen clearly from Eq. (8) that there exists a simple linear relationship between road friction coefficient μ and maximum aligning moment $M_{a\text{max}}$, if BTM is made use of. Besides, all the parameters in Eq. (8) can be measured or calculated easily: the tire contact length l can be obtained by using semi-analytical approach [9] when the characteristic of tire structure and contact between elastic bodies are adequately taken into account. Caster trail ξ_c is connected with geometrical relationship among steering structures, and it is up to kinematic relationship among structures [4, 10]. The vertical load of front axle can be figured out by considering the load longitudinal distribution [11]. And the maximum aligning moment of steering system $M_{a\text{max}}$ can be obtained by solving the torque equilibrium equation of steering system when the torque of steering wheel is measurable.

3.2 Judgment Method for the Point of Aligning Moment Reaching Maximum

The difficulty of maximum aligning moment method is to judge when M_a reaches the peak. Because this method is only used to estimate road friction but not the tire slip angle, the point of maximum aligning moment cannot be acquired by measuring slip angle which satisfies Eq. (6). However, if aligning moment reaches maximum, Eq. (9) below holds.

$$\frac{\partial M_a}{\partial |\gamma|} = 0 \quad (9)$$

Although $\partial M_a / \partial |\gamma|$ is difficult to be measured directly, it can be estimated approximatively under some assumptions.

First of all, within a small scope of μ , μ and C_{zf} are constant, thus:

$$\frac{dM_a}{dt} \approx \frac{\partial M_a}{\partial |\gamma|} \frac{\partial |\gamma|}{\partial \alpha} \frac{d\alpha}{dt} \quad (10)$$

And tire slip angle is usually small, so the equation $\tan(\alpha) \approx \alpha$ holds. Therefore, Eq. (10) can be rewritten as:

$$\frac{\partial M_a}{\partial |\gamma|} = \frac{dM_a/dt}{\text{sign}(\gamma) \frac{C_{zf}}{3\mu F_z} d\alpha/dt} \quad (11)$$

$d\alpha/dt$ is hard to be measured without extra sensors, but it finds that there exists almost same variation trend between $d\alpha/dt$ and $-d\delta/dt$ by calculation, as it is shown in Fig. 3.

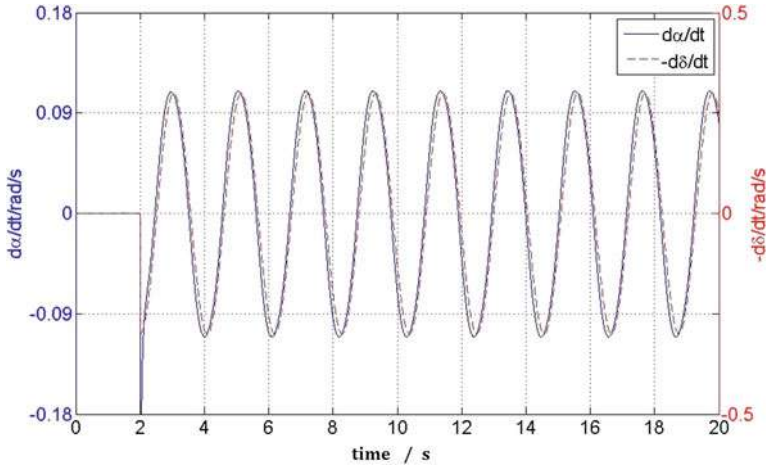


Fig. 3 $-d\delta/dt$ and $d\alpha/dt$ to time

Hence, the third consumption is:

$$\frac{d\alpha}{dt} \approx -k_{z\delta} \frac{d\delta}{dt} \quad (12)$$

whereby $k_{z\delta}$ is a constant.

Substituting Eqs. (11) and (12) into the previous Eq. (9):

$$\frac{\partial M_a / \partial t}{\partial \delta / \partial t} \approx 0 \quad (13)$$

The numerator and denominator in Eq. (13) can be obtained by steering system model. The above derivation process shows that M_a is approximatively regarded as maximum when Eq. (13) holds. Then, μ can be computed by Eq. (8).

In particular, if the vehicle equipped with Electric Power Steering (EPS) or other advanced steering systems which can measure steering torque and steering angle, it can be seen from the derivation process that the road friction coefficient can be estimated without any extra sensors when using the maximum aligning moment method, and it has huge market potential.

3.3 Validation of Estimated Model

In order to verify the estimated algorithm, the test results of Pylon course slalom are imported into estimated model. The friction coefficient of concrete pavement testing ground is 0.7–0.8, and vehicle speed is about 45 km/h. The vehicle steering occurs after 5 s for vehicle stability. Figure 4 shows the estimated results of road friction coefficient. During the early 6.5–8.5 s, road friction coefficient is underestimated,

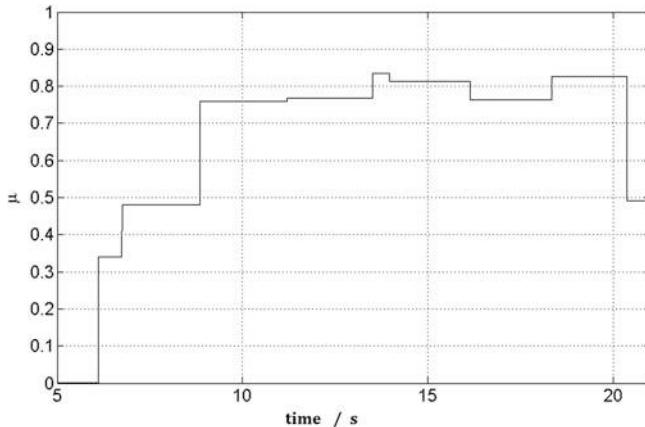


Fig. 4 Estimated results of road friction coefficient

because wheel steering angle is too small. With the increase of steering angle, the estimated value quickly achieves its actual value and basically remains stable.

4 Control Strategy of Cornering Braking

The control aim of cornering braking is to make vehicle get braking force as big as possible and keep lateral stability well. In order to get maximal braking force, the wheel slip ratio should be controlled near maximum adhesion coefficient region. During vehicle braking, to keep well lateral stability needs to hold vehicle turning radius steady, moreover, not to lead to over-steering or under-steering.

Keep vehicle neutral-steering that means:

$$R/R_0 = 1 \quad (14)$$

where R is transient turning radius $R = u/\omega_r$, R_0 is turning radius as front wheel angle constant, vehicle speed low and lateral acceleration close to 0, $R_0 = \delta/L$, u is vehicle speed, ω_r is yaw velocity, δ is steering angle of front wheel, L is wheelbase.

In Eq. (14), only the vehicle speed u and yaw velocity ω_r change when steering angle of front wheel is constant. Because of vehicle speed is affected by braking, it will decrease constantly. The primary mechanism for designing control strategy during cornering braking is to adjust the vehicle yaw velocity by controlling slip ratio; consequently, vehicle lateral stability can be kept.

Figure 5 shows the relationship between longitudinal and lateral adhesion coefficients to slip ratio under the same slip angle. It can be seen from Fig. 5 that longitudinal adhesion coefficient reduces little and lateral adhesion coefficient enhances significantly, while the slip ratio corresponding to maximum adhesion coefficient sharply decreases from s_μ to $s_{\mu d}$.

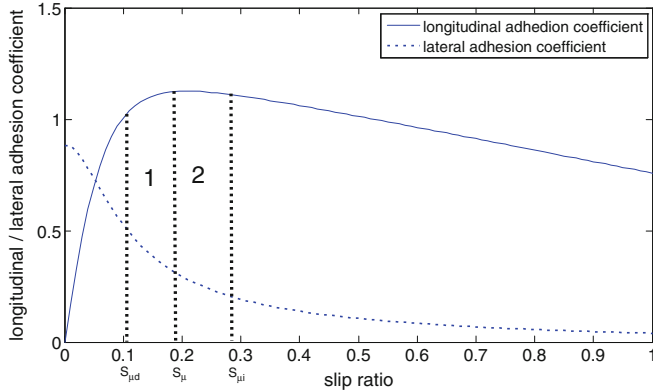


Fig. 5 Longitudinal and lateral adhesion coefficients to slip ratio under the same slip angle

Similarly, if the slip ratio corresponding to maximum adhesion coefficient increases from s_μ to $s_{\mu i}$, then the longitudinal adhesion coefficient enhances little while lateral adhesion coefficient decreases drastically. That means if ranges of region 1 and 2 are set to be reasonable, the vehicle lateral stability can be improved without influencing braking efficiency.

Table 1 shows the yaw velocity behavior caused by slip ratio change of each wheel. It can be summarized that when vehicle has over-steer characteristics, yaw velocity should reduce and slip ratio of inner front wheel should increase. Likewise, when vehicle has under-steer characteristics, both yaw velocity and slip ratio of outer front wheel should increase, but slip ratio of outer rear wheel should increase. It should be pointed that the precondition of ESBS controlling slip ratio is brake pressure of brake master cylinder high enough to make the wheel in big braking slip ratio region. Figure 6 shows flow diagram of ESBS control strategy.

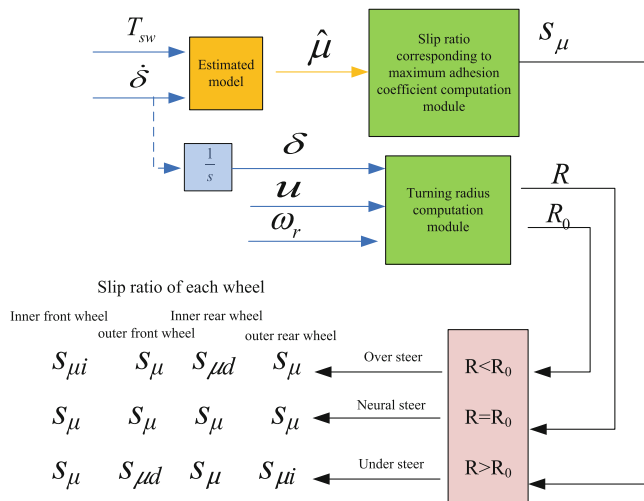
5 Braking Performance Analysis

In order to validate the effectiveness of control strategy based on road identification during cornering braking, analysis of high and low adhesion roads ($\mu = 0.8, 0.3$) are simulated respectively. In the simulation parameters of vehicle are as follow: vehicle mass $m = 1535$ kg, front and rear longitudinal distances between the tire axles and the mass center are separately $a = 1.423$ m, $b = 1.117$ m, moment of inertia about z axle is $I_z = 2248.1$ kg · m^2 . In simulation, the vehicle turns left from 2th second and holds the steering angle in 4th second, then vehicle brakes from 8th second until it stops.

Figure 7a shows the transient steering radius on big adhesion coefficient road, of which ABS means traditional target slip ratio method ($s = -0.2$), ABS op is optimal control strategy of ABS target slip ratio changes with road, and ESBS is

Table 1 Yaw velocity behavior caused by slip ratio change of each wheel

	Slip ratio increasing			Slip ratio decreasing		
	Longitudinal force	Lateral force	Yaw velocity	Longitudinal force	Lateral force	Yaw velocity
Inner front wheel	Decrease	Decrease	Decrease	Decrease	Increase	Uncertainly
Outer front wheel	Decrease	Decrease	Uncertainly	Decrease	Increase	Increase
Inner rear wheel	Decrease	Decrease	Uncertainly	Decrease	Increase	Decrease
Outer rear wheel	Decrease	Decrease	Increase	Decrease	Increase	Uncertainly

**Fig. 6** Flow diagram of ESBS control strategy

added cornering braking control strategy based on ABS op. From the curves in Fig. 7a, it can be seen that whether ABS or ABS op, both results have over-steer characteristics during cornering braking. However, under the ESBS control, braking distance increases a little, but the vehicle finally keeps neural-steer characteristics after transient over steering, so ESBS can effectively improve the vehicle lateral stability. Meanwhile the slip ratio corresponding to maximum adhesion coefficient is about -0.2 , so there is little difference between ABS and ABS op results.

Figure 7b shows slip ratios with ESBS control on high adhesion road. From the curves in Fig. 7b, it can be seen that slip ratio of left rear wheel (inner) decreases and slip ratio of left front wheel (inner) increases, because vehicle has over-steer characteristics after braking. Vehicle remains stable during cornering braking by the influence of both slip ratios. It should be explained that slip ratio is positive

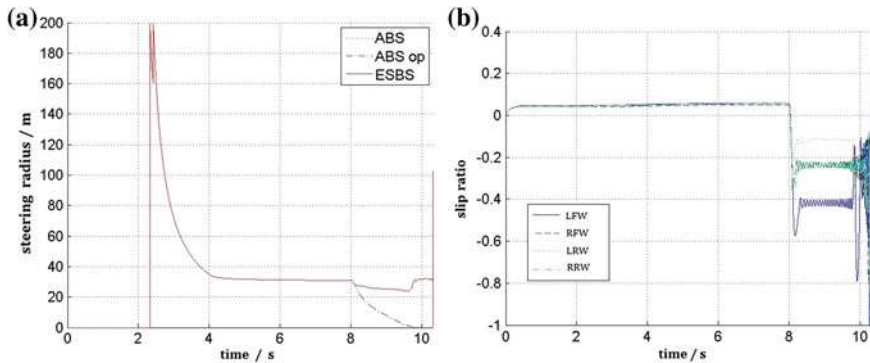


Fig. 7 Transient steering radiiuses/slip ratios with ESBS control on high adhesion road. **a** Transient steering radiiuses. **b** Slip ratios with ESBS control

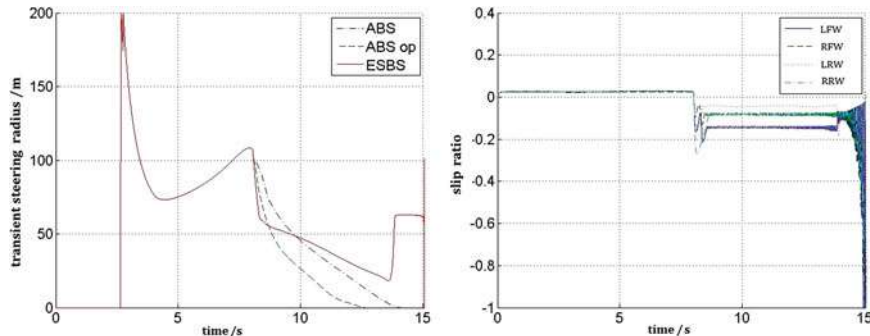


Fig. 8 Transient steering radiiuses/slip ratios with ESBS control on low adhesion road. **a** Transient steering radiiuses. **b** Slip ratios with ESBS control

when the car drives and it is negative when braking, so-called slip ratio in the paper means the absolute value of slip ratio.

Figure 8a shows the transient steering radius on low adhesion coefficient road. From the curves in Fig. 8a, it can be seen that when vehicle just starts to brake, it has under-steer characteristics, and vehicle transient steering radius with effect of ESBS decreases faster than other two methods'. When vehicle is under over-steer characteristics, ESBS can make steering radius increase, and yet the other methods lead to severe over-steer characteristics. Meanwhile it can be learnt that there exist huge differences between slip ratio corresponding to maximum adhesion coefficient and -0.2 , so ABS op can take full advantage of road adhesion ability, and braking distance lowers obviously compared with traditional ABS.

Figure 8b shows slip ratios with ESBS control on low adhesion road. From the curves in Fig. 8b, it can be seen that the slip ratio of right front wheel (outer) decreases while the slip ratio of right rear wheel (outer) increases, because vehicle

has under-steer characteristics after starting to brake. When vehicle is under over-steer characteristics, the slip ratio of left rear wheel decreases and the slip ratio of left front wheel increases separately, and during cornering braking, the change of slip ratio always accords with ESBS control, then it can improve vehicle stability effectively.

6 Conclusion

A cornering braking control strategy based on road identification is proposed in this paper; meanwhile road identification method and establishment of control strategy are expounded particularly. It is shown from the pylon course slalom test on concrete pavement that the estimated method based on maximum aligning moment for road friction coefficient is accurate and effective. The results from high and low adhesion road simulation show that the vehicle lateral stability and braking safety are effectively improved by ESBS control strategy during cornering braking. Because of the control strategy basically continuing to use the hardware and control logic of ABS, it has high value of practical application.

References

1. Yu F, Lin Y (2005) Vehicle system dynamics. China machine press, Beijing
2. Lei X (2005) A study on control strategy of vehicle stability during cornering braking. Shanghai Jiao Tong University engineering master thesis, Shanghai
3. Mauer GF (1995) A fuzzy logic controller for ABS braking system. IEEE Trans Fuzzy Syst 3:381–388
4. Ahn C et al (2009) Estimation of road friction for enhanced active safety systems: dynamic approach. In: American control conference, St Louis, MO, USA
5. Hsu Y et al (2006) A method to estimate the friction coefficient and tire slip angle using steering torque. In: 2006 ASME international mechanical engineering congress and exposition, Chicago, Illinois, pp 1–10
6. Li J, Yu F, Zhang J et al (2001) An investigation into optimal target slip ratio control for simulation of an anti-lock braking system of vehicles. J Syst Simul 13(6):789–793
7. Pacejka HB (2006) Tire and vehicle dynamics. Society of Automotive Engineers, USA
8. Abe M (2009) Vehicle handling dynamics. Elsevier, UK
9. Zhu X, Xie Z, Yan X et al (1998) Determination for ground contact length and static radial stiffness of tire. Tire Ind 18(8):458–461
10. Laws S et al (2005) Steer-by-wire suspension and steering design for controllability and observability. IFAC World congress, Prague
11. Zhisheng Yu (2000) Vehicle theory. China machine press, Beijing

Van Traffic Accident Analysis. A Holistic Approach

**Blanca Arenas Ramírez, Javier Páez Ayuso,
José M. Mira McWilliams, Felipe Jiménez Alonso,
Arturo Furones Crespo and Francisco Aparicio Izquierdo**

Abstract From 2003 on, the numbers of accidents and victims have decreased significantly in Spain: the number of deaths was in 2010 54 % below that of 2003. This has been to a great extent the results of several safety policy measures such as the penalty point system, surveillance and control campaigns and a considerable increase in the media of road safety-related issues. However, accidents with involvement of vans (LGV's less than 3500 kg) have not followed this trend, and thus the contribution of this kind of vehicles to the global figures has risen. Within this context, INSIA has conducted an ambitious research project, developed with the purpose of an integrated analysis of the different factors which can explain the accidental behavior of this kind of vehicles. In this paper analyze in greater depth the validity of one of the initial hypothesis: "vans may have a different dynamic behavior from passenger cars, and thus accident rates may be higher if they are driven like a passenger car". The basis of the working hypotheses are essentially related to the behavior of the vehicle with respect to safety distances, reaction times and braking capacities of the vehicle behind, and on the influence of loads.

Keywords Vans · LGV's accident analysis · Dynamic test program · Nationwide mobility survey

F2012-F08-015

B. Arenas Ramírez (✉) · J. Páez Ayuso · J. M. Mira McWilliams ·
F. Jiménez Alonso · A. Furones Crespo · F. Aparicio Izquierdo
Automobile Research Institute (INSIA), Technical University of Madrid (UPM),
Madrid, Spain

1 Introduction

It is well known that road accidents are a very complex socio-economic problem given the large number of variables which influence the risk conditions and the capabilities of drivers and vehicles to overcome them. Additionally, there exists the problem of the estimation of the exposure levels for given groups of road users, as well as the availability of sufficient information concerning the accidents and other incidents in which only random circumstances, difficult to identify, prevented a dramatic outcome which would have turned the incident into an accident of the kind above.

The studies on accidents which have been carried out to date are usually based on in-depth analyses, which are expensive and only applicable to small samples and of great interest to identify and evaluate the influence factors. The most relevant are driver, vehicle and road characteristics. More or less sophisticated statistical methods are also applied to describe the process on a macroscopic level, or identify correlations between given factors, and the occurrence of accidents and victims. However, the techniques are seldom part of an integrated methodology which allows for a deeper and more complete knowledge of the relationship between the different variables, as intended in this work.

Through the research Project FURGOSEG [1], in the framework of which, this paper is included, an integrated methodology has been proposed for the analysis of van accidents and similar vehicles, which includes different techniques: in-depth accident analysis, econometric and data mining models, surveys, road inspections, track tests safety systems.

For the study a “van” is defined as a light freight transport vehicle and the different types belong to any of the following four groups: G1: pick-up, G2: Chassis cabin truck max weight: 3,500 kg, G3: Vans and combi-type commercial vehicles y G4: Vans and passenger car-derived LVS, in general over 2,000 kg (see Annex 1). This classification is one of the results of the project and has been a priori obtained from expert opinion and confirmed *ex-post* by the result analysis.

In this paper we focus on the results obtained around the hypothesis “vans could have a dynamic behavior different from passenger cars, so that van accidents could increase if driven like a passenger car”.

For verification o rejection of the hypothesis we have developed an integrated analysis with three steps:

1. Survey on 3,693 van drivers to determine van driver perception, the % of who do not perceive differences between driving of vans and cars.
2. Track tests to determine if dynamic behavior of vans is changing due to load conditions and displacement of center of gravity due to changes in loads.
3. Data mining models to address the important issue of whether vans and cars shown different patterns in crash accidents.

2 Nation-Wide Mobility Survey: Driver Perception of Vans Dynamic Behavior

In the interurban mobility survey carried out for 3,693 van drivers, we have included several items to record driver's opinions on how this kind of vehicle is driven. The first is formulated as Q1: do you believe that this kind of vehicle is driven like a passenger car? 58.7 % of drivers think the opposite, but this proportion depends on the van type: for G4 it rises to 72.3 %, for G3 51.3 %, for G1 63.3 %. Even for light truck drivers, 27.7 % believes that it is driven differently. A summary of the responses is shown on Table 1.

The second question is formulated as follows: Q2: why do you believe that this vehicle is driven like a passenger car? There is an open question in which the driver could explain the reasons for his answer, negative or positive, we have thus grouped the possible answers in the following categories: Factor 1—Weight/Measures: in this factor we have included the answers related with the vehicle characteristics. The drivers could have answered that driving is different because either the sizes or weights are different or that they are driven the same because the measures and weights coincide.

Factor 2—Maneuvrability/Comfort: here we have grouped answers such as: it is driven like a passenger car, with greater difficulty.

Factor 3—Safety/Visibility: here we include answers related to safety aspects such as ABS or comments where the surveyed driver indicates if the vehicle is more or less safe, as well as the comments on larger or smaller visibility.

Factor 4—Load/Stability: in this case the surveyed drivers mentioned the lower stability of this kind of vehicles, the different driving when loaded, instability caused by wind and in curves, etc.

Factor 5—Similar to Passenger Cars: this factor is a grouping of the comments of surveyed drivers indicating the similarity between passenger car and van driving.

Factor 6—More Critical Braking: comments on how braking distances are larger, or worse braking conditions.

Factor 7—NS/NC: where the surveyed driver has not answered or has explicitly indicated that he/she does not know the answer.

The results (negative responses) for each group of factors are shown on Table 2.

According to the drivers surveyed the most frequent reason for which a van is not driven like a passenger car is the difference in weights and measures and secondly the load and its role in vehicle safety.

The third question was Q3: do you believe that his vehicle, when loaded, should be driven in interurban roads differently as when non-loaded? 73 % answered on the affirmative, but it is significant that 27 % does not acknowledge that the vehicle should be driven differently when loaded. As for the type of vehicle, the proportion of negative answers is 20.4 % within truck drivers, 32 % in passenger—car—likes, 22.7 % for pure vans and 29 % for pick-ups.

Table 1 Answers to the question Q1: do you believe that this type of vehicle should be driven like a passenger car?

		Yes (%)	No (%)
P 30- Vans type	G1: PickUp	63.3	36.7
	G2: Chassis cabin truck	27.7	72.3
	G3: Vans and combi type-commercial vehicles	51.3	48.7
	G4: Vans and passenger car-derived LVS	72.8	27.2
	Global	58.7	41.3

Table 2 Answers to the question “Q2: why do you believe that this vehicle is driven like a passenger car?”

F1	Weight/measures	645	42.2 %
F2	Maneuvrability/comfort	190	12.4 %
F3	Safety/visibility	204	13.4 %
F7	NS/NC	38	2.5 %
F4	Load/stability	340	22.3 %
F6	More critical breaking	51	3.3 %
F5	Similar to passenger cars	59	3.9 %
	Total	1,527	100.00 %

In the fourth question the drivers were requested to indicate if they would change their driving under heavier loads occasionally, frequently or always under the following assumptions: (a) driving at lower speed (b) maintaining following distances (c) others, to be specified in a text field.

The two most frequent behaviors are:

- “I drive more slowly” for 78 %, and “I keep a larger safety distance” for 71.8 % of cases. This means that between 20 and 30 % do not show a different driving behavior in both situations. Drivers of passenger-cars like vans only reduce speed occasionally in 28.5 of cases and those of Vans and 19 % for combi-type commercial vehicles.
- A larger following distance is observed occasionally by 22.7 % of passenger-like vans and 14.8 % of those of Vans and combi type-commercial vehicles.

Each question has been analyzed cross-examining with respect to others such as age, gender, distances covered on a standard working day and we may highlight the following:

- The average distances are moderate or even low for most of the surveyed, thus this factor does not seem to justify a pressure which could lead them to, e.g., drive fast or the need of long driving journeys.
- A very large proportion of drivers believe that this type of vehicle is driven like a passenger car. The figure is even larger for women (69.4 %).

- The proportion of drivers that believes that the load does affect driving is larger but that of drivers who believe the opposite is still too high (between 20 and 30 %) and this can be considered a significant risk factor since in most cases it does not coincide with objective reality.
- Among experienced drivers, there exists a smaller perception of driving differences.

These results are of great interest if one takes into account that the driving license for passenger cars is also valid for vans below 3,500 kg.

3 Track Tests

With the purpose of examining the dynamic behavior of the vehicles, a track test plan has been developed for braking and steering with passenger cars and vans under different loads for the latter. In turn, the test has been repeated 3 times, and our intention here is to assess if there exist significant differences between the dynamic behavior of passenger cars and vans, as well as analyzing the influence of load in such behavior.

Namely, 3 loads have been considered under the following tests:

- Braking tests with initial speed of 30 km/h to 80 km/h with and without ABS
- Steering wheel tests at constant radius, constant speed and constant direction angle.

As example for illustration, we show the results obtained when testing an IVECO Daly van. The instrumentation employed was the following:

- Gyroscopic platform RMS FES 33 which provides angles rotated on the three axes the corresponding angular velocities and linear accelerations.
- Non-contact Speed sensor Correvit L-CE
- Receptor GPS Astech G12 which provides the vehicle paths.
- Connection to the CAN vehicle bus to obtain direction angles

As indicated above, the tests have been carried out under 3 different loads as shown in Table 3, where the zero load just includes the driver and instruments. The maximum load allowed is 3,500 kg, although here it has been slightly surpassed, while the overload is 20 % above Maximum Weight.

Table 4 shows the results obtained in several braking tests with and without ABS. It is observed that the maximum possible deceleration is recorded as the vehicle load increases, although the differences are not important between the so-called “empty” and “loaded” vehicles, the decrease is larger for overload, significantly lower for vans without ABS than for those with it. It should be noted that the maximum possible deceleration is smaller than that obtainable with a passenger car under similar tests conditions, which have been above 9 m/s^2 . On the

Table 3 Load conditions (in kg)

Load condition	Front axle	Rear axle	Total
Empty	1,530	1,380	2,910
Loaded	1,530	2,160	3,690
Overloaded	1,520	2,790	4,310

Table 4 Maximum decelerations reached (m/s^2)

Load condition	With ABS	Without ABS
Empty	8.6	6.8
Loaded	8.4	6.7
Overloaded	7.8	–

other hand, the test speeds were not very high given the characteristics of the test track.

The tests carried out on vans and passenger cars allow us to highlight that:

- The vehicles without ABS tested do not show significant differences in braking with respect to unloaded ones.
- The load is influential on braking implying a large braking distance on ABS equipped vehicles.
- A great difference can be observed in the performance of vehicles equipped with ABS with respect to those that don't. In the full set of tests, the extreme values of the recorded accelerations are 8.6 m/s^2 for ABS-equipped vans, unloaded, and 6.7 m/s^2 for non ABS-equipped vans; this difference amounts to 28 % of the braking capacity.

This last factor is specially relevant in Spain considering that for vans, both in fleets and in recent additions, there exist large differences between populations of vans and passenger cars, equipped with ABS. In the year 2008, 100 % of all new passenger cars had ABS, while for vans this proportion is only 63 and 10 % does not even include it as an option.

On the other hand, the turning behavior of the vehicle was analyzed under the 3 loads from the steering tests (constant radius) on a circular path of radius = 20 m. Fig. 1 shows the results for the first load condition. The following simplified model has been fitted to the experimental data:

$$\delta = \frac{L}{R} + K_V \frac{v^2}{gR}$$

We have to fit the scatterplot to a parabola without the linear term. Thus, the coefficient of the quadratic term can be related to the turning coefficient (k_v) and we can see if the vehicle shows understeering, oversteering or neutral behavior in the range of test conditions with side accelerations between 1 and 5 m/s^2 .

The least-squares fit provide the following values of k_v :

Fig. 1 Results of vehicle behavior in a path of constant radius

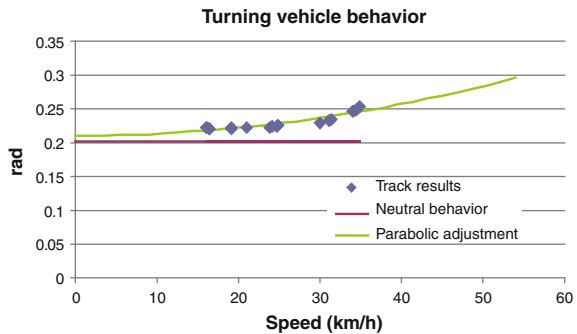
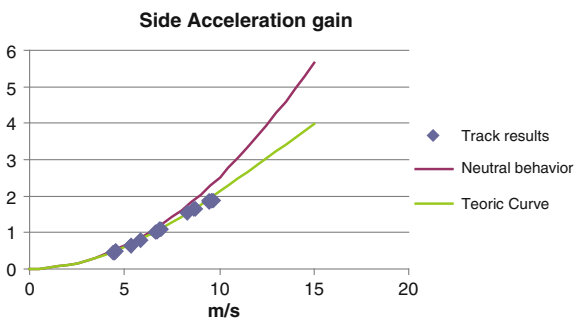


Fig. 2 Side acceleration gain for “empty” vehicle



- Empty: $K_v = 0.075$
- Loaded: $K_v = 0.109$
- Overload: $K_v = 0.078$

From the results of the model fitted above, the side acceleration gain has been analyzed as well as the yaw speed and curvature. As may be observed as example for illustration in Fig. 2, the experimental evidence is coherent with the model above. As can be observed, the vehicle presents understeering behavior and the changes in load do not cause changes which, although they are not a significant modification, as for example switching from understeering to oversteering, could, for instance, affect vehicle response to evasive manouevres.

The tests conditions do not allow for drawing final conclusions but one can not discard the possible influence of this variable in accidents, so that it may be advisable to carry out new tests under more severe conditions as far as speed, side acceleration, with scenarios of possible load displacement and other influence factors.

4 Data Mining Models

A data mining analysis has been carried out based on the data from the records of the Accident Data Base of the General Traffic Directorate (DGT) [2], with the purpose of the identification of influencing factors related to the dynamic behavior of the vehicle in the moment of the accident and subsequently to determine if there is different behavior of vans with respect to cars in two specific crash scenarios. The scenarios takes into account differences in braking and dynamic response, related to loads as it is expected to be more common in vans than cars.

Approximately 90,000 accidents are recorded on the base per year, being the period studied 2000–2009. The data base contains more than 100 variables related to the environment, vehicles and persons involved, and in which at least one person has been injured.

For the data mining analysis the CART (Classification and Regression Trees) techniques, developed by Breiman et al. [3], have been applied. It is a multivariate non-parametric technique, particularly suitable for prediction and classification. Some advantages of this tool for accident analysis are (a) its capacity for dealing simultaneously with different types of data (numerical, categorical) as well with missing data for both the explanatory and response variables, (b) building of the tree is simple, and (c) the results are easy to interpret. As growing procedure we have used the CRT algorithm included in the statistical software SPSS v17 [4].

The accident database we have used does not include variables indicating the dynamic behavior of the vehicle in the moment of the accident. To deal with this lack of information we have chosen two accident scenarios where the dynamic behavior of the van derived from its own characteristics and as different from those of passenger cars could have been influential in causing the accident.

In the scenario 1 we have selected vans involved in rear-end collisions, and they crash into the vehicle in front of it. The hypothesis is that the braking distance for vans is larger than for passenger cars and thus they are more likely to impact on preceding vehicle. The characteristics of the accidents analyzed are: 2 vehicles involved, rear end accident and where at least one of the two drivers is not respecting safety distance, although this information is usually the result of a subjective assessment from the road agent.

The response variable is “vehicle colliding in the rear-end crash”. If the driver of the vehicle involved has not respected the safety distance, it is considered as vehicle impacting in the rear-end crash” and the other driver is impacted vehicle”. This variable is dichotomous. In this case the tree identifies significant differences with respect to different vehicle variables, distinguishing vans from the rest. It is observed that for rear-end crash the proportion of vehicles impacting is larger for vans (53.9 %) than for passenger cars (43.3 %) and additionally vehicle type is the most relevant explanatory variable in the model.

In the scenario 2 we have analysed vans involved in accidents with a pre-crash sudden maneuver. Similarly, we want to analyze the turning behavior or if the position of the center of mass of the van are influential on their accident rate.

The characteristics of the accidents analyzed under this scenario are: a single vehicle involved, which may be a van or a passenger car, and the driver perform a sudden manoeuvre just before the accident occurs. In a similar way to previous scenario, the response variable is type of vehicle, (binary) passenger car or van, and the explanatory variables are the same as for previous CART model.

The analysis shows that sudden manoeuvres accidents, there are significant differences between vans and other vehicles: there is an increase in the proportion of vans (6.9 % to 14.5 %) when the type of accident is overturn. In pedestrian accidents we also observe an increase in vans although in a smaller proportion (1.7 %).

In rear-end collisions, the main influence factors were the safety distance and the braking capacity. The first is not fully objective and depends on the driver, the second on the vehicle and, as mentioned above, by means of tests, differences have been detected between the braking performances of both types of vehicles, turning out larger under loaded vans.

In sudden manouevres accidents which end up in overturn, they may be related to the height of the center of mass under certain load conditions of the van, and with possible problems of load displacement. Although these factors have not been verified experimentally, it is an (easy to show) physical truth that both: a larger height of the center of mass of the vehicle (which occurs in most cases under loads), and a side displacement of the load, reduce the overturn threshold, (maximum side acceleration which the vehicle may endure before overturning). This is a distinguishing factor of passenger cars and vans and between different van types as well, although stronger for vans and combi type-commercial vehicles and chassis cabin truck types.

Although no tests have been carried out on the influence on safety and specially under sudden manouevres, of ESP systems, their influence is well established and its presence in vehicle fleets and new vehicles is smaller than for ABS for vans as it has been determined in the fleet vans study for year 2008.

5 Conclusions

The results of the survey indicate that a certain number of vehicles which are driven with overloads and thus could divert even more from the behavior of passenger cars, with a negative effect on safety. Most of van drivers believe that their vehicles should be driven like passenger cars, and there is a small proportion that believes that driving need not change under heavier loads. For these it can be remarked the inadequate risk perception of a great number of van drivers, who are not aware of the special characteristics of their vehicles with respect to passenger cars, which, are allowed to drive these vehicles without additional driving licenses.

The results obtained for the directional behavior of these light freight transport vehicles support the hypothesis of the influence of loads on the dynamic behavior and also of the difference with respect to passenger cars.

From data mining results, it has been identified significant differences between vehicle types: mainly vans and passenger cars, which may influence the occurrence of certain types of accidents.

Besides, in Spain, the study revealed the vans have less safety equipment as ABS and ESP than passenger cars.

Bearing in mind these results, it would be advisable the establishment of new requirements for drivers, and some policies devoted to promote vans fleet renewal increasing safety equipment presence.

Annex 1: LGV vehicle classification

For the definition we have taken into account the different vehicle classifications of the General Traffic Directorate (DGT) as well as definitions from the general vehicle Regulations. The four LGV groups of our analysis are:

- G1: pick-up vehicles used to carry (simultaneously or not) people, goods or both, with a single or double 5 to 6 people non-integrated cabin, the load-carrying receptacle can be open in the upper side and the sides may be abatable or fixed, with 2 or more-axis traction, particularly suited to difficult roads, the passenger cabin looking more like an SUVs than a passenger cars.
- G2: Chassis cabin truck or bodywork commercial vehicle: designed for goods transport: including a single or double cabin, carrying up to 7 people (driver included) the cabin is non-integrated with the rest, different sections or boxes may be adapted to the chassis, the vehicle looks like a small truck and the cabin resembles that of a van.
 - G2.1. Boxcar type.
 - G2.2. Box van type variant.
- G3: Vans and combi type-commercial vehicles: they are designed for (simultaneous or not) transport of people, goods or both, with a simple cabin carrying up to 9 people (driver included) integrated with the rest of the vehicle, it looks like a classical goods distribution van, possibly carrying more than one row of sets when combi type-commercial vehicles.
 - G3.1. Vans.
 - G3.2. Combi variant/mixed transport.
- G4: Vans and passenger car-derived LVS, in general over 2,000 kg.
 - G4.1. Car- van is a vehicle devoted to servicing or 100 % goods transport, derived from a passenger car keeping the bodywork, with a single row of seats, it looks exactly like rear-blinded car.
 - G4.2. Passenger car-derived LVS derived from passenger cars, devoted to (simultaneous or not) transport of goods, people or both, carrying up to 7

(driver included), the cabin is integrated, it looks like passenger cars in front, but higher and typically with a double rear door.

- G4.2.1. Van variant.
- G4.2.2. Combi variant.

Acknowledgments This work has been carried out in the framework of the research Project FURGOSEG - P24/08 “Development and application of an integrated methodology for the study of road accidents with involvement of vans”, of the Spanish national Research Plan 2008–2011. MICINN.

References

1. Project FURGOSEG - P24/08 (2011) Development and application of an integrated methodology for the study of road accidents with involvement of vans, of the Spanish National Research Plan 2008–2011. MICINN, 2011
2. General Traffic Directorate (2000–2009) Internal Affairs Ministry. (DGT). Data base accidents
3. Breiman L, Friedman JH, Olshen RA, Stone CJ (1984) Classification and regression trees. Wadsworth International Group, Belmont
4. SPSS Statistics (computer program V 17), 2008

Study on Rollover Prevention of Heavy-Duty Vehicles by Using Flywheel Energy Storage Systems

**Suda Yoshihiro, Huh Junhoi, Aki Masahiko, Shihpin Lin,
Ryoichi Takahata and Naomasa Mukaide**

Abstract This paper deals with rollover prevention of a vehicle using a flywheel. The authors have proposed to use a flywheel as a stabilizer for a heavy vehicle by using gyroscopic effect. A typical flywheel is composed of a rotating disk and gimbals which absorb the gyroscopic effect while supporting the rotor. To produce the gyroscopic effect to stabilize the heavy vehicle, the proposed system constrains a gimbal when the roll of the vehicle becomes large and reach beyond the threshold value. The stability of the heavy vehicle with the proposed flywheel system is examined by multibody dynamics simulations and the experiment. It was found that the proposed control system is effective for rollover prevention.

Keywords Flywheel battery system · Rollover prevention · Heavy-duty vehicle · Gyro effect · Experiment

1 Introduction

Heavy vehicles have played an important role in land transportation. Of them, the use of long articulated vehicles is economically attractive due to lower costs per mass of cargo. However, it has been shown that articulated vehicles can suffer

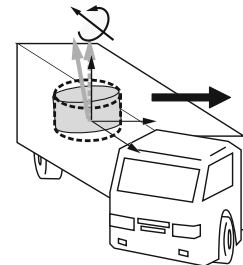
F2012-F08-016

S. Yoshihiro (✉) · H. Junhoi · A. Masahiko · S. Lin
Institute of Industrial Science, The University of Tokyo, Japan

RyoichiTakahata · N. Mukaide
JTEKT Corporation, Japan

Table 1 Mass of vehicle

Tractor	Trailer	Container
7,000 kg	3,550 kg	24,000 kg (Maximum Load)

Fig. 1 Rollover prevention by using flywheel

from dangerous rollover instabilities from its distinct structure [1]. And it is very difficult for drivers to perceive their proximity to rollover while driving [2].

The authors propose to use flywheel energy storage systems as a stabilizer for articulated vehicles by using gyroscopic effect. The flywheel has the gyroscopic effect, and several studies have reported that the flywheel can be used for the attitude controls such as satellite and gondola [3, 4]. The authors reported that the gyroscopic effect of the flywheel is utilized as the stability control device for motion of railway vehicle [5, 6]. In this paper, the authors developed a simulation model of the articulated vehicle to estimate effect of rollover prevention of articulated vehicles by using the flywheel energy storage system (Fig. 1). The stability of the articulated vehicle with the flywheel systems is examined using the multibody dynamics software ADAMS. Parameters of the articulated vehicle model used for simulation are based on a real scale tractor semi-trailer combination for 40 ft freight container loaded maximum weight. Specifications of the vehicle are shown in Table 1. The vehicle model turns under rough running condition that is able to cause rollover accident. It was found that the proposed control system is effective for rollover prevention.

This paper dealt with rollover prevention of an articulated vehicle using a flywheel. To indicate the proposed rollover prevention system, dynamical simulation of a semi-trailer was calculated. Those results showed the effectiveness of the proposed system for rollover prevention.

2 Gyro Effect

When a disturbance angular velocity acts on a rotating body which has angular momentum, torque is generated to the rotating body. This is called as gyro effect. This is formulated as (1).

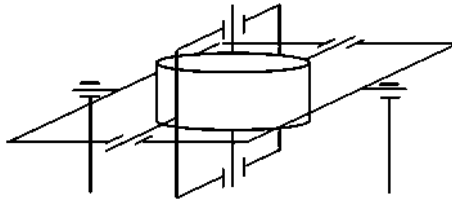


Fig. 2 Double gimbaled flywheel

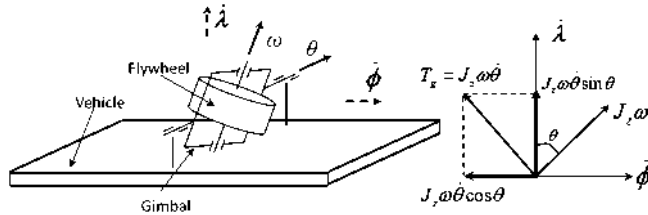


Fig. 3 Gyro effects of single gimbaled flywheel

A flywheel has different dynamic characteristics by each gimbal type. When a flywheel is supported by double gimbals (Fig. 2), dynamics of the flywheel is isolated from dynamics of a base of the flywheel. Therefore, a gyro effect is not appeared by motion of the flywheel.

On the other hand, when a flywheel is supported by single gimbals, roll and yaw angular velocities of a vehicle become disturbances to the gimbals. Therefore, the gyro effect (Eqs. (3) and (4)) influence on the dynamics of the vehicle (Fig. 3). In this study, rollover prevention by using the gyro effect of an articulated vehicle is treated. Figure 3 shows the concept of rollover prevention for the on-board flywheel battery system. When the vehicle has a roll angle, the flywheel with single gimbal generates an anti-rollover moment with a pitching motion.

$$H \times \Omega = T_g \quad (1)$$

$$J_y \ddot{\theta} + c \dot{\theta} + k \theta = J_z \omega \dot{\phi} \cos \theta - J_z \omega \dot{\lambda} \sin \theta \quad (2)$$

$$I_x \ddot{\phi} + C_x \dot{\phi} + k_x \phi = -J_z \omega \dot{\theta} \cos \theta + T_x \quad (3)$$

$$I_Z \ddot{\lambda} + C_Z \dot{\lambda} + K_Z \lambda = J_Z \omega \dot{\theta} \sin \theta + T_Z \quad (4)$$

3 Concept of Rollover Prevention

Until recently, the flywheel energy storage system was loaded on a vehicle with a double gimbal support device to avoid a bad influence of the gyro effect on the motion of the vehicle. However, the flywheel energy storage systems have to be



Fig. 4 Concept of rollover prevention. (a) Double gimbal. (b) Constraint a gimbal. (c) Single gimbal

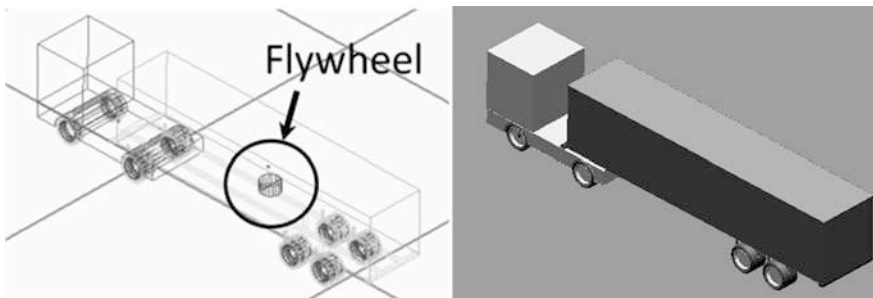
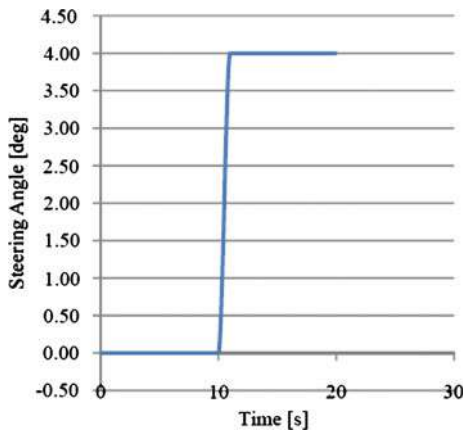
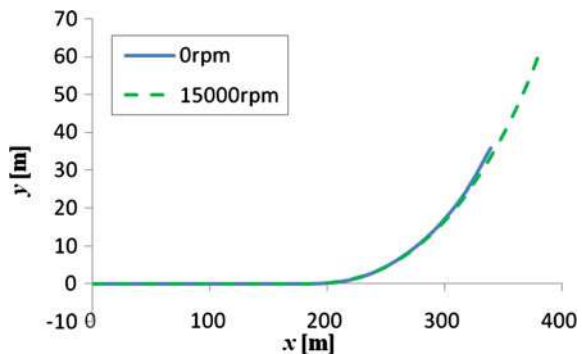
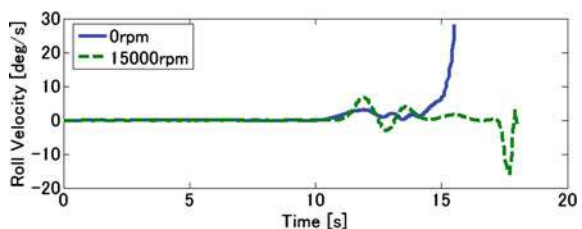


Fig. 5 Overview of simulation model

supported by single gimbal to use gyroscopic effect of the flywheel for rollover prevention. The authors propose fundamental concept of rollover prevention by using flywheel energy storage system. In ordinary running condition, the flywheel is supported by a double gimbal to avoid bad influence of the gyro effect, and when the lateral acceleration and the roll angle of vehicle are so large for the vehicle to have a potential to rollover, the external gimbal is constrained to prevent rollover (Fig. 4).

4 Rollover Prevent Effect by Simulation

The stability of the articulated vehicle with the flywheel systems is examined using the multibody dynamics software; ADAMS. The articulated vehicle is consisted by a tractor, a trailer and container. Moreover, a flywheel is mounted on the trailer. Figure 5 shows an overview of the articulated vehicle model by ADAMS. Parameters of the articulated vehicle model used for simulation are based on a real scale tractor semi-trailer combination for 40 ft freight container loaded maximum weight. Specifications of the vehicle are shown in Table 1. The vehicle model turns under rough running condition (Figs. 6 and 7) that is able to cause rollover accident. Figure 8 shows roll angular velocities of the trailer and Fig. 9 shows roll angle of the trailer. Solid lines show no control results and dotted lines show

Fig. 6 Steering condition**Fig. 7** Vehicular swept path**Fig. 8** Roll angular velocity of trailer

control results. The no control result shows a roll angle of the trailer monotonically increased. On the other hand, the control result shows a roll angle of the trailer was stabilized to a steady state. Figure 7 shows the vehicular swept path. A swept path with no control stopped by the rollover. On the other hand, a swept path with control kept running state after the sudden steering maneuver.

These results show effectiveness of the proposed control system. It was found that the gyroscopic effect of the flywheel energy storage system is effective for rollover prevention.

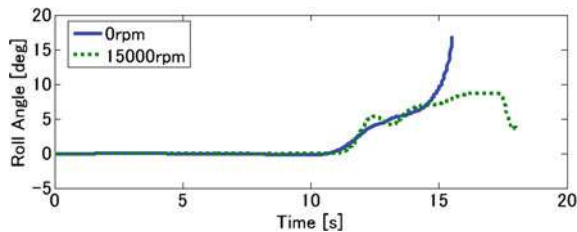


Fig. 9 Roll angle of trailer

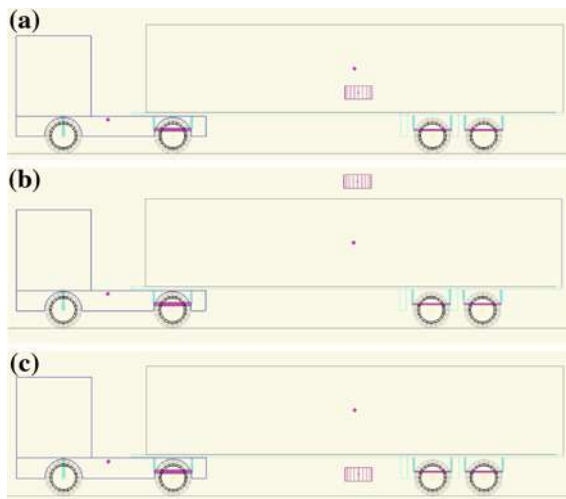


Fig. 10 Flywheel mounted position. (a) Flywheel mounted in the container. (b) Flywheel mounted above the container. (c) Flywheel mounted under the trailer

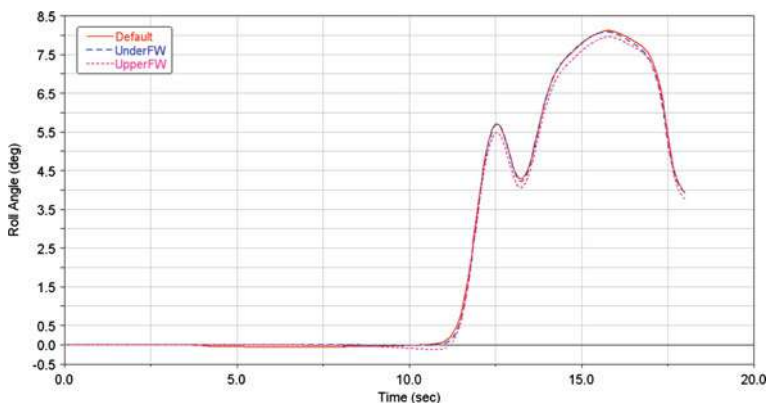


Fig. 11 Roll angle of trailer

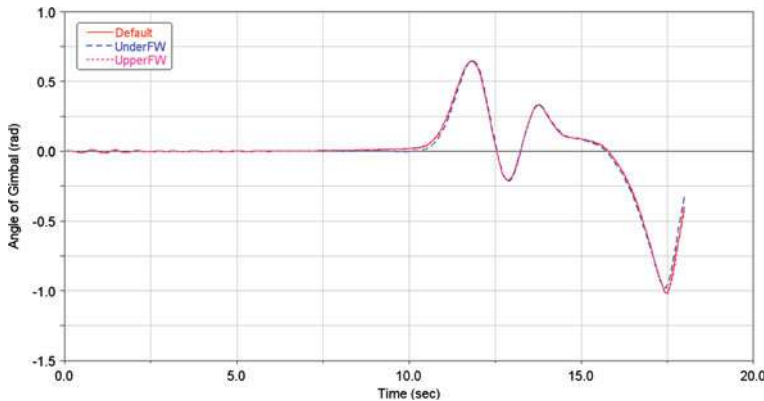


Fig. 12 Gimbal angle

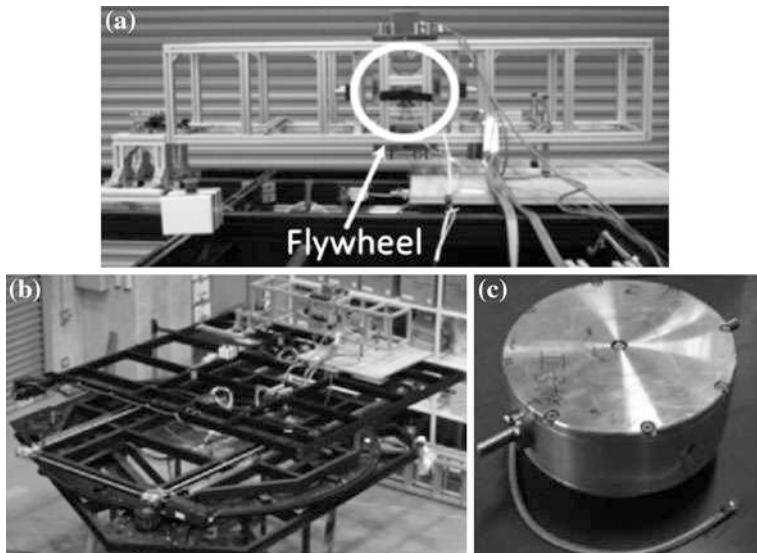


Fig. 13 Experimental apparatus. (a) 1/8-scaled trailer. (b) Turntable + XYstage. (c) Flywheel

5 Effect of Flywheel Mounted Location

Effect of flywheel mounted position is examined for practical use of flywheel battery for rollover prevention. In this paper, the mounted location effect is considered along height direction. Figure 10 shows conditions of flywheel mounted location. The three conditions are; (a) in the container (b) above the container and (c) under the trailer. By using these mounted conditions, dynamic analysis was carried out. A steering condition of the vehicle was used as the Fig. 6.

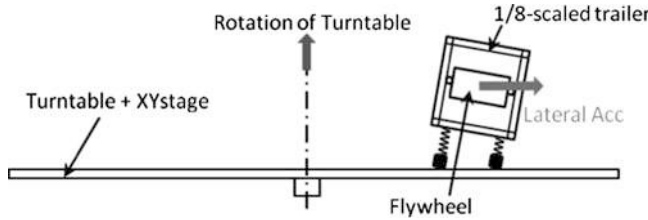


Fig. 14 Schematic diagram of the experimental setup

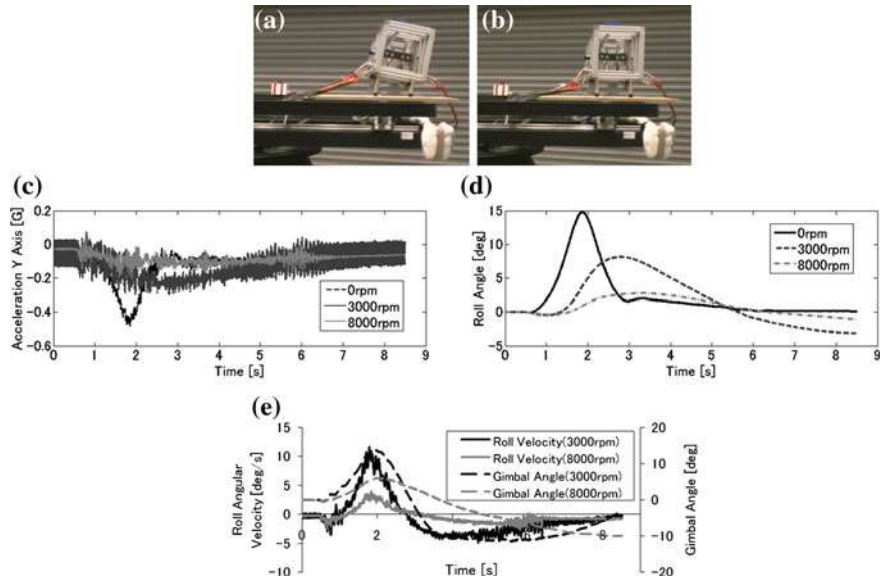


Fig. 15 Experimental result. (a) No Control (0 rpm). (b) Control (8,000 rpm). (c) Lateral acceleration. (d) Roll angle. (e) Roll angular velocity—gimbal angle

Figure 11 shows roll angles of the trailer and Fig. 12 shows gimbal motions of the flywheel battery. A red solid line shows the condition (a) which is an original condition. A blue dotted line shows the condition (b), and a pink dotted line shows the condition (c). These three conditions have the same control effects because the anti-rollover moment by the flywheel does not affect the act point. In addition, the slightly differences of the trailer response between three conditions came from the changing of the center of gravity by the flywheel battery position.

It is need to set the center of gravity to a lower position. Therefore, a realistic location of the flywheel battery is under the trailer.

6 Experiment with a Semi-Trailler Model

Experimental setup was conducted by a semi-trailer model, a flywheel. The semi-trailer model was made as 1/8 scaled model. The experimental setup was mounted on a turntable and translational motion stage. A situation of rollover was realized by rotation of the turntable system (Fig. 13). The mechanism of rollover is shown in Fig. 14.

Experimental results are shown in Fig. 15. Figure 15(a, b) show experimental scenes. Figure 15(c, d) show control effects. By these results, when rotational speed of the flywheel increase, the control effects also increase.

7 Conclusions

This paper dealt with rollover prevention of an articulated vehicle using a flywheel. To indicate the proposed rollover prevention system, dynamical simulation of a semi-trailer was calculated. The dynamic analysis showed the effectiveness of the proposed system for rollover prevention. Moreover, the effect of flywheel mounted location was also examined. Moreover, the experiment with a semi-trailer model was carried out. Those results showed the effectiveness of the proposed system for rollover prevention.

References

1. Rajamani R (2012) Vehicle dynamics and control, Springer, pp 427–456
2. Winkler CB, Blower D, Ervin RD, Chalasani RM (2000) Rollover of heavy commercial vehicles, SAE
3. Kanki H, Nekomoto Y, Monobe H, Ogura H, Kobayashi K (1994) Development of CMG active vibration control device for gondola. JAME Int J Series C 37(3):468–470
4. Kurosawa H (1989) Attitude control by using control moment gyro. Syst Control Inform 33(4):157–164 (In Japanese)
5. Okamoto H, Lin S, Kotani M, Yabuno H, Suda Y (2006) Stabilization control for hunting motion of railway vehicle by gyroscopic damper. In: VSDIA2006
6. Suda Y, Ando T, Nakano K, Huh J (2009) Roll motion control of vehicles by gyroscopic moment with flywheel battery. In : IAVSD2009

Part VIII

**Safety Standards and International
Regulations**

Iso 26262 Impact on Development of Powertrain Control System

Hui Guo, Jiaxi Liu, Shitao Yu and Jun Li

Abstract More and more Electronic/Electrical (E/E) systems with safety related functionalities are being integrated on modern vehicles, which increase system complexity and thus increase system risk. This trend strengthens the demand for functional safety development processes. ISO 26262, which has been published in November 2011, provide necessary requirements and standardizes the processes for functional safety development in automotive industry. Safety related E/E systems should be developed following the guidance of this standard. According to ISO 26262, more than 100 work products could be required for powertrain control system development. How to meet such requirements is a challenging topic. This paper proposes an approach to comply with ISO 26262 by adding a few essential work products to the conventional V-Model development processes, which could be a sufficient way as first step. An example from powertrain control system is used to illustrate the proposed approach.

Keywords ISO 26262 · Functional safety · Powertrain control system · Impact · Work product

1 Introduction

Social expectation for automotive safety is continuously rising. In parallel, safety related functionalities with complex software and mechatronic implementation increase system complexity. It finally increases risks resulted from systematic

F2012-F09-003

H. Guo (✉) · J. Liu · S. Yu · J. Li
United Automotive Electronic Systems Co. Ltd, Shanghai, China

failures and random hardware failures. ISO 26262 is an international standard for functional safety of E/E systems on road vehicles. This new standard addresses possible hazards caused by malfunctioning behaviour of safety-related E/E systems, and provides guidance to identify, evaluate and control these risks [1].

Due to product liability issues, safety related automotive E/E systems have to comply with ISO 26262 after its publication [2]. Requirements in ISO 26262 should be followed and consequent work products should be documented to provide safety proof. The implementation of ISO 26262 is a concern for most of the E/E system suppliers.

There are researches on implementation case study of ISO 26262 [3, 4]. However, analysis is not seen in literature about the impact of ISO 26262 on the conventional V-model development process for powertrain control system. It will be helpful for organizations to adapt existing well organized process and integrate ‘add-on’ work products required by ISO 26262. In following sections, the essential ‘add-on’ work products from ISO 26262 are recommended and a function development case in powertrain control system is used to illustrate how to implement these work products.

2 Iso 26262 Essential Work Products

V-model based product development process is widely used for development of automotive E/E systems, including powertrain control system, as shown in Fig. 1. ISO 26262 defines a complete automotive safety lifecycle, in which the development phase is also based on V-model. Therefore implementation of ISO 26262 will not fundamentally change product development process of powertrain control system. The impact will be the requirement to provide a well-structured and convincing safety case.

To construct the safety case, a few essential work products needs to be added on the original V-model development process, as shown in black rectangle mark in Fig. 1.

In concept phase, three work products are needed, which are Item Definition (ID), Hazard Analysis & Risk Assessment (H&R), and Functional Safety Concept (FCO). As OEMs have the overview of the interaction between E/E systems on the vehicle, it is optimal to provide these work products by them and communicate the results with suppliers. Before stepping into product development phase, an Impact Analysis (IA) can be used to check the changed part of the functional safety concept and determine tailoring of the process.

A Development Interface Agreement (DIA) will help the powertrain control system suppliers to define the responsibilities and work products exchange with OEMs.

Suppliers of powertrain control system will be responsible for functional safety development in product development phase. On the left side of V-model, the safety requirements should be explicitly identified as safety related. Therefore work products of Technical Safety Concept (TCO), System Design Specification

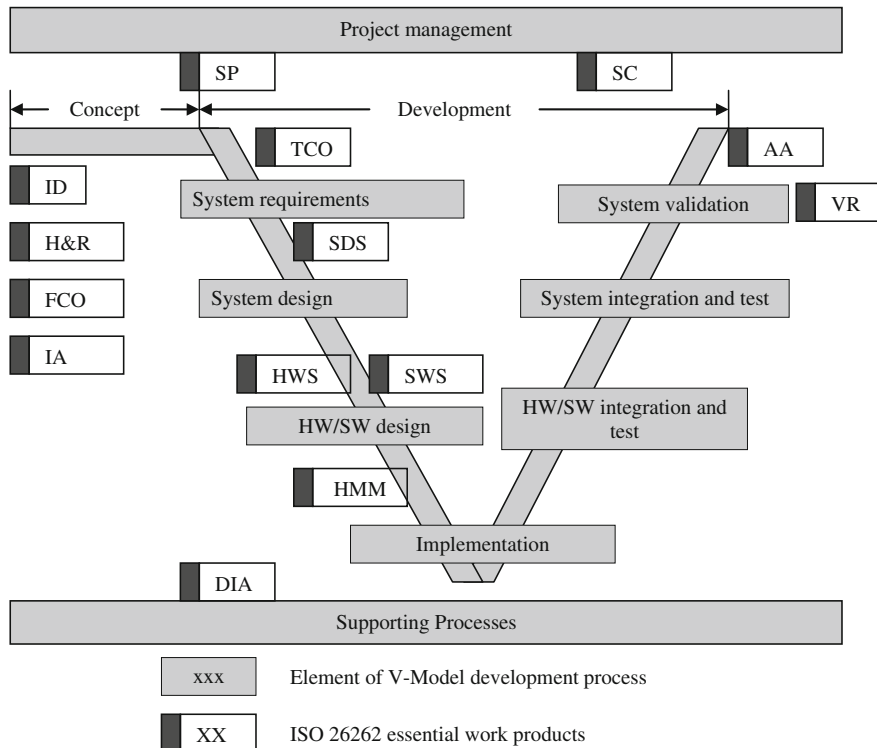


Fig. 1 ISO 26262 impact on V-model development process of powertrain control system

(Safety) (SDS), Hardware Safety Specification (HWS), Software Safety Specification (SWS) should be conducted. On the right side of V-model, i.e. the verification and validation side, a safety Validation Report (VR) is required to confirm all safety goals being archived on vehicle level.

For products which have risks classified with higher Automotive Safety Integrity Levels (ASIL C or ASIL D), a functional safety Audit & Assessment (AA) with sufficient independent level should be conducted to check whether the development follows the guidance in ISO 26262. Also for these products, quantitative Hardware Architectural Metrics and Reliability Metrics (HMM) should be calculated to verify that system reaches safety goals considering hardware random failure.

All the work products need to be planned and managed in Safety Plan (SP). For this reason, a project safety manager will be nominated. At last, the whole functional safety documentation is summarized in Safety Case (SC).

ISO 26262 not only has requirements on above essential work products, but also has many other requirements. For example, ISO 26262 also has requirements on unit tests, integration tests and so on. However, based on our experience and analysis, most of these requirements can be covered by already existing well

organized V-model development process. It can be a sufficient way to fulfill ISO 26262 by focusing on the essential work products at first.

3 Implementation Hints for Essential Work Products

To make the implementation hints for the essential work products comprehensible, an example will be given. The background of the example is to add Start/Stop function in a vehicle with manual transmission. The implementation of Start/Stop control is intended to be in Engine Control Unit (ECU).

3.1 Item Definition

Item definition serves to define the item under development and provides sufficient information to support subsequent sub-phases, such as hazard analysis and risk assessment. The item's functionalities, primary elements, interfaces and constraints can be described. And the scope for the project can be outlined. Take Start/Stop function for example, the basic functionality is to automatically switch engine off when the vehicle stops moving and start the engine again when the driver pulls away. Primary elements may contain software algorithm of Start/Stop function which will be implemented in Engine Control Unit, and other necessary sensors and actuators. Start/Stop function may share some sensors and actuators (e.g. engine speed sensor) with engine control, and therefore has interfaces with engine control. Constraints in this example could be that the Start/Stop function is developed for vehicles with manual transmission.

3.2 Hazard Analysis and Risk Assessment

Hazard analysis and risk assessment identifies potential hazards based on the information provided by item definition and classifies these hazards according to risk levels. Adequate techniques, including brainstorming, checklists, FMEA, etc., should be used in hazard identification to collectively address potential hazards. The risk of identified hazards should be assessed based on three categories: the severity of potential harm (S), the probability of exposure regarding operational situations (E) and the controllability of each hazardous event by the driver or other persons potentially at risk (C). For Start/Stop function described above, two possible hazards are fault engine start which causes unintended vehicle movement and fault engine stop which causes unintended vehicle stop. Risk assessment example of these two hazards is as illustrated in Table 1.

Table 1 Example for ASIL classification of Start/Stop system

Hazard: Fault engine start which causes unintended vehicle movement					
Considered situation: Vehicle is parked on hill top, gear is engaged to secure the car but without handbrake					
E	E2	C	S	S3	ASIL B
Parking on hill top, E3		C3			
Using gear to secure the car other than handbrake, E2		Driver left vehicle, no access to control, C3	Vehicle moves, and accelerates due to slope, pedestrian may be crashed seriously. S3		
Hazard: Fault engine stop which causes unintended vehicle stop					
Considered situation: overtaking on country road					
E	E2	C	C1	S3	ASIL
Overtaking, E3		Driver can cancel overtaking by braking, C1		May crash to on-coming vehicle. S3	QM
On-coming vehicle from opposite direction, E2					

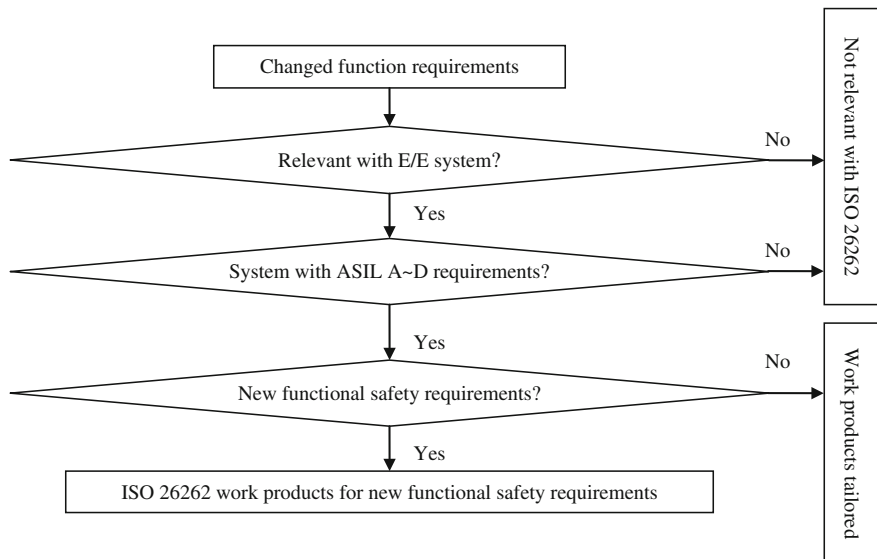


Fig. 2 Impact analysis work flow

A safety goal should be specified for every identified hazard with ASIL classification, along with its safe state and fault tolerance time. Safety goal inherits ASIL of corresponding hazard, and the ASIL will be passed throughout entire lifecycle. In above example, safety goal of Start/Stop function is to avoid unintended vehicle movement caused by fault automatic engine start (ASIL B). Safe state could be engine stop.

3.3 Functional Safety Concept

The objective of functional safety concept is to define necessary functions designed to achieve safety goals. Functional safety concept contains functional safety requirements and their allocation to elements in primary system architecture of the item. Functional safety requirements may contain measures for fault detection, fault mitigation, driver warning, etc. For the example of Start/Stop function, the functional safety requirements can be specified as this: inhibit engine automatic start when drive train is engaged (ASIL B). In this way, starting engine will not cause vehicle movement. If Start/Stop function is implemented in Engine Control Unit, the functional safety requirements can be allocated to it.

Table 2 DIA example

Customer: xx Project Name: xxxx				Supplier: xx		
Development Interface Agreement						
DIA IA	Work product name	Document link	Provided by customer/supplier	Deliver to	Date	Coversheet/Original document
...
3.2	Safety goals	Attachment 3.2	Customer	Supplier	xx-xx-xx	Original document
...
5.1	Validation report	Attachment 5.1	Supplier	Customer	xx-xx-xx	Coversheet
...

3.4 Impact Analysis

For most of the customer projects, it is not necessary to develop a completely new powertrain control system. Customer requires new features on already developed systems. The new function requirements can be analyzed by functional safety impact analysis, as shown in Fig. 2. The safety experts will check whether the new function requirements bring new functional safety requirements (ASIL A to D). If the answer is yes, subsequent ISO 26262 work products implementation is required. Otherwise, the safety lifecycle of ISO 26262 is tailored according to the results of this analysis. Most of the technical work products will not be reworked, such as technical safety concept, software safety requirements, hardware safety requirements, etc. For powertrain control system development, even though the hardware and software program are not changed, the safety validation report would be needed considering application data change from project to project. The impact analysis process and result should be recorded as a work product.

For the example of Start/Stop function, as there are new functional safety requirements with ASIL B, subsequent ISO 26262 work products are required.

3.5 Development Interface Agreement

The Development Interface Agreement (DIA) is a protocol between customer and powertrain control system supplier. It defines the responsibilities for functional safety work products in the distributed development, as shown in Table 2.

For example, functional safety concept is provided by OEM in distributed development. However, functional safety concept may be adjusted between OEM and suppliers to ensure technical feasibility. This can be recorded in the DIA as an agreement of the cooperation between customer and powertrain control system supplier.

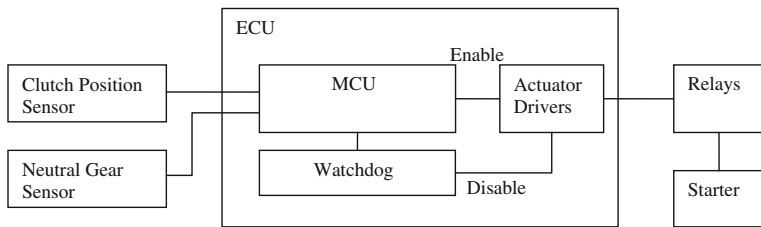


Fig. 3 Example for system design

To make an efficient DIA communication, it is recommended that a project safety manager is nominated on each side. And they take the responsibility to build up DIA.

3.6 Safety Plan

Safety Plan (SP) is used to define and follow all activities to achieve functional safety during entire lifecycle of the item. Safety plan can be conducted after functional safety concept and impact analysis are available. At this point development tasks and process tailoring have been determined. Safety plan may include deadlines, milestones, responsibilities and necessary resources, and it should be adjusted according to project plan.

3.7 Technical Safety Concept

Technical safety concept is technical solution of functional safety concept. It includes technical safety requirements and their allocation to elements in system structure. It is the responsibility of system supplier to define technical safety concept, because various technical solutions may exist for one functional safety concept. For example, at least two possible technical solutions exist for functional safety concept of above mentioned Start/Stop function. One possible solution is that the ECU gets drive train status information through neutral gear sensor and clutch sensor, and ensure automatic engine start can only happen when drive train is open. Another possible solution is to implement hardware circuit with neutral gear switch and clutch bottom switch which ensures the starter can only be energized when gear is neutral or clutch is pressed to bottom.

3.8 System Design Specification (Safety)

System design illustrates how system elements cooperate and interact to implement technical safety concept. System design may be documented through block diagrams or other graphical representations. The elements which are responsible to implement safety requirements should be marked and safety mechanisms should be described. If safety requirements are implemented by hardware and software package, hardware and software interfaces should be defined. A sketch of system design of Start/Stop function is illustrated in Fig. 3. The signals from clutch position sensor and neutral gear sensor reflect drive train status. Software algorithm of Start/Stop function is running in Micro Controller Unit (MCU). It ensures engine can be automatically started only when drive train is open. MCU control relays of starter through actuator drivers. The MCU and watchdog architecture ensure the hardware platform can fulfill safety requirements with ASIL B classification.

3.9 Hardware Safety Specification

Hardware safety specification specifies necessary requirements from hardware side to meet the requirements of technical safety concept and system design. Hardware safety requirements may contain requirements for input ports of sensors with safety purpose, safety related actuator drivers, feedback circuit to detect errors and so on. In above example, the system utilizes clutch position sensor and neutral gear sensor. Hardware safety requirements may include following contents: ECU provides input ports according to signal types of the two sensors, MCU and watchdog architecture is required and so on. These hardware safety requirements will inherit ASIL B classification from technical safety concept.

3.10 Hardware Architectural Metrics and Hardware Reliability Metrics

The objective of quantitative metrics is to provide a valid argument that the hardware design is sufficient to control random hardware faults according to the assigned ASIL. They are mandatory for safety goals with ASIL C or ASIL D classification. Quantitative metrics include hardware architectural metrics and hardware reliability metrics. Hardware architectural metrics measure hardware architecture design. A good hardware architecture design should use safety mechanism with high diagnosis coverage to detect safety critical failure modes of elements with high failure rate. Hardware reliability metrics measure the probability of violating safety goal due to random hardware faults. Quantitative fault

tree analysis and Failure Mode Effect and Diagnosis Analysis can be used for quantitative metrics calculation. In above example, safety goals for Start/Stop function is classified as ASIL B, it is not necessary to provide quantitative metrics.

3.11 Software Safety Specification

Software safety specification specifies necessary requirements from software side to meet the requirements of technical safety concept and system design. Software safety requirements may contain software based self-test mechanisms, software measures to detect errors, and so on. In above example of Start/Stop function, one of the software safety requirements is to inhibit automatic engine start when drive train is open. Other software safety requirements may contain diagnosis of sensor signal, self-test of ECU and so on.

3.12 Safety Validation Report

The purpose of safety validation is to confirm functional safety at vehicle level. It is necessary to examine that specific safety goals are sufficient to guarantee functional safety of the item, and all safety goals are fulfilled. A safety validation report for above mentioned Start/Stop function may contain a software configuration check to ensure safety related software modules are updated and integrated, and special test cases to verify that Start/Stop function will not start the engine when drive train is engaged.

3.13 Functional Safety Audit and Assessment

For item with ASIL C or ASIL D safety goals, ISO 26262 requires functional safety audit and assessment to evaluate the achieved functional safety. Work products compliance with ISO 26262, the implementation of functional safety process (functional safety audit), and the implementation of safety measures will be evaluated. A functional safety assessment report needs to give a clear result for acceptance, conditional acceptance, or rejection of the functional safety of the item. If the result is rejection of the functional safety of the item, the product can not be released for production.

In above example, safety goals for Start/Stop function is classified as ASIL B, it is not necessary to provide functional safety assessment report (including functional safety audit).

3.14 Safety Case

Safety Case (SC) is a complete collection of all functional safety work products. It should be under configuration management in safety life cycle. Experience from good practice is to create a template folder for projects and put functional safety work products in the sub-folders with a summary list. The safety plan can be reused as the summary list as all the functional safety work products are planned and recorded there.

4 Conclusion

ISO 26262 impact on development of powertrain control system is analyzed from viewpoint of work products based on existing V-model development process. The essential work products are identified and implementation hints for these work products are provided. According to the research, it is feasible to integrate the essential work products required by ISO 26262 into existing development process for powertrain control system.

References

1. ISO 26262, 1st edn, ISO, 2011
2. Hamann R, Saufer J, Kriso S, Grote W (2009) Application of ISO 26262 in distributed development ISO 26262 in reality. SAE Int (2009-01-0758)
3. Schubotz H (2008) Experience with ISO WD 26262 in automotive safety projects. SAE Int (2008-01-0126)
4. Meti LG, Dr. –Ing. Zerflwski D (2009) New functional safety standard WD ISO 26262 and the potential impact on the ECU development for the Indian market. SAE Int (2009-28-0021)

Analysis and Improvement for the Failure of Seat Belt Anchor of a Car Based on Simulation and Experiment

**Yongsheng Li, Hong Peng, Bing Rong, Yongxin Men
and Fuquan Zhao**

Abstract A numerical simulation and improvement was performed for the failure of seat belt anchor of a car, because of large deformation of roof and tearing of floor during certification test. Firstly, an appropriate loading curve according to ECER14 was chosen; secondly, adjust the FE model of broken area in order to reflect the real structure; At last, the simulation result was coincidental with the test result through defining the failure rule for material of metal. Based on this model, improvement methods were provided: decreasing deformation of roof by installing back door and enhancing load capacity by adding nut stiffening plate. The result showed that these two methods can increase deformation resistance ability and loading capacity of body substantially, which has been applied to real car and helps to pass the regulation certificates.

Keywords Seatbelt · Strength · Simulation · Test · Failure

1 Introduction

Seatbelt is one of the main protective devices of drivers' constrained system. It plays a significant role in protecting drivers as well as passengers. The strength of the fixed point is regarded as an important factor of passive safety. And it is forced to be examined in state safe quality examination and vehicle announcement test [1, 2]. Meanwhile, with the development of the auto-mobile manufacture, a large number of vehicles have been sold abroad. Different countries and districts

F2012-F09-004

Y. Li (✉) · H. Peng · B. Rong · Y. Men · F. Zhao
Zhejiang Geely Automobile Research Institute CO. LTD, Hangzhou, China

have strict requirements for strength of the safety belts' fixed points. So the designing for the fixed points of safety points is important [3].

In this paper, a series of simulations and improvements were performed on rear seatbelt anchor of a certain vehicle, and conclusions were obtained: set back doors to decrease the deformation of the headers; add nut plates and weld spots to improve loading capacity of fixed points. The result shows that simulation is approximately consistent with experimental data. The methods mentioned above can observably improve the carrying ability and against deformation, which helped pass the regulations after being used in reality.

2 Strength Analysis of Seat Belt Anchor

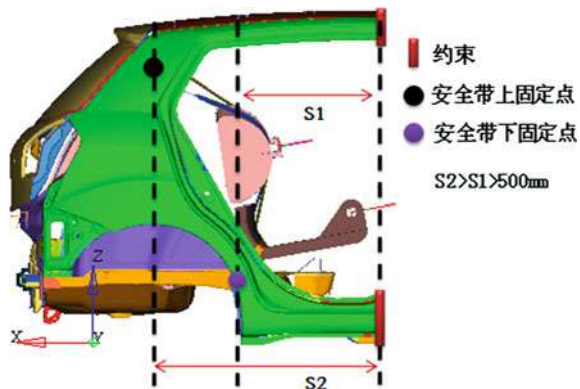
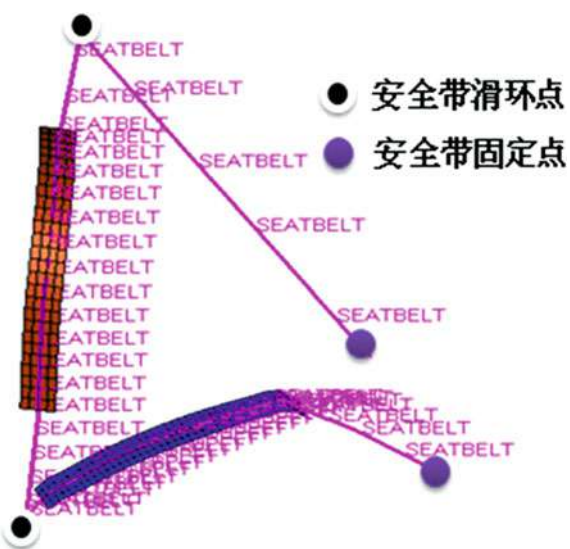
2.1 Finite Element Modeling

Construction and adjustment of finite element model usually spent most of the time in process of CAE analysis. However, according to different types of analysis, we should make every effort to shorten modelling time and operating time of computer under the premise that ensures the accuracy of the results. In order to simulate and calculate the strength ability of seatbelt anchor accurately and satisfy the requirement: fixed installation should be away from seatbelt anchor 500 mm in front and 300 mm in rear [4], a finite element model of 1/2 part of body in white was built; seatbelt components, shoulder and lap block were installed on it, as shown in Fig. 1.

In order to get accurate analysis results, the parameters should be set properly. During the actual test, plates nearby the seatbelt anchor maybe torn. In order to accurately simulate the failure condition, strain failure value of material is set whilst defining full-integral method and five integral points is chosen along thickness direction, which can avoid the hourglass shape of white body structure and improve the precision of simulation. Slip ring of seatbelt can be well simulated using 1D element, whilst contact area between human module and belt use 2D shell element, as shown in Fig. 2. Here, 1D element is set material "MAT_SEATBELT", the mass of belts in length and strain-stress relationship under loading and unloading (Fig. 3) is defined, which can simulate seatbelt performance well. 2D shell element used elastic material with lower stiffness, to define the contacting relationship between seat belts and human module and help assign load to each fixed point.

2.2 Applying Boundary Condition

According to ECE-R14, under the premise of not affecting the stiffness near the seatbelt anchor, constraint white body all degree of freedom (DOF). In this model, the rear seat standard is for three people, seatbelt are three-level cross device, and

Fig. 1 Assembly drawing**Fig. 2** Seatbelt model

all seat belt anchor are installed in the floor of body, applying the concentrated load with 13,500 N along longitudinal and 10°upward at the place of shoulder and lap module (Fig. 4).

2.3 Quasi-Static Fem Model Validation

The strength test of seatbelt anchorage is a quasi-static problem. We can use the implicit and explicit method to solve it. But this simulation relates to an extremely complex contact problem which may cause no convergence. Here, explicit integral

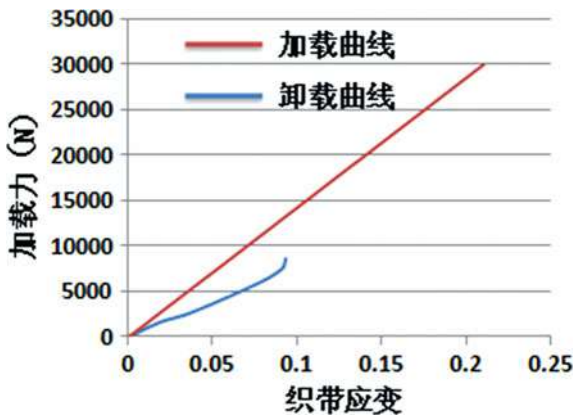


Fig. 3 Material curve of belt

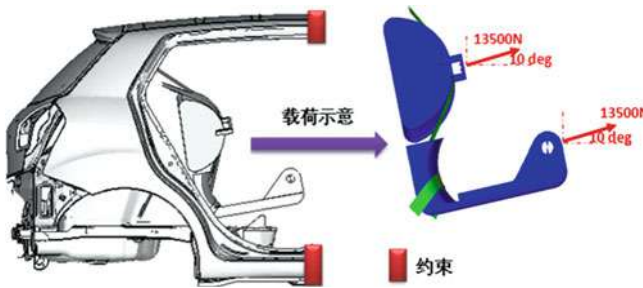


Fig. 4 Boundary condition

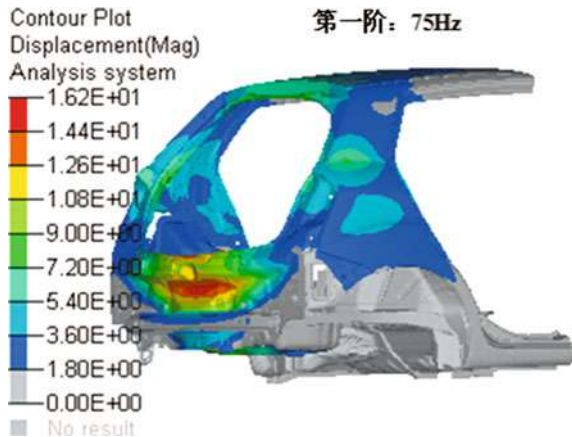
method has an advantage of dealing with complex contact issue and is adopted to solve quasi-static problem.

There are two other problems: reasonable loading time and loading curve.

It is obvious that we should not reduce the quasi-static solution quality when enhancing the loading speed in order to spend less time. If the loading speed exceed the target, inertial effect would happen, which may cause localized solution, so simulation result does not consist with experiment; accurate and efficient quasi-static analysis require a smoothly loading, a sudden and rapid movements may cause stress wave and make an uncorrected simulation result [5].

Generally speaking, loading time should be ten times larger than the first modal period and with sine function curve transition at turning points to make sure that the simulation process is quasi-static [6]. Here, the first mode frequency of the constrained module is 75 Hz, as shown in Fig. 5. According to the above theory, we can know that analysis of load time should not be less than 0.133 s. The loading curve is shown in Fig. 6: the loading period from 0 to 1 time of standard load is 0.08 s with sine curve transition. The load duration is 0.06 S in order to accurately reflect stress condition under 1 time of standard load. At the same time,

Fig. 5 Mode calculation result



considering safety factor 1.5, amplitude of loading curve is extended to 1.5 times of the standard load, so total computation time is 0.25 s.

2.4 Correlation Analysis between Simulation and Test

On the strength analysis of seatbelt according to ECE-R14 regulations, common failure situation mainly includes the following two forms: 1. Part of body crush largely; 2. The panel around fixed point will be torn. These two kinds of failure can both lead to the result that rated load capacity of the structure fall sharply, which could not satisfy the ECE-R14 code requirements.

At the present time, in seatbelt anchor strength test, there is no requirements for components of car except seatbelt fixed point and areas beside it Such as interior, exterior, open/closure, which sometimes make a great effect on result.

2.5 Simulation of Seatbelt Anchor Strength Without Back Door

Without considering the back door, the displacement picture of body is shown in Fig. 7, the largest deformation appears at the upper fixed point of seatbelt for middle seat, the maximum displacement is 331.82 mm, and structural deformation is very serious. Therefore it can be judged that body in this area has produced the whole crushing, which cannot bear external load. Under the same condition, the deformation in test is shown in Fig. 6; the way and area of crushing on the body in white are completely consistent with simulation result, which verifies the correctness of CAE analysis (Fig. 8).

In order to reveal the relationship between displacement and load, displacement curve of upper seatbelt anchor for middle seat is obtained and shown in Fig. 9.

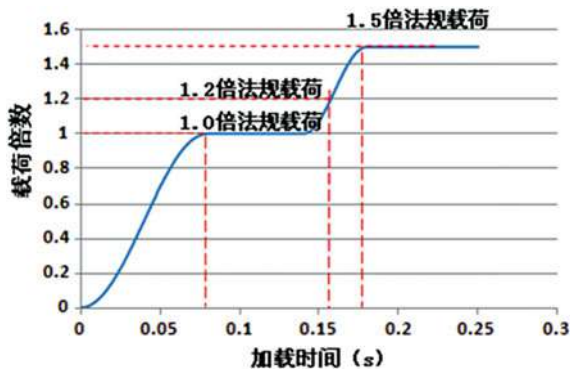


Fig. 6 Loading curve

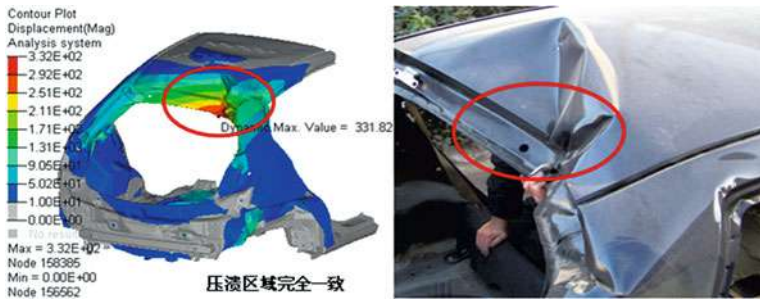


Fig. 7 Comparison of CAE analysis and test deformation

Fig. 8 Middle seatbelt anchor

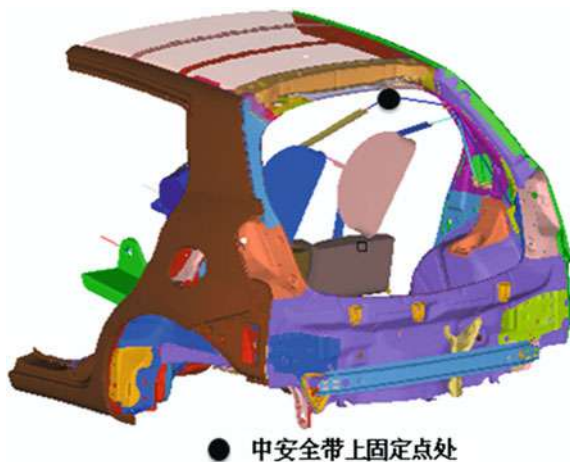
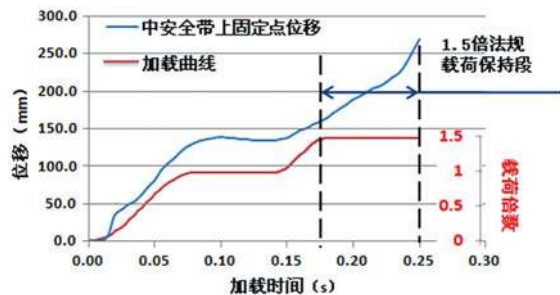


Fig. 9 Comparison of load curve and displacement



At the period of 1.5 times of load in regulations, the displacement of that point is steadily increase, whilst the loading curve keeps level all the time, which further explains the area fail to bear the load, but will continue to deform, eventually the seatbelt anchor strength cannot meet regulations requirements.

2.6 Simulation of Seatbelt Anchor Strength with Back Door

Because back door has an effect to strengthen the stiffness of door frame in body, the deformation of seatbelt anchor has a 50 % reduction, and the largest value is only 149 mm as shown in Fig. 8. It can be further verified from displacement-load curve in Fig. 9 that: at the period of 1.5 times of load in regulation, the displacement of upper seatbelt anchor for middle seat keeps the trend, which explains that the structure is strong enough to bear load continuously and will not crush (Figs. 10 and 11).

On the other hand, if sheet metal is torn, it will be unable to withstand the load, so we must assure that there is no risk tearing sheet metal parts, i.e. the maximum equivalent plastic strain is within the allowable value. Analyze the strength of seatbelt anchor and sheet metal nearby, the equivalent plastic strain of reinforced plate at fixed point and floor is shown in Figs. 12 and 13. The maximum equivalent plastic strain of reinforced plate is 0.657, which is far greater than the permissible value of 0.306, and then the strengthening plate will be torn. Because of no failure setting for material, although the maximum equivalent plastic strain of floor is less than the permissible value of 0.343, in actual condition, load will be totally transferred to floor and equivalent strain increase rapidly in short time. Figure 14 gives the result of applying load on floor alone; the strain value is higher than limitation of material and has a high risk of being torn.

Fig. 10 Displacement of BIW

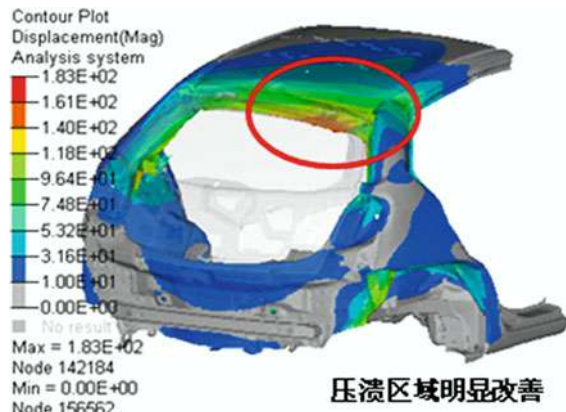


Fig. 11 Upper fixed point of middle seatbelt

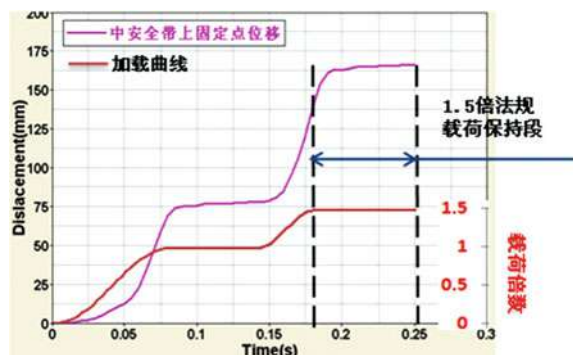


Fig. 12 Equivalent plastic strain of reinforced plate



2.7 Relationship Analysis between Simulation and Test

An experiment was carrying out to evaluate the strength of seatbelt anchor with backdoor installed. When the load reached 7,845 N, it dropped to zero rapidly, as shown in Fig. 15: right down fixed point on floor of left seatbelt was torn,

Fig. 13 Equivalent plastic strain of floor

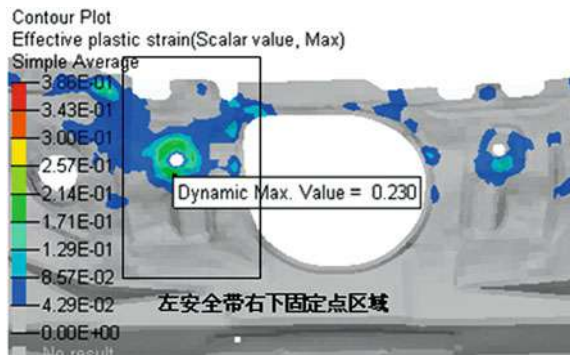


Fig. 14 Equivalent plastic strain of floor

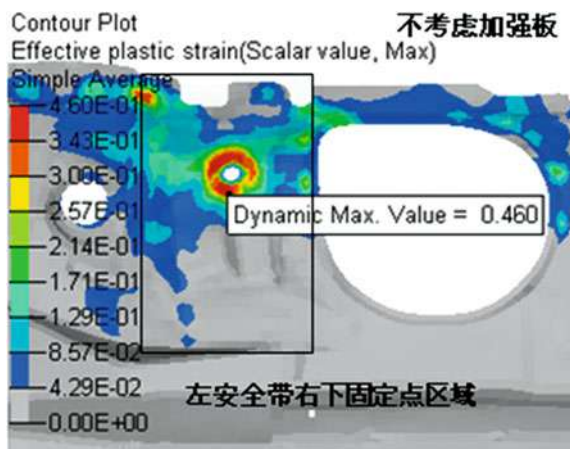
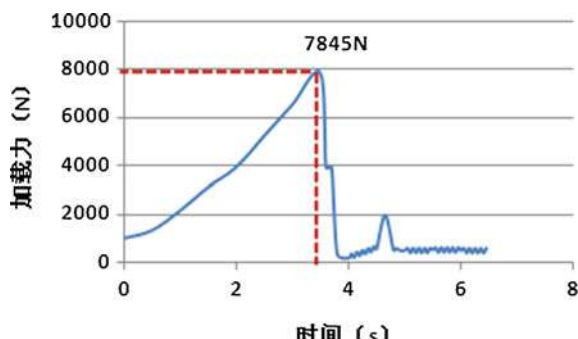


Fig. 15 Loading curve of test



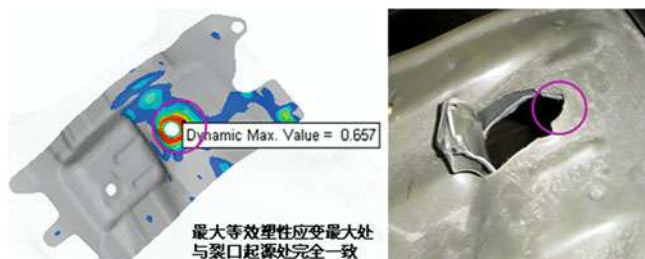
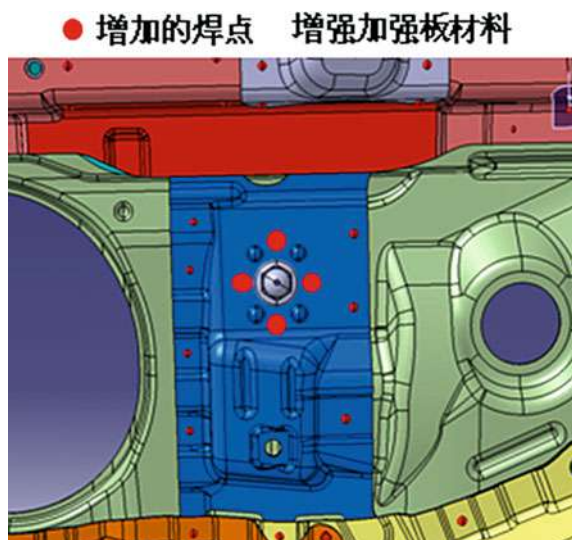


Fig. 16 Critical area of simulation and test

Fig. 17 Scheme 1



experiment failed. Further CAE analysis results show that: in simulation, when the load reaches 7,200 N, maximum equivalent plastic strain of reinforced plate on right down fixed point is 0.306, which is equal to target value of material, so there is tearing risk, as shown in Fig. 16, the dangerous area is right down fixed point of left seatbelt that is completely consistent with test result.

3 Improvement and Optimisation

Through previous analysis, it is known that with the consideration of the back door, the main reason for the failure of seatbelt anchor strength is the tearing of sheet metal. In order to improve, a simple and efficient method is to reinforce the

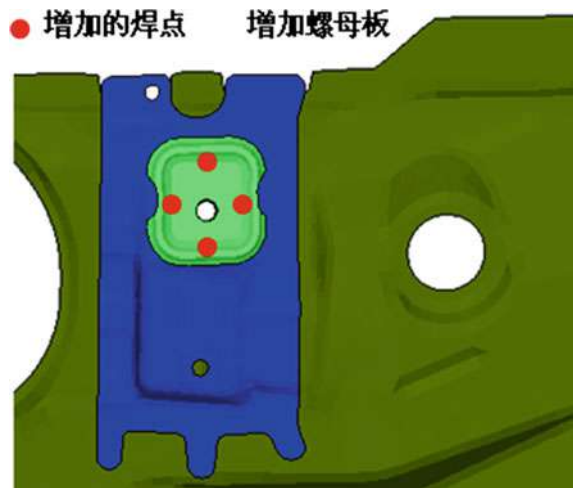
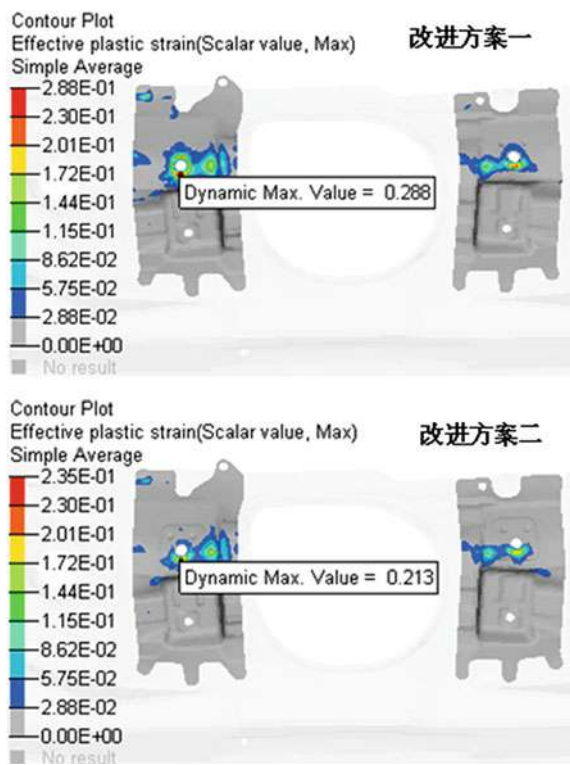
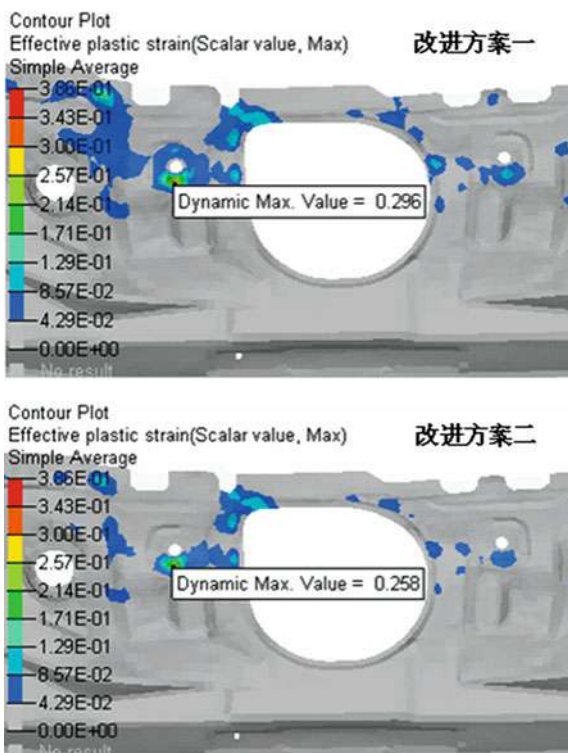
Fig. 18 Scheme 1**Fig. 19** Equivalent strain of reinforced plate

Fig. 20 Equivalent strain of floor



sheet metal wholly or partially. This paper mainly provides the following two improvements:

First, adopt a better material for reinforcing plate, and added 4 weld spots between the floor and plate, it is shown in Fig. 17.

Secondly, on the basis of above improvement, a nut plate is added to reduce the stress concentration as shown in Fig. 18.

It is known from previous analysis that although installation of the back door solved the problem of roof crush, seatbelt anchor on the floor is not able to bear the load, and the most risky parts are the floor and reinforced plates, so more attention should be paid to these regions. Under the rule of 1.5 times load, the comparison of the maximum equivalent plastic strain of all improved cases is shown in Figs. 19, 20, 21, and the result comparison between former case and modified case is shown in Table 1.

3.1 Simulation Result Analysis of Scheme 1

In improved scheme 1, the maximum equivalent plastic strain value of the floor reinforced plate is 0.288 which improved by 56 % (Table 1), but is also greater

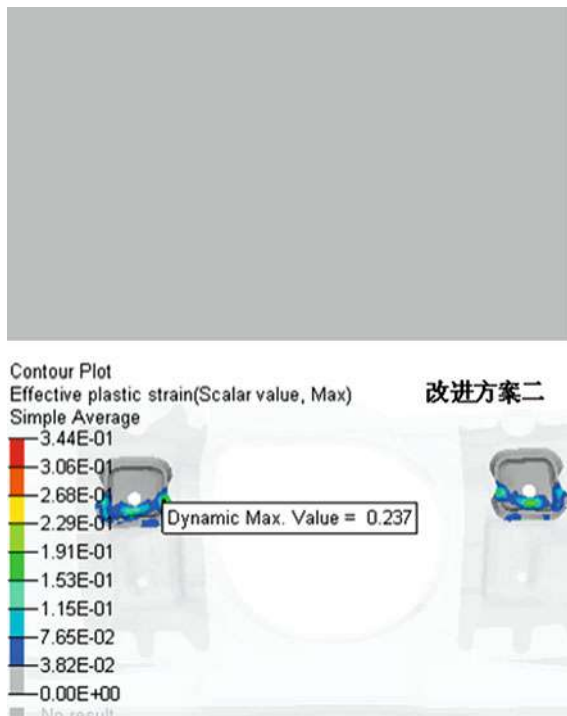


Fig. 21 Equivalent strain of nut plate

Table 1 Max equivalent strain comparison of different cases

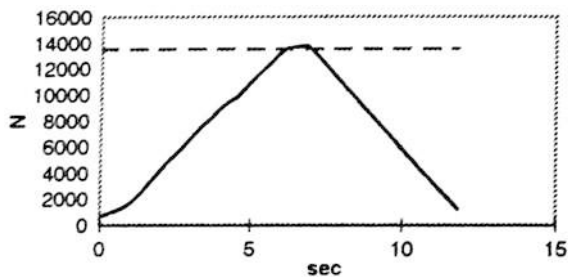
Origin	Scheme 1			Scheme 2	
	Max plastic strain	Max plastic strain	Improvement ratio to original (%)	Max plastic strain	Improvement ratio to scheme1 (%)
Reinforced plate	0.657	0.288	56	0.213	26
Floor	0.230	0.296	-29	0.259	13
Nut plate	-	-	-	0.237	-

than the permissible value of 0.237 and may cause risks of tearing. The maximum equivalent plastic strain location is near the right down fixed point of left seatbelt which is consistent with the test cracking position. Due to the reinforced plate, more loads are distributed on the floor, so the maximum equivalent plastic strain of the floor decreased by 29 % compared with the original scheme. Comprehensive considering the strain of reinforce plate and floor, this scheme is still at the risk of tearing, the seatbelt anchor intensity can't pass through the regulation test. But the system maximum bearing load increased by 87 % and reached 13,500 N.

Fig. 22 Comparisons of loading ability for different cases



Fig. 23 Loading and unloading curve



3.2 Simulation Result Analysis of Scheme 2

In improved scheme 2, the maximum equivalent plastic strain of reinforced plate, the vehicle floor and the nut plate is 0.213, 0.258 and 0.237, which is less than the material permissible stress and meets the strength design requirements. Compared with the scheme 1, the equivalent plastic strain of the reinforced plate has improved by 26 % and the floor by 13 % (Table 1).

Meanwhile, in the instance of installing the back door, white body overall structure has no local collapse and subsidence, so based on the improvement and optimization of scheme 2, the strength of rear seatbelt anchor in this vehicle meets ECE-R14 regulation. In a word, the bearing capacities of different schemes are shown in Fig. 22.

Ultimately, the vehicle passed law Random testing by adopting the scheme 2, and the accuracy of CAE analysis results is verified by test, as shown in Fig. 23.

4 Conclusions

According to the ECE-R14 regulation, a numerical simulation analysis and test certification was performed. Firstly, the analysis model is validated and the loading curve is confirmed according to the quasi-static theory. Secondly, the reason

analysis of the failure during test process is conducted and the design improved. Following conclusions were obtained:

Installing the back door can effectively improve the loading ability of the body, reducing the deformation and avoiding crushing invalidation.

Aiming at tearing failure mode of seatbelt fixed point, add nut panel and the number of welding spots to improve the maximum loading ability and meet the design requirements.

During the test authentication and simulation process of seat belt fixed point, the crushing deformation and tearing of the sheet metal are two primary failure modes. These two modes interact mutually, so they should be both considered in the design process.

References

1. Xu Z, Fan X, Xia G (2010) Vehicle seatbelt anchor analysis based on LY-DYNA. *Mech Eng* 03
2. Du Z, Wen X (2004) The analysis and optimization of the fastened point intensity on automobile safety belt. *J Chongqing Jiaotong Univ* 10
3. Vehicle Standard (Australian Design Rule 5/05-Anchorages for Seatbelts) (2006)
4. ECE-R14 (1998) Uniform provisions concerning the approval of vehicles with regard to safety-belt anchorages, 12
5. Zhuo Z translates (1988) ABAQUS/explicit finite element software guide. Tsinghua University press, beijing, 12
6. Huang Z, Chen S, Bai Y (2011) Discussion about explicit quasi-static loading method. *J Wuhan Univ Technol* 6

Passengers' Safety Evaluation Research Based on Vehicle with Freeway Guardrail Impact

Hui Tang, Yongxin Men, Qingxiang Guo, Jianxun Liu
and Fuquan Zhao

Abstract *Research and/or Engineering Questions/Objective* The passengers' damage mechanism of vehicle with freeway guardrail impact is different from the vehicle front crash and side crash, and there is not a unified passenger's evaluation standard. So compare the passengers' safety evaluation methods of vehicle with freeway guardrail impact in other countries and identify appropriate evaluation index limit for our country will be as the research objectives. *Methodology* First, compare and analysis the passengers' safety evaluation methods and evaluation indexes of vehicle with freeway guardrail Impact in theories in other country, and construct transformation models between each evaluation indexes. Then, based on the real vehicle crash test data which collected by Shojaati, Bmst who are from Swiss Fed Inst Tech—Zurich Switzerland and the main drafters of our country's *The Evaluation Specification For Highway Safety Barriers* such as Yu Shuping and Qiao Xiyong. Third, by using the cftool platform of MATLAB, according to the Exponential index approximation methods for data fitting. Finally, finite element models and vehicle-guardrail system is created through HyperMesh, and calculated by LS-DYNA. Verify the adaptability of limit on the basis of the dynamic response of vehicle and the guardrail. *Results* The level of the passengers' safety standard about vehicle impact with freeway guardrail is low in the existing rules. The new limit of passengers' safety evaluation indexes was identified, which would be useful to modify the rules. *Limitations of this study* The indexes limit is limited to the passengers' safety evaluation which is a vehicle impact with guideline in the research. *What does the paper offer that is new in the field in*

F2012-F09-005

H. Tang (✉) · Y. Men · Q. Guo · F. Zhao
Zhejiang Geely Automobile Research Institute CO. LTD, Hangzhou, China

J. Liu
School of Transportation, Chongqing Jiaotong University, Chongqing, China

comparison to other works of the author The Mathematical regression model HPC and ASI have been constructed, and the limits of HPC in different safety level have been identified. *Conclusion* In the process of vehicle with freeway guardrail impact, where ASI is safety level A, $HPC \leq 180.27$, where ASI is safety level B, $180.27 \leq HPC \leq 295.45$, where ASI is safety level C, $HPC \leq 557.45$.

Keywords Vehicle · Guardrail · Impact · Passenger · Safety evaluation

1 Preface

In recent years, with the automobiles' ownerships and highway's mileage constantly increasing, the number of traffic accidents, one-third of which were caused by the collision of cars and guardrails, on the road rises year by year. Besides, the micro-miniaturization, giant scale and heavy-weight of vehicles decrease their self-protection ability, causing massive life-killings and damage of properties. Researching the safety evaluation system of cars and guardrails' collision is the significant approach to guaranteeing the crew's security and reducing the property loss.

Currently, there are basically two formed foreign systems for vehicles' guardrail collision' evaluation approaches [1]: European Union's EN1317-2 in 2010 [2] and American MASH2009 [3]. Both of the systems are based on flail space model to evaluate. Our country puts it into practice according to *The Evaluation Specification for Highway Safety Barriers (JTG/TF83-01-2004)* [4] (abbreviated as F83 Criteria as follows), adopting passengers' frontal crash safety evaluation approach to make judgments. A number of academics worldwide conduct the research about the relationships between systems. Shojaati, Bmst [5, 6] explored the link between passengers' acceleration injury index and heads' injury indicators. Shu Ping Yu and Xi Yong Qiao [7] and so forth Cheng hu Wong [8] etc. Discovered even the opposite conclusions reached by Chinese, American and European union's assessment systems through automobile testaments.

Therefore, how to assess the passengers' security within collision of vehicles and guardrails by reasonable crew safety evaluation approaches have become the key points for the research. This passage explores the difference between evaluation approaches from several countries and decides on the suitable evaluation limitative index for our country by comparing and analyzing evaluation approaches to collision of vehicles and guardrail at homes and abroad, in order to provide reference for domestic guardrail crash testament criteria for passengers' security.

2 Evaluation Criteria of Passengers' Security

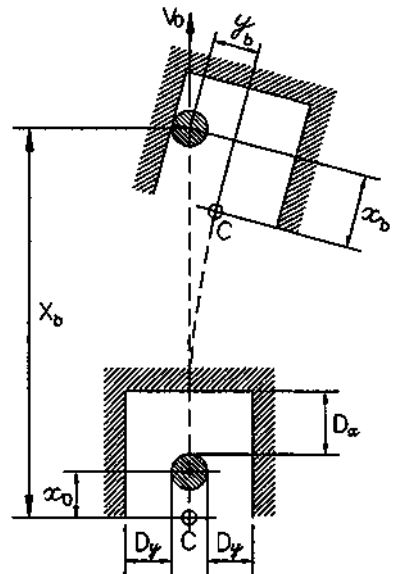
Assessment approaches to passengers' security are normally categorized into direct assessment and indirect assessment. Indirect assessment is an approach which calculates the passengers' injury index and tests passengers' risk by applying to the simplified vehicle crash models. The strength of it is that it's easy to test with and test repeatedly if adopted. The drawback is that it's impossible to describe the feeling of every single part of the human bodies during the collision. Direct assessment is to place fake fresh into cars and test parts of the bodies' physical index by sensor measurement to acquire passengers' injury index. The strength is that it can comparatively completely reflect parts of bodies' injury situations, while one of the drawbacks can be that it cannot be repeated possibly. European Union and American adopt indirect assessment mostly while both approaches are adopted in China.

2.1 Indirect Evaluation Method

Indirect evaluation method is divided into three categories, (1) Speed evaluation index, which includes Theoretical Head Impact Velocity (THIV) and Occupant Impact Velocities (OIV); (2) Acceleration evaluation index, which is composed of Post-impact Head Deceleration (PHD) and Occupant Ride down Accelerations (ORA) and the vehicle 10 ms average acceleration; (3) Acceleration rate evaluation index, which is Acceleration Severity Index (ASI). All the above indexes based on the Flail Space Model except the vehicle 10 ms average acceleration only.

The head of driver was simplified as a free moving point and the longitudinal movement, lateral movement and transverse moving of vehicle was considered during the impact process between vehicle and barrier in Flail Space Model [1-3] (see Fig. 1), the impact process was divided into three stages by t_1 which is the start contact moment between vehicle and guardrail and t_2 which is the initiate time when driver impact the occupant compartment.

- (1) The early collision stage ($t < t_1$), the period is before vehicle contact with barrier, and the acceleration of driver is the same as vehicle's. Then the distance between the head of driver and the centre gravity of vehicle was defined as x_0 , while D_x and D_y is the distance from driver's head to cockpit in longitudinal direction and in lateral separately.
- (2) Main collision stage ($t_1 \leq t \leq t_2$), the period is from vehicle contact with guardrail to driver contact with cockpit, and relative movement between the head of driver and vehicle is happen. We therefore define x_b is the distance from driver's head to the centre gravity of vehicle in longitudinal direction, while y_b is in lateral direction, then driver's head will impact the front of cockpit if $x_b \geq D_x + x_0$, or the head will crash the left of cockpit if $y_b \geq D_y$.

Fig. 1 Flail space model

- (3) Post main collision stage ($t > t_2$), the period is after the beginning of driver contact cockpit. And the acceleration of the head of driver is the same as the vehicle.

2.1.1 Speed Evaluation Index

The speed evaluation index is observing the severe degree which driver impact cockpit during main collision stage. The THIV was used in the standard of European Union (EN1317-2:2010) while USA by OIV in MASH2009, the first one is a merge data of longitudinal direction and lateral, but the second is the date in longitudinal direction or lateral lonely.

(1) Theoretical Head Impact Velocity

$$\text{THIV} = \left[V_x^2(t) + V_y^2(t) \right]^{1/2} \quad (1)$$

Where $V_x(t)$ is the velocity of the vehicle of the head of driver in x direction and $V_y(t)$ is the velocity its in y direction.

(2) Occupant Impact Velocities

In the simplified the Flail Space Model which ignores both vehicle's transverse moving and $x_0 = 0$, Occupant Impact Velocities is

$$V_{X,Y} = \int_0^{t*} a_{x,y} dt \quad (2)$$

Where $V_{X,Y}$ is the velocity of driver in x or y direction and $a_{x,y}$ is the acceleration of the centre gravity of vehicle and is the shorter time that is given by

$$X, Y = \int_0^{t^*} \int_0^{t^*} a_{x,y} dt^2 \quad (3)$$

Where X is 0.6 meter, Y is 0.3 meter.

2.1.2 Acceleration Evaluation Index

The acceleration evaluation index is focus on the maximum value of acceleration in driver during post main collision stage. The vehicle 10 ms average acceleration was usually used in China, while European Union uses PHD and ORA In the United States. PHD is a merge data of longitudinal and lateral direction, ORA is the individual data in longitudinal direction or lateral, while the vehicle 10 ms average acceleration includes the two calculate method as before.

(1) The Vehicle 10 ms Average Acceleration

This index makes 10 ms average acceleration of the centre gravity of vehicle as the driver's acceleration value.

(2) Post-Impact Head Deceleration

Post-impact Head Deceleration is the maximum value of the acceleration as follow,

$$\text{PHD} = \text{MAX}[(\ddot{x}_c(t) + \ddot{y}_c(t))^{1/2}] (t > t_2) \quad (4)$$

where $\ddot{x}_c(t)$ is the acceleration of vehicle in x direction and $\ddot{y}_c(t)$ is the acceleration of vehicle in y direction. PHD was defined and often used in EN 1317-2:1998, but was cancelled in new version EN 1317-2:2010.

(3) Occupant Ride Down Accelerations

In the simplified the Flail Space Model which ignores both vehicle's transverse moving and $x_0 = 0$, ORA is the maximum value of the vehicle 10 ms average acceleration in x direction or y direction.

2.1.3 Acceleration Rate Evaluation Index

Acceleration rate evaluation index is to pay close attention to the changed of vehicle's acceleration during the whole crash process by ASI, which computed with the following formula,

$$\text{ASI}(t) = \left[(\bar{a}_x/\hat{a}_x)^2 + (\bar{a}_y/\hat{a}_y)^2 + (\bar{a}_z/\hat{a}_z)^2 \right]^{1/2} \quad (5)$$

Where \hat{a}_x , \hat{a}_y , \hat{a}_z are limit values for the components of the acceleration in x , y and z direction; then $\hat{a}_x = 12\text{ g}$, $\hat{a}_y = 9\text{ g}$, $\hat{a}_z = 10\text{ g}$ if the occupants wearing safety belts, $g = 9.81\text{ m/s}^2$ is the magnitude of the acceleration of gravity; and \bar{a}_x , \bar{a}_y , \bar{a}_z are the components of the acceleration of the centre gravity of velocity, which are give by

$$\bar{a}_x = \frac{1}{\delta} \int_t^{t+\delta} a_x dt, \quad \bar{a}_y = \frac{1}{\delta} \int_t^{t+\delta} a_y dt, \quad \bar{a}_z = \frac{1}{\delta} \int_t^{t+\delta} a_z dt \quad (6)$$

2.2 Direct Evaluation Method

Direct evaluation method adopting the Head Performance Criterion (HPC), Thorax Performance Criterion (THPC), and Femur Performance Criterion (FPC) which is frontal impact occupant safety evaluation index in F83 standards in China.

(1) Head Performance Criterion

$$HPC = (t_2 - t_1) \left[\frac{1}{t_2 - t_1} \int_{t_1}^{t_2} adt \right]^{2.5} \leq 1000 \quad (7)$$

Where t is the anytime ‘window’ ($t_2 - t_1$) up to 36 ms and a is the resultant head acceleration from the three components a_x , a_y and a_z .

(2) Thorax Performance Criterion

Using this index is to measure the chest compression displacement.

(3) Femur Performance Criterion

Femur Performance Criterion is test the force in legs of dummy.

2.3 Occupant Evaluation Standard

The occupant evaluation standards for the impact between vehicle and freeway safety barriers in EU, U.S. and CHN are show Table 1.

3 The Lack of Current Occupant Estimate

3.1 Not Complete in Indirect Evaluation Method

The indirect method mainly use the jointed space model calculation crew member’s injury, But the model only the crew’s head set to a simple particle, other parts

Table 1 Assessment comparison of the person's damage degree

Index country	Evaluation index	Limit range	
EU	ASI _{Δt=50 ms}	Class A ASI ≤ 1.0 Class B $1.0 < \text{ASI} \leq 1.4$ Class C $1.4 < \text{ASI} \leq 1.9$	
	PHD _{Δt=10 ms} (Abolish)	Merge data of longitudinal and lateral direction $\leq 20 g$	
THIV		$\leq 33 \text{ km/h}$	
U.S.	OIV	Longitudinal: Recommend, 3 m/s; Max, 5 m/s Longitudinal and transverse direction: Recommend, 9 m/s; Max, 12 m/s	
	ORA _{Δt=10ms}	Longitudinal and transverse direction: Recommend, 15 g; Max, 20 g	
CHN	F83 Dummy	HPC _{Δt=36ms} THPC FPC	≤ 1000 $\leq 75 \text{ mm}$ $\leq 10 \text{ kN}$
D80 ^a	Vehicle	The vehicle 10 ms average acceleration	x, y and z direction $\leq 20 g$
D81 ^b	Vehicle	The vehicle 10 ms average acceleration	$\leq 20 g$
		Merge x, y and z direction	$\leq 200 \text{ m/s}^2 (\approx 20.4 g)$

Remark ^a General specification of freeway traffic engineering and roadside facilities, JTG D80-2006; ^b Guidelines for design of highway safety facilities, JTG/T D81-2006

of the body not be considered, and could not describe damage degree the parts of crew neck, shoulder and other in a collision.

3.2 Deviations in Direct Evaluation Standards

Direct evaluation method at present test by factors, foreign relative standard gradually be cancelled. Our country F83 standard is holding the evaluation method, but use positive impact evaluation method and the crew vehicle collision barrier, there are certain deviation, the main differences as follow:

1. Different Impacting Angle

There are certain impacting Angle when vehicles contact with the guardrail, a large number of accident data shows, the vehicles and the guardrail impacting Angle mainly focus on 15–25°, the Angle of collision is 20° in Our country F83 standards all the real car crash test, Angle for test, and *The protection of the occupants in the event of a frontal collision for passenger car (GB 11551-2003)* [9]

in the collision test according to the standard definition of barrier Angle should be 90°, there is large difference in both Collision Angle.

2. Collision Speed Different

Vehicles and fence in the crash test, our country F83 standard according to different car will be divided into small collision speed bus 100 km/h, large bus 80 km/h, large truck 60 km/h, while the front collision passenger car, the occupant protection “regulation passenger car collision speed of 50 km/h, both collision speed difference between.

3. Collision Object Different

Vehicles and fence in the crash test, collision object for guardrail (rigid guardrail, semi-rigid guardrail and flexible guardrail), and positive impact test is rigid wall.

4. Vehicle Movement Condition Is Different

Vehicles and guardrail in the crash test, vehicle and guardrail collision does not stop immediately, but in the guardrail guidance, to carry on the guardrail gradually recovered to normal driving direction; And vehicles in the frontal collision test, the body of the car stop movement was directly for rigid wall intercept.

5. Different Motion State Members

Vehicles and guardrail in the crash test, there are great changes in vehicles longitudinal and transverse movement, crew motion state also along with the change of motion of the body and change, the crew has Frontal crash the longitudinal motion characteristics and side impact the lateral movement characteristics; And in the frontal crash tests, the false man no obvious lateral movement phenomenon.

Therefore, indirect evaluation method should be directly evaluation method for the supplement, direct evaluation laws to indirect evaluation method as a benchmark. In order to accurately describe in the direct evaluation method the crew in the vehicle and guardrail in collision the damage situation, establish direct and indirect evaluation index of mathematical model, and through the model for the calculation of the direct evaluation index for occupant safety evaluation limit a kind of effective method.

4 Building Regress Math Model

Based on the Swiss federal institute of technology, such as Shojaati,Bmst [5, 6] and F83 standards [7] in our country main writer YuShuping, QiaoXiyong scholars the real car crash test data, with the aid of the MATLAB software cftool platform, using Exponential binomial index data processing approximation algorithm, establish the head of crew performance index and the crew acceleration damage index mathematical regression model [10], such as the type of 8 shows, the relation curves shown in Fig. 2.

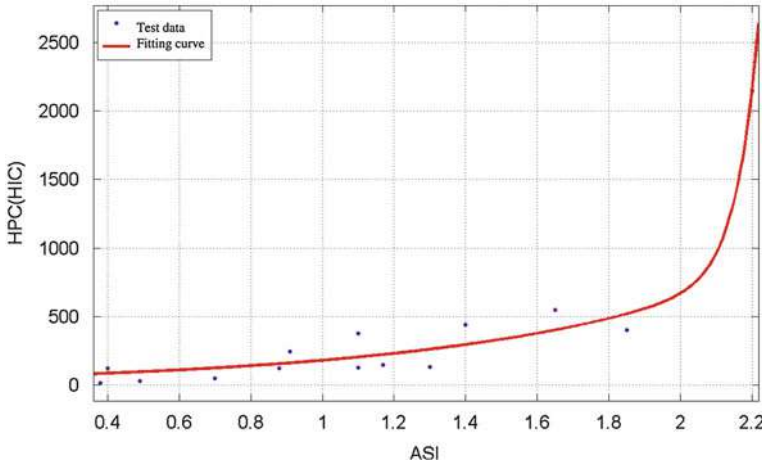


Fig. 2 ASI and HPC relations diagram

$$HPC = 52.43 \cdot e^{1.235 \times ASI} + 2.468 \times 10^{-13} \cdot e^{16.47 \times ASI} \quad (8)$$

Where ASI is the acceleration damage index and HPC crew the head performance indicators.

Coefficient of determination R^2 is judge fitting degree of regression model quality the most commonly used quantitative index, the higher the value that the higher the degree of model fitting. The regression model coefficient of determination $R^2 = 0.9636$, the author thinks that goodness-of-fit is better. The HPC was calculated in each hazard grade according to the Eq. 8, as shown in Table 2. It is not difficult to find that, when the crew head performance index at 557.45, crew acceleration damage index ASI has reached the most dangerous grade C.

5 Model Validations

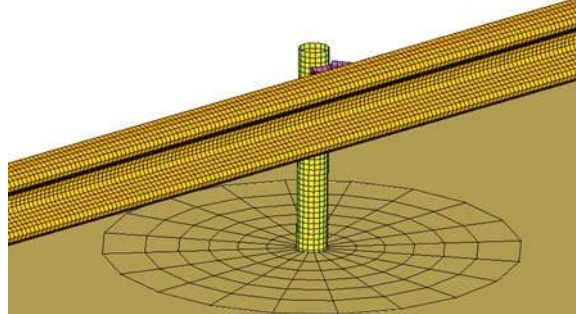
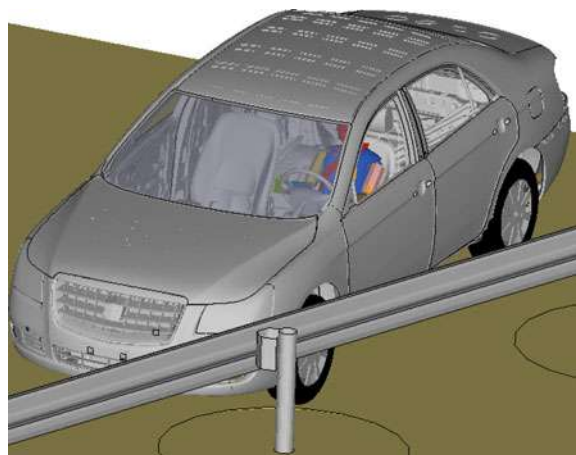
Due to time and experimental conditions, the real car cannot crash test, and now through the computer simulation method to mathematical regression model is validated.

5.1 Establish Simulation Model

First, through the CATIA software to create semi-rigid double wave barrier and soil geometry model, import HyperMesh10.0 software and established the guardrail and soil finite element model, as shown in Fig. 3, Fence board, pillar and

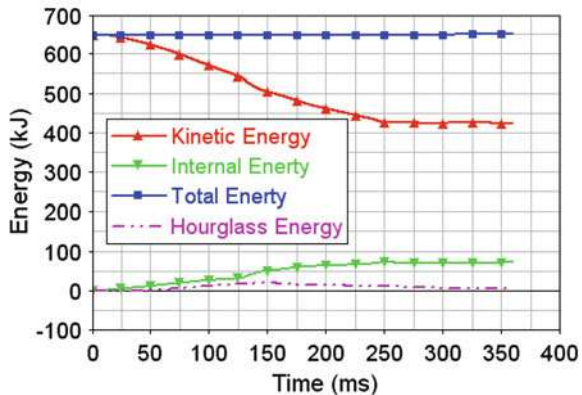
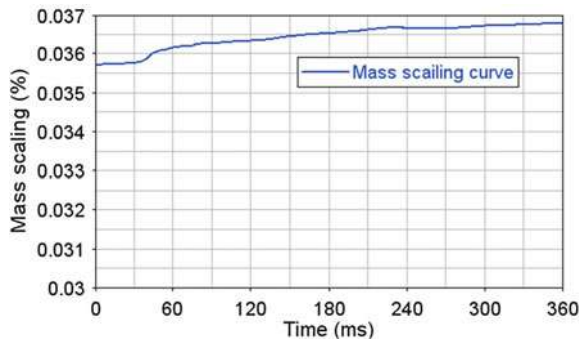
Table 2 ASI and HPC translation table

Class	ASI	HPC
ASI-A	≤ 1.0	≤ 180.27
ASI-B	$1.0 < \text{ASI} \leq 1.4$	$180.27 < \text{HPC} \leq 295.45$
ASI-C	$1.4 < \text{ASI} \leq 1.9$	$295.45 < \text{HPC} \leq 557.45$

Fig. 3 Guardrail and soil model**Fig. 4** Vehicle collision barrier and the coupling model

prevention piece of the * MAT_PIECEWISE_LINEAR_PLASTICITY elastic-plastic material type, its material parameters is: density $\text{Rho} = 7.865\text{E}-9 \text{ t/mm}^3$, elastic modulus $E = 2.0\text{E}5 \text{ MPa}$, Poisson ratio $\text{NU} = 0.27$, yield stress $\text{SIGY} = 310 \text{ MPa}$, shear modulus $\text{ETAN} = 763 \text{ MPa}$, strain rate $C = 40$, $P = 5$. The material type* MAT_SOIL_AND_FOAM_FAILURE, soil mass density $\rho = 1.874\text{E}3 \text{ kg/m}^3$, Poisson ratio $\nu = 0.35$, shear modulus $G = 49.5 \text{ MPa}$, tensile stress end $\text{Pc} = 0.55 \text{ MPa}$, bulk modulus $K = 134.55 \text{ MPa}$ [11].

Secondly, based on a domestic independent brand a car models and LSTC 50 percentage a dummy, establish occupant restraint system model. False man with

Fig. 5 Energy curve**Fig. 6** Quality percentage increase graph

seat belt, seat and the crew compartment parts by * CONTACT_AUTOMATIC_SINGLE_SURFACE type.

Finally, according to the F83 standard test requirements definition boundary conditions, establish a finite element model of the collision, as shown in Fig. 4 shows. Vehicle and guardrail contact with *CONTACT_AUTOMATIC_SINGLE_SURFACE. The whole model including 1,298,545 nodes, 1,780,572 elements, and the mass of vehicle is 1.6 t, vehicle initial velocity for 100 km/h, 20° Angle for the collision, the time for 360 ms.

5.2 The Simulation Result Analysis

Collision model energy curve shown in Fig. 5, each energy curve trend is reasonable, the total energy of the basic conservation. The mass increase curve shown in Fig. 6, the mass increase $0.036 < 5\%$. Visibly, the model is suitable for this condition to analysis.

The simulation results of Vehicle and dummy is shown in Fig. 7, according to the type of 5-6 calculated acceleration severity index ASI = 1.04, generation into

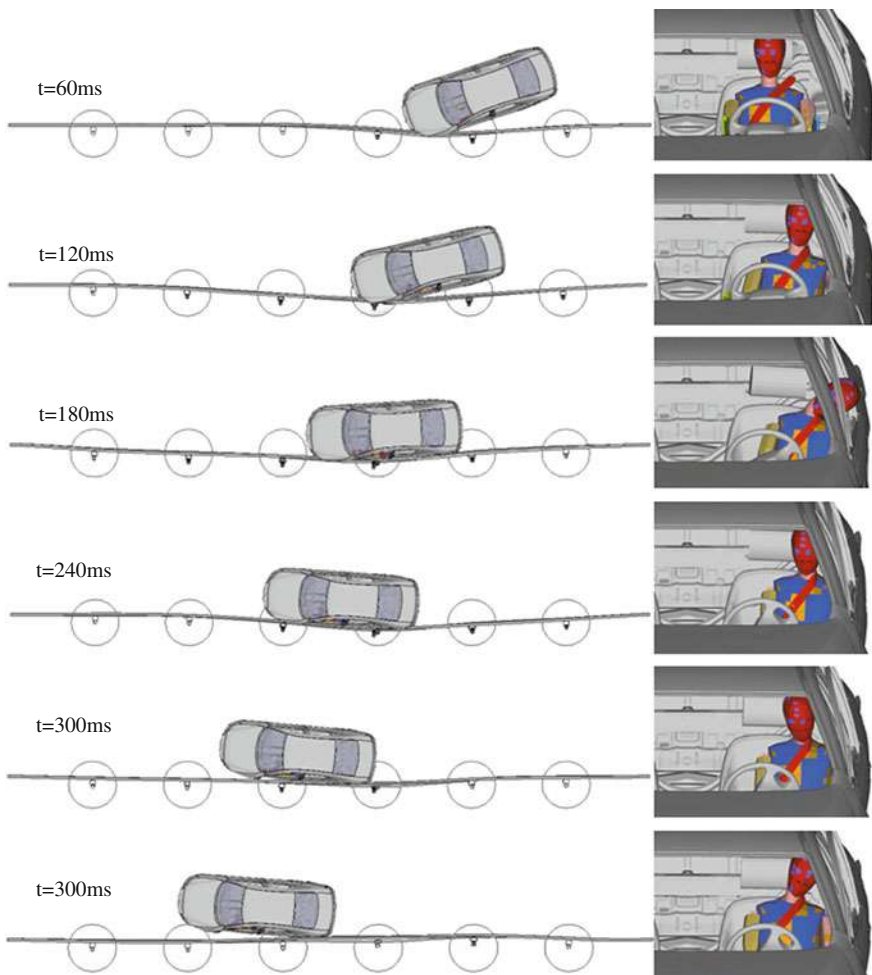


Fig. 7 Simulation results of vehicle and dummy

the ASI and HPC mathematical regression model (type 8) get a head fake performance index $HPC = 186.7$; And according to the type of 7 calculated $HPC = 184.6$, compared to find both numerical approaches. Therefore, HPC and ASI mathematical model basic correctly, actual reaction false people hurt objectively.

6 Conclusions

The passenger damage mechanism in crash between vehicle and freeway guardrail is different from that in vehicle front crash and side crash, and the level of passenger safety standards on vehicle crash with freeway guardrail is loose in the existing rules. The new limit of passenger safety evaluation index is established as follows. In the vehicle with high speed and guardrail collision process, when ASI is level A dangerous, HPC is less than 180.27; ASI is level B dangerous, HPC between 180.27 and 295.45; ASI is level C dangerous, HPC should not be more than 557.45.

Acknowledgments The authors wish to acknowledge the contributions of many individuals and groups who contributed to this research: Hong PENG, Huicai LU, Zelong WANG, Zhitao WANG, Liyong YAN, Yan ZHANG; in addition, LSTC for providing the LS-DYNA finite element solver software and Altair Engineering for providing the HyperWorks pre- and post-processing software.

References

1. Wang Y, Gao Y, Jia N, Gao S, Yan S (2011) The situation and analysis of freeway guardrail occupant risk assessment technology in Foreign countries. *J China & Foreign Highway* 31(6):282–285
2. EUROPEAN STANDARD BS EN1317-2 (1998) Road restraint systems. Part2: performance classes, impact test acceptance criteria and test methods for safety berries. CEN 1998
3. Manual for Assessing Safety Hardware (MASH) (2010) American Association of State Highway and Transportation Officials (AASHTO)
4. JTGF83-01-2004 (2004).The evaluation specification for highway safety barriers. People's Communications Publishing House, Beijing, pp 8–10
5. Shojaati M (2003) Correlation between injury risk and impact severity index ASI. In: 3rd Swiss transport research conference, Monte Verità/Ascona, 2003
6. Bmst (2010) Passenger safety on modern vehicle restraint systems. 16th IRF World Road Meeting, Lisbon, p 5
7. Yu S, Qiao X, Wang W, Yang, R (2004) Research for correlation between acceleration severity index (Asi) and head injury criterion (Hic) for highway safety barrier. In: Automotive safety technology international conference. pp 99–104
8. Zhou Z, Wang C (2011) Occupant Risk evaluation for crash testing of guardrails. In: The 9th international forum of automotive traffic safety (INFATS), Changsha, China, Dec 2011
9. GB 11551-2003 (2003) The protection of the occupants in the event of a frontal collision for passenger car. People's Communications Publishing House, Beijing
10. Tang H (2011) Physical design of freeway double-bar semi-rigid guardrail and impact simulation of vehicle-guardrails. Chongqing Jiaotong University, Chongqing, p 4
11. Schauer D, Tokarz F, Kay G (1997) Preliminary vehicle in pact simulation technology advancement Publication, NO.FHWA-RD-96-059, Federal Highway administration

Protection of Occupants for Survival Space as per ECE R29: A Study of Regulatory Requirements, New Proposals and Challenges of Implementation in Global Context

Mukesh Sharma

Abstract The uniform provisions concerning the approval of vehicles with regard to the protection of the occupants of the cab of a commercial vehicle as per ECE R29 [1], was implemented in October 2008 in India. The cab must be designed in such a way that in event of crash, sufficient survival space is ensured for the occupants. ECE-R 29 uses prescribed limits of cabin crush to ensure occupant protection rather measuring occupant injury based on Anthropomorphic Test Devices (ATDs), or dummies. The “Swing Bob” dynamic test procedure specified in ECE R29 is used for the evaluation of survival space. With evolving times various informal proposals were raised by different countries in GRSP meetings to modify the existing regulation to newer requirements. Though India has mandated the standard but it was realized during the implementation process that there are some areas, which are not addressed by the standard. This paper discusses about the modification proposals submitted by different countries and practical problems incurred during implementation of the standard in Indian context. The paper also discusses a case study of light commercial vehicle less than 1,500 kg, the problems in meeting survival space requirements and highlights the rationalization of standard for lighter vehicles.

Abbreviations

GRSP	Working group on passive safety
R Point	Seat reference point (SRP)
OICA	The International Organization of Motor Vehicle Manufacturers
SCDR	Steering center distance from R panel
RFFD	Right foot floor distance from dash panel

F2012-F09-008

M. Sharma (✉)

Satyam Computer Services Co Ltd, Room no 23 102 no 498, Gushoujing road,
Shanghai, China

LFFD	Left foot floor distance from dash panel
RKD	Right knee distance from dash panel
LKD	Left knee distance from dash panel

1 Introduction

At present the occupant safety in vehicles is covered by regulations listed in Table 1 at macro level. Occupant safety in frontal collision is governed by regulation ECE R94 for M1 category of vehicles with GVW less than 2,500 kg. Safety in side impact collision is governed by ECE R95 for M1 and N1 category of vehicles with a condition that R point of the vehicle shall not be more than 700 mm. Safety in rear collision is governed by ECE R34 for M1 category of vehicle. Another regulation, ECE R29 covers the survival space requirements for N category vehicles.

Traffic accident analysis is without a doubt, the main source to furnish information for the development of automotive vehicles concerning safety. A study conducted in U.S about the heavy truck accidents revealed three major accident modes [2].

- Rollover
- Collision with fixed objects
- Collision with vehicles in support

The other highlights of the US study revealed that the primary nature of impact is largely frontal type, however when rollover occurs it frequently becomes the most fatal accident.

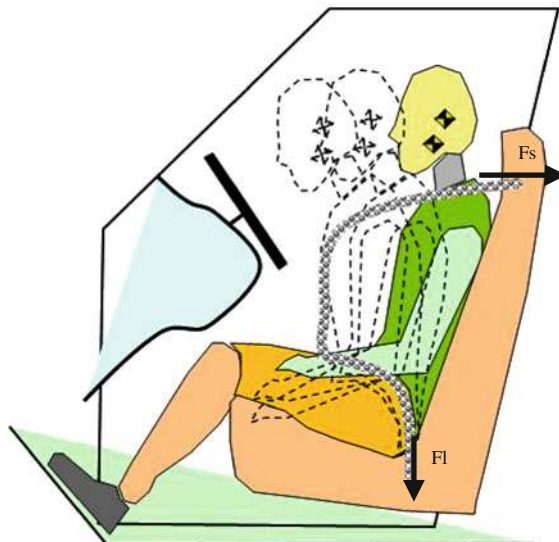
In general, occupant's protection requires two design considerations:

- reduction of decelerations on the occupant (restrained by a belt) by intentional deformability of the structure;
- limitation of passenger's compartment deformation to avoid passenger crushing. It is thought that the second trend should have basic importance. It is necessary to ensure a minimum space called "survival space." This is also necessary in the event of severe crashes [3].

A typical auto crash can be viewed as having two collisions. The "first collision" occurs when the vehicle impacts another vehicle or a fixed object. The "second collision" occurs when a vehicle occupant impacts the interior of the vehicle or is ejected and hits the ground. The second collision immediately follows, often only by milliseconds, the first collision. The seat belt prevents the second collision or minimizes its injury-producing potential. A snug fitting lap and shoulder belt "ties" the occupant to the passenger compartment and allows him or

Table 1 Description of regulations covering occupant safety

S.no	Occupant safety	Type of vehicles	Safety regulation
1	Safety in frontal collision	M1 \leq 2.5 tonne	ECE R 94
2	Safety in side impact	M1 & N1	ECE R95
3.	Safety in rear impact	M1	ECE R34
4.	Survival space requirement	N category	ECE R 29

Fig. 1 Movement of occupant during a frontal collision

her to “ride down” the crash, thereby minimizing or eliminating injurious occupant contact with the vehicle interior, such as the windshield, steering wheel or the roof.

During the car crash test, the seat belt is subject to large load as shown in Fig. 1. The buckle assembly resists the load that is applied to belt in the passive belt system. Belt system is basically important for improving the safety performance [4].

ECER R29 does not consider the measurement of injuries for the evaluation of safety but it considers the survival space as an important criteria for ensuring the safety of the truck cabin occupants. Figure 2 shows a typical accident on road. The picture shows that the truck collides with the rear of a loaded truck. This kind of accident directly affects the survival space of the occupants in the cab. A more representative demonstration is shown in Fig. 3. The Fig. 3 shows that lower section of the cab under goes deformation. This is a typical road crash that commonly happens on the road. A statistics of traffic accidents involving heavy trucks is shown in Table 2 [5].

Following observations are made from Table 2:

- 21 % of accidents occur in offroad conditions
- Rollover constitutes a total of 36 % accidents
- Front to front and front to rear constitute approximately 24 % of accidents

Fig. 2 Collision of truck on high way



Fig. 3 Frontal impact on moving truck

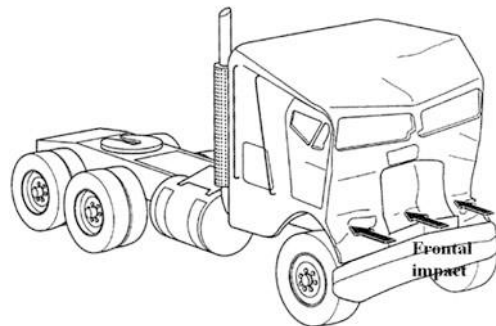


Table 2 Traffic accident involving heavy trucks

S.no	Type of accident	Percentage (%)
1	Off road	21
2	Roll over	36
3	Front to front	14
4	Front to side	3
5	Front to back	10
6	Truck to car	15
7	Truck to other	2

- Front to side and other constitute 20 % of accidents in totality.

2 Scope

The paper will focus on the following:

- Description of Regulatory requirements
- An overview of GRSP proposals and new test methods
- Test configuration
- Test methodology
- Case study of a light commercial vehicle
- Results and discussion
- Conclusion.

3 Description of Regulatory Requirements

ECE R29 outlines the requirement of measuring survival space using a manikin. This regulation applies to commercial vehicles which are intended for the carriage of goods. The regulation describes following three test that are required to be conducted.

3.1 *Front Impact Test (Swing Bob Impact Test)*

The swing bob is made of steel with evenly distributed mass of $1,500 \pm 250$ kg. It has a rectangular striking surface which is 2,500 mm(l) wide and 800 mm(h) high. The center of gravity of the swing bob is in the median longitudinal plane of the vehicle and lying $50 + 5/-0$ mm (H(R)) below the R point of the driver (Fig. 4).

The swing strikes the front of the cab in the rear direction in horizontally in plane parallel to the median longitudinal of the plane.

The impact energy requirements are shown in Table 3.

3.2 *Roof Strength Test*

The roof of the cab shall withstand the static load equivalent to weight of front axle or axles subject to a maximum of 10 tonnes. The load is uniformly distributed over the roof by means of a suitably shaped rigid former (Fig. 5).

3.3 *Partition Test*

The rear wall of the cab shall be capable of withstanding a static load of 200 kgf per tonne of permissible useful load. The load shall be applied by means of a rigid barrier perpendicular to the longitudinal median axis of vehicle, covering at least

Fig. 4 Position of swing bob before impact (side view)

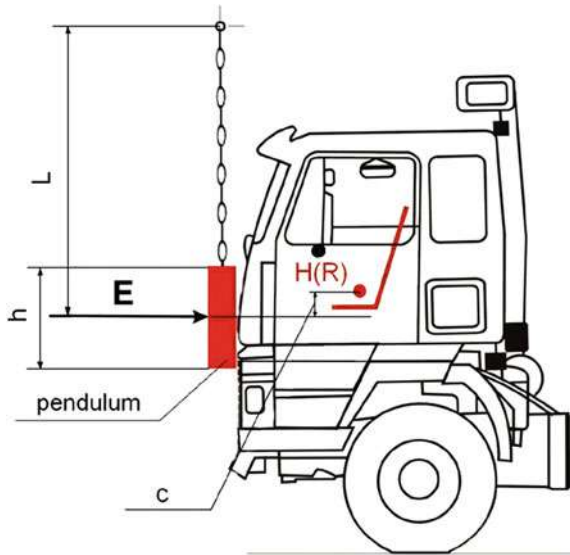


Table 3 Impact energy requirements as per ECE R29

S.no	Gross weight of the vehicle(GVW), in Kg	Energy in mkgf
1	GVW < 7,000 kg	3,000 mkgf
2	GVW \geq 7,000 kg	4,500 mkgf

the whole of the cab rear wall situated above the chassis frame, and moving parallel to that axis (Fig. 6).

4 An Overview of Grsp Proposals and New Test Methods

The regulation ECE R29 is undergoing discussion for appropriate modifications in GRSP(Working group on passive safety).No final conclusions have been reached till September 2008. This section will discuss few proposals discussed in recent years. The purpose of this literature study is to highlight important facts concerning the modification of regulation.

Sweden raised a pertinent issue about the definition of cab in GRSP meetings. The definition of cab is not present in the existing ECE R29 regulation. According to the proposal, Sweden proposed a definition of cab as follows:

“Cab” means a system of integrated structural elements or other structural element which form part of the outer geometry of the cab, the primarily aim of which is to protect the driver and passenger in case of frontal-impact or overturning. The above definition attempts to define the cab in some form and

Fig. 5 Position of swing bob before impact (front view)

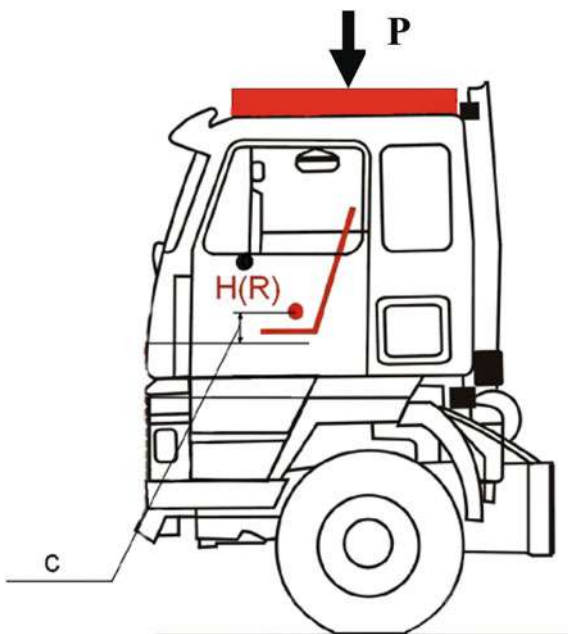
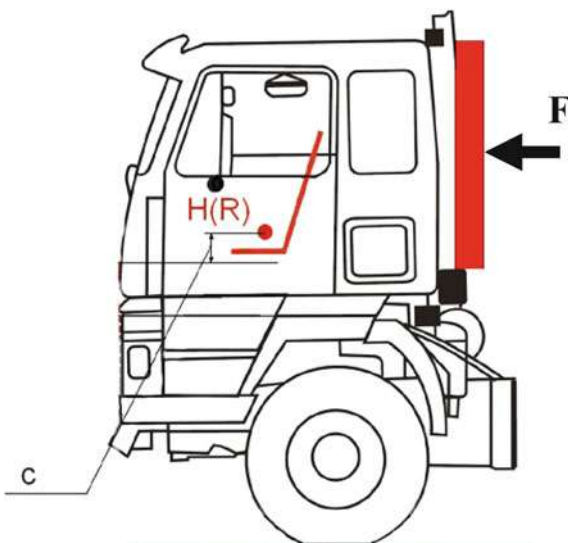


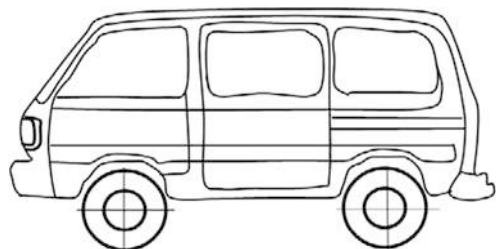
Fig. 6 Position of swing bob before impact (front view)



addresses the basic flaw in the regulation. The absence of a definition a cab puts a question mark on the status of N1 vehicles which are derived from M1 and have a common roof structure with driver-passenger as shown in Fig. 7.

Though it is possible to carry out the test in these kind of vehicles but it is difficult to carry out the test B, roof crush in this category of vehicle. Therefore a

Fig. 7 Description of vehicle with common cabin and roof structure



clear definition of cab will remove this ambiguity and vehicle with common cabin and roof structure will not come under direct scope of this regulation. Infact, Swedish proposal attempts to consider scope of the regulation applicable to separate driver cabin.

Studies conducted in USA [2] suggested that trucks with GVW > 15,000 kg accounted for 83 % fatalities and vehicles less than 15,000 kg represent only a minor part of it. Cluster analysis on the basis of FARS indicated three major accident modes: rollover, collision with fixed objects, collision with other motor vehicles. Head on collisions (front to front) show a large offset and often extremely high energy levels and deformations that can be considered “catastrophic”, where passive safety measures are unlikely to result in any benefit.

Studies conducted by Volvo [6], on the basis of 455 traffic accidents with injured truck drivers concluded that rollover is involved in one way or other in 68 % of accidents with injuries. In 21 % of cases the A pillar was also deformed during rollover accident.

Studies conducted by Japan [7], on the basis of study of 55 accidents with rollovers show that injuries are present in 31 % of the cases (there was no injury in 47 % of the cases); furthermore a large majority (87 %) were 90° rollovers, 180° rollovers representing only 4 %. Cab deformations as a result of 1 90° rollover is minor in 34 % of the cases, but upper A pillar deformation was seen in 21 % (confirming to Volvo data).

OICA proposal follows the current UNECE R29 approach, but with higher energy levels, Russia proposes an offset test, considering this is the most frequent accident configuration. Therefore the energy levels shall be increased in line with the energies of frontal impact. The other opinion pointed out that front-rear impacts are usually of high overlaps and if there is an escape maneuver, resulting in offset, the differential speed would be much lower than in a head on collision, thereby reducing the energy levels. In any case, energy levels as seen in car frontal impacts would be totally unrealistic for trucks.

The Russian federation however noted that the offset test would ensure higher safety levels and considered that its proposal (40 % overlap and 40 kJ) would be equivalent to OICA test (full width), 80–100 kJ energy.

OICA also proposed 180° rollover tests with a rigid platen inclined at 20° to the vertical with an impact of energy level 17.6 kJ. The direction of the impact is perpendicular to the longitudinal axis of the cab. In addition to this a quasi static

load is applied on the same cab with a rigid platen in vertical direction as shown in figure.

The other test proposed by OICA is 90° rollover with subsequent impact on A pillar. This test is based on Swedish requirements having steel pendulum greater than 1,000 kg. The pendulum is inclined 45° to vertical and 15° in horizontal XZ plane. The actual impact direction is 15° to vehicle longitudinal axis, However the impact energy is 30 kJ.

AIS 029 is an equivalent standard in India, derived from ECE R29. Survival Space for protection of occupants of Cabs of commercial Vehicles is derived from ECE R 29 which is not mandatory in Europe however in India the same has been notified for all N categories of vehicles.

However, certain N category vehicles that have been derived from M1, M2 & M3 category have a different type of body construction which does not fall in the conventional type of truck construction with a cab and load body. These include:

- Monocoque bodies as in the case of passenger vehicles converted to delivery vans.
- Ladder frame chassis vehicles derived from Utility passenger vehicles as base models.

Currently, the Pendulum Impact Test in AIS 029 has two steps of 3,000 m kgf impact energy for vehicles up to 7,000 kg GVW and 4,500 m kgf impact energy for vehicles greater than 7,000 kg GVW.

As per AIS 029, 3,000 m kgf of impact energy is imparted for vehicles up to 7,000 kg GVW. It is a large amount of energy which makes it more stringent for lighter vehicles, especially those in the 1,000–3,500 kg GVW range. i.e.; higher impact speeds for lighter vehicles.

For example:

$$\text{Impact speed} = \sqrt{2E/M}, \text{ m/s}$$

where E = Impact Energy, m kgf

M = vehicle mass (GVW), kg

For M = 1500 kg, the Impact speed = 6.26 m/s or 22.53 km/h

Accordingly, impact speed for different GVW of the vehicles is calculated in Table 4 given below. From the table, it can be seen that the impact speed for lighter vehicle is higher and for heavier vehicle the impact speed is lower for the same mass of the vehicle. It is clear that in effect the severity of impact would be higher for smaller and lighter vehicles in comparison to heavier vehicles.

Further to above, smaller vehicles have primary crash absorbing members fitted in lower portion and most of the impact is distributed to only cab structure. On the contrary the converted vehicles (M1 to N1 category) have less leg space that makes the regulation more stringent for such vehicles. The position of the pendulum impactor plays an important role in deciding impact severity.

The use of manikin as specified in ECE R29 has called for a review because the dimensions are little different from Hybrid III 50 % dummy. Further there is no flexibility allowed in opening of thigh areas as it is there in Hybrid III.

Therefore following issues need careful address in regard to ECE R29.

Table 4 Description of impact speed for fixed impact energies

Energy of impact	GVW, kg	Speed of impact km/h
3,000 mkgf	1,500	22.5
	2,000	19.5
	2,500	17.5
	3,000	15.9
	3,500	14.8
	4,000	13.8
	4,500	13.0
	5,000	12.3
	5,500	11.8
	6,000	11.3
	6,500	10.8
	7,000	10.4
	7,001	12.8
4,500 mkgf	8,000	12.0
	9,000	11.3
	10,000	10.7

- a. A plausible definition of Cab is required in the regulation.
- b. The modified impact test regulation that can cover real life accidents.
- c. Rationalisation of impact energies for different GVW vehicles.
- d. Commonisation of dummy dimension and alternate use of Hybrid III 50 % dummy.

5 Test Configuration

In order to cover the design aspect of the vehicle for meeting ECE R29, we considered a CAE model simulation test to understand the effect of pendulum impactor position on the strength of a standard model.

A cab model was considered and different test configuration were decided to evaluate the effect.

Table 5 shows three impact configurations. Configuration B is the condition specified in ECE R29 regulation. Figure 8 shows the positioning of impactors in three different configurations. Configuration A is 50 mm above the position defined in regulation and configuration C is 50 mm below the position defined in regulation.

6 Test Methodology

Figure 9 shows the test methodology that has been adopted to study the effect of different test configurations.

First of all a physical test was carried out on a vehicle and deformation measurements were done for the cabin. The CAE model was created and the results of

Table 5 Description of test configurations

Configuration	Pendulum impactor position	Remarks
B	C.G-50 mm	As per ECE R29 regulation
A	C.G	50 mm up from existing regulation condition
C	C.G-100 mm	50 mm below from existing regulation condition

simulation tests were compared with physical test to validate the model. After the model validation the CAE model was used to evaluate the effect of different test configurations. The result comparison is done and finally conclusions are drawn.

7 Case Study: Light Commercial Vehicle

7.1 LS-DYNA Model Creation and Correlation with Lab Test Results

7.1.1 Description of LS DYNA model

The calculation of the pendulum impact on front facia of the commercial vehicle has been done with explicit dynamic code LS DYNA. Finite element model of all the relevant parts and connecting members were considered in the model. The non deforming part observed after first development test were not consider. There is no major deformation in the front door but it is the main load bearing member, hence door stiffness for the frontal impact is modeled with beam elements. Besides this the major components considered are as follows:

- Front Portion of the vehicle
- Front tire and suspension
- A Pipe and steering control
- Front floor and longitudinal members (Fig. 10).

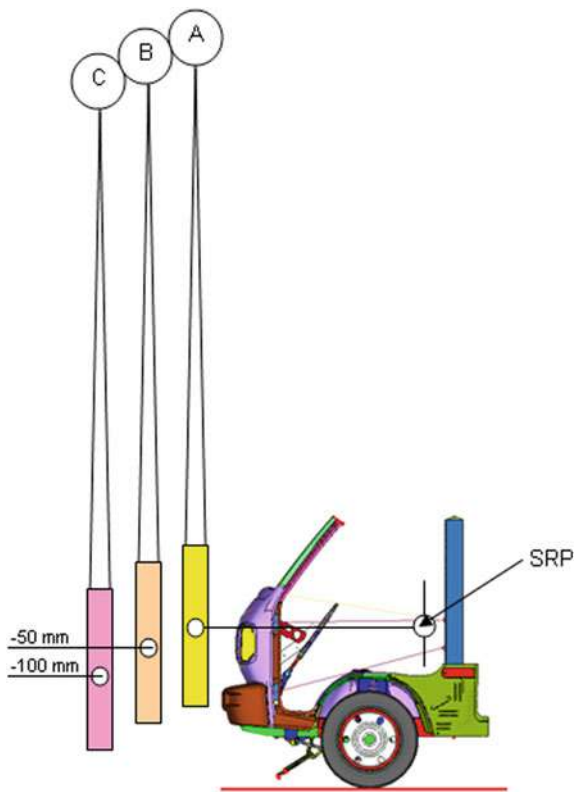
7.1.2 FE Model Creation

The FE model of front half of the vehicle is prepared. Model consists of 134,750 shell, 2,700 beam elements and 2,530 solid elements. Element details is as given below.

Front portion of the vehicle The main load bearing part of the vehicle during pendulum impact modeled with Belytschko T say 2D shell elements, type S16 (fully integrated) are used so that they can carry plane bending loads.

Front tire and suspension Front Tires are modeled with 2D shell elements. To incorporate the tire cushion effect tire pressure (28 Psi) is modeled with control

Fig. 8 Position of swing bob before impact (side view)



volume. Front Suspension consist of shock absorber are modeled with discrete elements and joints are used for tire movements during impact.

A Pipe and steering control The steering movement is critical during pendulum impact. Steering assembly along with A pipe is meshed with 2D shell elements. The sliding motion of the steering column is simulated with cylindrical joints between steering column and tie rod.

Front Floor and under body components The impact energy is absorber by floor and under body members. These are modeled with 2d shell element of S16 type.

Door The front door has crucial role of energy transfer between AB pillar. Doors are represented with beam elements created between hinge and striker location.

Body parts were connected with spot welds and other subassembly like A pipe, steering column and bull bar were connected with body through bolts. The spot welds were modeled with beam element (Type 9). The bolts are model with combination of beam and shell elements. The bolt modeling is given below.

The Front face deformation was correlated with Physical test result with adjustment in beam diameter used for door modeling. Model consists of 134,750 shell element and 2,700 beam elements.

Fig. 9 Description of test methodology

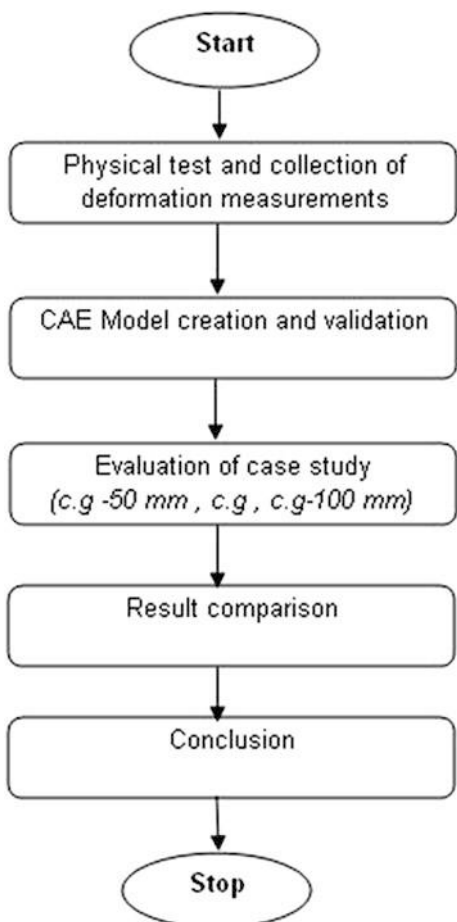
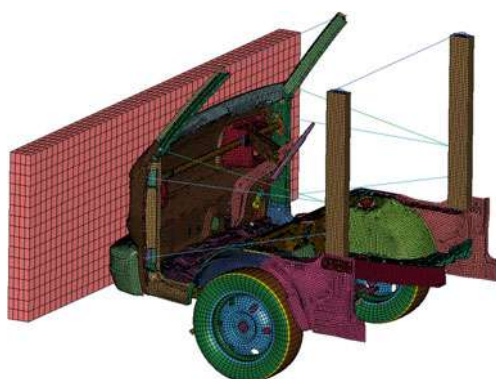


Fig. 10 Description of CAE model



Body parts were connected with spot welds and other subassembly like A pipe, steering column and bull bar were connected with body through bolts. The spot welds were modeled with beam element (Type 9). The bolts are model with combination of beam and shell elements. The bolt modeling is given below.

7.1.3 Material Details

Shell and beam elements used for bolt modeling had assigned the elastic material. The elastic–plastic material model (MAT_PIECEWISE_LINEAR_PLASTICITY, type 24) was used for all the components having high deformation. Strain rate effects were considered by stress versus strain curve for various strain rate.

Mass balancing is not required due vehicle in stationary condition.

7.1.4 Front Impact Test

The pendulum was modeled with shell structure. Rigid material was assigned to pendulum through MAT_RIGID card. The impact energy was controlled via density adjustment. The reference points was connected with pendulum through beam elements. At same time reference point is constrained for all DOF except A axis rotation. Body is fixed with the help of holding hook. Hooks are constrained for all the DOF. The rear part of the body is constrained for translational DOF

To verify the influence of the change of pendulum level on survival space, front impact test was numerically simulated with change in pendulum vertical position. The center of gravity of the pendulum was changed relative to R point of the driver seat in center position. The details as given below:-

- As per ECE-R 29
- CG of pendulum kept 100 mm below R point
- CG of pendulum kept 50 mm above R point.

7.1.5 Result Correlation

To develop the base model for other case study CAE model is validated with physical test result. The correlation is establish for front portion and A pipe deformations. The deformation pattern at critical area shows the similarity between CAE and test results.

Figure 11 shows the correlation of dash panel deformation between simulation and physical test. The characteristic of the deformation near head lamp area is very similar. The folding of floor area and lower portion of the dash panel is quite similar (Fig. 12).

Figure 13 shows the correlation of A pipe deformation in simulation and physical test results.

Fig. 11 Description of T bolt modelling



Figure 14 shows the objective points for which the correlation between physical and simulation test was carried out. The points were chosen in driver's R plane and Co driver's R plane. The objective correlation of simulation and physical test results are shown in Figs. 14 and 15. Measurements are taken on front facia and floor to get the scale factor. A good correlation is obtained between physical and simulation test results.

Figure 14 shows the correlation between simulation test and physical test results. The x axis shows the dimension in longitudinal direction. The y axis shows the dimension in vertical direction. The graph displays the post impact deformation profile of the dash panel. The correlation between simulation and physical test matches very well in lamp housing area. The deformation in areas above lamp housing and near lower floor area shows a good correlation. The CAE model deformation is slightly higher on the top. This is probably due to the presence of windshield in physical vehicle and the windshield offers some resistance to decrease the deformation at the top in physical model. Similar correlation is evident from Fig. 15 for co driver side. In general the CAE model showed deformations on the severe side thus validating the model.

Refer annexure for the detail. A correlation of more than 90 % was obtained in deformation measurements (Fig. 16).

7.1.6 CAE Measurement Matrix

The following measurements were done to evaluate the survival space of driver. The Fig. 14 displays the nomenclature of critical measurements.

- The movement of steering wheel in longitudinal direction is shown by Steering Center Distance from R Plane (SCDR).
- The distance between knee and the dash panel is shown by Knee Distance from dash panel (KD).
- The distance between the foot tip and dash panel is shown by Foot Floor Distance from dash panel(FFD) (Fig. 17, Table 6).

The prefix “d” is for driver and the prefix “p” is for passenger.

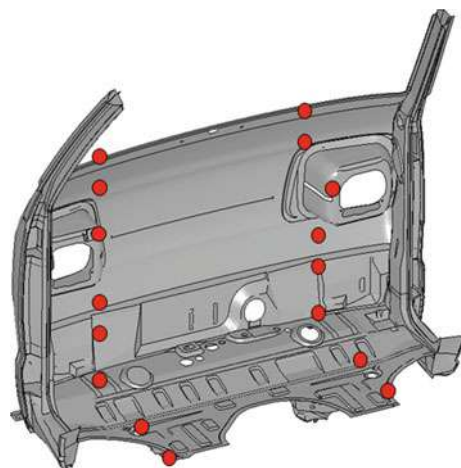


Fig. 12 Correlation of dash panel deformation—physical test vs CAE

Fig. 13 Correlation of A Pipe deformation—physical test vs CAE



Fig. 14 Selection of correlation points on dash panel



The pendulum first strikes the bumper, over which the energy of the pendulum is applied to lower part of the front panel, this causes high deformation in floor and

Fig. 15 Driver side correlation—physical vs simulation result

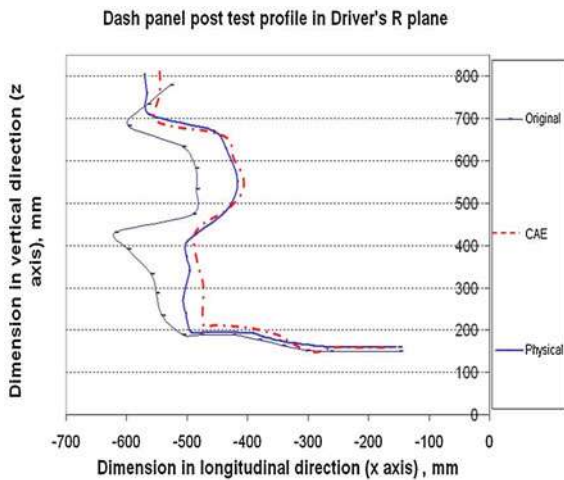
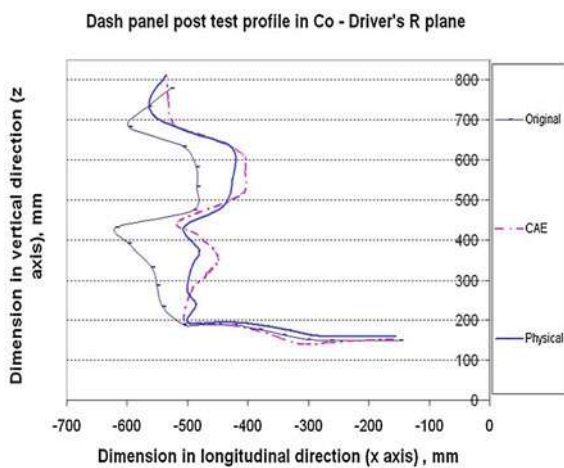


Fig. 16 Co driver side correlation—physical vs simulation result



lower part of the front panel. The front panel deformation and steering column displacement are critical for the driver survival space. The next section describes survival space measurement in different test configurations.

7.1.7 Results and Discussions

The comparison of deformation and displacement in case of driver is shown in Table 7.

The negative value for d-RFFD and d-LFFD indicates that it was not possible to assemble the foot of the dummy inside the vehicle. The assembly fell short by 87 and 72 mm for d-RFFD and d-LFFD respectively.

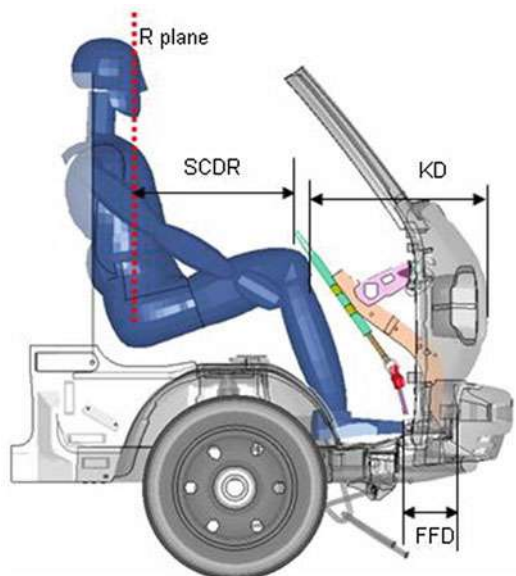


Fig. 17 Description of critical measurements for survival space

Table 6 Description of measurement ID—driver and passenger

S.no	Measurement ID— driver	Measurement ID— passenger	Description
1	d-RFFD	p-RFFD	Right foot floor distance from dash panel
2	d-LFFD	p-LFFD	Left foot floor distance from dash panel
3	d-RKD	p-RKD	Right knee distance from dash panel
4	d-LKD	p-LKD	Left knee distance from dash panel
5	d-SCDR	Not applicable	Steering center distance from R plane

Table 7 Description of deformation and displacement measurement in case of driver

S.no	Measurement ID—driver	C.G	C.G-50 mm	C.G-100 mm
1	d-RFFD	-87	82	95
2	d-LFFD	-72	58	70
3	d-RKD	310	402	412
4	d-LKD	306	389	400
5	d-SCM	309	404	412

Fig. 18 Comparison of deformation and displacement in case of driver

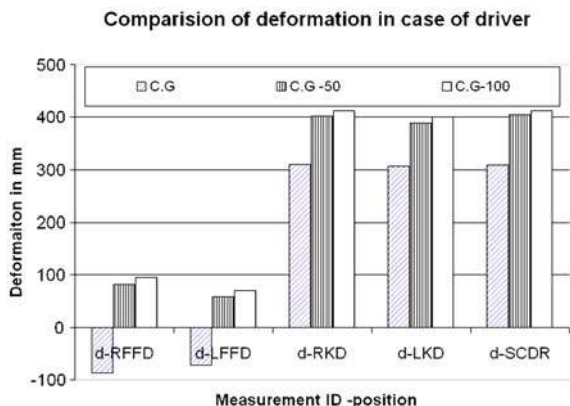


Figure 15 shows the comparison of deformation at various locations in three different case (C.G, C.G-50 & C.G-100 mm) (Fig. 18).

Table 8 shows the comparison of percentage differences between C.G and C.G-50 mm and between C.G-50 mm and C.G-100 mm.

Following observations are made from Table 8:

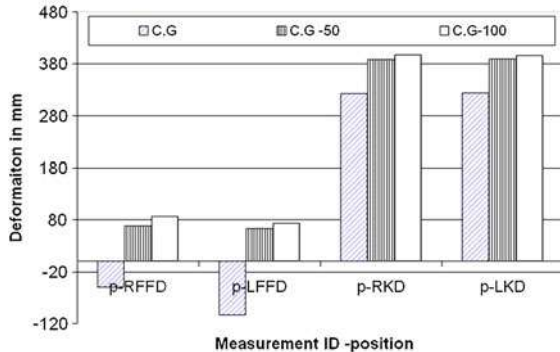
- Deformation of dash panel measured at right foot position of the driver dummy is 206 % higher in the case where the center of gravity of pendulum is position in line with the seat reference point (R point) than in the case where the center of gravity is 50 mm below the seat reference point.. Similarly, deformation in dash panel at left foot position of driver dummy is higher by 224 %.
- Deformation of dash panel measured at right knee location of the driver dummy is 23 % higher and 21 % higher in left knee location.
- The movement of steering center is 24 % higher in the case where the center of gravity of pendulum is position in line with the seat reference point (R point) than in the case where the center of gravity is 50 mm below the seat reference point.
- The comparisons between c.g-50 mm and c.g-100 mm pendulum positions show that deformations in c.g-100 mm case are less by 16 % for RFFD, less by 21 % for LFFD, less by 2–3 % for other measurement locations like RKD and SCDR (Fig. 19, Table 9).

Following observations are made from Table 10:

- Deformation of dash panel measured at right foot position of the driver dummy is 171 % higher in the case where the center of gravity of pendulum is position in line with the seat reference point (R point) than in the case where the center of gravity is 50 mm below the seat reference point.. Similarly, deformation in dash panel at left foot position of driver dummy is higher by 263 %.
- Deformation of dash panel measured at right knee location of the driver and co driver side is higher by 17.

Table 8 Description of deformation and displacement measurement in case of driver

% difference	d-RFFD (%)	d-LFFD (%)	d-RKD (%)	d-LKD (%)	d-SCDR (%)
C.G-50 VS C.G	206	224	23	21	24
C.G -50 vs C.G-100	16	21	2	3	2

Comparision of deformation in case of co-driver**Fig. 19** Co driver side correlation—physical vs simulation result**Table 9** Steering column displacement along longitudinal direction

S.no	Measurement ID-driver	C.G	C.G-50 mm	C.G-100 mm
1	p-RFFD	-49	69	87
2	p-LFFD	-103	63	74
3	p-RKD	323	388	397
4	p-LKD	324	390	396
5	p-SCM	Not applicable		

Table 10 Description of deformation and displacement measurement in case of driver

% difference	p-RFFD (%)	p-LFFD	p-RKD	p-LKD	p-SCDR
C.G-50 vs C.G	171	263	17	17	NA
C.G -50 vs C.G-100	26	17	2	2	NA

- The comparisons between c.g-50 mm and c.g-100 mm pendulum positions show that deformations in c.g-100 mm case are less by 26 % for RFFD, less by 17 % for LFFD, less by 2 % for knee locations.

8 Conclusion

Following are the conclusions that can be deduced:

- The vehicles converted from M1 to N1 category with common roof structures do not have their load bearing structures in line with the pendulum impactor therefore the impacting pendulum surface has a tendency to miss the load bearing structure or just partially overlapping it, as shown in Fig. 8. The impactor face is not able to strike the load bearing member of the cab. The impactor strikes the dash panel only and that may not offer huge resistance in case of small vehicles.
- The results show that there is approximately a difference of more than 200 % in deformation near foot area, if the impactor plate misses the longitudinal cross members then it becomes impossible to assemble the foot.
- It is evident from the experimental simulation results that the pendulum position plays a critical role in determining the survival space. The distance between the center of impactor surface and the seat reference point defines the severity of the impact.
- It is concluded that small vehicles of N1 category which are derived from M1 category have their crash bearing structure in lower area and it is evident from the experimental results that such kind of vehicles must be tested with the impactor plate positioning in lower area.
- The impactor plate shall be positioned based on the location of load bearing members of smaller vehicles which have been converted from M1 to N1 category.

Therefore it is well understood from the study carried out in this paper that small vehicles that are used for carriage of goods in India shall be tested as per ECE R 29 (or AIS-29) with some modifications in the placement of impactor plate.

References

1. ECE R29, Uniform provisions concerning the approvals of vehicles with regard to the protection of the occupants of the cab of a commercial vehicle
2. Heavy Truck Accidents in US (2007) GRSP INF/CS/02, Informal group on truck cab strength, 1st Meeting (April 2007). www.unece.org
3. National Highway Traffic Safety Administration, Traffic Safety Facts 2000 A Public Information Fact Sheet on Motor Vehicle and Traffic Safety Published by the National Highway Traffic Safety Administration's National Center for Statistics and Analysis
4. Sharma M et al (2008) Experimental evaluation of performance of effective upper belt anchorage (EUBA), lower belt anchorage (LBA) and floor deformation under different test configuration as per ECE R14. SAE (2008-01-0185)
5. Truck cab crashworthiness in real world accidents. Renault Trucks, GRSP/INF/CS/02e, Informal group on truck cab strength. www.unece.org
6. Traffic accidents heavy trucks, Volvo, GRSP/INF/CS/03, Informal group on truck cab strength. www.unece.org
7. Accident types—Truck drivers, Japan, GRSP/INF/CS/05, Informal group on truck cab strength. www.unece.org

Additional Sources

NHTSA website. <http://www.safercar.gov>

IIHS website—<http://www.safercar.gov>

SAE Website—<http://www.sae.org/>

UNECE website. <http://www.unece.org>

Automotive Functional Safety Compliance Requirements with ISO 26262: HW Architectural Metrics with an Example

T. Chitra

Abstract The newly released automotive safety standard ISO 26262 entitled ‘Road vehicles—Functional Safety’ gives the guidelines to demonstrate safety compliance of a product design. The standard describes the safety implementation process considering the total product life cycle. Based on the hazard and risk analysis carried out on the functionality of an item, the functional safety requirements are derived. For each of these functional safety requirements the technical safety requirements are specified with respect to Hardware and Software design. The standard has several requirements in order to prove the safety compliance with respect to Hardware and software design. In this paper one of the requirements in the hardware design which is known as HW Architectural metrics and Probabilistic Metric for random Hardware Failures is discussed. This is a quantitative assessment of a design with respect to technical safety requirements. The merits of each of these calculations are demonstrated using a simple example of a solenoid valve driver control circuit. The paper also discusses certain challenges in carrying out these analyses.

Keywords Hardware safety • Hardware architectural Metrics • ISO 26262 compliance • SPPM-LPFM

F2012-F09-009

T. Chitra (✉)
Consultant Mahindra Satyam, Bangalore, India

1 Introduction

Safety turns out to be one of the most important issues of present day automobile development. The whole challenge is how we ascertain that the safety related electrical/electronic systems are adequately designed to avoid systematic and random failures. The newly introduced automotive safety standard ISO 26262 provides the necessary guidelines to design a product with adequate safety. The standard has ten parts. Each part addresses the requirements with respect to different aspects of product life cycle. In order to carry out the safety analysis of any product the first and foremost activity is to carry out the hazard analysis of the function and to identify the risks associated with them. The objective of the hazard analysis is to identify and categorize those malfunctions of the item and formulate the safety goals related to the prevention or mitigation of the hazardous events in order to avoid unreasonable risk.

Safety goals are top-level safety requirements for the item. The safety goals guide in deriving the functional safety requirements required in avoiding the unreasonable risk associated with the hazardous event. The safety goals are expressed in terms of functional objectives. The risk associated with the hazards is measured qualitatively by Automotive Safety Integrity Level (ASIL). There are four levels of the ASIL namely ASIL A, ASIL B, ASILC, ASILD where ASIL A is the lowest safety integrity level and ASIL D the highest one. The ASILs are determined based on the severity, exposure and controllability associated with each hazardous event. The part 3 of the ISO 26262 standard has the detailed description of the ASIL determination for a given hazard.

Having defined the safety goal for an item based on its functionality we derive the functional safety requirements in order to mitigate the risks in the design. For each of the functional safety requirement we derive the technical safety concept which in turn results in hardware and software technical safety requirements. Part 5 of the standard details the hardware level requirements in the product development and Part 6 details the software level requirements. These guidelines as described in Part 5 and Part 6 help in designing the product with adequate safety in order to realize a safe product as envisaged by the functional safety requirements.

In this paper we address the quantitative requirements as described in ISO 26262 part-5 as one of the requirements to comply with. These quantitative requirements are referred to as Hardware Architectural Metrics and Probability of Random Hardware Failure in the standard. These metrics essentially evaluate the design against technical safety requirements with respect to the diagnostic coverage provided in terms of safety mechanisms for the random hardware failures. A simple example of a solenoid driver circuit is considered in order to demonstrate the methods explained in the standard.

2 Quantitative Evaluation of the Hardware Architecture

The standard describes two independent requirements with respect to quantification of the evaluation of the Hardware design. This evaluation quantification metrics are mandatory for all safety goals with ASIL B/ASIL C/ASIL D rating. The two requirements are detailed in Sections. 8 and 9 of the ISO 26262 [1] standard Part 5. The two analyses are:

- Evaluation of Hardware Architectural Metrics (ISO 26262-5 Section 8)
- Evaluation of safety goal violation due to Random Hardware failures (ISO 26262-5 Section 9).

2.1 Hardware Architectural Metrics

The objective of this evaluation is to validate fault handling techniques against the implementation of the safety requirements in the architectural design of the item. The evaluation deals with two aspects namely single point failure metric and Latent point failure metric (SPFM/LPFM). In order to carry out this analysis all the hardware components in the architecture are considered. The analysis is carried out as per the following steps

1. Consider each component in the architecture.
2. Determine whether the components are Safety related or non-safety related.
Only the safety related components are of concern for this analysis.
3. Get the failure rate for each component (either from an established standard data base such as MIL 217F, IEC 62380, SN 29500..., Field failure rate or Component vendor provided data).
4. For each component identify all the failure modes.
5. For each failure mode determine whether it violates the safety goal or not.
6. If the failure mode violates the safety goal then identify the relevant available safety mechanism which would help in overcoming the SG violation. List all the Safety Mechanism (SM).
7. For the listed SM determine the Diagnostic Coverage (DC) in % using the guidelines given in Appendix D of ISO 26262-5.(Tables D1 to D12).
8. If a particular failure mode does not violate the SG provide the justification for the same.
9. Calculate the residual failure rate $\lambda_{\text{Residual}}$ for each failure mode of the safety related component. The single point residual failure rate for each failure mode is given by

$$\lambda_{\text{Residual}} = \lambda_{\text{Res}} = \lambda * (\text{failure mod e ratio}) * \left(1 - \frac{DC}{100}\right)$$

Table 1 Target values for SPFM and LPFM for various ASILs

	ASIL B (%)	ASIL C (%)	ASIL D (%)
Single point faults metric	>90	>97	>99
Latent faults metric	>60	>80	>90

Where λ is the failure rate of the component.

10. Examine whether there is a possibility of the failure mode becoming latent. This is a possibility with a common cause driving multiple point failures which may result in the safety mechanism provided also fails.
11. If the failure mode is a candidate for violating the SG as a latent point then identify safety mechanism that would prevent the SG violation. Determine the DC coverage as in Step 7.
12. The residual failure rate for the latent failure ($\lambda_{\text{Multiple point latent}}$) with respect to each failure mode of the safety related components are calculated as in step 9 using the DC corresponding to the latent failure.

$$\lambda_{\text{multiple point Latent}} = \lambda_{MPFL} = \lambda * (\text{failure mod e ratio}) * \left(1 - \frac{DC}{100}\right)$$

13. SPFM and LPFM are calculated using the formula given in Appendix C (C2 for single point fault metric and C3 for Latent point fault Metric). The SPFM is calculated taking the ratio of summation of residual failures of all the failure modes of the safety related elements to that of the summation of the total failure rate of safety related elements.

$$SPFM = 1 - \frac{\sum \lambda_{\text{Res}}}{\sum \lambda_S}$$

The LPFM is calculated taking the ratio of the summation of the multiple point latent failures to that of the latent faults remaining in the system.

$$LPFM = 1 - \frac{\sum \lambda_{MPFL}}{\sum (\lambda_S - \lambda_{\text{Res}})}$$

where λ_S is the failure rate of safety related items of the system.

14. The obtained values of SPFM and LPFM are compared with the table given below for compliance (Table 1).

If the target values are not met then the design is revisited for improving the safety mechanisms with higher diagnostic coverage and introducing redundancy to avoid single point failures. Also the multiple point failures leading to latent failures can be examined for the common cause and improve the design for avoiding/preventing the same. The failure rates of the individual components can be examined for better reliability using higher quality components and better de-rating to improve the reliability.

Table 2 Random Hardware failure Target values

ASIL	Random HW failure target values
D	$<10^{(-8)}/\text{h}$
C	$<10^{(-7)}/\text{h}$
B	$<10^{(-7)}/\text{h}$

2.2 Evaluation of Safety Goal Violation due to Random HW Failures

The main objective of this evaluation is to have a rationale that the residual risk of a safety goal violation due to random hardware failures of the item is sufficiently low. Sufficiently low refers to comparison with similar items already in use. Two alternative approaches are given in the standard to evaluate the safety goal violation with respect to the residual failures of the safety related components in the hardware architecture.

Method 1 In this method we use a probabilistic metric called “Probabilistic method for random hardware failures” (PMHF) to evaluate the violation of safety goal using quantified Fault Tree Analysis (FTA). The FTA is constructed for the safety goal of concern considering all the safety related components whose failure is responsible for violating the safety goal.

The safety goal violation being the top event of the FTA the probability of occurrence of the top event is calculated considering the failure rates of all the base events. This value of probability of occurrence is compared with a target value. Sample target values are given in the Table 2 below as given in the standard. One can use field data from similar well-trusted designs or quantitative analysis techniques applied to similar well-trusted design principles using failure rates from standard failure rate data bases

Method 2 In this method we evaluate each single point fault, residual fault and dual point fault leading to the SG violation. Some part of this analysis is already carried out in Sect. 2.1. The single point and residual failure rates of components violating the safety goal is already available as part of the analysis. The same could be evaluated for the said target values as mentioned in the standard for this method. This is one reason method 2 is preferred to method 1 by most of the people. The target values are set such that the faults are evaluated using a criteria combining the occurrence of the fault and the efficiency of the safety mechanism.

The target values for evaluation is referred to as Failure Rate classes (FRC). The failure rate classes are categorized as FRC-1, FRC-2, FRC-3,... etc., These classes are analogous to the occurrence levels 1, 2, and 3 used in FMEA, where 1 represents failure modes which have lowest occurrence rate. Following the guidance given in the standard the following Table 3 represents the failure rate targets for each FRC.

Similar tables are available for single point fault, Dual point fault in the part 5 of the standard. Thus consider the failure mode for each and every safety related

Table 3 Failure rate targets corresponding to each failure rate class

FRC	Target value	Remarks
FRC-1	$10^{(-6)}/\text{h}$	ASIL D failure target in Table 2 divided by 100
FRC-2	$10^{(-5)}/\text{h}$	Ten Times FRC-1 value
FRC-3	$10^{(-4)}/\text{hr}$	100 times FRC-1 value
FRC-4	$10^{(-3)}/\text{hr}$	The failure rate corresponding to failure rate class $i > 3$ shall be less than or equal to $10^{(i-1)}$ times failure rate corresponding to FRC-1
FRD-5	$10^{(-2)}/\text{hr}$	

Table 4 Max. failure rate classes for a given DC of the HW part—residual faults

ASIL of the safety goal	Diagnostic Coverage (DC) with respect to residual faults			
	$\geq 99.9 \%$	$\geq 99 \%$	$\geq 90 \%$	$< 90 \%$
D	Failure rate class 4	Failure rate class 3	Failure rate class 4	Failure rate class 4 + dedicated measures
C	Failure rate class 5	Failure rate class 4	Failure rate class 3	Failure rate class 2 + dedicated measures
B	Failure rate class 5	Failure rate class 4	Failure rate class 3	Failure rate class 2

One can refer to 9.4.2.4 of ISO 26262-part 5 for examples of dedicated measures

component in the HW architecture determine whether the particular failure mode is responsible for violating the SG. Following the steps given in Sect. 2.2 (steps 1 through 9) determine the residual failure or single point failure. Comparing the failure rates/residual failure rates with the target values one can determine whether FRC is satisfied or not. This method helps in finding out whether there is any single potential component responsible for violating the safety goal (Table 4).

3 Example

Consider the Hardware Schematic given in Fig. 1. The circuit diagram describes solenoid valve functionality.

4 Description of the Schematic

The circuit has the following components: 12 V battery, 5 V voltage regulator, MCU input sensor circuit, MOSFETs, Induction coil, Freewheel Diode, LED indicators and Resistors. 12 V Battery supplies power to voltage regulator and voltage regulator gives 5 V power to MCU. This in turn gives power to MOSFETs, when the solenoid valve has to be activated based on the signals received from input sensor. The solenoid valve is activated only when both high side and low

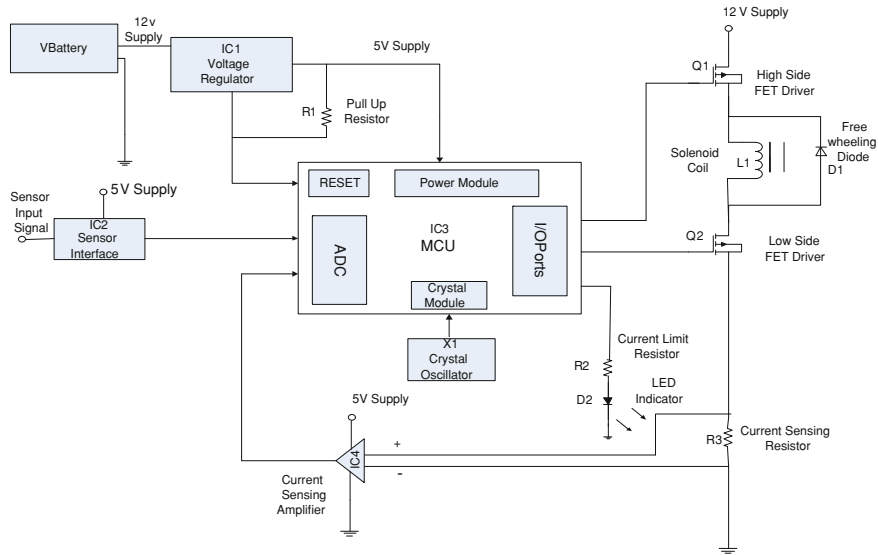


Fig. 1 Circuit diagram for solenoid valve activation

side MosFets are activated. Input voltage to the MCU is very important and thus the 5 V regulator generates RESET signal when the voltage threshold exceeds the limit and the same signal is connected to Micro through R1. Current sensor resistor R4 senses the current flowing through the inductor and this signal is connected to the Micro which in turn enables the LED to show the valve driver activation.

4.1 Safety Goal for the Soleniod Valve Driver

One of the safety goal related to the solenoid valve functionality is to prevent unintended activation of the solenoid valve. Thus we formulate the SG as

To Prevent false activation of Solenoid Valve. This SG has been assigned ASIL C in this example.

4.2 Safety Issues Foreseen

The Safety issues foreseen in this functionality are higher voltage supply to the MCU can burn the processor thus unable to drive the solenoid. The input sensor to provide the right input and thus the input signals to be monitored periodically. Micro processor to be monitored for its memory and the SW processing to be monitored by self test. The functionality of Mosfets to be monitored so that MCU

Table 5 Safety mechanism with the DC coverage

Safety mechanism	SM—Ref.	Description	DC coverage (%)
SM-Sensor	SM1	Test pattern/Sensor monitored outputs	99
SM OP voltage	SM2	Voltage or current control	99
SM current sensor	SM3	Input comparison/voting (1oo2, 2oo3 or better redundancy)	99
SM micro ADC	SM4	Monitored outputs	99
SM micro memory	SM5	Memory monitoring using error-detection-correction codes (EDC)	99
SM micro processing	SM6	Self-test by software: limited number of patterns (one channel)	90
SM micro watchdog	SM7	Watchdog with separate time base and time-window	90

has the information that the valve driver functionality is monitored by the MCU. These are some of the factors which are taken care in the design by various means. The following are the safety mechanisms present in the design. The DC coverage is as per the tables given in Appendix D of ISO-26262-5 (Table 5). Table 6 gives the detailed Single point and latent point failure metric calculations using the Safety mechanisms mentioned below:

The above table gives the detailed analysis of the SPFm and LPFM calculation of the Solenoid valve driver for the Safety goal *To prevent false activation of Solenoid Valve* which is rated as ASIL C in this example. We see that the SPFm and LPFM satisfy the target value set by the standard. The compliance of the SPFm and LPFM tells us that the design is adequate with respect to the safety mechanisms provided for the Safety goal analysed.

The application of the HW metric as described by method 1 in Sect. 2.2 is carried out for the example. The first method requires the FTA done for the safety goal violation. The sample FTA is shown below (Fig. 2):

Each of these boxes (Senosr failure, MCU failure, Coil Driver circuit failure) are analysed further for the causes and the same is evaluated with the FIT rates considered in the previous analysis. It is found that the probability of failure of the top event (which is the safety goal—False activation of Solenoid valve) is approximately equal to 0.3×10^{-7} . We find that this value satisfies the order of magnitude given as target value given in Table 2.

The example is also evaluated by the method 2 as described in Sect. 2.2 where in we need to examine each and every failure mode of a component which would violate the safety goal has a residual failure rate satisfying the FRC specified in Tables 3 and 4. The residual failure for the failure modes violating the safety goal is available in the SPFm/LPFM table above. The residual failures lie in the interval $[7.4 \times 10^{-12}, 6.4 \times 10^{-10}]$ which shows the FRC conditions are satisfied

Table 6 SPFML/PFM calculation for the example

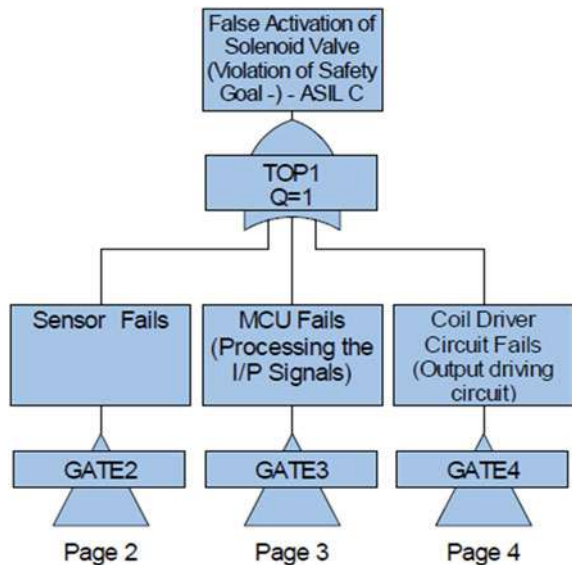
Component name	FIT—failure rate	Safety Related (SR)/Not Safety Related (NSR)	Failure Mode (FM)	Failure distribution (%)	FM has potential to violate safety goal in absence of SM SMechanism?	Safety mechanism(s) allowing prevention of FM violating SG	SM(s) allowing prevention of FM violating SG (%)	Residual FIT/Hour (Single point)	FM has potential to violate SG in combination with an independent failure of another component/item? SGI	Detection mean? safety mechanism(s) allowing prevention of FM being latent?	FM coverage estimated to achieve with the SM (%)	Residual latent failure FIT/Hour (Latent point)
D1	3.23	SR	Short	80	No	No	No	No	No	No	No	0.255
D2	22.05	NSR	Open Short	20 80	No No	No Yes	No Yes	No Yes	SM3	99	99	0.12385
L1	30	SR	Open Short	15 85	No No	No Yes	No Yes	No Yes	SM3	99	99	0.12385
Q1	14.57	SR	Open Short	15 85	No No	No Yes	No Yes	No Yes	SM3	99	99	0.12385
Q2	14.57	SR	Open Over I/P voltage	15 17	No No	No No	No No	No No	No No	No No	No No	0.12385
			Low I/P voltage	17	No	No	No	No				
			O/P Volt. drift to high side	17	No	No	No	No				
IC1	5.0	SR	No voltage	17	No	No	No	No	No	No	No	No
			Oscil.O/P voltage	17	No	No	No	No				
			Pwr spikes on O/P voltage	17	NO	NO	NO	NO				
			No sensor data	14	No	SM1	99	0.036	No	No	No	No
			Signal offset	14	Yes	SM1	99	0.036	No	No	No	No
			Signal drift	14	Yes	SM1	99	0.036	No	No	No	No
			Sensitivity error	14	Yes	SM1	99	0.036	No	No	No	No
			Inverted sign	14	Yes	SM1	99	0.036	No	No	No	No
			Peaks on signal	14	Yes	SM1	99	0.036	No	No	No	No
			Stuck signal	14	Yes	SM1	99	0.036	No	No	No	No
			No Pwr supply to micro	9	No							
			Over voltage	9	Yes	SM2	99	0.064	No	No	No	No
			Under voltage	9	Yes	SM2	99	0.064	No	No	No	No
			Noisy supply	9	Yes	SM2	99	0.064	No	No	No	No

(continued)

Table 6 (continued)

Component name	FIT—failure rate	Safety Related (SR)/Not Safety Related (NSR)	Failure Moe (FM)	Failure distribution (%)	FM has potential to violate safety goal in absence of SM SMechanism?	Safety mechanism(s) allowing prevention of FM violating SG (%)	SM(s) allowing prevention of FM violating SG (%)	Residual FIT/Hour (Single point)	FM has potential to violate SG in combination with another independent failure mechanism? safety means? safety mechanism(s) allowing prevention of another component/item?	Detection means? safety mechanism(s) allowing prevention of FM being latent?	FM coverage estimated to achieve with the SM (%)	Residual FIT/Hour (Latent point)
IC3	70.0	SR	Memory failure	9	Yes	SM5	99	0.064	No			
			ADC failure	9	Yes	SM4	99	0.064	No			
			Processing fail	9	Yes	SM6	90	0.064	No			
			Incorrect reset	9	Yes	SM7	90	0.064	No			
			Incorrect CLK i/p signal	9	Yes	SM7	90	0.064	No			
			Incorrect Reg execution	9	Yes	SM6	90	0.064	No			
			Incorrect read of comparator signals	9	Yes	SM4	99	0.064	No			
IC4	12.0	SR	No Volt to IC4 current	17	No				No			
			Incorrect read current	17	No				No			
			Peaks on signal	17	No				No			
			Signl drift	17	No				No			
			High offset error	17	No				No			
			Offset error	17	No				No			
R1	0.1852	SR	Open	40	Yes	SM7	90	0.0075	No			
			Short	20	No				Yes			
			Drift	40	No				No			
			Open	40	No							
R2	0.1531	NSR	Short	20	No							
			Drift	40	No							
R3	0.2056	SR	Open	80	No							
			Short	10	No							
			Drift	10	No							
X4		SR	Open	60	No							
			Short	40	No							
			Total of residual failures	Single point and latent point					3.149			
			SFPM calculated =	98.11					LPFM calculated = 99.71			
			This is >97 % which is the requirement ASIL C						This is >80 % which is the requirement for ASIL C			

Fig. 2 Sample FTA for the SG false activation of solenoid valve (ASIL-C)



for the components and thus we can conclude that there is no potential component with its failure mode responsible for violating the safety goal.

5 Limitations and Challenges

For the evaluation of the HW metrics and PMHF the major requirement is the failure mechanisms of the components and their failure rate. If it is a standard component the failure rates are picked up from the available standard databases. The consistency of the failure rate between the standard data base plays a critical role. Also the custom made component like ASIC and other Commercial off the Shelf (COTS) components throws a challenge in getting the failure rate as well as the failure mechanisms from the manufacturers. The limitation thrown here is the dependency of the available failure rates, details of the design of the custom made components which are used in the calculation. Thus the confidence one can gain in meeting the target values is a challenge.

6 Summary and Conclusion

The quantitative evaluation of Hardware Metrics as required by ISO 26262-5 has been discussed and the same has been illustrated with an example. The quantitative metrics serves as a good tool in evaluating the safety mechanisms provided in the HW

design against their coverage and residual failures. However testing the safety mechanisms with various vehicle scenarios would add more confidence to the design.

Acknowledgments The author would like to thank Mr. Kirana Anantha Rao and Mr Surendra Reddy of safety team in Mahindra Satyam for the fruitful discussions held during the preparation of this paper.

Reference

1. ISO 26262-2011(E) Road vehicles—functional safety, First edn—2011-11-15

Part IX

Other

Research on Vehicle Transportation Safety Risk Assessment and Control

Jie Yang and Xinpeng Tang

Abstract Introduce the theory of vehicle transportation security risk assessment and control, and apply it in the automobile unit (division)'s vehicle transportation support tasks. The paper is introduced in Fuzzy Analytic Hierarchy Process (FAHP) and Fuzzy Comprehensive Evaluation (FCE) to obtain the comprehensive priority of the risk factors and the risk level of the entire system, and accordingly give the risk control measures, finally verified by an example, indicate the effectiveness and feasibility of this method for the transportation security management forecast and decision making.

Keywords Vehicle transportation safety · Risk assessment · FAHP · FCE · Control measures

1 Introduction

With the increasing of vehicle ownership in China, there are greater hazard in vehicle transport safety, accidents occur frequently. In the army, the transportation support tasks at all levels are heavy, with complex environment, difficult conditions, plus drivers team placed quickly. These lead to more transportation safety risk factors, the safety management is extremely difficult. According to statistics,

F2012-F10-002

J. Yang (✉) · X. Tang
School of Mechanical Science and Engineering, Huazhong University of Science and Technology, Hubei, China

the number of accidents caused by military vehicle transportation is more than 60 % of the total every year. Preventing vehicle accident is the top priority of the military safety works, so it becomes the urgent matter to improve ways and means of vehicle safety management. Along with the time development and the progress of science and technology, new security measures appear more and more, however, not all safety measures lead to increased safety [1]. Risk management is a comprehensive management functions to assess and address the risks faced by an organization [2]. The use of risk assessment and control can predict the risk factors in the transport process comprehensively, accurately grasp of the safety risk level, and formulate target-oriented risk control measures in accordance with the assessment result, thus effectively reduce the occurrence of risk event, improve the security of vehicle transport.

Safety risk assessment and control, means that after taking comprehensive prediction and assessment of system risk, according to the results, take targeted restrictive measures on the system risks and countermeasures to control risks incident [3]. Vehicle transportation safety risk assessment and control, means to combine the risk management and road transport security theory, based on the risk identification, make a qualitative or quantitative assessment of transportation safety risk, and formulate appropriate safety measures with risk control theory. The goal includes: minimizing risk of pre-accidents events, minimizing risk transport accidents, minimizing transport accidents effects, minimizing effects of transport catastrophes [4].

Common strategic methods of risk control includes: risk avoidance, risk reduction, risk transfer and risks acceptance. Technical method includes: remove, replace, mitigate, isolation, process control, protection and discipline [5]. Vehicle transportation safety risk control measures roughly divide into two classes: One is to prevent the accidents, such as the vehicle examines annually, another is to mitigate the injuries after the accident, such as the use of seat belts [6].

Implementing vehicle transportation safety risk assessment and control, Should first set up a specialized organization, make them clear the duties and basic procedures, then according to the actual task, analyse the risk factors, implement risk assessment, formulate corresponding risk control scheme by the assessment results analysis, and perfect in the process of implementing the control scheme, in order to control over the security risks of the whole task process.

This paper selects the assessment methods based on the fuzzy analytic hierarchy process to determine the weight. The method concentrates reflection the respective advantages of analytic hierarchy process and fuzzy comprehensive assessment method, not only overcomes the limitations of the traditional risk assessment methods to quantify the risk factors difficultly, but also solves the problem that there is partial more uncertainty in the process of assessment, and it carries out a clear analysis difficultly when using other methods. Risk control takes target control mode in management control learn, that is a tracking control way, implemented by the operating procedures “setting the overall objective—the decomposition of objective—implementation and achievement of objective—the feedback objective achievement” [7]. Finally, the paper combines with an

Table 1 Military vehicle transportation security risk assessment index system

The first level index layer	The second level index layer
Driver(U_1)	Physical condition(U_{11}), Psychological quality(U_{12}), Professional ethics and attitude discipline(U_{13}), Driving technical experience(U_{14})
Vehicle technology condition(U_2)	Handling stability(U_{21}), Braking performance(U_{22}), Wheels and tires(U_{23}), Light signal(U_{24}), Assembly components reliability(U_{25})
Environmental condition(U_3)	Road conditions(U_{31}), Traffic environment(U_{32}), Weather and climate conditions(U_{33}), Task itself(U_{34}), Time period(U_{35})
Organization and management(U_4)	Timeliness of safety education(U_{41}), Task program establishment and implement(U_{42}), Tool and Spare parts equipped with(U_{43}), Maintenance and safety checks(U_{44}), Medical and maintenance support on the way(U_{45})
Others(U_5)	Other traffic participants' behaviour (U_{51}), Natural geological disasters(U_{52})

example, gives the comprehensive sort of a transportation task safety risk sub-factors relative to the overall goal, comes to the comprehensive security risk rating score of the task, and gives the appropriate risk control scheme.

2 Instruction of the Assessment Method

2.1 Setting up the Assessment Index System

A risk management system is a detailed and systematic process to identify risks and understand the likelihood and potential consequences of [8]. Transportation support tasks taken up by automobile unit (division) responsible, not only include general daily transport, but also include important transport task such as combat exercises, the large-scale persons and goods transport and etc. And the risks are often with the characteristics of the difficult environment, complex condition, quantity of personnel and vehicles participating, so the risk factors involved in the tasks are also very complex. The establishment of a risk index system should fully consider all the risk factors affecting transportation safety, and systematically classify risk factors, screen out the typical indicators which can represent the various components of the transportation security system. The indicators selected should not only follow the law of traffic accidents, but also grasp the key points of the task itself, it is necessary to be able to reflect on a part of the risk factors, but also to guarantee the independence of the indicators.

In accordance with the principles above and the actual military transport safety, automobile unit (division) transportation safety risk assessment index system can be established as the construction below (as shown in Table 1).

Table 2 0.1–0.9 scale meaning table

Scale	Meaning	Explanation
0.5	Equally important	Compared to two factors, both are equally important
0.6	Slightly important	Compared to two factors, the former than the latter slightly
0.7	Obviously important	Compared to two factors, the former than the latter extremely
0.8	Strongly important	Compared to two factors, the former than the latter strongly
0.9	Extremely important	Compared to two factors, the former than the latter is extremely
0.1–0.4	Contrary to the above	Contrary to the above

2.2 Based on FAHP to Determine the Weight

After establishing the index hierarchy, it also determined the affiliation of risk indicators factors. Following from the above hierarchy and expert advice, use the method of constructing fuzzy consistent matrix to obtain the weight of the factors at all indicators layers. Now introduce the concept of the fuzzy consistent matrix [9] firstly:

Definition 1: Set matrix $R = (r_{ij})_{n \times n}$, if meet $0 \leq r_{ij} \leq 1$, ($i, j = 1, 2, \dots, n$), it says R is a fuzzy matrix.

Definition 2: Set fuzzy matrix $R = (r_{ij})_{n \times n}$, if meet $r_{ij} + r_{ji} = 1$, ($i, j = 1, 2, \dots, n$), it says fuzzy matrix R is a fuzzy complementary matrix.

Definition 3: Set fuzzy matrix $R = (r_{ij})_{n \times n}$, if i, j, k meet $r_{ij} = r_{ik} - r_{kj} + 0.5$, it says fuzzy matrix R is a fuzzy consistent matrix.

(1) Structure the fuzzy complementary matrix. Combined with expert advice, by the comparison between each two factors, construct fuzzy complementary matrix $R = (a_{ij})_{n \times n}$. It indicates the relative importance between this layer related factors for relative upper index. Quantitative description for the importance of the each two factors comparison shows such as 0.1–0.9 scale meaning table (as shown in Table 2).

(2) Get fuzzy consistent matrix. Check out whether the fuzzy complementary matrix constructed has the consistency from definition 3, if not, get the fuzzy consistent matrix by the following methods: First sum the fuzzy complementary matrix as per row, written for $r_i = \sum_{k=1}^n a_{ik}$, ($i = 1, 2, \dots, n$), and make the following mathematical transformation $r_{ij} = \frac{r_i - r_j}{2n} + 0.5$, thus established matrix $R = (r_{ij})_{n \times n}$ is fuzzy consistent.

(3) Calculate all levels factors weights. Take the line and normalization method to fuzzy consistent matrix $R = (r_{ij})_{n \times n}$ to calculate all levels factors weights $W = (w_1, w_2, \dots, w_n)$, where the weights meet

$$w_i = \frac{\sum_{i=1}^n r_{ij} - 1 + \frac{n}{2}}{n(n-1)} = , (i = 1, 2, \dots, n), n \text{ is the order of } R.$$

(4) Calculate integrated sort weights of the level factors relative to the target layer. Calculate from target layer to bottom layer, the importance of comparing all the factors in same layer relative to the target layer is used by integrated sort weight. If the sort weights of the factors b_1, b_2, \dots, b_m in the first layer relative to the target layer is $w_{b_1}, w_{b_2}, \dots, w_{b_m}$, and the sort weights of the factors c_1, c_2, \dots, c_n in the second layer relative to the factor b_i is $w_{c_1}, w_{c_2}, \dots, w_{c_n}$. When c_i and b_j are not linked, w_{c_j} is 0. The integrated sort weight of the factor c_i in the second layer relative to the target layer is $W_i^T = \sum_{i=1}^n w_{b_i} \cdot w_{c_j}$, in which $j = 1, 2, \dots, n$. Repeating the process to the bottom, can obtain the security risks integrated sort weight of all sub-factors relative to target layer.

2.3 Fuzzy Comprehensive Evaluation Method [10] to Conduct Comprehensive Assessment

(1) Establish the Factors Set. Accordance with the hierarchy of the index system, establish the security risk factor sets in the first layer $U = \{U_1, U_2, \dots, U_m\}$, divide factors set U into m sub-factor sets $U_i = (U_{i1}, U_{i2}, U_{i3}, \dots, U_{it})$, in which $i = 1, 2, \dots, m; j = 1, 2, \dots, t$.

(2) Establish the Comments Set. In accordance with the degree of influence risk factors, transportation security risk rating is divided into {High, higher, generally, lower}, with $V = (v_1, v_2, v_3, v_4)$ to represent.

(3) Evaluation of Factor Sets in the Second Level

i: Single factor evaluation: Regard sub-factor U_{ij} to the comments set V as a fuzzy mapping, it can determine the fuzzy membership of single sub-factor U_{ij} attach to each comment, thus get the fuzzy evaluation vector of sub-factor U_{ij} on $V: r_{ij} = (r_{ij1}, r_{ij2}, r_{ij3}, r_{ij4})$.

ii: Construct sub-factors set evaluation matrix: According to the fuzzy evaluation vector of the sub-factors U_{ij} , it can determine the fuzzy evaluation mem-

bership degree matrix of $U_i: R_i = (R_{i1}, R_{i2}, \dots, R_{im})^T = \begin{pmatrix} r_{i11} & r_{i12} & r_{i13} & r_{i14} \\ r_{i21} & r_{i22} & r_{i23} & r_{i24} \\ \dots & \dots & \dots & \dots \\ r_{im2} & r_{im2} & r_{im3} & r_{im4} \end{pmatrix}$

iii: Determine the sub-factor weight: Second-level factors weight is represented by $W_i = (w_{i1}, w_{i2}, \dots, w_{ij})$, can be established by fuzzy analytic hierarchy process.

iv: Establishment of a single-level fuzzy evaluation model: According to the fuzzy theory, get the evaluation result of U_i using fuzzy synthetic relationship operations: $C_i = W_i \circ R_i = (c_{i1}, c_{i2}, \dots, c_{i4})$, in which “ \circ ” is fuzzy synthetic relationship operator. Fuzzy synthetic relationship operator generally includes three

types: main factors determine type $M(\wedge, \vee)$ or $M(\vee, \wedge)$, main factors of outstanding $M(\vee, \cdot)$, weighted average type $M(\cdot, +)$ and etc. The operator is generally selected according to the actual situation.

v: Comprehensive Evaluation of the Overall Goal. Regard every factor set U_i as a factor, use C_i as its single factor evaluation, it can obtain a fuzzy mapping from factors set U to V , that is the fuzzy judgment matrix of U relative to V , $R = (C_1, C_2, C_3, \dots, C_s)^T$, combining with the sub-factors weight of $U:W = (w_1, w_2, \dots, w_s)$. Then it could obtain the fuzzy comprehensive evaluation vector of overall goal $C = W \circ R = (c_1, c_2, \dots, c_4)$. This approach can be used for three or even more advanced fuzzy comprehensive evaluation.

3 An Application Example

A border regiment plans to transport winter goods and materials for directly under border station. The time is the whole day on October 7, ** years. Transportation line: Regiment headquarters—X border station. Task: Transport several all kinds of materials 48 tons and 18 rotation officers and soldiers. Dispatched vehicles: Ten (One command vehicle, eight 6 t truck, one passenger car). The other personnel: main drive, co-pilot a total of 12, 4 led cadres. Road conditions: 360 km (National highway about 180 km, Gobi simple road about 100 km, mountain road about 80 km). Environment condition: The winding mountain road, early winter cold climate, accompanied by the mountains of snow, cold, windy weather, complex situation. In order to ensure that the whole transportation task are completed safely and smoothly, league organizations relevant leaders and business personnel to carry out security risk assessment in the assessment index system on the basis of Table 1, and make the risk control scheme according to the assessment results.

3.1 Using FAHP to obtain all Levels of Factors Weights and the Integrated Sort Weight

By the expert survey and FAHP above, calculate the factor weights of each level and its integrated weight on target layer. The result is shown in Table 3.

3.2 Fuzzy Comprehensive Evaluation

Invite 10 experts to collect the survey comments, obtain the fuzzy evaluation matrix of the sub-factors sets on secondary index layer U_i to reviews V . Select

Table 3 Factor weights and its integrated sort weight

First level index layer	Weight w_i	Secondary index layer	Weight w_{ij}	Integrated sort weight	Integrated sort
Driver	0.2125	Physical condition	0.2567	0.0545	4
		Psychological quality	0.2433	0.0517	5
		Professional ethics and attitude discipline	0.2700	0.0574	3
		Driving technical experience	0.2300	0.0489	7
Vehicle technology condition	0.1875	Handling stability	0.2250	0.0422	12
		Braking performance	0.2125	0.0398	15
		Wheels and tires	0.2000	0.0375	16
		Light signal	0.1750	0.0328	19
		Assembly components reliability	0.1875	0.0352	17
Environmental condition	0.2250	Road conditions	0.2150	0.0484	8
		Traffic environment	0.1900	0.0428	10
		Weather and climate conditions	0.2275	0.0512	6
		Task itself	0.1775	0.0399	14
Organization and management	0.2000	Time period	0.1900	0.0428	10
		Timeliness of safety education	0.2125	0.0425	11
		Task program establishment and implement	0.2250	0.0450	9
		Tool and Spare parts equipped with	0.1750	0.0350	18
		Maintenance and safety checks	0.2000	0.0400	13
Others	0.1750	Medical and maintenance support on the way	0.1875	0.0375	16
		Other traffic participants' behaviour	0.5200	0.0910	1
		Natural geological disasters	0.4800	0.0840	2

$M(\cdot, +)$ type, that is weighted average type fuzzy synthetic relationship operator to do evaluate plan of the various sub-factors set on secondary index layer:

$$C_1 = W_1 \circ R_1 = (0.1040, 0.2337, 0.3487, 0.3137),$$

$$C_2 = (0.0438, 0.1100, 0.3313, 0.5150), \quad C_3 = (0.1113, 0.3770, 0.2938, 0.2180), \\ C_4 = (0.2375, 0.2125, 0.2750, 0.2750), \quad C_5 = (0, 0.052, 0.2520, 0.6960).$$

Now we can know the fuzzy comprehensive evaluation matrix of overall goal U is $R = (C_1, C_2, C_3, C_4, C_5)^T$, ultimately the overall risk evaluation result got is $C = W \circ R = (0.1029, 0.2067, 0.3014, 0.3891)$.

Table 4 Safety risk reviews set score table

Goal scoring (A perfect 100 points)	Fuzzy reviews set	Index reviews set
≥ 80	High	
70 – 80	Higher	$V = \{\text{high, higher, general, lower}\}$
60 – 70	General	
40 – 60	Lower	

4 Results Analysis and Risk Control

4.1 Results Analysis

The results above shows that, the proportion of the transportation task comprehensive security risk accounts for the “high”, “high”, “Normal”, “lower” is 10.29, 20.67, 30.14, 38.91 %. Now contrasting to the safety risk reviews set score table (Table 4), take $V = \{90, 80, 65, 50\}$, the risk composite score $k = \sum_{i=1}^4 c_i v_i = 64.8430$, so the security risk level of the transport task is “general”.

Similarly, the risk level of the main risk factors to affect the overall security risk is: “driver” in general, “vehicle technical condition” in lower, “environmental conditions” in general, “organization and management” in general, “others” in lower.

From the sort of individual security risk factors relative to the overall impact, we can see that the risk fact should be caused enough attention of policymakers, such as “Other traffic participants’ behaviour”, “natural geological disasters”, “professional ethics and attitude discipline” and etc.

4.2 Risk Control

According to the integrated sort of factor risk, combining with risk control theory, formulate appropriate risk control measures in order. And make the risk control measures enacted itemized list in chronological order, ultimately form the transportation tasks security risk control report (as shown in Table 5).

5 Conclusions

The use of FAHP to determine the weight of the transport safety risk factors, overcomes the disadvantages of the traditional AHP, and determines importance order of risk factors more comprehensively and reasonably. The example shows

Table 5 transportation tasks security risk control report

Order number	Risk factor	Risk control measure
1	Other traffic participants' behaviour	Strict safety education and driving organization
2	Natural geological disasters	Perfect plan, strengthen investigation, strict driving organization
3	Professional ethics and attitude discipline	Adjust drivers, Strict safety education and management
4	Physical condition	Adjust drivers, health care
5	Psychological quality	Adjust drivers, psychological counselling
6	Weather and climate conditions	Grasp meteorological information anytime, perfect plan roundly, Strengthen safety guidance and driving organization
7	Driving technical experience	Strictly select drivers, strengthen safety guidance
8	Road conditions	Strengthen safety guidance and driving organization
9	Task program establishment and implement	Review and check the scheme seriously, improve anytime
10	Time period	Avoid danger period, arrange rest time scientifically
11	Traffic environment	Strengthen safety guidance and key sections organization
12	Timeliness of safety education	Strengthen implement, tracking guide organization
13	Handling stability	Strengthen specific technical guidance
14	Maintenance and safety checks	Strict accountability, strengthen the work coordination
15	Task itself	Clear responsibility, strengthen the organization and inspection
16	Braking performance	Strengthening technical guidance, take auxiliary measures
17	Medical and maintenance support on the way	Clear responsibility, strengthen coordination
18	Wheels and tires	Strengthening safety guidance, Perfect plan
19	Assembly components reliability	Strictly select and check for vehicles
20	Tool and Spare parts equipped with	Strengthen supervision and check, full consideration
21	Light signal	Strict maintenance and inspection

that, this method used for comprehensive assessment of the vehicle transportation safety risk factors, can determine the priority of the risk factors, and also can obtain the risk level of the whole system combined with the risk factors scores. The assessment results draw closer to the people's way of thinking and the actual qualitative assessment, and the decision-making information provided are more broad and accurate. Consequently provide a better basis for the development of risk control measures. The use of vehicle transportation security risk assessment

and control, could predict the risk factors during the vehicle transport more intuitive and assess accurately, establish the risk control measures more targeted, provide a good method means for army to prevent vehicle accident. This method also applies to the safety management of professional vehicle transportation enterprises.

References

1. Bjarne R (2003) The RISIT research programme—risk and safety in the transport sector. The Research Council of Norway, Oslo
2. Liu X (2006) Risk management . Peking University Press, Beijing
3. Lin B (2007) Safety system engineering. China Labor Social Security Press, Beijing
4. Andrzej S (2010) Defence-in-depth strategy in transport risk management. In: TST 2010, CCIS vol 104, pp 51–58
5. Chen G (2007) Risk engineering. National Defense Industry Press, Beijing
6. Tang H (2006) Risk control and road traffic safety. Chinese Mark (26):84–85
7. Du D (2006) Management control learn. Tsinghua University Press, Beijing
8. WorkCover Corporation (2003) Road freight transport industry occupational health and safety. Work Cover Corporation of South Australia, Adelaide
9. Feng Kong (2008) The fuzzy multiple attribute decision theory, methods and the application. China's Agricultural Science and Technology Press, Beijing
10. Song X (2004) Fuzzy mathematical theory and method. China's mining industry press, Xuzhou

Reliability in Automotive Engineering by Fuzzy Rule-Based FMEA

László Pokorádi and Tímea Fülep

Abstract The Failure Modes and Effects Analysis (FMEA) is a reliability estimation method intended to identify potential failures which have significant consequences affecting the system performance. In a Failure Modes and Effects Analysis the Probability of Failure (PoF), Consequence of Failure (CoF) and Detectability of Failure (DoF) may be determined using engineering judgment and/or based mathematical models, where the result is expressed in a term. The terms qualities and quantities are sometimes used to distinguish these methods. The fuzzy FMEA is a quantitative method of reliability or risk analysis which involves the study of the failure modes can occur in every part of an integrated system. The aim of this paper is to show the possibility of use of fuzzy set theory to estimate failure criticality level theoretically and practically by exemplification of case study of process' risk assessment.

Keywords Reliability analysis · Fuzzy set theory · FMEA

1 Introduction

The Failure Modes and Effects Analysis (FMEA) is a method of reliability analysis intended to identify potential failures which have significant consequences affecting the system performance and/or process consequence. Detail procedure on

F2012-F10-003

L. Pokorádi (✉)
University of Debrecen Debrecen, Hungary

T. Fülep
Széchenyi István University Győr, Hungary

how to carry out FMEA has been documented by IEC Standard Publication 812 [1]. During the analysis, experts discover the potential system failures and determine their efficient causes. The criticality level of causes—the Risk Priority Number (PRN)—determined above are assessed depend on they Probability of Failure (PoF), Consequence of Failure (CoF) and Detectability of Failure (DoF). Fuzzy logic seems to be a powerful mathematical tool capable of combining linguistic and numeric variables in order to estimate the subjectiveness involved in risk analysis and determine whether a risk or criticality level is acceptable or not [2]. Johanyák presented a research-development activity, which aims making Design FMEA more and more efficient with the help of network technologies, artificial intelligence and the modification of the original FMEA methodology [3]. The aim of our paper is to show fuzzy set theory-based Failure Mode and Effect Analysis.

2 Traditional FMEA

The applied techniques to enhance reliability can also call tools to their aid, e.g. fuzzy logic. The most wide-spread and legally prescribed (e.g. UN-ECE Reg. 13, Annex 18, 3.4.4.) two techniques are the FMEA and Fault Tree Analysis (FTA), which are usually combined before their use with systematic, functional techniques, e.g. Reliability Block Diagram. It can be ambivalent how to classify these techniques, because on the one hand it is stated and visible that FTA has proper quantitative nature, but on the other hand it has also qualitative nature, because of e.g. sensitivity analysis. For FMEA there are solutions about integrating failure costs [4] into these forms and to order according their highness. According to this aspect we can call FMEA a quantitative technique as well, however not from the reliability point of view, but the possible integrated expenditure for it.

The literary work of FMEA is quite extensive and in terms of interpretation and explanation the understood is extremely flexible. It can be stated facetiously that ‘So many houses, so many customs’. It refers also to the used terminology of types, the forms, the ranking. There are FMEAs mentioned at a specified functional level (Functional FMEA) and at the component level (Detailed FMEA) [5]. These kinds of differences can give rise to misunderstanding, because it can be comprehended like similarities and compared to the fundamentally accepted types: system, design, process. In these cases negotiations should be accepted; obviously it makes the comprehension impede.

A FMEA is a good means to analyze risks caused by individual failures. The individual risks are weight against each other to recognize priorities. FMEA does not provide a statement on the total failure risk. For the analysis of failure combinations, the fault-tree analysis is more appropriate. The advantages of a FMEA prove that the efforts to prevent failures from the beginning of the development process of a product are justified because the very much higher resulting costs are eliminated later. Advantages are, e.g.:

- prevention of failures in design and development,
- prevention of repeated failures through systematic consideration of expert/failure knowledge on the product or process,
- less subsequent product changes and thus reduction of costs.

The FMEA Risk Priority Number method is intrinsically subjective because guidelines for rating severity, occurrence and detection vary from one institution to another. The same risk priority number can be obtained using a number of different combinations of severity, occurrence and detection factors. The risk priority number does not distinguish among the linguistic variations possible for a risk priority number [6]. The FMEA scales for severity and detection are only qualitative. For instance, a rank 8 severity is not twice as severe as a rank 4. When the severity, detection and occurrence are multiplied together to form the risk priority number, the ratings are treated as if they represent numeric quantities. The calculation erroneously implies that a two-fold increase in one factor (e.g. severity) can be offset by a corresponding decrease of half in another factor [7].

The idea of expressing an RPN as a likelihood value lends itself to perhaps redefining an RPN as a probability value. However, a modification needs to be introduced to ensure that any RPN lies in the range of values between 0 and 1. No confusion is anticipated here, as the analyst can still use values in the range 1–10 for the rankings and the software will simply divide the calculated product by 1,000. Summing the three rankings together has its advantages in that the calculated sum in terms of a percentage give a better understanding of the importance of the RPN. This can be demonstrated by the following special example where the severity rating is very high compared with the occurrence and detection ratings [8].

Suppose that:

- PoF = 1 (1 out of 10)
- CoF = 9 (9 out of 10)
- DoF = 1 (1 out of 10)

Multiplying the rating together gives: $PoF \times CoF \times DF = 1 \times 9 \times 1 = 9$ (9 out of 1,000), 0,9 %, summing the ratings together gives: $PoF + CoF + DF = 1 + 9 + 1 = 11$ (11 out of 30), 37 %.

According to the first calculation the accepted intervention limit is at 10 % (RPN = 100), but this value can also be different per ranking catalogues.

2.1 How Weighting Can Influence RPN Value

Taking into consideration the different opinions during a moderated evaluation meeting deriving from the diverse experience and proficiency regarding the concerned system (subsystem or process) the objectivity can be queried. In order to avoid making compulsory compromises the following solution can be applied to decrease subjectivity. Figure 1 shows the differences between opinions of

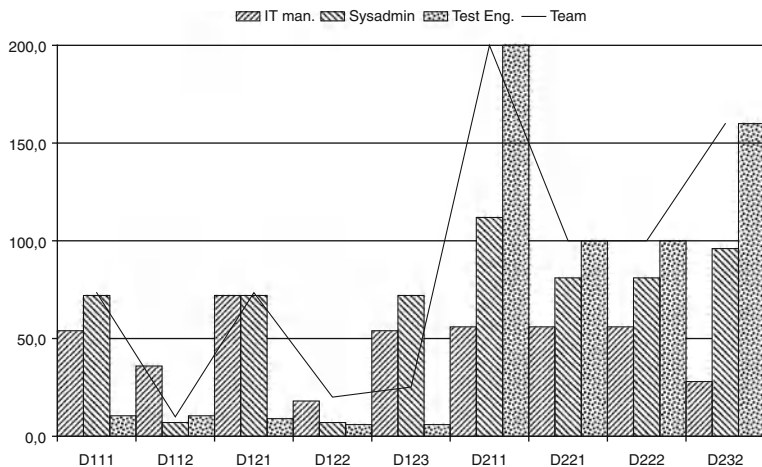


Fig. 1 Results of traditional FMEA

members of work team and compromised result using traditional FMEA, where the DXXX means the specific failure mode.

In the following a more complex method is going to be presented referring the above described question—how weighting can influence the RPN value.

3 The Fuzzy Logic Based Criticality Assessment

To prepare the fuzzy logic-based FMEA firstly the occurrence, severity, detectability and criticality level categories—as linguistic ones—and membership functions of these characteristics should be determined with an eye to characters of analyzed system or process.

The categories and short definitions, which determined by FMEA work team, are shown by Table 1. The Figs. 2, 3, 4 and 5 show membership functions of categories determined above. Figure 6 determines the rule base of investigation, which has 120 logical rules. Next step is to define fuzzy PRN assessment model. A multi-input fuzzy assessment model considers more than one (in our case 3) attributes. The rule base of fuzzy FMEA consists of a collection of IF–THEN rules using AND connections. Each fuzzy rule can be represented as (for example):

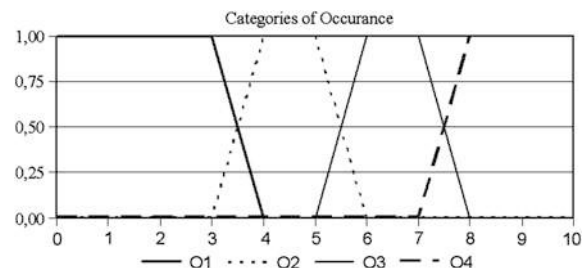
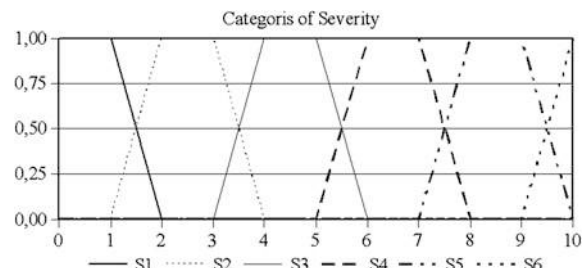
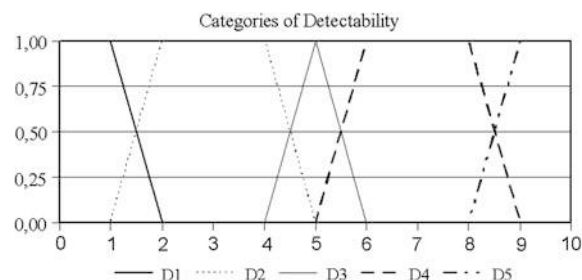
$$\text{IF_}(PoF \text{ is } O1)\text{_AND_}(DoF \text{ is } D1)\text{_AND_}(CoF \text{ is } S1)\text{_THEN_}(PRN \text{ is } C1) \quad (1)$$

Because of the FMEA has three input variables, the rule base can be demonstrated as a Rubik Cube, which has 125 rules (see Fig. 6).

During the analysis, the experts identify the possible failure modes, they occurrence, severity, detectability levels using linguistic categories and scales

Table 1 Categories

Occurrence categories		Criticality level categories	
O1	Yearly or rarely	C1	Low
O2	Few time is a year	C2	Medium
O3	Few time is a month	C3	High
O4	Few time is a week	C4	Extra High
Severity categories		Detectability categories	
S1	Incommodity	D1	IT immediately
S2	Alternative solution	D2	IT later
S3	Brake down in the near future	D3	User immediately
S4	Reduced capacity	D4	User later
S5	Brake down	D5	Later, accidentally
S6	False test result		

Fig. 2 Membership functions of occurrence categories**Fig. 3** Membership functions of severity categories**Fig. 4** Membership functions of detectability categories

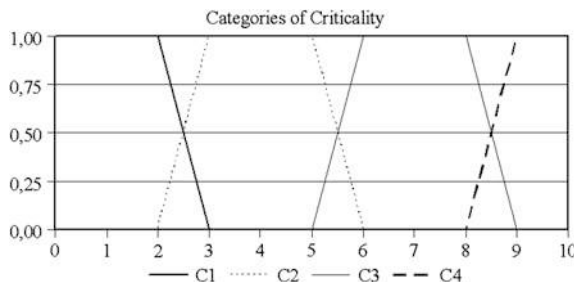


Fig. 5 Membership functions of criticality categories

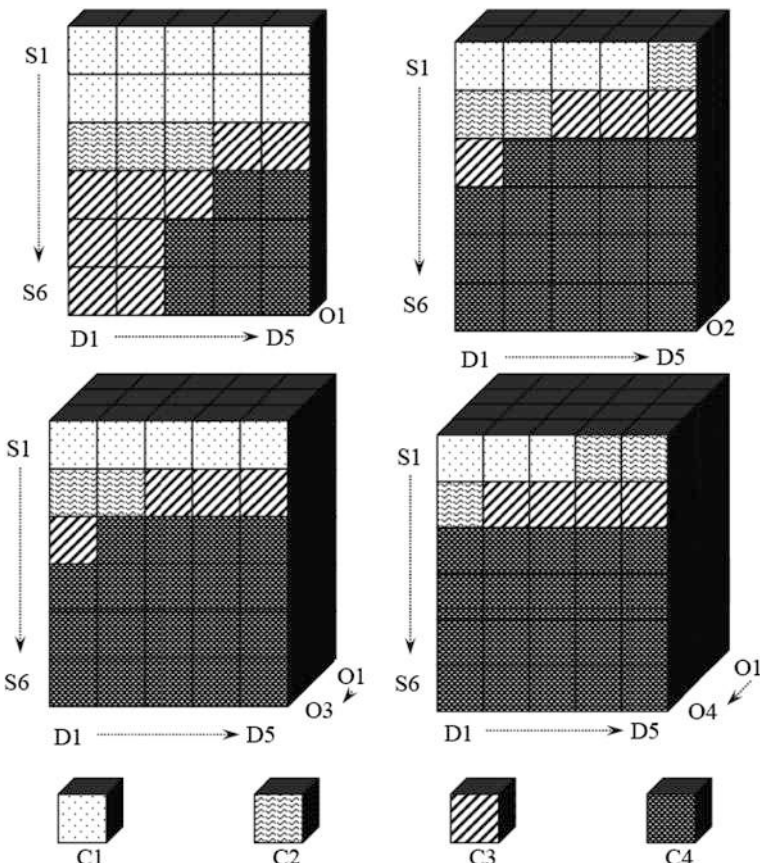


Fig. 6 Fuzzy FMEA rule base

determined above. A fuzzy logic-based criticality level assessment process uses several rules simultaneously. The attribute of set of rules mentioned above is that their solution by classical logic can be different or antinomical at the same time. Practically, this inconsistency can be untied by the fuzzy logic.

Table 2 Results of traditional and fuzzy FMEA

Code	IT man.				Sysadmin				Test Eng.				Tr. team	Fuzzy team
	O	S	D.	RPN	O	S	D	RPN	O	S	D	RPN		
D111	3.0	6.0	3.0	54.0	3.0	4.0	6.0	72.0	3.5	3.0	1.0	10.5	73.5	5.282
D112	2.0	6.0	3.0	36.0	1.0	7.0	1.0	7.0	3.5	3.0	1.0	10.5	10.0	4.000
D121	2.0	4.0	9.0	72.0	3.0	4.0	6.0	72.0	3.0	3.0	1.0	9.0	73.5	2.663
D122	1.0	6.0	3.0	18.0	1.0	7.0	1.0	7.0	2.0	3.0	1.0	6.0	20.0	4.000
D123	3.0	6.0	3.0	54.0	3.0	4.0	6.0	72.0	2.0	3.0	1.0	6.0	25.2	4.000
D211	2.0	4.0	7.0	56.0	4.0	4.0	7.0	112.0	4.0	5.0	10.0	200.0	200.0	8.125
D221	2.0	4.0	7.0	56.0	3.0	3.0	9.0	81.0	4.0	5.0	5.0	100.0	100.0	7.531
D222	2.0	4.0	7.0	56.0	3.0	3.0	9.0	81.0	4.0	5.0	5.0	100.0	100.0	7.531
D232	1.0	4.0	7.0	28.0	3.0	4.0	8.0	96.0	4.0	5.0	8.0	160.0	160.0	7.000

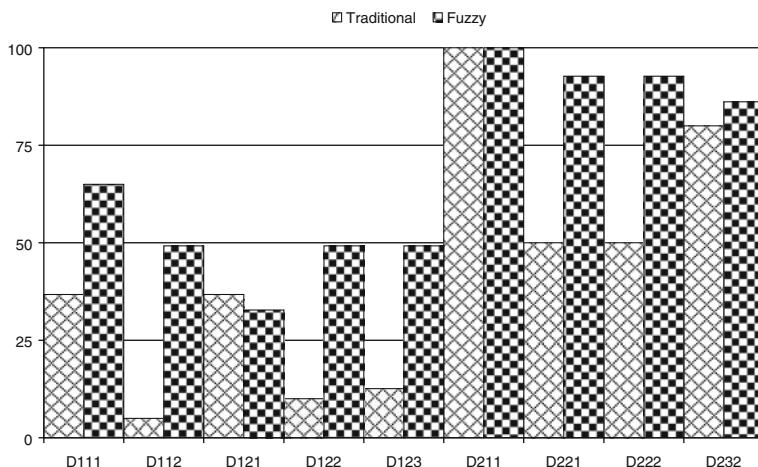
**Fig. 7** Comparison of result traditional and fuzzy FMEA

Table 2 shows results of the investigations mentioned above. Traditional (1–1000) and Fuzzy (1–10) FMEA use different scales. Therefore to compare them their relative values are shown by Fig. 7. The relative values were determined by maximum PRN that in both situation D211's ones.

References

1. IEC (1985) Analysis techniques for system reliability procedure for failure mode and effects analysis (FMEA), IEC Publication 812
2. Pokorádi L (2008) Systems and processes modelling. Campus Kiadó, Debrecen, pp 242. ISBN (in Hungarian)

3. Johanyák ZC (2000) Knowledge-based FMEA in networking environment. *Analele Universităii Eftimie Murgu Resita*, Anul VII, Nr. 2, TOME I, 2000, ISSN 1453-7394, pp 176–179. <http://johanyak.hu>
4. Signor M (2002) The failure-analysis matrix: a kinder, gentler alternative to FMEA for information systems. Proceedings of annual reliability and maintainability symposium, Seattle, pp 173–177
5. Savakoor DS, Bowles JB, Bonnel RD (1993) Combining sneak circuit analysis and failure modes and effects analysis. Proceedings of annual reliability and maintainability symposium, Atlanta, pp 199–205
6. Kara-Zaitri C, Fleming PV (1997) Application of fuzzy inference methods to failure modes effects and criticality analysis (FMECA). In: International conference on safety and reliability, pp 2403–2414
7. Bowles JB (1998) The new SAE FMECA standard. Proceedings of annual reliability and maintainability symposium, Anaheim, pp 48–53
8. Kara-Zaitri C, Keller AZ, Barody I, Fleming PV (1991) An improved FMEA methodology. Proceedings of annual reliability and maintainability symposium, Orlando, pp 248–252

Back Muscle Activity While Operating a Vehicle

Chaoyang Chen, Bo Cheng, Zhengguang Wang, Dawei Chen,
Xin Tao and John M Cavanaugh

Abstract *Research and/or Engineering Questions/Objective* Low Back Disorder (LBD) is common in automobile drivers and prominent in truck drivers. Rate of LBD was found to be 40 % among all truck drivers and 65 % among professional drivers with 15 years behind the wheel. Whole-body vibration (WBV) has repeatedly been identified as a risk factor for LBD. Sitting in awkward postures while exposed to vibration increases the rate of LBD fourfold. However, the injury mechanisms that link vibration to LBD are still not completely understood. The long term purposes of our study are to determine muscle contribution to associated LBD while operating a vehicle. The specific aim of this study was to determine back muscle activity in response to lumbar inclination angles and vibrations from driving on different road surfaces. *Methodology* The Surface Electromyography (sEMG) of latissimus dorsi and lumbar erector spinae muscles were recorded from eight adults (seven male, one female, age from 18–45) using Biopac Data Acquisition System (Model MP30, Biopac Systems Inc, Goleta, CA) and analysed using Acqknowledge software (Ver. 4.2). Two accelerometers (Model TSD109F, Biopac Systems Inc, Goleta, CA) were attached to the driver waist and vehicle floor respectively. sEMG and vibration data was recorded simultaneously under various operating conditions including: sitting with several lumbar inclination angles, engine idling, and driving on smooth, pebble, potholed roads, and freeway. Correlation between sEMG (normalized to individual Maximum Voluntary Contraction (MVC)) and vibration measures (mean, median, peak frequency; Root Mean Square (RMS); and Power (G^2/Hz)) was analyzed. ANOVA, Kruskal-Wallis,

F2012-F10-010

C. Chaoyang (✉) · C. Bo · Z. Wang · D. Chen
Department of Biomedical Engineering, Wayne State University, Detroit, MI, USA

T. Xin · C. J. M
State Key Laboratory of Automotive Safety and Energy, Tsinghua University,
Beijing, China

correlation and regression, and other statistical methods were used to analyse EMG and vibration variables under different operating conditions using SPSS software with $p < 0.05$ considered as a significant level. *Results* A quadratic correlation between normalized sEMG (%MVC) and lumbar inclination angle was found. Each driver had a lumbar inclination angle that elicited only a lowest %MVC. This angle ranked from 0 to 23° (13.14 ± 4.14 , Mean \pm SEM). The inclination angle from the most desirable driving posture was not correlated with the inclination angle with the lowest %MVC (χ^2 test, $p = 0.304$). Driving on potholed road elicited a highest %MVC and highest acceleration power (G^2/Hz) (ANOVA, $p < 0.05$). The highest %MVC was 18 % in potholed road driving. The vibration acceleration power (G^2/Hz) had a linear correlation with %MVC EMG activity (Pearson test, $p < 0.00$). Mean, median, or peak frequency of vibration did not have a linear correlation with EMG Power (V^2/Hz) or RMS (Pearson test, $p > 0.05$). The vibration frequency, RMS, and power of vibration (G^2/Hz) recorded from lumbar region were lower than that recorded from the vehicle floor (Paired t test, $p = 0.000$). *Limitations of this study* The limitation of this study is that the road testing time period was shorter than the realistic driving conditions which have a longer time period. Muscle fatigue or secondary pain over the long driving time period was not determined in this study. *What does the paper offer that is new in the field including in comparison to other work by the authors* Currently, most research uses Root Mean Square (RMS) to measure the magnitude of and intensity of vibration, as well as EMG response. This study demonstrated that magnitude of vibration (G^2/Hz) corresponded to power (V^2/Hz) of EMG better than other EMG measures including RMS and frequency analysis. In addition, various vibration curves under different operating conditions were obtained in this study; these vibration curves are required for input of vibration loading conditions during finite element analysis fatigue analysis. *Conclusions:* The probability for driver to develop muscle fatigue is higher when driving on potholed road because intermittent muscle contractions were more than 10 % MVC under this condition. Sitting posture has effects on muscle activity. Driver's comfort did not show a direct correlation to the lumbar inclination angle that elicited the lowest %MVC. The seat may absorb some of the vibration energy from the vehicle, reducing the intensity of vibration transferred to the human body. In this study, power (G^2/Hz in vibration and V^2/Hz in EMG) was more sensitive and specific for analysis of the magnitude of vibration and corresponding EMGs.

Keywords Back muscle · Electromyography · Vehicle vibration

1 Introduction

Vehicle drivers are exposed to vibratory environments and ergonomically unfavourable working conditions, which can lead to back pain over a time period. Driver vibrates predominantly at frequencies related to the vibration from the

engine and driving on different road surfaces. Vehicle drivers are therefore subjected to vibrations coinciding with the resonant frequencies of their body (4–20 Hz) [1]. Vehicles subject drivers to vibrations over a frequency range that coincides with the resonant frequencies of the body, which enlarges the vibration intensity to the body that may cause body injury. Cab ergonomics is becoming an interesting research area for occupant concerns on safety and health, which can be addressed by physiological and biomechanical analysis.

One of the most important health problems is the onset of Low Back Pain (LBP) due to straining of Erector Spinae (ES) muscle. Low Back Disorder (LBD) is common in automobile drivers and prominent in truck drivers. Rate of LBD was found to be 40 % among all truck drivers and 65 % among professional drivers with 15 years behind the wheel. Whole body vibration [2, 3] and postural factors [4] are the main contributors to the occurrence of LBP. Whole-Body Vibration (WBV) has repeatedly been identified as a risk factor for LBD. Sitting in awkward postures while exposed to vibration increases the rate of LBD fourfold [3].

Studies relating to LBP aspects of vehicle operators or occupants have relied on the basis of questionnaire study. While the results are very relevant, they have not been able to accurately point whether the problem exists entirely due to whole body vibration [2]; or to posture [4, 5] or a combination of both the factors [6]. Whole body vibrations and postures lead to weakening of muscles, which result in higher fatigue rate than compared to a healthy muscle [7–9].

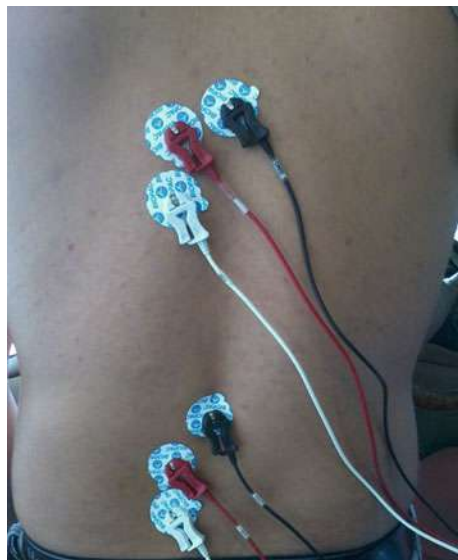
Fatigue is defined as the time-dependent summation of internal and external influences, which adversely affects human performance, irrespective of any subjective awareness either of the influences or of the impairment [2]. Surface electromyography (sEMG) parameters associated with either onset or occurrences of fatigue include EMG signal amplitude, power, mean and median frequencies of the power density spectrum. It has been reported that, during fatigue, there is an increase in the sEMG signal amplitude and power [10], and a decrease (or left shift) in the both mean and median frequencies [6].

However, the injury mechanisms that link vibration to LBD are still not completely understood. The long term purposes of our study are to determine muscle contribution to associated LBD while operating a vehicle. The specific aim of this study was to determine back muscle activity in response to lumbar inclination angles and vibrations from driving on different road surfaces.

2 Materials and Methods

Subjects: Eight adults (seven male, one female, age of 18–45) participated in this study. The average age was 24.88 years (SEM = 3.37 years). None of the selected participants had physical disability or discomfort problem. Experiments were performed using a min-van. All volunteers also read and signed an informed consent before participating.

Fig. 1 Shows the sEMG recording locations on thoracic paraspinal muscle and lumbar erector spinae. Read lead is probe electrode, white lead is reference electrode, the black lead is ground electrode which was placed on the spinal process



EMG data acquisition: Muscles considered for this study were the thoracic paraspinal muscle (2 cm lateral to midpoint of T7 spinal process) and erector spinae (ES) (2 cm lateral to midpoint of L3 spinal process) (Fig. 1).

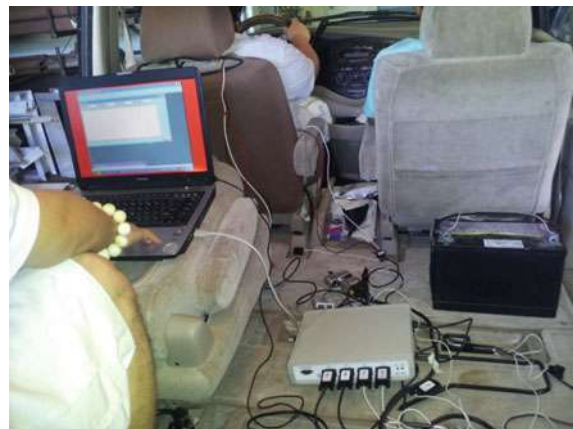
Both these muscle groups are fairly large and easy to identify on test subjects. sEMG signals were recorded at a sampling frequency of 1,000 Hz using BioPac Data Acquisition System (Model MP30, Biopac Systems Inc, Goleta, CA) was used with BSL PRO 3.6.7 software to collect the data and analyzed using Acqknowledge software (Ver. 4.2, Biopac Systems Inc). Two EMG electrodes were attached to the upper-back trapezius and paraspinal muscle (deep to trapezius) and lower-back erector spinae (ES) of the test subject, with two ground EMGs attached to the spinal process.

Vibration data acquisition: One accelerometer (Model TSD109F, Biopac Systems Inc, Goleta, CA) was attached to the waist, with the other accelerometer attached to the floor of the car, respectively. In this study, only vertical vibration (Y-axis) was recorded. Using these four channels, the MP30 collected all the data simultaneously (Fig. 2). The data was analyzed using the AcqKnowledge 4.2 software, where the mean of the EMG data was compared to the subject's maximum voluntary contraction (MVC) EMG data, expressed as a percentage for comparisons between different subjects.

sEMG and vibration data was recorded simultaneously under various operating conditions. Data recorded included: sitting with several lumbar inclination angles, engine idling, and driving on smooth, pebble, potholed roads, and freeway (Fig. 3).

In order to complete all tests in an identical manner, all equipment was stationed inside the same vehicle for the duration of the testing period. The BioPac

Fig. 2 Demonstrates the recording setting in the vehicle



Systems MP30 data collection hardware was used to collect all data, and a laptop running the BSL 3.6.7 software was used to display and save the data (Fig. 2). The MP30 system has four channel connections: Channel one collected lower back sEMG data, Channel two collected upper back sEMG data.

Channel three collect: vibration from 50 g accelerometer attached to the volunteer body, and Channel four collected the vibration data from 50 g accelerometer attached to the vehicle floor.

Tests with inclination angels: Data collection started with a seat angle that was forward past the upright position about 10–20°. The angle taken was the angle of the lumbar spine of the volunteer from the vertical position. The data was collected for ten seconds, and then the seat was repositioned, and the angle of the lumbar spine was changed at five to ten degrees increments.

The last inclination test was “the most comfortable” sitting position, in which the volunteer adjusted the seat to the most desirable position, after which the angle and EMG data was collected during driving on different road surfaces.

Tests on different road surface driving: There were five stages to the driving portion of testing: (1) the first test involved idling the engine for 10 s; (2) the next test involved driving along a smooth road at a speed of 25 mph (3) the third test involved driving across a brick road, which creates a high frequency vibration; (4) the fourth test involved driving through a road with many potholes; (5) then the vehicle test moved to the freeway driving at a speed of 60 mph; (6) the final test was EMG data acquisition of maximum voluntary contraction (MVC) in order to calibrate all previous testing EMG response into % MVC (Fig. 4).

Data analysis: Correlation between sEMG (normalized to individual maximum voluntary contraction (MVC)) and vibration measures (mean, median, peak frequency; root mean square (RMS); and Power (G^2/Hz)) was analyzed. ANOVA, Kruskal-Wallis, correlation and regression, and other statistical methods were used to analyze EMG and vibration variables under different operating conditions using SPSS software with $p < 0.05$ considered as a significant level.



Fig. 3 Demonstrated the different road surface conditions. **a** Smooth surface road **b** High frequency vibration pebble rod **c** Low frequency vibration potholed road **d** Smooth surface freeway



Fig. 4 Shows the how the Maximum Voluntary Contraction (MVC) EMG was recorded. Volunteer extended the spine at the maximum effort during EMG recording

3 Results

It was found in the study that the chosen “most comfortable angle” (MCA) (or the most desirable inclination angle) did not match the inclination angle of lowest EMG activity (%MVC) (Table 1). This inclination angle from the most desirable driving posture was not correlated with the inclination angle with the lowest %MVC (χ^2 test, $p = 0.304$).

Table 1 Correlation between chosen MCA and inclination of lowest % MVC

Personal ID	Chosen MCA	LumL % MVC	Match?	ThorL % MVC	Match?
I	23	23	Yes	23	Yes
A	40	40	No	10	No
2D	30	30	No	15	No
2C	23	23	No	10	No
Z	25	25	No	25	Yes
Y	17	17	No	17	Yes
P	28	28	No	28	Yes
L	45	45	Yes	35	No
Average	28.875	13.125		20.375	

LumL%MVC lumbar inclination of lowest %MVC, *ThorL%MVC* thoracic lowest % MVC. Thoracic inclination angle was measured by setting perpendicular protractor on the surface of the sternum

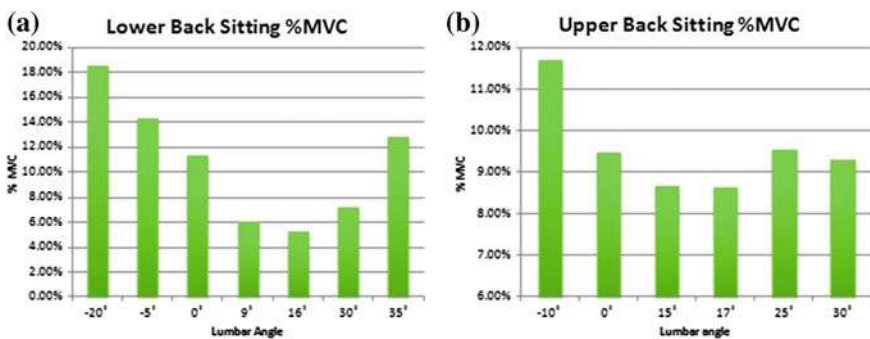


Fig. 5 **a.** shows a quadratic correlation between normalized sEMG (%MVC) and lumbar inclination angle from a volunteer. **b** shows the correlation at the thoracic region. Negative degrees indicate backward inclination while positive degrees indicate forward inclination

A quadratic correlation between normalized sEMG (%MVC) and lumbar inclination angle was found. Each driver had a lumbar inclination angle that elicited only a lowest %MVC. This angle ranked from 0 to 23 degree from different individual. Lumbar inclination angle demonstrated a better quadratic correlation with normalized sEMG (%MVC) (Fig. 5a, b).

For the driving tests, driving on potholed road caused low frequency high magnitude vibration, while driving on pebble road caused high frequency and low magnitude vibration. Driving on potholed road elicited the highest muscle activity (%MVC) in both lower back (Fig. 6a) and upper back (Fig. 6b) muscles compared to other road type driving (ANOVA, $p < 0.01$).

Driving on potholed road also elicited the highest acceleration power (G^2/Hz) compared to other road type driving (ANOVA, $p < 0.05$). The highest %MVC was 18 % found in upper back while driving on the potholed road. The vibration power (G^2/Hz) had a linear correlation with EMG activity (%MVC) (Pearson test, $p < 0.00$). While the mean, median, or peak frequency of vibration did not

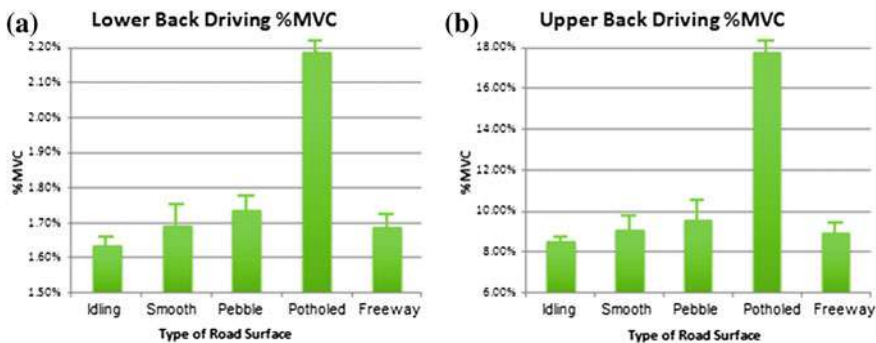


Fig. 6 Lower back (a) and upper back muscle activity (%MVC, AVE \pm SEM) in response to driving on various type roads

demonstrate a linear correlation with EMG Power (V^2/Hz) or root mean square (RMS) (Pearson test, $p > 0.05$). The vibration frequency, RMS, and G^2/Hz recorded from lumbar region were lower than that recorded from the vehicle floor (Paired t test, $p = 0.000$).

4 Discussions

Exposure to vibration has been reported to cause muscle-skeletal pain of the spine [2, 11, 12] with radiological pathologic findings occurring earlier in the spine of individuals exposed to long periods of vibration [12]. A relationship between whole-body vibration (WBV) and low back pain (LBP) has been investigated [13–15]. To the date, the anatomic components that have been considered to cause back pain include the intervertebral disks, paraspinal muscles, ligaments, facet joint capsules, and the adjacent nerve tissues.

Epidemiological studies [11] have revealed an increased incidence of intervertebral disc disorders in professionals exposed to many years of vibration. It has been suggested [16, 17] that WBV increases compression of intervertebral disks. WBV leads to disturbances in the diffusion between intervertebral disks and surrounding tissues, resulting in more rapid disc degeneration [12]. Additionally, it has been suggested that WBV may induce vascular damage within the spine [18] and may affect the ultrastructure of tissues of the dorsal root ganglia [19]. This has been linked to the observed biochemical alteration of pain related neuropeptides and might explain the source of vibration-induced back pain.

Paraspinal muscle may play an important role in back pain generation. This has been found to be more prominent in helicopter pilots. The cyclic response of the erector spinae (ES) due to WBV might lead to muscle fatigue, causing LBP in pilots. Epidemiological studies in helicopter pilots have also suggested that LBP is associated with WBV [2, 4, 20]. The helicopter produces cyclic and constant vibration, hence leading to chronic LBP. The spectra of vibration in some

helicopters show a concentration of energy to provoke a response in the ES muscle. Another hypothesis for LBP is based on the asymmetric posture pilots are required to maintain during vehicle operating. Such asymmetric posture may lead to different intensities in the EMG of right and left ES in sitting with a rotated trunk [2, 9, 20]. All these literatures demonstrate that sitting posture and vibration associated with muscle fatigue and back pain are interesting topics for ergonomic research regarding to driver's comfort and safety.

EMG is an import approach for these ergonomic researches. Vertical sinusoidal vibration at very low frequencies (0.315–5 Hz) led to a synchronized response in the electromyogram (EMG) of the erector spinae (ES) muscles at the lumbar level [18]. The torque increased on the lumbar spine due to vibration between 3 and 10 Hz together with the increase of the EMG response [21]. The effects of 4.5 Hz vibration on the EMG of the ES in three different seated postures (1° , 35° trunk flexion, and 10° trunk extension) were studied and it was found that EMG modulation by vibration was more prominent in cases showing higher baseline EMG before exposure to vibration [22]. sEMG indices have also been developed for the assessment of back muscle weakness, muscle fiber composition and fatigability [23]. The correlations between muscle force and EMG have been studied, in which logarithmic relationship has been identified [24]. Based on the measured EMG activity, the force contraction force can now be evaluated; the data can be used in building mathematic model such as finite element model with muscle bio-fidelity.

The present study collected the preliminary data on muscle activity related to sitting postures and driving on different road conditions. These data will be used for future human mathematical modelling with better bio-fidelity. It also provided muscle responding patterns required for muscle fatigue and pain studies. The EMG data obtained in this study can also be used for muscle fatigue studies to determine the muscle fatigue life under different %MVC. It has been hypothesized that higher muscle activity leads to quicker muscle fatigue. More than 10 % MVC can trigger a fatigue associated with injury and performance [25]. Accordingly, less %MVC should be seen in more comfort sitting posture. However, this study showed that the lowest %MVC lumbar inclination angle did not match the most comfortable sitting lumbar inclination angle. It is possibly that proprioceptive sensory system in other locations such as limbs sensory system, and vestibular sensory system for head position may also play roles in selection of the most comfortable sitting posture.

The probability for driver to develop muscle fatigue is higher when driving on potholed road because intermittent muscle contractions showed the highest %MVC under this road condition. Thoracic paraspinal muscle showed a higher %MVC than lumbar paraspinal muscle. This could be resulted from the upper back muscle might be involved in control the steering wheel during driving on potholed road.

In this study, the power of vibration recorded from the human body was less than that recorded from the vehicle floor indicted that the vibration energy was absorbed partially by the seat, reducing the intensity of vibration transferred to the

human body. Power (G^2/Hz in vibration and V^2/Hz in EMG) was more sensitive and specific for analysis of the magnitude of vibration and corresponding EMG.

Currently, most researchers have used root mean square (RMS) to measure the magnitude and intensity of vibration, and EMG response. To investigate if there is a better measurement that can also better correlate the relationship between vibration and EMG, EMG frequency, RMS and power have been measured in this study. It appeared to be in this study that magnitude of vibration power (G^2/Hz) corresponded to power (V^2/Hz) of EMG better than other measures including RMS and frequency analysis. Hence, power analysis can be an alternative approach for vibration and muscle activity correlation studies in addition to using RMS for correlation studies. In addition, various vibration curves under different operating conditions were obtained in this study; these vibration curves are required for input of vibration loading conditions during finite element analysis fatigue analysis.

Limitations of this study: The limitation of this study is that the road testing time period was shorter than the realistic driving time period which is much longer. Muscle fatigue or secondary pain over the long driving time period was not determined in this study.

Conclusions: The probability for driver to develop muscle fatigue is postulated to be higher when driving on potholed road than other types of roads because intermittent muscle contractions could be more than 10 % MVC under this condition. Sitting posture has effects on muscle activity. Driver's comfort did not show a direct correlation to the lumbar inclination angle that elicited the lowest %MVC. The seat may absorb some of the vibration energy from the vehicle, reducing the intensity of vibration transferred to the human body. In this study, power (G^2/Hz in vibration and V^2/Hz in EMG) was more sensitive and specific for the analysis of the magnitude of vibration and EMGs correlation.

Acknowledgments This research was supported by an Opening Fund of State Key Laboratory of Automotive Safety and Energy of Tsinghua University, Beijing, China (KF11011).

References

1. Mansfield NJ (2005) Impedance methods (apparent mass, driving point mechanical impedance and absorbed power) for assessment of the biomechanical response of the seated person to whole-body vibration. *Ind Health* 43(3):378–389
2. Bongers PM, Hulshof CT, Dijkstra L, Boshuizen HC, Groenhout HJ, Valken E (1990) Back pain and exposure to whole body vibration in helicopter pilots. *Ergonomics* 33(8):1007–1026
3. Lis AM, Black KM, Korn H, Nordin M (2007) Association between sitting and occupational LBP. *European Spine Journal : official publication of the European Spine Society, the European Spinal Deformity Society, and the European Section of the Cervical Spine Research Society* 16(2):283–298
4. Froom P, Hanegbi R, Ribak J, Gross M (1987) Low back pain in the AH-1 Cobra helicopter. *Aviat Space Environ Med* 58(4):315–318
5. Hansen OB, Wagstaff AS (2001) Low back pain in Norwegian helicopter aircrew. *Aviat Space Environ Med* 72(3):161–164

6. de Oliveira CG, Nadal J (2004) Back muscle EMG of helicopter pilots in flight: effects of fatigue, vibration, and posture. *Aviat Space Environ Med* 75(4):317–322
7. de Oliveira CG, Simpson DM, Nadal J (2001) Lumbar back muscle activity of helicopter pilots and whole-body vibration. *J Biomech* 34(10):1309–1315
8. Toren A (2001) Muscle activity and range of motion during active trunk rotation in a sitting posture. *Appl ergonomics* 32(6):583–591
9. Wilder DG, Pope MH (1996) Epidemiological and aetiological aspects of low back pain in vibration environments—an update. *Clin Biomech* 11(2):61–73
10. Bonato P, Roy SH, Knaflitz M, De Luca CJ (2001) Time-frequency parameters of the surface myoelectric signal for assessing muscle fatigue during cyclic dynamic contractions. *IEEE Trans Bio-med Eng* 48(7):745–753
11. Dupuis H (1994) Medical and occupational preconditions for vibration-induced spinal disorders: occupational disease no. 2110 in Germany. *Int Arch Occup Environ Health* 66(5):303–308
12. Dupuis H, Zerlett G (1987) Whole-body vibration and disorders of the spine. *Int Arch Occup Environ Health* 59(4):323–336
13. Tiemessen IJ, Hulshof CT, Frings-Dresen MH (2008) Low back pain in drivers exposed to whole body vibration: analysis of a dose-response pattern. *Occup Environ Med* 65(10):667–675
14. Frymoyer JW, Pope MH, Costanza MC, Rosen JC, Goggin JE, Wilder DG (1980) Epidemiologic studies of low-back pain. *Spine* 5(5):419–423
15. Lings S, Leboeuf-Yde C (2000) Whole-body vibration and low back pain: a systematic, critical review of the epidemiological literature 1992–1999. *Int Arch Occup Environ Health* 73(5):290–297
16. Kasra M, Shirazi-Adl A, Drouin G (1992) Dynamics of human lumbar intervertebral joints. Experimental and finite-element investigations. *Spine* 17(1):93–102
17. Guo LX, Teo EC, Lee KK, Zhang QH (2005) Vibration characteristics of the human spine under axial cyclic loads: effect of frequency and damping. *Spine* 30(6):631–637
18. Seidel H (1988) Myoelectric reactions to ultra-low frequency and low-frequency whole body vibration. *Eur J Appl Physiol* 57(5):558–562
19. McLain RF, Weinstein JN (1994) Effects of whole body vibration on dorsal root ganglion neurons. Changes in neuronal nuclei. *Spine* 19(13):1455–1461
20. Shanahan DF, Reading TE (1984) Helicopter pilot back pain: a preliminary study. *Aviat Space Environ Med* 55(2):117–121
21. Seroussi RE, Wilder DG, Pope MH (1989) Trunk muscle electromyography and whole body vibration. *J Biomech* 22(3):219–229
22. Zimmermann CL, Cook TM, Goel VK (1993) Effects of seated posture on erector spinae EMG activity during whole body vibration. *Ergonomics* 36(6):667–675
23. Lariviere C, Arsenault AB, Gravel D, Gagnon D, Loisel P (2003) Surface electromyography assessment of back muscle intrinsic properties. *Journal of electromyography and kinesiology : official journal of the International Society of Electrophysiological Kinesiology* 13(4): 305–318
24. Ramirez A, Grasa J, Alonso A, Soteras F, Osta R, Munoz MJ, Calvo B (2010) Active response of skeletal muscle: in vivo experimental results and model formulation. *J Theor Biol* 267(4):546–553
25. Sogaard K, Blangsted AK, Jorgensen LV, Madeleine P, Sjogaard G (2003) Evidence of long term muscle fatigue following prolonged intermittent contractions based on mechano- and electromyograms. *Journal of electromyography and kinesiology : official journal of the International Society of Electrophysiological Kinesiology* 13(5):441–450

Development of Lightweight Front Side Member Through Hydroforming Technology

K. J. Sung, D. H. Kim, K. S. Kim and Y. K. Kim

Abstract In order to improve fuel efficiency and to reduce emissions, reduction in vehicle weight is a major concern. Reduction in vehicle weight is a necessity in the automobile industry to improve fuel efficiency and reduce emissions. New technologies, such as hydroforming and hot-press forming, have been applied to high strength steel, contributing to reduction in vehicle weight. Our team, in cooperation with an automobile manufacturer, have developed Body in White (BIW) manufacturing to provide vehicle weight reduction. Based upon this, we have developed a new front side member product. Before being put to use, the new front side member needs to be subjecting to testing. By using a high strength and thin plate, we were able to reduce vehicle weight while improving performance. Hydroforming Technology is popular among advanced automotive companies in Asia, the US and Europe as it enable reduction in vehicle weight, cost reduction, dimension precision, etc. This study investigates a front side member developed through hydroforming technology.

Keywords Hydroforming · Lightweight · High strength material

F2012-F10-017

K. J. Sung (✉) · D. H. Kim · K. S. Kim · Y. K. Kim
Hyundai Hysco R&D Center, 265, Yeompo-dong, Buk-gu, Ulsan, Korea

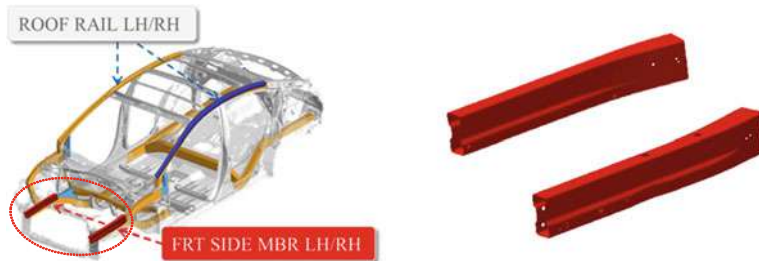


Fig. 1 Front side member

1 Introduction

Hydroforming technology is widely applied to engine compartments, rear axle side members and chassis, etc. We have mass produced many hydroformed products in line with global automotive manufacturing trends and now we are developing new products using new technical methods such as hot-press forming and Tailor Welded Blank (TWB). The goals of this project were to advance automotive hydroformed product development and automotive company competitiveness through actual vehicle test [1–4]. Our object product is front side member in the subcompact segment, and this part is constructed to car Body in White (BIW) and it serves to guarantee passenger safety in the event of a collision (Fig. 1).

2 FEA Simulation

FEA simulations for part and tool were conducted in order to optimize formability and tool reliability.

2.1 Manufacturing Process

We started to design hydroforming model on the basis of the press type model. Above all, we thoroughly examined the overall manufacturing process. Hydroforming technology normally consists of bending, preforming and hydroforming. Especially, preforming tools can address local expansion and wrinkling that occur in the hydroforming process. Hydroforming produces a final product using high pressure water and piercing precise holes. These processes should be optimized before making tool and early part design stage. We omit a bending process because total forming of the product was near straight shape (Fig. 2).

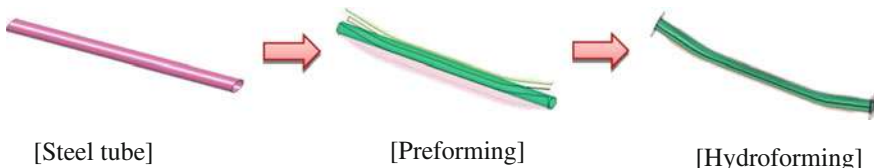


Fig. 2 Hydroforming manufacturing process



Fig. 3 Press type and hydroforming type

2.2 Materials

We mainly used 38 or 45 kgf grade materials for hydroforming. These materials were selected in view of material price and forming properties. We have tried to design modeling, forming analysis and mass production development. Application of high strength materials to new products is a recent area of interest. If automotive parts are applied to high strength materials, it will be possible to achieve reduction in vehicle weight through use of thinner products. Our aim was to produce a lightweight front side member that does not deteriorate vehicle performance, used high strength thin materials (DP590). But we concerned roll mark when it occurred Electric Resistance Welding (ERW) pipe manufacturing because it is applied high strength materials. So we has tested pipe that can be available expansion rate 20 % and roll mark was not appeared for many times. Additional research needs to be conducted before mass production is possible as the pipe we produced is only a prototype.

2.3 Process Design

After developing prototypes, we started to design concept model. Our basic model was welding type as 1.4t outer panel and 2.3t inner panel. If it is designed hydroforming type, it can come true close section member structure without welding line. Furthermore it is expected weight decrease through reduction parts count (Fig. 3).

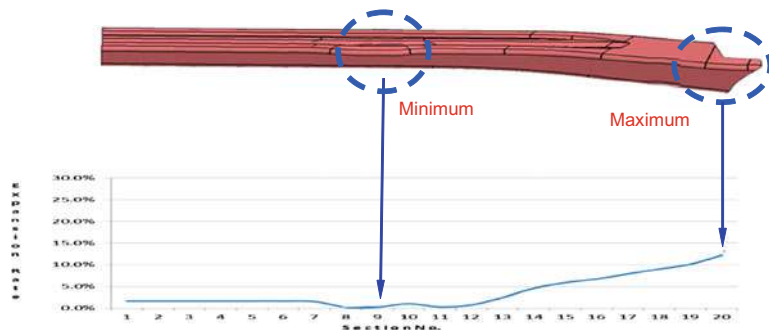


Fig. 4 Hydroforming model expansion rate

When we developed our hydroforming model, we had to consider expansion rate. Hydroformed products get burn when it could make expansion materials to stick into die. Mass-produced hydroformed products developed to date typically exhibit an expansion rate under 5 %. However the parts were manufactured on the basis of good forming property, this part is concerned forming property because high strength materials. In consideration of this, we developed a hydroforming model that exhibits an expansion rate under 2 %, excluding end sections (Fig. 4).

2.4 Forming Analysis

In the following we evaluate forming properties on the basis of former designed model. Although it is difficult to establish conditions that accurately reflect the conditions on an actual manufacturing line, we attempted to design a forming process that closely mirrored actual workplace conditions. When we action forming analysis, many conditions were considered such as forming pressure, feed rate and material properties. There was a few difference property actual and products that was developed until now, we had always offered revision value. It was not easy offering revision value to product because this item was applied to a high strength material. Nevertheless, product forming properties far exceeded expectations. The result of forming analysis was good as wrinkles and cracking did not occur. Also, minimum thick decrease rate was good by 9.5 % level. Overall it will not occur big trouble in the way of product manufacture (Fig. 5).

3 Proto Manufacturing

We have manufactured proto model on the basis of design and forming analysis. Die was made two type as preforming die and hydroforming die. Heat treatment was not applied as it was just die for proto manufacturing use. First, pre-forming

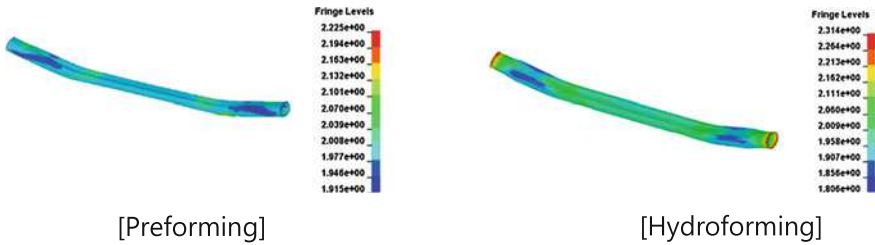


Fig. 5 Forming analysis result

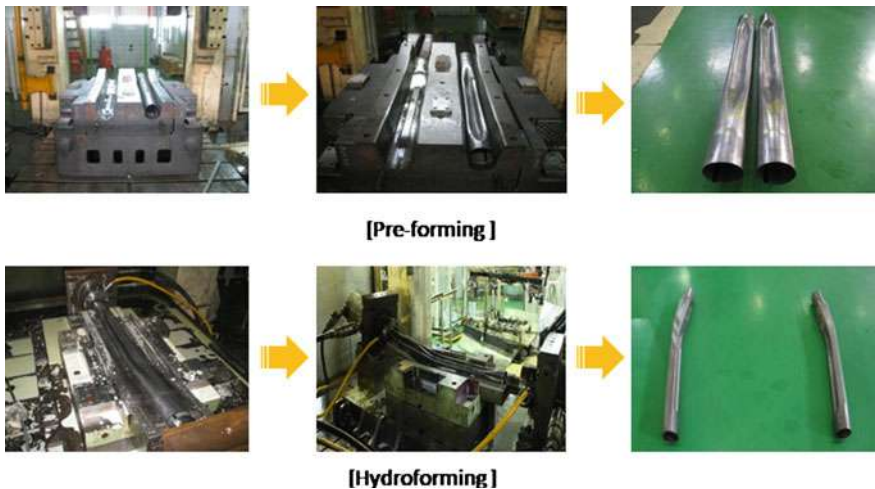


Fig. 6 Product manufacturing

process was started, the result of total product shape was not bad. However, dimples occurred in the bead and a V-shaped groove was present. Accordingly, we redesigned our preforming die to facilitate hydroforming. Especially upper die was primarily revised, after that we performed number hydroforming tests. Finally we developed a hydroforming product that is consistent with exact object shape by two times tryout. This product was transferred assembly company, and it was assembled with other parts. Now carmakers have manufactured to BIW, it will be evaluate to satisfy as fatigue and crash performance (Fig. 6).

4 Conclusion

We have developed a front side member applied high strength thin steel through hydroforming technology. The product we developed has a number of advantages as well be discussed below.

- (1) We have found applying the solution of hydroforming technology and high strength thin steel manufacturing technology about car body parts.
- (2) It will be available contribution at to car lightweight by new technology.
- (3) By applying this product to a car body, we optimized design structure and improved car body twist resistance.

References

1. Kim HY, Lim HT, Suh CH, Lee WS (2003) Numerical modeling of tube hydroforming process considering prebending and preforming effect. In: International workshop on tube hydroforming proceeding of the TUBEHYDRO 2003
2. Kim YS, Won SY, Park JW, Choi SG (2003) Analysis of forming limit in tube hydroforming process. In: International workshop on tube hydroforming proceeding of the TUBEHYDRO 2003
3. Hur JH, Kim YG, Kim HS, Kim DH (2005) The development of hydro-formability improving technology using FEA. In: SME, North America hydroforming conference, 2005, production ID TP06PUB110
4. Kim DH, Kim YG, Kim YJ, Moon MB (2011) Optimization of hydroforming tools and formability for trailing arm of passenger car. TUBEHYDRO2011